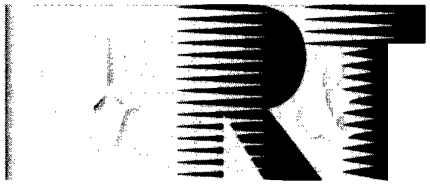
RTO-EN-4
AC/323(AVT)TP/6

RTO-EN-4

NORTH ATLANTIC TREATY ORGANIZATION



RESEARCH AND TECHNOLOGY ORGANIZATION

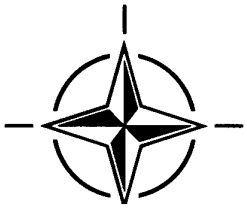
BP 25, 7 RUE ANCELLE, F-92201 NEUILLY-SUR-SEINE CEDEX, FRANCE

RTO EDUCATIONAL NOTES 4

Fluid Dynamics Research on Supersonic Aircraft

(les Travaux de recherche en dynamique des fluides relatifs aux aéronefs supersoniques)

This report is a compilation of the edited proceedings of the Special Course on "Fluid Dynamics Research on Supersonic Aircraft" held at the von Kármán Institute for Fluid Dynamics (VKI) in Rhode-Saint-Genèse, Belgium, 25-29 May 1998.



19990120 080

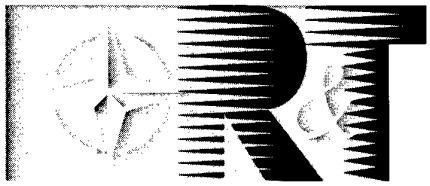
DISTRIBUTION STATEMENT A:
Approved for Public Release -
Distribution Unlimited

Published November 1998

Distribution and Availability on Back Cover

RTO-EN-4
AC/323(AVT)TP/6

NORTH ATLANTIC TREATY ORGANIZATION



RESEARCH AND TECHNOLOGY ORGANIZATION

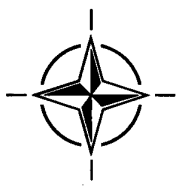
BP 25, 7 RUE ANCELLE, F-92201 NEUILLY-SUR-SEINE CEDEX, FRANCE

RTO EDUCATIONAL NOTES 4

Fluid Dynamics Research on Supersonic Aircraft

(les Travaux de recherche en dynamique des fluides relatifs aux aéronefs supersoniques)

This report is a compilation of the edited proceedings of the Special Course on "Fluid Dynamics Research on Supersonic Aircraft" held at the von Kármán Institute for Fluid Dynamics (VKI) in Rhode-Saint-Genèse, Belgium, 25-29 May 1998.



The Research and Technology Organization (RTO) of NATO

RTO is the single focus in NATO for Defence Research and Technology activities. Its mission is to conduct and promote cooperative research and information exchange. The objective is to support the development and effective use of national defence research and technology and to meet the military needs of the Alliance, to maintain a technological lead, and to provide advice to NATO and national decision makers. The RTO performs its mission with the support of an extensive network of national experts. It also ensures effective coordination with other NATO bodies involved in R&T activities.

RTO reports both to the Military Committee of NATO and to the Conference of National Armament Directors. It comprises a Research and Technology Board (RTB) as the highest level of national representation and the Research and Technology Agency (RTA), a dedicated staff with its headquarters in Neuilly, near Paris, France. In order to facilitate contacts with the military users and other NATO activities, a small part of the RTA staff is located in NATO Headquarters in Brussels. The Brussels staff also coordinates RTO's cooperation with nations in Middle and Eastern Europe, to which RTO attaches particular importance especially as working together in the field of research is one of the more promising areas of initial cooperation.

The total spectrum of R&T activities is covered by 6 Panels, dealing with:

- SAS Studies, Analysis and Simulation
- SCI Systems Concepts and Integration
- SET Sensors and Electronics Technology
- IST Information Systems Technology
- AVT Applied Vehicle Technology
- HFM Human Factors and Medicine

These Panels are made up of national representatives as well as generally recognised 'world class' scientists. The Panels also provide a communication link to military users and other NATO bodies. RTO's scientific and technological work is carried out by Technical Teams, created for specific activities and with a specific duration. Such Technical Teams can organise workshops, symposia, field trials, lecture series and training courses. An important function of these Technical Teams is to ensure the continuity of the expert networks.

RTO builds upon earlier cooperation in defence research and technology as set-up under the Advisory Group for Aerospace Research and Development (AGARD) and the Defence Research Group (DRG). AGARD and the DRG share common roots in that they were both established at the initiative of Dr Theodore von Kármán, a leading aerospace scientist, who early on recognised the importance of scientific support for the Allied Armed Forces. RTO is capitalising on these common roots in order to provide the Alliance and the NATO nations with a strong scientific and technological basis that will guarantee a solid base for the future.

The content of this publication has been reproduced
directly from material supplied by RTO or the authors.



Printed on recycled paper

Published November 1998

Copyright © RTO/NATO 1998
All Rights Reserved

ISBN 92-837-1007-X



Printed by Canada Communication Group Inc.
(A St. Joseph Corporation Company)
45 Sacré-Cœur Blvd., Hull (Québec), Canada K1A 0S7

Fluid Dynamics Research on Supersonic Aircraft

(RTO EN-4)

Executive Summary

This report is a compilation of the edited proceedings of the Special Course on "Fluid Dynamics Research on Supersonic Aircraft" held at the von Kármán Institute for Fluid Dynamics (VKI) in Rhode-Saint-Genèse, Belgium, 25-29 May, 1998.

Considering the growth in air travel demand on long range routes, high speed transportation is now being seriously considered. The evaluation of the current state-of-the-art in high speed aerodynamic research and its coupling with connected fields, namely those related to economical feasibility and environmental aspects, is mandatory to determine the status of the critical technologies which are necessary for the development of high speed transport aircraft. It should be noted that many of the current critical technologies relate both to commercial and military aircraft.

This series of lectures, supported by the RTO Applied Vehicle and Technology Panel and the von Kármán Institute for Fluid Dynamics, reviewed the current major supersonic transport programs of Europe, Japan, Russia and the United States; and included detailed lectures addressing aerodynamic design methods including optimization of L/D, laminar flow control, vortical flow and aerodynamic interference; environmental aspects including sonic boom and emissions; and propulsion integration.

The environmental and economic barriers to high-speed flight remain a challenge. There is some thought that a supersonic corporate jet may be the first supersonic civil aircraft of the next generation to be produced. Military technology and excess production capacity may provide the basis for making such an aircraft affordable.

DTIC QUALITY INSPECTED

Les travaux de recherche en dynamique des fluides relatifs aux aéronefs supersoniques

(RTO EN-4)

Synthèse

Ce rapport est un recueil du compte rendu du cours spécial sur "La recherche en dynamique des fluides pour les aéronefs supersoniques" organisé à l'Institut von Kármán (VKI) à Rhode-Saint-Genèse en Belgique, du 25 au 29 mai 1998.

Vu la croissance de la demande de places sur les lignes long courrier, des efforts considérables sont actuellement consacrés à l'étude du transport à grande vitesse. Par conséquent, il est nécessaire d'évaluer l'état actuel des connaissances dans le domaine de la recherche en aérodynamique supersonique, ainsi que ses liens avec certains domaines connexes, comme la faisabilité économique et l'environnement, afin de déterminer l'état d'avancement des technologies critiques nécessaires au développement des avions de transport à grande vitesse. Il y a lieu de noter que bon nombre de ces technologies déterminantes s'appliquent à la fois aux aéronefs civils et militaires.

Ce cours, présenté sous l'égide conjointe de la Commission RTO des technologies appliquées aux véhicules et l'Institut von Kármán, a fait le point des grands programmes concernant les avions de transport supersoniques actuellement en cours de développement en Europe, au Japon, en Russie et aux États-Unis. Le programme a inclu notamment des présentations très complètes sur les méthodes de conception aérodynamique y compris l'optimisation de la portance/traînée, le contrôle des écoulements laminaires, les écoulements tourbillonnaires et l'interférence aérodynamique, ainsi que l'intégration de la propulsion. En ce qui concerne l'environnement, le bang sonique et les émissions ont également été examinés.

A l'heure actuelle, les défis posés par les barrières économiques et écologiques au vol à grande vitesse restent à relever. A l'avis de certains, le premier aéronef supersonique civil de la prochaine génération à être réalisé pourrait être un jet privé, auquel cas, l'acceptabilité financière d'un tel aéronef pourrait être obtenue par le biais des technologies militaires, associées à un excédent de capacité de production.

Contents

	Page
Executive Summary	iii
Synthèse	iv
Recent Publications of the Former Fluid Dynamics Panel of AGARD	vii
Special Course Staff	ix

	Reference
History and Economics of, and Prospects for, Commercial Supersonic Transport by R. Seebass and J.R. Woodhull	1
Supersonic Aerodynamics: Lift and Drag by R. Seebass and J.R. Woodhull	2
Turbulent Boundary Layer Methods for Supersonic Flow by A.G.T. Cross	3
Complex Experimental Studies of SST **Part I. Aerodynamics of Individual Elements** by A.M. Kharitonov	4
Required Technologies for Supersonic Transport Aircraft by J. Mertens	5
Sonic Boom Minimization by R. Seebass and J.R. Woodhull	6
Complex Experimental Studies of SST **Part II. Aerodynamic Interference of Various Elements** by A.M. Kharitonov	7
Multi Point Design Challenges for Supersonic Transports by J. Mertens	8
Vortex-Plume Interaction Research by P.M. Sforza	9
Status of NASA High-Speed Research Program by A.H. Whitehead, Jr.	10
Geometry Tools for Multidisciplinary Optimization by H. Sobieczky	11
Impact of Environmental Issues on the High-Speed Civil Transport by A.H. Whitehead, Jr.	12

Propulsion System Design for the European Supersonic Civil Transport Aircraft 13
by D. Prat

Application of CFD Methods to Propulsion System Integration in the Future Supersonic Transport Aircraft 14
by D. Prat, T. Surply and D. Gisquet

Overview of NAL's Program Including the Aerodynamic Design of the Scaled Supersonic Experimental Airplane 15
by K. Yoshida

Shock-Vortex Interaction Research 16
by P.M. Sforza

Aerodynamic Research for a Second Generation SST in Japan Including Laminar Flow Control & Low Sonic Boom Design 17
by K. Yoshida

The Aerodynamics of the Future Supersonic Transport Aircraft: Research Activities at ONERA 18
by J.J. Thibert

Aspects of Wing Design for Transonic and Supersonic Combat Aircraft 19
by B. Probert

Recent Publications of the Former Fluid Dynamics Panel of AGARD

AGARDOGRAPHS (AG)

Turbulent Boundary Layers in Subsonic and Supersonic Flow
AGARD AG-335, July 1996

Computational Aerodynamics Based on the Euler Equations
AGARD AG-325, September 1994

Scale Effects on Aircraft and Weapon Aerodynamics
AGARD AG-323 (E), July 1994

Design and Testing of High-Performance Parachutes
AGARD AG-319, November 1991

Experimental Techniques in the Field of Low Density Aerodynamics
AGARD AG-318 (E), April 1991

Techniques Expérimentales Liées à l'Aérodynamique à Basse Densité
AGARD AG-318 (FR), April 1990

A Survey of Measurements and Measuring Techniques in Rapidly Distorted Compressible Turbulent Boundary Layers
AGARD AG-315, May 1989

REPORTS (R)

High Speed Body Motion in Water
AGARD R-827, February 1998

Turbulence in Compressible Flows
AGARD R-819, Special Course Notes, June 1997

Advances in Cryogenic Wind Tunnel Technology
AGARD R-812, Special Course Notes, January 1997

Aerothermodynamics and Propulsion Integration for Hypersonic Vehicles
AGARD R-813, Special Course Notes, October 1996

Parallel Computing in CFD
AGARD R-807, Special Course Notes, October 1995

Optimum Design Methods for Aerodynamics
AGARD R-803, Special Course Notes, November 1994

Missile Aerodynamics
AGARD R-804, Special Course Notes, May 1994

Progress in Transition Modelling
AGARD R-793, Special Course Notes, April 1994

Shock-Wave/Boundary-Layer Interactions in Supersonic and Hypersonic Flows
AGARD R-792, Special Course Notes, August 1993

Unstructured Grid Methods for Advection Dominated Flows
AGARD R-787, Special Course Notes, May 1992

Skin Friction Drag Reduction
AGARD R-786, Special Course Notes, March 1992

Engineering Methods in Aerodynamic Analysis and Design of Aircraft
AGARD R-783, Special Course Notes, January 1992

ADVISORY REPORTS (AR)

A Selection of Test Cases for the Validation of Large-Eddy Simulations of Turbulent Flows
AGARD AR-345, April 1998

Ice Accretion Simulation
AGARD AR-344, Report of WG-20, December 1997

Sonic Nozzles for Mass Flow Measurement and Reference Nozzles for Thrust Verification
AGARD AR-321, Report of WG-19, June 1997

Cooperative Programme on Dynamic Wind Tunnel Experiments for Manoeuvring Aircraft
AGARD AR-305, Report of WG-16, October 1996

Hypersonic Experimental and Computational Capability, Improvement and Validation
AGARD AR-319, Vol. I, Report of WG-18, May 1996

Aerodynamics of 3-D Aircraft Afterbodies
AGARD AR-318, Report of WG-17, September 1995

A Selection of Experimental Test Cases for the Validation of CFD Codes
AGARD AR-303, Vols. I and II, Report of WG-14, August 1994

Quality Assessment for Wind Tunnel Testing
AGARD AR-304, Report of WG-15, July 1994

Air Intakes of High Speed Vehicles
AGARD AR-270, Report of WG-13, September 1991

Appraisal of the Suitability of Turbulence Models in Flow Calculations
AGARD AR-291, Technical Status Review, July 1991

Rotary-Balance Testing for Aircraft Dynamics
AGARD AR-265, Report of WG11, December 1990

Calculation of 3D Separated Turbulent Flows in Boundary Layer Limit
AGARD AR-255, Report of WG10, May 1990

CONFERENCE PROCEEDINGS (CP)

Advanced Aerodynamic Measurement Technology
AGARD CP-601, May 1998

Aerodynamics of Wind Tunnel Circuits and Their Components
AGARD CP-585, June 1997

The Characterization & Modification of Wakes from Lifting Vehicles in Fluids
AGARD CP-584, November 1996

Progress and Challenges in CFD Methods and Algorithms
AGARD CP-578, April 1996

Aerodynamics of Store Integration and Separation
AGARD CP-570, February 1996

Aerodynamics and Aeroacoustics of Rotorcraft
AGARD CP-552, August 1995

Application of Direct and Large Eddy Simulation to Transition and Turbulence
AGARD CP-551, December 1994

Wall Interference, Support Interference, and Flow Field Measurements
AGARD CP-535, July 1994

Computational and Experimental Assessment of Jets in Cross Flow
AGARD CP-534, November 1993

High-Lift System Aerodynamics
AGARD CP-515, September 1993

Theoretical and Experimental Methods in Hypersonic Flows
AGARD CP-514, April 1993

Aerodynamic Engine/Airframe Integration for High Performance Aircraft and Missiles
AGARD CP-498, September 1992

Effects of Adverse Weather on Aerodynamics
AGARD CP-496, December 1991

Manoeuvring Aerodynamics
AGARD CP-497, November 1991

Vortex Flow Aerodynamics
AGARD CP-494, July 1991

Missile Aerodynamics
AGARD CP-493, October 1990

Aerodynamics of Combat Aircraft Controls and of Ground Effects
AGARD CP-465, April 1990

Computational Methods for Aerodynamic Design (Inverse) and Optimization
AGARD CP-463, March 1990

Applications of Mesh Generation to Complex 3-D Configurations
AGARD CP-464, March 1990

Fluid Dynamics of Three-Dimensional Turbulent Shear Flows and Transition
AGARD CP-438, April 1989

Special Course Staff

COURSE DIRECTORS

Professor R. SEEBASS
University of Colorado
Aerospace Engineering Sciences
Campus Box 429
Bourder, CO 80303-0429
United States

Professor J-M. CHARBONNIER
von Kármán Institute for Fluid Dynamics
Chaussée de Waterloo, 72
1640 Rhode-Saint-Genèse
Belgium

LECTURERS

Dr. D. PRAT
Aérospatiale-Aéronautique
Direction Technique
Service A/BTE/EG/Aéro
316, Route de Bayonne
31060 Toulouse Cedex, France

Doctor J.J. THIBERT
ONERA
Directeur Aérodynamique Appliquée
29, Avenue Division Leclerc
B.P. 72
92322 Châtillon Cedex, France

Dr. J. MERTENS
Daimler-Benz Aerospace-Airbus GmbH
D-28183 Bremen, Germany

Professor H. SOBIECZKY
DLR German Aerospace Center
Department SM/SK
Bunsenstrasse, 10
D-37073 Gottingen, Germany

Doctor K. YOSHIDA
Advanced Tech. Aircraft Project Center
National Aerospace Laboratory
6-13-1, Osawa, Mitaka
Tokyo, 181-0015, Japan

Professor A. KHARITONOV
Head of Aerodynamic Division
Institute of Theoretical and
Applied Mechanics SB RAS (ITAM)
Instituskaya 4/1
Novosibirsk, 630090, Russia

Mr. A. CROSS
Aerodynamic Technology Dept
British Aerospace Military Aircraft
and Aerostructures
Brough, East Riding of Yorkshire, HU15 1EQ
United Kingdom

Mr. B. PROBERT
Aerodynamics Dept (W310P)
British Aerospace Military Aircraft
and Aerostructures
Warton Aerodrome
Preston, Lancashire PR4 1AX
United Kingdom

Professor R. SEEBASS
University of Colorado
Aerospace Engineering Sciences
Campus Box 429
Bourder, CO 80303-0429, USA

Professor P. SFORZA
Director Graduate Research
and Engineering Center
University of Florida
1350 N. Poquito Road
Shalimar, FL 32579, USA

Mr. A. WHITEHEAD
Manager of High Speed Research Project
Environmental Impact Team
NASA Langley Research Center
Hampton, VA 23665-5225, USA

PANEL EXECUTIVE

Mr. J.K. MOLLOY

Mail from Europe:
RTA/OTAN
BP 25
7, rue Ancelle
F-92201 Neuilly-sur-Seine Cedex
France

Mail from USA and Canada:
RTA/NATO
Unit PSC 116
APO AE 0977

Tel: 33 (1) 55 61 22 75
Fax: 33 (1) 55 61 22 98

History and Economics of, and Prospects for, Commercial Supersonic Transport

Richard Seebass

John R. Woodhull Professor and Chair,
Aerospace Engineering Sciences
Campus Box 429
University of Colorado
Boulder CO 80303-0429, USA

Introduction

Commercial transport at supersonic speeds has been a reality since 1976. Indeed, it has been a great technical success. The Concorde fleet has flown approximately 350,000 hours, most of them at supersonic speeds, and it has done so with high reliability. The twelve Concordes operating today have accumulated more supersonic fight hours than all of the world's military aircraft [1]. These Concordes will be in service for many years to come [2].

Scheduled Concorde flights are principally London - New York, Paris - New York. Reports on the Concorde indicate that the dozen now in service are well, but not always fully, utilized [3,4]. The Concorde has been a success for the two airlines that operate this small fleet. Does a second generation SST make sense? This paper reviews the past programs and provides the author's own conclusion regarding the prospects for commercial supersonic transport.

The Concorde

The Concorde derives from parallel studies in Britain and in France on supersonic transport, following the introduction of the turbojet powered Comet aircraft. The British had the first meeting of the Supersonic Transport Aircraft Committee (STAC) on November 5, 1956. Some members had privately concluded that the US Douglas DC-8 and Boeing 707 would capture so much of the subsonic market for commercial aircraft that the best options available were to go above the speed of sound or to give up the market [5].

In March 1959 STAC urged the controller of aircraft in the Ministry of Supply to consider the development of a supersonic transport, estimating a market of 125-175 aircraft. The British then approached the French about a joint program, with one goal being their admission to the European Common Market, then dominated by France. A simple, irrevocable, two page treaty between the United Kingdom and the French Republic, was signed on November 29, 1963 [6]. Shortly thereafter de Gaulle vetoed British membership in the Common Market. Later attempts by Britain to cancel their participation in the Concorde were rebuffed by President de Gaulle who correctly insisted they were bound by an irrevocable treaty [7].

In a 17 March 1960 address to the Royal Aeronautical Society, M. B. Morgan, the Scientific Advisor to the Air Ministry, foretold much of what was to become a realty in the Concorde, missing only the problems the sonic boom would cause [8]. Just short of 12 years later, with the pre-production Concorde then flying, Sir Morgan, then Director of the Royal Aircraft Establishment, in the 60th Wilbur and Orville Wright Memorial Lecture recounted the aerodynamic decisions that shaped this remarkable aircraft [9].

Commercial flight operations began in January, 1976, with British Airways (then BOAC) flying between London and Bahrain, and Air France operating between Paris and Rio de Janeiro [10]. In a carefully considered decision, Secretary of Transportation Coleman, on February 4, 1976, permitted limited scheduled flights of the Concorde into the United States, initially for a trial period of 16 months [6]. Two flights per day for each carrier were to be allowed into Kennedy, and one flight per day for each carrier was to be allowed for Dulles. Because the FAA operated Dulles, there was no difficulty in obtaining permission to operate there, and commercial service began at Dulles on May 24, 1976. The New York Port Authority banned such flights in March 1976, but this ban was overturned in court and commercial operations began there on November 27, 1977.

Copyright © 1998 by the author. This article derives from an earlier version that appeared in *New Concepts for High Speed Transport Design*, H. Sobieczky ed., 1997.

Paper presented at the RTO AVT Course on "Fluid Dynamics Research on Supersonic Aircraft", held in Rhode-Saint-Genèse, Belgium, 25-29 May 1998, and published in RTO EN-4.

Important national goals were achieved by the Concorde program for both Britain and France. Perhaps the most important was the development of a successful European community aircraft consortium. It is unknown, and not knowable, whether the joint British-French venture to develop the Concorde was the best or the only route to this end. It was achieved, however, and this must be attributed, at least in part, to the joint venture to develop the Concorde. The French also gained a considerable technological advance in their aircraft. Together, they proved the reliability and safety of public transport at supersonic speeds.

The program's cost, through March 1976, was put at between 1.5 and 2.1 billion in 1976 pounds sterling, or between $3.6 and $5.1 billion in 1977 US dollars (yearly weighted exchange rates) [11].

The round trip fares from Kennedy International Airport to Heathrow Airport on British Airways, or to Charles de Gaulle Airport on Air France, for the summer season, 1998, are $9,239 for London, and $9,401 for Paris. The corresponding subsonic fares for London are: first class, $8,676; business class, $5,344; and full coach,$2,664. And for Paris they are: $7,637; $5,331; and $2,013 respectively. Discount coach fares are $388 for London and $795 for Paris. The two airline average of Concorde fares has increased 32% in the last two years; the average discount coach fare has decreased by 17% from the average 1996 fare. This reflects, presumably, strong demand for the Concorde flights.

We can assume that this fare is covering the direct operating cost of the Concorde, exclusive of the depreciation or amortization of the aircraft itself. At these fares the market for supersonic travel is clearly limited, but no doubt considerably larger than that served by current Concorde operations.

The US SST

The US SST program began in June 1963 when President Kennedy, in a commencement speech at the Air Force Academy, said, "As a testament to our strong faith in the future of air power.... I am announcing today that the United States will commit itself to an important new program in civil aviation.... a plane that will move ahead at a speed faster than Mach 2, more than twice the speed of sound, to all corners of the globe." The day before this speech the president of Pan American World Airlines had made the announcement that Pan Am was taking options on six Concordes. Prior to that Air France and British Airways had ordered eight Concordes each. A few days later President Kennedy followed up his commencement address with a formal message to Congress in which he said, "In no event will the government investment be permitted to exceed $750 million" [7]. Development costs were then estimated to be approximately $1 billion.

This program soon evolved into two competitive aircraft designs, one by Lockheed and the other by Boeing, and two competitive engine designs, one by General Electric and the other by Pratt & Whitney. Boeing and General Electric were the eventual winners of this competition with the Boeing 2707-100, a swing wing, Mach 2.7, 300 passenger aircraft with a presumed range of 3500 nautical miles, weighing 750,000 pounds, an aircraft that was not then - and perhaps is not now - technically realizable. The swing wing provided both airport noise reductions and improved aerodynamic performance at lower speeds. The weight of the mechanism used to pivot the wings, however, resulted in unacceptably low range, or inadequate payload, or both.

The Boeing design evolved to a fixed wing, titanium aircraft, not unlike that proposed by Lockheed. The government's investment, including interest, was to be repaid with the delivery of the 300th aircraft by royalties on aircraft sales.

The US SST Program died in the Senate in May 1971, in part from concerns about noise in the airport environs, in part from concerns about its impact on the stratosphere, in part due to politics, and in part because its economic success seemed far from certain. Today, twenty-seven years later, these remain legitimate concerns.

Air Traffic

The current trends in air traffic are well known [13]. Growth has been positive for most of the past twenty-five years. International travel is growing faster than developed countries' domestic travel, leisure travel is growing faster than business travel, and Asia-Pacific traffic had, until recently, the largest regional growth rate. Air travel has become a commodity in the following sense: 40% of the travel is discount coach travel; the remaining 60% of the travel is comprised of 20% full fare coach, 30% business class and 10% first class. One would be wrong to conclude, however, that full-fare passengers comprise 60% of travel. Due to

frequent flyer upgrades and business and other traveller discounts, only 30% of the passengers on international routes pay full fare.

In 1968 nearly eight million international passengers arrived at or departed from Kennedy International Airport with 97 thousand arrivals and departures. In 1982 over eleven million passengers arrived at or departed from Kennedy. The introduction of wide-body aircraft allowed this travel to be accommodated with under 55 thousand arrivals and departures. In 1993 fifteen million international passengers used Kennedy, requiring 92 thousand arrivals and departures. Once again aircraft arrivals and departures there are close to the airport's capacity.

Expected growth in air traffic cannot be accommodated for long with the world's current airports and aircraft. In developed countries there are few airports that can be added. Thus, it is presumed that some of the increased traffic will be accommodated by larger aircraft. One SST configuration, a wing with passengers inside, flying obliquely, must be large and responds to both the SST and the large aircraft market.

Market

Within a few months of the first flight of the Soviet Union's TU-144 and the French and the British Concorde prototypes (December 31, 1968; March 2, and April 9, 1969), the US SST finalist, the Boeing 2707, had booked 122 options from 26 airlines to purchase aircraft. The Concorde had booked 74 options from 16 airlines. Thus, nearly 200 SSTs were "on order." A year later, in 1970, the FAA predicted 500-800 SSTs would be in operation by 1990. It is now 1998.

Twelve Concordes operate today. These aircraft need only pay their operating costs exclusive of the amortization of their purchase; they were essentially free to the two airlines flying them. What happened? The fares required to pay for their operation deter their use. In 1994 British Airways officials said maintenance costs were seven times those of a 747 and fuel costs per passenger mile were several times those of the 747.

Studies by Boeing and by McDonnell Douglas predict a market for 600 to 1500 SSTs [15, 16]. Mizuno of Japan Aircraft Development predicted a market for 600 Mach 2.5 SSTs with a 5500 nautical mile range, and estimated perhaps a 50% increase in this market derived from its stimulation by the travel time saved [17]. The distinguished airline economist R. E. G. Davies, on the other hand, found it to be between 9 and 36 aircraft, depending on how optimistic one is [18]. The enormous differences among these studies stems from what one projects for the fare required to cover the aircraft's total operating costs. It takes a long time to sell one thousand aircraft. The first Boeing 747 began commercial flights in 1970; twenty-four years later one thousand 747s had been delivered.

The challenge is to design, build, certify and operate an SST at marginally increased fares while providing the airlines a return on investment comparable to a similar investment in subsonic aircraft. The marginal increase in fares, however, depends upon many factors, including fuel prices.

Marginally increased fares - what does that mean? Assume such transport effectively saves the traveler some fraction of a day, or at most, a whole day. Whatever that traveler's expenses would be for that day, or, correspondingly, whatever their income might be for that day, provides a reliable guide as to what they would be willing to pay to save a fraction of a day of business travel, or have as extra time for their vacation. This intuitive judgment agrees with studies which predict little falloff in ticket sales for a 10% surcharge [16,17].

As noted earlier, non-discount passengers comprise 30% of the international market. To secure a significant fraction of this market, most argue, an SST will need to provide three-class service. Current Boeing studies reflect this, and show an SST with about 9% of the passengers in first class, 19% in business class, and 72% in economy. Can an SST succeed if it fills empty seats with discount coach passengers? Can it succeed if it does not? The Concorde provides only one class of service. The flight I was on in May 1998 from New York to London was 80% full; the earlier flight that day was sold out.

Technology has progressed steadily since the Concorde was conceived. But the Concorde was decades ahead of its time and today, nearly 40 years later, we cannot do significantly better than the Concorde [1]. Reduced energy efficiency, the sonic bang, engine emissions, and airport noise remain deterrents to the economic success and acceptability of an SST. Let me now turn to the environmental barriers facing a future SST.

Energy Consumption

The fuel consumed per passenger mile by SSTs of traditional design is several times that of subsonic transports. This derives in part from the addition of supersonic wave drag. Wave drag due to lift is inescapable except for an infinitely long swept wing, best approximated by the way, by an oblique wing. Volume can be moved through the air supersonically with no wave drag, but at considerable expense in skin friction drag. So it, too, entails a supersonic drag penalty. High speeds require high wing sweep, reducing the span and increasing induced drag. This increase in drag for a given lift more than offsets the improvement in propulsive efficiency with speed and results in increased fuel consumption.

Sixty countries have ratified a treaty that commits them to better manage their generation of greenhouse gases [19]. Developed countries are to provide plans by the end of this century that show how they will return to 1990 levels of greenhouse gas generation. But as Secretary of Transportation Coleman said in his decision to let the Concorde operate: "It would border on hypocrisy to choose the Concorde as the place to set an example... (for energy efficiency) while ignoring the inefficiency of private jets, cabin cruisers, or an assortment of energy profligates of American manufacture" [6].

The Concorde achieves 17 seat miles per gallon and, at 67% load factor, is equivalent to a car achieving 12 miles per gallon with only the driver. But the Concorde's passengers are going more than twenty times as fast and following nearly a straight line to their destination. A future SST should not and will not be rejected because of energy considerations. However, its economics are more sensitive to fuel costs than its subsonic counterparts and these are not only variable, but fuels may eventually be taxed for their carbon content.

Sonic Boom

Just as wave drag due to lift is inescapable so is the sonic bang. Adolf Busemann liked to illustrate this by depicting the conical shock wave system and its reflection from the ground as the crowbar that supported the weight of the aircraft [20]. In the US we call the sonic "bang" the sonic "boom." The "bang" in the sonic boom derives from the abrupt pressure increases through the two, and sometimes more, shock waves emanating from a supersonic aircraft. We call the integral of the positive phase of the pressure with respect to time the "impulse." The bang is directly related to the outdoor annoyance of animals and humans; both the bang and the impulse govern structural response and indoor annoyance.

The increasing acoustic impedance (i.e., the product of the density and the sound speed) below the aircraft in a real atmosphere freezes the shape of the pressure signature before it reaches the ground. In the approximation of an isothermal atmosphere this occurs in $\pi/2$ atmospheric scale heights, or at about 40,000 feet. This knowledge set me and my colleague Al George to tackle the minimization of various parameters of the sonic boom signature, including its bang and its boom, or any weighted average you might use of the parameters. Indeed, for the cruise characteristics of the proposed Mach 2.7 Boeing 2707 at 60,000 feet lifting 600,000 pounds, an aircraft 528 feet long need not have a sonic bang at all, i.e., the pressure field below the aircraft need not steepen into shock waves [21]. But as we noted then, reducing or eliminating the sonic boom increased the impulse, or total pressure loading, for obvious reasons: the bang part of the boom, that is, the shock waves, dissipates the energy in the signature. Consequently, reducing or eliminating the shock waves makes the impulse worse, increasing indoor annoyance.

Very considerable studies by the NASA over the past decade have explored whether or not such shaping of the sonic boom signature would lead to an acceptable sonic boom. The NASA's conclusion reinforces ours of over two decades ago: commercial transport-size aircraft cannot be reshaped to have an acceptable sonic boom. Very small supersonic aircraft, such as a corporate supersonic transport, may well have an acceptable, indeed nearly inaudible, sonic boom. This would stem not only from their size and design, but also from the thickening of their very weak shock waves by vibrational relaxation.

Commercial supersonic transports will be constrained to subsonic operation over populated areas, and perhaps to supersonic operation over the oceans alone. For aircraft traveling less than the speed of sound in sea water, this is simply a travelling source of acoustic radiation. Commercial transport at supersonic speeds over the oceans, and perhaps over unpopulated areas, is likely to continue to be acceptable. Flights over areas with significant wildlife may not be allowed. Through

constraints on aircraft routes we can avoid the problems caused by sonic booms, but in doing so we reduce the market for a second generation SST.

Atmospheric Impact

Whenever we burn hydrocarbon fuels using air, we impact the atmosphere and, in some cases, the local air quality. Whatever fuel we burn using air will produce oxides of nitrogen. A concern during the late 1960s was the effect of water vapor from SST engine exhausts on stratospheric ozone levels. It was soon realized, however, that the oxides of nitrogen were much more important [22]. This led the Department of Transportation, in 1972, to launch the Climatic Impact Assessment Program. This monumental and highly regarded 7200 page study, comprising the work of over 500 individuals, concluded that a limited fleet of supersonic transports, such as the 30 Concordes and TU-144s then envisioned, posed an insignificant threat to the atmosphere. This study also aided the extraordinary discovery of the reduction of atmospheric ozone by CFC refrigerants (Freon 11 and 12), culminating in the Montreal Protocol (1987) which will lead to the eventual elimination of these refrigerants.

The oxides of nitrogen catalytically destroy ozone above about 42,500 feet at mid-latitudes. Aircraft emissions are the major unnatural source of these oxides in the stratosphere. They are also an important source of them in the upper troposphere, at least at mid-latitudes in the northern hemisphere [23]. Thus it appears that SSTs in the stratosphere may reduce our protection from ultraviolet radiation by ozone. The calculated ozone column change due to the injection of the amount of NO_x expected from a full fleet of SSTs was about -12% in 1975. New knowledge changed this to +3% in 1979. Since that time, increasing knowledge provided a result of -10% in 1988, about double the -5% predicted ozone depletion if CFC releases remained at their 1974 rate [24]. So we have yet to determine what their impact might be. Recent results show NO_x to be less significant than was once thought, but raise the issue of the effects of engine emissions on stratospheric aerosol surface area. This could also play a role in depleting stratospheric ozone [25].

Airport Noise

Remarkable advances have been made in propulsion since jet engines were introduced. Over the past 25 years there has been about a 20% reduction in the amount of fuel required to produce a unit of thrust [26]. Because much of this gain has come from higher bypass ratios, takeoff noise levels have fallen in some cases below those required by current noise regulations. Current SST engine concepts, without augmented suppression systems, are probably 15-20 decibels (equivalent perceived noise decibels) above these standards. Recent NASA data indicates that the required noise suppression adds about 6500 pounds per engine, which for four engines is equivalent to about 90 passengers for a 300 passenger HSCT. At the moment there are sound ideas, but no proven technologies, on how to accomplish this noise reduction with acceptable weight increases. Unlike the sonic boom, however, we are not up against a fundamental momentum balance. A breakthrough is possible. Given that subsonic transport noise levels continue to fall, and the near certainty that conventional supersonic transports will operate only from selected coastal cities, current noise regulations need to be examined to see what airport noise levels might be acceptable from a moderate size fleet of supersonic aircraft.

The Prospects

The development of a supersonic transport that can be operated at a profit by the airlines, and sold in sufficient numbers for the airframe and engine manufacturers to realize a profit as well, remains a challenge. The US and European supersonic research programs involve the companies that profit from the sale of their subsonic jets. It would take some bold competitive vision, not unlike that which led to the Concorde, for a supersonic transport production program to emerge from these studies.

For unconventional configurations the technical and risk barriers are very high. It appears that an oblique flying wing could provide a Mach 1.4 -1.6 transport that operates with no surcharge over future subsonic transports and compete with them over land as well [27]. This could also be quite a large aircraft [28]. But without further research, considerable experimentation, and flight tests, this remains a conjecture. Such an aircraft would also require rethinking of selected aviation regulations and perhaps even some minor reconfiguration of airports. Both were required with the introduction of the Boeing 747.

A conventional configuration, operating at Mach 1.8 - 2.0, benefits from high productivity and substantially reduced travel times. Because of past and current government research programs, including that which led to the Concorde, the needed

research is largely done and the technology mature. Consequently, the development costs of such an aircraft appear to be quite reasonable. As a fleet, its contribution to the acoustic environment in and around selected airports may be small enough to deserve continued regulatory relief.

A small, corporate, supersonic transport appears to have a significant market and, if small enough, might be certifiable for supersonic operation over most land areas. Military technology and excess production capacity provide the basis for making such an aircraft affordable. It may be a long time before we can fly twice current speeds at affordable fares. And we may even have to fly obliquely to do so. Long before this happens, some will have travelled at Concorde speeds in corporate supersonic transports.

References

[1] Mertens, J., "Son of Concorde, a Technology Challenge," *New Concepts in High Speed Transport Design*, H. Sobieczky, ed., pp. 31-52, Springer, 1997.

[2] "Concorde Set to Fly into Next Century," *Aviation Week*, February 12, 1996, p. 39.

[3] Quintanilla, C., "Unsold Seats Sully Concorde's Snooty Image," *Wall Street Journal*, February 23, 1996, p. B1.

[4] Shifrin, C. A., and Sparco, P., "Air France Contemplates Additional Concorde Flights," *Aviation Week & Space Technology*, January 5, 1998, p. 38.

[5] Costello, J., and Hughes, T., *The Concorde Conspiracy*, New York: Charles Scribner, 1976, 302 pp.

[6] Horwitch, M., *Clipped Wings*, Cambridge Massachusetts: The Net Press, 1982, 472 pp.

[7] Heppenheimer, T. A., *Turbulent Skies*, John Wiley and Sons, 1995, 389 pp.

[8] Morgan, M. B., "Supersonic Aircraft - Promise and Problems," *J. Royal Aeronautical Society*, Vol. 64, No. 494, pp. 315-334, 1960.

[9] Morgan, Sir M., "A New Shape in the Sky," *Aeronautical J.*, pp. 1-18, January 1972.

[10] Orlebar, C., *The Concorde Story*, London: Temple Press, 1986, 144 pp.

[11] Henderson, P. D., "Two British Errors: Their Probable Size and Some Possible Lessons," *Oxford Economic Papers*, pp. 160-205, 1977.

[12] Dwiggins, D., *The SST: Here It Comes, Ready or Not*, Doubleday: New York, 1968, 249 pp.

[13] *International Aviation, Trends and Issues*, Report 86, Bureau of Transport and Communications Economics, Australian Government Publishing Service, 1994.

[14] Grey, J., "The New Orient Express," *Discover*, January 1986, pp. 73-81.

[15] *High-Speed Civil Transport Study*, Boeing Commercial Airplanes, NASA CR 4233, 1989.

[16] *Study of High-Speed Civil Transports*, Douglas Aircraft Company, NASA CR 4236, 1990.

[17] Mizuno, H. "Operations and Market," *High Speed Commercial Flight*, H. Loomis ed., pp. 83-97, Columbus: Battelle Press, 1989.

[18] Davies, R. E. G., "The Supersonic Unmarket," *Airways*, pp. 41-46, September/October 1995.

[19] "Turning up the Heat," *The Economist*, March 19, 1994, p. 15.

[20] Busemann, A., "The Relationship between Minimizing Drag and Noise at Supersonic Speeds," *High Speed Aeronautics*, Brooklyn: Polytechnic Institute of Brooklyn, 1955.

[21] Seebass, A. R., and George, A. R., "Sonic Boom Minimization," *J. Acoustical Society*, Vol. 51, No. 2, 1972, pp. 686-694.

[22] Johnston, H., "Reduction of Stratospheric Ozone by Nitrogen Oxide Catalysis from Supersonic Transport Exhaust," *Science*, 6 August 1971, pp. 517-522.

[23] Enhalt, D. H., Rohrer, F., and Wahner, A., "Sources and Distribution of NO_x in the Upper Troposphere at Northern Mid-Latitudes," *J. Geophysical Research*, Vol. 97, No. D4, March 20, 1992, pp. 3725-3737.

[24] Johnston, H. S., Prather, M. J., and Watson, R. T., "The Atmospheric Effects of Stratospheric Aircraft: A Topical Review," NASA Reference Publication, 1250, January 1991.

[25] Fahey, D. W., et al., "Emission Measurements of the Concorde Supersonic Aircraft in the Lower Stratosphere," *Science*, Vol. 270, October 6, 1995, pp. 70-74.

[26] Koff, B. L., "Spanning the Globe with Jet Propulsion," William Littlewood Memorial Lecture, May 1991, AIAA Paper No. 2987.

[27] Van der Velden, A., "The Oblique Flying Wing Transport," *New Concepts in High Speed Transport Design*, H. Sobieczky, ed., pp. 291-316, Springer, 1997.

[28] Li, P., Seebass, R., and Sobieczky, H., "The Oblique Flying Wing as the New Large Aircraft," *Proceedings, 20th International Council of the Aeronautical Sciences Congress*, 96.4.4.2, 1996.

Supersonic Aerodynamics: Lift and Drag

Richard Seebass

John R. Woodhull Professor and Chair,
Aerospace Engineering Sciences
Campus Box 429
University of Colorado
Boulder CO 80303-0429, USA

Introduction

We briefly review here the fundamentals of generating lift, and what this costs us in inviscid drag at supersonic speeds in the context of the optimum aerodynamic design. The supersonic area rule tells us how to determine the wave drag and this leads to the minimum possible inviscid drag for a supersonic aircraft. We understand from this, then, the trade-off between induced drag and wave drag due to lift. Finally, viscous effects are considered briefly. These determine the altitude at which the aircraft will fly and this sets its C_L and thereby its aerodynamic performance.

Lift and Drag

If we consider a flat plate airfoil, at angle of attack, α, in a flow of subsonic Mach number M, with $\beta^2 = |M^2 - 1|$, then its lift is

$$c_l = 2\pi\alpha/\beta.$$

Since the pressure must be normal to this flat plate one would expect a component of drag with $c_d = \alpha c_l$. And yet we know that in two-dimensional subsonic flow the inviscid drag is zero. How can this be? If we consider the leading edge of the flat plate to be a small circle of radius ε, then we may using conformal mapping to compute the force on this circle and the flat plate. If we then let $\varepsilon \to 0$, the result is, as we know, that the leading edge thrust precisely offsets the drag due to the plate's inclination.

So we escape drag due to lift in two-dimensional subsonic flows. But wings must be finite in span, so we next consider this effect. The wing's lift must be distributed elliptically along its span to minimize the drag that derives from the axial momentum lost to the swirling motion of the wing tip vortices. This itself derives from the pressure difference between the lower and upper surface. This we call the induced drag:

$$D_{induced} = \frac{L^2}{\pi q s^2}.$$

Here L is the lift, distributed elliptically, s is the wing span, and q the dynamic pressure.

At supersonic speeds the same flat plate airfoil gives a lift coefficient of

$$c_l = 4\alpha/\beta.$$

In this case there is no possibility of leading edge suction. The pressure coefficient is uniform and of equal magnitude, but opposite sign, on each side of the plate. So we must accept the resulting drag of αc_l that drives from the waves this airfoil sends to infinity:

$$D_{wave} = \beta L^2/4,$$

but we now have no induced drag.

Busemann,[1,2] and later Jones,[3,4] were the first to point out that, for supersonic flow over an infinite swept wing, it is the normal velocity component that matters. Thus infinite yawed wings with their leading edges swept sufficiently behind the Mach cone (subsonic leading edges) can avoid this wave drag. Again, the tilt of the lift vector is overcome by leading edge suction. For a finite wing not all of the theoretically available suction can be realized. How much can be realized depends on, among other variables such as sweep and leading edge radius, the Reynolds number. See Carlson[5] for a recent review of this subject.

Of course we cannot have infinite wings in supersonic flow either and, consequently, with subsonic leading edges we will have induced drag and wave drag. Sweeping a single wing is more advantageous than considering the wing to have two halves, both of which are swept back or swept forward. As R. T.

Copyright © 1998 by the author. Published here with the author's permission.

Paper presented at the RTO AVT Course on "Fluid Dynamics Research on Supersonic Aircraft", held in Rhode-Saint-Genèse, Belgium, 25-29 May 1998, and published in RTO EN-4.

Jones observed long ago, an oblique wing is the best compromise between forward sweep and backward sweep.

The wave drag of a body of revolution is easily computed. If we let its cross-sectional area be $S(x)$, and its length l, then $2\pi D/q$

$$= \int_0^l S''(x)dx \int_0^l S''(\xi)\log|2(x-\xi)|d\xi$$

plus terms that are multiplied by $S'(l)$.

Wave Drag

The supersonic area rule tells us that the wave drag of an aircraft in a steady supersonic flow is identical to the average wave drag of a series of equivalent bodies of revolution. These bodies of revolution are defined by the cuts through the aircraft made by the tangents to the fore Mach cone from a distant point aft of the aircraft at an azimuthal angle θ, as shown in Fig.1. This average is over all azimuthal angles.

For each azimuthal angle the cross-sectional area of the equivalent body of revolution is given by the sum of two quantities: the cross-sectional area created by the oblique section from the tangent to the fore Mach cone's intersection with the aircraft, projected onto a plane normal to the free stream; and a term proportional to the component of force on the contour of this oblique cut, lying in the θ = constant plane, and normal to the free stream.[6,7] The minimum wave drag associated with a given lift requires that all oblique loadings projected by the Mach planes be elliptical. This is the same as saying that each equivalent body of revolution should be a Kármán ogive, which is the shape that minimizes the fore-body drag of a body of revolution of given base area.

The drag of a supersonic wing with subsonic leading edges and an elliptic spanwise loading can be expressed using our theoretical understanding of drag at supersonic speeds.

This drag is given by:

$$D = qS_f C_f + \frac{L^2}{\pi q s^2} + \frac{\beta^2 L^2}{\pi q l_l^2} + \frac{128 q V^2}{\pi l_V^4} \cdot \qquad (1)$$

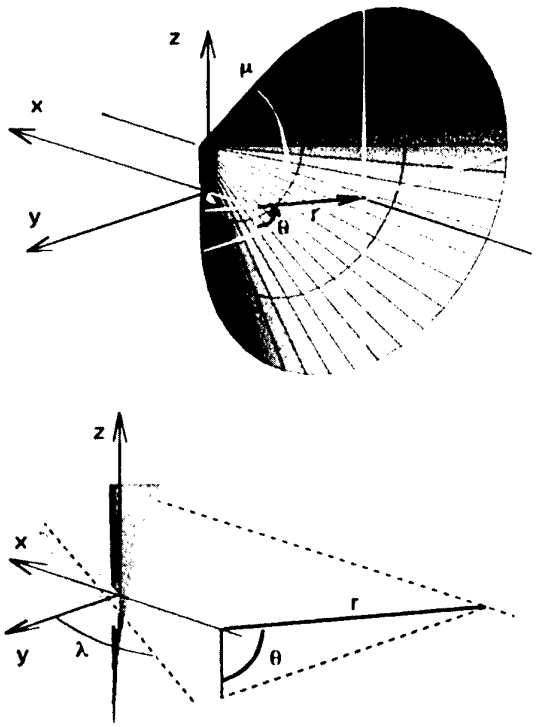


Fig. 1. Fore Mach cone (above) and its intersection with an oblique wing aircraft (below). Courtesy H. Sobieczky.

Here S_f is the wetted area, and C_f is the average skin friction coefficient. Thus the first term represents the skin friction drag which we may accurately approximate by the turbulent drag on a flat plate of the same area and average streamwise chord.

The second term is the induced drag for an elliptically loaded wing. We recognize this expression as the induced drag of the wing in the flow normal to it, that is as $L^2/(\pi q_n b^2)$, where q_n is the dynamic pressure of the normal flow and b is the unswept wing's span. The third and fourth terms are the wave drag due to lift and the wave drag due to volume, where V is the wing's volume. The two lengths, l_l and l_V are the averages over all azimuthal angles of the individual lengths of the equivalent bodies of revolution, appropriately adjusted for the variation of the component of the force lying in the θ = constant plane.

Oblique Wing Aerodynamics

As noted earlier, for the minimum wave drag due to lift, the loading in each oblique plane must be elliptical; that is, the equivalent body of revolution in each azimuthal plane is a Kármán ogive.[8] This is readily realized in an oblique wing with an elliptic planform. With an elliptical spanwise load, every loading projected by the oblique Mach planes is also elliptical.

For the minimum wave drag due to volume each equivalent body must be a Sears-Haack body.[9,10] This minimizes the wave drag for a given volume. If we minimize the wing's thickness, that is, the caliber of the equivalent body, then for the same caliber body as the Sears-Haack body, the volume in Eq. (1) is reduced by $\sqrt{(8/9)}$.

Smith[11] noted that the Sears-Haack area distribution is the product of an elliptic distribution and a parabolic distribution. The lengths of the chords cut by parallel planes on an elliptic planform are distributed elliptically. Thus, if all sections of wing were parabolic, each area distribution of the equivalent body of revolution due to volume would be the product of an elliptic and a parabolic distribution and the wave drag of the wing would be a minimum for given volume.

The lengths in the last two terms are the average over all azimuthal angles of the effective length for lift, and volume, for each azimuthal angle, as determined by the supersonic area rule. To calculate these lengths we must determine the angle at which the tangent to the Mach cone cuts the plane of the wing.

For simplicity we assume that the wing lies in a horizontal plane. We recognize, but ignore, the fact that the wing must incline its lift vector slightly to offset the leading edge suction which occurs on only one side of the wing. In practical cases this results in wing plane inclination of less than two degrees.

If we write down the expression for the fore Mach cone depicted in Fig. 1, and consider its apex to be at a large radial (and thereby axial) location, this equation becomes that for its tangent plane. This plane intersects the horizontal plane and thereby the wing, in a line that makes an angle, φ, given by

$$\tan\varphi = \pm\beta\sin\theta,$$

with the y-axis. Now that we know the angle cut by the tangent to the Mach cone, we also know the length of the equivalent body of revolution for that plane is

$$l(\theta) = b\sin\lambda - \beta\cos\lambda\sin\theta.$$

We may then determine the two lengths l_l and l_v to find the now classical results of an oblique wing:

$$\frac{1}{l_l^2} = \frac{1}{2\pi}\int_0^{2\pi}\frac{(\cos\theta)^2}{l^2(\theta)}d\theta \qquad (2)$$

$$= \frac{1}{m^2b^2(\sin\lambda)^2}\left(\frac{1}{\sqrt{1-m^2}} - 1\right),$$

$$\frac{1}{l_v^4} = \frac{1}{2\pi}\int_0^{2\pi}\frac{d\theta}{l^4(\theta)} \qquad (3)$$

$$= \frac{2+3m^2}{2b^4(\sin\lambda)^4(1-m^2)^{7/2}},$$

where $m = \beta\cot\lambda$.[12,13] For a wing with a subsonic leading edge m is less than 1. The drag arising from the lift of an elliptic wing, i.e., the sum of the induced drag and wave drag due to lift, can also be determined by applying Kogan's theory.[14] And this theory can be used to show that an oblique, elliptically loaded, wing has the minimum inviscid drag for a given lift.[15]

We may use Eqs. (2) and (3) to determine the inviscid drag for an oblique lifting line, that is for m << 1. This gives, for the inviscid flow past a lifting line,

$$D = \frac{L^2}{\pi q s^2\sqrt{1-m^2}}. \qquad (4)$$

We should note here that the large sweep approximation, then the drag due to lift is predominately induced drag. Then we may rewrite Eq.(1) in the classical form for minimum drag:[16]

$$D_{min} = qS_fC_f + \frac{L^2}{\pi q s^2} + \frac{\beta^2L^2}{2\pi q\ell^2} + \frac{128qV^2}{\pi\ell^4}. \qquad (5)$$

Here ℓ is the aircraft's length, which in the case of an oblique wing is its streamwise length. The linear result for an arbitrary elliptic wing is more com-

plex.[12,13,17]

An oblique elliptic wing simultaneously provides large span and large lifting length. The reduction in the drag for an oblique wing of finite span comes from being able to provide the optimum distribution of lift and volume in all oblique planes. To achieve an elliptic load distribution, twist variation along the wing span, or bending the wing up at the tips, is needed. The proper wing cross-section area distribution then gives the minimum wave drag due to volume or thickness. Fig. 2 provides the inviscid *L/D* for an elliptic planform oblique wing with a 10:1 axis ratio as a function of C_L and sweep as determined by Euler computations.[20] From this we conclude that for inviscid flow the optimum occurs with a sweep of about 68 degrees at $C_L = 0.068$.

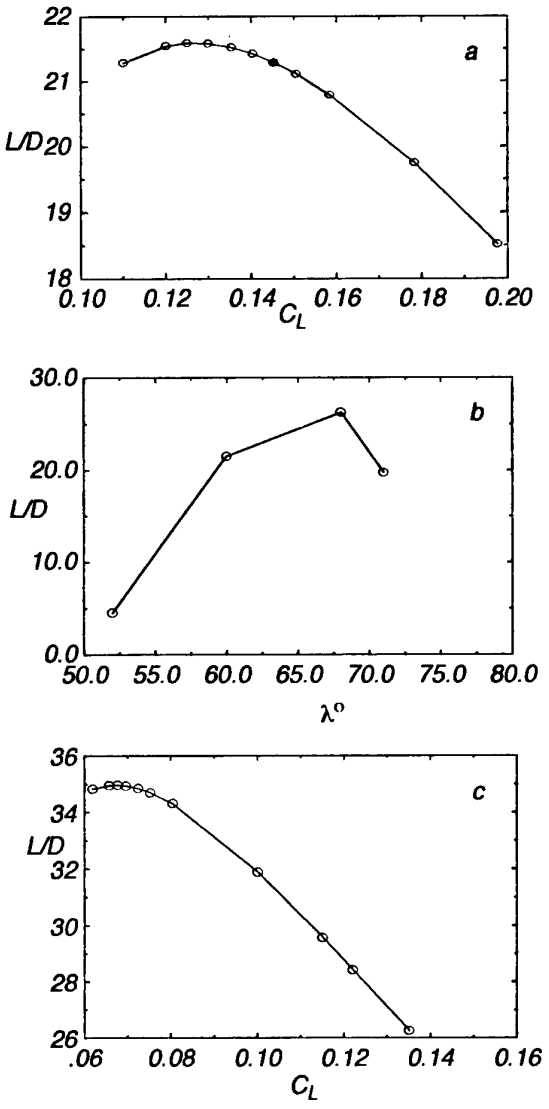


Fig. 2. Inviscid *L/D* as a function of: a) C_L for $\lambda = 60^\circ$, c) C_L for $\lambda = 68^\circ$, b) λ for $C_L = .068$.

Viscous Effects

We may approximate the viscous drag by that on a flat plate of equivalent wetted area. Here we follow Peterson[18] in applying the *T'* method of Sommer and Short[19] to determine the skin friction on a flat plate at supersonic Mach numbers. We assume here that the wing is at the recovery temperature. For an oblique wing we may use twice the planform area as the wetted area with good accuracy. Aircraft fly whenever possible at the altitude that, considering viscous effects, maximizes *L/D*. We may improve *L/D* by flying higher and thereby reducing skin friction drag because *q* is lower, although the increased C_L means a lower inviscid *L/D*.

To determine what altitude, and thereby what C_L, gives maximum viscous *L/D*, we must first determine the appropriate Reynolds numbers and develop a table of C_f, and determine the skin friction drag. The streamwise chord used was the mean chord divided by cosλ. Because viscous drag is $2qSC_f$, where C_f is the average skin friction coefficient, and $L = qSC_L$, we can write for the drag:

$$D/L = (D/L)_{inviscid} + 2C_f/C_D. \qquad (6)$$

To be specific, previous design studies[17,20,21] suggest an OFW with a 10:1 axis ratio, a 550 foot span, and a maximum chord of 55 feet. This gives a planform area, *S*, of 23,758 square feet, and with a maximum thickness of 19% gives a volume of 124,140 cubic feet. Such an aircraft might accommodate 800 passengers. The studies of Rawdon et al.[21] suggest an estimated takeoff weight of 1.575 million pounds, a weight upon entering cruise of 1.5 million pounds, and a weight upon leaving cruise of 0.9 million pounds. The mid-cruise weight would be 1.2 million pounds.

To determine the density and viscosity in, and indeed the Reynolds number for, the boundary layer we need an appropriate reference temperature, *T'*. This we may determine for a given wall temperature from Peterson.[18] Given this reference temperature, and thereby the freestream Reynolds number for a given flight altitude, we may construct Fig. 3.

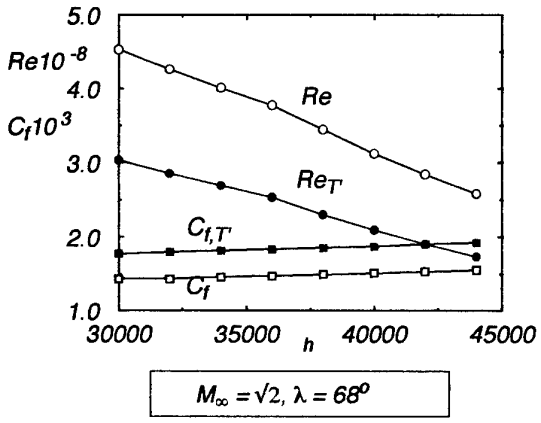


Fig. 3. Freestream and reference temperature Reynolds number and C_f versus flight altitude, h.

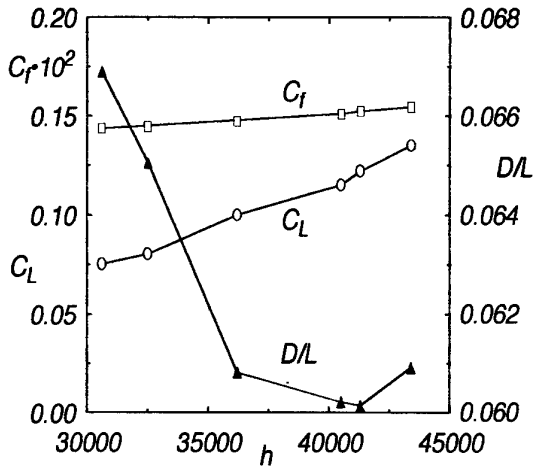


Fig. 4: Lift coefficient, skin friction coefficient and drag-to lift ratio, D/L, as a function of flight altitude.

Knowing C_f as a function of altitude, h, and given the aircraft's weight, say 1.5 million pounds upon entering cruise, we can determine the $C_L(h)$ needed to fly at that altitude. Equation (6) then provides D/L as a function of altitude as shown in Fig. 4. As Fig. 4 depicts, the viscous drag-to-lift ratio is a minimum at 41,300 feet; here $C_L = 0.1221$ and $C_f = 0.001523$.

We then analyze the flow under these conditions to find a new value for the inviscid L/D of 28.42, down from the value of 35.0 depicted in Fig. 2c. Equation (6) then gives us the viscous L/D,

$$\left(\frac{L}{D}\right)_{opt} = \left[\frac{1}{28.42} + \frac{2 \times 0.001523}{0.1221}\right]^{-1}$$

or 16.6 to the accuracy with which we might believe this result. This corresponds to an ML/D of 23.5, which is close to the linear theory optimum of 25.2. Given the flight altitude of 41,300 feet and C_f, the viscous drag is determined to be 37,420 pounds. We have reduced inviscid L/D from its maximum of 35.0 to 28.4 by increasing C_L to fly higher, but we have improved the viscous L/D by nearly 10%.

For nominal conditions we might take the weight to be 1.2 million pounds, the volume to be 85,800 cubic feet and the altitude to be 42,000 feet. Using Eq. (1) and the nominal conditions, we calculate the turbulent skin friction drag on a flat plate, and more directly, the other terms to conclude that the drag in pounds is:

$D = 73.5 * 10^3 = 73.5 * 10^3$[0.583 (skin friction)+ 0.221 (induced)+ 0.05 (wave-lift)+ 0.147 (wave-volume)].

We see that for this aerodynamic optimum aircraft the viscous drag is 58%, the induced drag is 22%, and the wave drag is 20%, with most of this due to volume. The drag due to lift is 27%. This maximum ML/D is for the untrimmed aircraft. Some drag penalty will be incurred by trimming the aircraft. The L/D of 16.6 is nearly double the maximum L/D for swept wing aircraft of the same swept span and length.

Summary

The simplest and most important components of the drag of aerodynamic optimum supersonic aircraft have been delineated. Knowledge of induced drag and the area rule makes it possible to determine the inviscid drag of the aerodynamically optimum aircraft. Viscous effects may be estimated using flat plate skin friction coefficients. They are important in determining the aircraft's flight altitude and cruise lift coefficient.

For this optimized aircraft nearly 60% of its drag is skin friction drag, just over 20% is induced drag, and just under 20% is wave drag. Less than 30% of the drag is due to lift.

References

1. Busemann, A., "Aerodynamischer Autreib bei Übershallgeschwindigkeit," *Proceedings, Volta Congress*, pp. 328-369, 1935.

2. Busemann, A., "Pheilflügel bei Hochgeschwindigkeit," *Lilienthal-Gesellschaft für Luftfahrt*, Bericht 164, 1943.

3. Jones, R. T., "Wing Plan Forms for High-Speed Flight," NACA TN 863, 1947.

4. Jones, R. T., "Effects of Sweepback on Boundary Layer Separation," NACA Rep. 884, 1947.

5. Carlson, H. W., McElroy, M. O., Lessard, W. B., and McCullers, L. A., "Improved Method for Prediction of Attainable Wing Leading-Edge Thrust," NASA TP 3537, April 1996.

6. Lomax, H., "The Wave Drag of Arbitrary Configurations in Linearized Flow as Determined by Areas and Forces in Oblique Planes," NACA RM A55A18, 1955.

7. Lomax, H., and Heaslet, M. B., "Recent Developments in the Theory of Wing-Body Wave Drag," *J. Aero. S.*, Vol. 23, No. 12, pp. 1061-1074, 1956.

8. Von Kármán, Th., and Burgers, J. M., *Aerodynamic Theory*, W. F. Durand ed., Vol. 2, Springer, pp. 172-175, 1934.

9. Sears, W. R., "On Projectiles of Minimum Wave Drag," *Quart. Appl. Math.*, Vol. 4, No. 4, pp. 361-366, 1947.

10. Haack, W., "Geschossformen kleinsten Wellenwiderstandes," *Lilienthal-Gesellschaft für Luftfahrt*, Bericht 139, pp. 14-28, 1941.

11. Smith, J. H. B., "Lift/Drag Ratios of Optimized Slewed Elliptic Wings at Supersonic Speeds," *Aeronautical Quart.*, Vol. 12, pp. 201-218, 1961.

12. Jones, R. T., "The Minimum Drag of Thin Wings in Frictionless Flow," *J. Aero. Sci.*, Vol. 18, No. 2, pp. 75-81, 1951.

13. Jones, R. T., "Theoretical Determination of the Minimum Drag of Airfoils at Supersonic Speeds," *J. Aero. Sci.*, Vol. 19, No. 12, pp. 813-822, 1952.

14. Kogan, M. N., "On Bodies of Minimum Drag in a Supersonic Gas Flow," *Prikl. Mat. Mekh.*, Vol. 21, No. 2, pp. 207-212, 1957.

15. Jones, R. T., "The Minimum Drag of Thin Wings at Supersonic Speeds According to Kogan's Theory," *Theoretical and Computational Fluid Dynamics*, Vol. 1, pp. 97-103, 1989.

16. Küchemann, D., *The Aerodynamic Design of Aircraft*, Oxford, Pergamon Press, p. 119, 1978.

17. Li, P., Seebass, R., and Sobieczky, H., "Oblique Flying Wing Aerodynamics," AIAA Paper No. 96-2120, 1996.

18. Sommer, S. C., and Short, B. J., "Free-Flight Measurements of Turbulent-Boundary-Layer Skin Friction in the Presence of Severe Aerodynamic Heating at Mach Numbers from 2.8 to 7.0," NACA TN 3391, March 1955.

19. Peterson, J. B., "A Comparison of Experimental and Theoretical Results for the Compressible Turbulent-Boundary-Layer Skin Friction with Zero Pressure Gradient," NASA TN D-1795, March 1963.

20. Li, P., Seebass, R., and Sobieczky, H., "Manual Optimization of an Oblique Flying Wing," AIAA Paper No. 98-0598, 1998.

21. Rawdon, B. K., Scott, P. W., Liebeck, R. H., Page, M. A., Bird, R. S., and Wechsler, J., "Oblique All-Wing SST Concept," McDonnell Douglas Contractor Report, NAS1-19345, 1994.

TURBULENT BOUNDARY LAYER METHODS FOR SUPERSONIC FLOW

A.G.T. Cross
Aerodynamic Technology Department
British Aerospace, Military Aircraft and Aerostructures
Brough, East Riding of Yorkshire, HU15 1EQ
United. Kingdom.

SUMMARY

This paper considers the application of integral boundary layer theory to, turbulent, supersonic flow. Starting from the three-dimensional boundary layer equations the requirements for closure are addressed for the most general case. In particular, closure requires an accurate and consistent treatment of both the temperature and velocity profiles. Further, for supersonic flow the treatment must include an appropriate model for the effects of compressibility.

It is shown how a consistent approach to closure can be achieved based on the law of the wall and wake velocity profile. This allows important Reynolds number and pressure gradient effects to be modelled.

An important requirement for supersonic flow is the ability to model shock boundary layer interaction. For such flows involving wings the combined effects of Reynolds number and pressure gradient determine the limits and type of separation. Through application involving a viscous Euler calculation method, evidence is provided of the practical use of integral boundary layer methods based on the law of the wall and wake. This use includes application to wing flow involving three-dimensional shock boundary layer interaction.

LIST OF SYMBOLS

Main symbols:-

A	Law of the wall constant.
B	Wake scale factor.
C_E	Entrainment coefficient.
C_f	Skin friction coefficient.
C_l	Lift coefficient.
H	Shape parameter, $H = \delta^*/\theta$.
$\overline{H}$	Equivalent incompressible value of H.
H^*	Head's shape parameter, $H^* = (\delta - \delta^*)/\theta$.
K_s	Streamline curvature, at $z = \delta$.
K_n	Streamline normal curvature.
k	Prandtl's mixing length constant.
M	Mach number.
p	Pressure.
P_r	Prandtl number.
Q	Scalar component of velocity vector.
Q_s	Velocity component in the streamline direction.
Q_c	Velocity component in the streamline normal or cross-flow direction.
q	The non-dimensional friction velocity, $\sqrt{C_f/2}$.
R_δ	The Reynolds number based on δ, $\rho_e Q_e \delta/\mu_e$.
$R_{\delta'}$	The Reynolds number based on δ', $\rho_e Q_e \delta'/\mu_e$.
$R'_{\delta'}$	Transformed $R_{\delta'}$, $(T_w/T_e)\rho_e Q_e \delta'/\mu_e$.
r	Recovery factor.
s, n	Streamline co-ordinates.
T	Temperature in boundary layer.
T_r	Recovery temperature.
T_{te}	Total temperature, at $z = \delta$.
T_w	Bounding surface or wall Temperature.
V_T	Transpiration velocity.
z	Distance measured from and normal to the bounding surface.

Paper presented at the RTO AVT Course on "Fluid Dynamics Research on Supersonic Aircraft", held in Rhode-Saint-Genèse, Belgium, 25-29 May 1998, and published in RTO EN-4.

β_o Limiting streamline angle.
χ Wake exponent.
δ Actual boundary layer thickness.
δ^* Boundary layer displacement thickness.
μ Viscosity.
θ Boundary layer momentum thickness.
ρ Density.

General subscripts:-
e Value at boundary layer outer edge.
∞ Free stream value.
s Streamline value or component.
c Cross-flow value or component.

General superscript:-
$'$ Equivalent incompressible value.

1. INTRODUCTION

The design of high speed air vehicles involves both supersonic flow and high Reynolds number. Starting with the direct effects of supersonic flight speed, figure 1 shows how lift coefficient varies with Mach number. In the figure the curves are lines of constant overall lift at constant pressure altitude; i.e.,

$$C_l M_\infty^2 = constant.$$

The figure shows how at supersonic speeds very low values of lift coefficient are required relative to the subsonic and transonic speed regimes. As it is easier to generate the required lift for supersonic flight the emphasis at high speed is often on achieving attached flow and low drag.

Figure 2 shows how flight Reynolds number, based on a unit length scale, varies with both altitude and Mach number. As a reference, also included in the figure are contours of constant drag based on the use of supersonic and subsonic similarity rules. The application of these rules requires that,

$$\frac{p_\infty M_\infty^2}{\left(M_\infty^2 - 1\right)^{1/2}} = constant. \quad \text{for} \quad M_\infty > 1$$

$$\frac{p_\infty M_\infty^2}{2\left(1 - M_\infty^2\right)^{1/2}} = constant. \quad \text{for} \quad M_\infty < 1$$

The figure 2 gives an indication of the high Reynolds numbers associated with supersonic flight and some indication of the expected Reynolds number variation.

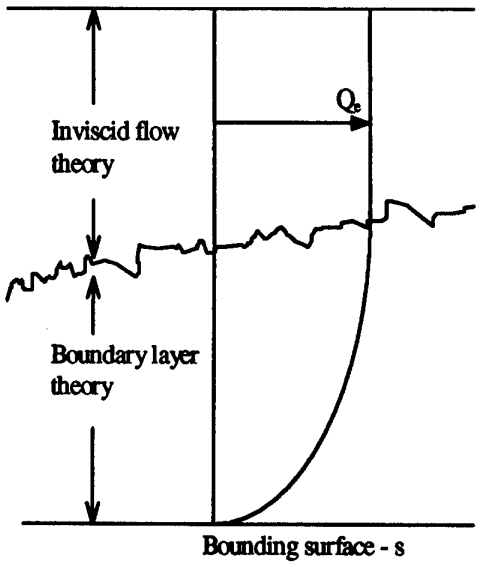
Due to the predominant design requirements of attached flow and high Reynolds number, turbulent boundary layer theory has long been used to develop supersonic air vehicle design methods.

At transonic flight speeds there are significant local regions of supersonic flow and boundary layer theory can again be used to advantage. However, in this case the levels of lift coefficient are much higher than for the fully supersonic case. Operation close to the buffet boundary becomes a consequence of the higher lift and so there is more of a need to model separation.

For the transonic case both shock induced and trailing edge separation must be modelled. Further, the relative importance of these forms of separation is strongly dependent on Reynolds number. Clearly the effects of Reynolds number must be accurately represented in transonic design methods and the underlying theory on which these methods are based. For this reason, the ability to model separation and the effects of Reynolds number at transonic flow speeds predominately determine the requirements for the more general capability that can be applied to fully supersonic flow.

The advantage of the boundary layer approach is that the viscous effects are all confined to a thin layer of fluid close to the bounding surface of the flight vehicle. Sketch 1 illustrates the basic concept of the boundary layer model.

The inviscid flow regime illustrated in the sketch can be modelled with Euler methods. Further, viscous-inviscid coupling theory can be used for addressing the interaction between the inviscid and boundary layer flows. This is important when the interactions are strong, such as when trailing edges, shock waves and separation are involved. In this paper we focus our deliberations largely on closure of the boundary layer equations with viscous Euler design methods and applications in mind.



Sketch 1. Boundary layer flow.

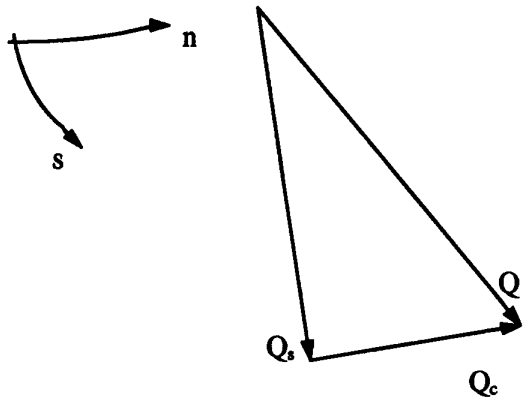
Integral methods are considered in this paper as these are very efficient in terms of computing requirements. This is particularly so for turbulent flow at high Reynolds number. One of the key advantages is realised when the integral boundary layer method is included within a viscous Euler method. This is because the computational grid used for a viscous Euler calculation is largely independent of Reynolds number. In this case a common grid can be used and the numerical errors associated with Reynolds number dependent grids are avoided. Reference 1 describes a scale effect study for a low speed wing. In this case the changing form of separation with increasing Reynolds number, from trailing to leading edge, was successfully modelled by a viscous Euler method using a common grid.

2. GOVERNING EQUATIONS

It is important here to start any discussion of boundary layer methods by reference to the three-dimensional boundary layer equations. This is to ensure that the methods considered are as general as is practicable.

In particular, three-dimensional separation effects are important on wings and bodies and so the primary requirement for accuracy requires consideration of three-dimensional flow. The boundary layer equations are developed in a co-ordinate system determined by the streamline and streamline normal at the outer edge of the boundary layer. This so-called streamline co-ordinate system lies in the plane of the bounding surface and is as illustrated in sketch 2. Also included in the sketch are the definitions of the streamline and cross-flow components of the velocity in the boundary layer. By definition of the streamline direction, it follows that at the outer edge of the boundary layer the streamline and cross-flow velocity components are given by,

$$Q_s = Q_e \text{ and } Q_c = 0.$$



Sketch 2. Streamline co-ordinates and velocity components.

For the three-dimensional turbulent boundary layer, the entrainment and momentum integral equations apply. The compressible flow version of these equations will now be considered in the form given by Smith[2]:

First the continuity, or entrainment, equation,

$$\frac{\partial(\delta-\delta_s^*)}{\partial s}-\frac{\partial \delta_c^*}{\partial n}$$
$$+(\delta-\delta_s^*)\left[\frac{1}{\rho_e Q_e}\frac{\partial(\rho_e Q_e)}{\partial s}-K_s\right]$$
$$-\delta_c^*\left[\frac{1}{\rho_e Q_e}\frac{\partial(\rho_e Q_e)}{\partial n}-K_n\right]=C_E \qquad \textbf{2.1.1}$$

The streamline momentum equation,

$$\frac{\partial \theta_{ss}}{\partial s}+\frac{\partial \theta_{sc}}{\partial n}$$
$$+\theta_{ss}\left[\frac{(H_s+1)}{Q_e}\frac{\partial Q_e}{\partial s}+\frac{1}{\rho_e Q_e}\frac{\partial(\rho_e Q_e)}{\partial s}-K_s\right]$$
$$+\theta_{sc}\left[\frac{1}{Q_e}\frac{\partial Q_e}{\partial n}+\frac{1}{\rho_e Q_e}\frac{\partial(\rho_e Q_e)}{\partial n}-2K_n\right]$$
$$+\delta_c^*\left[\frac{1}{Q_e}\frac{\partial Q_e}{\partial n}-K_n\right]+\theta_{cc}K_s=\frac{C_{fs}}{2} \qquad 2.1.2$$

The cross-flow momentum equation,

$$\frac{\partial \theta_{cs}}{\partial s}+\frac{\partial \theta_{cc}}{\partial n}$$
$$+\theta_{cc}\left[\frac{1}{Q_e}\frac{\partial Q_e}{\partial n}+\frac{1}{\rho_e Q_e}\frac{\partial(\rho_e Q_e)}{\partial n}-K_n\right]$$
$$+\theta_{cs}\left[\frac{1}{Q_e}\frac{\partial Q_e}{\partial s}+\frac{1}{\rho_e Q_e}\frac{\partial(\rho_e Q_e)}{\partial s}-2K_s\right]$$
$$+\theta_{ss}(H_s+1)K_n=\frac{C_{fc}}{2} \qquad 2.1.3$$

2.1 Auxiliary Equations

The governing equations, equations 2.1, involve many unknowns and so require the use of auxiliary closure equations in order to effect their solution. The shape parameter in the streamline direction is given by,

$$H_s=\delta_s^*/\theta_{ss}\,.$$

Thus, the governing equations primarily involve the boundary layer integral thickness parameters that are defined as,

$$\delta_s^*=\int_0^d\left[1-\frac{\rho}{\rho_e}\frac{Q_s}{Q_e}\right]dz \qquad 2.2.1$$

$$\delta_c^*=-\int_0^d\frac{\rho}{\rho_e}\frac{Q_c}{Q_e}dz \qquad 2.2.2$$

$$\theta_{ss}=\int_0^d\left[1-\frac{Q_s}{Q_e}\right]\frac{\rho}{\rho_e}\frac{Q_s}{Q_e}dz \qquad 2.2.3$$

$$\theta_{cc}=-\int_0^d\frac{\rho}{\rho_e}\frac{Q_c^2}{Q_e^2}dz \qquad 2.2.4$$

$$\theta_{sc}=\int_0^d\left[1-\frac{Q_s}{Q_e}\right]\frac{\rho}{\rho_e}\frac{Q_c}{Q_e}dz \qquad 2.2.5$$

$$\theta_{cs}=-\int_0^d\frac{\rho}{\rho_e}\frac{Q_c}{Q_e}\frac{Q_s}{Q_e}dz \qquad 2.2.6$$

Clearly from the above we also have,

$$\theta_{cs}=\theta_{sc}+\delta_c^* \qquad 2.3$$

As a result of this large number of integral thickness parameters the three-dimensional integral boundary layer equations are strongly dependent on the form of the velocity profile that determines Q_s and Q_c. This dependence is much greater than for the two-dimensional case and is why direct use of the velocity profile has to be the starting point for defining closure. As transonic flow requires accuracy in order to model the effects of Reynolds number on separation, this is a particular reason why direct use of the velocity profile is necessary.

3. BOUNDARY LAYER PROFILES

In general integral boundary layer theory requires consideration of the velocity profile. Direct reference to the velocity profile is necessary in the three-dimensional case if a consistent and reliable means of closure is to be achieved. For the compressible case there is also a need to consider the temperature and density profiles. However, Prandtl's boundary layer model involves the inviscid, external flow, pressure being impressed on the boundary layer. Therefore the pressure across the layer is constant and the equation of state requires the density profile to be simply the inverse of the temperature profile. For these reasons our interest in high speed flows and compressibility must start with a consideration of the velocity

and temperature profiles. In particular, analytic forms are required that can be used to provide closure of the boundary layer integral equations.

3.1 Velocity Profile

Figures 3a and 3b show some high Reynolds number two-dimensional boundary layer profiles measured by Winter and Gaudet[3]. These profiles were measured on the side walls of a large transonic wind tunnel as a means of obtaining high Reynolds numbers that would have been unobtainable on a wind tunnel model. The figures cover ranges of Mach number at two different Reynolds numbers. The figures also include an analytic fit to the experimental data based on a form of the law of the wall and wake proposed in reference[4]. The two-dimensional form of the theoretical velocity profile used in the figures is as follows,

$$Q/Q_e = q/k\left\{\frac{1}{2}\log(R_\delta\ q\,z/\delta)^2 + A\right\} + B\sin^{\chi}(\pi\ z/2\delta) \qquad 3.1$$

This profile involves a slight revision of the more usual logarithmic term in order that separated flow can be considered. Beyond the separation point the friction velocity q is negative and so we must replace the usual term,

$$\log(\ )$$

by the identity,

$$\frac{1}{2}\log(\ )^2.$$

It should be noted that at the separation point itself the friction velocity is zero. Thus from equation 3.1 and the application of L'Hopital's rule we obtain for the logarithmic wall region,

$$\lim_{q\to 0}\left(\frac{d\log q^2}{dq}\Big/\frac{dq^{-1}}{dq}\right) = 0.$$

Thus the law of the wall vanishes at the separation point leaving only the law of the wake.

Apart from the revision of the logarithmic term, the wake includes a variable exponent χ in order to allow for longitudinal pressure gradient. The variable exponent also provides a means of twisting, or skewing, the wake when the three-dimensional form is considered. For the law of the wake, $\chi = 2$ provides the usual analytic form of Coles[5] tabulated wake function, but in reference 4 this is assumed only to apply to equilibrium, that is self preserving flow. For self preserving flow the boundary layer shape parameter remains constant. It is shown in reference 4, relative to the equilibrium condition, that for adverse pressure gradients the wake exponent is less than the equilibrium value while for favourable pressure gradients larger values are applicable.

In order to consider the profile of equation 3.1 for closure of the boundary layer equations the wake scale factor B must satisfy the boundary condition,

$$Q = Q_e \text{ when } z = \delta.$$

This requires,

$$B = 1 - q/k\left\{\frac{1}{2}\log(R_\delta\ q)^2 + A\right\} \qquad 3.2$$

The theoretical profile as shown in figures 3a and 3b, was applied to the experimental data subject to using the appropriate values of χ that relate to zero pressure gradient. The fitted profiles were obtained by calculating optimum values of the friction velocity q and the boundary layer thickness δ such that the profiles gave a best fit to the data. From the figures it can be seen that the theoretical profiles give good agreement with the experimental data up to Mach 2.8, that was the highest Mach number case measured during the tests.

The law of the wall can be derived from Prandtl's mixing length hypothesis as was shown by Schlichting[6]. One of the fundamental assumptions for the derivation is that the shear stress close to the wall is constant. In extending the law of the wall to three-dimensions the equivalent and entirely consistent assumption is that the wall shear stress vector must be constant in both magnitude and direction. As a

consequence of this assumption, the law of the wall must simply lie in the direction of the limiting streamline that occurs at the bounding surface. The limiting streamline angle, measured relative to the streamline ordinate direction, is given by,

$$\beta_0 = \lim_{z \to 0} \left(\frac{dQ_c}{dz} \Big/ \frac{dQ_s}{dz} \right)$$

For this reason for the three-dimensional law of the wall we can simply write,

$$Q_s/Q_e = q_s/k \left\{ \frac{1}{2} \log(R_\delta \, q \, z/\delta)^2 + A \right\}$$

$$Q_c/Q_e = q_c/k \left\{ \frac{1}{2} \log(R_\delta \, q \, z/\delta)^2 + A \right\}$$

Where,

$$q^2 = q_s^2 + q_c^2, \qquad 3.3.1$$

$$q_s = q \cos\beta_o, \quad q_c = q \sin\beta_0. \qquad 3.3.2$$

Unfortunately, the law of the wake cannot be treated so easily. The wake does not simply resolve as it is skewed. As shown in reference 4, this skewing can be allowed for by having different wake exponents for the streamline and cross-flow directions. Thus, for the full form of the three-dimensional velocity profile we can write,

$$Q_s/Q_e = q_s/k \left\{ \frac{1}{2} \log(R_\delta \, q \, z/\delta)^2 + A \right\} + B_s \sin^{\chi_s}(\pi \, z/2\delta) \qquad 3.4.1$$

$$Q_c/Q_e = q_c/k \left\{ \frac{1}{2} \log(R_\delta \, q \, z/\delta)^2 + A \right\} + B_c \sin^{\chi_c}(\pi \, z/2\delta) \qquad 3.4.2$$

Separate wake scaling factors are also needed to apply the outer edge boundary conditions; given by $Q_s = Q_e$ and $Q_c = 0$ when $z = \delta$. Application of the boundary conditions give,

$$B_s = 1 - q_s/k \left\{ \frac{1}{2} \log(R_\delta \, q)^2 + A \right\} \qquad 3.5.1$$

$$B_c = -q_c/k \left\{ \frac{1}{2} \log(R_\delta \, q)^2 + A \right\} \qquad 3.5.2$$

$$B_c = (B_s - 1) q_c/q_s \qquad 3.5.3$$

Equation 3.5.3 is informative in relation to the behaviour of the wake, but not of direct use as it becomes indeterminate in the approach of two-dimensional separation; i.e. $q_s \to 0$.

3. 2 Temperature Profile

Having considered the velocity profile we now need to turn our attention to the temperature profile. As shown by Schlichting[6], for Prandtl numbers near unity the quadratic temperature-velocity relation becomes applicable. This relation applies for zero pressure gradient flow with heat transfer ($T_w \neq T_r$) or for adiabatic wall flows with pressure gradient ($T_w = T_r$). The theoretical temperature profile is therefor linked to the velocity profile through this relation which can be written as,

$$T = T_w + (T_r - T_w) Q/Q_e + (T_e - T_r) Q^2/Q_e^2 \qquad 3.6.1$$

where,

$$T_r = T_e + r\,(T_{te} - T_e). \qquad 3.6.2$$

For turbulent flow the recovery factor 'r' is obtained from the Prandtl number by,

$$r = P_r^{1/3} \qquad 3.6.3$$

Figures 4a and 4b show the result of comparing the temperature relation with the adiabatic wall data of Winter and Gaudet[3]. Winter and Gaudet measured the temperature and so were able to calculate the temperature ratio T/T_e within the boundary layer. However, by assuming constant pressure across the boundary layer they actually presented the results as a density ratio ρ/ρ_e. From the figures it can be seen that a very good

fit to the data is obtained using the quadratic temperature-velocity relation.

As temperature is a scalar variable it is usual to apply the quadratic temperature-velocity relation directly to the three-dimensional case. This approach was adopted by Smith[2], who used a power law for the velocity profile in the streamline direction. However, justification for its use with the law of the wall can be established by remembering that the logarithmic region is two-dimensional in character as it can be simply resolved by virtue of equations 3.3.2. As most of the velocity change within the attached boundary layer occurs within the logarithmic region, the effects of temperature and density are predominantly in the wall region where the temperature profile based on two-dimensional data is most relevant. For this reason the equation 3.6.1 is fully consistent with the three-dimensional form of the law of the wall.

4. COMPRESSIBILITY

In principle, now that we have analytical forms of the velocity and temperature profiles the integral thickness parameters defined by equations 2.2 can be evaluated to enable closure of the boundary layer equations. However, to simplify the analysis it is more usual to consider a compressibility transformation approach.

4.1 Spence Transformation

By consideration of the experimental data of Lobb, Winkler and Persh[7], Spence[8] showed that for Mach numbers up to a value of eight it was largely possible to represent the effects of compressibility by writing,

$$Q/Q_e = F(z'/\delta')$$

where,

$$z' = \int_0^z (\rho/\rho_e)\,dz \qquad \textbf{4.1.1}$$

$$\delta' = \int_0^d (\rho/\rho_e)\,dz \qquad \textbf{4.1.2}$$

These equations essentially define a transformation whereby the normal to the wall distance z and the boundary layer thickness δ are transformed to equivalent incompressible values z' and δ'. As such they can be used with a standard incompressible velocity profile.

Figures 5a and 5b show the result of applying the Spence transformation to the data of Winter and Gaudet[3] and then fitting the law of the wall and wake in similar fashion as for figures 3a and 3b. The theoretical profiles were fitted again using equation 3.1 but as a result of the transformation, δ' was substituted for all occurrences of δ and equivalent incompressible values of friction velocity were allowed for. As a result the profile is represented by writing,

$$Q/Q_e = q'/k\left\{\frac{1}{2}\log(R_{\delta'}\, q' z'/\delta')^2 + A\right\} + B\sin^{\chi}(\pi\, z'/2\delta') \qquad \textbf{4.2}$$

For the transformed profiles of figures 5a and 5b, the theoretical results appear to agree quite well with the experimental data and provide some confirmation of the general applicability of the Spence transformation. However, for values of Mach number above two, the results do not agree as well as those of the original non-transformed profiles of figures 3a and 3b.

4.2 Reynolds Number Transformation

It can be seen from figures 5a and 5b that the greatest errors in the velocity profile occur at the wall where $T = T_w$ and $\rho = \rho_w$. These errors and the previous results of figures 3a and 3b suggest that we need to nullify the effects of the Spence transformation in the law of the wall. A means of achieving this will now be considered. From the Spence transformation we can write for the region close to the wall,

$$z' = \int_0^z (\rho_w/\rho_e)\,dz$$

And so,

$$z' = (\rho_w/\rho_e)\, z$$

$$z' = (T_e/T_w)\, z$$

Thus we can nullify the effects of the transformation close to the wall if we effectively

use z rather than z' in the logarithmic region; i.e. equation 4.2 becomes,

$$Q/Q_e = q'/k\left\{\frac{1}{2}\log(T_w/T_e\, R_{\delta'}\, q'z'/\delta')^2 + A\right\} + B\sin^{\chi}(\pi\, z'/2\delta')$$

In effect this form of the velocity profile differs only from equation 4.2 in respect to the inclusion of a temperature ratio factor on the Reynolds number. For this reason we can retain the original form of equation 4.2 if we redefine the Reynolds number based on the equivalent incompressible boundary layer thickness. With this approach in mind we replace $R_{\delta'}$ by,

$$R'_{\delta'} = (T_w/T_e)(\delta'/\delta)R_{\delta} \qquad 4.3$$

Figures 6a and 6b show the result of this change on the transformed velocity profile and it can be seen that much better agreement is now obtained with the experiment of Winter and Gaudet. The results are now very similar to the original results of figures 3a and 3b. However, the revised profile has the advantage that it can be used with the Spence transformation.

4.3 Application To Three-Dimensions

It is now possible to write the three-dimensional velocity profile in the transformed form and so,

$$Q_s/Q_e = q'_s/k\left\{\frac{1}{2}\log(R'_{\delta'}\, q'z'/\delta')^2 + A\right\} + B_s\sin^{\chi_s}(\pi\, z'/2\delta') \qquad 4.4.1$$

$$Q_c/Q_e = q'_c/k\left\{\frac{1}{2}\log(R'_{\delta'}\, q'z'/\delta')^2 + A\right\} + B_c\sin^{\chi_c}(\pi\, z'/2\delta') \qquad 4.4.2$$

where,

$$B_s = 1 - q'_s/k\left\{\frac{1}{2}\log(R'_{\delta'}\, q')^2 + A\right\} \qquad 4.4.3$$

$$B_c = -q'_c/k\left\{\frac{1}{2}\log(R'_{\delta'}\, q')^2 + A\right\} \qquad 4.4.4$$

As a result of using the Spence transformation the integral thickness parameters defined by equation 2.2 can be rewritten along with a new thickness Δ_s such that,

$$\delta^*_s = \int_0^d dz - \int_0^{d'}\frac{Q_s}{Q_e}dz' \qquad 4.5.1$$

$$\delta^*_c = -\int_0^{d'}\frac{Q_c}{Q_e}dz' \qquad 4.5.2$$

$$\theta_{ss} = \int_0^{d'}\left[1-\frac{Q_s}{Q_e}\right]\frac{Q_s}{Q_e}dz' \qquad 4.5.3$$

$$\theta_{cc} = -\int_0^{d'}\frac{Q_c^2}{Q_e^2}dz' \qquad 4.5.4$$

$$\theta_{sc} = \int_0^{d'}\left[1-\frac{Q_s}{Q_e}\right]\frac{Q_c}{Q_e}dz' \qquad 4.5.5$$

$$\theta_{cs} = -\int_0^{d'}\frac{Q_c}{Q_e}\frac{Q_s}{Q_e}dz' \qquad 4.5.6$$

$$\Delta_s = \int_0^{d'}\left[1-\frac{Q_s}{Q_e}\right]dz' \qquad 4.5.7$$

It can be seen from these integrals that they generally transform to their equivalent incompressible form. That is they equate to equations 2.2 with $\rho = \rho_e$. The exception is for δ^*_s which is related to the equivalent incompressible thickness Δ_s through the identity:-

$$\delta^*_s = \Delta_s + \delta - \delta' \qquad 4.6$$

From equations 4.4 and 4.5 it should be clear that the integral thickness parameters can be calculated by direct integration of the theoretical velocity profile such that we can define the following functions,

$$\Delta_s/\delta' = F_1(q'_s, q'_c, \chi_s, R'_{\delta'}) \qquad 4.7.1$$

$$\delta_c^*/\delta' = F_2(q_s', q_c', \chi_c, R_{\delta'}') \qquad 4.7.2$$

$$\theta_{ss}/\delta' = F_3(q_s', q_c', \chi_s, R_{\delta'}') \qquad 4.7.3$$

$$\theta_{cc}/\delta' = F_4(q_s', q_c', \chi_c, R_{\delta'}') \qquad 4.7.4$$

$$\theta_{sc}/\delta' = F_5(q_s, q_c\chi_s, \chi_c R_{\delta'}') \qquad 4.7.5$$

$$\theta_{cs}/\delta' = \theta_{sc}/\delta' + \delta_c^*/\delta' \qquad 4.7.6$$

Further, from the Spence transformation, we can write,

$$\delta = \int_0^{\delta'} (\rho_e/\rho)\, dz'$$

or,

$$\delta = \int_0^{\delta'} (T/T_e)\, dz' .$$

In the latter case we can substitute the temperature-velocity relation, equation 3.6.1, for the temperature T and this allows direct integration to yield,

$$\delta = \delta' + (T_w/T_e - 1)\Delta_s + (T_r/T_e - 1)\theta_{ss} \qquad 4.8.1$$

By combining this result with equation 4.6 we obtain,

$$\delta_s^* = T_w/T_e\, \Delta_s + (T_r/T_e - 1)\theta_{ss} \qquad 4.9.1$$

$$H_s = T_w/T_e\, \overline{H}_s + T_r/T_e - 1 \qquad 4.9.2$$

The result of equation 4.9.1 is important as it provides the expression for δ_s^* that complements the results of equations 4.7.

4.4 Skin Friction Transformation

In addition to the integral thickness parameters, it is necessary to have an equation for the skin friction coefficient if closure of the boundary layer equations is to be achieved. This can also be provided by the law of the wall and wake velocity profile. Further by considering data for supersonic flow it is possible to further validate the compressibility transformation approach.

From the definition of the non-dimensional friction velocity and noting that we are dealing with equivalent incompressible values we can write for an equivalent incompressible skin friction coefficient,

$$C_f' = 2q'^2 \qquad 4.10$$

So far, from the consequences of the Spence transformation, equations 4.3 and 4.9, suggest a skin friction transformation of the form,

$$C_f/C_f' = F(T_r/T_e, T_w/T_e)$$

This form generally agrees with the adiabatic wall correlation of Green[9], Hoerner[10] and of Winter and Gaudet[3].

While determining the appropriate skin friction transformation for the law of the wall and wake velocity profile, we need to remember that when the transformed velocity profile was fitted to the experimental data we effectively chose the optimum value of q'. For this reason we can determine equivalent incompressible values of skin friction coefficient from q' and relate these to the actual measured values. When dealing with adiabatic wall data it is most appropriate to seek a correlation involving the temperature ratio T_r/T_e.

Reference	C_f/C_f'
Green.	$(1+0.13M_\infty^2)^{-0.76}$
Hoerner.	$(1+0.15M_\infty^2)^{-0.58}$
Winter and Gaudet.	$(1+0.20M_\infty^2)^{-0.5}$
T_r/T_e correlation.	$(T_r/T_e)^{-0.54}$
T_{te}/T_e correlation.	$(T_{te}/T_e)^{-0.51}$

Table 1. Skin friction transformations.

By using the data appropriate to figures 6a and 6b, values of C_f' are obtained for the data of Winter and Gaudet. These can be compared with the actual measured values to provide the ratio

C_f/C_f'. Figures 7a and 7b show the result of correlating the skin friction ratio first with T_r/T_e and then with T_{te}/T_e. From these results it can be seen that both forms of correlation apply equally well. The results of the correlation are compared in table 1 with equations provided by Green[9], Hoerner[10] and Winter and Gaudet[3].

It is encouraging that the transformation involving the total temperature T_{te} basically confirms Winter and Gaudet's own result; i.e.,

$$C_f/C_f' = (T_{te}/T_e)^{-0.5} \qquad 4.11$$

The good agreement primarily results from the introduction of equation 4.3 as it assures a good fit of the law of the wall to the measured velocity profile data.

5. VELOCITY PROFILE EFFECTS

So far we have demonstrated the suitability of the law of the wall and wake for compressible flow. By defining the equivalent incompressible Reynolds number, $R_{\delta'}'$, the accuracy of the law of the wall and wake as developed for incompressible flow can be maintained for the compressible case, while permitting the full advantages of the Spence transformation to be realised.

Now we will briefly consider some of the implications of this form of velocity profile.

5.1 Shape Parameter Relations

From equations 4.7 it can be seen that the boundary layer integral thickness parameters all relate directly to the actual boundary layer thickness such that the equations 4.7 effectively define a set of shape parameters.

These shape parameters are equivalent incompressible results and it is convenient now to consider the special case of two-dimensional flow. For the two-dimensional case we have two shape parameters,

$$\Delta/\delta' = F_1(q', \chi, R_{\delta'}'),$$

$$\theta/\delta' = F_3(q', \chi, R_{\delta'}').$$

However, if we resort to more usual two-dimensional shape parameters we have,

$$H = \delta^*/\theta .$$

While Head[11], as a consequence of developing the boundary layer entrainment method, introduced the shape parameter,

$$H^* = (\delta - \delta^*)/\theta .$$

For the equivalent incompressible case,

$$\overline{H} = \Delta/\theta .$$

While from equation 4.6, H^* remains unchanged after transformation but given by,

$$H^* = (\delta' - \Delta)/\theta .$$

For the law of the wall and wake these results can be written as,

$$\overline{H} = F_1(q', \chi, R_{\delta'}')/F_3(q', \chi, R_{\delta'}'), \qquad 5.1.1$$

$$H^* = \left(1 - F_1(q', \chi, R_{\delta'}')\right)/F_3(q', \chi, R_{\delta'}'). \qquad 5.1.2$$

Figure 8 shows the effect of Reynolds number on the relationship between these shape parameters for the law of the wall and wake. The figure shows curves of constant R_θ' for the equilibrium flow condition $\chi = 2$. In this case R_θ' is obtained from,

$$R_\theta' = R_{\delta'}'/(\overline{H} + H^*) \qquad 5.2$$

The figure shows that the effects of Reynolds number are confined to low values of $\overline{H}$. The higher values of $\overline{H}$ are associated with separation for which the logarithmic region becomes very thin and this is why the effects of Reynolds number become negligible. The most significant consequence of Reynolds number is that it influences the lower limit of $\overline{H}$. The

lower limit of $\overline{H}$ becomes important for accelerating flows such as those involving wings with actuated flaps and controls.

Figure 9 shows the effect on the shape parameter relation of varying the wake exponent χ at a constant R_θ'. The parameter χ is a function of pressure gradient and controls the shape of the wake. As the wake term dominates the velocity profile near separation its strongest influence is at large values of $\overline{H}$.

5.2 Skin Friction Law

As the equations 5.1 provide a direct link between the equivalent incompressible skin friction coefficient and the shape parameter relation their result is effectively a skin friction law.

To provide a familiar reference, figure 10 provides a graphical representation of the well known Ludwieg-Tillmann skin friction law. This is a function of H, or $\overline{H}$ and R_θ, or R_θ'. Figure 11 is based on equations 5.1 and 5.2 for the equilibrium flow condition.

From figure 11 it can be seen that the main departure of the law of the wall and wake from the Ludwieg-Tillmann skin friction law is for the higher values of $\overline{H}$.

6. ENTRAINMENT

So far we have considered the velocity and temperature profiles as the primary means of closure of the integral boundary layer equations for turbulent flow.

To complete closure of the governing equations it is necessary to provide the right hand side of equation 2.1.1; that is it is necessary to provide the entrainment coefficient C_E.

In Head's[11] original formulation of the incompressible, two-dimensional, entrainment method it was shown that the entrainment coefficient could be related by a simple algebraic function to the shape parameter H. While this simple approach worked quite well, the method was later improved by Head[12] and Patel such that departure from equilibrium conditions was directly allowed for. Green[13] extended the original entrainment method to compressible flow, while Green[14], Weeks and Brooman introduced history effects by use of the lag-entrainment equation. The lag-entrainment equation is an additional differential equation that is solved such that the calculated entrainment coefficient is dependent on the upstream history of the boundary layer.

It was shown by Smith[2] that Green's[13] two-dimensional algebraic entrainment equation could be directly applied to the three-dimensional case by using the appropriate streamline direction parameters.

As the lag-entrainment equation is widely recognised as being the most appropriate means of calculating the entrainment coefficient it has been applied to the three-dimensional case using the same approach as Smith[2].

7. DESIGN APPLICATION

The three-dimensional velocity profile has been used together with the lag-entrainment equation of Green[14] et al to provide closure of the boundary layer equations. The boundary layer equations are transformed to a general non orthogonal co-ordinate system as used originally by Myring[15] and later by Smith[2].

The boundary layer method has also been coupled to an inviscid Euler method to allow viscous Euler solutions to be obtained. This is particularly important as it allows the inverse solution of the boundary layer equations and so the consideration of separated flow.

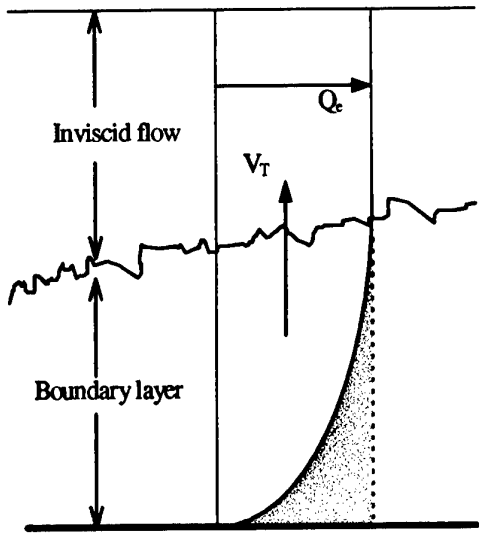
7.1 Transpiration Velocity

The coupling of the boundary layer and Euler equations is based on using the transpiration velocity, or equivalent source, approach of Lighthill[16]. Sketch 3 illustrates the basic concept of this approach in two-dimensions.

The mass flux within the boundary layer is less than that for the equivalent inviscid flow and the shaded area of the sketch portrays the deficit. By definition of the boundary layer displacement thickness, the deficit is given by $\rho_e Q_e \delta^*$. The rate of change of this deficit, along the bounding

surface, must also balance the transfer $\rho_e Q_e V_T$ to the inviscid flow and so,

$$V_t/Q_e = \frac{1}{\rho_e Q_e}\frac{\partial(\rho_e Q_e \delta^*)}{\partial s} \qquad 7.1$$



Sketch 3. Transpiration velocity model.

The equation for the transpiration velocity, when written for the three-dimensional case and in the streamline co-ordinate system is,

$$V_t/Q_e = \frac{\partial\delta_s^*}{\partial s} + \frac{\partial\delta_c^*}{\partial n} + \delta_s^*\left[\frac{1}{\rho_e Q_e}\frac{\partial(\rho_e Q_e)}{\partial s} - K_s\right] + \delta_c^*\left[\frac{1}{\rho_e Q_e}\frac{\partial(\rho_e Q_e)}{\partial .n} - K_n\right] \qquad 7.2$$

7.2 Viscous Coupling

The transpiration equation provides the link between the inviscid flow and boundary layer flow and all the relevant equations must be solved consistently to provide the overall compatible solution.

Due to the strong interaction between the inviscid flow and the boundary layer near separation the coupling problem requires special consideration. For two-dimensional flow the approach of Veldman[17] can be adopted whereby the inviscid flow equations are approximated. This alleviates the coupling problem by permitting a simultaneous solution of simpler equations so allowing the full equations to be driven to convergence through an iterative procedure. This forms the basis of the quasi-simultaneous solution method.

The quasi-simultaneous solution method can be used in three-dimensions and such a method is described in reference 18. This method effectively involves a linear treatment of both the inviscid flow and boundary layer equations in order to simplify the coupling equations. It is these simplified equations that are used to drive the solution of the full equations to convergence. Some results of using this method will now be briefly considered.

7.3 Airfoil Test Case

The viscous Euler method of reference 18 has been applied to the RAE 2822 airfoil experiment of Cook[19], McDonald and Firmin. While Cook et al did not cover supersonic free stream conditions, most of the cases considered were transonic and provided data involving local supersonic flow and shock boundary layer interaction. Here we consider viscous Euler results for 'case 6' and 'case 9'. Allowing for wind tunnel wall interference corrections the conditions for the two cases are summarised in table 2.

Data Item	Case 6	Case 9
Airfoil chord - $\bar{c}$.	0.61m	0.61m
Transition fixing point based on $\bar{c}$.	$x/\bar{c} = 0.03$	$x/\bar{c} = 0.03$
Transition fix, ballotini, diameter	.000254m	.000762m
Incidence - degrees.	2.52	2.79
Mach number, M_∞.	0.725	0.73
Reynolds number based on $\bar{c}$.	6.5×10^6	6.5×10^6

Table 2. RAE 2822 airfoil data.

From the table it can be seen that transition was fixed close to the airfoil leading edge. For this reason it is was necessary to fix transition in the calculations. Further, for the two cases, it can be seen that there was a significant difference in the size of the medium used to fix transition. This difference was not allowed for in the calculations.

Figure 12a shows viscous Euler pressure coefficient results for the RAE 2822 airfoil compared with the case 6 data of Cook et el. As a reference, also included in the figure is the result of an inviscid Euler calculation. Figure 12b shows similar results for case 9. For all the calculations a fine, 400 by 30, structured Euler grid was used. With 400 cells along the airfoil surface and wake centre line this gave a good resolution of the shock wave and trailing edge which both involve incipient separation.

Figures 12a and 12b show the significant effect of boundary layer displacement. They also show that the viscous Euler results agree favourably with the experimental data. The shock strength is reduced and the shock position moves forward as a result of the boundary layer.

Figures 13 and 14 compare with test data the boundary layer solution for these two cases. Figures 13a and 14a show the turbulent skin friction coefficient and demonstrate good agreement between test data and theory for both cases. The figures 13a and 14a also show that, while the flow conditions for case 6 and case 9 are fairly similar, case 9 is significantly closer to involving shock induced separation. Both cases are also very close to involving trailing edge separation.

Figures 13b and 14b show the development of the boundary layer shape parameter. From figure 13b it can be seen that for case 6 the agreement between the test data and theory is again quite good. For case 9, figure 14b shows the agreement to be less convincing and this is thought to be at least partly due to the effect of the thicker transition fixing medium.

For the upper surface of case 9 the laminar boundary layer calculation gives a momentum thickness of 0.000023m at the transition point. From table 2, this can be seen to be much smaller than the size of the transition fixing medium. Though the medium was sparsely distributed, some significant disturbance to the boundary layer, above and beyond simply causing transition, is to be expected.

7.4 Wing Test Case

In order to demonstrate the three-dimensional viscous Euler capability the Weybridge W4 wing test case is now considered. This test case is relevant here as it involves a three-dimensional shock boundary layer interaction on the wing upper surface. Further, as a result of the wing sweep effect the inviscid flow immediately downstream of the shock remains supersonic.

The history of the W4 wing and geometry definition are provided by Richards[20]. Figure 15 shows a plan view of the W4 wing and includes four of the lateral wing stations at which pressure measurements where made. Further table 3 provides details of the principal wing parameters and the particular test case conditions.

Data Item	Value
Aspect ratio.	7.965
Mean wing chord - $\bar{c}$.	0.1839m
Crank semi-span position.	$\eta = 0.411$
Leading edge sweep Λ_{le} - degrees.	28.30
Trailing edge sweep Λ_{te} - degrees.	3.50 for $\eta \leq 0.411$ 14.07 for $\eta \geq 0.411$
Incidence - degrees.	0.52
Mach number, M_∞.	0.78
Reynolds number based on $\bar{c}$.	8.5×10^6
Transition fixing loci based on local chord c.	upper, $x/c = 0.15$ lower, $x/c = 0.05$

Table 3. Weybridge W4 wing data.

Burton[21] has applied the three-dimensional viscous Euler capability to the W4 wing test case using a standard inviscid Euler structured grid. This grid involved 160 by 32 by 32 computation

cells which at the time was considered a "fine" grid solution.

Figure 16 shows the pressure coefficient distribution along the wing chord at the four wing stations illustrated in figure 15. Though not shown in the figures, the inviscid Euler shock is further rearward than the viscous Euler shock by some 11% of the local wing chord. From this it will be evident that the results of figure 16 are superficially quite similar to those of the two-dimensional airfoil. Basically that is, the displacement effect of the boundary layer pulls the otherwise inviscid shock forward with an appropriate weakening of its strength.

The W4 wing is of relatively high aspect ratio and the inviscid shock is basically an oblique shock and so quasi two-dimensional. However the shock is oblique to the boundary layer and so, the boundary layer can become highly three-dimensional. For this reason it is necessary to consider for the W4 wing the cross-flow development of the boundary layer. The cross-flow is characterised by the limiting streamline angle β_0 that is defined relative to the streamline direction ω_e at the outer edge of the boundary layer. The limiting streamline angle in Cartesian wing co-ordinates is therefor,

$$\omega_0 = \omega_e + \beta_0 \qquad 7.3.1$$

where,

$$\beta_0 = \tan^{-1}\left(q_c'/q_s'\right) \qquad 7.3.2$$

Figure 17 shows for the upper surface of the wing the local Mach number and development of ω_0. The increase of ω_0 through the shock can be noticed and this in turn can have a significant impact on its downstream development and the conditions for eventual separation.

The outboard part of the wing shows little lateral variation of the flow and for this reason it is appropriate to consider the tapered wing separation criterion. For the tapered wing involving separation, the separation line should follow a wing generator defined by a constant value of x/c. If Λ is the sweep angle of the wing generator, the limiting streamline angle for separation is simply,

$$\omega_0 = \pi/2 - \Lambda.$$

For the W4 wing the limiting streamline angle for separation over the outer part of the wing trailing edge is 75.9°. This compares with an actual attained value, from figure 17b, of 59.7° and so gives an indication of the close proximity of trailing edge separation.

By consideration of the cross-flow it should be clear that any increase in shock strength can either cause a local shock induced separation or push the trailing edge to the point of separation. It is for this reason that three-dimensional effects must be allowed for even when modelling wing flows involving moderate sweep.

8. CONCLUSIONS

Some developments of the law of the wall and wake have been reviewed with particular reference to three-dimensional and compressible flow.

These developments allow consistent closure of the three-dimensional turbulent boundary layer equations as they provide all the necessary shape parameter relations and the skin friction coefficient.

Compressibility has been largely addressed by consideration of the Spence transformation but with further improvement resulting from the specification of an equivalent incompressible Reynolds number.

It has been shown how this approach to closure can be used with a three-dimensional, entrainment, integral, boundary layer method. Some results have also been shown as a consequence of coupling the three-dimensional boundary layer method with an Euler method to produce a viscous Euler capability.

9. REFERENCES

1. Cross, A.G.T., "Use of a Computational Fluid Dynamics Method for Addressing Scale Effect", CEAS conference on "Wind Tunnels and Wind Tunnel Test Techniques", Churchill College Cambridge, U.K., April 1997.

2. Smith, P.D., "Direct and Inverse Integral Calculation Methods for Three-dimensional Turbulent Boundary layers", Aeronautical Journal, May 1984, Paper 1200/1.

3. Winter, K.G. and Gaudet, L., "Turbulent Boundary layer Studies at High Reynolds Numbers between 0.2 and 2.8", ARC R&M 3712, December 1970.

4. Cross, A.G.T.,"Boundary layer Calculation and Viscous inviscid Coupling", 15th Congress of Council of the Aeronautical Sciences, September 1986, ICAS-86-2.4.1.

5. Coles, D., "The Law of the Wake in Relation to Turbulent Boundary layers", Journal of Fluid Mechanics, 1956.

6. Schlichting, H.," Boundary layer Theory", McGraw-Hill series in Mechanical Engineering, Pergamon Press, 1955, pp 395-396 and pp 282-284.

7. Lobb, R.K., Winkler, E.M. and Persh, J., "Experimental Investigation of Turbulent Boundary layers in Hypersonic Flow", Journal of aeronautical Sciences, January 1955, pp 1-9.

8. Spence, D.A., "The Growth of Compressible Turbulent Boundary layers on Isothermal and Adiabatic Walls", ARC R&M 3191, June 1959.

9. Green, J.E., "The Prediction of Turbulent Boundary layer development in Compressible Flow", Journal of Fluid Mechanics, 1968.

10. Hoerner, S.F., "Fluid Dynamic Drag", Published by the author, USA, 1965.

11. Head, M.R., "Entrainment in the Turbulent Boundary layer" ARC R&M 3152, 1958.

12. Head, M.R. and Patel, V.C. "Improved Entrainment Method for Calculating Turbulent Boundary layer Development" ARC R&M 3643, 1968.

13. Green, J.E., "Application of Head's Entrainment Method to the Prediction of Turbulent Boundary Layers and Wakes in Compressible Flow", RAE TR 72079, June 1972.

14. Green, J.E., Weeks, D.J. and Brooman, J.W.F., "Prediction of Turbulent Boundary Layers and Wakes in Compressible Flow by a Lag-entrainment Method", RAE TR 72231, 1973.

15. Myring, D.F. "An Integral Prediction Method for Three-dimensional Turbulent Boundary layers", RAE TR 70147, 1970

16. Lighthill, M.J., "On Displacement Thickness", Journal Fluid Mechanics, 1958, Volume. 4.

17. Veldman, A.E.P., "The Calculation of Incompressible Boundary Layers with Strong Interaction", AGARD-CP-291, 1980, PAPER 12.

18. Cross, A.G.T., "Separated Flow Calculations Involving Integral Boundary layer Methods and Quasi-simultaneous Coupling", Conference on "The Prediction and Exploitation of Separated Flow", R.Ae.S., London, April 1989.

19. Cook, P.H. McDonald, M.A. and Firmin, M.C.P., "Aerofoil RAE 2822 - Pressure Distributions, and Boundary Layer and Wake measurements", RAE TM AERO 1725, September 1977.

20. Richards, G., "Report on the Geometry and Wind Tunnel Models of Wing W4 and the Computed Mesh used in Various Computer Codes for Wing W4", ESDU International, Memorandum 70, January 1991.

21. Burton, K.W., "W4 Wing-body EJ63V Calculations", British Aerospace MA&A, Brough, Aerodynamics, internal memorandum No. FDD1/KWB21, Brough, March 1988.

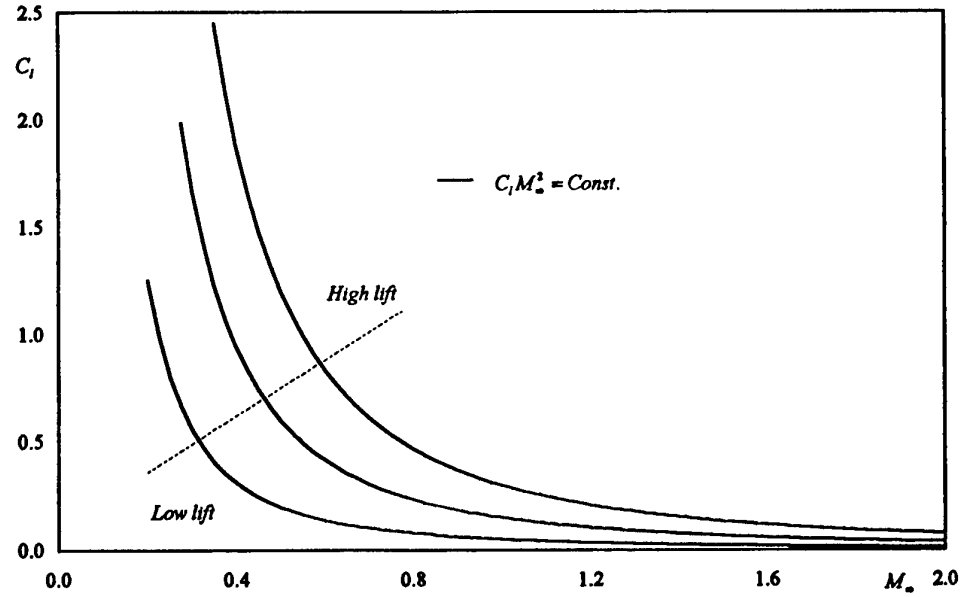


FIGURE 1. VARIATION OF LIFT COEFFICIENT WITH MACH NUMBER AT CONSTANT PRESSURE ALTITUDE AND CONSTANT LIFT.

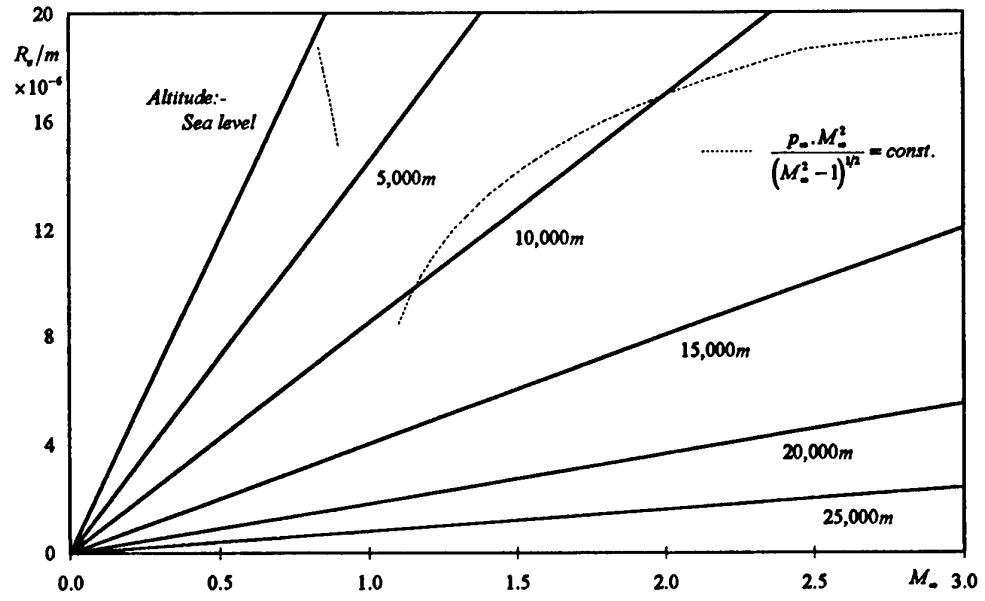


FIGURE 2. EFFECT OF ALTITUDE AND MACH NUMBER ON FLIGHT UNIT REYNOLDS NUMBER FOR THE INTERNATIONAL STANDARD ATMOSPHERE.

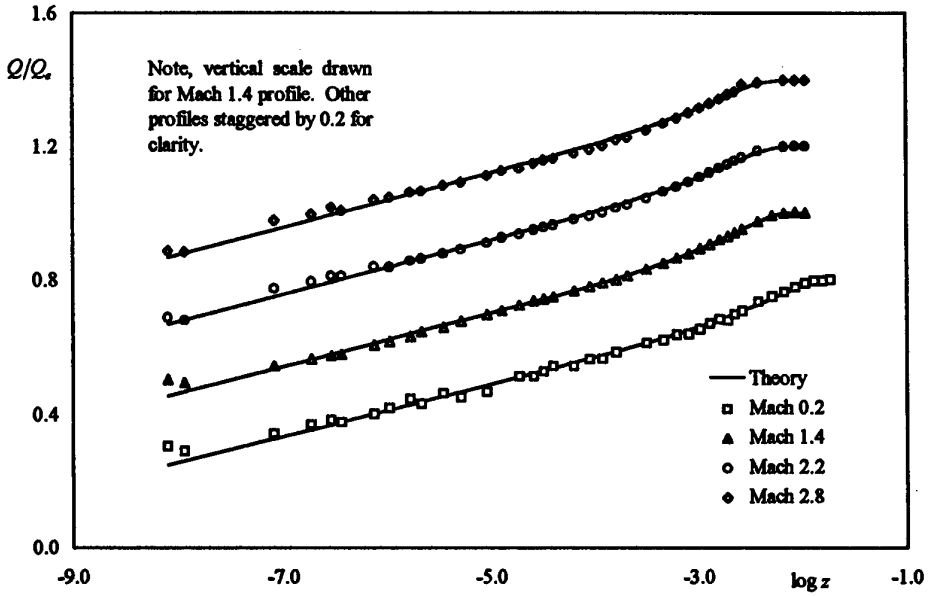


FIGURE 3a. TURBULENT VELOCITY PROFILES. COMPARISON BETWEEN EXPERIMENT AND THEORY FOR A REYNOLDS NUMBER OF 4×10^6 PER METER.

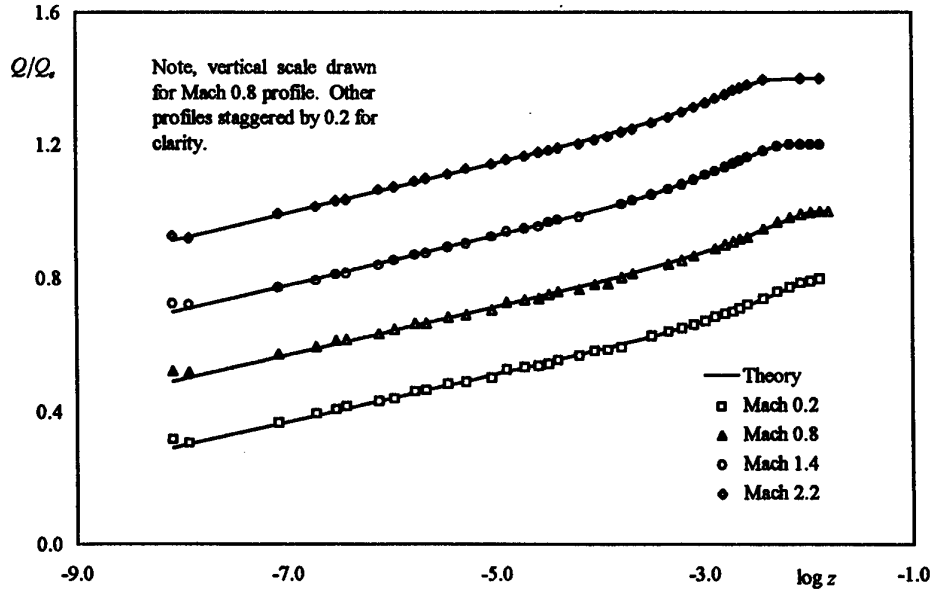


FIGURE 3b. TURBULENT VELOCITY PROFILES. COMPARISON BETWEEN EXPERIMENT AND THEORY FOR A REYNOLDS NUMBER OF 13×10^6 PER METER.

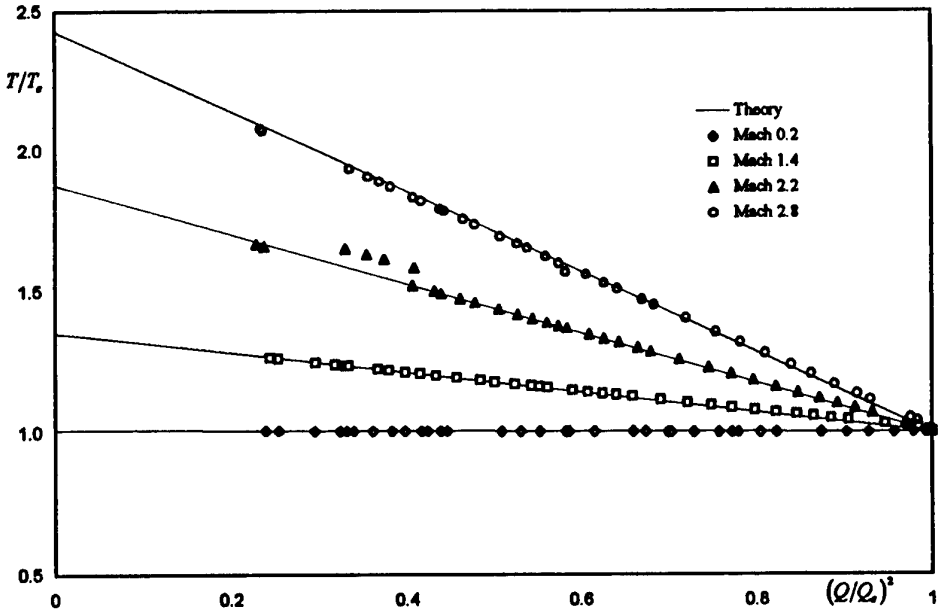


FIGURE 4a. BOUNDARY LAYER TEMPERATURE-VELOCITY RELATION FOR AN ADIABATIC WALL AND ZERO PRESSURE GRADIENT. REYNOLDS NUMBER 4 x 10^6 PER METER.

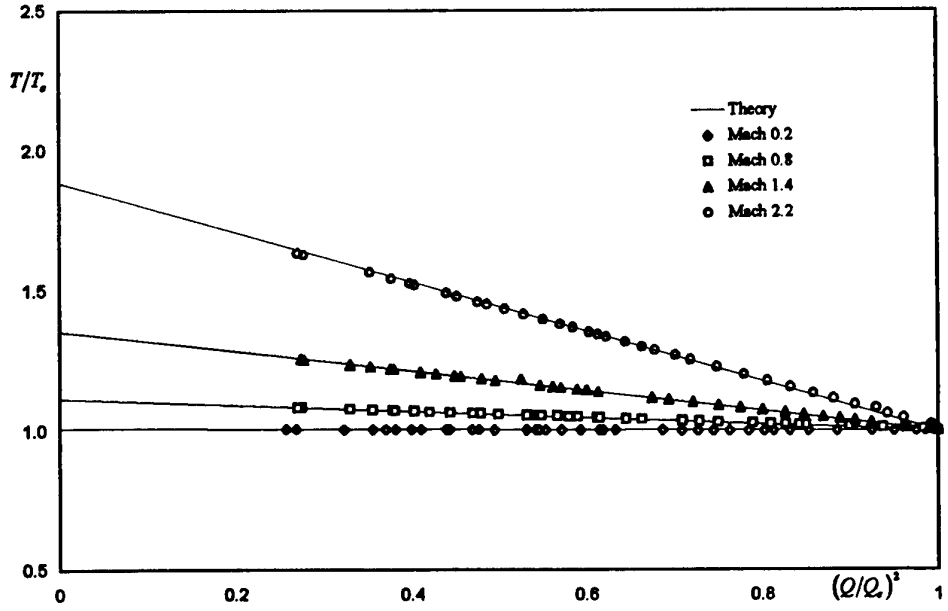


FIGURE 4b. BOUNDARY LAYER TEMPERATURE-VELOCITY RELATION FOR AN ADIABATIC WALL AND ZERO PRESSURE GRADIENT. REYNOLDS NUMBER 13 x 10^6 PER METER.

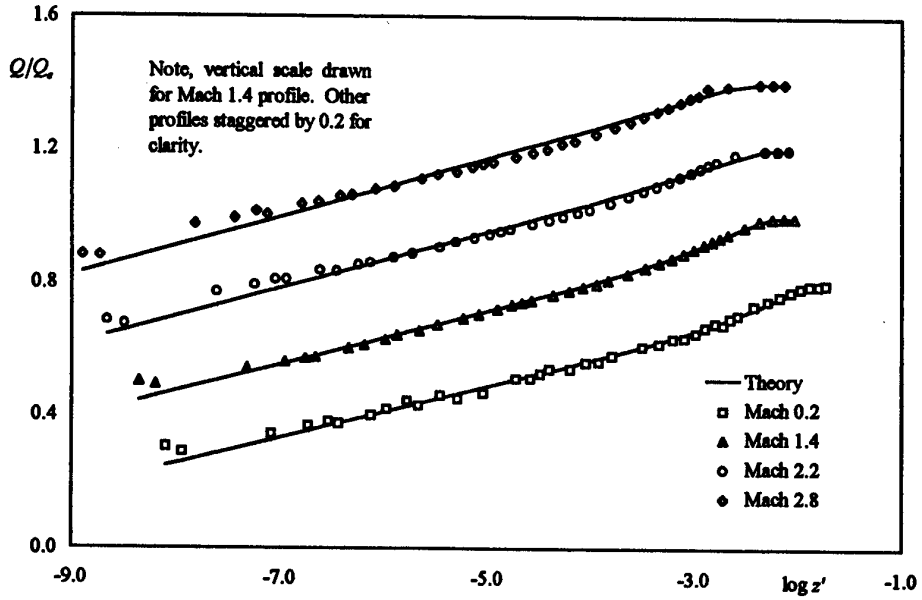


FIGURE 5a. TRANSFORMED TURBULENT VELOCITY PROFILES. COMPARISON BETWEEN EXPERIMENT AND THEORY FOR A REYNOLDS NUMBER OF 4 x 10^6 PER METER.

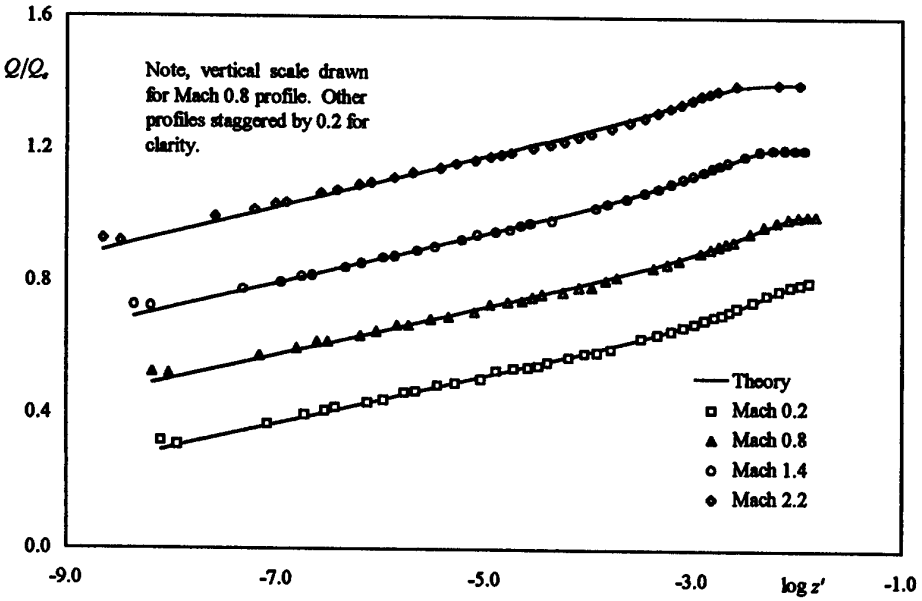


FIGURE 5b. TRANSFORMED TURBULENT VELOCITY PROFILES. COMPARISON BETWEEN EXPERIMENT AND THEORY FOR A REYNOLDS NUMBER OF 13 x 10^6 PER METER.

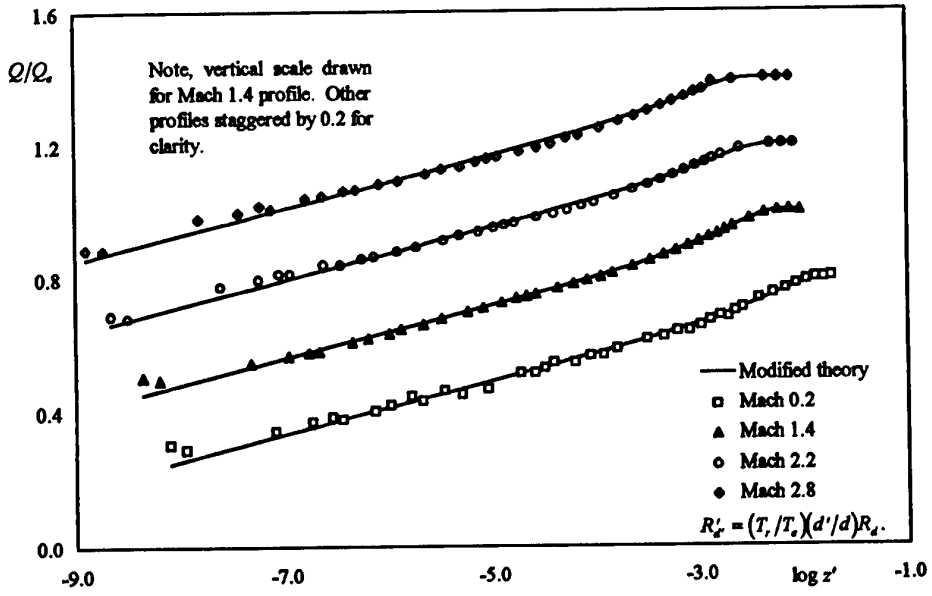


FIGURE 6a. TRANSFORMED TURBULENT VELOCITY PROFILES. COMPARISON BETWEEN EXPERIMENT AND THEORY FOR A REYNOLDS NUMBER OF 4 x 10^6 PER METER.

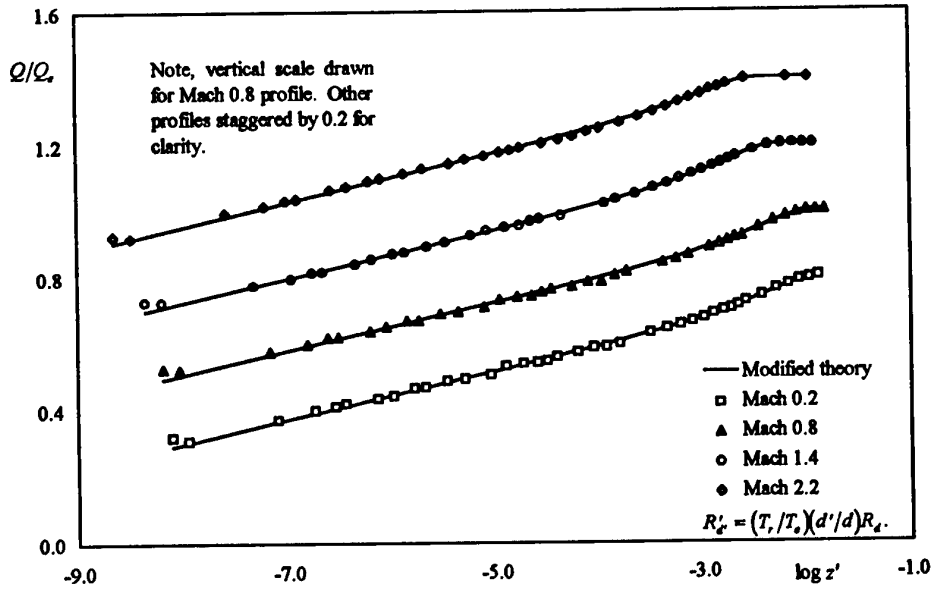


FIGURE 6b. TRANSFORMED TURBULENT VELOCITY PROFILES. COMPARISON BETWEEN EXPERIMENT AND THEORY FOR A REYNOLDS NUMBER OF 13 x 10^6 PER METER.

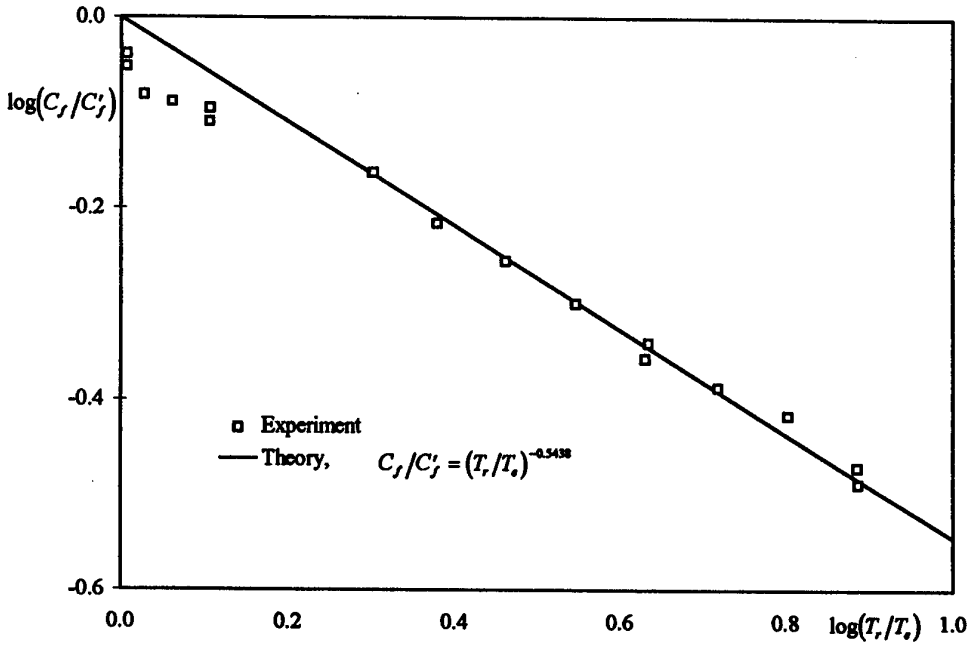


FIGURE 7a. COMPRESSIBILITY TRANSFORMATION FOR SKIN FRICTION COEFFICIENT BASED ON RECOVERY TEMPERATURE TO FREE STREAM TEMPERATURE RATIO.

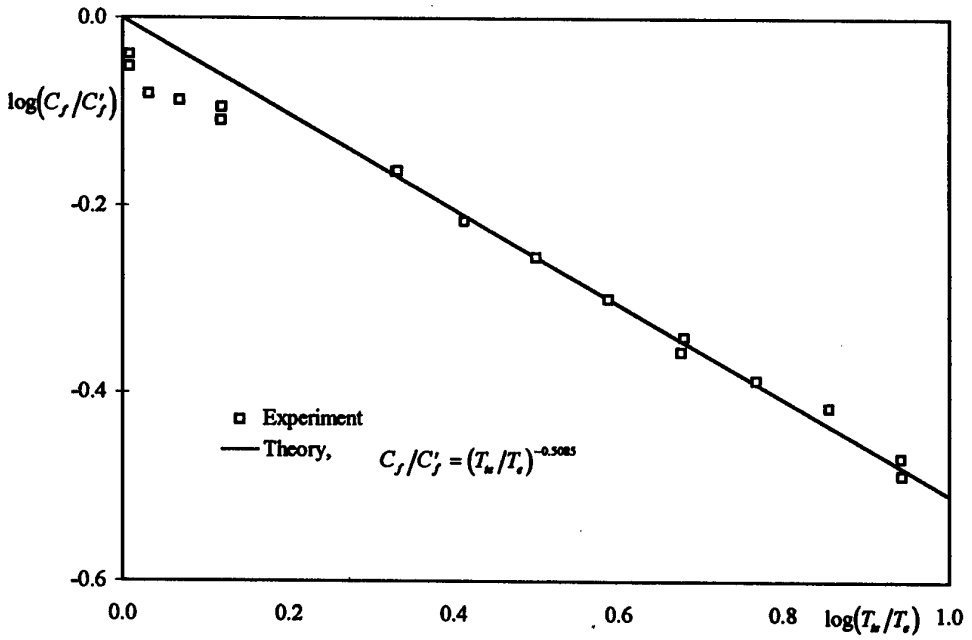


FIGURE 7b. COMPRESSIBILITY TRANSFORMATION FOR SKIN FRICTION COEFFICIENT BASED ON FREE STREAM TOTAL TO STATIC TEMPERATURE RATIO.

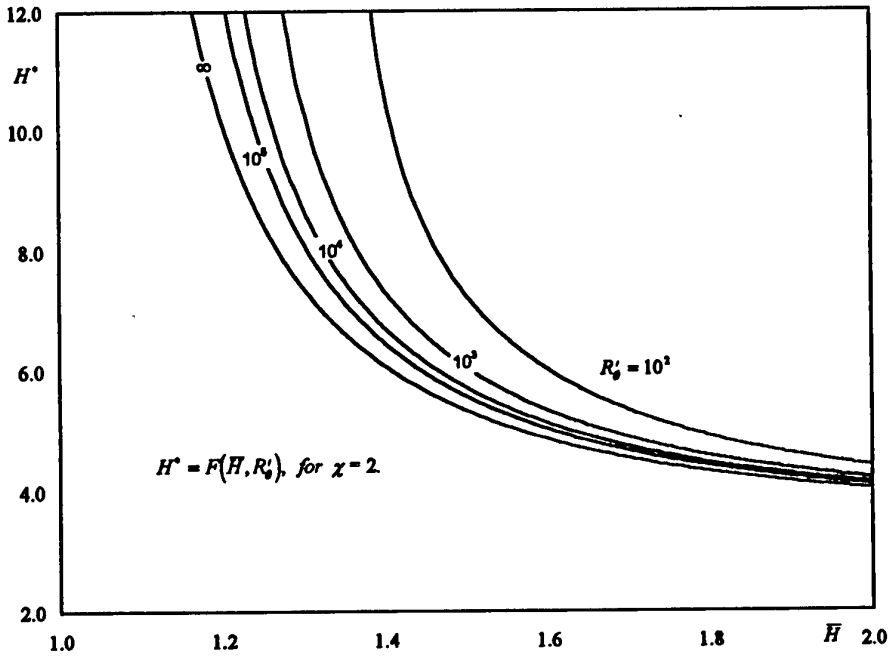


FIGURE 8. SHAPE PARAMETER RELATION FOR EQUILIBRIUM FLOW.

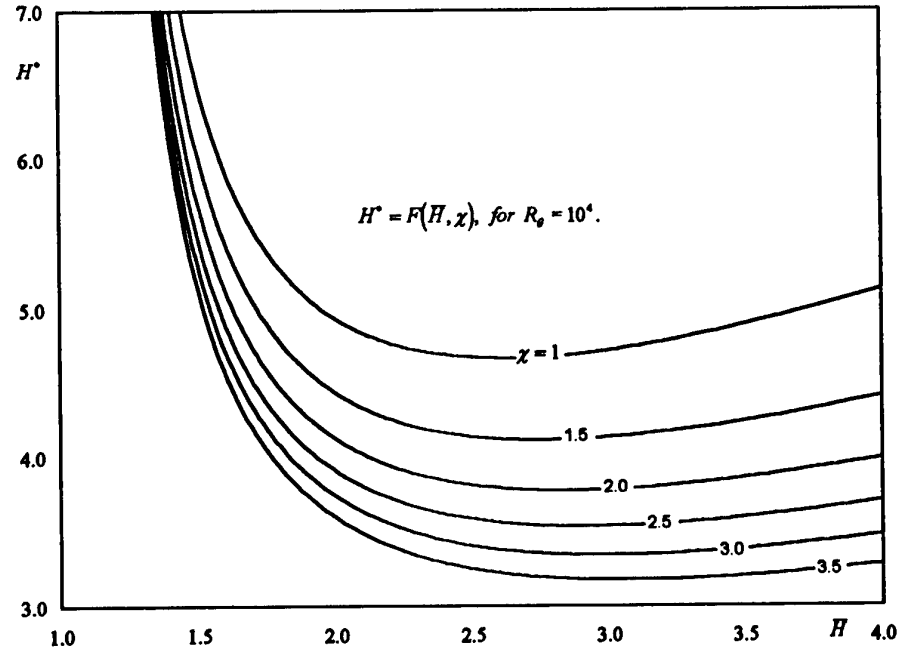


FIGURE 9. EFFECT OF WAKE DISTORTION ON THE SHAPE PARAMETER RELATION.

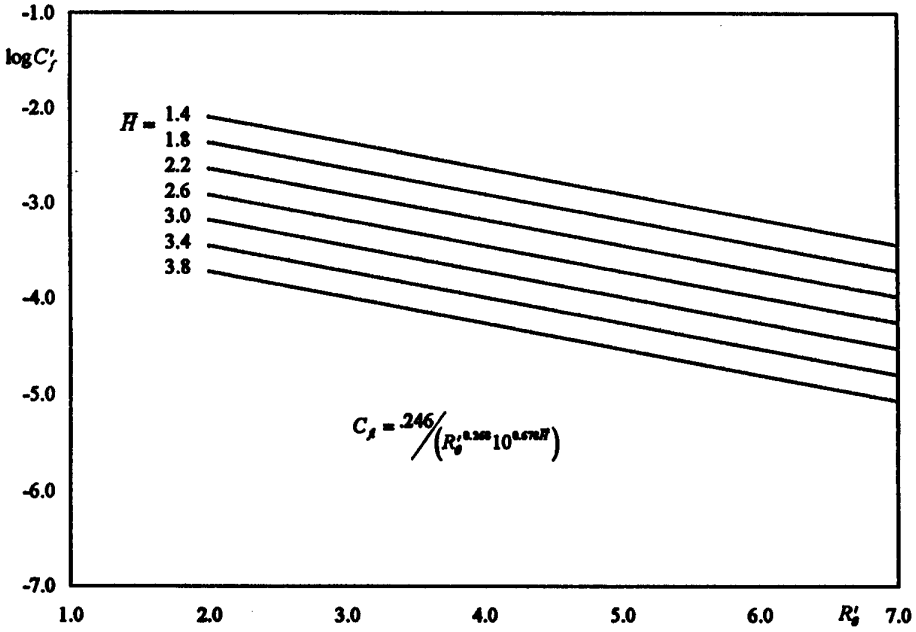


FIGURE 10. LUDWIEG-TILLMAN SKIN FRICTION RELATION.

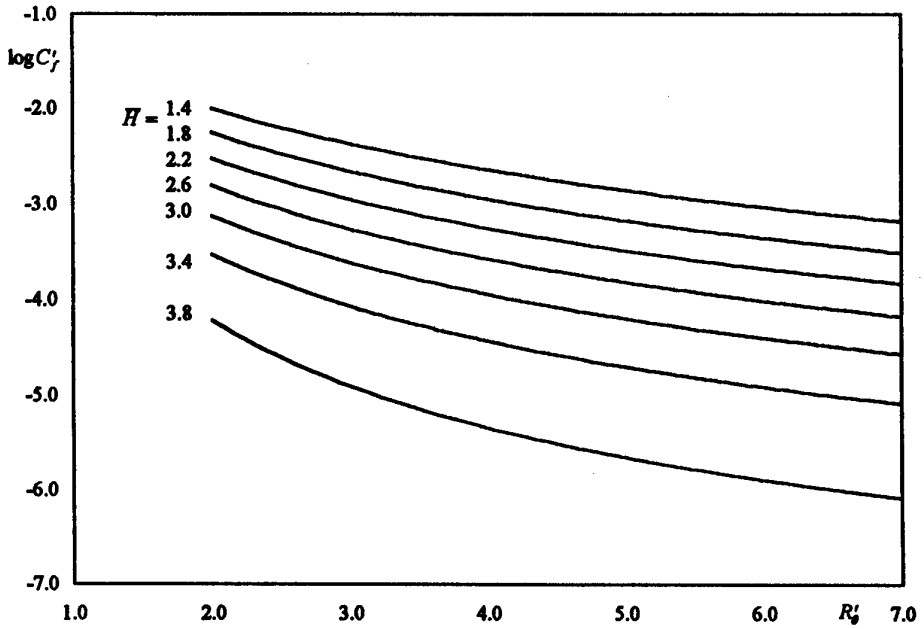


FIGURE 11. LAW OF THE WALL AND WAKE SKIN FRICTION RELATION FOR EQUILIBRIUM FLOW.

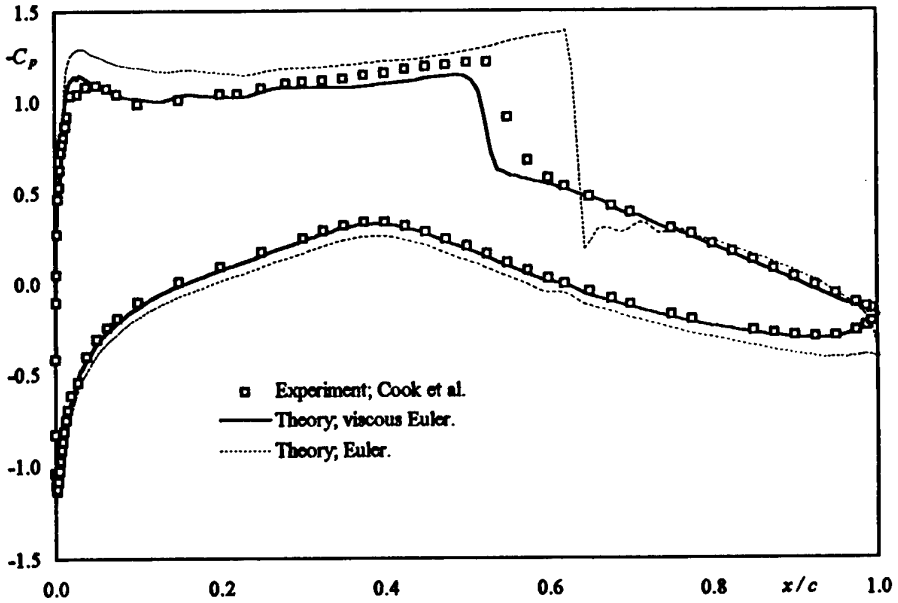


FIGURE 12a. COMPARISON OF INVISCID EULER AND VISCOUS EULER WITH EXPERIMENT FOR THE RAE 2822 AEROFOIL. CASE 6; MACH NUMBER 0.725, REYNOLDS NUMBER 6.5 x 10^6.

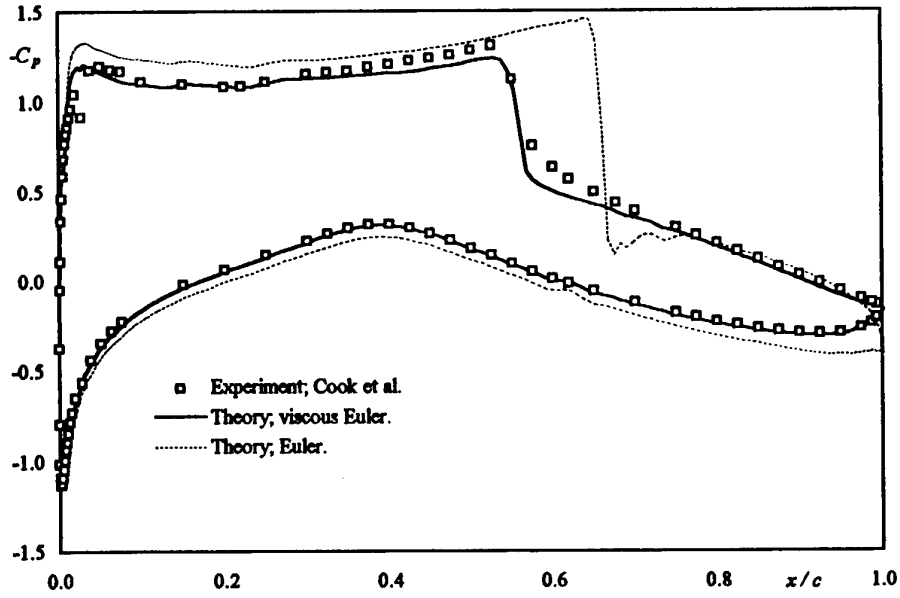


FIGURE 12b. COMPARISON OF INVISCID EULER AND VISCOUS EULER WITH EXPERIMENT FOR THE RAE 2822 AEROFOIL. CASE 9; MACH NUMBER 0.73, REYNOLDS NUMBER 6.5 x 10^6.

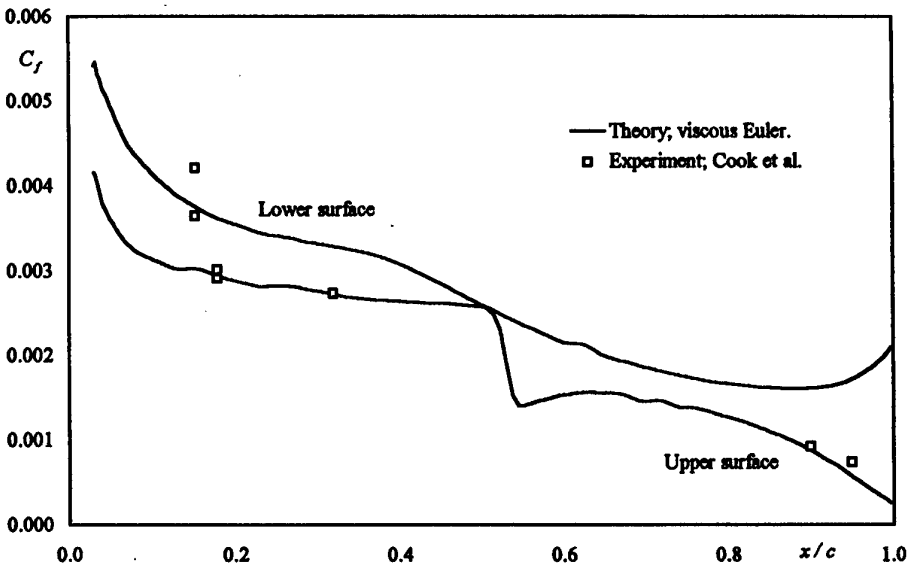


FIGURE 13a. VISCOUS EULER BOUNDARY LAYER SOLUTION COMPARED WITH EXPERIMENT FOR THE RAE 2822 AEROFOIL. CASE 6; MACH NUMBER 0.725, REYNOLDS NUMBER 6.5 x 10^6.

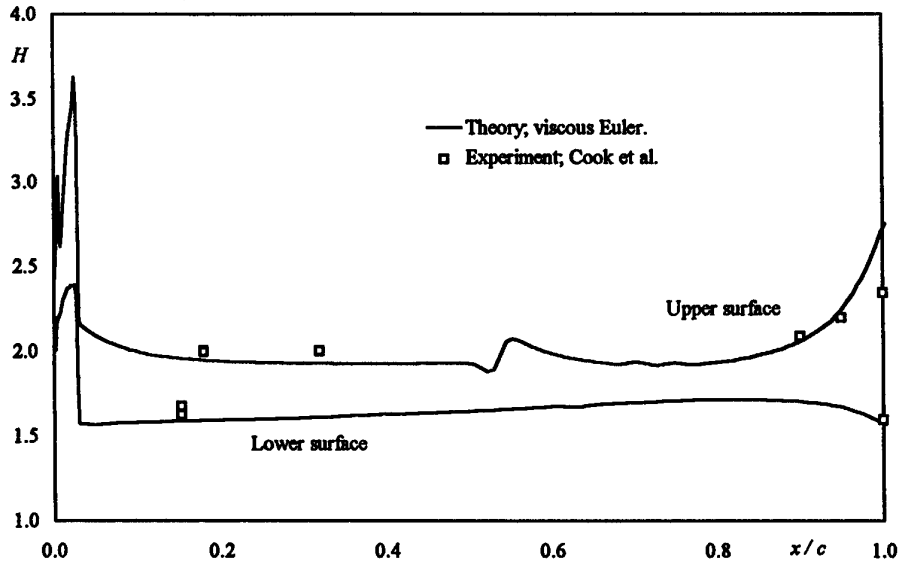


FIGURE 13b. VISCOUS EULER BOUNDARY LAYER SOLUTION COMPARED WITH EXPERIMENT FOR THE RAE 2822 AEROFOIL. CASE 6; MACH NUMBER 0.725, REYNOLDS NUMBER 6.5 x 10^6.

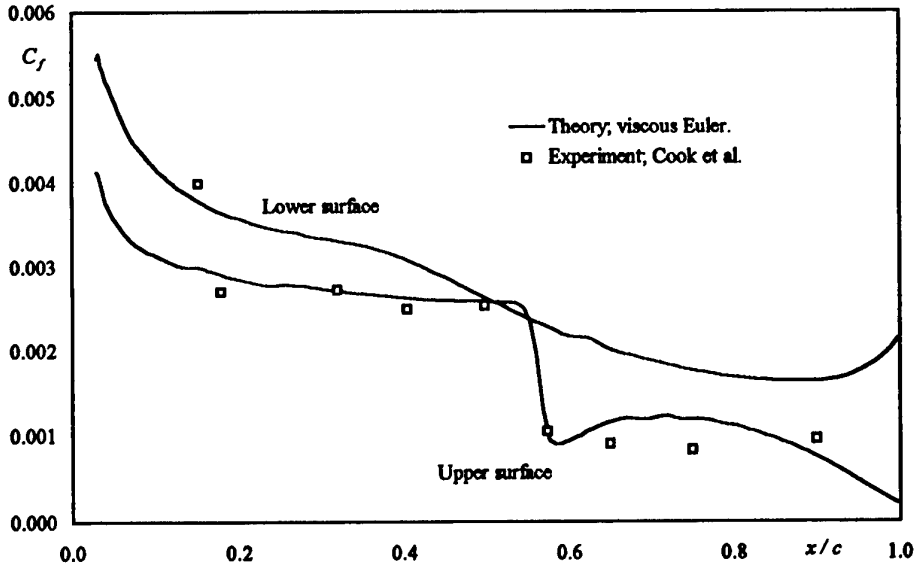


FIGURE 14a. VISCOUS EULER BOUNDARY LAYER SOLUTION COMPARED WITH EXPERIMENT FOR THE RAE 2822 AEROFOIL. CASE 9; MACH NUMBER 0.73, REYNOLDS NUMBER 6.5 x 10^6.

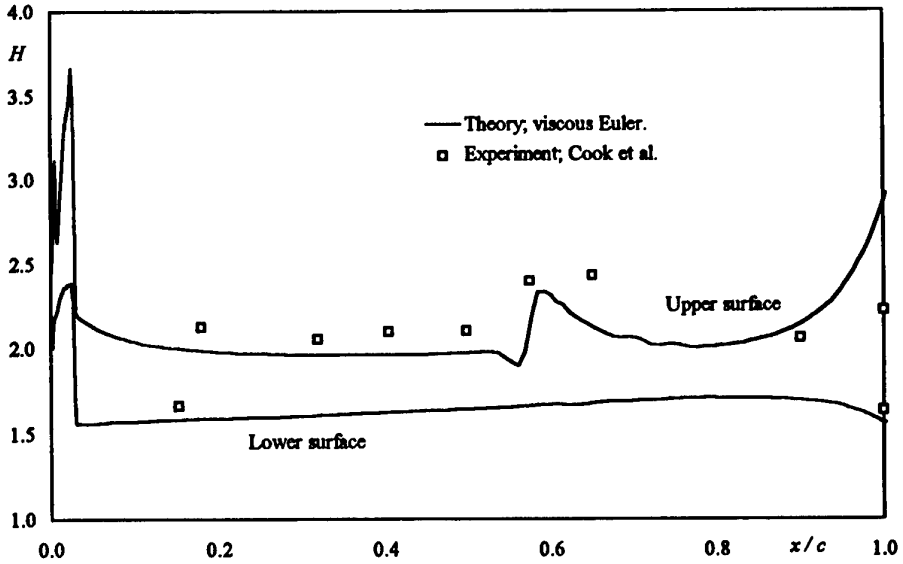


FIGURE 14b. VISCOUS EULER BOUNDARY LAYER SOLUTION COMPARED WITH EXPERIMENT FOR THE RAE 2822 AEROFOIL. CASE 9; MACH NUMBER 0.73, REYNOLDS NUMBER 6.5 x 10^6.

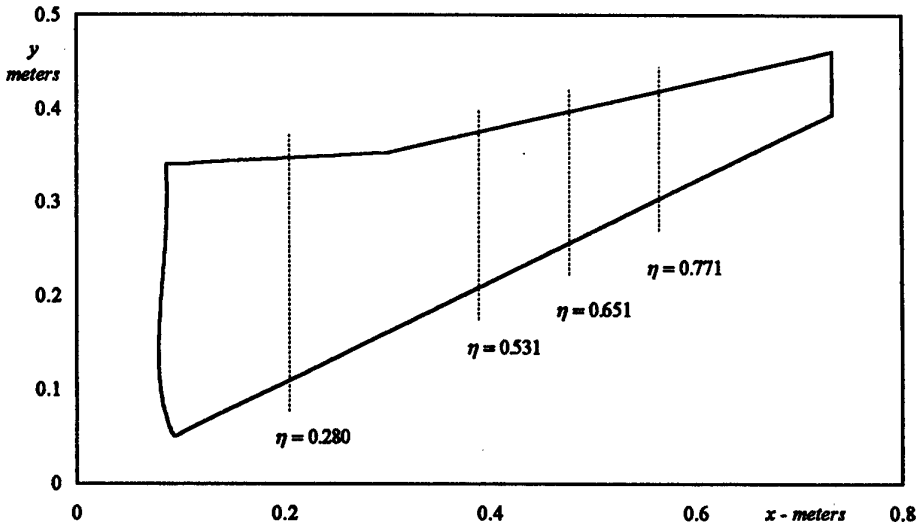


FIGURE 15. PLAN FORM OF W4 WING SHOWING PRESSURE MEASUREMENT STATIONS.

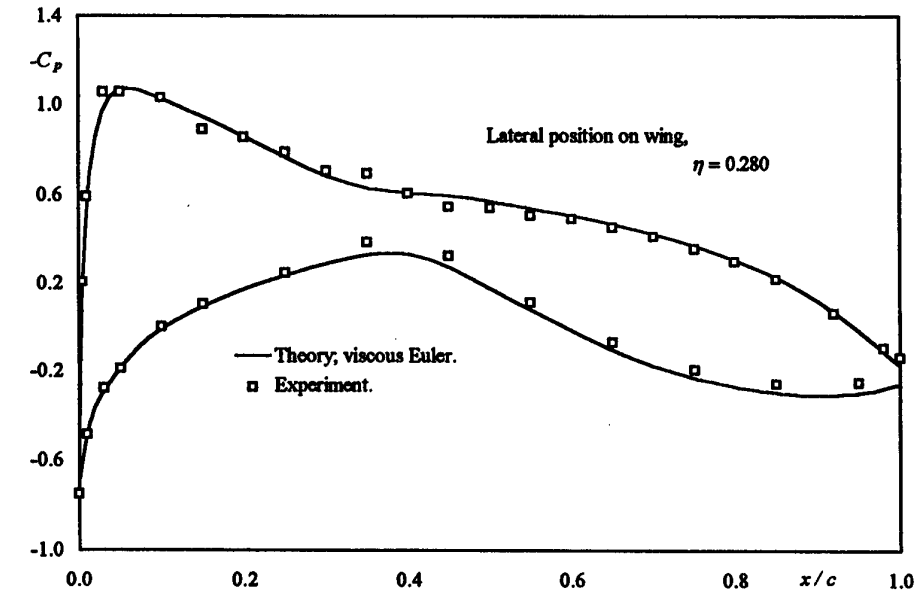


FIGURE 16a. COMPARISON OF VISCOUS EULER AND EXPERIMENT FOR THE W4 WING. INCIDENCE 0.52 DEGREES, MACH NUMBER 0.78, REYNOLDS NUMBER 8.5 x 106.

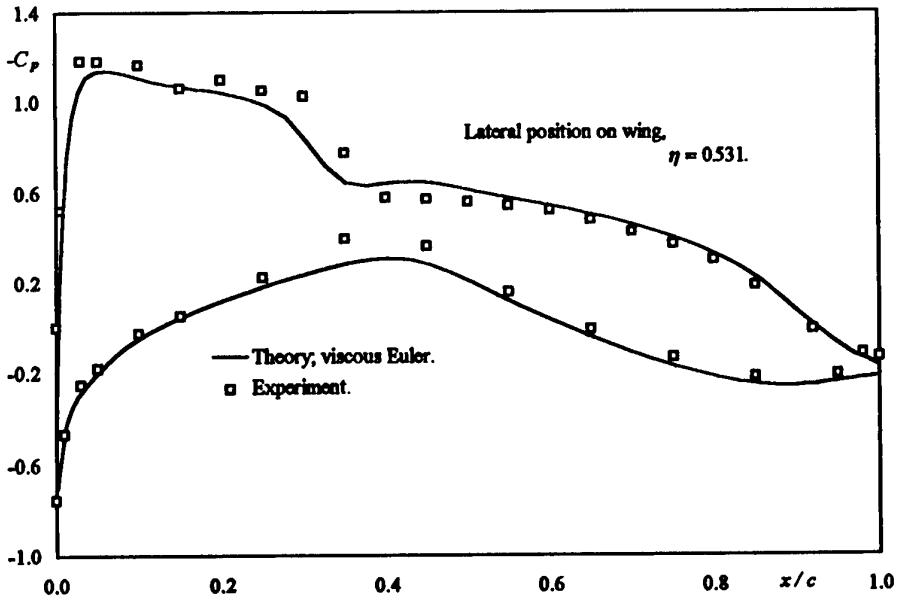


FIGURE 16b. COMPARISON OF VISCOUS EULER AND EXPERIMENT FOR THE W4 WING. INCIDENCE 0.52 DEGREES, MACH NUMBER 0.78, REYNOLDS NUMBER 8.5 x 106.

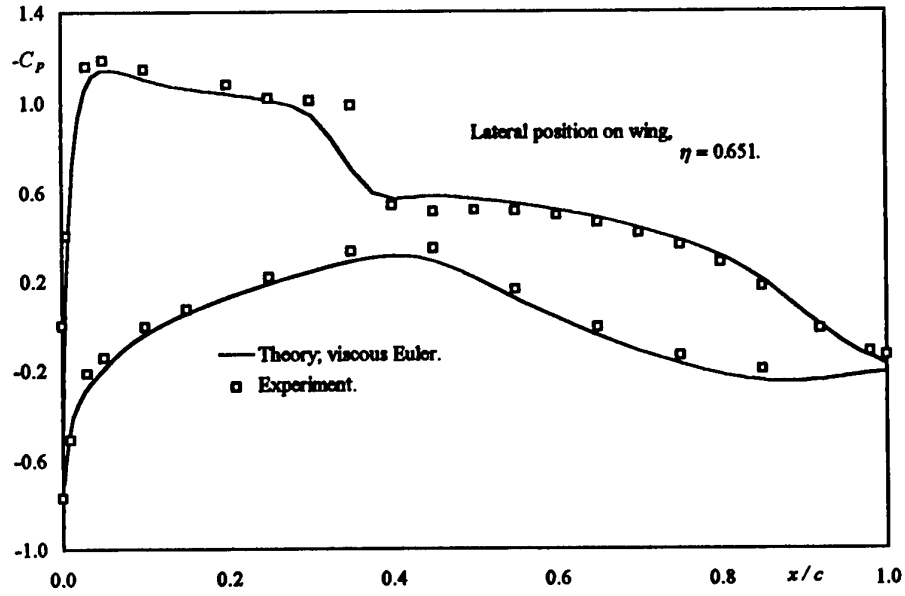


FIGURE 16c. COMPARISON OF VISCOUS EULER AND EXPERIMENT FOR THE W4 WING. INCIDENCE 0.52 DEGREES, MACH NUMBER 0.78, REYNOLDS NUMBER 8.5 x 106.

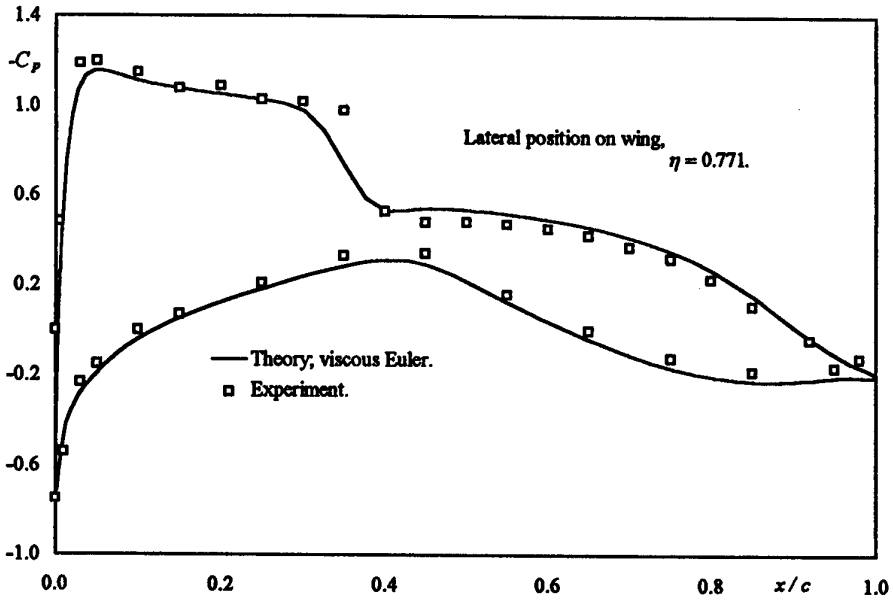


FIGURE 16d. COMPARISON OF VISCOUS EULER AND EXPERIMENT FOR THE W4 WING. INCIDENCE 0.52 DEGREES, MACH NUMBER 0.78, REYNOLDS NUMBER 8.5 x 106.

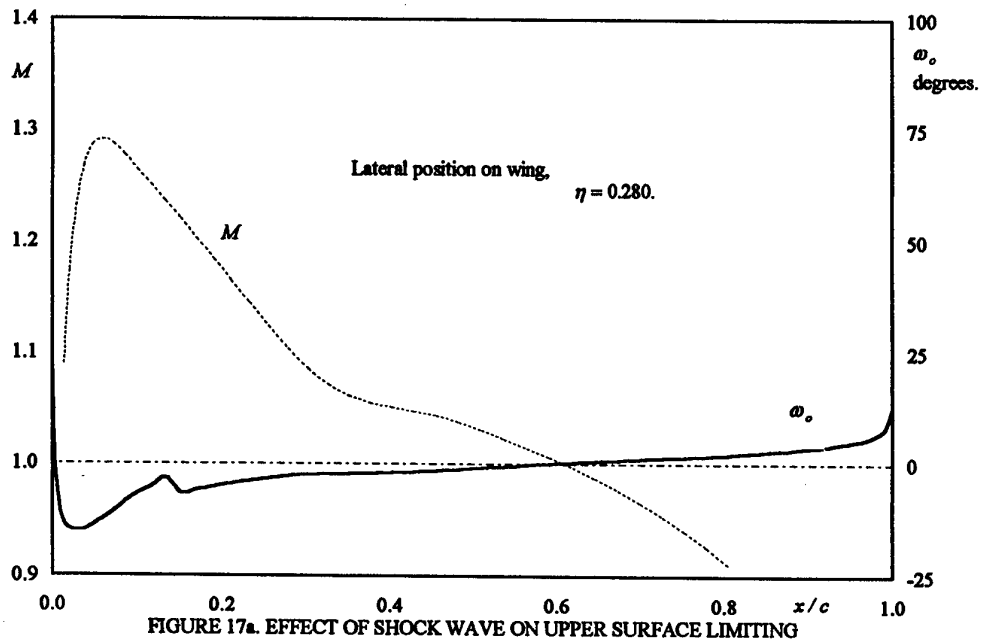


FIGURE 17a. EFFECT OF SHOCK WAVE ON UPPER SURFACE LIMITING STREAMLINE DEVELOPMENT FOR THE W4 WING.

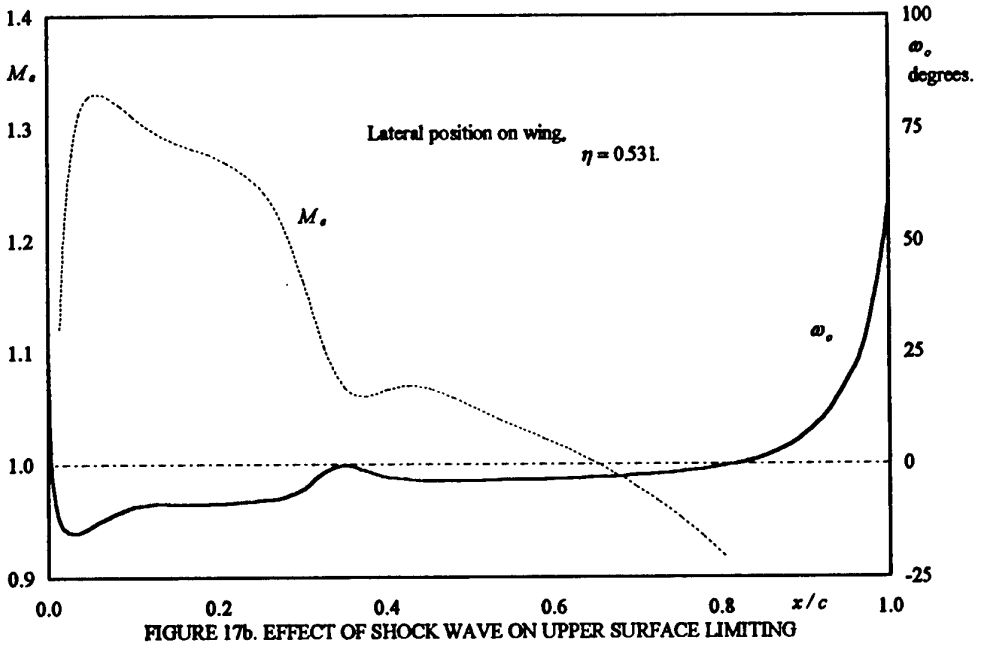


FIGURE 17b. EFFECT OF SHOCK WAVE ON UPPER SURFACE LIMITING STREAMLINE DEVELOPMENT FOR THE W4 WING.

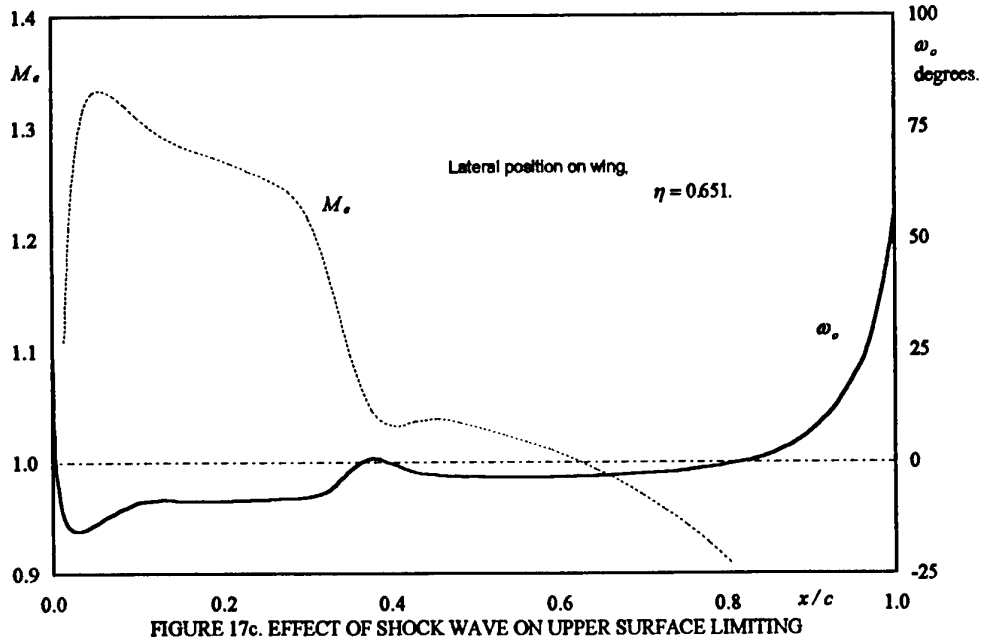


FIGURE 17c. EFFECT OF SHOCK WAVE ON UPPER SURFACE LIMITING STREAMLINE DEVELOPMENT FOR THE W4 WING.

COMPLEX EXPERIMENTAL STUDIES OF SST.

PART I. AERODYNAMICS OF INDIVIDUAL ELEMENTS

by

A.M. KHARITONOV

Institute of Theoretical and Applied Mechanics SB RAS (ITAM SB RAS), Instituskaya 4/1, Novosibirsk, 630090 Russia

Introduction.

The achievement of aerodynamic perfection of supersonic flying vehicles is determined to a large extent by the depth of understanding of aerodynamics of the main aircraft elements and the optimum use of aerodynamic interference of individual elements: wing, fuselage (airframe), engine nacelle, and other superstructures. A successful solution of these problems requires the study of regularities of three-dimensional flow around the developed geometric configurations, which is characterized at supersonic speeds by the presence of shock waves and expansion fans, and by their interaction with each other and with boundary layers. In most cases, these interactions involve multiple separations and reattachments of boundary layers, the size and position of separation regions are determined by the body geometries, flight conditions, and/or relative positions of the bodies in space.

These problems form one of the basic experimental research directions of the Aerodynamics Laboratory of the Institute of Theoretical and Applied Mechanics SB RAS. Vast experimental information has been accumulated on the flow around both schematic configurations of promising flying vehicles and models of specific aircraft under development. All experiments were conducted in the supersonic wind tunnel T-313 of ITAM SB RAS equipped with specially developed devices, methodology, and software for the study of interference of various aircraft elements. The wind tunnel T-313 of our Institute is a blowdown tunnel with square test section (size 0.6x0.6 m) and Mach number range from 2 to 6. A sketch of the wind tunnel and the main parameters are demonstrated in Fig. 1. The region of Reynolds number modeling is shown here with regard for all constructive restrictions.

A multiple statistical analysis for various Mach numbers allows one to characterize the nonuniformity of the field of velocities in the zone of model location for the last twenty-five years of the wind tunnel performance. The nonuniformity degree of the field of velocities in the test section is maintained at a level not exceeding 0.5% (Fig.2).

Multiple measurements of accuracy reference models as against the similar data obtained in various wind tunnels: VKF, ONERA, DLR, etc. are demonstrated in Figs. 3 and 4.

The present lecture is devoted to various aspects of HSCT aerodynamics which yield a notion of versatility and complexity of experiments and obtained results. Apart from their own significance, these results are of interest for verification of the computational fluid dynamics (CFD) models and methods.

All experimental investigations obtained in the Aerodynamics Laboratory of ITAM SB RAS were initiated and supported by the Aerodynamics Department of the Tupolev Aviation Company.

The authors of this paper are the ITAM scientists Dr. M.Brodetsky, Dr. V.Kornilov, Dr. A.Zheltovodov, and me.

List of symbols.

x,y,z	Cartesian coordinates
M_∞	freestream Mach number
Re	freestream Reynolds number
Re_x	Reynolds number based on the x ditance
Re_δ	Reynolds number based on the boundary layer thickness.
$C_P=(P-P_\infty)/q$	pressure coefficient
q	dynamic pressure
P	static pressure
P_0'	stagnation pressure behind the shock-wave

Paper presented at the RTO AVT Course on "Fluid Dynamics Research on Supersonic Aircraft", held in Rhode-Saint-Genèse, Belgium, 25-29 May 1998, and published in RTO EN-4.

Cy normal force coefficient

m_z pitching moment coefficient

Cx_{min} minimum drag coefficient

Cx_u induced wave drag coefficient

ΔCy increment of the lift coefficient

ΔCx_u increment of the induced wave drag coefficient

ΔK_u^n increment of the lift-to-drag coefficient

ΔK_{max} maximum gain of the lift-to-drag coefficient

$\Delta = \frac{C_x^f - C_x^{n.f.}}{C_x^f}$ gain of the induced wave drag coefficient

α angle of attack

$\Delta\alpha_M$ increment of local angle of attack

χ swept angles

$\bar{z} = z/\ell/2$ relative span distance

T_φ scale of the wing twist

T_f scale of the wing deformation

T_r recovery temperature

T_w wall temperature

u flow velocity

M_δ; Re_δ; u_δ based on the boundary layer thickness

$\xi = P_2/P_\infty$ shock wave intensity

R junction radius

h; h_A; h_B size of the 3D boundary layer area

δ_B/δ_A relation of the boundary layer thickness on the corner faces

ω_x vorticity of fluid

σ root-mean-square deviation

AERODYNAMIC CHARACTERISTICS OF NON-FLAT WINGS.

It is known that one of the methods of increasing the lift-to-drag ratio of HSCT is the choice and optimization of non-flat wings. A non-flat lifting surface is usually understood as the curvature of the medium lines of wing and fuselage profiles, transverse cambers of the wing and its geometric twist. The distribution of the initial profile thickness should be retained. Multiple numerical and experimental studies [1-8] showed that a non-flat lifting surface allows one to increase the lift-to-drag ratio by decreasing the inductive-wave drag and the losses for aerodynamic balancing. Various numerical methods of optimization of such wings are either confined to consideration of a specific class of surfaces or ignore the gas viscosity and wing thickness, or do not allow for realization of the optimum lift force distribution. It is also very difficult to determine experimentally the optimum parameters of wing deformation and twist. However, on the basis of numerical calculations it is possible to perform a parametric study of the characteristics of non-flat wings in a certain class of surfaces. Such an approach developed in [5, 6] is considered below.

The authors suggested an original method and studied experimentally the distributed aerodynamic characteristics of five isolated wings with equal shape and planform area (Fig. 5). Wing 2 is a flat one, and the remaining wings differ from it only by the type and scale of mid-surface deformation. The local angles of attack of the mid-surface of wing 1 are determined by a six-order parametric polynomial of the form

$$\alpha = a_{\infty} + a_{10}\cdot x + a_{11}\cdot x\cdot|z| + a_{20}\cdot x^2 + a_{01}\cdot|z| + a_{02}\cdot z^2$$

The coefficients of this polynomial were calculated by solving the inverse variational problem using the method [3] from the condition of obtaining the minimum inductive-wave drag for specified values of the Mach number M=2, lift force coefficient Cy=0.1 and pitching moment m_z=0.005. The law of profile mid-surface variation for a number of cross-sections of this wing and the spanwise twist are presented in Figs. 6 and 7. The scale coefficients of wing deformation are listed in Table 1.

Table 1.

Wing	1	2	3	4	5
T_φ	1	0	1	0	0
T_f	1	0	0	1	0.5

Here wing 2 is a flat one with a symmetric parabolic profile. Wing 3 and 4 are obtained by separating the deformation components (twist and camber) of the mid-surface of wing 1. Wing 5 has the same type of deformation as wing 4, but a different scale. The non-flat wings have the same distribution of profile thickness as the flat wing. The twist axis of wings 1 and 3 in each cross-section passes through the leading edge.

To study the conditions of forming the gain in inductive-wave drag due to mid-surface deformation, the static pressure distributions were measured on all the wings [9]. In doing so, the pressure was measured on the lower surface on one half of the wing and on the upper surface on the other half. A scheme of pressure taps is shown in Fig. 5. The tests were performed for M=2.03 and $Re_1=26\cdot10^6$ m^{-1} within the range Cy=0-0.35. The root-mean-square error of the pressure coefficient Cp is $\sigma_{Cp}=0.02$, and the difference in these coefficients in the corresponding points of flat and non-flat wings is estimated as $\sigma_{Cp}=0.01$. Reliability of the obtained results is also confirmed by the comparison of integral characteristics of the examined wings obtained on the basis of pressure distribution measurements and balance tests. These data are presented in Fig. 8 as inductive polars. The same figure shows the computational results [7]. It is seen that in the range $Cy\le0.15$ the results of balance and pressure measurement tests are in reasonable agreement. At higher values of Cy, the inclination angle of pressure polars is slightly larger than that of balance polars. The calculated polars are in satisfactory agreement with the balance results in a wider range of Cy, though they have a slightly larger angle, too. The calculated values of Cx_{min} are by 0.0005 smaller for wing 1 and by 0.0004 larger for wing 4 than those obtained by the balance and pressure measurement methods.

Figure 9 shows the curves of the relative decrease in inductive-wave drag of non-flat wings 1 and 4 in comparison with a flat wing Δ for an equal lift force. The characteristics $\Delta(Cy)$ obtained from the balance and pressure measurements are in fairly good agreement with each other. This allows one to use the pressure measurement results for a more detailed analysis aimed at studying the mechanism of decreasing inductive-wave drag due to mid-surface deformation.

The influence of the mid-surface camber on the local aerodynamic characteristics is analyzed in [6] by using the increments of aerodynamic characteristics with respect to the corresponding values for a flat wing. Thus, for various cross-sections $\bar{z}$ of the wings under consideration it is possible to study and compare the chordwise distribution of the following increments: local angles of attack $\Delta\alpha_M(\bar{x})$, local lift force coefficients $\Delta C_y^M(\bar{x})$, and inductive-wave drag $\Delta C_{x_u}^M(\bar{x})$, for the lower and upper surfaces separately and for the cross-section as a whole, for an angle of attack of the maximum lift-to-drag ratio α_{Km}. As an illustration, Figure 10 shows these curves for the cross-section $\bar{z}=0.8$, M=2.0, $\alpha=3°$. The open symbols refer to wing 4, and the closed symbols to wing 5. The circles indicate the corresponding increments of ΔCy and $\Delta C_{x_u}^M$, and the squares denote the increment of ΔK_u^n.

Since in each cross-section the dependence $\Delta\alpha_M(\bar{x})$ is the same for the upper and lower surfaces, being equal to the corresponding characteristic for the medium lines, we can confine ourselves to consideration of the functions $\Delta\alpha_M(\bar{x})$ only for the lower surface. The same figure shows the increments of the lift force coefficient $\Delta C_y^n(\bar{x})$ and inductive-wave drag $\Delta C_{x_u}^n(\bar{x})$ accumulated along the chord, which are integral characteristics of appropriate local increments. The accumulated increments of inductive-wave lift-to-drag ratio $\Delta K_u^n(\bar{x})$ can be considered in a similar way:

$$\Delta K_u^n(\bar{x}) = \left[\frac{C_y^n(\bar{x})}{C_x^n(\bar{x})}\right]^{n.f} - \left[\frac{C_y^n(\bar{x})}{C_x^n(\bar{x})}\right]^{f}.$$

On the whole, the increments of the local lift force values ΔC_y^M for non-flat wings are in agreement with the increments of the local angles of attack and decrease as the deformation scale decreases. The difference in ΔC_y^M and $\Delta C_{x_u}^M$ values caused by the deformation scale changes is small and lie within the experimental error for a considerable part of the wing planform area. This is especially typical of wing panels, where $\Delta\alpha_M$ due to deformation scale changes does not exceed 1°. The influence of deformation itself on the local characteristics is sufficiently reliable and has the same character for the wings under consideration. Thus, the local lift coefficients on the fore sections of non-flat wing profiles vary insignificantly despite considerably lower values of the local angle of attack in comparison with a flat wing. The lift force increases downstream on the remaining portion of the surface, where the increments $\Delta\alpha_M$ are positive. The analysis of integral characteristics $\Delta C_y^n(\bar{x})$ shows that this increase not only compensates for the lift force decrease on the

wing forebody, but also creates an additional lift, as compared with a flat wing.

The local coefficient of inductive-wave drag is determined by the value of $Cp \cdot \alpha$. Therefore, on those surface portions where $\Delta\alpha_M<0$ the inductive-wave drag of non-flat wings is smaller than that of a flat wing until the local angles of attack and pressure coefficients change the sign. This situation is realized on the lower surface of the fore section of the wing. Further downstream, where $\Delta\alpha>0$ and $\Delta C_y^M>0$, the drag of non-flat wings increases. On the upper surface in the nose part of root sections, despite large negative values of $\Delta\alpha_M$, the inductive-wave drag does not decrease in comparison with the flat wing and is even higher in sections $\bar{z}\leq 0.1$. This is explained by significant deformation which results in appearance of a negative lift force on these surface portions at an angle of attack α_{Km}, and the inductive-wave drag increases in comparison with a flat wing. On the wing panel ($\bar{z}>0.4$) on the upper surface of the fore section the gain in inductive-wave drag is also smaller for non-flat wings than on the lower one, despite lower values of the local lift coefficients. This is caused by the fact that the local angles of attack on these surface portions are close to zero when a flat wing is positioned at an angle of attack α_{Km}. Therefore, the deformation cannot yield a significant gain in inductive-wave drag and leads mainly to decreasing lift force. At the rear sections of wing panel profiles the increments $\Delta C_{x_u}^M$ on the upper surface are much larger than on the lower surface for almost equal values of ΔC_y^M. This is related to the fact that at an angle of attack α_{Km} a negative lift force is realized on the lower surface of the wing panel in the rear sections of wing profiles where the local angles of attack are close to zero. For non-flat wings the Cp coefficients in this region are positive but small in magnitude. As a result, the local values of $C_{x_u}^M$ and $\Delta C_{x_u}^M$ are close to zero in the both cases. The lift force on the upper surface in this region is positive both for flat and deformed wings, being larger for the latter. But the local angles of attack are also larger here. As a result, with an equal change in the lift force, the drag force on the lower surface in the rear sections of wing panels of non-flat wings remains practically the same as for a flat wing and increases on the upper surface.

The considered peculiarities of the distribution of local characteristics become more explicit if we examine the integral increments ΔC_y^n, ΔC_x^n, and ΔK_u^n. Thus, the lift force on the lower surface of non-flat wings starts to increase in comparison with a flat wing practically from the leading edge. At the same time, the inductive-wave drag increases more slowly than ΔCy because of negative ΔCx_u values on the fore sections of the profile and above-considered peculiarities of the rear sections. This results in a higher inductive-wave lift-to-drag ratio of the lower surface of examined wings than for a flat wing, except for the root sections of wing 4. The inductive-wave drag on the upper surface increases more substantially than the lift force, which yields a lower lift-to-drag ratio than a flat wing. Hence, the obtained gain in inductive-wave drag for the wings under consideration at $Cy=Cy_{Km}$ is provided by the lower surface and formed in the fore and rear sections of the profiles.

A decrease in deformation scale on the whole leads to a decrease of the increments of the considered characteristics. As a result, both the gains and losses in inductive-wave drag decrease in comparison with a flat wing. Hence, the gain in the maximum lift-to-drag ratio for wing 5 in comparison with a flat wing is ensured by the lower surface.

To determine the overall effect of the upper surface on the value of Δ_{Km} a combined wing was considered, whose lower surface corresponds to wing 5 and its upper surface corresponds to the flat wing 2. It was assumed that the pressure distribution on the combined wing is the same as on the corresponding surfaces of wings 2 and 5. The calculation of integral characteristics of this wing using experimental pressure coefficients showed that the gain in the maximum lift-to-drag ratio for this wing, as compared with a flat wing (taking into account the friction drag), is $\Delta_{Km}=0.6$. To check this result, wing 6 was experimentally studied. The lower surface of this wing corresponds to wing 5, and the upper surface to wing 2. A comparison of the lift-to-drag ratio for wings 2, 5, and 6 versus the lift coefficient is shown in Fig. 11. Indeed, the gain in the maximum lift-to-drag ratio for wing 5 is $\Delta_{Km}=0.23$, as compared with a flat wing, and the corresponding value for wing 6 is $\Delta_{Km}=0.45$. Thus, the value of Δ_{Km} realized on this wing is by 0.15 smaller than predicted in calculations. This

disagreement can be caused by the fact that the condition of independent flow past the upper and lower wing surfaces is not fully fulfilled and, probably, by the pressure measurement errors on wings 2 and 5. For Cy>0.15 the lift-to-drag ratio of wing 6 is lower than that of wing 5. This confirms the above mentioned peculiarity that the gain in aerodynamic efficiency of deformed wings at large values of Cy occurs due to more effective operation of the upper surface.

Thus, the presented results show that the gain in aerodynamic efficiency obtained by cambering the medium surface, as compared with a flat wing, are mainly ensured by the lower surface. This indicates that symmetric airfoils with low wave drag in combination with a deformed medium surface are not probably optimum from the viewpoint of the minimum inductive-wave drag. Hence, the wing surface should be optimized with regard for wing thickness. It is reasonable to consider the upper and lower surfaces separately, preserving a prescribed wing volume or the maximum wing thickness. Such an approach can ensure an additional gain in aerodynamic efficiency in comparison with a flat wing.

On the whole, an original method of analysis [6] of the distributions of local and integral characteristics of wings with different deformation of the medium surface is demonstrated here, which allows for a deeper understanding of the conditions of formation of the gain in inductive-wave lift-to-drag ratio. Appropriate recommendations for designing HSCT wings have been worked out on the basis of this method.

THE FLOW AROUND BOUNDARY LAYER DIVERTERS

It is known that the improvement of inlet characteristics of engine nacelles located on wing surfaces is achieved by mounting them on boundary layer diverters (Fig. 12). Since arrangement solutions of this kind are usually accompanied by a considerable increase in aircraft drag, a search for diverter configurations with minimum drag is demanded. The flows around such diverters are accompanied by 3D flow separation extending to other aircraft elements and adversely affecting their performance. In this case we usually observe complex 3D flows, interference effects in the flow around intersecting surfaces, considerable viscous effects, which makes the numerical calculation of these configurations more difficult. Therefore, complex experimental investigations of diverters with different geometry were conducted in the wind tunnel T-313 for M_∞=2.25 and $Re_1=25\cdot10^6$ m^{-1} [11]. The drag, pressure distribution, near-wall flow topography on diverters and in their vicinity, and the pressure field at the inlet simulator entrance were studied. A special technique was developed for this purpose: an appropriate diverter configuration with inlet simulator was mounted on the side wall of the test section (Fig. 13a). A schematized model of diverter 1 with inlet simulator 2 was placed using sting 3 on the four-component mechanical balance. This allowed one to measure the drag coefficient to a high accuracy. The diverter was located in a developed turbulent boundary layer on the wind tunnel wall. Figure 13b shows the geometry of examined wedges. Variants 2-5 differ from the initial one by the leading edge sweep angle χ, while the half-angle θ was constant over the height of the diverters. The wedge tip coincided with the leading edge of the inlet simulator. Variants 6-9 have a forebody extending upstream with respect to the inlet simulator. Half-angles θ are listed in the table (Fig. 13b). The cross-sections of these wedges were antiparallelograms or isoscales triangles (for the extended forebody). The upper part of diverters 7-9 is analogous to variant 1, while the lower part repeats the geometry of variant 6.

Figure 14 shows the results of drag coefficient measurements for ten variants under consideration. The results were obtained with allowance for the pressure force acting upon sting 3 and for the base pressure registered by a Pitot rake in the base cavity 4 (Fig. 13a). An explicit gain in drag $\Delta Cx_1=Cx_i-Cx_1$ for the considered variants with respect to initial one is clearly seen. The value of ΔCx_1 was determined using the mean values of the coefficients Cx_i and Cx_1 obtained in three series of multiple experiments. Systematic errors were eliminated, wherever possible, and the confidence interval of random error, equal to $2\sigma=\pm0.0083$ was obtained for the initial wedge (variant 1). As it follows from Fig. 14, a noticeable gain in drag of 15-25% is observed for variants 6-9. The overall effect in these cases is caused by favorable influence of a large sweep angle of the leading edge and by a decrease of wedge angle when approaching its base. It seems that in each particular case, having chosen a wedge configuration with minimum drag, one has also to bear in mind that the wedge can generate disturbances that enter the inlet. In reality, in all cases the boundary layer diverter generates

a 3D shock wave which interacts with the boundary layers on various surfaces. The flow in the drain slot is characterized by merging boundary layers which separated and/or effuse in the crossflow direction under the action of adverse pressure gradients. Such complicated flows can affect the flow entering the inlet. These problems were studied in detail in [12, 13]. As an illustration, let us consider here the topography of the limiting streamlines on the diverter and lifting surface (Fig. 15), which was obtained by using the oil-film visualization. The shock wave generated by the wedge interacts with boundary layers developed on the lifting surface and on the lower surface of inlet simulator. Because of that, the boundary layers separate along the separation lines S_1 and S_3 and reattach again along the reattachment lines R_1 and R_3, respectively (Fig. 15b). Three-dimensional λ-configurations of shock waves with tangential discontinuities emanating from triple points are formed near these lines. An intense vortex is formed near the corner junction of the side surface of the wedge and the lifting surface, which gives rise to the separation line S_2. Regions of plane-parallel flow (marked by dots) are observed at the side surface of the wedge and lower surface of the simulator. The flow along the wedge is characterized by weak overflow of the gas from the drain slot to the side surface of the inlet simulator. Leaving the slot and passing around the vertex of the streamwise corner formed by the lower and side surfaces of the inlet simulator, the flow separates along the separation line S_4 (Fig. 15a and b) and reattaches along the reattachment line R_3. The flow pattern on the side surface of the inlet simulator is presented in the characteristic cross-section III normal to this wedge face and to the intersection line of diffracted shock wave with this face.

A vortex enclosed between the lines S_3 and R_3 (cross-section I) is formed on the lower surface of the inlet simulator. This vortex extends in the transverse direction, penetrating onto the side surface of the inlet simulator. In this case, secondary lines of separation S_3 and reattachment R_3 are observed in the reverse flow region.

Hence, the action of a transverse vortex on the side surface of the inlet simulator is similar to that of the near-wall stream inclined with respect to the free stream. The flow around this near-wall stream is characterized by an adverse pressure gradient, which is evidenced by the deflection of the limiting streamlines on the side surface of the inlet simulator (Fig. 15a). A thin boundary layer developing on this surface separated along the line S_5 and reattaches along the line R_5.

Thus, the shock wave generated by the leading edge of the wedge causes the boundary layer separation on the lifting surface and, diffracting on the streamwise corner of the inlet simulator and interacting with its boundary layer, it also causes a separated flow on the external surface of the inlet nacelle. In case a diverter combination with a forebody extending upstream of the inlet is used (variant 6), the intensity of the shock wave propagating from the wedge vertex is insufficient to cause the boundary layer separation on the lifting surface. Therefore, the limiting streamlines curve near the vortex without forming a separation line. The separation line S_1 is slightly shifted downstream, which is caused by variation of the half-angle over the wedge height, which favors a change in the critical pressure ratio. Contrary to the first case, the separation region extends to the wedge face. The flow pattern around wedge 7-9 differs only by the fact that the lines S_1 and R_1 pass over the wedge face from the leading edge inflection point. The analysis and comparison of the limiting streamlines on the HSTC model near the diverters confirmed their qualitative agreement. The use of diverters (variants 7-9) with an upstream extended forebody allows for decreasing the drag, and the leading edge inflection helps to eliminate possible penetration of disturbances into the inlet.

Thus, this example gives evidence that the study of 2D and 3D separated flows on schematized models allows for a more profound analysis of rather complex flow structures around combinations of the boundary layer diverters and inlets of flying vehicles. This approach allows one to study in detail the local characteristics of complex flows and find the ways for further decreasing the drag of these elements.

VISCOUS NEAR-WALL FLOWS IN REGIONS OF AERODYNAMIC SURFACE JUNCTIONS

1. Interaction of boundary layers.

The flows along the intersection line of two surfaces which form a streamwise corner refer to complex 3D flows frequently encountered in various HSCT configurations. These flows are formed at places of junction of various elements,

such as wing-fuselage, wing-prismatic superstructures, turbomachine blades, etc.

Various aspects of this problem have been studied in different years by L.G.Loitsyansky, V.I.Subbotin, V.I.Kornilov in Russia, P.Bradshow, A.D.Young, F.B.Gessner, E.A.Eichelbrenner, and others in foreign countries.

The near-wall flows in corner configurations are formed under the influence of numerous factors. Thus, intersecting surfaces can be non-flat, have junction radius other than zero, or have swept and blunted leading edges. The flows induced by asymmetrically developed boundary layers should be also mentioned. Much more complicated is the flow in a corner configuration formed under the influence of outside impinging oblique shock wave. In this case, the flow is characterized by separation in the regions of surface junctions and becomes significantly unsteady with large strength of the impinging shock.

In the general case the flows near the bisector plane of corner configurations are characterized by complex vortex flows and versatile governing parameters.

Such incompressible flows were the object of investigation in numerous studies [14-20]. These are only some experimental researches dealing mainly with open straight corner configurations. Much less attention is paid in experimental research to supersonic flows in the corners, the works [21-24] can be mentioned here. Numerical calculation of near-wall turbulent flows in corner configurations is still a complicated problem; thus, the most reliable notion about the structure and characteristics of these flows have been obtained by experimental methods. Let us consider some results obtained in the Aerodynamics Laboratory of ITAM. Models reproducing symmetrical and asymmetrical interactions of boundary layers were used for these purposes (Fig. 16a and b, respectively). These models are straight streamwise corners formed by flat plates with varied geometry of the leading edges and face junction radii. The experiments were performed for Mach numbers M_∞=2, 3, and 4 and Reynolds numbers $Re_1=(15\text{-}57)\cdot 10^6$ m^{-1}. The Mach number distributions in the boundary layer were determined on the basis of P_0' and P values measured by pressure probes with orifice size 0.25x1.0 mm. The position of the boundary layer transition was either fixed by boundary layer trips or measured. It is known that secondary flows arise near the bisector plane of a streamwise corner. These flows are observed in the interaction region of laminar boundary layers and directed along the bisector plane towards the external flow. They arise and develop mainly under the action of local pressure gradient near the leading edges of intersecting surfaces. Hence, the leading edge of the corner initiates disturbances in the boundary layer in the form of paired vortices. As the flow passes to a turbulent state, these vortices are pressed out by secondary flows originating due to turbulent transfer [19]. The above-mentioned local effects should be taken into account when designing the regions of surface junction. This, in turn, requires the knowledge about the integral characteristics of the boundary layer in the vicinity of bisector plane. These data are presented in Fig. 17 as $Re_\delta=f(Re_x)$. These results characterize the boundary layer evolution in the bisector plane of a straight streamwise corner for a temperature factor $\bar{T}w=Tw/Tr=1$. For comparison, this figure shows also the values of Re_δ for 2D flow calculated using the empirical formula [25]. In logarithmic coordinates the experimental values of Re_δ in the bisector plane of the corner are adequately approximated by linear dependences. However, contrary to the flow past a flat plate, a substantial dependence of Re_δ on M_∞ is observed, which is apparently caused by secondary flows depending on the Mach number. Exactly secondary flows determine slightly less intense development of the boundary layer than outside the interaction region, which can be deduced from the slope of the $Re_\delta=f(Re_x)$ curves.

If we use the product $M_\delta^{0.6}Re_x$ as an argument, then the experimental values of Re_δ under examined conditions are generalized by a single dependence which is approximated by the formula

$$Re_\delta = \frac{0.32\cdot\left(M_\delta^{0.6}\cdot Re_x\right)}{\left[\lg\left(M_\delta^{0.6}\cdot Re_x\right)-3.6\right]\cdot\lg\left(M_\delta^{0.6}\cdot Re_\delta\right)}.$$

As it follows from Fig. 18, the maximum difference between the calculated and experimental curves lies within 11%.

The length of 3D region in the vicinity of the bisector plane of a corner is usually determined by the distribution of equal velocity lines (isotachs) in a cross-section. A typical distribution of isotachs at subsonic and supersonic speeds is presented in Fig. 19. The velocity ratio is u/u_δ=0.5 (curve 1), 0.70 (2), 0.80 (3), 0.90 (4),

and 0.99 (5). These results testify to an almost complete symmetry of isotachs with respect to the bisector plane of the corner and to a similarity of these flows at subsonic and supersonic speeds. Two regions are clearly seen here. The isotachs are located parallel to the corner face in one region and significantly curved in the other. The transition from one region to the other takes place asymptotically, therefore, the determination of the length **h** is approximate to a certain extent. This quantity was determined graphically as a distance z_1 (or y_1) beginning from which the isotach u/u_δ=0.99 deviates from the direction parallel to the corner face. The determination of **h** on the basis of integral spanwise characteristics δ_1 and δ_2 showed that the results differ by no more than ±3%.

An introduction of corner face junction radius other than zero eliminates the corner line and, as a consequence, the characteristic features of boundary layer interaction degenerate. In particular, as the junction radius increases, the velocity distribution in the bisector plane gradually changes, approaching the corresponding profiles in 2D flow region.

Figure 20 shows the functions $Re_\delta=f(Re_x \cdot R)$ for various values of junction radius R between the corner faces. An asymptotic transition from 3D to 2D flow is observed already at $R/\delta_{2D}=6$, when the boundary layer thickness δ_{2D} in the bisector plane corresponds to the 2D case. This is also confirmed by the distribution of isotachs shown in Fig. 21.

Thus, when a certain value of the junction radius of the corner faces is achieved, the vortex drag degenerates completely. For practical applications it is important to know the limiting values of the junction radius, for which the flow near the bisector plane becomes two-dimensional and vortex-free. Increasing of these values of the junction radius leads only to useless area increase and, hence, to additional airfoil drag.

Asymmetrical interactions are often encountered on flying vehicles, when the boundary layer prehistory is different on different corner faces.

The degree of asymmetry can be conventionally characterized by the ratio of thickness of boundary layers developing on neighboring faces, δ_B/δ_A, which varied in this case from 1 (symmetrical case) to 2.3. The state of boundary layers on neighboring faces, their equilibrium state was verified by the 2D flow characteristics: measured profiles of mean velocity $u/u_\delta=f(y/\delta_1)$, fluctuations of the streamwise component, skin friction coefficients and distribution of pressure coefficients along the face B (see Fig. 16).

Figure 22 for M_∞=3 [26] shows isotachs obtained for the interaction of compressible boundary layers in the range of sweep angles of one of the corner faces χ=0-70°. The distribution of isotachs is also asymmetrical about the bisector plane of the corner. As it should be expected, an increase of sweep angle decreases the asymmetry of isotachs. The same figure shows the interaction region length versus the Reynolds number Re_x which is conventionally determined in two transverse directions h_A and h_B. The number Re_x is based on parameters at the boundary layer edge and on the coordinate x from the actual beginning of turbulent boundary layer development along the intersection line of the surfaces. The function $h/\delta_{2D}=f(Re_x)$ in this interpretation has the same form as in the case of interaction of symmetrical boundary layers and is practically independent of the sweep angle χ of the leading edge of one of the faces. The structure of asymmetrically developed streamwise vortices can be represented as the mean vorticity distribution along the x axis. The measurement results of transverse velocity components v and w made it possible to calculate the lines of equal nondimensional vorticity ω_x=const, the distribution being shown in Fig. 23a and b for δ_B/δ_A=1.5 and 2.3, respectively. The character of distribution of these lines does not leave any doubts that in the case of asymmetrical interaction of boundary layers developing on the faces of a straight streamwise corner a pair of counter-rotating vortices is again formed with spanwise effusion from a certain dividing line (corner line in the symmetrical case). Judging from the maximum vorticity value $\omega_{x_{max}}$, as the asymmetry parameter δ_B/δ_A increases within the examined range 1.0÷2.3, a slight decrease in vortex flow intensity is observed in the region of less developed boundary layer, i.e. on face A. Nevertheless, principal changes characterized by a substantial restructuring of the flow do not occur. On the whole, as the parameter δ_B/δ_A increases in the examined range, a certain tendency can be noted to gradual diminishing of the vortex A and, vice versa, to expanding of the vortex B to larger areas of the boundary layer.

2. Shock wave/boundary layer interaction.

Various situations of shock wave/turbulent boundary layer interaction are encountered in external and internal aerodynamics. This makes the complex flow in corner configurations even more complicated [27, 28]. Typical examples of such flows are the flows around junction regions of wing-fuselage, wing-rectangular engine nacelle, etc. Experimental studies of these flows were performed on schematized models of straight streamwise corner [29-32]. A sketch of such a model is shown in Fig. 24. Here 1 is a straight streamwise corner formed by vertical V and horizontal H faces with sharp leading edges, 2 is the shock wave generator, 3 and 5 are struts, 4 are pressure orifices (133 points), 6 are top plugs, 7 is the boundary layer trip, and 8 is the traverse gear. The oblique shock intensity ξ was varied by changing the angle of attack of the shock wave generator within the range of angles α_G from 8.6° to 16.6°, which corresponds to calculated values of ξ from 1.86 to 3.11. Here P_2 is the pressure behind the oblique shock, P_∞ is the free-stream static pressure. The experiments were performed for Mach numbers M_∞=2, 3, 4 and unit Reynolds numbers $Re_1=(9.7\text{-}48)10^6$ m^{-1} with zero angles of attack and sideslip.

The flow structure formed on corner faces was studied on the basis of measured static pressure distributions and visualization of the limiting streamlines by the oil-film method, the flow fields were obtained by the laser sheet method. As an example, Figure 25 shows the topography of the surface streamlines for the shock strength ξ=2.43 and Mach number M_∞=3. Here SW is the calculated position of the shock trace, RS is the reflected shock, S and R are the primary and secondary lines of flow separation and reattachment, SP is the saddle point, F is the vortex. A schematic flow pattern is presented below for cross-sections I-I and II-II. The impinging shock wave (dashed line), which is glancing for the face V, leads to the formation on the latter of an explicit separation line S_1 characterizing the flow separation with its subsequent reattachment along the line R_1. A detailed analysis [29, 30] showed that separation takes place already for the shock strength ξ=1.86 and becomes large-scale as ξ increases. In the region limited by the lines S_1 and SW there are signs of the formation of secondary separation, which is characterized by the appearance of separation line S_2. This line extends to the overall interaction region as the shock strength increases, and merges the line S_1.

On the horizontal face H, the impinging shock wave forms the separation line S_3 that has a curved front over the entire span. Being separated along this line, the boundary layer reattaches along the line R_3 to form a circulation flow.

The curvature of the line S_3 near the corner bisector plane can be explained as follows. As already noted, even without external disturbances of the shock wave type, the shear flow in this region has a 3D character due to usual interaction of neighboring boundary layers. An intense braking of the flow favors a considerable reduction of turbulent friction near the corner rib, as compared with a 2D case. Disturbances propagate upstream over the subsonic part of the layer, whose thickness is larger than in the corresponding 2D analog, thus increasing the pressure level and favoring an earlier flow separation near the streamwise corner rib. This is the reason for a characteristic upstream "bulging" of the 3D separation bubble, which manifests itself in the form of curvature of the line S_3 in this region (corner separation). In most cases, the spanwise length of the separation region does not exceed (2.5-4.0)δ. For high values of shock strength it can reach (10-12)δ.

As is seen from Fig. 25, the interaction of the impinging shock wave and a 3D flow along the corner line is accompanied by the development of a large-scale vortex with the center at point F and formation of a saddle point SP. The streamwise length of the separation region (x_{R_3}-x_{S_3}) in the plane of this point (SP) for the maximum value of examined shock strength ξ is approximately 26δ.

The pressure fields in the interaction region are more clearly represented as isolines P/P_∞=const and isosurfaces of the relative pressure P/P_∞ in Figs. 26a and b, respectively. Here P_∞ and P are the static pressures in the free stream and in a current point on the model surface, respectively, x_u is the distance from the leading edge of the model to the point of pressure growth beginning, determined at a distance **z** from the corner line where the flow is in a state close to quasi-two-dimensional one, δ is the boundary layer thickness at the point of pressure growth beginning x_u. The dashed line shows the shock wave trace calculated ignoring the effect of boundary layer on the shock wave generator. On the whole, the isobar pictures reveal an obvious analogy for different values of ξ. It is seen (Fig. 26a) that downstream of the shock wave trace the 2D flow

character is violated on the entire examined surface of the streamwise corner, even for a small strength of the shock. The flow pattern upstream of the shock wave trace is significantly different. An explicit 3D flow region is formed near the corner rib ($y/\delta=z/\delta=0$), which is characterized by upstream deformation of isolines P/P_∞=const. The length of this region $\Delta x/\delta$ from the point of shock incidence onto the horizontal face in the mentioned direction is 16.3. (Note that the value of the coordinate $(x-x_u)/\delta$ determining the shock wave position on the horizontal face for ξ=2.43 is 14.4. A perspective view of isosurfaces of the relative pressure P/P_∞ is presented in Fig. 26b for the same value of shock strength. It is seen that an impinging shock wave produces a pressure wave front at the vertical face (coordinate y/δ) whose level noticeably grows as ξ increases. In this case, the flow structure, at least at negative values of the coordinate $(x-x_u)/\delta$, is almost completely determined by the process of shock wave interaction with the boundary layer on the vertical face. The flow on the horizontal face at a certain distance from the corner rib along the coordinate z/δ under these conditions is in an undisturbed state, i.e., the pressure distribution in this region is the same as without the shock wave.

A 3D separation bubble is formed near the streamwise corner rib ($y/\delta=z/\delta\leq$5-6). Its influence extends upstream and provokes pressure growth there [29]. The separation bubble length weakly depends on the shock wave strength and amounts to approximately 40δ, while its transverse dimensions do not exceed (3.5-4.0)δ.

A detailed analysis of all results obtained allows one to draw a tentative picture of 3D flow, which is shown in Fig. 27 [34, 35]. For a more clear representation, the finite-width arrows (A), (B),., (K),.,(U) show the elements of the most typical stream surfaces. DS refers to surface elements of the dividing layer, which divides the near-wall flow and the external flow that hardly takes any part in the formation of vortex flow. It can be expected that this surface has a variable height from the wall in the spanwise direction, which increases near the streamwise corner rib where a 3D flow is observed even without external influence. The flow on the vertical face is characterized by stream tubes (cross-section I) with different velocity depending on the distance from the wall (K, L, M, N, Q). Low-velocity stream tubes, such as K, that cannot overcome the adverse pressure gradient, deflect in the transverse direction along the line S_1 and involved into the vortex flow F. Stream tubes with larger velocity, such as L, penetrate behind the line S_1 spreading along it; being unable to overcome the elevated pressure, these stream tubes pass along the separation line (S_1+S_2). In a similar way we can trace the stream tubes M which form a secondary separation S_2 in the reverse flow. This is evidenced by the laser sheet photo in which a λ-shock is seen. The stream tubes with the largest velocity, Q, located higher than the DS, completely overcome the counter-pressure and pass down to the surface along the line R_1. Their further evolution is determined by the reflected barrel shock RS arising on the horizontal face.

As already noted, the flow on the horizontal face is characterized by a curved front of the separation line S_3 and reattachment line R_3, and by the formation of the vortex F and flow turning to the free side edge. The near-wall flow directed from the initial layer (cross-section I), the reverse flow behind the line S_3, and the flow effusion in the transverse direction lead to the formation of a clearly seen saddle point SP. Finally, the most high-speed stream tubes E' and D located above the DS come down to the surface along the reattachment line R_3 and propagate downstream, being affected by comparatively weak transverse pressure gradient. Therefore, the streamlines deflect here insignificantly from the free-stream direction.

It should be noted that a very complex flow pattern is described here only on the basis of the measurement of steady parameters. In reality, following [27, 28] it can be assumed that the flow in the separation region is unsteady. It is strongly suggested in [36, 37] that these flows in corner configurations are characterized by high-frequency fluctuations of surface pressure, which were registered by supersmall pressure probes, such as Kulite. This is also confirmed by energy spectra of pressure fluctuations on the surface. The surface pressure in the unsteady flow region rapidly increases and becomes higher than the pressure obtained from the correlation for an oblique shock.

Thus, in the presence of an impinging shock wave the flow on the most part of the streamwise corner surface has a large-scale 3D character, which is caused by the onset of developed separation and by the formation of vortex and circulation flow region.

The effects of pure viscous interaction caused by the interference of neighboring boundary layers

considered above are substantially weaker that the corresponding interaction initiated by the impinging shock. Therefore, it is not possible to identify here a 2D flow region, which is clearly registered under the absence of external influence.

The flow pattern presented here can be considered as the first version of interpretation of experimental data for creating the physical model of these flows. At the same time the data obtained extend the knowledge about this complex flow and can form the basis for developing numerical methods.

Conclusions.

Three examples of the flow around HSCT elements are presented: aerodynamics of non-flat wings, the flow around boundary layer diverters, and the flow in junction regions of aerodynamic surfaces. Each of these events contains complex 3D flows with boundary layer separation and reattachment. Numerical calculations of these turbulent flows do not adequately simulate such flows yet. Therefore, the optimization of aerodynamically perfect surfaces still has some limitations. In a limited class of geometry, the presented results of experimental studies allow one to give recommendations concerning the shapes of considered elements that ensure the maximum lift-to-drag ratio. The developed experimental techniques illustrate the possibilities of extending the notion about rather complicated flows by using schematized models. The results obtained in each case, in turn, can be used for the development and verification of numerical models and methods.

REFERENCES

1. Kogan M.I. About bodies with minimum drag in a supersonic gas flow, J. Appl. Mech. and Math., Vol. 21, 1957.
2. Zhilin Yu.Ya. Wings with minimum drag, J. Appl. Mech. and Math., Vol. 21, 1957.
3. Shcherbak Ya.S., Kosyachenko L.M. A numerical method of calculating supersonic aerodynamic characteristics of a non-flat wind with variable sweep, Trudy VAUGA, Iss. 37 and 41, 1969 and 1970.
4. Gladkov A.A. Calculation of aerodynamic characteristics of wings in a supersonic flow, Trudy TsAGI, Iss. 1235, 1971.
5. Brodetsky M.D., Koscheev A.B., Cheremukhin G.A. Experimental study of non-flat wings at supersonic speeds, Izv. SO AN SSSR, Ser. tekh. nauk, Iss. 3, 1974.
6. Brodetsky M.D., Koscheev A.B., Cheremukhin G.A. Experimental study of distributed aerodynamic characteristics of non-flat wings at supersonic speeds, in: "Investigations of non-flat wing aerodynamics" (collection of papers of ITAM SB RAS), Novosibirsk, 1977, pp. 114-159.
7. Bokovikov Yu.G. A software system "Wing" for calculating aerodynamic characteristics of wings at supersonic speeds, in: "Investigations of non-flat wing aerodynamics" (collection of papers of ITAM SB RAS), Novosibirsk, 1977, pp. 43-93.
8. Brodetsky M.D., Koscheev A.B., Cheremukhin G.A. Estimation of the influence of deformation on the lift-to-drag ratio of a flying vehicle, in: "Investigations of non-flat wing aerodynamics" (collection of papers of ITAM SB RAS), Novosibirsk, 1977, pp. 159-175.
9. Brodetsky M.D., Bruk S.M., Makhnin A.M. A study of errors in determining the pressure coefficients at supersonic speeds, in: "Investigations of non-flat wing aerodynamics" (collection of papers of ITAM SB RAS), Novosibirsk, 1977, pp. 94-114.
10. Bokovikov Yu.G. Izv. SO AN SSSR, Ser. tekh. nauk, No. 8, 1974.
11. Zheltovodov A.A., Rafaelyants A.A., Filatov V.M. A study of peculiarities of the flow around boundary layer diverters and their drag, in: "Aerodynamic interference of the flow around 3D bodies" (ed. A.M.Kharitonov) (collection of papers of ITAM SB RAS), Novosibirsk, 1980, pp. 63-82.
12. Zheltovodov A.A. Physical peculiarities and some properties of 2D and 3D separated flows at supersonic speeds, Izv. AN SSSR, Mekhanika Zhidkosti i Gaza, No. 3, 1979.
13. Zheltovodov A.A. Shock waves/turbulent boundary-layer interactions - fundamental studies and applications, AIAA Paper 96-1977, 1996, 27 p.
14. Zamir M., Young A.D., Experimental investigation of the boundary layer in a streamwise corner, The Aeron. Quart., Vol. XXI, p.4, 1970.
15. Moiola O.O., Young A.D., An experimental investigation of the turbulent boundary layer along a streamwise corner, AGARD-CP-93, 1971.
16. Gessner F.B. The origin of secondary flow in turbulent flow along a corner, J. Fluid Mech., Vol. 58, No. 1, 1978.
17. Kornilov V.I., Kharitonov A.M., Interaction of turbulent boundary layers in a straight streamwise corner, J. Appl. Mech. Tech. Phys., No. 3, 1978.

18. Kornilov V.I., Kharitonov A.M., The development of transverse flows in a longitudinal flow along a straight streamwise corner, J. Appl. Mech. Tech. Phys., No. 1, 1979.

19. Kornilov V.I., Kharitonov A.M. Investigation of the structure of turbulent flows in streamwise asymmetric corner configurations, Experiments in Fluids, Vol. 2, 1984.

20. Shabaka J.M.M.A., Bradshaw P. Turbulent flow measurements in an idealized wing/body junction, AIAA J., Vol. 19, No. 2, 1981.

21. Weinderg B.C., Rubin S.G. Compressible corner flow, J. Fluid Mech., Vol. 56, p. 4, 1972.

22. Kornilov V.I., Kharitonov A.M., An experimental study of compressible boundary layer near the intersection line of two plates forming a straight corner, Izv. SO AN SSSR, Ser. tekh. nauk, No. 8, Iss. 2, 1974.

23. Dem'yanenko V.S., Igumnov V.A. Three-dimensional shock wave/turbulent boundary layer interaction in the interference region of intersecting surfaces, Izv. SO AN SSSR, Ser. tekh. nauk, No. 8, Iss. 2, 1975.

24. Sheig D.S., Hancky V.L., Petty D.S. Three-dimensional supersonic turbulent flow in a streamwise corner, RTK, Vol. 17, No. 7, 1979.

25. Chappel P.D. Some correlations for the turbulent boundary layer on a flat plate, The Aeronaut. J., Vol. 74, No. 6, 1970.

26. Kornilov V.I., Kharitonov A.M. Some peculiarities of viscous flows in corner configurations, in: "Studies of near-wall viscous flows" (collection of papers of ITAM SB RAS), Novosibirsk, 1979.

27. Bogdonoff S.M., Poddar K., An exploratory study of a three-dimensional shock wave turbulent boundary layer interaction in a corner, AIAA Paper No. 0525, 1991, 17 p.

28. Batcho P., Sullivan J. The 3D flowfield in a supersonic shock boundary layer corner interaction, AIAA Paper 88-0307, 1988, 10 p.

29. Kornilov V.I., Kharitonov A.M. Three-dimensional flow in corner configuration under the conditions of outside impinging shock wave, Sib. Fiz.-Tekh. Zhurn., Iss. 5, 1993, pp. 75-82.

30. Kornilov V.I. Formation peculiarities of the flow structure in a corner configuration under the conditions of interaction with incident oblique shock wave, Thermophysics and Aeromechanics, Vol. 2, No. 2, 1995, pp. 95-104.

31. Kornilov V.I. Flow structure peculiarities in a streamwise corner under the conditions of shock wave/boundary layer interaction, Eur. J. Mech. B/Fluids, Vol. 15, No. 6, 1996, pp. 831-846.

32. Kornilov V.I. Interaction of an external incident oblique shock wave with the boundary layer in a rectangular half-channel, Thermophysics and Aeromechanics, Vol. 2, No. 3, 1995, pp. 191-202.

33. Kornilov V.I. Interaction between outside-impinging shock wave and boundary layer in a rectangular half-channel, Eur. J. Mech. B/Fluids, 1996, Vol. 15, No. 6, pp. 847-864.

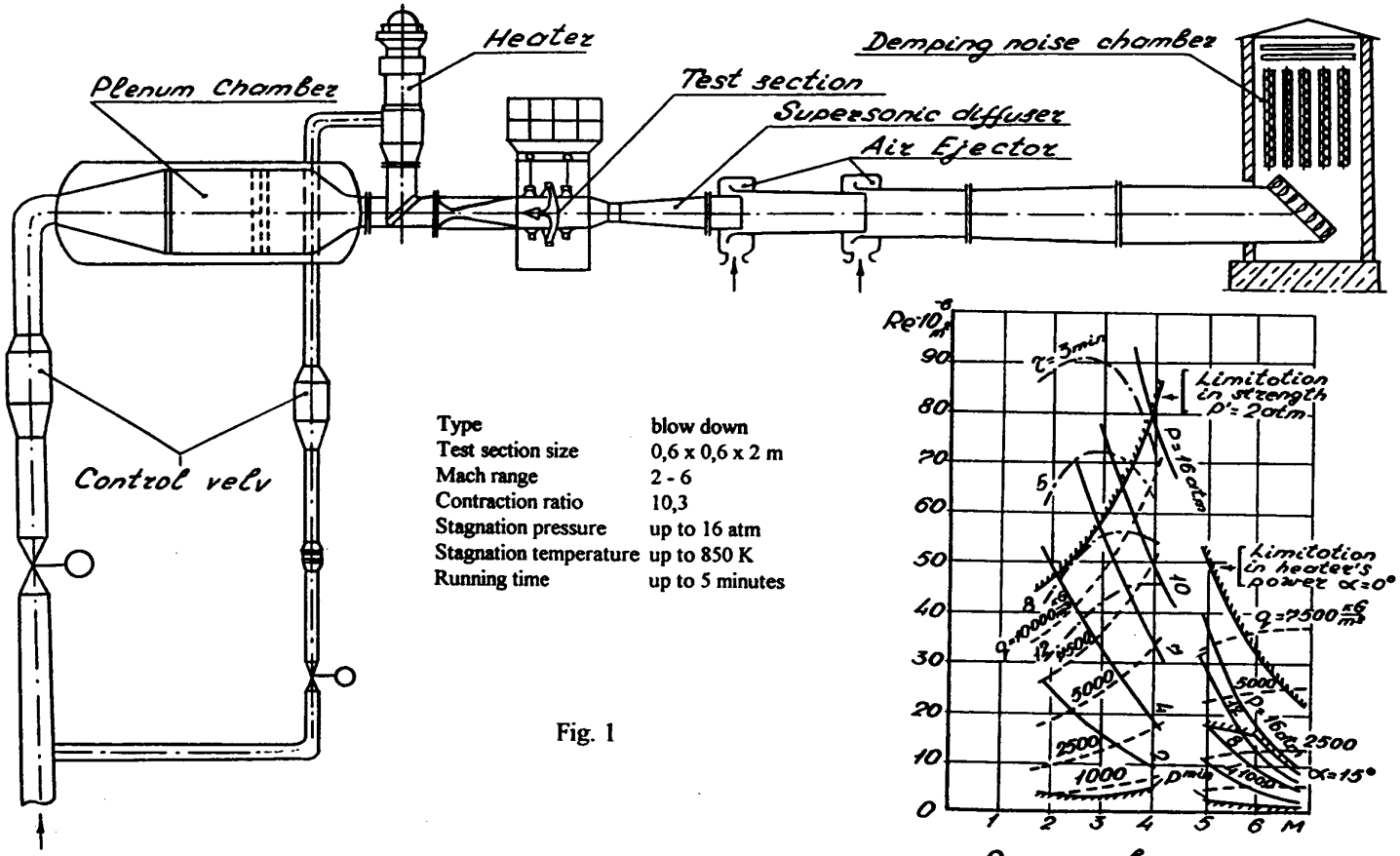
34. Kornilov V.I., Kharitonov A.M. Three-dimensional flow in a corner configuration under the condition of interaction with the outside-impinging incident shock wave, ICAR Paper (scientific report of ICAR at ITAM SB RAS), No. 2-94, 1994, 10 p.

35. Kornilov V.I. Three-dimensional turbulent flows in the regions of aerodynamic surfaces junctions, Proc. of Pacific int. Conf. on Aerospace Science and Technology, Dec. 6-9, 1993, Tainan, 1993, Vol. 3, pp. 1184-1190.

36. Poddar K., Bogdonoff S. A study of unsteadiness of crossing shock wave turbulent boundary layer interactions, AIAA Paper 90-1456, 1990, 13 p.

37. Tan D.K.M., Tran T.T., Bogdonoff S. Surface pressure fluctuations in three-dimensional shock wave turbulent boundary layer interaction, AIAA Paper 85-0125, 1985.

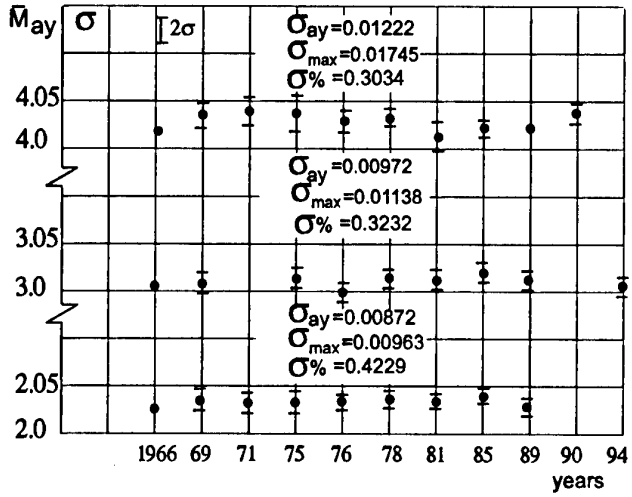
Sketch of ITAM wind tunnel T-313



Type	blow down
Test section size	0,6 x 0,6 x 2 m
Mach range	2 - 6
Contraction ratio	10,3
Stagnation pressure	up to 16 atm
Stagnation temperature	up to 850 K
Running time	up to 5 minutes

Fig. 1

Non-uniformity of the velocity fields in the test section T-313i



A multiple statistical analysis during the last 25 years makes it possible to assure that the maximum deviation at M=2, 3 and 4 is kept a level no higher than 0.5% .

Fig. 2

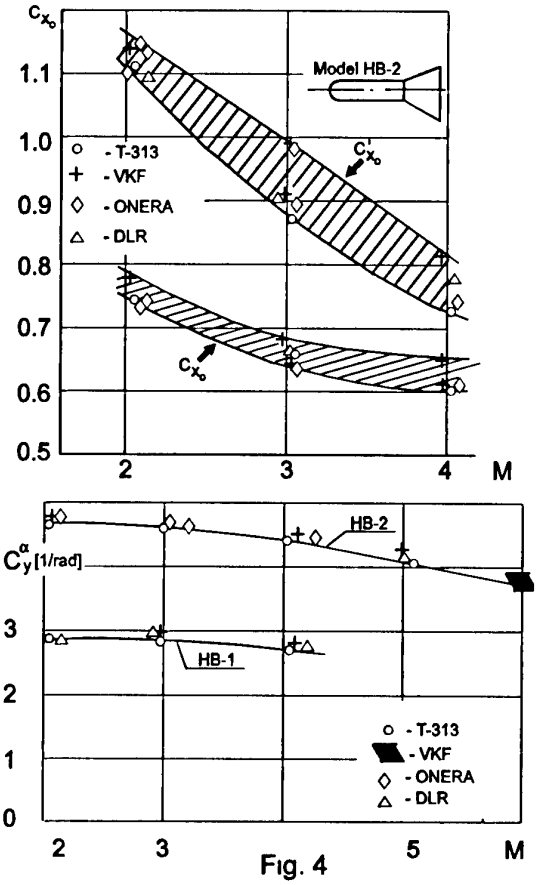
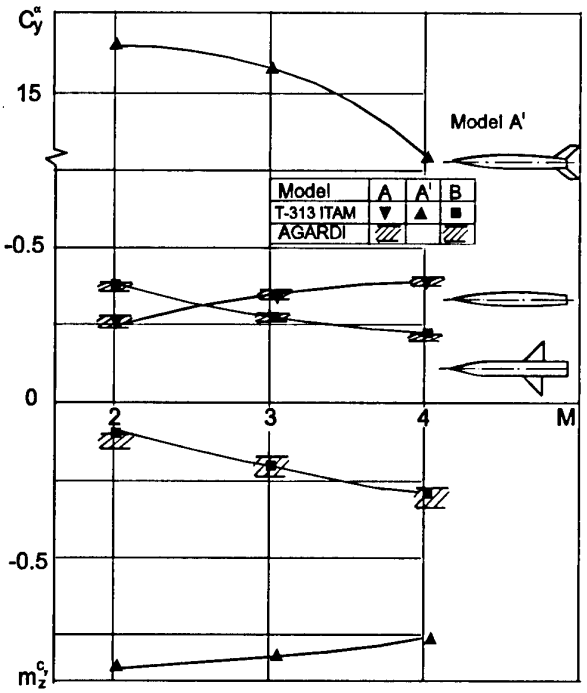
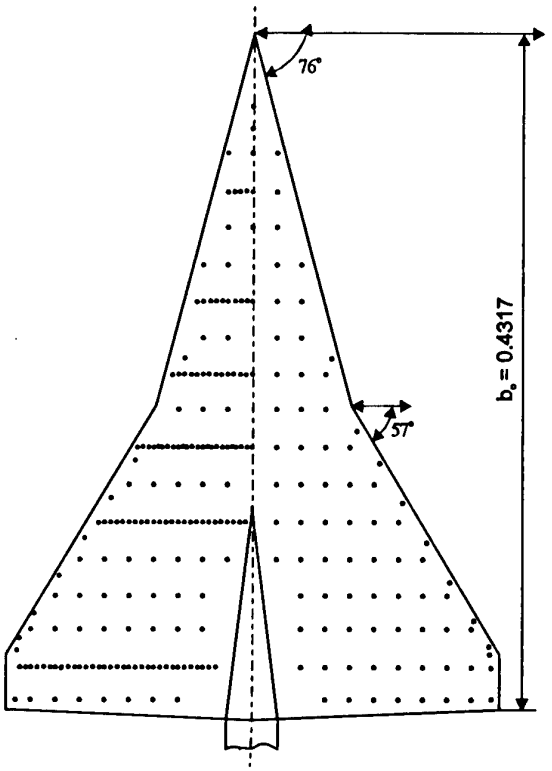


Fig. 4





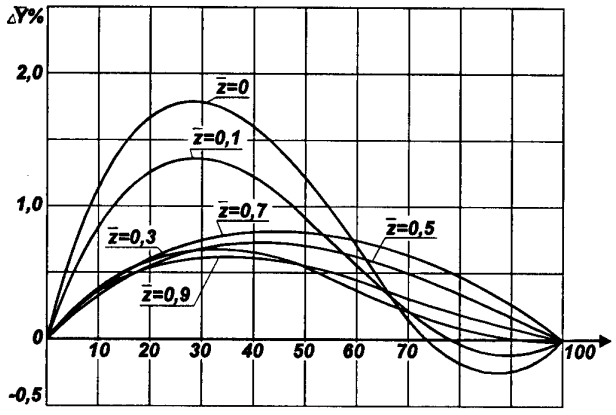


Fig. 6

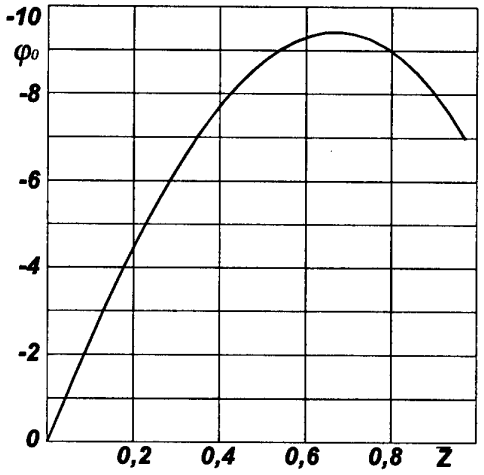


Fig. 7

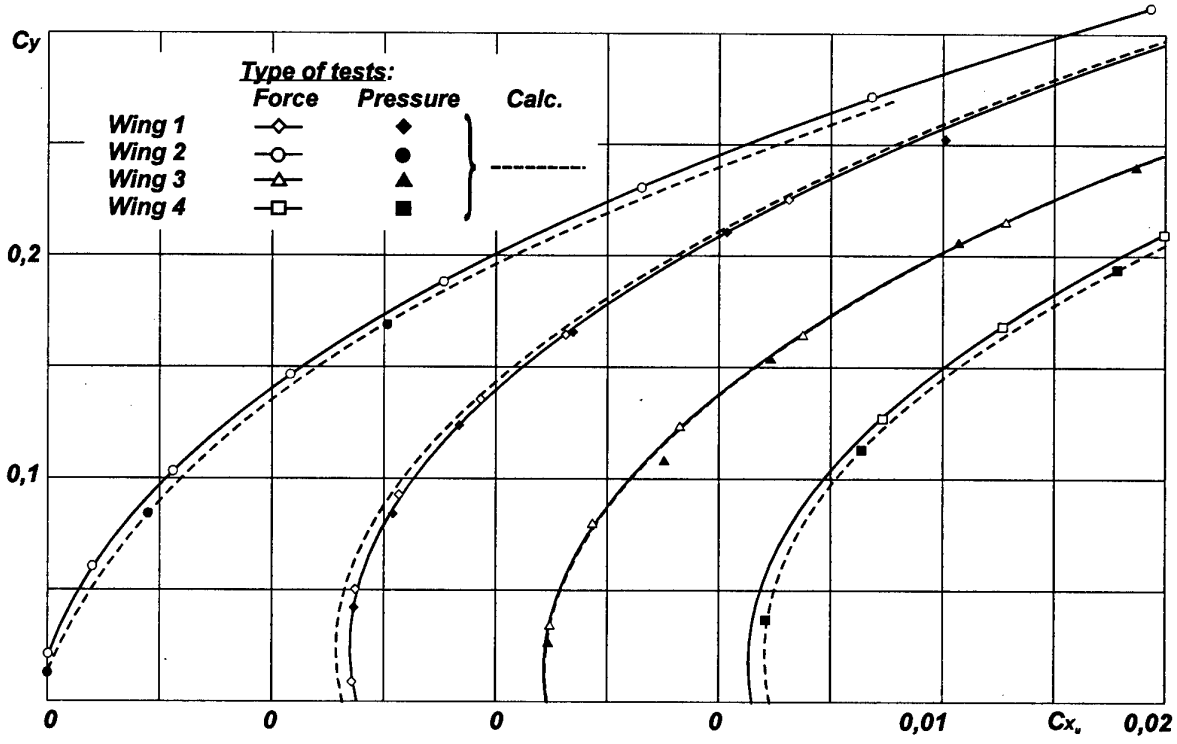


Fig. 8

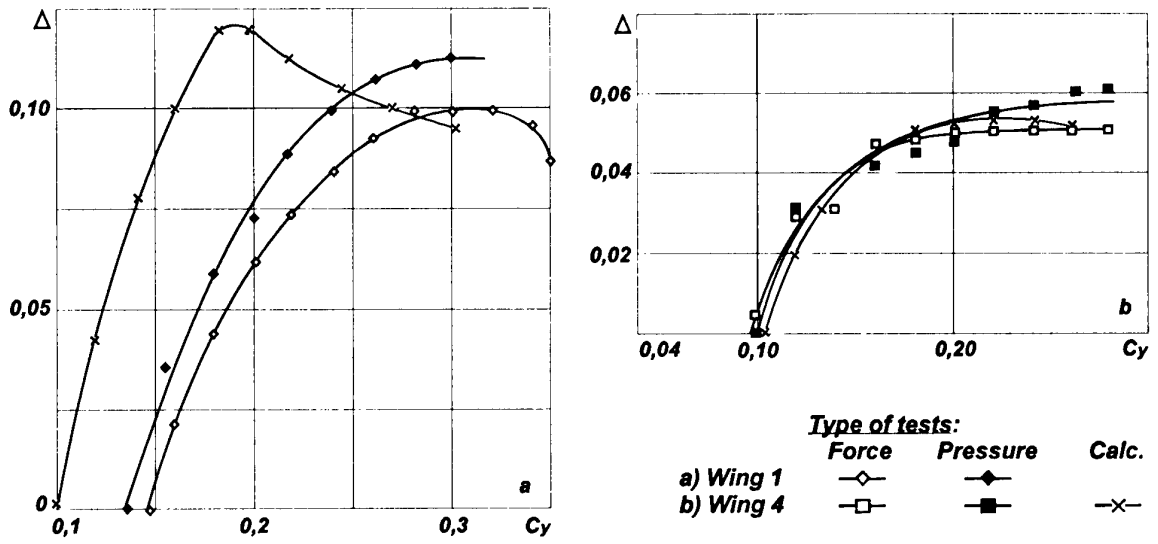

Δ
0,10
0,05
0
0,1
0,2
0,3
Cy
a
Δ
0,06
0,04
0,02
0,04
0,10
0,20
Cy
b
Type of tests:
Force
Pressure
Calc.
a) Wing 1
b) Wing 4

Fig. 9

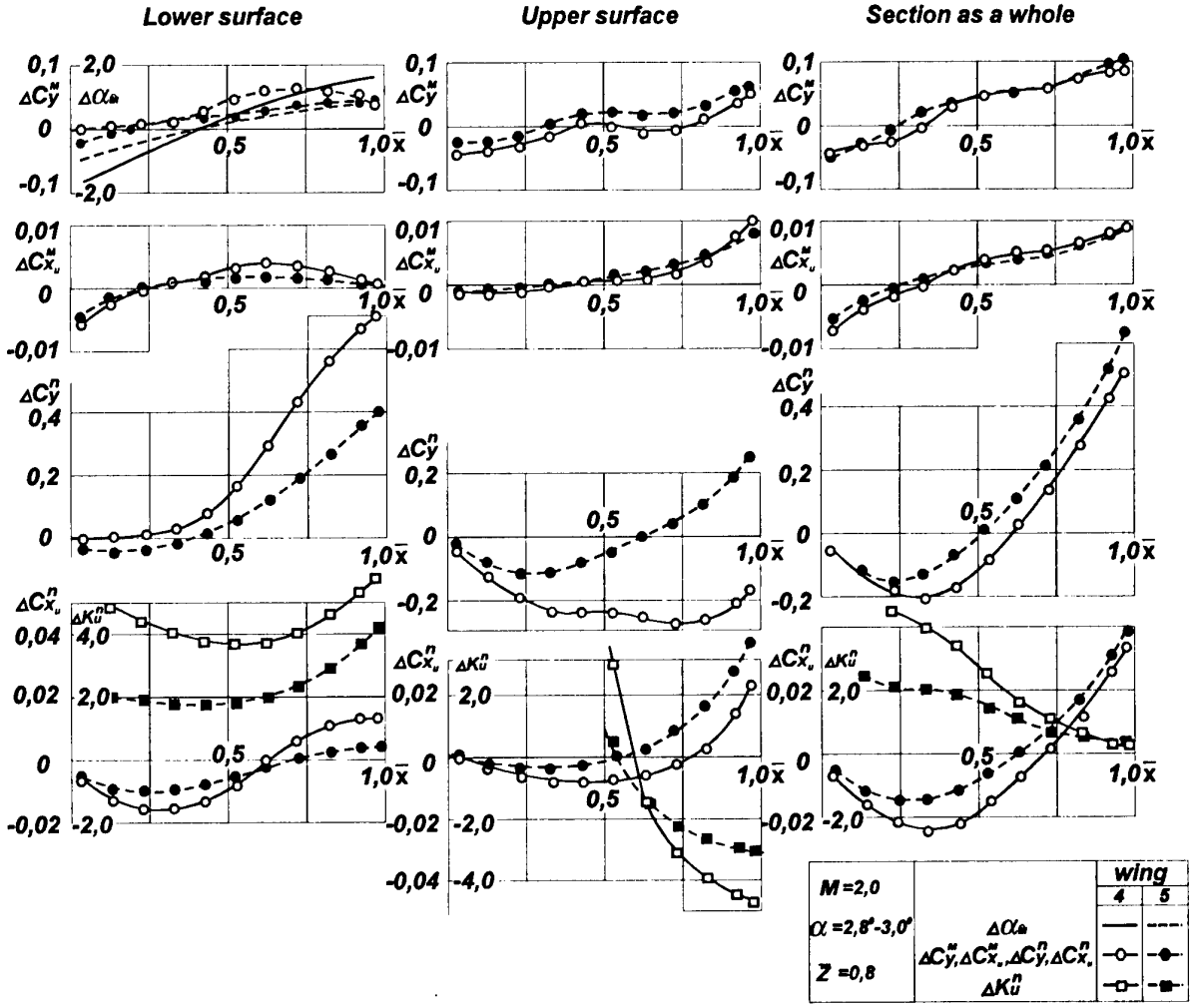

Lower surface
Upper surface
Section as a whole
M=2,0
α=2,6°-3,0°
Z=0,8
wing
4
5

Fig. 10

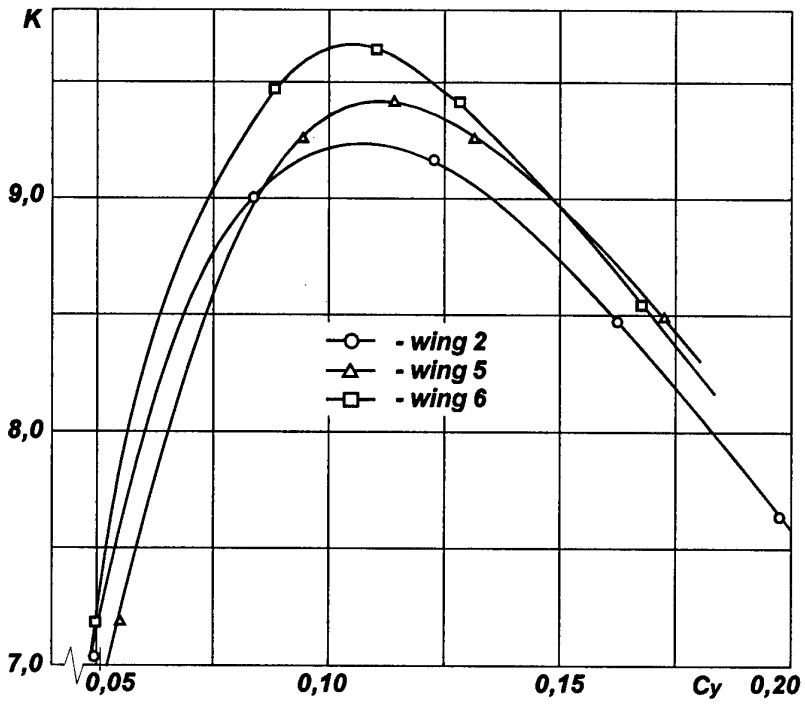


Fig. 11

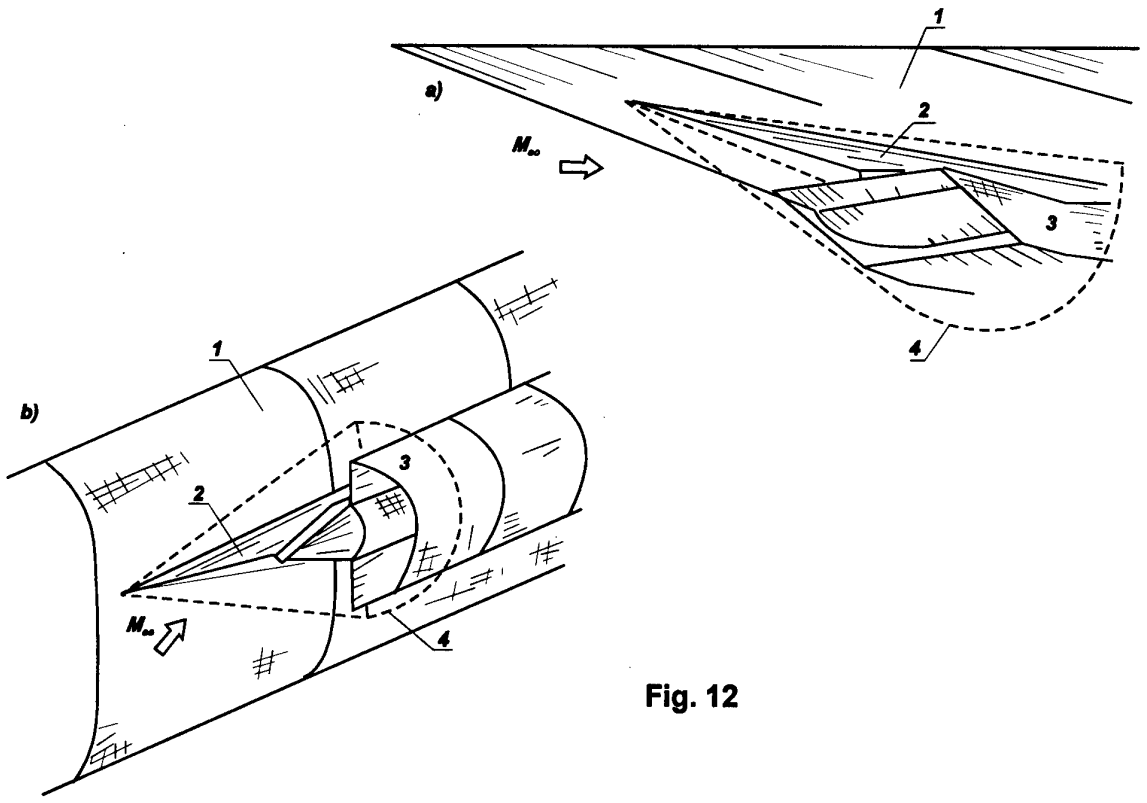
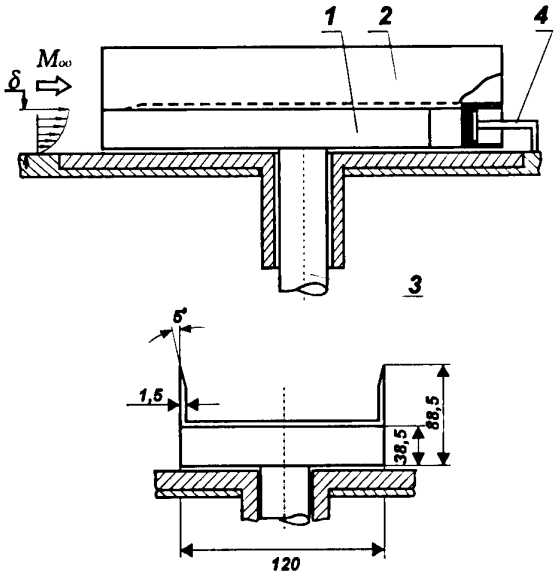


Fig. 12



variants	χ_0	$2\theta_0$	$\bar{h}=\frac{h_1}{h}$
1.	0°	26°	1
2.	−27°19′	26°	–
3.	−27°19′	26°	–
4.	−27°19′	26°	–
5.	45°54′	26°	–
6.	66°52′	θ= =9°44′+ 13°	0
7.	70°06′	–/–/–	0,156
8.	73°36′	–/–/–	0,312
9.	77°10′	–/–/–	0,468
10.	0°	var	–

Fig. 13

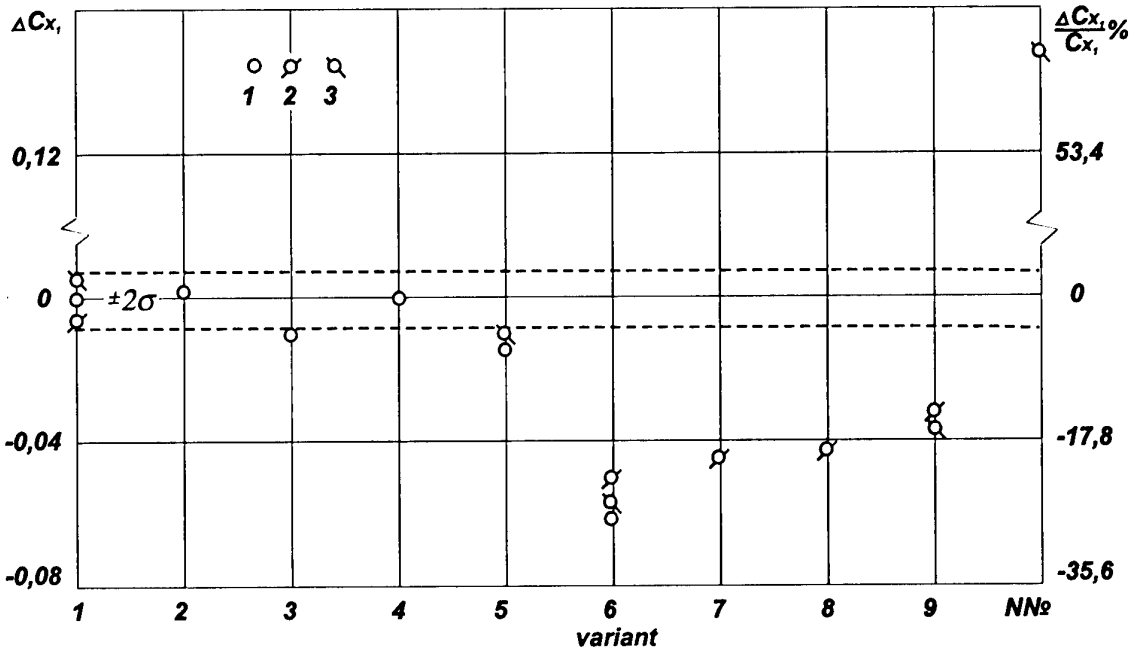


Fig. 14

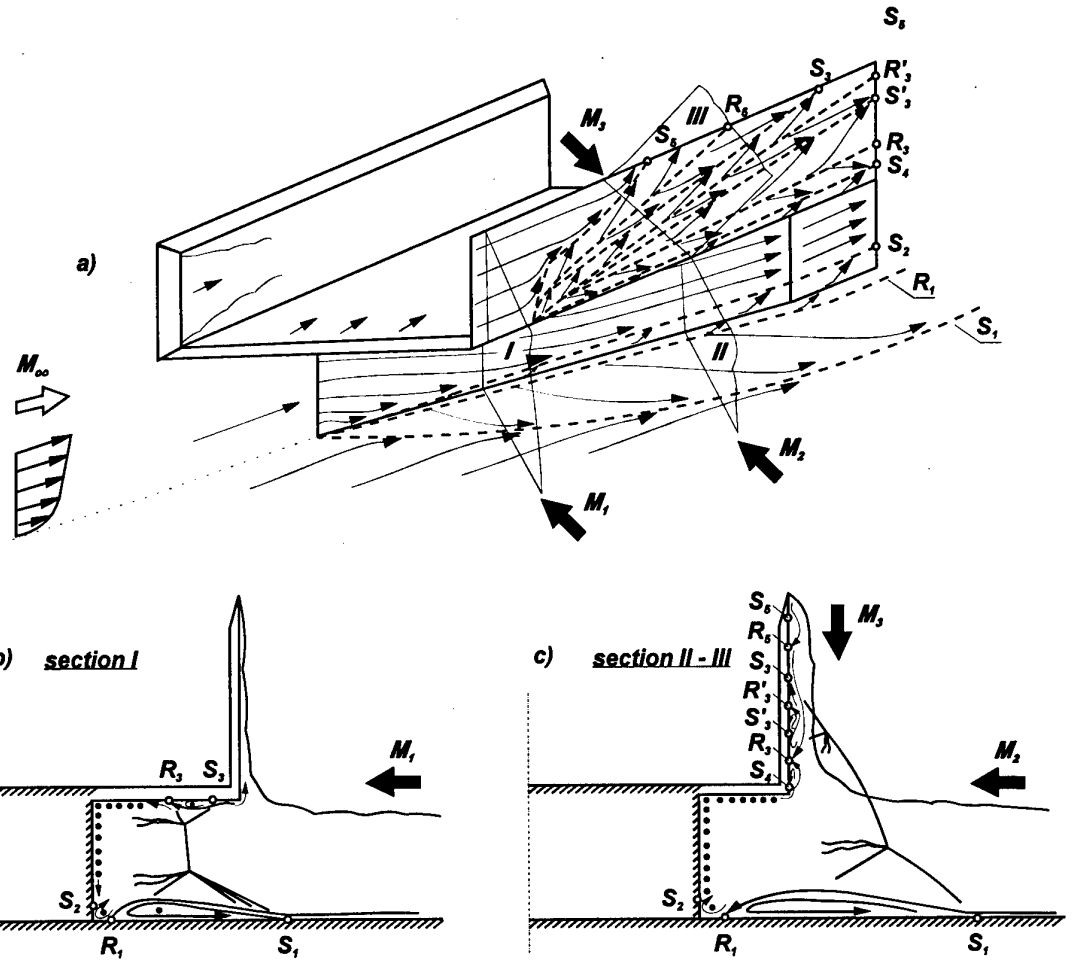

a)
M_∞
M_3
M_2
M_1
I
II
III
S_6
S_3
R'_3
S'_3
R_6
S_5
R_2
S_4
S_2
R_1
S_1
b) section I
R_2 S_2
M_1
S_2
R_1
S_1
c) section II - III
S_6
R_6
S_3
R'_3
S'_3
R_2
S_4
M_3
M_2
S_2
R_1
S_1

Fig. 15

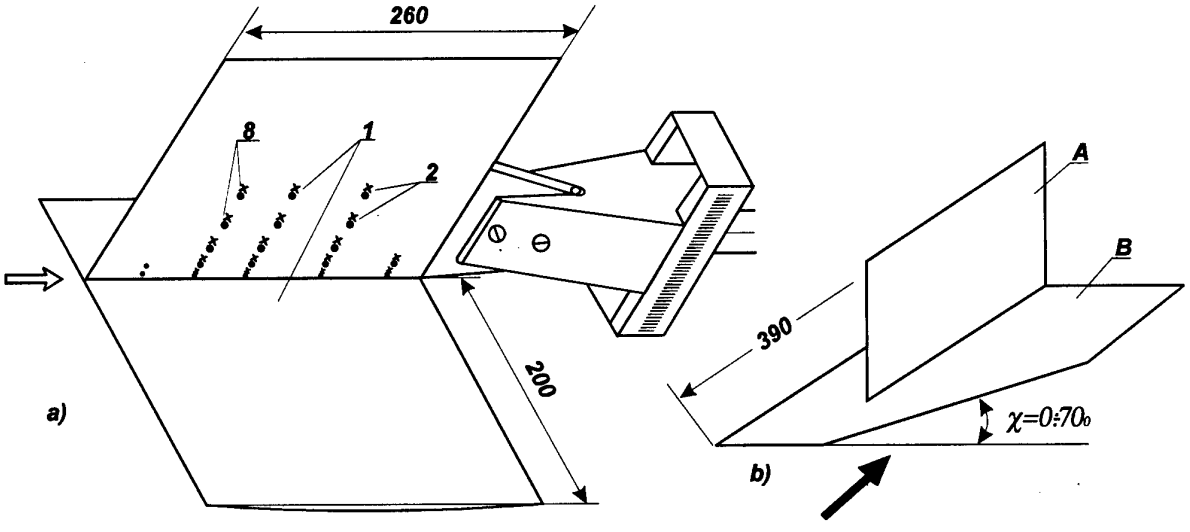

260
8
1
2
200
a)
A
B
390
χ=0÷70
b)

Fig. 16

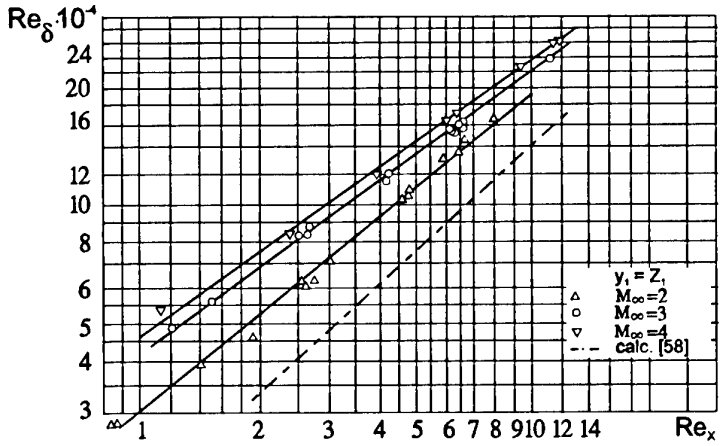


Fig. 17

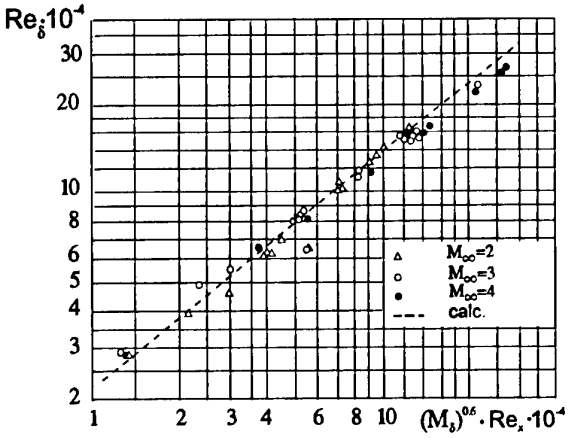


Fig. 18 Z_1=0.8mm, x - var

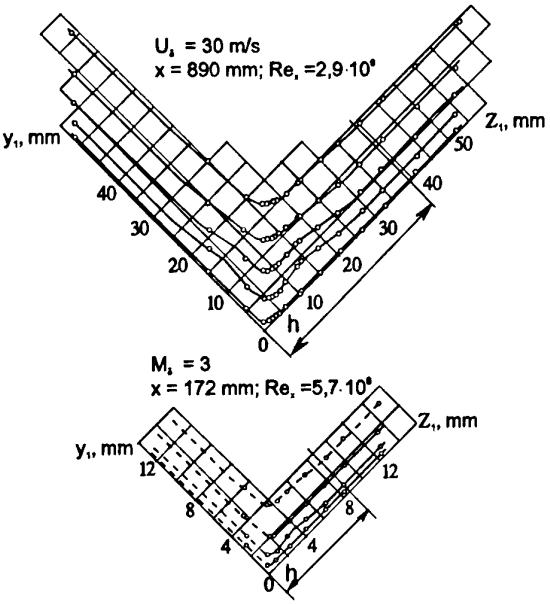


Fig.19 1 - U/U_δ = 0,50; 2 - 0,70; 3 - 0,89; 4 - 0,90; 5 - 0,99

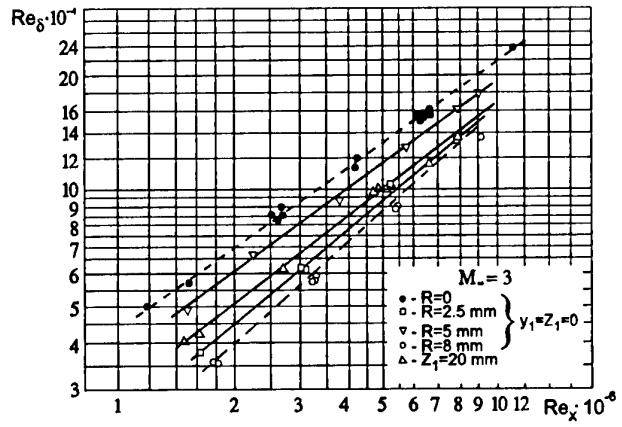


Fig. 20.

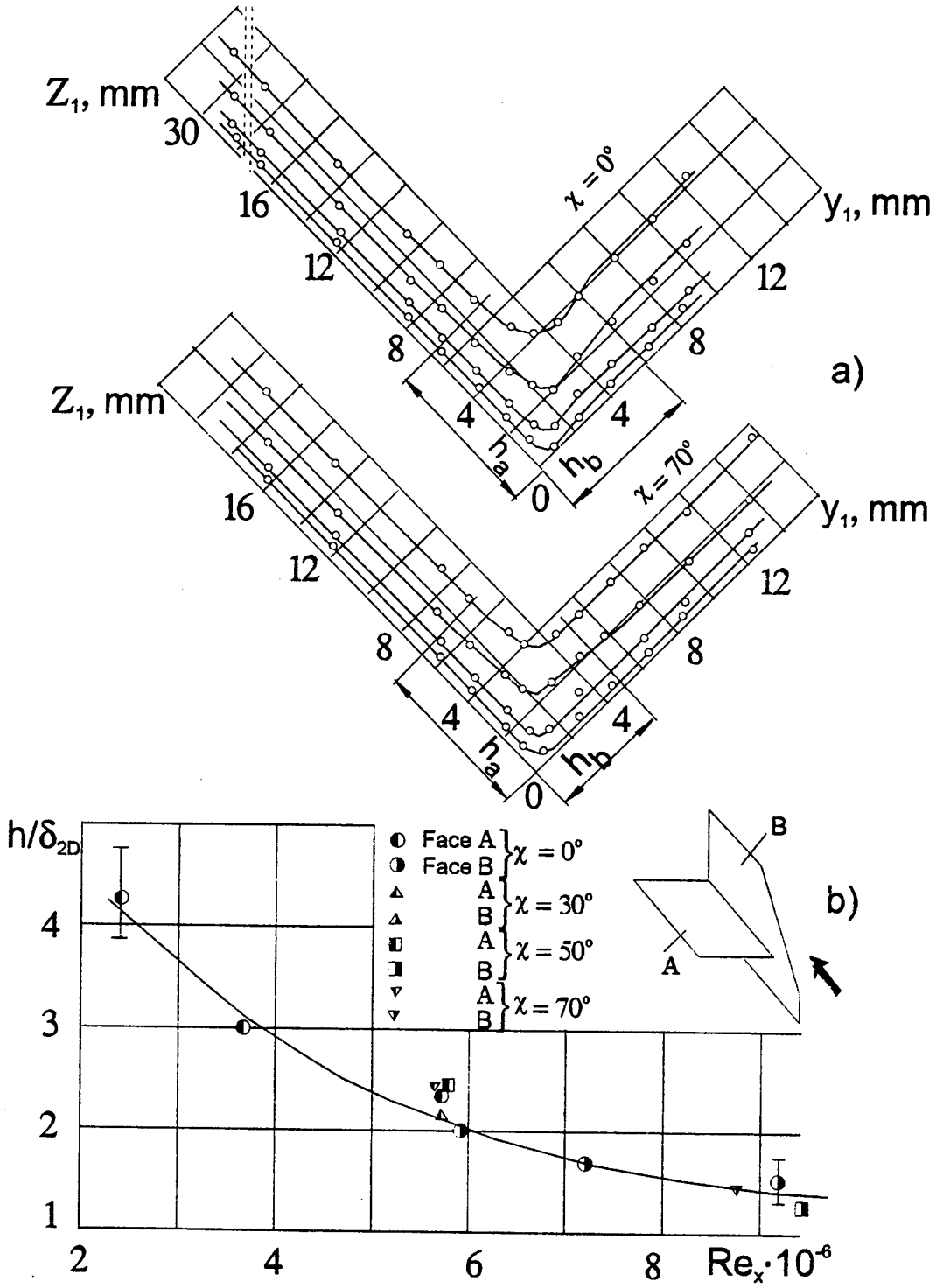


Fig. 22 M_∞=3, Re_1 =33·10^6 m^{-1}; 1 - U/U_δ = 0,7;
2 - 0,8; 3 - 0,9; 4 - 0,99

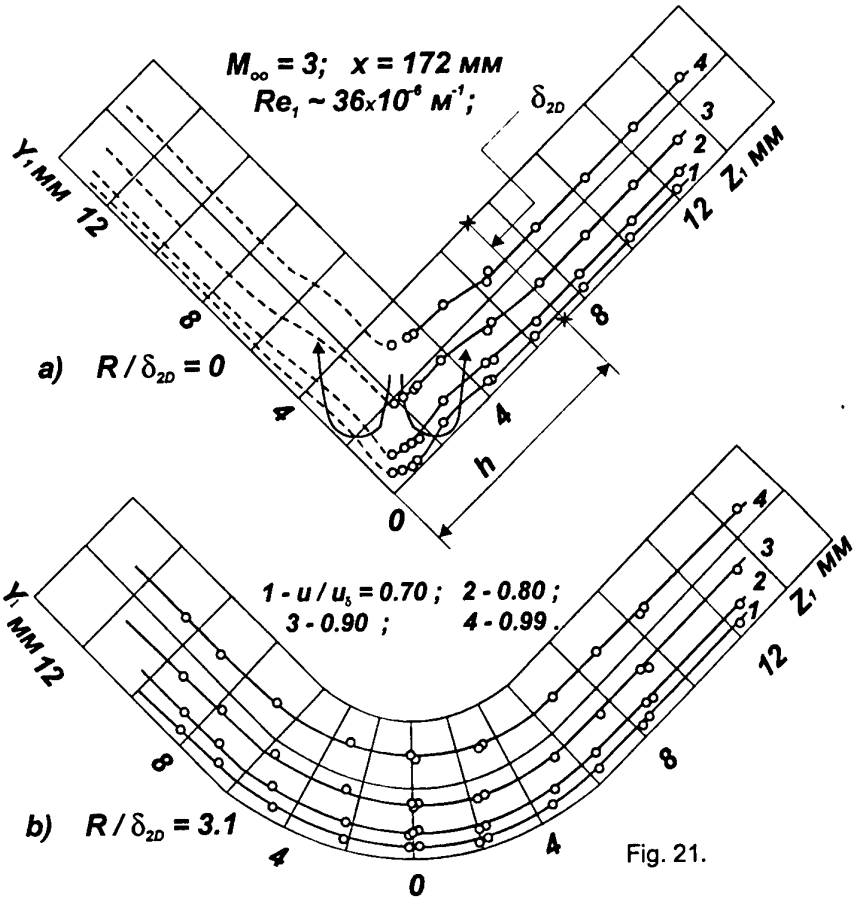

$M_\infty = 3$; $x = 172$ мм
$Re_1 \sim 36 \times 10^6$ м$^{-1}$;
δ_{2D}
Y, мм
Z, мм
a) $R/\delta_{2D} = 0$
h
1 - $u/u_\delta = 0.70$; 2 - 0.80 ;
3 - 0.90 ; 4 - 0.99 .
b) $R/\delta_{2D} = 3.1$

Fig. 21.

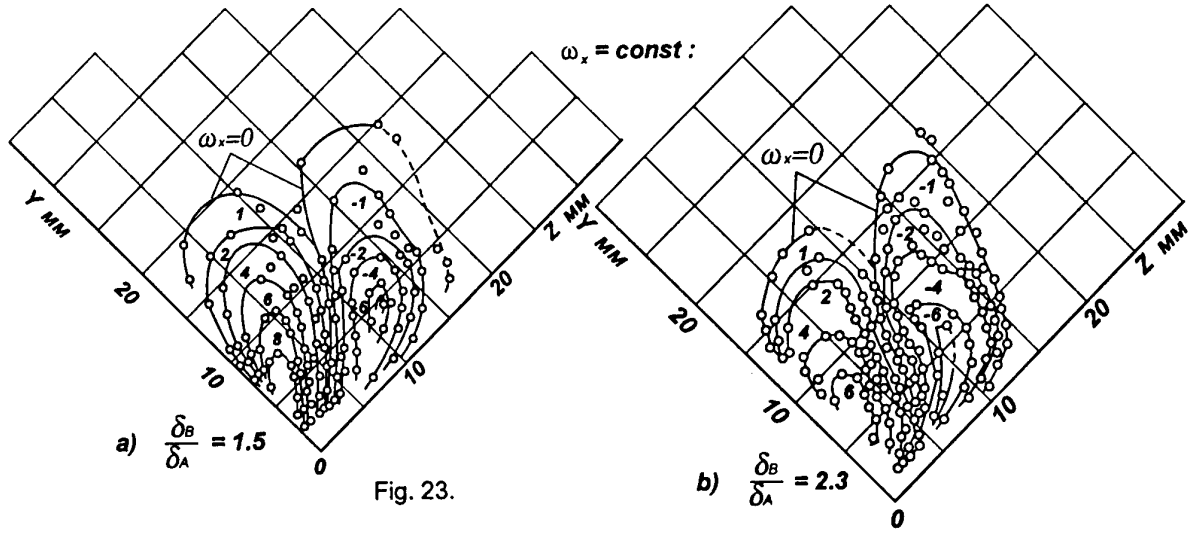

ω_x = const :
ω_x=0
Y мм
Z мм
a) $\frac{\delta_B}{\delta_A} = 1.5$
b) $\frac{\delta_B}{\delta_A} = 2.3$

Fig. 23.

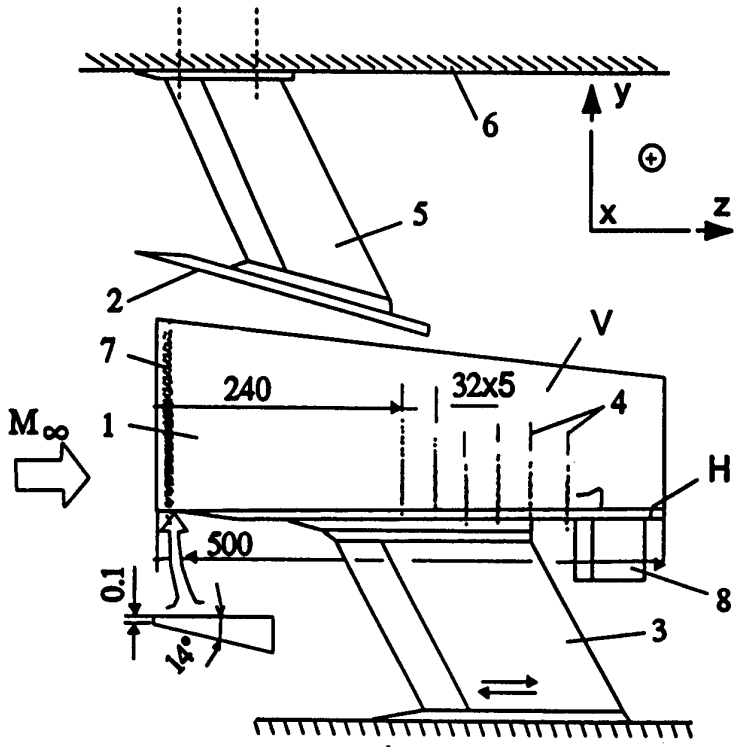

6
y
x
z
5
2
V
7
240
32x5
4
M_∞
1
H
500
0.1
8
3
14°

Fig. 24

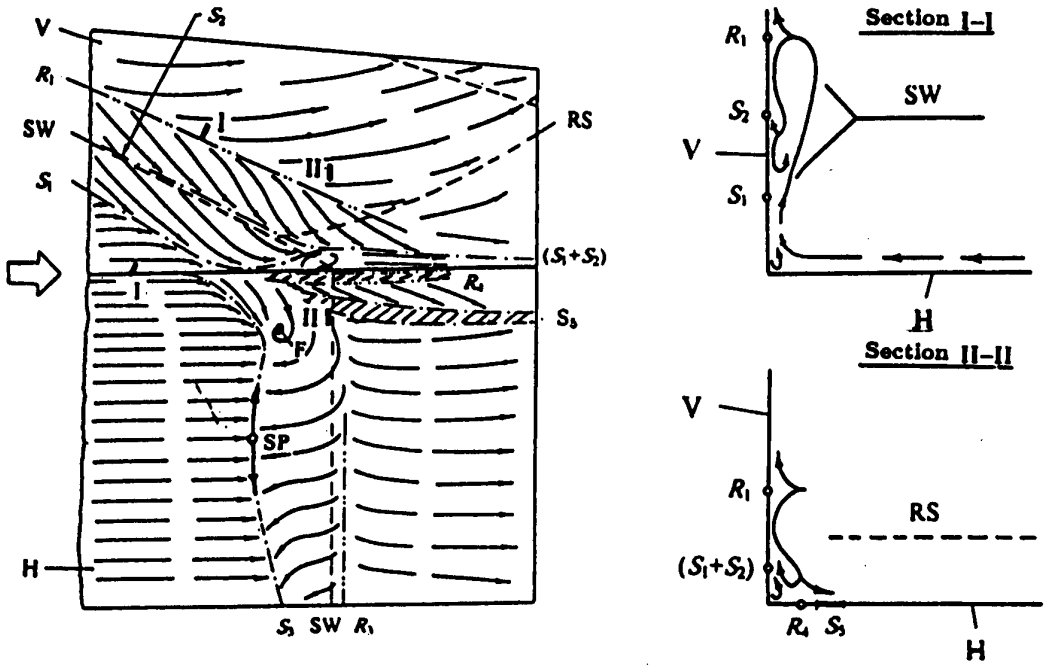

V
S_2
R_1
SW
S_1
RS
I
II
(S_1+S_2)
R_4
S_3
F
SP
H
S_3 SW R_1
Section I–I
R_1
S_2
V
S_1
SW
H
Section II–II
V
R_1
RS
(S_1+S_2)
R_4 S_3
H

Fig. 25

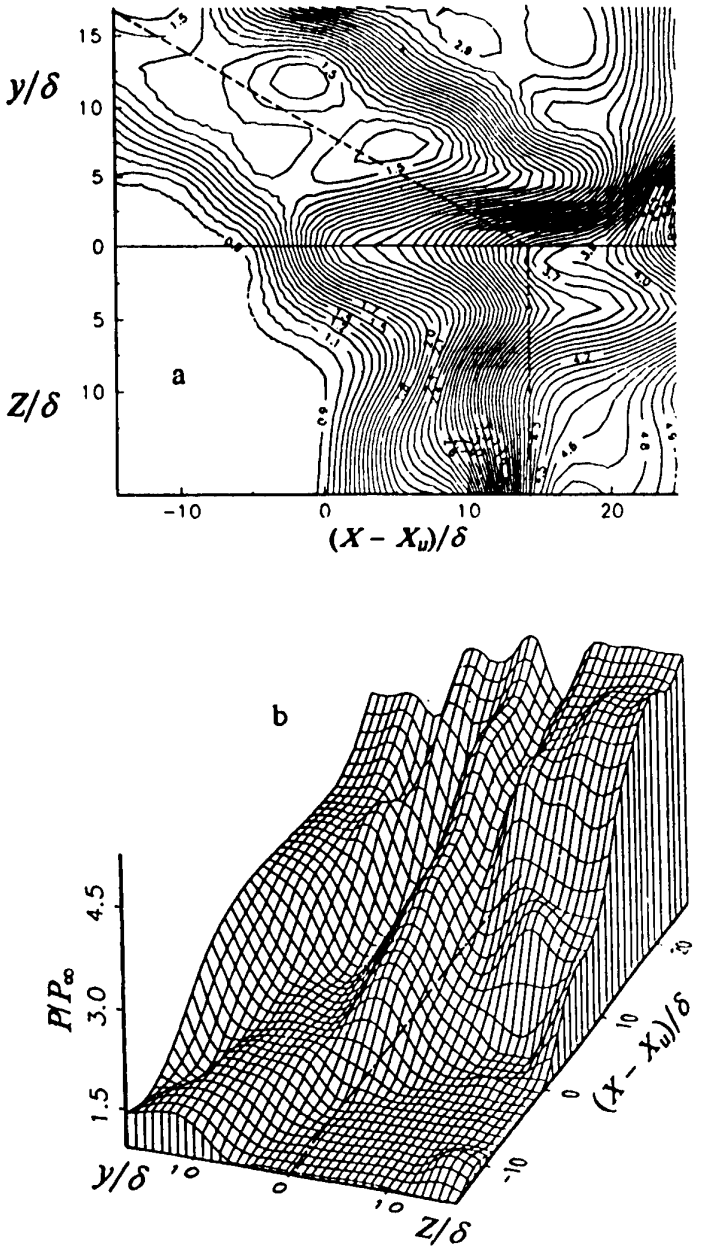


Fig. 26

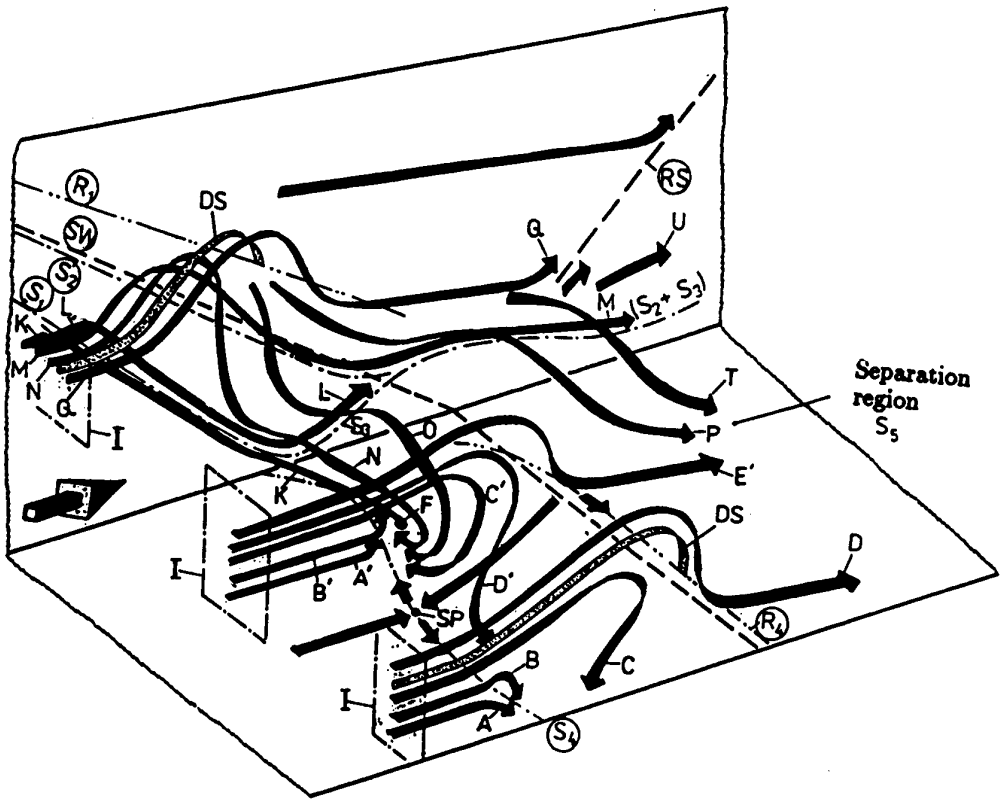

R1
DS
SW
S2
S
K
L
M
N
Q
I
RS
Q
U
M
(S2+S3)
T
Separation
region
S5
P
E'
L
O
N
K
F
C'
D'
SP
B'
A'
I
DS
D
R4
B
C
A
S4

Fig. 27

Required Technologies for Supersonic Transport Aircraft

Josef Mertens
Daimler-Benz Aerospace Airbus GmbH
D-28183 Bremen
Germany

SUMMARY
After referring to the remarkable technology level which Concorde has achieved, the most challenging new requirements for a future Supersonic Civil Transport are presented. It is proposed how to estimate influences of technology improvements on aircraft flight performance. A survey on key technologies follows with special emphasis on aerodynamic technologies.

1. CONCORDE TECHNOLOGY LEVEL

Concorde (fig. 1) is the only supersonic airliner which was introduced into regular passenger service. It is still in service at British Airways and Air France without any flight accidents, and probably will stay in service at least for ten more years.

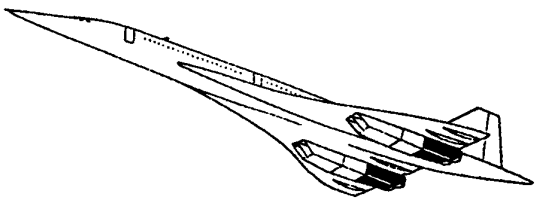


Figure 1: Concorde

Concorde has experienced the most supersonic flight hours and flight miles of all aircraft. Indeed, the only twelve flying Concordes have accumulated more supersonic flight hours than the total of all military aircraft all over the world. Concorde's range is about 6 500 km, whereas the best fighters like Su-27 or F-22 -so called "supercruisers"- achieve about 200 km in sustained low supersonic cruise, and military supersonic bombers or reconnaissence aircraft like B-1 or SR-71 reach about 3 500 km without refuelling. But although supersonic flight range of Concorde is by far better than for any other supersonic jet built, this range was the most important limiter for a commercial success of Concorde. A new viable supersonic airliner, called Supersonic Commercial Transport (SCT), must be able to serve the important trans-Pacific market requiring a range of 10 000 to 11 000 km. This is a tremendous improvement compared to the Concorde.

What are the differences between Concorde and a new SCT ? Besides the larger size, which improves a bit the range performance, technology improvements are cited to enable this big step forward. So, let's look at the technology improvements we have achieved in aviation since the Concorde design. As there is no other supersonic airliner, we have to compare Concorde's contemporary subsonic airliners with the newest generation of subsonic airliners [1].

Aircraft *flight performance* is governed by aerodynamics, structures and engines. All other disciplines -although often important for the viability of an aircraft- are only weakly related to *flight performance* of transport aircraft. Therefore we will look at the improvements in these main disciplines.

About the same development generation: B737-200, B747-100, Concorde
Modern aircraft, 25 years later: B737-500, B747-400, A340-300E

	OWE %	PAY %	OWE / PAY	F / PAY×Mm	Improvment %	Range Mm	PAX No.	MTOW Mg
Concorde	42,52	4,8	8,90	**1,647**	—	6,58	98	185,1
B737-200 *)	56,14	18,4	3,06	**0,398**	—	4,07	107	52,6
B737-500 *)	52,01	16,1	3,23	**0,436**	-9,55	4,48	108	60,6
B747-100	48,90	10,5	4,67	**0,458**	—	9,04	385	332,1
B747-400	45,99	9,61	4,79	**0,345**	24,67	13,27	420	394,6
A340-300E	47,90	9,82	4,88	**0,315**	31,32 (rel. to B747-100)	13,24	295	271

OWE: operating empty weight, PAY: payload, F: fuel
PAX: passengers MTOW: maximum take-off weight

Part of improvement was used to increase range, part to increase payload
Performance comparison by fuel per passenger-kilometer

*) Data base for the different B737-versions seems to be inconsistent; because the more efficient engine of the B737-500 (CFM-56 instead of JT-8D for B737-200) should improve aircraft efficiency, at least for long ranges

Figure 2: Weight improvements since Concorde

Paper presented at the RTO AVT Course on "Fluid Dynamics Research on Supersonic Aircraft", held in Rhode-Saint-Genèse, Belgium, 25-29 May 1998, and published in RTO EN-4.

1.1 Concorde structure weight still "comparable" - 25 years later

The first example of technologies concerns weight improvements, listed in figure 2.

Boeing B737-200 and B747-100 were developed in parallel with Concorde [2]. The new generation aircraft of comparable size are B737-500, B747-400 and Airbus A340-300E [3]; the latter beeing handicaped when compared with the B747-400, because it is a bit smaller. Improvements of fuel per passenger-kilometers of more than 30% were achieved; but comparison to the old aircraft is difficult, because data base has changed (improved seating standards etc.).

When comparing Concorde's structure weight, it is still comparable to the A340. (Comparison can only be made and was made by designing both aircraft with the same design tool. Assuming several structure technology standards, results showed the weights to reach the actual values of Concorde resp. A340, when using the same structure standards for both designs [4]). But what are the technologies leading to the subsonic weight improvements or Concorde's advanced values ?

- Because Concorde has only a small payload fraction, it is much more sensitiv to weight increments; therefore more effort was spent for weight savings and expensive solutions became useful.
- Many (weight) improvements for transonic aircraft after B737-100, B747-100 were provided by interdisciplinary effects like
  high bypass engines or
  optimized (nonlinear) transonic aerodynamics (fig. 3) via increased wing profile thickness and volume or reduced wing sweep

  which cannot be transferred to a Concorde type configuration.

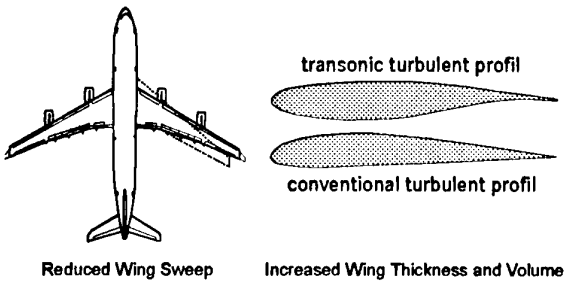


Figure 3: Improvements in Transonic Aerodynamics

- System weight was only marginally reduced since Concorde.
- Since Concorde's time many improvements in structure technology did not result in weight improvements, but were offset by advanced safety requirements; e.g. new requirements for pressure losses, cabin evacuation or fire resistance of cabin equipment. But this is the world where a new SCT must fly.

1.2 Limited aerodynamic improvement potential for a Concorde-like aircraft

When comparing aerodynamic improvements since Concorde time, we find strong differences in the aerodynamic efficiency between Concorde time subsonic aircraft like B747 or B737 and modern aircraft like B777, A340 or A320, expressed by improved L/D (lift/drag). These subsonic aircraft fly at high subsonic Mach numbers, when the air flow at the aircraft locally reaches partially subsonic, partially supersonic Mach numbers, which is named transonic flow. Physics of transonic flow include strong nonlinearities like shock waves, and the governing equations change from elliptic to hyperbolic type. Whereas the old aircraft were designed using pure subsonic linear potential flow theory combined with simple sweep theory, improvements were provided exploiting nonlinear theory; the latter require modern high performance computers not available for Concorde development.

But flow around supersonic airliners like the Concorde is dominated by small disturbances of the incoming flow, because strong disturbances would create high wave drag. Therefore, design (and especially sizing) of supersonic airliners can mostly be based on linearized potential flow theory, as was Concorde (slender body theory). Only for some parts nonlinear effects have to be respected for: strong interference effects like engine integration, fine tuning of the configuration and strongly nonlinear boundary layer flows. But, except for laminar flow, other strongly nonlinear boundary layer flows like separation are avoided because they are connected with large drag increases. Therefore, modern nonlinear aerodynamic theory can only provide limited improvements compared to Concorde (except for laminar flow).

Although, some aerodynamic improvements may be provided:

- New materials providing higher specific stiffness may allow a higher aspect ratio via interdisciplinary effects.
- Local optimization for nonlinear flow phenomena will provide reduced interference drag, especially for engine integration.
- Nonlinear calculations will speed up configuration optimisation.
- Supersonic laminar flow is the only new aerodynamic technology which can strongly improve performance. But it is still far away from realisation for large transport aircraft; and laminar design must not too much penalize wave drag design.

1.3 Olympus engine efficiency is still very good

When comparing engines we have to compare installed engine efficiencies (η_E), although mostly specific fuel consumption (SFC) is used.

SFC divides the fuel *flow* (i.e. an energy flow) by the thrust *force*; so physically it is not a meaningful value and can only be compared at the same speed (v = flight velocity). In contrast η_E is the amount of *energy flow* provided by the engine's thrust divided by the *energy flow* provided by the fuel (H = calorific value of fuel). η_E and SFC are connected via the equation

$$\eta_E \times H = v / SFC \qquad (1)$$

When not using a consistent system of units like SI, the respective unit conversions have to be applied. For Kerosen

H is given by

$$H = 42.817\ \text{MJ/kg} \qquad (2)$$

Now we can compare engines. At Mach 2.0-cruise, Olympus [2] and a proposed new supersonic engine are given as well as a modern high bypass transonic engine used for widebody aircraft [3]:

Olympus, M=2.0: SFC = 1.19 kg/daN/h η_E = 0,41 (3)

New engine, M=2.0: SFC = 1,13 kg/daN/h η_E = 0,43 (4)

CF6-80-C2, M=0,85: SFC = 0,56 kg/daN/h η_E = 0,37 (5)

We see that Olympus is still very good. The improvements of subsonic engines, mainly achieved by strongly increased bypass ratio, did not yet reach Olympus' efficiency. Indeed, at supersonic cruise a modern optimized engine with very low bypass ratio would provide slightly better values than the one given above. But this engine -like Olympus- will never meet the stringent noise criteria at take-off and landing which new SCT have to fulfill. Probably a bypass ratio of about 2 and extensive noise suppression (damping plus ejector) will be applied to meet noise criteria; this will decrease engine efficiency at supersonic cruise to values indicated above.

2. REQUIREMENTS FOR A NEW SUPERSONIC COMMERCIAL TRANSPORT (SCT)

There are only a few Concordes which serve a small, exclusive class of passengers over limited distances at high fares. For its rare presence Concorde is allowed to meet only elementary environmental criteria which will not become more stringent for Concorde itself. Especially for noise, ICAO Annex 16 and FAR 36 explicitly require for Concorde, that it must not become even more noisy than it was just at certification; and Concorde is very noisy. For new supersonic airliners those rules will never be applied; instead, a new SCT must fulfill new requirements which are not met by Concorde:

- It must comply with all valid certification rules,
- it must be economically viable,
- it must provide sufficient comfort.

A new SCT must be "just another aircraft" [5]. In the following paragraphs only those points are mentioned which will introduce significant new challenges compared to Concorde.

2.1 Relevant certification rules

Safety:

Concorde has proven to be save. But since Concorde certification some new rules were introduced by the authorities -e.g. FAA, JAA- which a new SCT has to meet [6]. The most obvious challenge is cabin pressure loss:

It is required, that aircraft and passengers can survive pressure loss in the cabin provoked by a sudden hole like a broken window. Therefore, sufficient pressure levels must be maintained in the aircraft when a hole opens. After DC10-accidents, when burst of underfloor cargo doors destroyed the floor of the aircraft with the hydraulic systems, size of the relevant hole was increased by pure geometrical definition (about the size of a door); for a wide body aircraft it has a size of 20 sqft (FAR 25). This poses extreme difficulties for flight altitudes above 40 000 ft. It is impossible to fight against this requirement by building a stronger aircraft, because there is no requirement on strength or probability of creation of such a hole, but only a given hole size. Concorde needs only to survive a hole in the hull of window size; and Concorde has small windows.

Environment:

- Concorde produces inacceptable noise at take-off and landing, although having less than 110 passengers. A new SCT, which will be of at least double the size of Concorde, has to meet current noise standards (FAR 36, stage 3) or even future more stringent ones. For comparison: FAR 36, stage 3 is just met by the B747-200. But SCT engines will not have a bypass ratio of about 5 like the B747-200 engines [2], but only one of about 2.
- Best aerodynamic performance L/D (lift/drag) is reached at elevated values of the lift coefficient (about C_L=0.5 for subsonic aircraft, below C_L=0.15 for supersonic flight). To fly at good aerodynamic performance, to maintain acceptable pressure levels in the inlets and engines, and to fill the engines with air, dynamic pressure at supersonic cruise will be in the range of about 20 to 30 kPa. Therefore, flight altitude depends on cruise speed and weight, for a Mach 2 aircraft about 16 km. And the higher the cruise altitude, the more sensitive is the atmosphere to pollution, especially the ozone layer. At the time beeing it seems, that a Mach 2-SCT will not harm the ozone layer; but this is based on calculations which still are questionable.

  Supersonic aircraft will burn more fuel per passenger kilometer than subsonic transports. Although CO_2 is not altitude sensitive, it is a well known greenhouse gas, and the large amount of CO_2 emitted has to be justified.

  In the future it has to be expected that the public becomes even more sensitive to environmental impacts. Therefore a new SCT has to demonstrate, that its impact on the earth' atmosphere is tolerable.
- A body cruising at supersonic speed generates a sonic boom which follows the body. This boom is an annoying and startling noise in an area of about 30 to 40 km at both sides of the SCT's track (fig. 4). To avoid harassment or

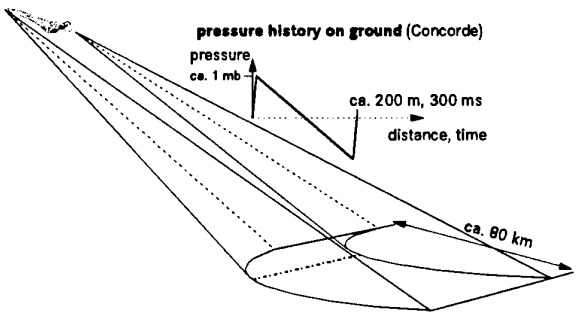


Figure 4: Sonic Boom

damage, civil supersonic flight will only be permitted over sea or perhaps uninhabited land. Because noise of the natural environment is so high on the sea, there is no

harassment or damage known to people, animals or ships below Concorde routes. In contrast to people on land, there exists no complaint about Concorde's sonic boom over sea [7].

Operations:
- Any new aircraft must be able to follow current and future ATC (air traffic control) procedures. In the future, steeper descent angles may be requested in the airport area which could be a challenge for SCT.
- New SCT must meet current ground load values, i.e. wheel number, size, loading and distribution. High ground load values may damage some airports, especially on aprons with tunnels.
- Loads on passenger and crew during operation must stay within acceptable boundaries. Especially long elastic fuselages provide strong vibrations during ground roll and in turbulence, and may impose high g-loads during rotation.

2.2 Economic viability

Range:

Concorde is only able to serve some of the medium range overwater routes. This is an inattractively limited part of the market. To gain a sufficient part of the market, future SCT must serve the important overwater long range routes. This, for the trans-Pacific routes, is more than 5 500 nm range. Range is even more important than speed ! For its limited range Concorde did not find a market, although Concorde's range was at the achievable limits. Also, the American SST, the Boeing B2707, failed for its insufficient range [8] and its uncontrolled growth of weight; even when environmental concerns were cited for stopping the program [9] (which luckily limited the liability of Boeing).

Operations:

Today, there exists a very expensive environment for air traffic operations: airports with its buildings and installations, hangars, air traffic control (ATC). New aircraft may require some additional installations, but the necessary investments must be paid by the money earned with those aircraft. And at least for the introduction of the new aircraft, success depends on the ability to cope with the existing environment. Time spent at the airport for de- and emparking of passengers, servicing of the aircraft, refueling etc. must be minimized:

- Aircraft dimensions (length, span or occupied ground area) must be compatible with existing installations at the relevant airports.
- Aircraft accessability (doors) must be compatible with existing airport installations; service ports should be compatible with usual procedures.
- Aircraft accessability must allow for parallel de-/embark, service, fueling, etc. to enable rapid turn-around.
- Aircraft supply needs must be compatible with existing (big) systems, e.g. fuel type.
- To serve the many routes with overland legs, subsonic cruise performance must be about as good as the supersonic one. Concorde has only poor subsonic performance.

Cost and fares:

A new SCT will only become a success, if the manufacturer of the aircraft and the airlines operating this aircraft will earn their money with this aircraft. This requires production of a sufficient number of aircraft at a profitable price for the manufacturer, and operationg cost which are lower than the money paid by the passengers [10, 11]:

- To reduce seat mile cost and to serve a large market, an SCT must transport many passengers (size effect), at least as much as subsonic long range aircraft (e.g. A340). (Smaller SCT would -at first- only serve full fare passengers; but after a short period airlines will begin to introduce reduced fares to fill empty seats -because empty seats are the most expensive seats-, and this leads to the situation today with mostly low fare tickets.)
- To gain a sufficient part of the market, a future SCT must serve all classes.
- Speed pays (see cars, trains, air traffic) but a surcharge must stay in acceptable limits. It seems, that the travelling public accepts surcharges of about the money they would earn for the time they saved by the increased speed -even for holiday trips.
- An SCT with those (low) fares must still allow a profit for manufacturer and airlines. And the manufacturer must sell many aircraft in order to provide an acceptable price. This becomes impossible with pure exclusivity.

2.3 Comfort

Passengers like comfort, and especially on long trips some level of comfort is necessary. But what is the special kind of comfort required for supersonic transports ?

Range:

Passengers select a faster transport to save time; and they pay for the time saved. But this is the time from airport to airport or even house to house. Therefore supersonic transport makes only sense, when the flight time is an essential part of the trip time, i.e. for long ranges.

And passengers do not like stop-overs; because they prolong flight time and are even more annoying than flight.

Therefore an SCT must provide long range capability, to connect at least the most important areas of the world: Europe, US and eastern Asia, all separated by up to 5 000 to 6 000 nm.

Speed:

Passengers pay for the time saved. Therefore overall trip time has to be reduced, as well by high cruise speed without stop-overs, but as importantly by accelerated check-in / check-out.

Additionally, many passengers feel very uncomfortable during and after trips of more than 6 hours flight duration, especially children, or disabled and elderly people, who will feel circulatory trouble.

Space:

Passengers want space like in comparable subsonic transports, i.e. medium range transports with same flight duration. The narrow Concorde fuselage is only accepted for Concorde's exclusivity.

3. ESTIMATION OF TECHNOLOGY INFLUENCE

There are several technologies to improve a new SCT. In order to evaluate the importance of a technology, we must be

able to estimate its influence on the realisation of an SCT. At present level of knowledge, there is a hierarchy of technologies from fulfillment of constraints over cruise performance to operations. The operations are still at the last position, because we are on search for a technical solution. When a solution is found, operations will become more important, because they contribute strongly to cost performance.

3.1 Technologies to fulfill constraints

Here technology estimation is possible looking for the relevant physical priciples. Influence of constraints on aircraft cruise performance and cost is indirect, but can be very strong and limiting.

The most important constraints for an SCT are:

- *Take-off:*
  Field length:
  The required *thrust* (i.e. engine size) is determined by *weight* (acceleration) and *aerodynamic lift* (span, wing area, rotation angle) at lift-off (i.e. minimum airspeed).
  Take-off field length is defined by runway length of the relevant airports to be used by SCT. Today about 11 000 ft are assumed.
  Climb rate:
  The required *thrust* is determined by *weight* and aerodynamic performance **L/D**.
  After take-off, a climb rate with one engine out must be maintained of
  0,5% with gear extended and
  3% with gear retracted.
- *Noise:*
  Noise is determined mainly by *exhaust velocity* of the jet engines (as long as the turbomachinery is well shielded by inlet and nozzle) and mass flow (i.e. *thrust*; take-off thrust = massflow · exhaust velocity). This means that an aircraft of same weight should have about the same nozzle area to produce comparable noise; e.g. SCT and B747.
  Stage 3 compliant low noise exhaust velocities are between 300 m/s (Airbus A340, well below stage 3 limits) and at most 400 m/s [12]; for compliance, bypass ratios of about 2 or comparable measures are required.
  Required low speed *thrust* is determined by **field** *acceleration*, by *weight* and *drag* during **climb**, and by *drag* during **approach**.

  In the rules ICAO, annex 16, chapter 3 and its derivations FAR 36, stage 3 or JAR etc., maximum noise allowed at take-off and landing is defined. Figure 5 shows the three points, where noise is measured. Maximum noise levels

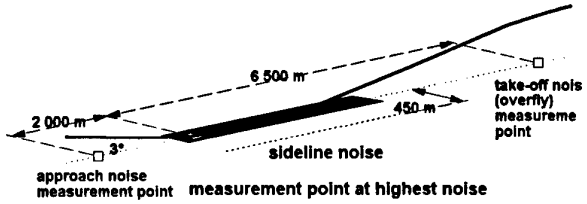


Figure 5: Noise measurement points

  allowed for the different points depend on aircraft weight and number of engines. Noise levels are measured in EPNdB which is a time integral of the EPNL(dB) weighted noise. Additionally, if noise at one point is only a little more elevated (at most 2 dB), it may be compensated by lower noise at the other points, following some complicated weighting.

- *Transonic acceleration:*
  The highest *wave drag* values and the worst ***engine efficiency*** nearly coincide at low supersonic speed; this may determine engine size.
  Best supersonic cruise performance does not make any sense, if the supersonic aircraft is not able to reach supersonic speed.

- *Range:*
  Fuel amounts to a very high portion of gross weight (50% or even more). Therefore *cruise efficiency* determines range capability.
  Airlines indicate, that a viable supersonic transport must be able to fly at least about 5 500 nm. Many routes include segments over inhabited land, where only subsonic speeds are allowed.
  Supersonic cruise:
  Reduce ***aerodynamic drag*** (here by slenderness), reduce *weight* and improve supersonic *engine efficiency* (here via decreased bypass ratio) to meet range requirements.
  Drag at supersonic cruise is dominated by wave drag, but friction drag and induced drag are important as well. Drag has to be balanced by thrust.
  Subsonic cruise:
  Improve subsonic *engine efficiency* (here via increased bypass ratio) and
  reduce *aerodynamic drag* (here mainly larger span);
  both reduce supersonic efficiency.
  Drag at subsonic cruise is dominated by by friction drag and induced drag, possibly vortex drag due to separation. Drag has to be balanced by thrust.

- *Controllability:*
  Provide *control authority* for all disturbances either external (gusts, manoeuvers) or internal (failure cases like inoperative engines, cabin pressure loss).

- *Emissions:*
  It seems, that most important will be *NOx-generation* for its influence on the ozone layer.
  NOx-generation is determined by peak temperatures which occur only at spot points in the burner, where stochiometric conditions are met. Low NOx-burners reduce peak temperatures, but still maintain high mean temperatures.

Some of those constraining influences work against each other. For estimation of values compare subsonic aircraft of similar weight, e.g. B747, but pay attention to the significant physical parameters.

3.2 Technologies to improve cruise performance

To estimate influences on cruise performance, at first we will estimate the most important physics of constant cruise. This is -for a real aircraft- some kind of oversimplification, because it ommits the important segments of take-off, climb, climb during cruise, acceleration and reserves for go-around and divert as well as the minor parts for descend, landing and

taxy. But for a long range aircraft it remains the most important segment.

Constant cruise is governed by the two equilibriums of lift (**L**) and weight (**W**), and of thrust (**T**) and drag (**D**):

$$L = W \qquad (6)$$

$$T = D \qquad (7)$$

Thrust is payed by fuel (**F**)

$$T \cdot SFC = dF/dt \qquad (8)$$

(SFC: specific fuel consumption, see eq. 1; t: time)
which reduces mass (**m**) or weight

$$dF = - dm, \qquad W = m \cdot g \qquad (9)$$

but provides range (**r**) via speed (**v**)

$$dr = v \cdot dt \qquad (10)$$

When introducing the other equations in (8), simple algebraic operations provide the differential Breguet equation

$$dr = - (v \cdot L/D) / (SFC \cdot g) \cdot dm/m \qquad (11)$$

or with engine efficiency η_E and calorific value of fuel **H** instead of specific fuel consumption SFC (eq. 1)

$$dr = - L/D \cdot \eta_E \cdot H/g \cdot dm/m \qquad (12)$$

After integration we have Breguet's range formula

$$r = L/D \cdot \eta_E \cdot H/g \cdot \ln [m_o / (m_o - F)] \qquad (13)$$

or

$$r = (v \cdot L/D) / (SFC \cdot g) \cdot \ln [m_o / (m_o - F)] \qquad (14)$$

r is the Breguet range which for a real aircraft is longer than the aircraft's range, but it allows for comparison of aircraft of similar weigths or designed for similar missions.

Aerodynamics determine aerodynamic performance **L/D** and so influence needed fuel **F**, but also provide requirements for structural layout and systems.
Fuel, structures, engines, equipment and payload are total mass at begin of cruise $\mathbf{m_o}$.
Engines contribute to mass and provide its efficiency η_E which influences needed fuel **F** and mass for fuel storage.
The selected cruise speed **v** or cruise Mach **M** influences achievable **L/D**, engine efficiency η_E or SFC, needed fuel **F**, and structure and equipment mass.

The Breguet equation allows simple estimation of range and comparison of range performance for different aircraft designs; but it is still difficult to estimate improvements by singular technologies. The Breguet equation provides a rough estimation of range improvements, when only one parameter is changed, e.g. range improvement Dr provided by a pure aerodynamic improvement DL/D for the same aircraft (η_E, m_o, F). Now equation (13) gives

$$\Delta r = \Delta L/D \cdot \eta_E \cdot H/g \cdot \ln [m_o / (m_o - F)] \qquad (15)$$

For fixed range, we can try to estimate the influences on fuel needed (**F**) by the inverse Breguet equation

$$m_o/(m_o - F) = \exp [r/(L/D \cdot \eta_E) \cdot g/H] \qquad (16)$$

But caution: usually now both m_o and F become strongly dependent on $\Delta L/D$ or $\Delta\eta_E$; because better drag or engine efficiency reduces fuel consumption F, and this reduces gross weight m_o. Therefore the inverse Breguet equation usually calculates an aircraft whose performance is not exploited. To exploit performance, the aircraft has to be resized. This cannot be calculated by a simple equation. As a first, very rough estimation, the unresized improvement for fuel consumption, calculated by the inverse Breguet equation (16), has to be multiplied by the factor:

$$1 + \text{(weight part under consideration)} / m_o \qquad (17)$$

e.g. for improvement of η_E: $(1 + F/m_o)$. But remember: Breguet equation only calculates idealised cruise flight. Therefore it may only be used for estimation of tendencies in long range flight.

Small improvements in fuel consumption by individual technologies may be *compared* by: percentage of the individual improvement, multiplied by

weight part influenced by this technology / payload (18)

This is explained in fig. 6 by several examples for an Airbus

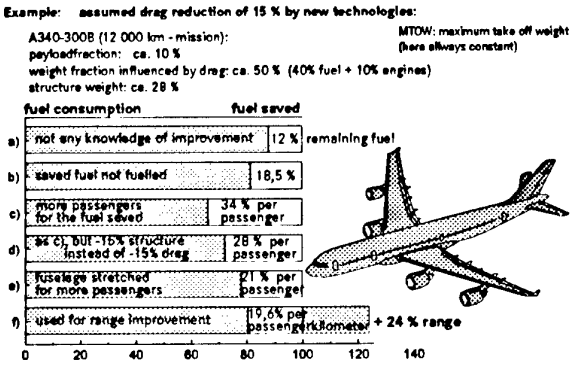


Figure 6: Improvement estimation
A340-300B with an assumed 15% pure drag improvement or a 15% structure weight reduction; for all examples the maximum take-off weight (MTOW) was maintained by adding fuel or payload.

3.3 Technologies to improve operations

Technologies for operational improvements usually are not directly connected to flight performance, but rather to operating costs. Therefore, simple estimation of their influence is difficult. Most of these technologies are not specifically related to SCT. Some of them are mentioned.

Materials with improved creep resistance for hot engine parts:

In supersonic engines temperatures remain high during cruise, whereas for subsonic aircraft peak temperatures are reached only at take-off. Therefore high temperature creep resistance becomes more important for SCT. It will allow higher engine (cruise) efficiency and/or reduce maintenance costs.

Special control systems to guaranty controllability:

Because SCT-configurations strongly differ from subsonic or military aircraft, some different control problems may occur; e.g.

- inoperative engines with high lever arms in supersonic flight; if this determines control surface loads (mainly rudder, but also aileron, elevator) special surfaces or procedures may provide improved solutions
- after a sudden pressure loss
  - special devices or differently sized devices to produce high drag may enable rapid descent and deceleration to reach sufficient atmospheric pressure levels
  - special devices may help to maintain sufficient pressure and temperature in the cabin.

If needed, appropriate systems must be developed.

Neutral point and center of pressure vary strongly when going from take-off over transonic flight to supersonic cruise and back for landing. For optimum flight performance during supersonic cruise, only very small control flap deflections are allowed.

Both require a highly sophisticated fuel trim system.

Artificial vision will avoid the heavy Concorde-like droop nose.

Artificial vision is just under development for CAT III landings and ground roll of subsonic aircraft.

Manoeuver and gust load alleviation may reduce wing weight.

Just in use for several aircraft (L1011-500, A320, A330/A340) and will be improved for future ones (A3XX).

Systems for reduced turn-around time improve aircraft productivity.

Such systems are under development all the time, especially for expensive, very large aircraft like A3XX. Special problems for SCT are

- a large wing root blocks accessability to large parts of the fuselage
- a narrow fuselage retards boarding/deboarding and ground cabin service (like cleaning)
- the large fuel amount requires several points or long time for fuelling.

Systems to reduce maintenance costs are under development for subsonic aircraft all the time. Specialities for SCT are:

- Supersonic inlet and nozzle are specific to SCT.
- Accessability to the engines is reduced by supersonic inlet and nozzle, and possibly by installation just at the wing.
- In many areas of the SCT space is very limited (small thickness at movables, tail, nose).
- Dissimilar SCT-geometry requires different procedures.
- Elevated temperatures during cruise introduce dissimilar loads and load cycles which alter maintenance, sometimes even in favor for SCT (e.g. corrosion).

Active landing gear allows better damping of roll vibrations, ground loads and supports take-off rotation.

Just under development for very large aircraft like A3XX.

Improved ATC-systems.

Strongly required are new ATC systems and procedures, especially for long range overwater guidance and area navigation (direct flight, not restricted to airways linking ATC-control points), and automated data links (FANS = Future Air Navigation System). They are not specific to SCT and are just under development for subsonic aircraft.

4. TECHNOLOGIES FOR A CONCORDE SUCCESSOR: KIND AND RISKS

We have seen, that many technologies required for a new SCT are just developed or under development for subsonic aircraft. Other technology improvements cannot be transferred to an SCT. And Concorde's technology level is still "comparable". But what are the new technologies which will enable realisation of a competitive SCT with sufficient range and operating costs ?

4.1 Aerodynamic technologies

This course mainly deals with aerodynamics; in chapter 5 aerodynamic technologies are prescribed in more detail. Therefore, here only the important points are mentioned.

Aerodynamic multi point design:

For subsonic aircraft, in the first design step usually a two point design is made for

- high speed cruise and
- low speed take-off and landing.

Often this is achieved via a nearly pure one point design for high speed cruise, whereas low speed performance is achieved using rather complicated flap systems.

A supersonic aircraft must be able to cruise economically at supersonic speed over uninhabited areas and at high subsonic speed over inhabited land. And supersonic cruise only becomes possible, if transonic acceleration can be realized. So, we have to design for four points:

- supersonic cruise,
- high subsonic cruise,
- low speed take-off and landing and
- transonic acceleration.

Moreover, low speed performance cannot be achieved using additional large flap surfaces like fowlers. Since an SCT has a large wing surface, effect of (fowler) flaps is very limited. And lift slope ($C_{L\alpha}$) decreases for small aspect ratio. But lift via high angle of attack, as used for Concorde, is accompanied by large drag which requires noise producing thrust.

Therefore a best combination of aerodynamic's (and other discipline's) design principles is required to meet the

diverging requirements. Most important part is selection of a suited configuration, for which aerodynamics contribute strongly in meeting the four aerodynamic design points.

Nonlinear aerodynamics:

Nonlinear aerodynamics enable minimisation of interference losses, e.g. engine and wing-fuselage integration. It is beeing developed for subsonic transports; but it becomes more challenging for supersonic transports by the combination of nonlinear effects with very weak oblique shocks, strongly three dimensional geometries and boundary layers, and strong shocks around the engines and in the inlets, even with reflected shocks.

Control surfaces:

Design of the control surfaces depends strongly on the configuration selected. Smart solutions may decide on the viability of a configuration or strongly ease design and operation.

Aeroelastics:

New approaches like aeroelastic tailoring or aeroelastic control are beeing developed for large subsonic transports. For the slender SCT-configuration, inclusion of aeroelastics in the early design stage is a prerequisite, at least for static aeroelastics (i.e. inclusion of the shape variation due to aerodynamic loads, but still without vibrations). For many SCT-configurations, flutter itself is as important, but hitherto it can be checked only at a more matured design stage, when a more detailed data base was built up.

Aerodynamics, especially nonstationary aerodynamics, and dynamic structure calculations are much more challenging for an SCT than for subsonic transports, at least for the flutter sensitive symmetric (Concorde-like) configurations. Because flow and structure dimensionally has to be treated completely three dimensional, 2D- or quasi-2D approximations like airfoil flow, sweep theory or beam approximations are not possible.

Aerodynamic damping decreases with speed. Therefore supersonic cruise becomes flutter sensitive. But the nonlinear transonic aerodynamics (here high subsonic) also decrease flutter damping -the so called transonic dip. So there is a second high subsonic flutter case which mostly is even more flutter critical than supersonic cruise [13]. This is one of the most challenging calculations in SCT design.

Supersonic laminar flow (SSLF):

Supersonic laminar flow (SSLF) may provide strong improvements during cruise flight. But it is still far away from realisation and many questions are unresolved; even some physical principles are still not yet understood [14].

Today, we postulate a reference SCT to be viable without SSLF. Because, when a new subsonic aircraft will benefit from laminar flow, also the SCT must be improved by SSLF in order to maintain its competitiveness.

4.2 Material technologies

An SCT has only a small payload fraction; therefore it becomes very weight sensitive. To make a Concorde-like SCT viable, the necessary reduction of structure weight (compared to available technology, e.g. A340) will be about

30% for a Mach 1.6 SCT

40% for a Mach 2.0 SCT

50% for a Mach 2.4 SCT.

Even when considering for the high unit price of an SCT, this seems to be very risky! But still some improvements in other technologies -especially configuration selection- may reduce the weight improvement requirements given above.

New Materials:

For Mach numbers below 1.8, highest temperatures occur in sun shine on the ground. For Mach numbers above 1.8, cruise temperature becomes important, especially in respect to life time. Below Mach 2.0, for the airframe emphasis is still more on light weight than on temperature. Some materials envisaged are carbon fibers (CFRP), metal matrix composites (MMC) for highly loaded parts, ceramics.

For supersonic engines creep resistant high temperature materials are required (peak temperature during cruise).

Manufacture:

New methods are required to manufacture very light weight structures and elements. For new materials, methods must be developed to fabricate parts and to join them to assemblies.

Concepts for inspection, repair and crashworthiness are required.

All these have to be qualified early.

Structure design:

Materials and manufacturing principles must be integrated in the design process. For higher Mach numbers, the design must respect for thermal dilatation and stress.

Optimisation methods will reduce weight and integrate structure design with other discipline's needs.

Aeroelastics:

Provide data early in the design process, to direct the interdisciplinary design to an optimum solution which respects for aeroelastic deformation and which will have a save flutter margin.

Integrate stiffness (and thermal) design with aerodynamic design (aeroelastic/ aerothermoelastic tailoring).

Certification:

New materials and manufacture methods must be certified, before being considered in design. Both require a long time, especially for fatigue and thermal fatigue proving.

For Mach numbers above 1.8, thermal fatigue properties must be demonstrated for the materials, for structural concepts, and for the aircraft itself [6].

4.3 Engine technologies

Engines must fulfill several requirements at different design points, like the aircraft.

Efficiency:

SCT-engines must be very efficient at supersonic and high subsonic cruise, and

must provide sufficient thrust at take-off, transonic (low supersonic) acceleration and cruise.

Emissions:

To protect the atmosphere, pollution has to be minimized. Especially low NOx-burners are developed. This is even more stringent than for subsonic aircraft, because SCT fly

higher and burn at higher temperatures during cruise.

Noise:

Engine noise during take-off and landing must be comparable to subsonic aircraft (ICAO annex 16, chapter 3; FAR 36, stage 3). This requires large nozzle exit areas, comparable to subsonic aircraft of the same weight.

The multipoint capabilities of the engines are strongly related to the configuration selected. E.g. thrust available during take-off and landing depends on engine bypass ratio, noise reduction by suppression or simply throttling down, possible integration of noise suppressors in the airframe etc. This influences engine weight, thrust available and engine efficiency in the other design points. On the other hand, thrust required in the different design points is determined by the configuration, mainly aerodynamic performance and weight.

4.4 System technologies

Most systems are comparable with the ones of subsonic aircrafts. Emphasis is on low weight, small space and possibly high temperatures. Special systems for SCT are:

Inlet and nozzle control

Supersonic engines work at subsonic speeds. The inlet must decelerate the flow to subsonic speed, the nozzle must adapt to free stream pressure. Inlet control with several shocks and tuning with nozzle state is especially challenging. Concorde's solution is still state-of-the-art.

CG-control

From subsonic to supersonic flight, the center of pressure varies strongly. Control is provided by center of gravity (CG) control via fuel transfer. This system is proved in Concorde and applied in several subsonic jets as well.

Control of OEI (One Engine Inoperable) during supersonic flight

Sudden inoperability of one engine (OEI) or inlet surge / inlet unstart during supersonic flight must be covered by the flight control system. During this time no excessive loads must be provided to the airframe or the passengers. Possibly special control devices will support this failure case. E.g. Concorde and SR-71 switch off the symmetric engine and restart both engines symmetrically to control this asymmetric failure case.

Scheduled systems

In order to meet noise requirements at take-off and landing, it is envisaged to use an automated system for scheduling of flight path, flap settings and engine controls. This is envisaged for subsonic aircraft as well. But an SCT will depend more on such a system.

4.5 Multidisciplinary Design Optimisation (MDO)

A "classical" Concorde-like design has to reach technology limits of all relevant disciplines. This requires perfect harmonisation of all aspects in the design.

An unconventional configuration can improve performance over the limits of the "classical" configuration. But it requires a new kind of cooperation between the individual disciplines, with dissimilar interfaces between the disciplines compared to the "classical" approach.

In both cases, a solution requires the toolbox of Multidisciplinary Design Optimisation (MDO) [15, 16, 17].

There are three objectives of MDO, each of them of equal importance.

Harmonize multiple disciplines:

Organize cooperation and data transfer between all relevant disciplines.

Although all over the world companies talk about introducing MDO, total quality management (TQM), concurrent engineering (CE) etc., in real life there are strong objections of hierarchies against any kind of cooperation between departments. Future will show, if market competition will improve the situation.

Cooperative design:

Data to be respected for harmonisation and tools applied have to be carefully selected and must be ordered from crude predesign to detailed final design. Data transfer, from predesign to the more detailed design steps and vice versa for iteration steps, must be organized and fit into the data selected for interdisciplinary transfer.

Combine the relevant data into a design which must be evaluated by all participating disciplines.

The design process must be able to update the design exploiting the data corrections occured in the cooperative evaluation.

Optimisation:

Use optimisation tools which are well adapted to the different design stages in order to exploit the best combination of the available technologies. Especially for interdisciplinary development steps, numerical optimisation is recommended.

MDO is the **key technology** for a new supersonic transport. For subsonic transports remarkable improvements are also expected.

5. AERODYNAMIC TECHNOLOGIES

A well balanced contribution of new technologies in all major disciplines is required for realisation of a new **S**upersonic **C**ommercial **T**ransport (SCT). One of them -as usual one of the most important for aircraft- is aerodynamics. Here, the required "pure" aerodynamic technologies are specified in more detail, according to our present knowledge. Increasing insight into the problems may change the balance of importance of the individual technologies and may require some more contributions. We must never confine our knowledge to the knowledge base of an expert (or expert system) at a given time, but must stay open for new insights [18].

5.1 Aerodynamic knowledge base

Physics of flow will be presented in another lecture. Here some unresolved or not completely understood problems are presented which require some aerodynamic knowledge improvements.

5.1.1 Unresolved problems in the supersonic flow regime

Suction force:

Compared to lower flight speeds, in supersonic flow the efficiency of leading edge suction becomes more and more inefficient. Basically this should be correlated to the Mach number components normal to the leading edge, trailing edge, maximum thickness line etc. But following M. Mann and H. Carlson [19], it should be correlated to free stream Mach number.

Reasons for loss of suction force are:

- Low pressures generate suction forces, but reduce density. This diminishes efficiency of suction forces, especially in combination with shock losses. Both are compressibility effects which should (mainly) be related to (l.e.) normal Mach numbers.
- Supersonic trailing edges inhibit circulation efficiency and so reduce suction force recovery. For supersonic leading edges suction force is lost.
- The flow field in the vicinity of the wing is governed by radiation processes. These processes are not exactly modeled by numerical calculations: linearized theory does not model effects of local Mach number variations and therefore is unable to produce the correct radiation directions (characteristics). Most nonlinear methods respect for the local Mach numbers, but do not exactly model radiation; so numerical diffusion smears out radiation transport.
- Supersonic wings are mainly designed for minimum wave drag. This leads to nearly conical flow situations. At higher Mach numbers with smaller Mach angles this introduces strong pressure gradients in spanwise direction, i.e. normal to the free stream direction. Boundary layer flow tends to follow local pressure gradients; so, boundary layer air will accumulate in the low pressure valleys on the wing and may modify the designed low wave drag pressure distributions. This effect should strongly depend on Reynolds number and might be stronger in low Reynolds wind tunnel tests than in free flight. This effect is mainly related to free stream Mach number.

Complete understanding of the limitations of linearized solutions, CFD-solutions and low Reynolds wind tunnel tests remains open.

Radiation in CFD solutions:

Linearized theory does not respect for local Mach number variations. Usual CFD-methods do respect these, but only marginally model radiation properties. Numerical stability is achieved usually by addition of numerical viscosity. Without proper modelling of radiation properties, though, random contributions are introduced into the solution or valid contributions are neglected. Upwind schemes should model radiation, but most upwind schemes are basically one-dimensional and cannot model radiation direction, like all the upwind schemes which only fulfill the eigenvalue sign; i.e. they approximate the radiation direction by an accuracy of up to ±90°. Only CFD methods which are carefully based on the method of characteristics (MOC) provide good radiation properties, but these methods usually are not suited for universal CFD codes, especially for their rather inflexible handling of complicated geometries. A challenge remains to improve the tools for supersonic CFD.

Physical drag contributions:

To improve the aerodynamic design of an aircraft, it is very helpfull to know the different contributors for physical drag:

- Wave drag (radiated energy plus entropy already generated by shocks)
- induced drag
- friction drag
- separation drag.

For subsonic flow and linearized supersonic flow, methods exist largely based on far field balances, e.g. [20], but for nonlinear supersonic flow the far field results are poor, because of inexact radiation models. Also, due to the small leading edge radii, surface integration accuracy is more difficult to achieve; only friction drag can easily be extracted.

The following tasks summarize the challenges of supersonic aerodynamic design:

- Provide aerodynamic data suited for interdisciplinary design optimisation. These data must not be at the achievable accuracy limits, but must be reliable within specified accuracies for a wide range of configurations.
- Maximize aerodynamic performance (Lift/Drag = L/D) for given geometrical constraints:
  - improve quality of aerodynamic tools to reflect flow physics,
  - balance wave drag, induced drag, friction drag (including laminarisation concepts, riblets) for minimum overall drag.
- Determine the limits of special flow phenomena, like suction force.

5.1.2 Low speed tasks:

At take-off, it is necessary to

- improve lift
- maintain control
- improve L/D by limitation of drag;

whereas at landing it is required to

- improve lift
- increase drag, possibly by drag control devices
- guarantee handling qualities, especially when using partially separated flow
- and allow for go-arounds (sufficient thrust and/or rapid drag reduction).

5.1.3 Transonic tasks:

At high subsonic cruise optimize L/D:

avoid separation

minimize induced drag.

For transonic acceleration:

- minimize wave drag which is dominated by interference effects
- provide control of the aircraft
- provide control of engine inlet and nozzle.

5.2 Flap effectiveness

5.2.1 Supersonic hinge lines

At control surfaces with supersonic hinge lines, shocks occur at the hinge line. Shocks produce pressure losses and so reduce flap effectiveness. Additionally, the shock can provoke boundary layer separation bubbles (fig. 7); pressure in those bubbles is lower than behind the final shock. This reduces the flap force significantly. Because of the system of the three shocks behaving very sensitive to variations in the incoming flow and fluctuations in the separation bubble, strong vibration loads can arise.

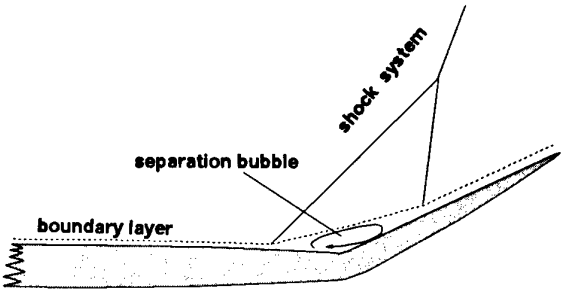


Figure 7: Shock-boundary layer interference

5.2.2 Trailing edge flaps on highly swept wings

On wings with highly swept (subsonic) trailing edges (OFW, arrow wings), the boundary layer is deflected by the spanwise pressure gradients and tends to become nearly parallel to the trailing edge, or even separates (fig. 8). Tendencies, known from lower sweep angles, and results for very high sweep angles, are not conclusive. Further theoretical and experimental investigations are required to understand flap efficiency at relevant sweep angles.

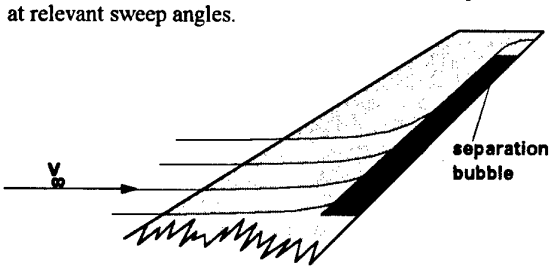


Figure 8: Highly swept trailing edge

5.3 Wind tunnel measurements

5.3.1 Wind tunnels

Wind tunnel experiments are essential

- to get insight into still unknown flow physics like separation, turbulence, transition
- to validate numerical calculations
- to generate data for complicated configurations including interference effects
- to check aerodynamic designs and to generate data for improvements
- to establish aerodynamic data for pre-flight validation of new aircraft.

But wind tunnels have limitations as well. For SCT-development the most important limitations for wind tunnel investigations are:

Reynolds number:

Reynolds number in wind tunnel testing usually is an order of magnitude lower than in free flight, for supersonic testing often up to two orders of magnitude. For drag measurements the boundary layer is tripped; i.e. transition strips provoke transition from laminar to turbulent flow at defined positions. This allows for calibrated friction measurements, but the boundary layer is thicker at lower Reynolds numbers. Therefore the interference effects, especially shock-boundary layer interference, in the wind tunnel remain different compared to free flight. Technologies better to transpose interference prediction from wind tunnel to free flight need to be developed.

Transition control:

Transition strips must be as small as possible. Thick or wide transition strips generate to much strip drag and thicken the boundary layer. On the other hand, if transition strips are too small, no transition or even relaminarisation occurs which does not allow useful drag measurements. Therefore the control of transition in experiments is always required, i.e. to identify the laminar and turbulent boundary layer regions on the whole aircraft model. Most common transition control techniques -like the acenaphtene technique- require wind tunnel runs at constant flow conditions. This is impossible in wind tunnels of blow-down type; and many supersonic wind tunnels are blow-down tunnels. Other transition control technologies are required here; possibly the techniques devoleped for cryogenic wind tunnels (like very sensitive infrared measurements) can be adapted here, or special liquid cristal techniques with sufficiently smooth surfaces.

Testing around Mach 1:

At near sonic speeds the flow around the model contains large supersonic flow domains. In the supersonic regions the wind tunnel model radiates disturbances to the wind tunnel wall which are (at least partially) reflected by the wall back onto the model. In contrast to free flight conditions, this reflection strongly changes pressures and flow properties at the model.

At high subsonic speeds, the supersonic regions can reach the wall and so generate a choked supersonic nozzle flow over the aircraft instead of the open supersonic bubble over the free flying aircraft. This (partial) nozzle flow changes the whole flow field and does not further resemble to free flight conditions.

Most transonic wind tunnels have slotted or perforated walls in order to minimize wall reflections. This minimisation, though, is only sufficient, if the supersonic bubble does not reach the wall or the important reflections do not meet the model. This requires test flow conditions avoiding the vicinity of Mach 1. New transonic wind tunnels use flexible walls (adaptive walls), where the wall geometry is adapted during the test to follow a free stream path line. This allows for better adaption of near sonic test conditions. But quality of adaption depends on the technical concept of the adaption mechanism; usually only a plane wall adaption is possible for two of the four walls

surrounding the test chamber. Although two-dimensional adaption in the most important direction is better than no adaption, three-dimensional adaption for three-dimensional models is not yet realized for relevant wind tunnels.

Engine simulation:

Usually, engines in supersonic tests are modeled by simple through-flow nozzles. But it is difficult to design spillage-free through-flow nozzles: nozzles often are choked and consume energy, whereas an engine adds energy. Wind tunnel simulation therefore often is restricted to limited cases including spillage. Additionally nozzle base drag is added due to internal naccelle drag. It can be corrected by pressure measurements, but these will correct only the individual nozzle base drag, and not the additional interference wave drag.

Laminar tests:

There exists only one wind tunnel for supersonic laminar flow tests between Mach 1.5 and 2.5. This is a refurbished facility at the University of Stuttgart, Germany. For more information, see e.g. [14]. More supersonic quiet wind tunnels in the Mach number range of interest are under construction or evaluation.

5.3.2 Measurement techniques

Measurement techniques have been developed for exploiting wind tunnel experiments. Some of these techniques are state of the art and provided by all wind tunnels: force measurement and pressure measurement via small holes in the model surface. The simpler optical methods like shadowgraphs, Schlieren or interferograms are best suited for 2D-measurements and available where suited. More refined techniques are available and will be applied to supersonic testing, especially optical methods for flow field measurements:

Pressure sensitive paint (PSP):

Special paints are developed which, when illuminated by a suited light source, emit light depending on the amount of O_2-molecules embedded by the paint surface. In air the amount of O_2-molecules directly correlates to air density. This allows for direct measurement of air density distribution on the model surface and, when temperature is known, indirectly for the measurement of pressure distribution, see. e.g. [21, 22, 23]. This technique is new and needs further improvements before it can be applied as a stand alone pressure measurement technique. Especially paint toxity, thickness or durability, painting, illumination technique and related automatic data processing need further research.

Liquid cristal coatings:

Surface coatings based on liquid cristal technology allow for various mapping techniques of relevant flow parameters on the model's surface like shear stress, temperature. This allows simultaneous measurement on large parts of the model. Problems result from the mostly relatively rough coating surface, the limited view angles and often the multiple sensitivities of the coatings which require careful separation of the measured effects. These problems still allow only for limited use of the technique in aerodynamic measurements.

Field mapping measurements in the free flow field:

Several new techniques allow for measurements in a selected plane of the flow field. Most common is Particle Image Velocity (PIV), see e.g. [24]: The flow field of interest is seeded with microscopic particles, commonly droplets of about 1 µm diameter. In the plane of interest, those droplets are photographed twice within a short time interval. The movement of the droplets is identified to provide the droplet's speed which is equal to flow velocity except at a shock. New developments are aimed at larger measurement fields and measuring all three velocity components. In the future, PIV measurements will be usable even for complicated interference flow measurements.

Several other flow field measurement techniques are developed, but either still in its infancy, restricted to high Mach numbers, suitable only for very specific cases or just of poor accuracy.

Laser-Doppler anemometry:

In the last years Laser-Doppler Anemometry (LDA) was developed as a tool for accurate, pointwise, nonintrusive flow field measurements [25]. The flow is seeded with droplets (like for PIV) which are observed within a small measurement volume. This volume is established by the crossing of two laser beams, where interference produces a sequence of light and shadow like a grid. Observed is the motion of the droplets through the interference grid, where the frequency of reflected light spots is correlated to the droplet's speed. LDA allows for accurate measuring of mean and fluctuating values, even resolution of boundary layer flow; but it requires relatively long measurement time.

Complementary to the experimental measurements, *correction methods* for experimental errors or insufficient simulation are needed. Here the most important corrections required are:

- accurate correction of wall interference
- correction of Reynolds effects, especially for interferencies
- spillage and nozzle base drag correction.

5.4 Aeroelastics

5.4.1 Static aeroelastics

In classical aerodynamic design, the aerodynamic wing shape is designed for one design point M_C (cruise Mach at a given weight and altitude). Knowledge based margins provide the ability to cope with the off-design points:

Some off-design points cover the (cruise) flight regime (like M_{MO} = maximum operating Mach, M_{CS} = subsonic cruise Mach, other aircraft weights for begin of cruise or end of cruise, altitude variations ...). Others concern exceptional points which do not occur in normal cruise, but only e.g. for emergencies like M_D (dive Mach).

Aerodynamics assume the geometry to be rigid. Once the aerodynamic (flight) shape is fixed and the aerodynamic loads are known, structure loads are determined, structure is designed and static aeroelastic deformation is calculated. This deformation at the design point is taken into account when the shape to be built (jig shape) is defined. The

procedure reestablishs the designed aerodynamic shape at the design point flight loads (M_C, design weight and altitude). But for any deviation of the design point, the aircraft will have a different shape. This deviation becomes important if the wing is not very stiff and if the deviations from the design point a large. Both occur for SCTs with thin wings and multiple design conditions.

To find the best compromise for an elastic wing flying at different design points, aeroelastic deformation must be considered in the aerodynamic design. For aerodynamics this can be a rather simple formulation, like a beam formulation for a slender arrow wing or an OFW, or a simple shell formulation for some kind of delta wing, including bending and torsion. The difficult problem is the "simple" estimation of structural values, because this requires simultaneous estimation of loads, mass distribution and structural thicknesses.

5.4.2 Flutter

Concorde has inacceptable take-off noise levels. For a Concorde-type SCT lower noise levels can only be achieved using larger engine diameters and larger wing span. But to maintain or even increase cruise performance, wing thickness must to be reduced. Such wings become very flutter sensitive.

Aerodynamic damping is an indicator for flutter onset. It is the smaller, the higher the flight speed is. But at high subsonic speeds, nonlinear transonic aerodynamics reduce aerodynamic damping, the so called transonic dip (fig. 9) [13]. A new SCT has therefore to be investigated for flutter at transonic speeds and at supersonic cruise speeds.

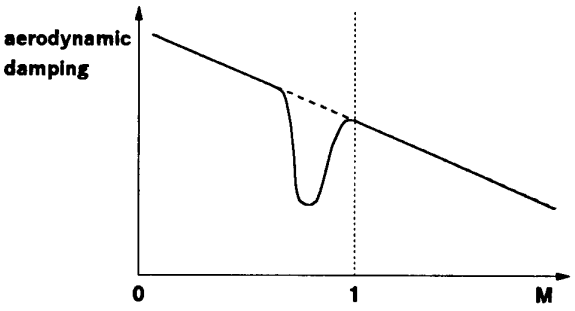


Figure 9: Transonic dip

Because of flutter becoming very critical for the thin wings of symmetric (Concorde-like) SCT-configurations, at least a rough approximation of flutter tendencies must be included in the first steps of configuration optimisation. Hitherto nobody knows how to do it. Perhaps, artificial flutter damping can be applied in the future, if its certification becomes possible.

5.5 Geometry generation

Aerodynamic design is development of a suited shape. For SCT development, extensive application of numerical optimizers is required [26, 27]. When using optimizers, the first very important step is to describe the space of possible shapes by as few parameters as possible, but still without inacceptable restrictions. In the first step of interdisciplinary optimisation, only global parameters are needed to described the basic aircraft geometry. The more refined the investigations are, the more sophisticated the numerical methods are, the more detailed the geometry must be described. But for all levels the same requirements for geometry generation hold:

For geometry generation by a human design engineer:

Geometry must be described by a limited set of parameters. But those parameters must be meaningful and well ordered in order to allow a human to reach geometric design goals. Alternative ways are allowed, e.g. multiple parameter sets or parameter set selections.

For automatic geometry generation by a numerical optimizer:

Geometry must be described by as few independent parameters as possible. Those parameters may have any level of abstraction. Not allowed are alternatives to the optimizer for selection between different, but equivalent parameter sets.

Any geometry generator must provide smooth shapes not tending to wiggles:

If wiggles cannot be avoided, smoothing procedures must be provided. For human applications, the smoothing procedures can be applied off-line as the last step of geometry generation. For numerical optimizers smoothing, if not avoidable, must be included in the geometry generation.

Any geometry generator must provide interfaces to and from CAD-systems:

When aerodynamics has developed a shape, this shape will be transferred to other company work groups like project, structure, aeroelastics, model design and fabrication. All aircraft related data transfer uses CAD-systems. The aerodynamic shape therefore has to be transferred into the CAD-system without intolerable accuracy losses.

On the other side, aerodynamics has to use input from other departments for geometry constraints like fairing size etc. Or the real model geometry has to be checked prior to a wind tunnel test. Or geometries generated by a partner must be investigated. Or wind tunnel results -like pressure measurements- have to be applied to a given geometry for aerodynamic improvements. In all those cases it must be possible to transfer the CAD-geometry into the aerodynamic geometry generator as an input geometry, e.g. to start an improvement calculation.

Especially for application of numerical optimisation strategies, more progress in systematic shape definition is needed. Sometimes it is proposed to use the CAD-systems directly for geometry generation, but CAD-systems are oriented towards structural design: these do not contain geometry definition tools suitable for aerodynamic optimisation. Powerful aerodynamic 3D-geometry generators are under development as preprocessor for CAD systems [28]

5.6 Fast computer codes for aircraft design

In the first interdisciplinary design loop, the whole aircraft is investigated. To allow the optimizer an investigation of the whole flight mission of a sufficient number of configurations, the individual calculations must be very fast and use only few variables. In more detailed investigations, not all disciplines are involved at the same time, and perhaps not all mission points. The aerodynamic code can therefore use more time

and variables to become more accurate. As a result, available turn around time, variables involved and accuracy achieved rise from step to step until the ultimate step of the flying aircraft.

As long as design modifications by theoretical predictions are relevant, turn around times are needed which allow for many repeated design loops. This is, depending on the design step: one hour, one night, one weekend.

Very fast codes are closed formulas for the interdisciplinary investigations. They only need some main geometry parameters as input for global estimation of the aircraft's performance to allow for configuration selection.

Fast codes are all codes which allow for turn around times of one hour for pure aerodynamic calculations (with many individual code calls) or one night/weekend for inter-disciplinary tasks. Fast codes relay on linearized theory with empirical corrections. They need more geometry parameters to allow for a first aerodynamic design optimisation including volume distribution and a first approximation of twist and camber; and they check the aerodynamic predictions of the interdisciplinary model.

Both codes calculate (at different accuracy levels) the global aerodynamic coefficients for performance calculations and first flight mechanics estimations. They identify the physical drag contributors and provide a load estimation.

As any code used for numerical optimisation, the codes must be robust. This means:

The code should be able to calculate all problems which the optimizer may pose, even some strange parameter combinations. If the code breaks down, this must not stop the design process, but the code should deliver an inacceptably bad result which is the worse the heavier the code crash was. For instance, if negative pressures occur, the result can be a bad value proportional to the detected negative pressure value. This leads an optimizer to solutions, where the code does not crash. If the code is reliable, only those are interesting solutions. Such cases must be controlled by the design engineer !

Today, most research effort is devoted to highly sophisticated CFD-codes. These codes are needed and must be improved furthermore, but for a better and practical *interdisciplinary* aircraft *optimisation*, quality and applicability of the simple fast codes must be improved. Much more research effort is needed in this direction.

5.7 Accurate computer codes

Accurate computer codes here are CFD-codes based on solutions of the Euler equations, sometimes with a coupled boundary layer solution and solutions of the Navier-Stokes equations. They are used for:

- configuration optimisation, to check and improve the previous design steps based on simpler codes, and to include results of wind tunnel tests,
- interference drag reduction, which is impossible using simpler codes,
- inlet and nozzle design with strong shock/boundary layer interactions.

To allow efficient exploitation of CFD-codes, the codes must fulfill the following requirements:

- They must represent the relevant physical properties. For SCT design, these are:
  reliable radiation of disturbances (not fulfilled by most CFD-codes),
  prediction of shocks and shock reflections,
  prediction of separations (this still requires much more research on turbulence).
- They must be able to use the exact geometry definitions including suited numerical grids.
- They must provide insight in flow physics by visualisation postprocessing of results.
- They must be able to predict aerodynamic loads.
- They must provide reliable performance predictions (drag prediction is still difficult for most CFD-codes).
- They must be able to identify the different physical contributiors of drag (still a research task, especially for supersonic flow with strong radiation properties).
- They must provide reliable aerodynamic derivatives for flight mechanics calculations.
- They must support the analysis of experiments.

If those codes are only used to check some results of previous predictions, the old fashioned procedure of man hour consuming grid adaption and numerical fine tuning may be applied. But as soon as the code is used for configuration optimisation, new requirements must be fulfilled:

- A geometry generator with very few variable parameters must model the variations of interest which the optimizer has to investigate.
- The grid generator must automatically provide a suited grid of high quality.
- The code must fast and automatically converge to a useful result. If the code breaks down, a (bad) result must be provided which directs the optimizer to useful variations.
- The results produced by the optimizer's parameter variations must reflect the variation of physical results.

5.8 Inverse design capabilities

Since the introduction of direct numerical optimisation, importance of inverse design methods has decreased. Sometimes inverse design is seen as a relict of old design techniques. But inverse design remains important. There are still cases, where the numerical effort of direct optimisation is still inacceptable. Though this will change in future, there remain other cases: Inverse design allows to construct solutions for comparison with incomplete or defective solutions. E.g. using only partial inputs or other than geometry inputs, a geometry can be designed to be compared with the geometry used for a CFD-calculation. Research is needed here, especially, if not only the classical inverse pressure design methods are to be used, but also other input alternatives [29, 15].

5.9 Special control devices

An SCT has a flight envelope strongly enlarged in comparison to subsonic transports. All new configurations, either Concorde-like aircraft with thin wings or an OFW, may provide some configuration deficiencies unknown for subsonic transports. If the existing control devices cannot

handle specific situations, or if the handling of those situations heavily penalizes those devices, then special control devices may improve handling of these situations.

Examples:

If one engine stalls or an engine burst occurs at supersonic speed (OEI = One Engine Inoperative), strong lateral moments and rolling moments can establish. If handling of them penalizes rudder (and/or aileron) sizing, a special spoiler deflection on the other wing may compensate the occuring yaw, roll and pitching moments. Fine tuning is possible using the conventional controls.

The oblique wing has superior aerodynamic performance, especially at low speeds. This may inhibit an acceptable landing procedure with steep descent. Special devices can produce the requested drag without inacceptable introduction of pitching moments.

Such devices strongly depend on the selected configuration. They are only recommended, if they considerably reduce size, weight or complexity of the already existing system. It is possible, that such devices ease design of the control system layout, but complicating the system may occur as well.

5.10 Ejector flaps

A new SCT, especially a Concorde-type SCT, has difficulties to fulfill take-off noise requirements. Any possibility to improve take-off performance and reduce noise must therefore be investigated.

The engine companies have proposed several engine types for SCT. There are engines which provide so much high pressure air at take-off, that they can only apply full (thermal) power if a large amount of bleed air is used elsewhere. It is worth therefore to investigate ejector flaps (fig. 10), mainly to increase thrust. Problems to be investigated are:

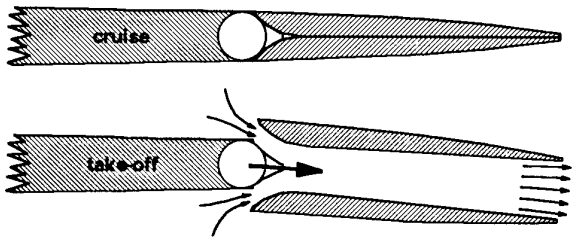


Figure 10: Ejector flaps

- What is the efficiency of the complex tubing and ejector flap system ?
- Does the additional installation weight of the complex tubing and flap system offset the improvement of take-off performance ?
- How complex and reliable will the system be ?
- What is the noise of such an ejector system ? The F117 is an example providing low noise, but design goal was mainly radar and infrared signature.
- Will exploitation of the ejector system for lift generation improve the design, when trim penalties and safety requirements are respected ?

To estimate the pros and cons of such a system, probably an SCT optimized without ejector flaps must be compared with a completely independent optimum design which is adapted to the exploitation of the ejector flaps.

5.11 Supersonic laminar flow (SSLF)

Supersonic transports are very drag sensitive. Technology to reduce drag by application of laminar flow, therefore, will be important; it is a prerequisite to achieve very long range capability, or to reduce aerodynamic heating at higher cruise Mach numbers [30]. In earlier studies it was assumed that SCTs would only become possible by application of laminar flow [31]. But today, we request an SCT to be viable without application of laminar flow in order to maintain its competitiveness when laminar flow becomes available for subsonic and supersonic transports. By reducing fuel burned, laminar flow drag reduction reduces size and weight of the aircraft, or increases range capability -whereas otherwise size and weight would grow towards infinity. Transition mechanisms from laminar to turbulent state of the boundary layer flow (ALT, CFI, TSI) function as for transonic transports, but at more severe conditions: higher sweep angles, cooled surfaces; higher mode instabilities (HMI) must at least be taken into account, although they may not become important below Mach 3. Hitherto there is a worldwide lack of ground test facilities to investigate TSI at the expected cruise Mach numbers between 1.6 and 2.4; in Stuttgart, Germany one such facility -a Ludwieg tube- is in the validation phase. A quiet Ludwieg tunnel could be a favourable choice for Europe. But it will require a new approach in designing aircraft which includes improved theoretical predictions, usage of classical wind tunnels for turbulent flow and flight tests for validation. A more detailed overview is given in [14].

6. CONCLUSION

A new SCT will only become reality, if many technologies are improved or newly developed. Some of them are aerodynamic technologies, as mentioned above. But many of them require contributions by other disciplines or need interdisciplinary connection with others. Both pure aerodynamics and interdisciplinary problems provide enough opportunities for many new intelligent contributions.

7. REFERENCES

1 J. Mertens: Son of Concorde, a Technology Challenge "New Design Concepts for High Speed Air Transport", H. Sobieczky ed., CISM 366, Springer Wien NewYork, 1997, pp. 31-51

2 Jane's - All the World's Aircraft, 1977/78

3 Jane's - All the World's Aircraft, 1995/96

4 A. Van der Velden, D. von Reith: Multi-Disciplinary SCT Design at Deutsche Aerospace Airbus
Proceedings of the 7th European Aerospace Conference EAC'94 "The Supersonic Transport of Second Generation", Toulouse, 25-27 October 1994, paper 3.61

5 C. Frantzen: Introduction to Regulatory Aspects of Supersonic Transports
Proceedings of the European Symposium on Future Supersonic Hypersonic Transportation Systems, Strasbourg, November 6-8, 1989, paper II, 3.1

6 J. Mertens: Certification of Supersonic Civil Transports "New Design Concepts for High Speed Air Transport", H.

Sobieczky ed., CISM 366, Springer Wien NewYork, 1997, pp. 97-103

7 J. Mertens: Sonic Boom Overwater Issues and Past Test Data, Review and Recommendations
DA-Report DA-010-93 / EF-1971, Bremen, 6.10.1993

8 M. Goldring: A Second Generation Supersonic Transport, the Lessons from Concorde
Proceedings of the 7th European Aerospace Conference EAC'94 "The Supersonic Transport of Second Generation", Toulouse, 25-27 October 1994, paper 2.31

9 J.M. Swihart: Prospects for a Second Generation High Speed Civil Transport
Proceedings of the 7th European Aerospace Conference EAC'94 "The Supersonic Transport of Second Generation", Toulouse, 25-27 October 1994, paper 2.33

10 A.R. Sebass: The Prospects for Commercial Supersonic Transport
"New Design Concepts for High Speed Air Transport", H. Sobieczky ed., CISM 366, Springer Wien NewYork, 1997, pp. 1-12

11 A. Van der Velden: Aircraft Economy for Design Tradeoffs
"New Design Concepts for High Speed Air Transport", H. Sobieczky ed., CISM 366, Springer Wien NewYork, 1997, pp. 13-30

12 U. Michel: How to Satisfy the Takeoff Noise Requirements for a Supersonic Transport
AIAA-paper AIAA-87-2726, AIAA 11th Aeroacoustics Conference, Oct. 19-21, 1987, Palo Alto, CA, USA

13 R. Barreau, T. Renard (Reporters): BRITE EURAM Program "Supersonic Flow Phenomena", Final Report Subtask 1.3 "Preliminary Aeroelastic Investigation of Supersonic Transport Aircraft Configuration"

14 J, Mertens: Laminar Flow for Supersonic Transports
"New Design Concepts for High Speed Air Transport", H. Sobieczky ed., CISM 366, Springer Wien NewYork, 1997, pp. 275-290

15 G.S. Dulikravich: Multidisciplinary Inverse Design and Optimization (MIDO)
"New Design Concepts for High Speed Air Transport", H. Sobieczky ed., CISM 366, Springer Wien NewYork, 1997, pp. 223-236

16 A. Van der Velden: Multi-Disciplinary Supersonic Transport Design
"New Design Concepts for High Speed Air Transport", H. Sobieczky ed., CISM 366, Springer Wien NewYork, 1997, pp. 251-273

17 A. Van der Velden: Tools for Applied Engineering Optimization
VKI lecture series in Optimum Design Methods in Aerodynamics, AGARD R 803, April 1994

18 J. Mertens: Required Aerodynamic Technologies
"New Design Concepts for High Speed Air Transport", H. Sobieczky ed., CISM 366, Springer Wien NewYork, 1997, pp. 69-96

19 M.J. Mann, H.W. Carlson: Aerodynamic Design of Supersonic Cruise Wings with a Calibrated Linearized Theory
Journal of Aircraft, **31**, 1, Jan.-Feb. 1994, pp. 35-40

20 A. Van der Velden: Aerodynamic Design and Synthesis of the Oblique Flying Wing Supersonic Transport
PhD-thesis Stanford University, Dept. Aero Astro SUDDAR 621, Univ. Microfilms no. DA9234183, June 1992

21 R.H. Engler, K. Hartmann, B. Schulze: Aerodynamic Assessment of an Optical Pressure Measurement System (OPMS) by Comparison with Conventional Pressure Measurements in a High Speed Wind Tunnel
Paper, presented at ICIASF '91, Washington D.D., 8 pages

22 A. Vollan, L. Alati: A new Optical Pressure Measurement System
Paper, presented at ICIASF '91, Washington D.D., 7 pages

23 B.G. McLachlan, J.H. Bell, H. Park, R.A. Kennelly, J.A. Schreiner, S.C. Smith, J.M. Strong: Pressure-Sensitive Paint Measurements on a Supersonic High-Sweep Oblique Wing Model
Journal of Aircraft, **32**, 2, March-April 1995, 217-227

24 C.E. Willert: A Comparison of Several Particle Image Velocimetry Systems
DGLR-Bericht 94-04 "Strömungen mit Ablösung", Erlangen, 4.-7.10.1994, 266-271

25 H. Lienhart, T. Böhnert: Grenzschichtmessungen an einem Laminarflügelprofil mit einem Laser-Doppler-Anemometer
DGLR-Bericht 92-07 "Strömungen mit Ablösung", Köln-Porz, 10.-12.11.1992, 471-476

26 A. Van der Velden: Aerodynamic Shape Optimization
VKI lecture series in Optimum Design Methods in Aerodynamics, AGARD R 803, April 1994

27 A Van der Velden: Supersonic Aircraft Shape Optimization
"New Design Concepts for High Speed Air Transport", H. Sobieczky ed., CISM 366, Springer Wien NewYork, 1997, pp. 237-250

28 H. Sobieczky: Geometry Generator for CFD and Applied Aerodynamics
"New Design Concepts for High Speed Air Transport", H. Sobieczky ed., CISM 366, Springer Wien NewYork, 1997, pp. 137-157

29 G.S. Dulikravich: Combined Optimization and Inverse Design of 3-D Aerodynamic Shapes
"New Design Concepts for High Speed Air Transport", H. Sobieczky ed., CISM 366, Springer Wien NewYork, 1997, pp. 189-200

30 Boeing Commercial Airplane Company: Application of Laminar Flow Control to Supersonic Transport Configurations.
NASA Contract Report 181917, July 1990

31 J. Mertens: Laminar Flow for Supersonic Transports
in J. Szodruch (ed.): Proceedings of the First European Forum on Laminar Flow Technology, Hamburg, 16.-18.3.1992, DGLR-Report 92-06

Sonic Boom Minimization

Richard Seebass

John R. Woodhull Professor and Chair,
Aerospace Engineering Sciences
Campus Box 429
University of Colorado
Boulder CO 80303-0429, USA

Introduction

We revisit the classical Jones-Seebass-George-Darden theory of sonic boom minimization, noting that minimum achievable sonic boom is related to the aircraft's weight divided by the three-halves power of its length. We then summarize studies of sonic boom acceptability and the effects of vibrational relaxation on very weak shock waves. This leads us to conclude that a small, appropriately designed, supersonic business jet's sonic boom may be nearly inaudible outdoors and hardly discernible indoors.

It is important to note at the outset that any improvement in the traditional parameters that govern the efficiency of the aircraft that result in a reduction of the aircraft's weight also provide, thereby, a reduction in sonic boom overpressure and impulse. Improvements in the lift-to-drag ratio, the thrust-to-weight ratio, the specific fuel consumption and the structural efficiency can all result in sonic boom reductions for an aircraft with the same range. Conversely, aerodynamic changes that appear to reduce the sonic boom but that compromise any of these traditional figures of merit will probably increase the sonic boom.

One of the primary difficulties in this field has been knowing what is to be reduced or minimized in order to make the sonic boom acceptable. Here we know much more than we did twenty-five years ago. As it is experienced outdoors, the most annoying feature of the sonic boom is the shock wave that gives rise to the more descriptive appellation used in Europe, "sonic bang." For small aircraft this may be the principal parameter for sonic boom annoyance and loudness, indoors or outdoors. For large aircraft, when the sonic boom is experienced indoors, another significant parameter is undoubtedly the energy in the signature as a function of frequency, perhaps adequately characterized by the overpressure and the impulse of the signature. The impulse is the integral of the pressure with time over that period of time during which the pressure is positive. For commercial transport-size aircraft the impulse is also a significant parameter in studies of structural disturbances due to, and the indoor loudness and annoyance from, sonic booms.

*Copyright © 1998 by author. Published with the author's permission.

History

Sonic boom minimization began with Busemann[1] who told us how to eliminate the wave drag and sonic boom due to the aircraft's volume. Twenty years later he noted that the lift contribution was inescapable.[2] Ryhming[3] determined the minimum farfield overpressure for a fixed drag. Jones[4,5] relaxed the constraint on drag and obtained improved results for the farfield. McLean[6] then noted that for SSTs of practical length the pressure signature at the ground need not be the farfield waveform; specifically, he observed that the midfield region in a homogeneous atmosphere could extend several hundred body lengths. Hayes[7] then pointed out that the signature shape that is approached asymptotically below the aircraft in an isothermal atmosphere of scale height H, is the signature that occurs at a distance $\pi H/2$ below the aircraft in a homogeneous atmosphere. Thus, if midfield effects persist to $\pi H/2$ real-atmospheric scale heights in a homogeneous atmosphere, then they will persist indefinitely below the aircraft in the real atmosphere.

Paper presented at the RTO AVT Course on "Fluid Dynamics Research on Supersonic Aircraft", held in Rhode-Saint-Genèse, Belgium, 25-29 May 1998, and published in RTO EN-4.

Seebass,[8,9] George,[10] and George and Plotkin[11] explored the ramifications of this "freezing" of the overpressure signature and reported improved results for various signature parameters. About the same time Jones[12] extended his earlier results to include these midfield effects, but only for a homogeneous atmosphere. In general, these minimizations were limited to the positive phase of the overpressure signature, although Jones[12] did determine the strength of the resulting rear shock and Seebass[9] established an upper limit for the additional aircraft length needed to ensure the rear shock strength and overpressure were no larger than those in the front shock.

The first minimum for a full signature was given by Petty,[13] who determined the minimum shock strength under the proviso that the absolute value of the overpressure be everywhere less than or equal to the front shock pressure rise. Hayes and Weiskopf,[14] and George and Seebass[15-17] established the conditions under which both shock waves could be eliminated, and George and Seebass[15-17] gave general results for the minimum of the shock pressure rise, overpressure, and impulse possible for the full signature. Seebass and George made an approximation to the linear pressure field that was appropriate for sonic boom studies, but not for determining an aircraft's wave drag. Darden[18] extended what she called the "Seebass- George Theory" by removing the blunt nose approximation, and provided useful charts[19] of what sonic boom levels could be achieved for a transport aircraft operating at Mach numbers of 2.5 and 3.2. Given the important contributions of L. B. Jones, and C. M. Darden, we should refer to sonic boom minimization theory as the *Jones-Seebass-George-Darden* theory.

A number of exotic schemes to reduce or eliminate the sonic boom have been proposed over the last twenty-five years. A few of these are based on rational possibilities; others violate what we know about aircraft design; some violate the basic laws of physics. Those that embody the addition or removal of heat from the flow can be treated easily. Linear theory tells us that sources of heat and mass affect an aircraft's equivalent body of revolution in a simple additive way, and Miller and Carlson[20] explored the use of heat or mass addition to alleviate the sonic boom.

For mass or heat addition (or removal) to be effective in changing the aircraft's equivalent body of revolution, the mass or enthalpy flux added to the flow must be comparable to the aircraft's lift coefficient times the freestream mass or enthalpy flux through an area equal to the aircraft's wing area. This simple observation rules out the practical application of such concepts. Others utilize the known fact that wave drag due to volume, and consequently the sonic boom due to volume, can be eliminated, frequently confusing this with the sonic boom due to lift. This entails the high expense of additional skin friction. And for practical aircraft, the volume is an asset toward reducing the sonic boom, not a liability.

The sonic boom due to lift cannot be avoided. The aircraft's weight must be transmitted to the ground, although how this occurs is not obvious from the lowest-order theory. The first-order sonic boom N-wave provides a second-order broad pressure wave, largely behind the intersection of the two Mach cones with the ground, that carries this pressure and thereby supports the aircraft. But you cannot have the second-order term without the first-order N-wave that is the sonic boom.[21-23]

We assume that volume either contributes to reducing, or at least does not increase, the sonic boom. It may contribute to reducing the sonic boom by making the aircraft's lift development appear longer. The analysis revisited here includes all schemes that would reduce the sonic boom of slender aircraft without violating the conservation of mass, momentum, energy, and the second law of thermodynamics.

Aerodynamic Minimization

We asked nearly thirty years ago to what extent can we reduce the sonic boom by aerodynamic means? Specifically, how may we shape the aircraft so that the sonic boom would be acceptable, and improve, or at least not compromise, the aircraft's aerodynamic performance? We assumed that the aircraft's volume distribution is achieved without penalty and the aircraft is then simply characterized by its weight and effective length.

What the minimum sonic boom aircraft is, of course, depends on what features of the overpressure signature we choose to treat. There are trade-offs between the aerodynamic minimization of the sonic boom and maximizing the aircraft's performance.

Aircraft with the minimum wave drag do not have the minimum sonic boom, although these two are closely related. And while it is often thought that an increase in the altitude of flight will reduce the sonic boom, this is not the case for aircraft designed to minimize their sonic bang.

For simplicity we assume that the atmosphere is isothermal, as this makes all we do analytic. The differences in sonic boom signatures computed for an isothermal atmosphere with the proper scale height and those for the standard atmosphere are very small and immaterial when one considers the seasonal, not to mention the daily, variations in the real atmosphere.

We use the supersonic area rule, discussed next, and pose the appropriate sonic boom minimization question in terms of the aircraft's equivalent body of revolution for the vertical azimuthal plane. We ask, then, "How do we shape the equivalent body of revolution in the vertical plane below the aircraft to minimize one of three signature parameters on the ground directly below the aircraft?" The three parameters are the impulse, I, with its overpressure of p_J; the overpressure, with its maximum pressure p_{so}; and the pressure rise through the shock wave, p_s, followed over a designer set rise time, τ, to its maximum value, p_{max}. These parameters are shown in Fig. 1.

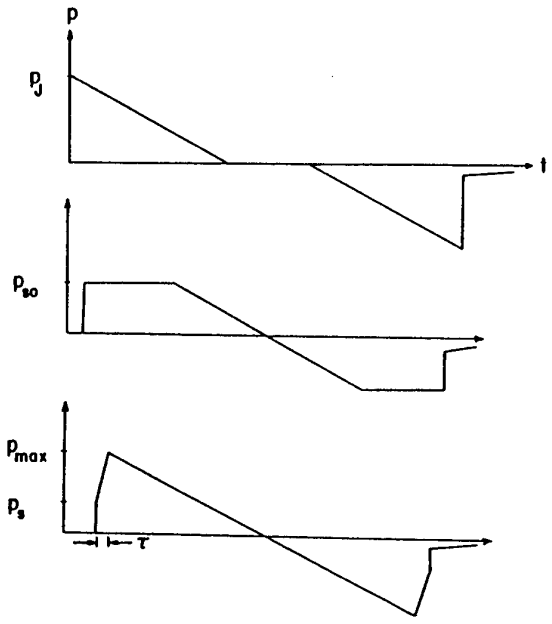


Figure 1. Overpressure signatures considered: 1) minimum impulse, I, with a shock pressure rise of p_J; 2) minimum overpressure, p_{so}; 3) minimum shock pressure rise, p_s, followed in a finite rise time, τ, to a maximum pressure, p_{max}.

Linear Theory

The supersonic area rule tells us that the wave drag of an aircraft in a steady supersonic flow is identical to the average wave drag of a series of equivalent bodies of revolution.[24] It also provides the linear farfield for the determination of the aircraft's sonic boom. These bodies of revolution are defined by the cuts through the aircraft made by the tangents to the fore Mach cone from a distant point aft of the aircraft at an azimuthal angle θ. The aerodynamic optimum supersonic aircraft is an elliptic wing flying obliquely, which we note is unusual in that its maximum sonic boom does not occur directly below the aircraft.[27]

For the azimuthal plane below the body, the cross-sectional area of the equivalent bodies of revolution is given by the sum of two quantities: 1) the cross-sectional area created by the oblique section cut by the tangent to the fore Mach cone's intersection with the aircraft, projected onto a plane normal to the free stream; 2) and a term proportional to the axial integral to the point considered of the lift defined by the contour of this oblique cut.

Aerodynamic Design

The deduction of the shape of the body of revolution that minimizes a given signature parameter below the aircraft is equivalent to the specification of the linear farfield pressure, or the Whitham F - function, for that azimuthal plane. The important facts are that the signal from the aircraft is essentially acoustic in nature, but that it is of finite amplitude. In the absence of winds, geometrical acoustics tells us that an acoustic signal conserves the Raleigh acoustic energy,

$$p_l^2 S/\rho a = \text{constant},$$

where p_l is the disturbance pressure from linear theory, S is the ray tube area, and ρa, the product of the density and the sound speed, is the acoustic impedance. For an isothermal atmosphere, in the

absence of nonlinear and atmospheric effects, the signal would decay below the aircraft as

$$p_l^2/p_{lo}^2 = Pz_o/P_o z, \qquad (1)$$

where the *o*-subscript refers to the linear reference conditions and P is the ambient pressure.

Because the signal is of finite amplitude compressions steepen. The amount they steepen at any phase of the signal is proportional to the amplitude there. Thus there is a nonlinear advance of some parts of the signal relative to other parts. In a homogeneous atmosphere this advance proceeds indefinitely; in an isothermal atmosphere, however, the increasing acoustic impedance below the aircraft means that the advance approaches a finite limit. Because of the nonlinear advance, shock waves may appear if not originally present. Once shock waves appear the decay of the pressure signal is enhanced by a factor that is asymptotically proportional to the inverse one-half power of this advance. With these facts in hand we may deduce the appropriate *F* - function to minimize a given signature parameter.

Because the pressure perturbation that must be induced by the aircraft to support itself is independent of altitude, while that induced by a given flow deflection angle due to the aircraft's shape is proportional to the ambient pressure, the lift contribution to the sonic boom decays less rapidly than that due to volume by a factor of exp (*h*/ 2*H*), where h is the aircraft's altitude and *H* the atmospheric scale height. The choice *H* = 25,000 models well the standard atmosphere.

At some large distance from the aircraft a pressure disturbance is sensed. We can think of that disturbance as being caused by a body of revolution with some effective base area equal to β times the aircraft's weight divided by twice the dynamic pressure plus any stream tube area changes caused by the engines, as shown in Fig. 2. This ultimate base area is achieved in some effective length, ℓ_{eff}. Frequently we will identify this length with the length of the aircraft, ℓ.

Aircraft Area Development

For a given ratio of front-to-rear shock strength, we consider, as noted earlier, the minimization of the following quantities: the impulse; the overpressure; the pressure rise through the shock wave with a specified rise time to the maximum pressure.

Recall that far from a body of revolution the linear pressure field is proportional to the Abel transform of the second derivative of the cross-sectional area:

$$\pi\sqrt{2\beta r}\, c_p(\chi;\theta) = \qquad (2)$$

$$\int_0^{\chi} \frac{[S''_L(\xi;\theta) + S''_V(\xi;\theta)]}{\sqrt{\chi-\xi}}\, d\xi \equiv 2\pi F(\chi;\theta).$$

The function $F(\chi;\theta)$ is often called the Whitham *F* - function; $\chi = x - \beta r$. A simple inversion of this formula leads to a relationship between the weight of the aircraft, which is proportional to the base area of the equivalent body of revolution, and the *F* - function:

$$S(\ell;0) = S_e(\ell;0) + \frac{\beta W}{\rho U^2} \qquad (3)$$

$$= 4\int_0^{\ell} F(t)\sqrt{(\ell-t)}\, dt,$$

where S_e accounts for the engine streamtube area increase. A further quadrature relates the volume and center of pressure location to another weighted integral of the *F* - function. For sonic boom (but not wave drag) prediction, discontinuities in the first derivative of the cross-sectional area can be most easily handled by considering the function to be a generalized one. Once the *F* - function is prescribed over the length of the body, then

$$F(t) = -\frac{1}{\pi\sqrt{t-\ell}}\left\{\int_0^{\ell} F(x)\frac{\sqrt{\ell-x}}{t-x}\, dx\right\} \qquad (4)$$

determines *F(t)* for all $t > \ell$.

If we ask: "For a given overpressure or shock pressure rise, how may we maximize the weight of the aircraft?" then we see from Eq. (3) that we should make *F* as large as possible as soon as possible. However, if shock waves are not to occur then there is a limit to the rate at which *F* can grow if the signal is not to steepen into shock waves. This leads to restriction on the maximum value of *F'*.

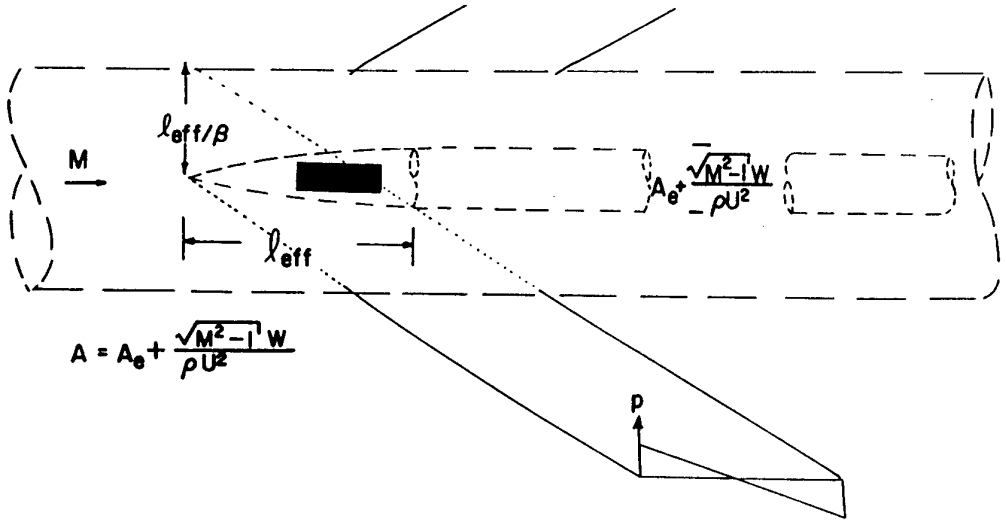


Figure 2. Representation of the aircraft, its effective length, base area, and the flow field.

Thus we are led to consider F - functions of the form shown in Fig. 4 with shocks introduced by the area balances indicated by the dashed lines. For the purposes of sonic boom minimization, but not wave drag, the F - function will have the form

$$F(y) = \mathcal{A}\delta(y) + \mathcal{B}y + \mathcal{C} \qquad (5)$$

for $y < \lambda$. Here we have represented the triangular pulse of Fig. 3 as a delta function, which is fine for the calculation of the sonic boom. Shock waves, as noted earlier, correspond to the dashed lines which, in the nonlinear evolution of the pressure signature, become vertical lines. Likewise we have for $\lambda < y < \ell$,

$$F(y) = \mathcal{B}y - \mathcal{D}. \qquad (6)$$

Here $\mathcal{A}$, $\mathcal{C}$ and $\mathcal{D}$, are constants yet to be determined. If we choose to minimize the overpressure, $\mathcal{B}$ is 0. If we choose to minimize the shock pressure rise and prescribe the rise time, then $\mathcal{B}$ is given by

$$\mathcal{B} = \left[\frac{\beta^{\frac{3}{2}}}{\Gamma M^4}\sqrt{\frac{1}{2\pi H}}\Big/\left(erf\sqrt{\frac{z}{2H}}\right)\right]\left(1 - \frac{Ma\tau}{\lambda}\right)$$

where a is the ambient sound speed. The value of τ needed to make a finite rise time sonic boom nearly inaudible may be less than 0.02 seconds.

The general procedures outlined in Reference 16 then lead to a system of four equations for the four unknowns $\mathcal{A}$, $\mathcal{D}$, λ and t. The four equations that determine these four unknowns are the two area balances, the fact that the line with slope $\mathcal{B}$ starting from ℓ must intersect the F - function at t, and a prescription of the ratio of the rear to the front shock strength, R. These four equations can be reduced to two complicated algebraic equations in λ and t. These two equations depend on a single parameter related to the aircraft's weight:

$$\tilde{W} = \alpha k\beta\left(\sqrt{\frac{h}{\ell}}\frac{W}{P_g\ell^2}\right)\exp\left(\frac{h}{H}\right). \qquad (7)$$

Here P_g is the ambient pressure at the ground, $\Gamma = (\gamma+1)/2$, h is the aircraft's flight altitude, α is the ratio of the real advance to the advance in a homogeneous atmosphere, and k depends only on Γ and on the Mach number:

$$\alpha = \sqrt{\frac{\pi H}{2h}}\,\mathrm{erf}\left(\sqrt{\frac{h}{2H}}\right),$$

$$k = \frac{2\Gamma}{(2\Gamma-1)}\frac{M^2}{\beta\sqrt{2\beta}}.$$

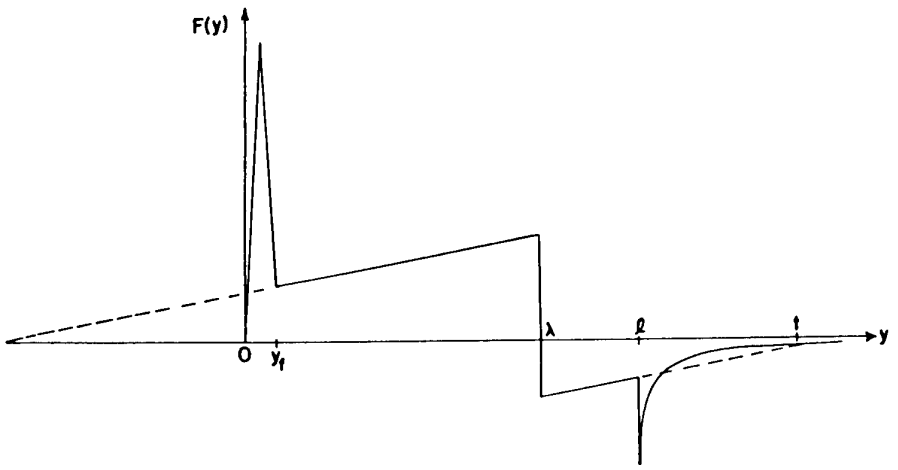


Figure 3. Whitham *F* - function for minimizing selected sonic boom signature parameters.

The numerical solution of these algebraic equations was effected by Lung[29] and Darden.[18]

The results for minimized bow shock overpressure and shock pressure rise can be given analytically. When both the front and rear shock are considered, the only numerical result needed is the additional length required to provide a rear shock strength *R* times that of the front shock.[17] This result for two ratios of the rear-to-front shock strength, *R*, is shown in Fig. 5. One set of curves applies to minimizing the overpressure; the other set applies to minimizing the shock pressure rise. When the ratio λ/ℓ is greater than or equal to 1, then there is no penalty for asking that the rear shock strength be *R* times that of the front shock. In the author's view, the only proper choice is $R = 1$.

The quantity $[\ell - \lambda]$ is the additional aircraft length required for the rear shock overpressure or shock pressure rise to be *R* times that of the front shock for an aircraft of length λ. The analytical result for the minimum overpressure for the positive phase of the signature is:

$$\frac{p_{so}}{P_g} = \frac{4\lambda e^{-h/2H}}{3h\alpha k\sqrt{2\beta}}\left[\left(1+\frac{9}{8}\tilde{W}_\lambda\right)^{1/2} - 1\right] \quad (8)$$

The analytical result for the minimum shock pressure rise for the positive phase of the signature, that is the bow shock pressure rise, is

$$\frac{p_s}{P_g} = \frac{4\lambda e^{-h/2H}}{3h\alpha k\sqrt{2\beta}} \times$$

$$\left\{\left[1+\frac{6}{5}\left(\frac{15\tilde{W}_\lambda}{16} - \left(1-\frac{Ma\tau}{\lambda}\right)\right)\right]^{1/2} - 1,\right\} \quad (9)$$

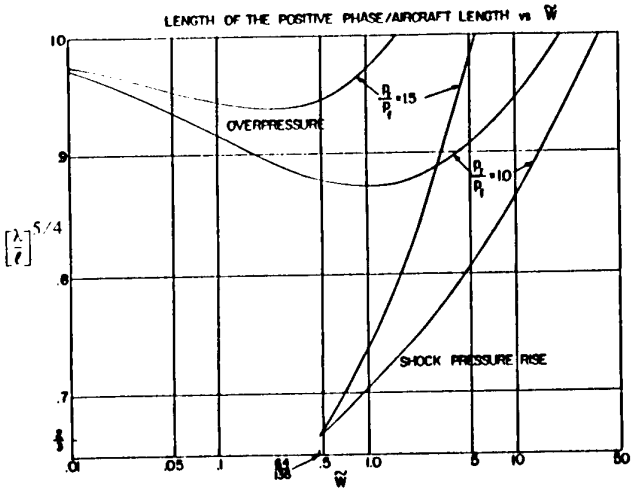


Figure 4. Fraction of the total aircraft length, λ/ℓ, needed for the positive phase of the *F*-function for two values of the rear-to-front shock strength, *R*.

with λ taken as the length in Eq. (7). These results then apply to the full signature with the aircraft's length determined from Fig. 5.

To illustrate this point, when $\tilde{W}$ is 64/135, then λ/ℓ is $(2/3)^{4/5}$. If $\tau = 0$, we find $\tilde{W}_\lambda = 16/15$, and so $p_s = 0$, i.e., no shock waves need occur. This corresponds to a length, λ, given by

$$\ell = \left[\frac{135}{64}\alpha k\beta e^{h/H}\left(\frac{W}{P_g}\right)\sqrt{h}\right]^{2/5}. \quad (10)$$

Once λ and t are known the F - function is determined, and with the F - function determined, the aircraft area development for $\theta = 0$ is known:

$$S(x) = 4\mathcal{A}x^{1/2} + \frac{16}{15}\mathcal{B}x^{5/2} + \frac{8}{3}\mathcal{C}x^{3/2} - \frac{8}{3}\mathbf{1}(x-\lambda)[\mathcal{C}+\mathcal{D}](x-\lambda)^{3/2}, \quad (11)$$

where $\mathbf{1}(x - \lambda)$ is the unit step function.

The introduction of the delta function into the F - function violates the small perturbation assumptions upon which the aerodynamic theory underlying our calculations is based. This local failure corresponds to a very slight nose blunting of the equivalent body of revolution and infinite drag. As Seebass first suggested[8] and Darden[18,30] showed, this can be resolved by considering the triangular pulses indicated in Fig. 4. Darden's results show that the triangular pulse requires about 5% additional body length and avoids infinite wave drag associated with the use of the delta function.

Figures 1A - 4A, provided in the appendix and taken from Reference 16, depict the variations of the minimum maximum pressure, p_{max}, for a finite rise time bow shock with a bow shock pressure rise of p_s, the minimum bow shock overpressure, p_{so}, and the minimum impulse bow shock pressure rise, p_J, and the corresponding impulses, after ground reflection, for values that correspond to a Mach 2.7, 300 ft. baseline aircraft weighing 600,000 lbs. and cruising at 60,000 ft. The scale height chosen (25,000 ft.) provides essentially the same results as the ICAO Standard Atmosphere. For the purpose of standardization we used a ground reflection factor of 2, noting that the 1.9 often used represents an average that is not applicable to hard surfaces. We remind the reader that an observer's experience of the sonic boom depends upon his or her position relative to reflective surfaces.

For this lift only case the minimum overpressure is insensitive to altitude and the impulse for all three cases grows (exponentially) with altitude. The pressure supporting the aircraft must be invariant with altitude, and the relative strength of the perturbation to the ambient pressure grows exponentially with altitude. This increases the extent to which the signal will advance and this, in turn, leads to this increase in the impulse with altitude. The overpressures are not very sensitive to Mach number and the impulses decrease slightly with increasing Mach number. The variation of the overpressure and impulse with aircraft weight is nearly linear. Finally we also observe that it is always beneficial to increase the aircraft's length and stretch out the pressure signal, and the impulse is essentially proportional to the aircraft's weight.

The above procedures can easily be generalized to include volume, center of pressure, and even wave drag constraints; the same general form of the Whitham F - function obtains.

Figure of Merit

Nearly thirty years ago Seebass and George showed that supersonic transports could be designed to have a less audible sonic boom as experienced outdoors. This was verified experimentally.[31] But this gain comes at the expense of higher maximum pressures and longer durations, and hence higher impulses.[16] Extensive field tests using F-104s flying supersonically over Oklahoma City[32] and B-58s flying supersonically over St. Louis,[33] and more controlled tests at Edwards Air Force Base (see Kryter, Ref. 34, for a complete discussion of community reaction) led the author to conclude then that, for transport-sized aircraft such as the Concorde, minimizing their sonic bang would mean higher impulses and not decrease significantly their annoyance when experienced indoors.

The minimum shock pressure rise, p_s, and $\exp(h/2H)$ times the resulting maximum pressure, p_{max}, and the minimum overpressure, p_{so}, all depend upon a

single parameter. This leads us to suggest as a figure of merit, FoM, the quantity:[16]

$$\text{FoM} = [\beta W/(P_g \ell^{3/2}\sqrt{h})]e^{h/(2H)}10^3.$$

The lower this FoM, which is proportional to the aircraft's weight divided by the three-halves power of the length, the better.

For the once proposed 300 ft., Mach 2.7 Boeing 2707, cruising at an altitude of 60,000 ft. and weighing 600,000 lbs., the FoM is about 1.9. For the 200 ft., Mach 2.0 Concorde cruising at an altitude of 50,000 ft. and weighing 300,000 lbs., the FoM is about 1.41. For a 100 ft., Mach 1.6 supersonic business jet cruising at an altitude of 40,000 ft. and weighing 60,000 lbs., the FoM is about 0.4.

Roskam[35] points out that for a great range of aircraft, the weight is proportional to the square root of the aircraft's pitching moment of inertia. This means that an aircraft's weight grows like the square of its length, which is consistent with its weight growing like the square of the wing span. Thus the FoM is roughly proportional to the quarter power of an aircraft's weight, and the smaller an aircraft, the better (lower) its figure of merit.

Could a 100 ft. long, Mach 1.6 supersonic business jet, cruising at an altitude of 40,000 ft. and weighing 60,000 lbs. have an acceptable sonic boom? From Fig. 4 and Eq. (9) one can quickly conclude that the minimum front and rear shock pressure rises ($R = 1$) with $\tau = 0.015$ are 0.247 lbs./ft.^{2} Would this be acceptable? To answer this question we must know more about acceptability.

Recent Studies of Acceptability

The University of Toronto's Institute for Aerospace Studies, Japan's Agency of Industrial Science and Technology, and NASA Langley developed simulators to better assess loudness and annoyance associated with minimized sonic booms as experienced outdoors.[40-42] Niedzwiecki and Ribner,[43,44] Shepherd and Sullivan,[45] among others,[46-51] improved existing methods for determining the subjective loudness of N-wave and minimized sonic boom signatures, establishing thereby a sound basis for reducing the outdoor annoyance of sonic booms. The seven principal conclusions of these studies (see Refs. 42-51) are:

1. Either the A-weighted sound exposure level or the perceived noise level can be used to establish a criteria for judging the acceptability of minimized sonic booms as experienced outdoors.

2. A post shock (secondary) rise time of 20 milliseconds is as effective as one of 50 milliseconds in reducing the loudness rating.

3. A loudness level of 1 or an A-weighted sound exposure level of 68 dB results in a sonic boom that is acceptable to 95% of those exposed to it.

4. This loudness level is achieved by a minimized signature in which the front (and rear) shock pressure rise is 0.25 lbs./ft. and the maximum (and minimum) pressure of 1.0 lbs./ft.^{2} occurs 20 milliseconds later (earlier).

5. The rise time of the shocks, governed by the physics of weak shocks, is an important variable.

6. The benefit of shaped minimized booms, when quantified by loudness, occurs equally indoors and outdoors.

7. The simulator tests found no unexplained effect of wave shape on either loudness or annoyance except that increased duration decreased subjective response.

The sixth conclusion, from Brown and Sutherland,[50] needs to be tested by field studies. But how would this be done? We have no aircraft designed to have a minimized boom. Perhaps the supersonic transport demonstrator planned by the National Aerospace laboratory in Japan could serve this purpose.[52] This group has conducted studies to minimize the sonic boom of supersonic transport.[53,54]

Mid 1990s flight tests at Edwards Air Force Base suggest that people's tolerance of sonic booms is very low and that for an aircraft to be certified to fly supersonically over populated areas, its sonic boom will have to be nearly inaudible outdoors, and hardly discernible indoors. About 5% of the those exposed will find anything they discern as unacceptable.

Effects of Vibrational Relaxation

For small aircraft with low shock pressure rises, we must also consider the beneficial effects of vibrational relaxation on these shock waves. These effects were well understood many years ago,[55-60] but we did not

consider them then in sonic boom minimization because they are not important in the sonic boom of transport-size aircraft. But for a small, slender, supersonic business jet, especially one of moderate cruise Mach number, say Mach 1.6-1.8, they may render the sonic boom essentially inaudible outdoors. With a minimized shock pressure rise and its thicker shock, more of the energy is in the lower frequencies, thereby reducing outdoor audibility and structural response.

Kang,[61] and Pierce and Kang,[62] considered vibrational relaxation effects in detail. Kang compares the theory for weak shock waves, including vibrational relaxation, with experimental results from explosions and supersonic aircraft flights. There is solid theoretical support and convincing experimental evidence that weak shock waves are considerably thickened and, when weak enough, disperse. This indicates that shock waves of the strength that may be achieved by supersonic business jets will have rise times of several tens of milliseconds.

Conclusion

We have revisited here the prescription for determining the minimum possible sonic boom signature parameters and conclude that while the outdoor annoyance of commercial transport size aircraft could be reduced, this is not the case for indoor annoyance, and therefore their sonic booms will remain unacceptable.

For small aircraft the shock pressure rise, maximum overpressure, and impulse can all be small. Would a small supersonic business jet have an acceptable sonic boom? There is considerable evidence that this is possible. But it will be difficult to establish that this is the case. A supersonic business jet can be designed to have only very weak shock waves in its pressure signature. These weak shocks will be considerably thickened, and in some cases dispersed, by vibrational relaxation. Will this nearly inaudible sonic boom be acceptable to those indoors? The answer is at least "perhaps," as the energy in this minimized boom is in the lowest frequencies, and thus it will contain less energy in the frequencies important in structural response and indoor annoyance.

Market studies indicate a considerable market for a supersonic business jet, but this market is nearly halved if it is restricted to supersonic flight over water.[63] A business plan for the development of a supersonic business jet must consider carefully whether or not there is a route to its certification for supersonic operations over populated areas. The lack of an established scheduled route structure may assist in this certification.

Thirty-year-old studies point the way for the design of a small supersonic business jet that may be certifiable for supersonic operations on many land routes. The case will rest on its sonic boom being a noise that is no more objectionable than that of current subsonic jet transports on ascent from, and descent to, still distant airports. This is a noise to which nearly all of us are exposed and which we have long accepted. Its duration is hundreds of seconds; the duration of the sonic boom of a supersonic business jet is a small fraction of a second.

It is the author's conjecture that to be certifiable for supersonic operation over land the sonic boom of a supersonic business jet will need to be acceptable to 95% of the population 95% of the time. This may well prove possible.

References

1. Busemann, A., "Aerodynamischer Auftreib bei Überschallgeswindigkeit," *Proceedings, Volta Congress*, pp. 315-317, 1935.

2. Busemann, A., "The Relation between Minimizing Drag and Noise at Supersonic Speeds," *Proceedings, High Speed Aerodynamics*, Polytechnic Institute of Brooklyn, pp. 133-144, 1955.

3. Ryhming, I. L., "The Supersonic Boom of a Projectile Related to Drag and Volume," *J. Aerospace Sciences*, Vol. 28, pp. 113-118, 1961.

4. Jones, L. B., "Lower Bounds for Sonic Bangs," *J. Royal Aeronautical Society*, Vol. 65, pp. 1-4,1961.

5. Jones, L. B., "Lower Bounds for Sonic Bang in the Far Field," *Aeronautical Quarterly*, Vol. XVIII, pp.1-21, 1967.

6. McLean, F. E., "Some Nonasymptotic Effects on the Sonic Boom of Large Airplanes," NASA TN D-2877, 1965.

7. Hayes, W. D., "Brief Review of the Basic Theory," *Sonic Boom Research*, R. Seebass, Ed., NASA SP-147,1967.

8. Seebass, R. "Minimum Sonic Boom Shock

Strengths and Overpressures," *Nature*, Vol. 221, pp. 651-653, 1969.

9. Seebass, R., "Sonic Boom Theory," *J. Aircraft*, Vol. 6, No. 3, 177-584, 1969.

10. George, A. R., "Lower Bounds for Sonic Booms in the Midfield," *AIAA J.*, Vol. 7, No. 8, p. 1542-1545, 1969.

11. George, A. R., and Plotkin, K. J., "Sonic Boom Waveforms and Amplitudes in a Real Atmosphere," *AIAA Journal*, Vol. 7, No. 10, pp. 1978-1981, 1969

12. Jones, L. B., "Lower Bounds for the Pressure Jump of the Bow Shock of a Supersonic Transport," *Aeronautical Quarterly*, Vol. XXI, pp. 1-17, 1970.

13. Petty, J. S., "Lower Bounds for Sonic Boom Considering the Negative Overpressure Region," *J. Aircraft*, Vol. 7, No. 4, pp. 375-377, 1970.

14. Hayes, W.D., and Weiskopf, F. B., Jr., "Optimum Configurations for Bangless Sonic Booms," *Quarterly of Applied Mathematics*, Vol. 30, pp. 311-328, 1972.

15. George, A. R., and Seebass, R., "Sonic Boom Minimization Including Both Front and Rear Shock Waves," *AIAA J.*, Vol. 10, No. 10, pp. 2091-2093, 1969.

16. Seebass, R., and George, A. R., "Sonic Boom Minimization," *Proceedings, Second Sonic Boom Symposium, J. Acoustical Society of America*, Vol. 51, No. 2 (Part 3), pp. 686-694, 1972.

17. Seebass, A. R., and George, A. R., "Design and Operation of Aircraft to Minimize Their Sonic Boom," *J. Aircraft*, Vol. 11, No. 9, pp. 509-517, 1974.

18. Darden, C. M., "Sonic Boom Minimization with Nose-Bluntness Relaxation," NASA TN 1348, 1979.

19. Darden, C. M., "Charts for Determining Potential Minimum Sonic Boom Overpressures for Supersonic Cruise Aircraft," NASA TP 1820, 1981.

20. Miller, D. S., and Carlson, H. W., "A Study of the Applications of Heat or Force Fields to the Sonic-Boom-Minimization Problem," NASA TN D-5582, Dec. 1969.

21. Warren, C. H. E., "A Note on the Sonic Bang Waveform of an Aircraft with Lift," *J. Royal Aeronautical Society*, Vol. 67, p. 95, 1963.

22. Seebass, R., and McLean, F. E., "Far-Field Sonic Boom Waveforms," *AIAA J.*, Vol. 6, No. 6, pp. 1153-1155, 1968.

23. Crow, S. C., and Bergmeier, G. G., "Active Sonic Boom Control," *1995 NASA High Speed Research Program Sonic Boom Workshop*, pp. 68 -111, 1996.

24. Hayes, W. D., "Linearized Supersonic Flow," Ph.D. thesis, California Institute of Technology, Pasadena (available as AMS Report 852, Princeton University), 1947.

25. Lomax, H., "The Wave Drag of Arbitrary Configurations in Linearized Flow as Determined by Areas and Forces in Oblique Planes," NACA RM A55A18, 1955.

26. Lomax, H., and Heaslet, M. B., "Recent Developments in the Theory of Wing-Body Wave Drag," *J. Aeronautical Sciences*, Vol. 23, No. 12, pp. 1061-1074, 1956.

27. Li, P., Seebass, R., and Sobieczky, H., "The Sonic Boom of an Oblique Flying Wing," *Proceedings, First Joint CEAS/AIAA Aeroacoustics Conference*, Vol. II, pp. 753-760, 1995.

28. von Kármán, Th., and Burgers, J. M., *Aerodynamic Theory*, W. F. Durand, ed., Vol. 2, Springer, pp. 172-175, 1934.

29. Sears, W. R., "On Projectiles of Minimum Wave Drag," *Quarterly of Applied Mathematics*, Vol. 4, No. 4, pp. 361-366, 1947.

30. Haack, W., "Geschossformen kleinsten Wellenwiderstandes," *Lilienthal-Gesellschaft für Luftfahrt*, Bericht 139, pp. 14-28, 1941.

31. Lighthill, M. J., "The Wave Drag at Zero Lift of Slender Delta Wings and Similar Configurations," *J. Fluid Mechanics*, Vol. 1, pp. 337, 1965.

32. Küchemann, D. *The Aerodynamic Design of Aircraft*, Pergamon, Oxford, 1978.

33. Darden, C. M., "Sonic Boom Theory: Its Status in Prediction and Minimization," *J. Aircraft*, Vol. 129, No. 6, pp. 569-576, 1977.

34. Lung, J. L., "A Computer Program for the Design of Supersonic Aircraft to Minimize Their Sonic Boom," M.S. Thesis, Cornell University, 1975.

35. Mack, R. J., and Darden, C. M., "Wind Tunnel Investigation of the Validly of a Sonic -Boom-Minimization Concept," NASA TP 1421, 1979.

36. Borsky, P. N., "Community Reactions to Sonic Booms in the Oklahoma City Area," (Parts I and II), Wright Patterson AFB Report AMRL-TR-65-37, 1965.

37. Nixon, C. W., and Hubbard, H. H., "Results of the USAF-NASA-FAA Flight Program to Study Commu-

nity Responses to Sonic Booms in the Greater St. Louis Area," NASA TN D-2705, 1965.

38. Kryter, K. D., "Sonic Boom from Supersonic Transport," *Science*, Vol. 163, 24 January, pp. 359-367, 1969.

39. Roskam, J., "Part V: Component Weight Estimation," *Airplane Design*, Roskam Aviation and Engineering, Ottawa, Kansas, 1989.

40. Glass, I. I., Ribner, H. S., and Gotlieb, J. J., "Canadian Sonic Boom Simulator Facilities, *Canadian Aeronautics and Space J.*, Vol. 18, No. 8, pp. 235-246, 1972.

41. Tokita, T., Nakamura, S., and Oda, A. "New Research Facilities for Sound Pressure Tests of Infra and Low Frequency Signals," *J. Acoustical Society of Japan*, Vol. 40, No. 10, 1984.

42. Leatherwood, J. D., Sheperd, K. P., and Sullivan, B.P.,"A New Simulator for Assessing Subjective Effects of Sonic Booms," NASA TM-104150, 1991.

43. Niedzwiecki, A., and Ribner, H. S., "Subjective Loudness of N-Wave Sonic Booms," *J. Acoustical Society of America*, Vol. 64, No. 6, pp. 1617-1621, 1978.

44. Niedzwiecki, A., and Ribner, H. S., "Subjective Loudness of 'Minimized' Sonic Boom Waveforms," *J. Acoustical Society of America*, Vol. 64, No. 6, pp. 1622-1626, 1978.

45. Shepherd, K. P., and Sullivan, B. P., "A Loudness Calculation Procedure Applied to Shaped Sonic Booms," NASA TP-3134, 1991.

46. Leatherwood, J. D., and Sullivan, B. M., "Laboratory Study of Effects of Sonic Boom Shaping on Subjective Loudness and Acceptability," NASA TP-3269, 1992.

47. Tokuyama, A., Sakai, K., and Taya, H., "Experimental Study of Sonic Boom Acceptance," AIAA Paper No. 93-3961, 1993.

48. McCurdy, D. A., "Subjective Response to Sonic Booms Having Different Shapes, and Durations," NASA TM-109090, 1994.

49. Wiggins, J. H., *The Effects of Sonic Boom*, Wiggins, Palos Verdes, 1969.

50. Brown, D., and Sutherland, L. C., "Evaluation of Outdoor-to-Indoor Response to Minimized Sonic Booms," NASA Contractor Report 18943, 1992.

51. McCurdy, D. A., Brown, S. A., and Hilliard, R. D., "The Effects of Simulated Sonic Booms on People in Their Homes," AIAA Paper No. 95-0834, 1995.

52. Shimbo, et al., "Aerodynamic Design of the Scaled Supersonic Experimental Airplane," *International CFD Workshop for Super-Sonic Transport Design*, National Aerospace Laboratory, Japan, pp. 62-67, 1998.

53. Makino, Y., et al., "The Effects of the Body Configuration on the Sonic-Boom Intensity," AIAA Paper No. 96-2466, 1996.

54. Makino, Y., et al., "Low-Boom Design Method by Numerical Optimization," AIAA Paper No. 98-2246, 1998.

55. Clarke, J, F., and McChesney, M., *Dynamics of Real Gases*, Butterworths, Washington, 1964.

56. Vincenti, W. G., and Kruger, C. H., *Introduction to Physical Gas Dynamics*, Wiley, New York, 1965.

55. Ockendon, H., and Spence, D. A., "Non-Linear Wave Propagation in a Relaxing Gas," *J. Fluid Mechanics*, Vol. 39, part 2, pp. 329-345, 1969.

57. Ryzhov, O. S., "Nonlinear Acoustics of Chemically Active Media," Prikl. Mat. Mekh. (PMM), Vol. 35, No. 6, pp. 1023-1037, 1971.

58. Hodgson, J. P., "Vibrational Relaxation Effects in Weak Shock Waves in Air and the Structure of Sonic Bangs," *J. Fluid Mechanics*, Vol. 58, Part 1, pp. 187-196, 1973.

59. Hung, C. M., and Seebass, R., "Reflexion of a Weak Shock Wave with Vibrational Relaxation," *J. Fluid Mechanics*, Vol. 65, Part 2, pp. 337-363, 1974.

60. Sinai, Y. H., and Clarke, J. F., "The Wave System Attached to a Finite Slender Body in a Supersonic Relaxing Gas Stream," *J. Fluid Mechanics*, Vol. 84, Part 4, pp. 717-741, 1978.

61. Kang, J., *Nonlinear Acoustic Propagation of Shock Waves through the Atmosphere with Molecular Relaxation*, Ph. D. Thesis, Pennsylvania State University, 1991.

62. Pierce, A. D., and Kang, J., "Molecular Relaxation Effects on Sonic Boom Waveforms," *Proceedings of the 12th ISNA Frontiers of Nonlinear Acoustics*, M. F. Hamilton and D. T. Blackstock, eds., Elsevier, pp. 165-170, 1990.

63. Greene, R., "The Market for a Corporate Supersonic Transport," Presentation: High Speed Civil Transport, Why and When?, AAAS Annual Meeting, Seattle, Washington (AAAS AS795 audio tape), 1997.

Appendix

The variation of the minimum bow shock pressure rise and the corresponding maximum pressure, minimum positive overpressure and minimum impulse with aircraft length, weight, altitude and Mach number for a M = 2.7, 300 ft., 600,00 lbs. baseline aircraft (taken from Ref. 16).

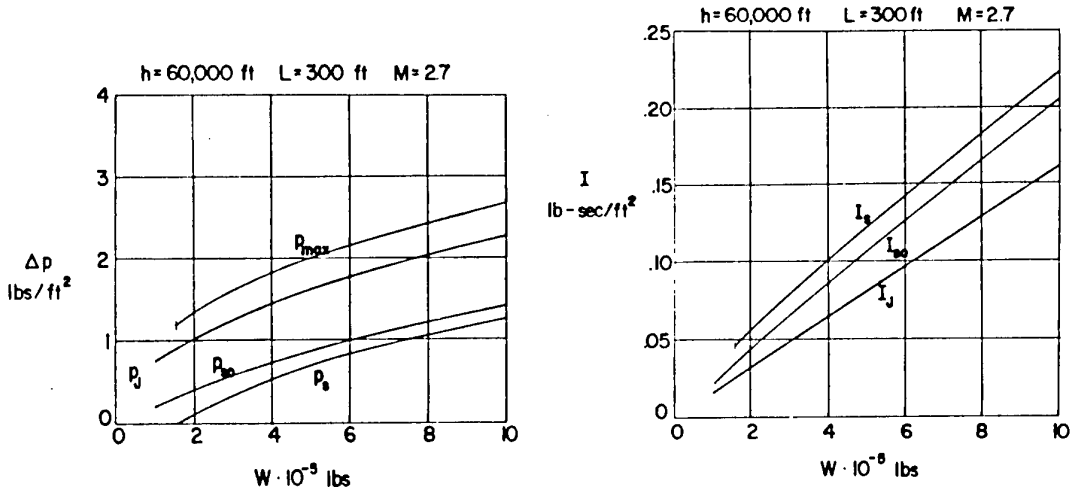


Figure 1A. Positive phase signature pressures and impulses as a function of aircraft weight (H = 25,000 ft.).

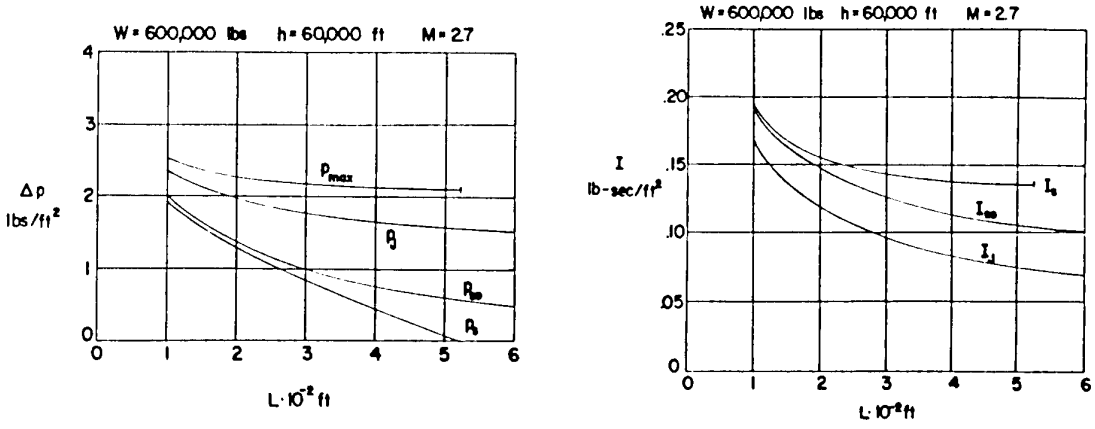


Figure 2A. Positive phase signature pressures and impulses as a function of aircraft length (H = 25,000 ft.).

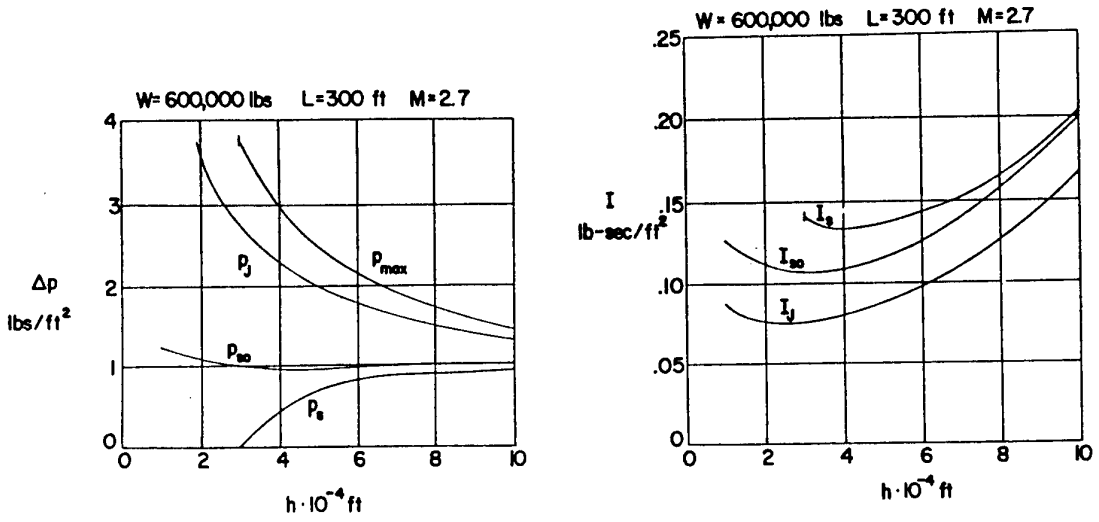


Figure 3A. Positive phase signature pressures and impulses as a function of flight altitude (H = 25,000 ft.).

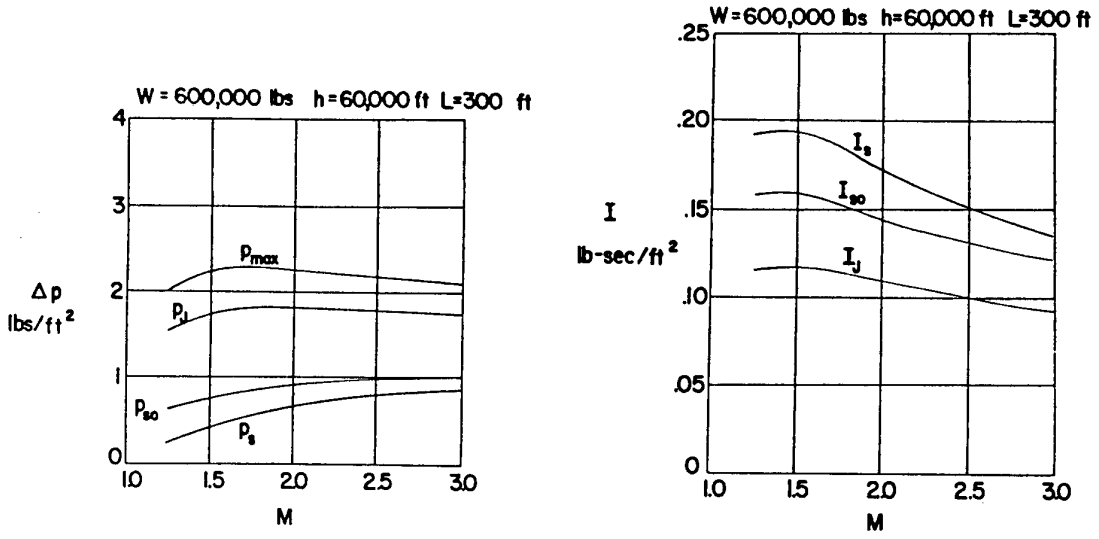


Figure 4A. Positive phase signature pressures and impulses as a function of Mach number (H = 25,000 ft.).

COMPLEX EXPERIMENTAL STUDIES OF SST.

PART II. AERODYNAMIC INTERFERENCE OF VARIOUS ELEMENTS

by

A.M. KHARITONOV

Institute of Theoretical and Applied Mechanics SB RAS (ITAM SB RAS), Instituskaya 4/1, Novosibirsk, 630090 Russia

Summary.

The results of complex experimental studies of aerodynamic interference of various elements of supersonic transport aircraft are presented. The objective was a detailed study of local SST aerodynamics, which was aimed at seeking the methods of increasing the aerodynamic perfectness of these vehicles. The results presented include the study of interference of a schematized wing with the body, wing with engine nacelles, wing with various superstructures, and wing with engine jets. A supersonic flow around all these configurations is accompanied by complex three-dimensional flows with shock wave/boundary layer interactions, boundary layers in the regions of surface junctions, diffraction flows, etc. Capabilities of the developed measurement techniques of the own aerodynamic characteristics of various elements and the contribution of the wing, the body, and the superstructures, as well as their mutual positions, to the characteristics of their combinations. The methods of increasing the lift-to-drag ratio of SST models are shown in a number of cases. At the same time, the results presented can be used as test cases for CFD validation.

List of symbols.

x,y,z	Cartesian coordinates
d	body diameter
l	span distance
$\bar{z}=Z/_{l/2}$	relative span distance
Δy	profile ordinate
x^*	coordinate of the wing position on the body
$\bar{x}_N=x_N/_{h_N}$	engine nacelle position
α	angle of attack
α_{Kmax}	angle of attack at maximum lift-to-drag ratio
β	slip angles
χ	swept angles
S	area of cross-section
f	relative wing thickness
M_∞	freestream Mach number
Re	freestream Reynolds number
q	dynamic pressure
P_0	stagnation pressure
P_0'	stagnation pressure behind the shock-wave
$C_P=(P-P_\infty)/q$	pressure coefficient
ΔC_P^{int}	interference increments of the pressure coefficient
$\bar{P}=P_{0j}/P_\infty$	relative total pressure in the jets
Cy_b	normal force coefficient of isolated body
Cy_w	normal force coefficient of isolated wing
Cy_w^b	normal force coefficient at present the body
Cy_b^w	normal force coefficient at present the wing
A_{Cy}	interference coefficient for normal force
K_{max}	maximum lift-to-drag ratio
n	nozzle pressure ratio
φ	inlet flow rate coefficient
m_z	pitching moment coefficient

Introduction

The second part of this lecture is devoted to aerodynamic interference of various SST elements. The interference phenomenon is known to be characterized by mutual flows over wing/body configurations, engine nacelles and various superstruc-

Paper presented at the RTO AVT Course on "Fluid Dynamics Research on Supersonic Aircraft", held in Rhode-Saint-Genèse, Belgium, 25-29 May 1998, and published in RTO EN-4.

tures with the lifting surface. These are usually complex three-dimensional turbulent flows which have been beyond adequate modeling. Careful and complete experimental data are needed for CFD validation. At the same time, such experimental data allow one to gain better insight into the structure and specific features of these flows, which defines the optimal mutual positions of elements and, hence, increases the aerodynamic efficiency.

The laboratory of aerodynamics of the Institute of Theoretical and Applied Mechanics SB RAS has devoted its efforts for many years to the problem of interference and accumulated vast experience of solving this kind of problems. The results of these experimental research of this laboratory have been conducted on the initiative and support of the Aerodynamics Department of the Tupolev Aviation Company and have been mainly published in Russian scientific journals and, thus, are known to a limited circle of scientists.

The authors of this paper are the ITAM scientists: Dr. M.Brodetsky, Dr. L.Vasenyov, Dr. A.Maksimov, Dr. A.Lokotko, and me.

AERODYNAMIC INTERFERENCE OF WING AND BODY

The experimental study of aerodynamic wing/body interference is very important for examining the structure and particular features of the flow around a wing/body combination with different positions of the wing on the body and for obtaining the data necessary for testing numerical methods. Let us consider detailed information on static pressure distribution, behavior of the limiting streamlines on the surface and the influence of relative wing area on interference parameters. For this purpose, we chose a combination of a triangular wing with a rhombic profile and an ogival-cylindrical body with a large aspect ratio (Fig. 1) [1-5].

The experiments were conducted in the supersonic wind tunnel T-313 based at the Institute of Theoretical and Applied Mechanics of the Siberian Branch of the Russian Academy of Sciences for free-stream velocities $M_\infty=2$ (subsonic leading edge of the wing) and $M_\infty=4$ (supersonic leading edge). The angles of attack of the model ranged within $\alpha=0\text{-}21°$. The corresponding Reynolds number calculated per 1 m amounted to $Re=(24 \text{ and } 56)\cdot10^6$ m^{-1}.

In the course of experiments the limiting streamlines on the surface and the flow pattern were visualized, the pressure distribution in various sections of wing and body and the total aerodynamic loads affecting the model were measured.

Comparison of these data with analogous ones for an isolated wing and isolated body allowed one to find the mechanism of their mutual effects and reveal the conditions when the positive interference is most fully realized.

The flow over this type of isolated wing occurs with a detached shock wave from the leading edges. The wave shape is conical with the apex at the wing tip, the wave shape in the cross-section is close to semielliptical. The pressure at the leeward surface of the wing increased in the direction from the root chord towards the leading edges. The wing profile affects the nature of pressure distribution in the wing cross-sections behind the line of maximum thickness. In the case of subsonic leading edges the flow over the leeward side of the wing is accompanied by the separation from the leading edges, and with an increase in the angle of attack - by the formation of a complex structure and internal shock waves. For example, under the angle of attack $\alpha=14.9°$ (Fig. 2) the presence of two vortex pairs - main vortices and secondary vortices - was detected when the trajectories are close to rectilinear in the vicinity of the wing. The above vortices condition a dramatic decrease of pressure

within a wide range over the wing with typical rarefaction peaks.

In the case of supersonic leading edges at small angles of attack there is no separation at the leeward side of the wing. With the growth of α, internal shock waves are formed in the flow field, which cause the boundary layer separation and the formation of a low-intensity vortex (Fig. 3). The visualization of limiting streamlines detects the presence of a part of the wing surface without separation, as well as the separation and reattachment lines as a result of the vortex existence. The effect of such a structure on the nature of pressure distribution, however, is not large.

A supersonic flow around bodies of revolution is also accompanied by flow separation, formation of vortices and internal shock waves. However, in contrast to delta wings, the nature of the flow over separate parts of sharpened wings, under certain conditions, can gradually change from nonseparated to a complicated flow involving both primary and secondary flow separations from the body surface, and vortex formation (Fig. 4). This circumstance is important for the case of wing/body combination, when the value of additional interference load essentially depends on the wing location on the body.

For subsonic leading edges at small and moderate angles of attack, the length of the separation region on the upper side of the wing panel with a characteristic low pressure increases because of the body effect (Fig. 5). The free vortex center on the wing moves also towards the body. If the wing is moved downstream of the body tip, then at high angles of attack ($\alpha \geq 15°$) the vortex system of the body presses out the free vortices of the wing to the leading edges, deforming their configuration and inducing the corresponding redistribution of pressure over some part of the wing surface. If the wing approaches gradually the body tip, then irrespective of the flow regime around it, a tendency to the pressure increase on the windward side of the wing is observed because of the flow deceleration behind the shock wave from the body. Under certain conditions — moderate supersonic velocities and low angles of attack — the wing can prevent the formation of body vortices.

Large portions of the surface with the pressure coefficient C_p, positive on the windward side and negative on the leeward one, are formed on the body in the presence of the wing, these C_p coefficients being much different from the values for an isolated body (see Fig. 5). The length of the wing influence regions in the longitudinal direction is proportional to the airborne chord length and increases in the presence of a rearbody.

The features of pressure distribution over the surfaces of the wing panel and cylindrical part of the body caused by their mutual influence lead to an increase of integral characteristics of the configuration, the value of the interference load being also dependent on the wing position on the body. This is evidenced by the change in the lift force derivative of the combination versus the wing position on the body (Fig.6). There exists a mutual position of the wing and the body such that the positive interference in the lift force achieves the maximum value.

An existence of the optimal position of the wing on the body is also validated by direct measurements of interference coefficients. For this purpose, it is possible to use the technique of separate measurements of aerodynamic loads affecting only the wing and only the body in their combination, the measurement being taken by a system of strain-gage balances (Fig. 7) [2]. This technique allows one to determine the own aerodynamic characteristics of elements of the combination and, thus, reveal the components of the total interference coefficient. As an illustration, Figure 8 shows the own characteristics of the wing and the body taking into account their mutual interference. The contribution of each element to the formation of total aerodynamic characteristics is clearly

seen. The influence of wing position on the body on the formation of interference loads can be characterized by interference coefficients, in particular, for normal forces:

for the wing $A_{C_{yw}} = \frac{C_{yw}^{b}}{C_{yw}}$; for the body $A_{C_{yb}} = \frac{C_{yb}^{w}}{C_{yb}}$.

The total interference coefficient for the wing/body combination is

$$A_{C_{ycomb}} = \frac{A_{C_{yw}}}{1+\frac{C_{yb}\cdot S_b}{C_{yw}\cdot S_w}} + \frac{A_{C_{yb}}}{1+\frac{C_{yw}\cdot S_w}{C_{yb}\cdot S_b}}.$$

Here C_{yw} and C_{yb} are the normal force coefficients of isolated wing and isolated body, respectively. The interference coefficients for the normal force A_{C_y} of the wing, body and their combination versus the parameter x^* for an angle of the maximum lift-to-drag ratio of the combination are plotted in Fig. 9. An interference increment is formed on the body, which is comparable with the normal force for an isolated body. A clearly expressed maximum was observed depending on the wing position x^*. The interference effect of the body on the wing is less pronounced. For $x^* = 0 \div 0.5$ the lifting properties of the wing in the presence of the body and those of an isolated wing are practically equal. Only when the wing moves further towards the body tip, an increase in the normal force of the wing is noticeable. On the whole, positive interference is observed for the wing/body combination within the entire range of x^* variation. The maximum value is achieved for $x^* \cong 0.8$.

Figure 10 shows the maximum lift-to-drag ratio of the configuration. For considered velocities and geometrical parameters it is always higher than the maximum lift-to-drag ratio of a configuration whose elements had no effect on each other. The value K_{max} of the configuration is proportional to the wing panel area and tends to the value K_{max} for an isolated wing with increasing this area.

The results obtained yield more profound understanding of formation conditions of the interference components of the aerodynamic load on the wing and body, and they are used for verification of numerical methods for computing such configurations [4, 5].

AERODYNAMIC INTERFERENCE OF PRISMATIC ENGINE NACELLES WITH A WING

This problem is typical of supersonic transport aircraft whose engines, located at the windward surface of the wing, reduce considerably the lift-to-drag ratio of the vehicle. The wish to minimize the lift-to-drag ratio reduction stipulated the necessity of detailed investigations of interference pressure fields [6]. In particular, Figure 11 shows the interference increments of the pressure coefficients induced by engine nacelles as isolines ΔC_p^{int} =const for the angle of attack of the maximum lift-to-drag ratio.

A very complex interference pattern was revealed for an engine nacelle placed by means of a boundary layer diverter at the lower wing surface. The shocks from the diverter and side cheeks of the inlet, the flow separation as a result of interaction of a shock from the diverter and the boundary layer on the wing, the flow turning in expansion waves from the inflection of the side wall of the engine nacelle, diffraction of shocks — all this conditions the formation of high-pressure (*1*, *3* in Fig. 11) and low-pressure (*1a*, *2*, *4* in Fig. 11) regions on the wing surface. As a result, the engine nacelles reduce the lift-to-drag ratio of the model.

The study of aerodynamic features of individual longitudinal sections of the wing showed that despite the overall negative result, there is some gain in the lift-to-drag

ratio on a part of the wing surface in the region $\bar{z} = 0.5$ due to the interference field of the nacelle. This gain is caused by the fact that the high-pressure region *3* in Fig.11 is formed at the rear part of the wing profiles, where the minimum local angles of attack are observed. As a result, additional lift force formed here does not lead to a noticeable growth of induction-wave drag, and the lift-to-drag ratio of these longitudinal sections of the wing become larger than without engine nacelles.

In the end sections of the wing ($\bar{z} > 0.7$) the high-pressure region *1* is already extended to the nose part with maximum local angles of attack, and the subsequent low-pressure region *2* is extended to the rear part. With such a redistribution of interference load, an additional overall induction-wave drag of longitudinal sections of the wing becomes larger than the additional lift force, and the lift-to-drag ratio decreases.

Two important conclusions follow from the analysis of local characteristics: firstly, the negative interference from the engine nacelles is mainly caused by the high-pressure *1* and low-pressure *2* regions; secondly, to increase the wing lift-to-drag ratio due to pressure field induced by the engine nacelle, it is necessary that high-pressure regions corresponded to surface sections with the minimum local angles of attack, and vice versa. Deeper understanding of formation conditions of the interference loads induced by engine nacelles made it possible to recommend the method of correcting the wing profile for increasing the lift-to-drag ratio. The idea of correction was that by changing the local angles of attack it is possible to design a wing with the same surface pressure distribution as the wing without the engine nacelle.

In this case the wing, having the same lift force as without the engine nacelle, has a lower induction wave drag and, hence, a higher lift-to-drag ratio. There are various approaches to calculating the corrected profiles. Let us consider the approach used in our work. It was assumed in calculating the correction that the downstream influence of wing portions with a changed profile is insignificant, and the engine nacelle pressure field is independent of profile changes.

In our case, it is reasonable to perform the correction in cross-sections $\bar{z} = 0.3 \div 0.8$ only in the first regions of high and low pressures, i.e., in regions *1* and *2* (see Fig. 11). The dependence $\Delta C_p^N(\alpha) = C_p^N(\alpha) - C_p^N(\alpha_{C_y=0})$ is constructed in this region for each cross-section. The values of derivatives $dC_p^N/d\alpha$ are determined from these dependences for an angle of attack $\alpha = 6.3°$. Using the engine nacelle pressure distributions ΔC_p^{int}, it is possible to calculate corrections to local angles of attack of the profile:

$$\Delta\alpha_l(\bar{x}_i) = \frac{\Delta C_p^{\text{int}}(\bar{x}_i)}{\frac{dC_p^N}{d\alpha^N}(\bar{x}_i)}.$$

Integrating this equation, it is possible to find the profile ordinates

$$\Delta y^n(\bar{x}) = \sum_{i=1}^{n} \Delta\alpha_l(\bar{x}_i) \cdot \Delta x$$

where Δy^n is the profile ordinate change at the nth step of integration. The region of corrections on the wing and an example of initial and modified profiles for two cross-sections are presented in Fig. 12. The calculation of such a wing using the linear theory validates the gain in aerodynamic efficiency. The lift force approaches the values for the wing without the engine nacelle, and the induction wave drag increases again.

The effectiveness of the proposed correction was validated by multiple control measurements of aerodynamic characteristics of an aircraft model with engine nacelles, whose wing had initial and modified profiles. As a result, it was obviously shown that the gain in the lift-to-drag ratio for an angle of attack $\alpha_{K_{\max}}$ is $\Delta K = 0.33$ (Fig. 13).

This example illustrates the existence of possible resources of increasing the lift-to-drag ratio of supersonic aircraft that can be found by detailed investigation of the local aerodynamics of flying vehicles.

AERODYNAMIC INTERFERENCE OF A WING WITH SUPERSTRUCTURES

Another example illustrating the possibility of increasing the lift-to-drag ratio of a supersonic aircraft is the use of positive interference of various superstructures located on the lifting surface [7, 8]. The research was carried out for a half-wing model placed on a suspension of the mechanical balance of the wind tunnel on a side sting (Fig. 14). Superstructures imitating the fairings of elevon control drivers were located at the windward side of the half-wing. The purpose of the experiment was to obtain the loads acting upon the superstructure as functions of the angle of attack, sideslip, and its external shape, and to determine the influence regions of superstructures and the values of pressures and loads induced by them. For this purpose, two of the six fairings ($\bar{z} = 0.35$ and 0.73) could be placed on a miniature two-component (longitudinal X and normal Y forces) strain-gage balance. If the balance was rotated by 90°, one could measure the normal Y and side Z forces in the half-wing-fixed coordinate system. Besides, a possibility of pressure registration on the wing surface near the superstructure was provided.

Direct measurements of loads acting upon the superstructure showed that among various geometric forms with the same mid-section, the least contribution to the wing drag is made by a superstructure with conical nose and rear parts. The measurements carried out for different slip angles β of the superstructure allowed one to obtain a generalized dependence of the latter on the wing angle of attack α, for which its contribution to the longitudinal force of the wing is minimal.

The interference pressure field formed by a conical superstructure on the wing surface for one of the flow regimes ($\beta = 0$, $\alpha = 4°$) is shown in Fig. 15 (here ΔC_p is the difference of pressure coefficients on the wing surface with and without the fairing). One can see that despite a comparatively simple shape of the fairing, a complex picture of excess pressure distributions is observed in its vicinity.

The results obtained allowed for the calculation of the coefficients of additional frontal drag ΔC_x and additional lift force ΔC_y of the half-wing caused by mounting of another conical superstructure. Similar increments (calculated for one superstructure) were determined from multiple measurements of the total characteristics of the half-wing model with six mounted superstructures and without them by a mechanical balance. The analysis of obtained data indicates a possibility of increasing the lift-to-drag ratio of the wing by means of superstructures mounted at the leeward side. The validity of this conclusion was supported by multiple measurements of the model of a supersonic passenger aircraft with seven conical superstructures mounted on the lower or upper surface of each wing panel. Thus, the results of a detailed study of interference characteristics of comparatively small superstructures allowed one in this case to recommend possible ways of increasing the lift-to-drag ratio on a cruising flight regime.

INTERFERENCE OF ENGINE JETS WITH A LIFTING SURFACE

The engine contribution to aerodynamic characteristics of a supersonic aircraft is determined by interference forces from the engine nacelle and from its jets. An example and some results of an experimental study of the influence of engine jets under their interaction with the wing surface on aerodynamic characteristics of an SST model are considered below [9, 10]. The method of separation of the airframe and

engine nacelles is used for that. The model (Fig. 16) is mounted on the suspension of the aerodynamic balance of the wind tunnel, while the engine nacelles are fixed on thin struts, which are connected with the lower surface of wing panels using a special device. The minimum possible gap of $0.3 \div 0.5$ mm between the engine nacelles and the wing surface is left. This gap is kept constant when changing the angle of attack. Besides, the engine nacelles can be moved along the chord, perpendicular to the wing plane, which allows one to study their optimal location along the x-axis. The external contours of engine nacelles, inlet configurations, and partly nozzles were modeled. A plane four-ramp inlet with mixed compression, which was common for two ducts, ensured a pressure increase by a factor of $5 \div 7$ within the range of angles of attack $0 \div 6°$. The duct configuration is shown in Fig. 17. The flow in engine nacelles is modeled with respect to the flow rate at the inlet entrance, relative total pressure in the jets, and partly with respect to the Mach number at the nozzle exit. For this purpose, the engine nacelle ducts are equipped with ejectors which are fed with compressed air at room temperature. Thus, the following parameters were varied in experiments: inlet flow rate within $\varphi = 0 \div 1$, relative total pressure in the jets $\overline{P} = P_{0j}/P_\infty = 6.6 \div 11.7$, and engine nacelle position with respect to the trailing edge of the wing along the chord. The engine nacelles were moved within $\overline{x}_N = x_N/h_N = 0.6 \div 3.5$. The nozzle pressure ratio varied within $n = 1.7 \div 2.0$ for the angle of attack $\alpha = 0 \div 6°$. The flow rate was varied by discrete replacement by nozzle with different throats. The flow rate coefficient φ was determined from the ratio of flow rate through the engine nacelle to flow rate in a free-stream tube with a cross-section equal to the inlet entrance area. The flow rate through the nozzle was determined from the total pressure fields measured in nozzle throats by miniature rakes in the passive duct regime. The averaging was performed over 9 points.

To exclude the influence of struts supporting the engine nacelles and elevated pressure in the slot between the engine nacelles and the wing, it seems reasonable to analyze the results in the form of increments of the corresponding characteristics.

As an illustration, Figure 18 shows the increments of the normal force and pitching moment coefficients as functions of the flow rate coefficient. The increments are the differences in characteristics without the engine nacelles and with them for various values of φ. The components ΔCy and Δm_z increase for the examined configuration as the flow rate coefficient decreases. The maximum values at $\varphi=0$ correspond to the choked inlets, when the interference loads due to the flow effusion play an important role. The flow rate coefficient $\varphi=1$ is realized in two cases: 1) passive flow regime (the air is not supplied through ejectors) and 2) regime with working ejectors when the nozzle throat area is chosen so that jet injection through ejectors does not affect the inlet flow. In this case the coincidence of polars is observed, which testifies to reliability of results obtained in the study of interaction of the engine jets. Let us note that for $\varphi < 1$ the absolute value of m_z decreases, which is due to an upstream shift of the center of mass.

The pressure distribution measurements in the zone of jet effects revealed a peak of positive pressure caused by flow underexpansion in the nozzle. Hence, the use of these effects can involve an increase of the normal force coefficient C_y. This can be achieved by extending the upper surface of a 2D nozzle relative to the lower surface or by shifting the engine nacelle upstream of the trailing edge of the wing, i.e., when the pressure peak is located on the wing surface. The experiments on checking a possibility of increasing the lift-to-drag ratio were conducted for $M_\infty = 2.27$ and $Re_1 = 25.5 \cdot 10^6$ m^{-1}. Engine nacelles with ejectors and nozzles, whose throat area was by 10% larger than that required by

the condition of geometric similarity, were used. The increments of aerodynamic characteristics of the SST model were measured versus the position of engine nacelles relative to the trailing edge of the wing and relative to the total pressure in the jets $\overline{P}$.

Figure 19 shows the increments of the maximum lift-to-drag ratio K_{max} of the model with jet/wing interaction. An equal increment $\Delta K_{max} \cong 0.2$ is observed in the range of displacement $\bar{x}_N = 0.9 \div 3.5$. Note that the following procedure was used for imitation of the nozzle with an extended upper surface. The characteristics in the extreme rear position of the engine nacelles ($\bar{x}_N = -0.6$) were determined when there was no interaction of jets with the wing surface. Then the wing edge was equipped with flaps (Fig. 16) located beneath the engine nacelles behind the nozzle exit in such a way that the positive pressure peak was fully located on these flaps. The increments ΔK_{max} in Fig. 19 correspond to the cases of modeling the quantity $\overline{P} = 11.7$ relative to the passive flow and comparison of the passive flow with and without the flaps. It is seen that for $\overline{P} = 11.7$ relative to the passive flow $\Delta K_{max} = 0.2$, while in the passive flow with and without the flaps $\Delta K_{max} = 0.15$.

Thus, when the aircraft engines operate in the regime of weak underexpansion of the jet, an arrangement of engine nacelles is possible that ensures a positive interference of jets with the airframe. The study of this effect can provide a considerable increase of the lift-to-drag ratio on the cruising regime.

Concluding remarks

Some particular examples of aerodynamic interference of the basic SST elements demonstrate possible ways of increasing the aerodynamic efficiency. In all cases, careful and detailed studies of various specific features of local aerodynamics of the interacting elements are needed.

REFERENCES

1. Vasenyov L.G. and Dem'yanenko V.S. Interference of a triangular wing and cylindrical body with an ogival nose part at supersonic speeds, Izv. SO AN SSSR, Ser. tekh. nauk, 1974, Iss. 1, No. 3, P.73 – 78.

2. Vasenyov L.G. and Kharitonov A.M. Interference of a triangular wing and cylindrical body at supersonic speeds, Preprint Inst. Theor. Appl. Mech., Sib. Branch, USSR Acad. Sci. No. 28, 1984, 53 p.

3. Vasenyov L.G. and Kharitonov A.M. Peculiarities of streamlining about the combination "delta wing-body". Proc. of the fifth Asian Congress of Fluid Mechanics, Korea, 1992.

4. Vasenyov L.G. and Kharitonov A.M. CFD validation experiments in problems of supersonic aerodynamics, Proc. Pacific Int. Conf. on aerospace science and technology, Vol. 1, Tainan, Taiwan, December 6–9, 1993b, P. 218 – 224.

5. Vasenyov L.G., Kharitonov A.M., Zabrodin A.V., et al. Comparative analysis of results of computational and experimental investigations of supersonic flows around typical aerodynamic objects "delta wing — body", Thermophysics and Aeromechanics, 1994, Vol. 1, No. 1, P. 35 – 43.

6. Brodetsky M.D., Rafaelyants A.A., Kharitonov A.M., and Cheremukhin G.A. Aerodynamic interference of prismatic engine nacelles with a wing at supersonic speeds, Uch. Zap. TsAGI, 1988, Vol. XIX, No. 1, P.13–21.

7. Brodetsky M.D., Maksimov A.I., and Kharitonov A.M. A technique of experimental investigation of aerodynamic interference of small superstructures with a lifting surface, Izv. SO AN SSSR, Ser. tekh. nauk, 1978, Iss. 3, No. 13, P. 81 – 86.

8. Brodetsky M.D., Maksimov A.I., Kharitonov A.M., et al. Aerodynamic interference of superstructures with a lifting

surface at supersonic speeds, Uch. Zap. TsAGI, 1981, Vol. XII, No. 3, P.110 – 115.

9. Lokotko A.V. A technique of determining the influence of engine jets on aerodynamic characteristics of the model, in: Proc. 2nd All-Union Conference on the Methods of Aerophysical Research, Pt. 2, Novosibirsk, 1979 (in Russian).

10. Lokotko A.V. The influence of the inlet flow rate coefficient and engine jets on aerodynamic characteristics of the model of supersonic passenger aircraft, in: A.M.Kharitonov (ed.) Aerodynamic Interference in the Flow around 3D Bodies, Novosibirsk, 1980, P. 55 – 62.

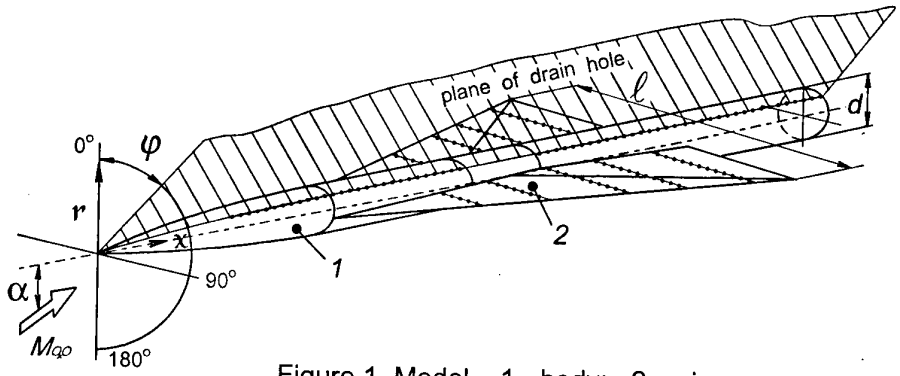


Figure 1. Model. 1 - body; 2 - wing.

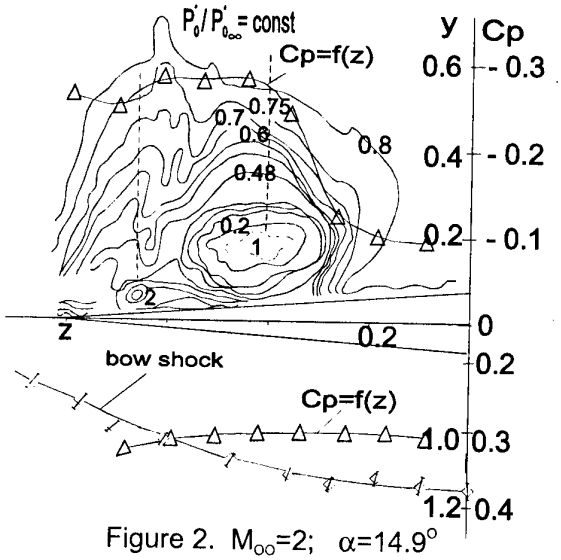


Figure 2. M_{∞}=2; α=14.9°

Subsonic leading edge (M_N=0.83);
1 - primary vortex; 2 - secondary vortex

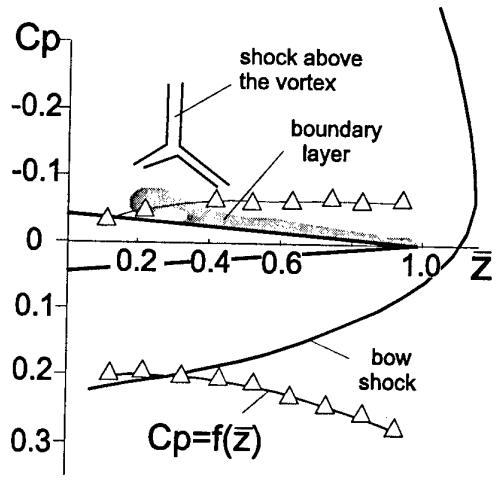


Figure 3. M_{∞}=4; α=14.5°

Supersonic leading edge (M_N=1.65)

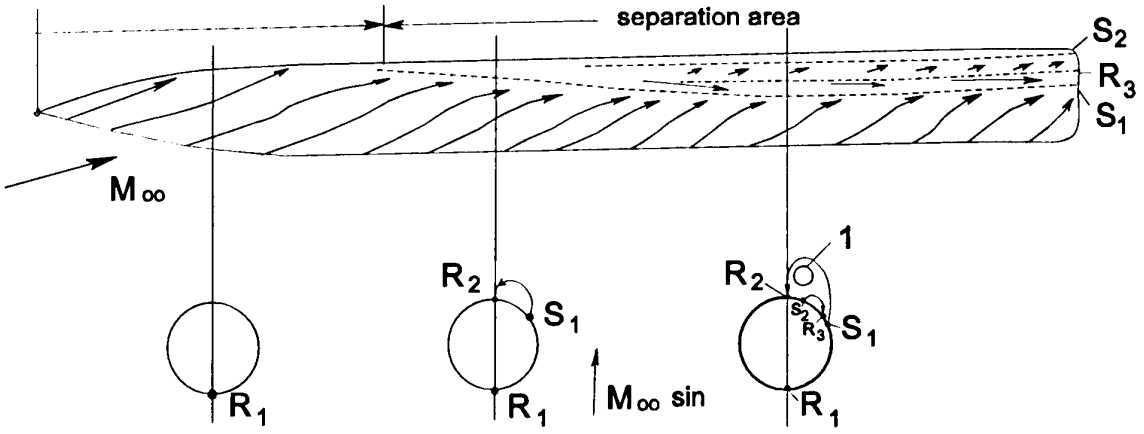


Figure 4. M_{∞}=2.03; α=10.3°

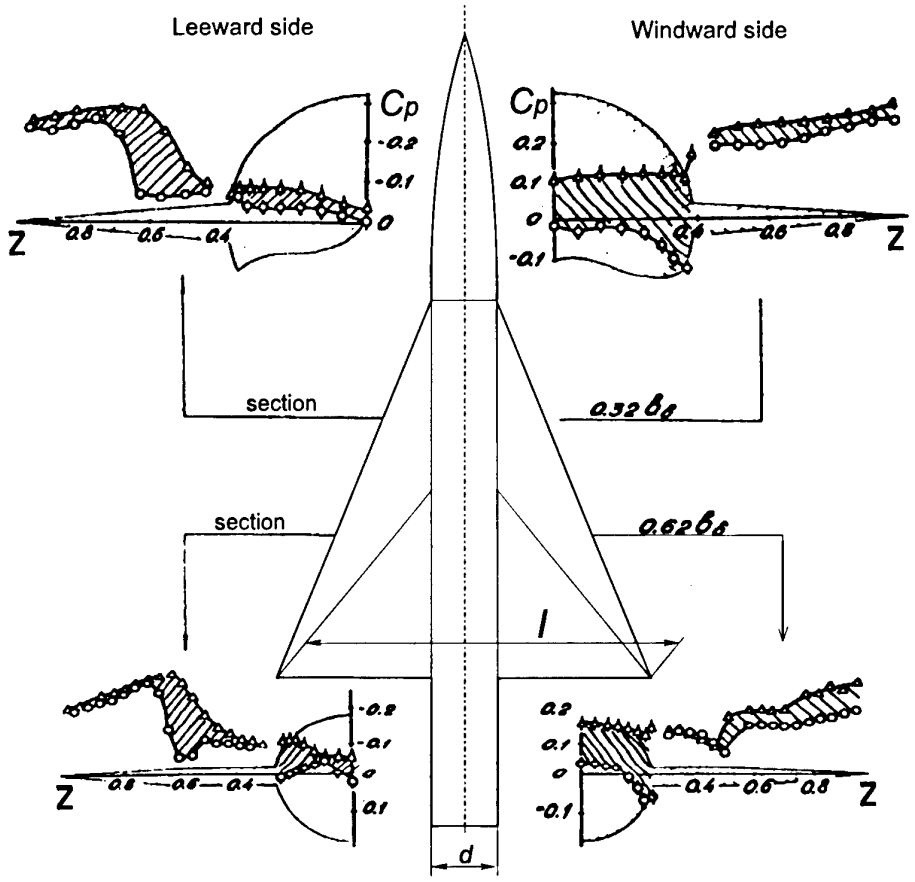


Figure 5.

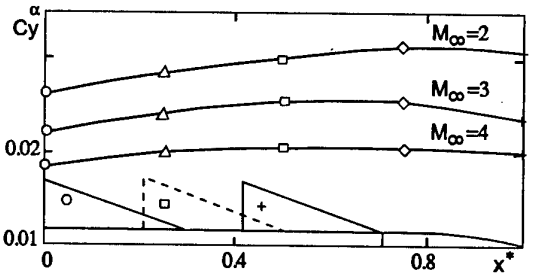
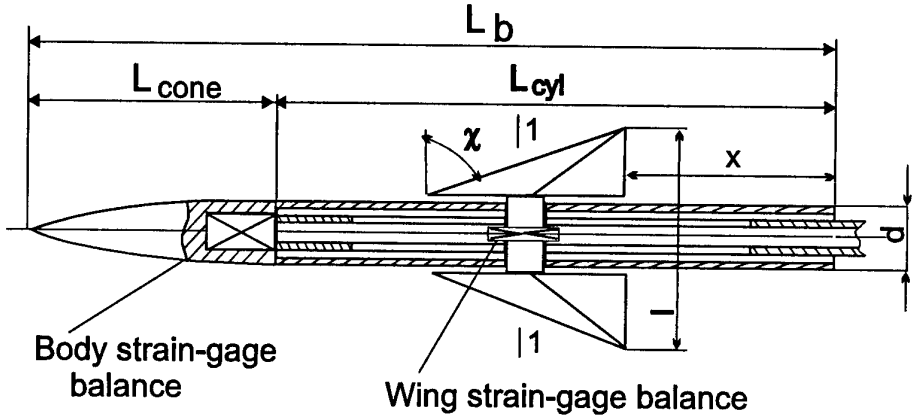


Figure 6. x* - wing location on body (d/l=0.265)

$$x^* = \frac{2(AR)_{rear}}{2(AR)_{cyl}\,[(1-d/l)/(d/l)]tg\chi}$$



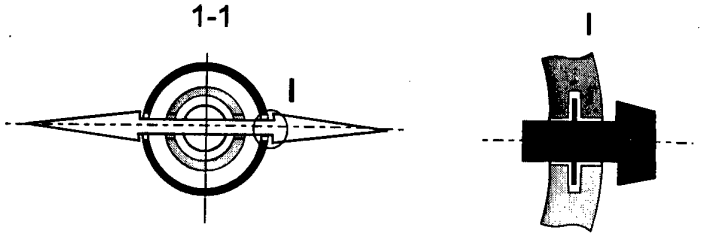


Figure 7.

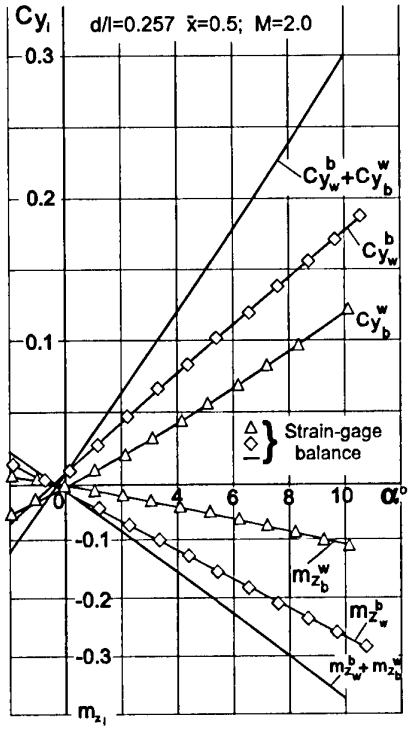


Figure 8.

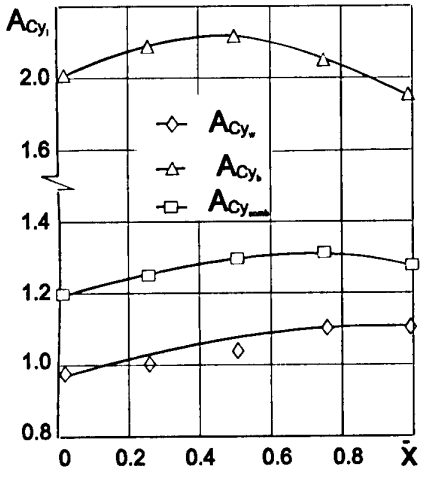


Figure 9. M_{oo}=2.03; d/l=0.257;

$\alpha_{Kmax}^{com.} = 6^{o}$

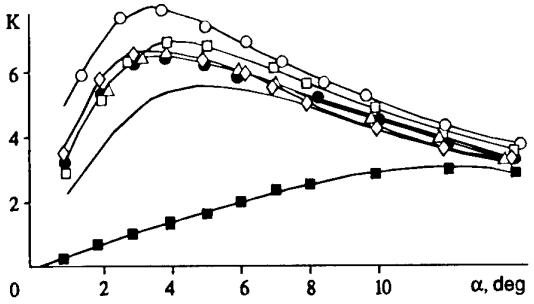


Figure 10. Lift-to-drag ratio versus the angle of attack for M_{oo} = 2.03, d/l = 0.173

○ - isolated wing; ■ - isolated body;

solid line - isolated body + isolated wing;

x = 0 (□); 0.5 (△); 0.75 (●), and 1.0 (◊)

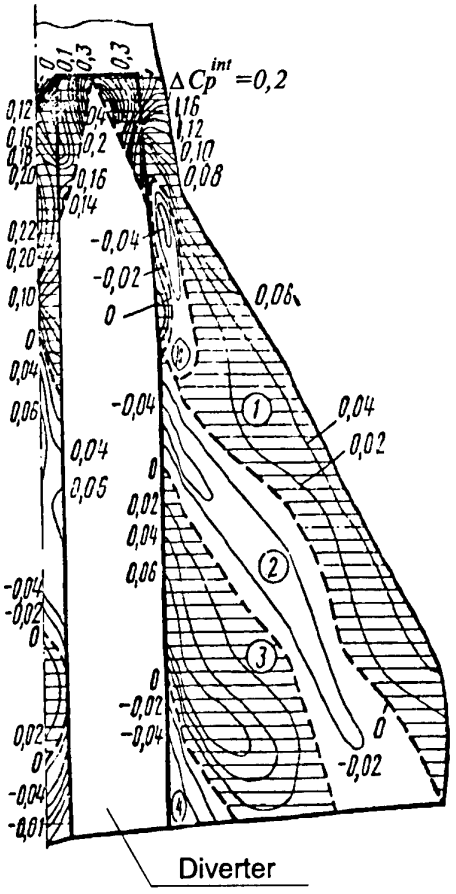


Figure 11. Interference pressure fields on the wing surface for M_{oo} = 2.27,

$\alpha = 6.3^{o}$ (Cy = 0.12)

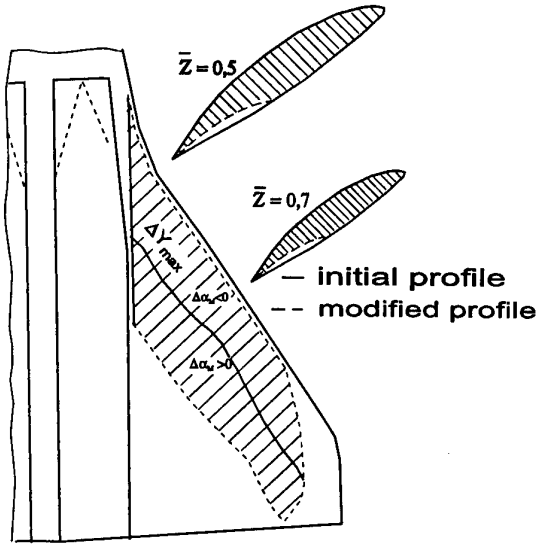
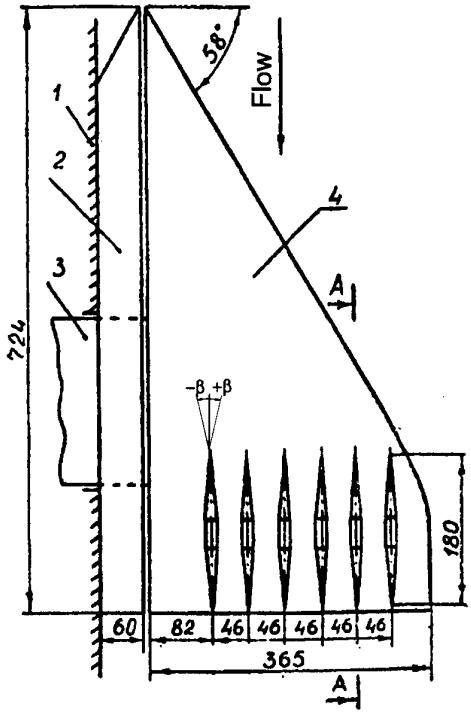


Figure 12.



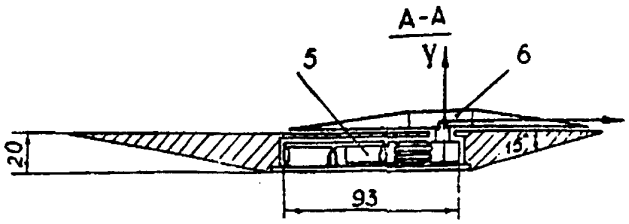


Figure 14.

1 - test section wall; 2 - "false" half-wing; 3 - side sting; 4 - model; 5 - strain-gage balance; 6 - superstructure.

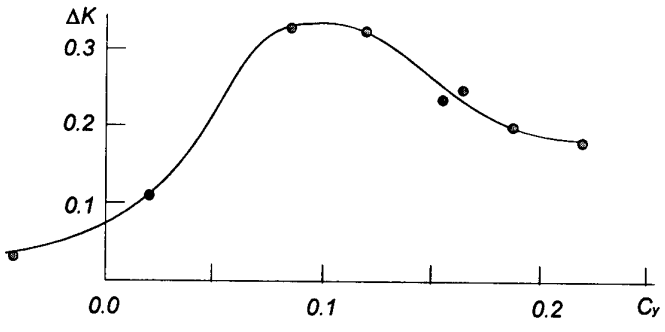


Figure 13.

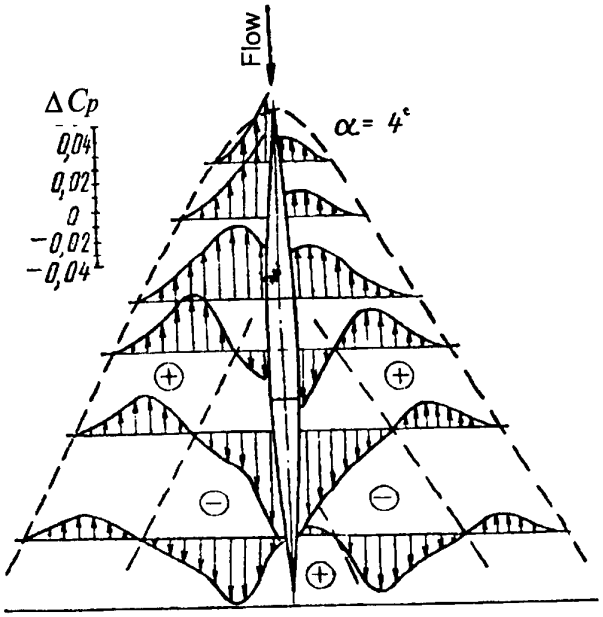


Figure 15.

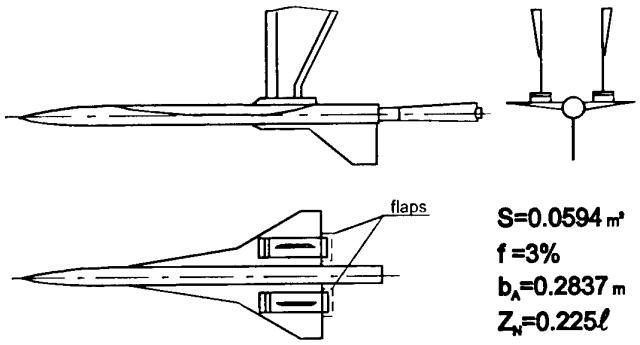


Figure 16.

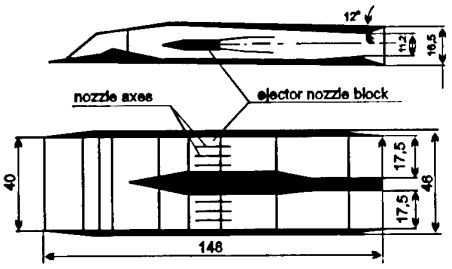


Figure 17.

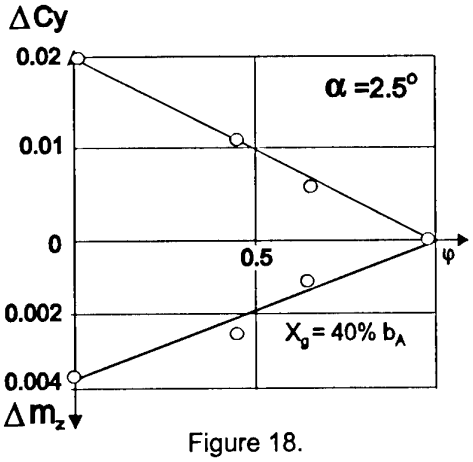


Figure 18.

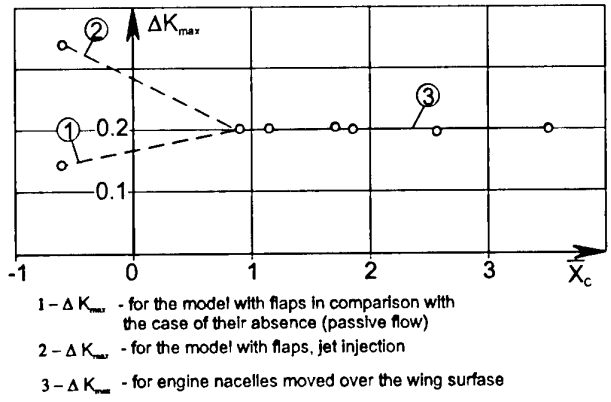


Figure 19.

Multi Point Design Challenges for Supersonic Transports

Josef Mertens
Daimler-Benz Aerospace Airbus GmbH
D-28183 Bremen
Germany

1. SUMMARY

In the lecture "Required Technologies for Supersonic Transport Aircraft" one of the new challenges for a Supersonic Commercial Transport (SCT) was multi point design for the four main design points:
- supersonic cruise
- transonic cruise
- transonic acceleration
- take-off and landing.

Besides engine technology, aerodynamics are most challenged by these differing requirements. But aerodynamic solutions will only become viable when contributing to an optimum of the whole aircraft; this is to be found in cooperation with all disciplines [1]. Here, we deal with the most important aerodynamic parameters at the different design points and consequences for aerodynamic design.

2. SUPERSONIC CRUISE

2.1 Physics of supersonic flow

Physics of supersonic flow are treated in the second lecture of this course by R. Seebass. Here, only some specific properties are mentioned.

In air, information of small disturbances propagates at the speed of sound. This information is transported by collisions between the molecules due to molecular thermal motion building up a bumping information chain at the speed of sound. At subsonic speeds, this propagation speed is faster than flight speed. Therefore, the air molecules around an aircraft are informed about the motion of the aircraft by bumping neighbouring molecules. Changes of air velocity and pressure are therefore smooth at subsonic speeds.

At supersonic flight speeds, the aircraft is faster than the information within the air. If we look at the disturbances produced by one small disturbance moving at supersonic speed v_∞ in three succeeding seconds (fig. 1), the disturbed

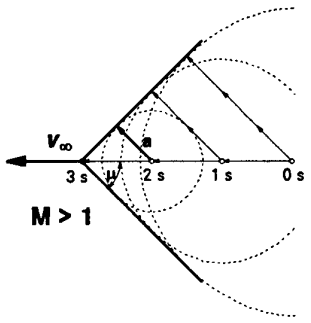


Figure 1: Mach cone

field is inside of a cone, the Mach cone. Outside this cone, air is not yet informed about the disturbance and nobody can hear anything of it. Important parameters are:

$$M = v / a, \qquad M: \text{Mach number} \qquad (1)$$

$$\sin \mu = a / v = 1 / M, \qquad \mu: \text{Mach angle} \qquad (2)$$

Information is spread only within the Mach cone. But the transport of individual informations from neighbouring point to point is even more confined, figure 2:

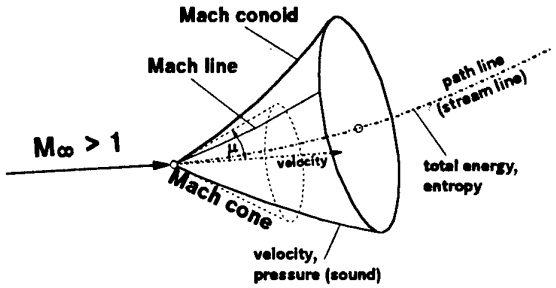


Figure 2: Propagation of supersonic perturbations

- Information about small perturbations in pressure and velocity is transferred only along Mach-lines in the Mach conoid (to which the Mach cone is the local tangent approximation).
- Information about small perturbations in total energy and entropy is transferred only along the path line or stream line (stationary flow).

The formulations above reflect at first only inviscid flow without thermal conductivity. Viscous fluxes and heat conduction exist normal to the Mach cone and path (stream) line. These additional fluxes become important along the path (stream) line in viscous dominated parts, i.e. only in the boundary layer and shear layers; along the Mach cone their influence is very low.

An aircraft flying at supersonic speed is not a small perturbation, but a rather strong perturbation. Because the air in front of the aircraft cannot be informed about the approaching perturbation, smooth reaction is impossible. Instead, the air reacts instantaneously on this strong perturbation and adapts by a strong reaction to this situation: Within some free path lengths of the molecules (about 7) the airflow changes mean velocity direction to follow the aircraft's surface. This sudden reaction not only requires a rapid flow change at the aircraft's surface, but also is radiated into the flow field, figure 3.

Air can transport information in smooth regions of the flow field only at the speed of sound, i.e. inside the Mach cone.

Paper presented at the RTO AVT Course on "Fluid Dynamics Research on Supersonic Aircraft", held in Rhode-Saint-Genèse, Belgium, 25-29 May 1998, and published in RTO EN-4.

This requires that
- the Mach angle in front of the shock is smaller than the shock angle (otherwise a shock would not be needed, because smooth information would be possible);
- the Mach angle behind the shock is larger than the shock angle, because otherwise no information would be available to build up a shock.

Speed of sound a only depends on temperature T:

$$a^2 = \gamma R T \qquad (3)$$

γ : adiabatic exponent (ratio of specific heats)
R : special gas constant for air

The shock moves at supersonic speed (in normal direction to the shock surface) with respect to the air before the shock. By passing the shock, air temperature (and speed of sound) increases to such an amount, that the shock moves only at subsonic (normal) speed relative to the air behind the shock. Behind strong shocks with high shock angles, the flow velocity is subsonic (relative to the aircraft), whereas for weak shocks with smaller shock angles the flow remains supersonic and only the component normal to the shock becomes subsonic, figure 3.

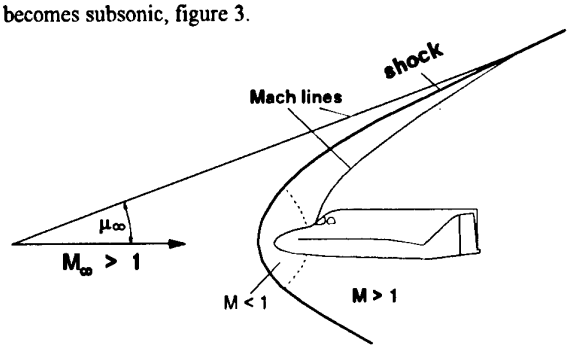


Figure 3: Strong perturbations

Shock energy remains in the shock surface and is radiated only along the shock surface. Furthermore, by conflicting informations from the Mach cones in front and aft of the shock, new energy is radiated into the shock. Therefore shock strength only very slowly decays with larger distance from the aircraft.

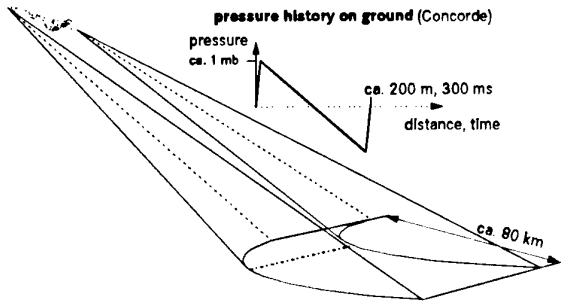


Figure 4: Sonic boom

An SCT flying at about 16 000 m altitude produces a strong shock on the ground, the sonic boom, figure 4. Usually, the pressure history of the sonic boom shows two shocks: a front shock, a rear shock, and in between a nearly linear decrase of pressure, the so called N-wave. All information of zones with higher temperature concentrate at the front shock; all other informations of the regions with decreasing temperatures are collected by the rear shock. So the stable N-wave builds up and can be heard as a double bang on the ground. It is possible to design pressure distributions around the aircraft which do not steepen up to the pure N-wave, but those pressure distributions are sensitive to variations in the vertical weather profile. Only minor changes in temperature or wind distribution of the air (weather conditions varying substantially in the real atmosphere) or flight conditions (Mach number, lift coefficient) destroy any carefully tuned pressure distribution and the N-wave becomes dominant.

The sonic boom is always to be heard, when an aircraft passes flying faster than speed of sound. The bang is the stronger the heavier and shorter the aircraft is, and the lower it flies. Because higher speed of sound (temperature) at low altitudes produces extinction of sideward disturbances, the lateral carpet size is limited; for Concorde the boom carpet has a lateral dimension of about 80 km. This lateral carpet size strongly depends on weather (temperature distribution) and speed of the aircraft with respect to the ground: carpet size is larger in winter and for aircraft tail winds. Boom strength usually is strongest about the middle of the carpet; at the side of the boom carpet, noise is lower and softer. Outside the cut-off distance no bang can be heard, but -if any- only the usual aircraft noise like a grumble.

2.2 Mathematics for solving supersonic flow problems

Mach conoid and path (stream) line (fig. 2) are singular surfaces called "characteristic surfaces"; their generating lines are Mach lines or "characteristics". Inviscid supersonic (or transient) flow is completely described by a set of partial differential equations (PDEs), called "compatibility equations", valid only along characteristics; they do not contain any derivatives across the characteristic surfaces, but allow for undefined jumps in these derivatives [2, 3, 4, 5, 6]. This means:

> Any other set of PDEs describing supersonic (or transient) flow contains *derivative components* normal to characteristic surfaces which are *not defined by the PDEs*! Solutions of those equations may use invalid information or produce solutions containing random parts. This may prohibit accurate or even useful solutions.

Inviscid supersonic (or transient) flow equations are hyperbolic. They describe radiation problems. The PDEs itself allow for discontinuities in the derivatives of the variables (like velocity, pressure, total energy, entropy). If, for a given problem, the initial conditions do not contain discontinuities of the derivatives, discontinuities may evolve in the flow field. Furthermore, any solution to these equations (except for the trivial identity solution, i.e. not any disturbance or flow change at all) is composed only by discontinuous elementary solution parts, maybe for higher derivatives. Estimating accuracy of numerical methods by Taylor series based approximation order may not be adequate for many hyperbolic problems, because the Taylor series' convergence towards discontinuos data is poor.

A straightforward formulation for characteristic directions

and compatibility equations was developed in the early 50ies by C. Heinz [7] at ISL, Saint Louis, France: Focusing on the essential normal characteristic direction, the number of equations used was reduced to the necessary minimum. This formulation is available in [5].

The above mentioned set of variables (velocity, pressure, entropy; total energy beeing dependent of pressure, velocity and entropy) is selected for decoupling of the variables in the compatibility equations. For other sets analogous formulations and discontinuities hold.

Viscous and heat conducting flow equations (Navier-Stokes equations) contain additional derivatives in all space directions without any preference. Those additional derivatives are of elliptical type; the resulting Navier-Stokes equations are of mixed or parabolic type. Viscous and heat flux influence is limited to thin layers (boundary layer, shear layers, shocks) and separation regions.

Shocks can develop in the flowfield by steeping up of solutions and at boundaries, where sudden changes of boundary conditions occur. Shocks are described by the Rankine-Hugoniot equations [2, 3, 5] which are derived by surface integration over a flat volume along the shock surface. Even the "inviscid" Rankine-Hugoniot equations contain viscous and heat fluxes across the shock surface. So the whole flowfield can be described by the inviscid equations, except the boundary layer, separation zones and viscosity in shear layers. In the free flow field, the discontinuous solution properties of the "inviscid" equations must be respected. Even when solving the Navier-Stokes equations for shocks, the thickness of a shock (about 7 molecule free path length) is below numerical resolution; within this small layer the number of molecules is not sufficient to establish equilibrium state variables as required for the continuum formulation of the Navier-Stokes equations. Therefore validity of solutions must be carefully checked. (Sometimes validity can be reached for special cases when carefully applying some continuity assumptions).

In frequent case studies the capturing of shocks in numerical solutions is improved by selection of so called conservative variables which should be conserved when passing a shock. Caution is needed, though: In the Rankine-Hugoniot equations, basically not the variables are conserved, but their fluxes normal to the shock. For example, normal to a stationary shock not density ρ is conserved, but $\rho \boldsymbol{v}\boldsymbol{n}_s$, $\boldsymbol{n}_s$ the shock normal vector; only by chance, the conservative velocity $\rho \boldsymbol{v}$ (i.e. momentum) is the flux of ρ. On the other hand, $\boldsymbol{v}_t$, the velocity component parallel to the shock surface, is conserved across the shock, but not $\rho \boldsymbol{v}_t$.

2.3 Dominating flow phenomena for SCTs

Wave drag:
In supersonic flow the disturbances are radiated away from the aircraft surface. Pressure balancing between aft and forward flow is impossible (fig. 5) or strongly limited for winged vehicles. The result is wave drag, corresponding to the radiated energy [8].

All energy is radiated along Mach lines. Pressure (and temperature) changes along the aircraft, resulting in crossing over of Mach lines at some distance. When Mach lines intersect, conflicting information arrives at this point which will be bridged by a shock. Eventually wave drag energy is captured by shock energy.

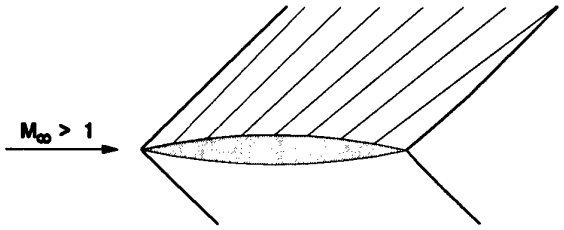


Figure 5: Wave drag

Circulation:
Disturbances can only propagate within the downstream Mach cone. This limits build-up of circulation for finite wings (fig. 6). Leading edge flow can only influence the downstream part of the leading edge, if the leading edge stays within the Mach cone (a so called *subsonic leading edge*). Information of the trailing edge can only reach other parts of the trailing edge to improve pressure recovery, if the trailing edge is located within the Mach cone (*subsonic trailing edge*). The trailing edge can improve the build-up of circulation only for parts of the leading edge within the trailing edge's Mach cone; this is only possible for low supersonic Mach numbers, high aspect ratio and high sweep angles.

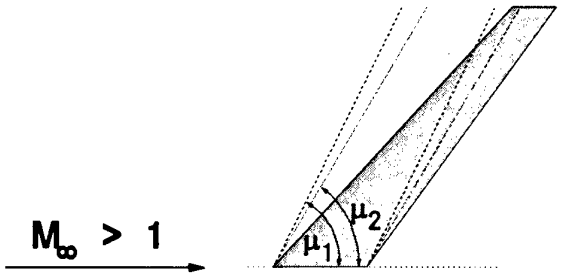


Figure 6: Subsonic leading and trailing edges

Kogans theorem:
Lift efficiency in subsonic flow is described by the energy bounded in the downwind field behind the aircraft: size, strength and downwind distribution determine the induced drag [8]. Kogan [9, 10] developed an similar theorem for supersonic flow: Any point of the aircraft surface can only influence air in its downwind Mach conoid; any point on the aircraft surface can only be influenced by air in its upwind Mach conoid. Kogan constructs the envelope of all downwind Mach conoids originating at the aircraft leading edges, and the envelope of all upwind Mach conoids originating at the aircraft trailing edges. The control surface defined by the intersection of those two envelopes contains all downwind information of the aircraft. Lift-dependend drag of an aircraft is the smaller, the larger this control surface area is, the smaller the mean downwind is and the less disturbed the downwind distribution is.

Interference drag:

Shocks generated on the surface of nacelles (and other interfering parts) are radiated to neighbouring parts like wing, other nacelles or the fuselage, where they are reflected, figure 7. Reflection conditions and drag is strongly influenced by shock-boundary layer interference. This requires reliable nonlinear calculation methods including viscous effects. Wind tunnel simulation must be able to simulate the viscous effects of high flight-Reynolds numbers.

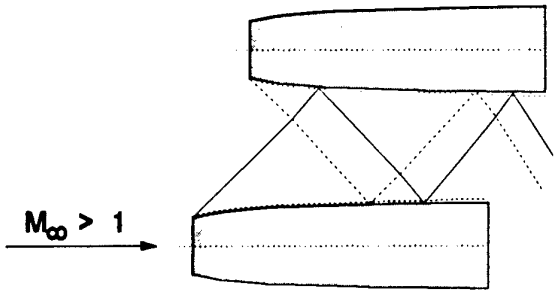


Figure 7: Shock reflection on neighbouring engines

Inlet flow:
Jet engines work at pure subsonic speeds. The inlet of an SCT, therefore, has to decelerate the incoming air from supersonic speed to subsonic velocities. This requires passing a shock system. To minimize shock losses, the air passes through several shocks (possibly including some isentropic compression). Adequate mathematical models for the generation of shocks, control of shocks, shock position and shock reflection, including important viscous effects, are strongly nonlinear. To enable stable flow conditions and engine operation, the inlet flow must be balanced with the nozzle flow; Concorde's aerodynamically coupled nozzle and inlet control is still state of the art, figure 8. Highly sophisticated numerical and wind tunnel simulations are required and must be combined with the control system and engine operation.

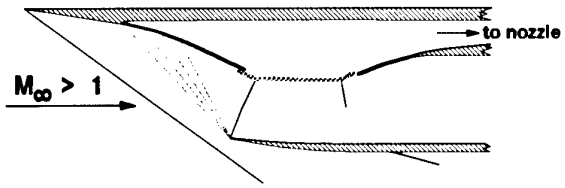


Figure 8: Inlet flow: Concorde principle

Hinge line shocks:

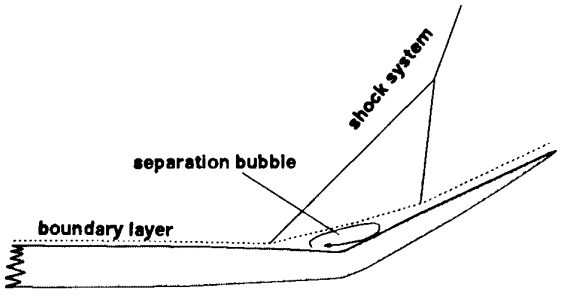


Figure 9: Shock-boundary layer interference

At control surfaces, shocks at the hinge line can provoke boundary layer separation bubbles strongly degrading flap efficiency and introducing vibrating airloads, figure 9.

2.4 Supersonic cruise design

Supersonic cruise is the longest cruise leg on those routes which are of interest for supersonic transport. So supersonic cruise performance largely determines range, weight and cost of an SCT. Supersonic cruise performance strongly relies on aerodynamic drag reduction. Drag related weights (i.e. fuel and engines) contribute about 60% to the SCT's MTOW (maximum take-off weight).

Here, we concentrate on drag reduction. Although, it has to be remembered, that drag minimization for itself is no goal for an aircraft: aerodynamic performance is L/D which is **L**ift divided by **D**rag or weight divided by drag; but, when looking for performance, more weight requires accordingly increased fuel consumption, see e.g. Breguet's formula (eqs. (11) to (14) in the lecture "Required Technologies for Supersonic Transport Aircraft"). A careful balance must be achieved when drag reduction requires a weight increase.

To estimate the influence of individual contributions to supersonic cruise drag, we look at the composition of (supersonic) drag. Contributors are friction drag, volume wave drag, lift dependent wave drag and induced drag. This is for the drag coefficient C_D

$$\mathbf{C_D} = \mathbf{A/S \cdot C_f} + \mathbf{K_V \cdot 128 V^2/(\pi S l_o^4)} + \mathbf{K_L \cdot \beta^2 S C_L^2 / (2\pi l^2)} + \mathbf{K_I \cdot S\, C_L^2 / (\pi b^2)} \qquad (4)$$

or in physical units for the drag force D

$$\mathbf{D} = \mathbf{A C_f q} + \mathbf{K_V \cdot 128 V^2/(\pi l_o^4) \cdot q} + \mathbf{K_L \cdot \beta^2 W^2/(2\pi q l^2)} + \mathbf{K_I \cdot W^2/(\pi q b^2)} \qquad (5)$$

with

A	total surface	
b	span	
C_D	drag coefficient	
C_f	friction coefficient	
C_L	lift coefficient	
D	drag	
K_I	shape parameter for induced drag (inverse Osswald factor)	
K_L	shape parameter for lift dependent wave drag	(6)
K_V	shape parameter for volume wave drag	
l	lifting length	
l_o	total (aircraft) length	
M	Mach number	
q	dynamic pressure	
S	wing (reference) area	
V	volume (aircraft + engine stream tube variation)	
W	weight	

and

$$\beta^2 = M^2 - 1 \qquad (7)$$

In the formulas (4) and (5) some parts are bold faced. These are the contributors which can significantly be influenced by design.

Skin friction drag:
The first term describes friction drag which is mainly determined by the aircraft's total surface A and the friction coefficient C_f. For minimisation both must be minimized.

Total aircraft surface A depends on the specified payload and the required fuel volume, aerodynamic lift, the slenderness and span requirements of other drag part minimisation, and (weakly) the aircraft's mechanical strength and stiffness. The total surface minimization is no goal for its own, it is rather only one aspect of drag minimisation to be balanced with other requirements.

Friction coefficient C_f here is the mean value of the local friction coefficients, weighted by surface area. It is mainly determined by the Reynolds-number. But it may be reduced by friction drag reduction techniques; those which are most well known are laminarisation and riblets.

Laminarisation maintains the low drag of laminar flow in the boundary layer, which reduces local C_f-values for an SCT by about 90%, but requires a huge technology effort [11]. Presently, we design our SCTs without laminar flow, although laminar flow promises strong improvements. But an SCT which will become viable *only* with application of laminar flow, may loose its competitiveness against subsonic aircraft as soon as the subsonic aircraft will utilize laminar flow. Most likely, subsonic aircraft will apply laminar flow earlier than SCTs. On the other hand, an SCT concept which is viable without laminar flow, may be improved by laminar flow just like the competing subsonic arcraft.

Riblets are streamwise microscopic valleys in the aircraft's surface which reduce aircraft turbulent drag locally by about 8% [12].

Other measures to reduce skin friction may arise in the future. Special (still exotic) surface coatings [13] such as some nano materials (thickness of only a few molecules) have been proposed which shall alter the wall condition ("no slip") for the boundary layer flow, e.g. by not completely diffuse reflection of the air molecules at the wall.

Volume wave drag:
The second term describes volume wave drag which is mainly determined by the aircraft's volume V and strongly by slenderness V/l_o^2, because l_o is squared and the whole term $(V/l_o^2)^2$ is squared once more.

Total aircraft volume V is, like surface A, given with the specified payload and the required fuel volume, the aircraft's mechanical strength and stiffness and the slenderness and span requirements. Due to the important volume wave drag contribution, volume of supersonic aircraft must be minimized, see Concorde's narrow and uncomfortable fuselage.

Larger total aircraft length l_o decreases volume wave drag, but decreases structure strength as well so that it increases aircraft weight and reduces stiffness. Both have to be kept in acceptable boundaries. Especially for large SCTs, i.e. long fuselages, fuselage flexibility poses big problems.
After Concorde's first landing at the old airport in Singapore, the pilots -although carefully fixed with seat belts in the tiny cockpit- hit the overhead panels with their heads due to strong bending oscillations of the slender fuselage on the rough runway. This was, for a long time, the last Concorde landing at Singapore.
Today airports request a maximum fuselage length of about 80 m, although most large SCT-designs (250 or more passengers) have fuselages of more than 90 m which is at the flexibility and weight limits.

The shape parameter K_V depends on the volume distribution of the whole aircraft including cross sectional variations of the engine stream tubes. At M=1 this is simply based on the distribution of the area normal to the flow direction (because Mach angle μ is 90°). At higher Mach numbers it becomes more complicated:
From each point of the aircraft's surface a perturbation wave is radiated downstream along a conoid which opens with Mach angle μ around the stream line, the Mach conoid (fig. 2). Therefore all areas along Mach conoids from and towards each surface point have to be respected. In practical applications for slender configurations, the following double integral approximation is used to compute the disturbances of the area distribution of an equivalent body of revolution:

On the most important perturbation line (e.g. the fuselage center line), the contributions of one Mach cone (of the undisturbed flow) are collected by integrating the projections of the cross sectional areas which are cut by a sufficient number of tangent planes to the Mach cone, so-called Mach planes (about 24 or more); the Mach planes osculate around the generating Mach cone; the projections are on a plane normal to the undisturbed flow. Along the perturbation line (center line) the contributions of several generating Mach cones (about 30 or more) are summed up [14], figure 10.

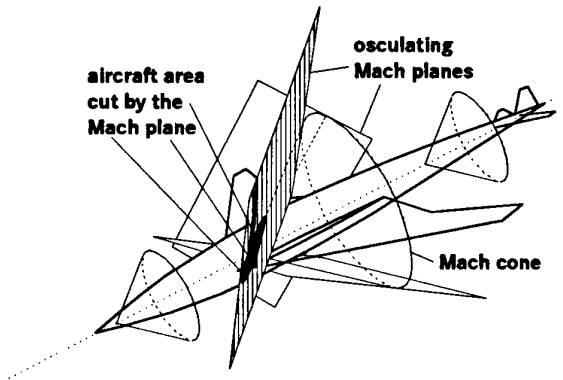


Figure 10: Wave drag calculation using Mach planes

As long as the aircraft is slender, it does not strongly alter the speed of the incoming flow; therefore the simple area approximation using the Mach planes of the incoming flow is valid. And aircraft which produce strong perturbations, will never be efficient. For simple bodies of revolution, the minimum drag area distribution is given by the Sears-Haack area distribution [15, 16].

Lift dependent wave drag:
The third term describes the lift dependent wave drag. It depends on speed (β^2 or β^2/q), aircraft weight W and aircraft *lifting* length l.

Lift dependend wave drag rises quadratically with weight W^2

or C_L^2, like the induced drag in the last term (therefore, for SCT typical C_L-values are 0.1 to 0.15, depending on the configuration selected). But in contrast to the induced drag which lowers with speed (q), the lift dependent wave drag increases with speed ($\beta^2/q \sim 1\text{-}1/M^2$).

Lift dependend wave drag lowers quadratically with lifting length l^2 requesting a slender wing with high sweep and small span.

The shape parameter K_L is minimized by a smooth lift distribution along lifting length l. Computation is demonstrated in [17, 18, 19]. Lowest values are achieved for a distribution given by the product of an ellipse and a parabola, e.g. an elliptical wing (OFW) with parabolic chordwise loading.

Induced drag:
The last term describes the well known induced drag. The drag coefficient C_D, which is referenced to wing area S, rises with lift coefficient squared C_L^2 and decreases with aspect ratio b^2/S; but the drag force D rises with weight squared W^2 and decreases with dynamic pressure q (speed squared) times span squared b^2.

Therefore: minimum induced drag requires a high span (b^2).

The shape factor K_I is the inverse of the well known Osswald factor, which becomes 1 for elliptical lift distribution over the span, see e.g. [8]. Elliptical lift distribution is achieved by plane wings of elliptical planform distribution and nearly by plane delta wings (as long as there is no leading edge separation). Best performance is reached with subsonic leading and trailing edges, i.e. edges within the Mach cone. Suction force is required for minimum induced drag, but for supersonic edges, in general it is lost. Pure supersonic wings (supersonic leading and trailing edges) have the maximum lift dependent drag of

$$C_D = C_L \tan\alpha, \qquad \alpha\text{: angle of attack} \qquad (8)$$

For other (wing) planforms, elliptical lift distribution can be approximated for one angle of attack by suited twist and camber distributions. Deviations of this design α produce additional induced drag according to the (wing) planform.

2.5 Summary:

To minimize supersonic drag we have to minimize certain flow parameters which requires optimisation of some configuration geometry parameters:

- minimize **friction drag** by optimizing **surface geometry and quality** (laminarisation),
- minimize **volume wave drag** by optimizing **slenderness** and **volume**,
- minimize **lift dependent wave drag** by optimizing **wing slenderness**,
- minimize **induced drag** by optimizing **span** resp. **aspect ratio**.

Wave drag minimisation requires slender configurations and slender wings, i.e. low b/l, whereas induced drag requests for high span b. Task is, to find the best combination of b and l, represented by the size of the rectangle

$$b \cdot l \qquad \text{or} \qquad b \cdot l_o \qquad (9)$$

given by span b and lifting length l or overall length l_o, figure 11.

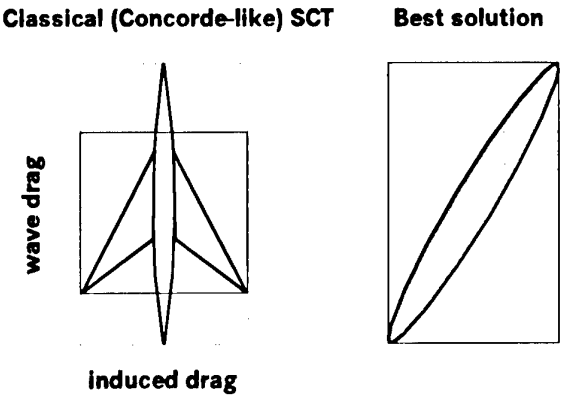


Figure 11: Wave drag and induced drag

The classical Concorde-like configuration only provides relatively low span for acceptable slenderness with (at least partially) subsonic leading edges. Because the leading edge is swept in different directions, it provides only half of the maximum possible lifting length l for a given span b and sweep angle. In contrast, the oblique flying wing (OFW) provides the maximum rectangle size $b \cdot l = b \cdot l_o$ because the wing uses the whole diagonal. Indeed, the elliptical OFW is the best solution reaching the theoretical drag minimum which was demonstrated by R.T. Jones [9].

For well balanced aircraft designs with turbulent boundary layer flows, the today achievable supersonic L/Ds for symmetric configurations are well below 10, for OFW a bit higher. Aircraft with better L/Ds can be designed, but at the expense of excessive weight. Application of laminar flow could improve supersonic L/D by about 1.

3. TRANSONIC CRUISE

3.1 Main properties of physics of transonic flow

If the flow field contains parts with subsonic flow and other parts with supersonic flow, the problem is called *transonic*. Properties in the flow field strongly change:

- In the subsonic parts, the flow field balances all flow properties in the field and is described by elliptic balance equations.
- In the supersonic parts, the flow field cannot balance properties, because flow speed is higher than information speed; it is described by hyperbolic radiation equations.

The supersonic parts usually are terminated by a strong shock. Whereas supersonic oblique shocks usually are kinematically fixed to the geometry, the strong normal shocks in transonic flow evolve in the flow field and are controlled by flow forces. Therefore they are prone to oscillations.

3.2 Mathematics of transonic flow

Mathematical models describing gas dynamics of those different flow types are strongly nonlinear, the equations are of mixed elliptic-hyperbolic type, even for the inviscid parts. Computational analysis usually follows transient formulations to avoid type changes within the flow. These enable quasi elliptic, hyperbolic and parabolic solution procedures. Some special mathematical models may be used for design purposes to calculate flows with desirable aerodynamic properties [20].

3.3 High subsonic cruise flight

The supersonic aircraft is firstly optimized for supersonic cruise performance. To achieve good transonic (i.e. high subsonic) cruise performance, preferably the configuration should adapt to the different requirements. The OFW performs this by adaption of sweep. A symmetric configuration (like Concorde) can use flaps:

- leading edge flaps, to avoid leading edge separation; this is especially important for sharp (supersonic) leading edges
- trailing edge flaps to control lift distribution for minimization of induced drag and load control during manoeuvers; this is supported by a pitch control surface like a horizontal tail.

3.4 Transonic cruise flight design

Because an SCT generates an annoying sonic boom as long as it flies faster than the speed of sound, supersonic operation will be limited to uninhabited areas, i.e. mainly over sea. Over populated areas SCTs have to cruise at subsonic speeds. But many important airports like Chicago, Atlanta, Denver, Frankfurt etc. are far away from sea and many routes contain an important part of flight over populated land. Therefore routings over uninhabited areas are preferred, even at slightly increasing distances; but large subsonic cruise legs remain, figure 12. It is estimated, that an SCT must be able to cruise subsonically during one fourth to one third of the whole distance.



Figure 12: Supersonic detour routing

Therefore a new SCT must provide good transonic (i.e. high subsonic) cruise performance, in contrast to Concorde's poor subsonic performance. In addition to engines which provide good subsonic efficiency, aerodynamic design is required to provide this performance.

At high subsonic (transonic) cruise, good performance is achieved without significant contribution of wave drag, i.e. just below drag rise. So, in the drag composition of eqs. (4) and (5) the two wave drag terms can be omitted:

$$C_D = A/S \cdot C_f + K_I \cdot S\, C_L^2 / (p\, b^2) \qquad (10)$$

or for the drag force

$$D = A\, C_f\, q + K_I \cdot W^2 / (p\, q\, b^2) \qquad (11)$$

Here mainly the sum of friction and induced drag has to be minimized and to be balanced with the other design requirements.

The terms for friction and induced drag are described in chapter 2 after eqs. (4) and (5). Because here the flight is subsonic, supersonic leading edges do not exist. But optimum angle of attack is higher than at supersonic cruise. Therefore flow at relatively sharp or even really wedge-sharp leading edges may separate, producing high vortex drag which has to be avoided by suited leading edge flap deflections.

State of the art symmetrical supersonic aircraft designs reach high subsonic cruise L/Ds of more than 15.

3.5 Summary

To minimize high subsonic drag, we have to minimize drag components by optimizing geometry components:

- minimize **friction drag** by optimizing **surface geometry and quality** (laminarisation),
- minimize **induced drag** by optimizing **span resp. aspect ratio**, and **avoid separation**.

Therefore subsonic airliners have highly loaded high aspect ratio wings, figure 13. This requirement contrasts to the supersonic cruise requirements. Here length l or l_o is only required to delay the drag rise Mach number, and for flight stability and control. The best solution would be a variable geometry, which was proposed by Boeing for the first US-SST. But the excessive weight for the large moving parts prevented such a solution. In contrast, the **O**blique **F**lying **W**ing (OFW) [9] provides variable geometry without large moving parts; therefore it can be the better solution.

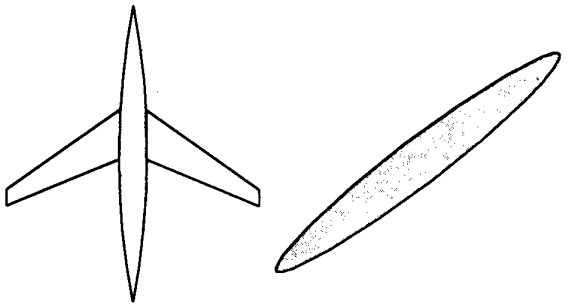


Figure 13: Transonic cruise aircraft

4. TRANSONIC ACCELERATION

4.1 Low supersonic acceleration flight

During transonic (i.e. low supersonic) acceleration, wave

drag is dominant. Here it strongly depends on interference of the different parts of the aircraft: fuselage, wing, nacelles with engine stream tubes, tail. Near Mach 1 even small changes in Mach number produce strong changes in Mach angle (i.e. radiation direction); strong shocks prevail with considerable shock-boundary layer interaction. As a cosequence, accurate drag prediction of the transonic interference phenomena requires nonlinear methods including the simulation of viscous effects.

4.2 Transonic control

Around flight Mach number 1 strong normal shocks are generated. These are very sensitive to small changes of the flow field and tend to oscillations.

Control flaps have to produce aerodynamic forces by pressure differences between the flap's and adjacent wing area's sides. Usually they generate a pressure rise on one side and a pressure drop on the other. Near Mach 1 the pressure rise at the hinge line provokes a strong shock with strong boundary layer interference including large separation zones. This easily results in vibrating loads (buffet) and weakens the flap's control forces. During transonic acceleration, therefore, the aircraft should not require strong control forces. Suited control flaps have swept hinge lines, hinge lines in less critical regions (for instance close to the trailing edge of the wing, because the shock has just moved to the trailing edge), or moving tails.

Engine efficiency is critical at low supersonic speeds. Especially the inlets have to cope with rapidly varying conditions due to sensitive Mach angle variations. The shock system, designed for supersonic cruise, cannot yet establish; an inlet control mechanism, designed only for supersonic cruise shocks, does not work. Measures are required, therefore, to allow for sufficient inlet efficiency, like special inlet doors.

4.3 Design for low supersonic flight

A supersonic jet is to cruise at supersonic speeds. But to reach supersonic speeds, it has to accelerate from take-off to the supersonic cruise speed. In between there is a speed regime with maximum wave drag and minimum engine performance which may determine engine size. This critical speed is the transonic acceleration point at low supersonic speed (about Mach 1.1).

Because wave drag is at its maximum, it dominates drag and (for rough estimations) the other parts may be omitted. So eqs. (4) or (5) become:

$$C_D = K_V \cdot 128V^2/(pSl_o^4) + K_L \cdot b^2 S C_L^2 / (2pl^2) \qquad (12)$$

or for the drag force

$$D = K_V \cdot 128V^2/(p\, l_o^4) \cdot q + K_L \cdot b^2 W^2/(2pql^2) \qquad (13)$$

where the first term for volume wave drag is dominant.

At Mach 2 the Mach-angle is 30°, at Mach 1.2 about 60° and at Mach 1 just 90°. This means, that at Mach 1 all



Figure 14: Drooped leading edge

disturbances produced by the aircraft are radiated in a plane normal to the flight path and so stay in the relative position to the plane, at least when neglecting the local Mach number variations. (But these local Mach number variations are the reason, that stationary or very slowly accelerated flight at Mach 1 is possible).

To minimize transonic wave drag, the configuration must be slender with a smooth variation of the total aircraft's cross sectional area distribution. These cross sections must include the variations of the engine's stream tubes. For the large Mach angles of about 90°, changes of cross sectional area must be balanced in a very short streamwise distance; but due to the nearly stationary propagation, the area distribution within each cross section is not so important. This leads to so called "Coke-bottle" fuselages which balance (strong) variations of wing, tailplane, engine areas by fuselage area changes.

To enable low wave drag at transonic *and* supersonic cruise speed, smooth area variations of all aircraft parts are recommended.

It is easy to design a perfect supersonic or hypersonic aircraft which will not be able to accelerate to supersonic speeds. This was demonstrated several times in the past! And Concorde needs its fuel guzzling afterburners to overcome this drag during a very slowly accelerated part of the flight. If Concorde does not succed in the first attempt to accelerate to supersonic speeds for a transatlantic flight, it has to return for refuelling! And this happens from time to time.

5. TAKE-OFF AND LANDING

5.1 Dominating flow phenomena

At take-off and landing, low speed of the aircraft generates only small dynamic pressures. Generation of aerodynamic forces, therefore, requires high specific aerodynamic loading, up to the separation limits.

Low speed lift generation:

To improve lift, span can be increased (variable geometry aircraft like the OFW), camber can be increased by flaps and wing area can be increased by Fowler flaps. Angle of attack can be increased (especially for highly swept wings) and engine air can be used directly for lift generation or for support of flap efficiency. Most SCT configurations have only limited possibilities to use flaps: the symmetric (Concorde-like) configurations have large wing areas, where flaps can contribute only marginally. For an arrow wing, inner wing flaps can be efficient, because they generate lift near to the center of gravity which reduces trim losses. For the OFW the pitching moments connected with camber or Fowler flaps limit their application.

Of special importance are leading edge flaps for symmetric

SCT configurations which do not generate lift, but reduce lift dependend drag. Concorde generates additional lift using the lifting vortices generated by leading edge separation on highly swept wings. Those vortices, on the other hand, produce high drag. For a new SCT it is intended, to use those vortices -if used at all- only at lift-off and perhaps flare. During climb, no vortices should separate at the leading edges to allow for lower climb drag. There are proposals to use droop flaps (fig. 14) or (proposed by Boeing) suction at the leading edge to delay leading edge vortex separation.

Separations:
At high aerodynamic loadings separation may occur. For landing, separation with separation drag is welcomed, but separation must always be controlled; it must not suddenly alter the flight handling. Leading edge separation must therefore be confined to highly swept leading edges, where the individual separation vortices are fit to the large lifting vortex. Trailing edge separation has to occur smoothly and at the selected parts, like for subsonic aircraft. Especially the OFW needs much drag for landing to inactivate its superior aerodynamic performance. Drag producing devices are then requested which introduce only minor pitching moments.

Controllability:
Due to the small dynamic pressure, control surfaces become less efficient. In addition, separation on control surfaces limits the achievable forces; separation on wing, fuselage and nacelles introduces additional disturbances.

Especially for highly swept trailing edges -like for arrow wings and OFW- the effectivity of control surfaces is not completely understood. Some additional research is needed here.

In order to exploit the wing's lift performance with droop leading edges and cambered or even fowlered trailing edges, it is necessary to balance the aircraft by an additional control surface like a horizontal tail or canard.

Performance:
At take-off, main emphasis is on good L/D to reduce thrust and noise. For landing, though, high drag is necessary to allow step descent and slow down, when the engines run at flight idle with still considerable thurst levels. On the other hand, enabling flare or allowing for go-around, drag must stay below some limits or must rapidly be reduced.

To allow for acceptable low drag levels at take-off and for go-around, actual designs apply low speed design angle of attack below about 12°. Then flight envelope includes angle of attack up to 18° to cover disturbance cases like gusts.

5.2 Mathematics
(Steady) subsonic flow problems are mainly of elliptic type in both the inviscid and viscous parts, which means that functions and all derivatives are continuous. Only the inviscid Euler equations allow for discontinuities normal to the path (stream) line. Methods are on the development level as available as for subsonic aircraft. Similar to subsonic aircraft technology, extremely complex flow separation is not yet really understood.

5.3 Design for take-off and landing
No aircraft can fly without take-off and landing. Therefore low-speed performance is crucial for the aircraft's viability. Low speed performance determines the required thrust during take-off and landing, and so strongly influences airport noise. For future SCT, meeting take-off noise is the most difficult requirement! And a viable SCT must be even quieter than what is required today by certification authorities (stage 3), since many airports do not accept noisy climbing aircraft which just comply to stage 3. They have to respect the concerns of the sourrounding communities and have to restrict noisy aircraft in order to maintain their airport certification.

In the US, airport certification is connected to a specified noise exposure area (maximum weighted and time integrated noise level in a specified area). If noise becomes higher, the whole airport noise certification process has to be repeated (environmental impact study) !
In Europe, many airports use their own noise rules, like noise related fees (most in Germany), sometimes related to the actual measured noise (Zurich), or noise related schedule restrictions (like London).

At low speeds, high lift or high angles of attack are required. Wave drag does not exist, friction drag is nearly constant, so induced drag (and separation drag) dominates. This leaves only the last term in eqs. (4) or (5).

$$C_D = K_I \cdot S\, C_L^2 / (p\, b^2) \qquad (14)$$

or for the drag force

$$D = K_I \cdot W^2 / (p\, q\, b^2) \qquad (15)$$

To minimize induced drag, we need a large span. This can be seen at high performance low speed planes like gliders, figure 15. Sweep does not help for drag, but special configurations (like the OFW) need it for stability and control. For SCTs, the variable geometry of the OFW helps for take-off drag minimization. But it also reduces drag at low landing speeds; therefore an OFW needs additional pitching moment free devices to produce drag for landing.

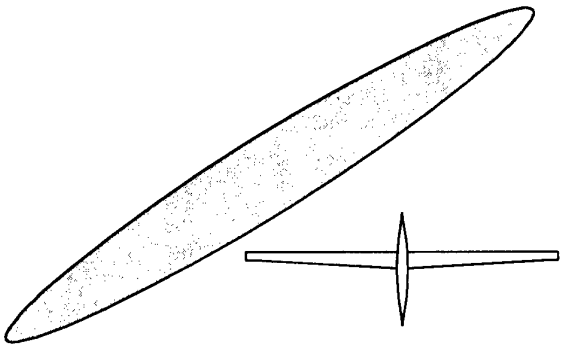


Figure 15: Low speed planes

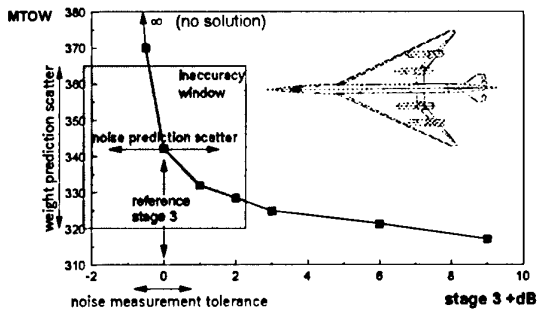


Figure 17: Challenge to meet stage 3

Additionally we must avoid separation:

- Separation limits pressure recovery. This adds pressure drag. On unswept wings, nose separation destroys lift and produces sudden, unstable flow conditions which provide unstable flight conditions. This must be avoided for safety reasons. Controlled trailing edge separation -e.g. on flaps- can be used to increase drag, e.g. for a steper glide path or

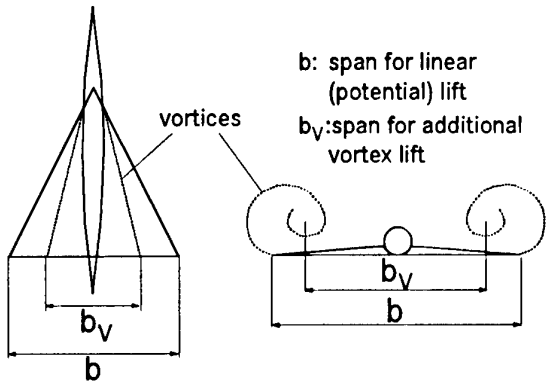


Figure 16: Vortex separation drag

deceleration during approach.

- On highly swept wings, leading edge separation is controlled and produces additional vortex lift which is used to increase Concorde's lift. But these lifting leading edge vortices are positioned above the wing at strongly reduced lifting span compared to the wing span itself. This reduced lifting span increases drastically the induced drag, figure 16. And Concorde needs its noisy afterburners to overcome this drag during take-off.

  A new SCT has to avoid leading edge separation during climb to enable low noise procedures.

Figure 17 shows a design exercise for a new "Concorde-like" SCT (250 passengers, 5 000 nm): Reference is a DA-design (DA: Daimler-Benz Aerospace Airbus) of an aircraft which is optimized just to meet stage 3. But because noise prediction is not very precise, the influence of aircraft noise on aircraft weight (MTOW) was investigated. Each square represents an optimized aircraft producing either more calculated noise than stage 3 (+ 0.5, to +9 dB) or less calculated noise (-0.5 dB). Weight strongly increases for lower noise, and just for -1 dB no solution was found (i.e. infinite MTOW). It has to be respected, that noise measurement at certification has a scatter of nearly 2 dB, calculated noise prediction about 3 dB and weight prediction has its scatter also. This means that our design was still very marginal !

6. CONSEQUENCES

Contradicting requirements are daily life for an engineer. But for a conventional SCT these four requirements really pose a design trap, mainly:

- high supersonic cruise performance requires
  a slender configuration with
  subsonic leading edges (i.e. limited span) or
  very thin wings with leading edge flaps or
  variable geometry
  low engine diameters,
- low take-off noise requires
  large span with
  round leading edges or leading edge flaps and
  large engine diameters.

At DA a screening of several promising configurations was performed, figure 18:

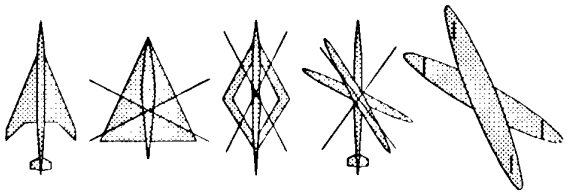


Figure 18: Search for a viable configuration

Remaining configurations were the conventional symmetric wing-body configuration at the left end, and the oblique flying wing (OFW) at the right end.

The blended wing-body lost for its poor slenderness. The optimizer simply concentrated the payload more and more at the center and spent more length for slenderness. So this configuration automatically transformed into the symmetrical wing-body.

The joined wing configuration has only limited span, does not provide enough fuel volume, does not provide space for an undercarriage and is structurally difficult, especially due to buckling.

The oblique wing-body combination is only interesting for rather small aircraft at low supersonic speeds [21, 22].

The extremely different aerodynamic requirements seem to prohibit a solution for the conventional symmetric wing-body, at least for large aircraft and long range. Only limit performance of all disciplines' technologies may reach the limit of viability. (Besides aerodynamics, severe problems are e.g. weight, flutter, engines, long flexible fuselage, undercarriage).
But this configuration has its merits for a smaller aircraft and shorter range, e.g. a 200 passenger transatlantic aircraft. Design becomes easier at lower design speed, mainly for the smaller sweep with larger span. This improves L/D at all

speeds and especially eases take off noise. Also engine and inlet design to cover all speed ranges becomes much more easier at lower cruise speeds.

The OFW is limited to large passenger aircraft, because profile height must be about 2.5 m or more. Therefore it is suited for SCTs with more than 250 passengers and subsonic aircraft with more than 400 passengers. The OFW provides variable geometry (aerodynamic span) without large moving parts, and best supersonic performance. It provides solutions to all the known problems of other configurations, like weight, noise, flutter, undercarriage, structural flexibility [18, 19]. In contrast it needs drag producing devices with controllable pitching moments to allow for a sufficiently steep descent and a short flare at touch down. Like with anything new there is still room for many new and perhaps surprising problems. Also, the interfaces between the individual disciplines are strongly different from conventional (subsonic) aircraft.

Both a conventional solution at design limits or an unconventional OFW-solution pose a strong challenge for aerodynamics and the other disciplines. The goal will only be met by new approaches using and further improving the techniques of Multidisciplinary Design Optimisation (MDO) [23, 18].

Because both solutions require many new, unapproved technologies, flying technology demonstrators are required in preparation of civil passenger traffic.

7. REFERENCES

1 J. Mertens
Aerodynamic Multipoint Design Challenge
"New Design Concepts for High Speed Air Transport", H. Sobieczky ed., CISM 366, Springer Wien NewYork, 1997, pp. 53-67

2 R. Courant, K.O. Friedrichs
Supersonic Flow and Shock Waves
Applied mathematical sciences, 21, Springer Verlag, New York, Berlin, Heidelberg, 1948/ 1976

3 R. Courant, D. Hilbert
Methoden der mathematischen Physik II
Springer, 1968

4 A. Jeffrey, T. Taniuti
Non-linear Wave Propagation with Applications to Physics and Magnetohydrodynamics
Academic Press, New York and London, 1964

5 J. Mertens
Instationäre Strömungen von Gasen mit brennbaren Partikeln, Kapitel A2
Dissertation RWTH Aachen, 1983

6 R. Sauer
Nichtstationäre Probleme der Gasdynamik
Springer, 1966

7 C. Heinz
Die Richtungs- und Verträglichkeitsbedingungen der Charakteristikentheorie
Institutsbericht, Lehrstuhl für Mechanik, RWTH Aachen, 1970

8 D. Küchemann
The aerodynamic design of aircraft
Pergamon Press, Oxford, 1978/ 1985

9 R.T. Jones
The Minimum Drag of Thin Wings at Supersonic Speed According to Kogan's Theory
Theoret. Comput. Fluid Dynamics (1989) 1: 97-103

10 M.N. Kogan
On Bodies of Minimum Drag in Supersonic Gas Flow
Prikl. Mat. Mekh., vol. XXI, no. 2, 1957, 207-212

11 J. Mertens
Laminar Flow for Supersonic Transports
"New Design Concepts for High Speed Air Transport", H. Sobieczky ed., CISM 366, Springer Wien NewYork, 1997, pp. 275-290

12 M. Bruse, D.W. Bechert, J.G.Th. van der Hoeven, W. Hage, G. Hoppe
Experiments with conventional and with novel adjustable drag-reducing surfaces
Near Wall Turbulent Flows, R.M.C. So, C.G. Speziale and B.E. Launder (Editors), Elsevier Science Publishers B.V., 1993

13 "New surface coating cuts drag", FLIGHT INTERNATIONAL 2-8 Nov. 1994, p. 24

14 H. Lomax
The Wave Drag of Arbitrary Configurations on Linearized Flow as Determined by Areas and Forces in Oblique Planes
Ames Aeronautical Laboratory, NACA RM A55A18, 1955

15 W. Haack
Geschoßformen kleinsten Wellenwiderstandes
Lilienthal-Gesellschaft, Bericht 139, 1947

16 W.R. Sears
On Projectiles of Minimum Drag
Quart. Appl. Math. 4., No. 4, 1957

17 A. Van der Velden
Aerodynamic Design and Synthesis of the Oblique Flying Wing Supersonic Transport
PhD-thesis Stanford University, Dept. Aero Astro SUDDAR 621, Univ. Microfilms no. DA9234183, June 1992

18 A. Van der Velden
The Oblique Flying Wing Transport
"New Design Concepts for High Speed Air Transport", H. Sobieczky ed., CISM 366, Springer Wien NewYork, 1997, pp. 291-315

19 A.R. Sebass
Oblique Flying Wing Studies

"New Design Concepts for High Speed Air Transport", H. Sobieczky ed., CISM 366, Springer Wien NewYork, 1997, pp. 317-336

20 H. Sobieczky
Gasdynamic Knowledge Base for High Speed Flow Modelling
"New Design Concepts for High Speed Air Transport", H. Sobieczky ed., CISM 366, Springer Wien NewYork, 1997, pp. 105-120

21 A. Van der Velden, D. von Reith
Multi-Disciplinary SCT Design at Deutsche Aerospace Airbus
Proceedings of the 7th European Aerospace Conference EAC'94 "The Supersonic Transport of Second Generation", Toulouse, 25-27 October 1994, paper 3.61

22 A. Van der Velden
Multi-Disciplinary Supersonic Transport Design
"New Design Concepts for High Speed Air Transport", H. Sobieczky ed., CISM 366, Springer Wien NewYork, 1997, pp. 251-273

23 G.S. Dulikravich
Multidisciplinary Inverse Design and Optimization (MIDO)
"New Design Concepts for High Speed Air Transport", H. Sobieczky ed., CISM 366, Springer Wien NewYork, 1997, pp. 223-236

VORTEX-PLUME INTERACTION RESEARCH

Pasquale M. Sforza
Graduate Engineering and Research Center
University of Florida, Shalimar, FL 32579

SUMMARY

The problem of the wake of an aircraft cruising at supersonic speed in the stratosphere is presented. The two major components of the flow field are the trailing vortex wake and the jet exhaust plumes. Accurate prediction of the dispersion of engine emissions resulting from interaction between the two has important consequences for determination of wake signatures. Research in the field is reviewed to provide an understanding of the present state of the art. Synthesis of these different jet and vortex studies provides a unified global description of aircraft wakes in terms of a length scale bA/C_L, based on the span, aspect ratio, and cruise lift coefficient. A model is developed in which the jet plumes, being immersed in the trailing vortex wake downwash, are assumed to deform into twin vortices typical of jets in a cross-flow. This permits the development of the wake flow field to be assessed with the relatively simple tools of vortex filament analysis. Wakes of both conventional high subsonic and supersonic aircraft may be accommodated by this approach, as would the wakes of wing-jet combination injectors for scramjet applications. Experimental studies that would aid in the development of more accurate prediction methods are also described.

1. INTRODUCTION

1.1 Background of the vortex wake problem

Wing tip vortices became a topic of rather widespread interest and scrutiny in the mid-1960s when it was recognized that they posed a hazard to following aircraft during low-speed terminal operations; see, for example, Jones (1970) and Sforza (1970). Airport safety considerations prompted substantial research efforts led by FAA and NASA through the mid-1970s. The fruits of that work are described in Hallock (1977) and Gessow (1977). During the same period the race to develop a supersonic transport (SST) was on, and uncertainty about the effect of its emissions on the stratosphere catalyzed research on supersonic aircraft vortex wakes. Because the prospects for a large SST fleet collapsed abruptly, study of vortex behavior in the supersonic end of the flight regime did not receive the sustained attention awarded the low-speed end and is characterized by a sparse database. Now, 20 years later, renewed interest in supersonic cruise vehicles, both commercial and military, has awakened a corresponding concern for fundamental insights regarding their vortex wakes. Three basic problems illuminate the practical need for such information:

(a) *entrainment* of engine plumes into wing vortices (or fuel jets into scramjet injector vortices). Engine emissions (or fuel species) trapped in the vortex wake are subjected to conditions different than those in the free stream thereby altering the subsequent chemistry. This also has implications for the characteristics of wake signatures.

(b) *confinement* of entrained material for long times after aircraft passage. This can increase residence times of possible pollutants.

(c) *interaction* of tip vortices with shock waves and flow fields over downstream surfaces. These can influence lift, drag, engine performance, and stability and control characteristics.

The present paper is concerned with the interpretation and application of the results of the few past and recent experiments to the first two problem areas of entrainment and confinement. The last problem, interaction, is dealt with in the associated companion paper, Sforza (1998).

1.2 Past studies of vortex wake entrainment

SST jet plumes stream through a wing wake flow field dominated by trailing vortices. Overcamp and Fay (1973) studied dispersion of SST exhaust products taking into account only global characteristics of trailing vortices and the stratospheric atmosphere. They considered the near wake to involve no appreciable interaction and the intermediate wake to be dominated by engulfment of the exhaust plume into the trailing vortex system. Conti, Hoshizaki, Redler, and Cassady (1973), Nielsen, Stahara, and Woolley (1974), and Holdeman (1974) all presented models for predicting behavior of jet exhaust plumes as they

Paper presented at the RTO AVT Course on "Fluid Dynamics Research on Supersonic Aircraft", held in Rhode-Saint-Genèse, Belgium, 25-29 May 1998, and published in RTO EN-4.

interact with the aircraft vortex wake. Farlow, *et al* (1974) presented flight measurements of overall wake dimensions and NO mixing ratios behind a supersonic NASA YF-12. Comparisons to results from the previously mentioned models demonstrated substantial differences between them.

Thereafter, for an extended period of almost 20 years, virtually no work along these lines appeared in the literature until Miake-Lye, Martinez-Sanchez, Brown, and Kolb (1991) presented a simplified *ad hoc* model to account for the capture of exhaust effluents by the trailing vortex system. They speculated on the existence of differences between supersonic and transonic aircraft wake systems which, they suggested, might lead to quite different dispersion characteristics. Quackenbush, Teske, and Bilanin (1993) incorporated a Reynolds-averaged turbulent flow model within a large-scale wake code to account for vortex entrainment of SST plumes. Dash and Kenzakowski (1994) presented Navier-Stokes (N-S) computations for the interaction of a subsonic jet and a low speed tip vortex in response to unpublished experiments carried out at NASA LaRC. Then, in a manner reminiscent of the events of the past, Fahey, *et al* (1995) presented measurements of reactive gases and particles in the wake of a Concorde cruising at supersonic speed in the stratosphere, but this time no comparisons to existing model predictions were given.

Most recently, Gerz and Ehret (1996), Jacquin and Garnier (1996), and Garnier, Jacquin, and Laverdant (1996) presented combined vortex filament and turbulent diffusion models for treating the interaction between the jet plumes and the trailing vortex field. Research into the far field of the trailing vortex system continued unabated, with Kandil, Adam, and Wong (1996) applying a compressible Reynolds-averaged Navier-Stokes (N-S) code; Quackenbush, Teske, and Bilanin (1996), and Teske, Quackenbush, and Bilanin (1997) further exploring the capabilities of their UNIWAKE code which is based on unsteady N-S equations with modeled turbulence; and Gerz and Ehret (1997) introducing a combination of vortex filament and large eddy simulation techniques to analyze the flow.

All of these studies were hampered by lack of a robust experimental database for validating the assumptions utilized, particularly with respect to initializing the plume mixing and reaction problem. As a consequence there is yet no unanimity regarding the mechanisms involved in the entrainment process.

The intense practical interest in the problem from an aircraft operations viewpoint has encouraged extensive efforts to compute the development of this extremely complex flow system. However, many, if not all, of the component mechanisms that interact in this problem are themselves imperfectly understood, as will be demonstrated in the subsequent sections.

2. THE VORTEX WAKE FLOW FIELD

2.1 Exploratory HSCT vortex wake experiments. Recent experimental studies of Mach 2.5 flow past a typical high speed commercial transport (HSCT) planform carried out by Wang, Sforza, and Pascali (1996) revealed a complex vortex wake system. The model geometry closely follows that of the NASA baseline 70°-45° cranked arrow wing configuration described by Fuhrmann (1993). Fig.1, a panoramic shadowgraph of the flow field for the case of 5° angle of attack, shows three distinct trailing vortices over the half-span of the model. There is a leading edge vortex from the inboard delta panel of the planform, a junction vortex from the crank in the leading edge, and a true tip vortex from the supersonic leading edge outboard panel.

Vapor screen visualization using a ruby laser as a light source was also employed to assess the evolution of the vortex wake. A schematic diagram illustrating the light sheet set-up is shown in Fig.2. The laser pulse duration was around 30ns and the light sheet thickness was about 2mm. Visualization experiments were performed at 1.2, 3.1, 4.8 and 8.8 tip chords downstream of the tip trailing edge using water droplets as the seed particles. Images from the CCD camera were captured by a frame grabber, stored in a file, and later digitally optimized to better reveal the three major structures in the vortex wake. Fig. 3 shows the typical frames of the enhanced light sheet photographed directly off the computer screen, in which the development of the flow field can be readily observed. The vortex cores appear as black spots because the light-scattering water droplets are unable to remain trapped in the swirling flow. This underscores the confinement capability of the inner region of a vortex for lighter species and particulates. On the other hand, the progressively brighter bands in the photographs

suggest enhancement of the population of scatterers. This appears to attest to the entrainment capability of the outer region of a vortex.

The wake of the HSCT model was also surveyed by means of a rake carrying 14 pitot pressure tubes as shown in Fig.4. The pitot probes are constructed of hypodermic tubes 25mm long and 0.61mm in internal diameter, and are spaced 6.35mm apart on centers. The rake was traversed vertically in increments of 1.27 to 2.54mm depending on location within the wake. Measurements were taken at downstream locations x/c_t=1.3, 7.8, and 16.3, where c_t is the tip chord, and the resulting pitot pressure contours are shown in Fig. 5. The three vortex structures are clearly evident as regions of pitot pressure deficit and the tip vortex is seen to migrate inboard as the downstream distance increases. The central vortex structure, which appears to emanate from the juncture of the inboard and outboard panels of the cranked wing, was found to be rotating in a sense opposite to that of the other two, stronger, vortices. There does seem to be relative motion between the three vortices in the transverse plane due to their mutual interaction suggesting a rather complex flow system in the near field.

The decay characteristics of the three predominant vortex structures as determined from the pitot pressure surveys are shown in Fig.6. Pitot pressure in the vortex is consistently lower than the free stream value and may be used a measure of its strength. Note that the vertical axis in Fig.6 has been inverted to emphasize that recovery of pitot pressure implies decay of vortex strength. The tip vortex is seen to have suffered little decay over the downstream distance surveyed while the leading edge vortex is declining more rapidly. Interestingly, the junction vortex is initially very strong, according to this measure, decays rapidly at first, and then matches the decay rate of the leading edge vortex.

A rake of 7 common sewing needles with 6.35mm spacing was positioned so as to lie in the plane of the three trailing vortices. Shadowgraphs reveal the disturbances generated by the sharp slender needles as Mach cones from which the Mach number distribution may be inferred. When the rake was placed so that the needle tips were immediately downstream of the wing, the waves generated in the juncture vortex (feature 6 in Fig.1) showed larger wave angles than those outside that region. But when the rake was moved back to x/C_t=2, all wave angles were found to be equal to within $\pm 1^\circ$, the resolution achievable with this technique. This uncertainty bounds the Mach number in the core to the range 3 to 3.3, a deviation of –3% to +6% of the free stream value. Therefore, within the resolution afforded by the photographs, the vortex wake appears to be convected downstream at the free stream Mach number very shortly after its generation. This implies that the Mach number components in the radial and tangential directions are much smaller than the axial component, a result in keeping with linearized supersonic flow theory. Then, assuming the stagnation temperature to be constant, that axial velocity in the vortex is the free stream value so that the Trefftz plane is reached within a short distance downstream. Although the expectation of constant stagnation temperature is reasonable for experiments in a blow-down wind tunnel, such is not the case for extended periods of supersonic cruise during which substantial heat transfer occurs.

2.2 Results from unswept wing experiments.

The same result of no measurable defect or excess in axial Mach number in the tip vortex of an unswept wing with aspect ratio A=3.12 at M=3.1 was reported by Wang and Sforza (1997). With the stagnation temperature and the axial Mach number being constant, the static temperature, and therefore the axial component of velocity, must also be constant, all being equal to their free stream values. Low speed experiments have shown axial velocity profiles that range all the way from jet-like to wake-like. To assess their result of approximately constant axial velocity they present an argument for compressible flow that is based on Batchelor's (1964) development for incompressible flow. They show that circulation promotes jet-like behavior while stagnation enthalpy loss promotes wake-like behavior, as found in incompressible flow. For the conditions of the experiment they calculate a jet-like behavior, but of sufficiently small magnitude that it lies within the bounds of uncertainty of the measurements.

When the wing is thin, as in the experiments of Davis (1952) and Adamson and Boatright (1957), or at least locally thin in the tip region due to chamfering, as in the experiments of Wang and Sforza (1997), no evidence of appreciable axial Mach Number excess or deficit is found. However, for thicker wings with flat, squared-off tips, Smart, Kalkhoran, and Bentson (1995) find a pronounced

axial Mach number deficit in the near field. Cross-flow separation around a thick, squared-off tip, according to Wang and Sforza, produces stagnation enthalpy losses sufficient to generate an axial Mach number deficit in the vortex. Rizetta's (1996) three-dimensional numerical analysis of the experiment performed by Smart, Kalkhoran, and Bentson appears to support this contention. A calculation of the flow field in the tip region is shown in Fig. 7 while results of the analysis for inviscid, laminar, and turbulent cases are compared to experiment in Fig. 8. Though the experimental results are under-predicted it is evident that the Mach number deficits in the vortex rise from negligible to moderate to substantial as the frictional losses increase.

Wang and Sforza (1997) explored the notion that chamfering the tip of a wing is tantamount to reducing the section thickness, as far as axial flow in the vortex is concerned. Typical pitot pressure contours measured at 2.3 chords behind the trailing edge for 5 and 10 degrees angle of attack are shown in Fig. 9. Using normalized values of the minimum pitot pressure in the vortex as a metric, they compared the few experimental data available in the literature. The results for small (~5°) and moderate (10°) angles of attack are shown in Fig. 10. The results for squared-off wing tips follow a simple power law curve for both angle of attack ranges while the chamfered tip results fall off those curves. For both angles of attack, the minimum pitot pressure for the chamfered tips of the 10.4% thick wing corresponds to an 8.2% thick wing with squared-off tips. Thus it appears that chamfering the wing tip may result in reduced losses due to cross-flow separation. However, as the vortex convects further downstream and circulation effects continue to compete with dissipation effects, a different axial flow profile in the vortex may ultimately develop. The relationship between axial flow deficits and the drag contribution represented by tip vortices is a subject of controversy.

Since the axial component of the Mach number and the static temperature are both essentially constant, the normalized pitot pressure profiles, shown in Fig. 11, may also be interpreted as profiles of stagnation pressure, static pressure, and density, all normalized by their respective free stream values. Although the vortex properties have been estimated under the linearized theory assumption that the radial and tangential components of velocity are much smaller than the axial component, it is still possible to recover swirl information. The radial component of Euler's equation reduces to $V^2=(r/\rho)(dp/dr)$ which can be calculated numerically from the profiles of pressure and density given in Fig. 11. The resulting swirl profiles are clearly similar to those found in low-speed vortices, being adequately described by Burger's vortex profile, as shown in Fig.12. The values of maximum swirl angles, defined as $\arctan(V/U)= 7.8\pm1.8$ and 12.4 ± 1.8 degrees for angles of attack of 5 and 10 degrees, respectively. These values are smaller than those typically reported for incompressible flows, which is in keeping with the physical intuition that it is difficult to turn a supersonic flow.

2.3 The near field: vortex roll-up

The nature of trailing vortex systems for slender, pointed supersonic planforms was set forth by Spreiter and Sacks (1951) in a comprehensive synthesis of NACA's extensive high speed research. They point out that for low aspect ratio wings small disturbance theory is valid in the vicinity of the wing and the inviscid wake at all Mach numbers and this fact permits them to describe, in some detail, the development of the vortex wake. During this period of high-speed research, attention was focused on predicting the downwash field encountered by the trailing control surfaces of aircraft or missiles rather than on details of the vortex system producing it.

A basic feature of the flow field behind the wing is the formation of concentrated trailing vortices from the distributed vorticity field generated by the wing, the so-called vortex roll-up process. On the basis of similarity arguments Spreiter and Sacks show that the downstream distance required to complete vortex roll-up is given by

$$x_r = kbA/C_L \qquad (1)$$

where A is the aspect ratio, b is the span, C_L is the lift coefficient, and k is a constant for any given wing and depends only on the planform shape and the span loading distribution. Kaden's (1931) analytic solution for the roll-up of a semi-infinite vortex sheet was used to determine k. For elliptical loading the constant k lies between 0.28 for rectangular wings and 0.14 for delta wings. For lift distributions more heavily loaded at outboard stations the values of k will decrease, and *vice versa*. This formulation appears to indicate that the number of span lengths necessary to fully roll up the vortices is larger for a conventional, high A, jet

transport than for a typical, low A, HSCT. However, the parameter $A/C_L = q/(W/b^2)$, where W is aircraft weight and q is the dynamic pressure, tends to be fairly constant for aircraft with similar missions. For large subsonic or supersonic, transport or bomber aircraft in cruise, A/C_L lies between 15 and 20. Thus in most cases one may expect the roll-up distance behind an elliptically loaded swept wing, according to Eq.1, to be around 2 or 3 spans for either subsonic or supersonic speeds.

Bilanin and Donaldson (1975) presented an alternate development for the roll-up distance based on the procedure of Betz (1932). They show that Kaden's result is limited to small times (or, equivalently, distances downstream) while theirs exhibits asymptotic behavior, but still with $x_r \sim A/C_L$. The difference between the two is that the constant k would be approximately an order of magnitude larger than that determined by Spreiter and Sacks. Rule and Bliss (1998) have incorporated a viscous core analysis to correct the shortcomings introduced by the vortex core singularity in Betz's inviscid approach. It is interesting to note that the quantity $(\pi^2 A/C_L)^{-1}$ naturally arises in their analysis as the only parameter. As this small parameter approaches zero their solution approaches the inviscid Betz limit. There apparently has been no systematic validation of any estimate for roll-up distance and its determination still appears to be an open question. Rossow (1997) evaluated extended Betz methods and concluded that for complex lift-generated vortex sheets they only provide notional information and more reliable methods, e.g. numerical analysis must be applied.

In addition, laboratory models are seldom twisted and therefore are more heavily loaded near the tip resulting in the shortest roll-up distances. The low speed experiments of Jacob, Savas, and Liepmann (1997) show the measured vorticity to be contained within a tightly rolled-up vortex pair only 5 chords downstream of the trailing edge of a rectangular wing with A/C_L= 11.4. For this untwisted rectangular wing the results of Spreiter and Sacks yield k=0.066 and therefore a roll-up distance of x_r/b=0.75 or x_r/c= 6. The method of Bilanin and Donaldson for this case would instead suggest x_r/c=60. Similarly, Ramaprian and Zheng (1997) show vorticity contours which include indicate that virtually all the measurable vorticity is concentrated prior to x_r/c=3. Calculations for the conditions of the experiment according to Eq. 1 yield x_r/c=2.3, in agreement with the observations.

The importance of rapid roll-up lies in the utility afforded by dealing with concentrated vortices in analytic or computational studies of the aircraft wake. Now, however, CFD codes often include determination, by one means or another, of the evolution of the vortex sheet leaving the wing. The difficulty is that there is no evidence of experimental validation of any of these approaches. Recent experiments by Miranda and Devenport (1998) provide detailed measurements of flow properties in the wake of a half-wing at low speed. Probing of the entire wake at a location 10 chords downstream revealed drastic thinning of the wake as it was wrapping up in a spiral around the vortex core. Since the CFD codes are applied to the interaction of the vortex wake with jet engine plumes in order to predict the ultimate fate of emissions it would seem vital to validate the vortex wake initialization process.

In the supersonic speed range there is much less data available on vortex wakes. Indeed, the experimental measurements of Wang, Sforza, and Pascali (1996) indicate that the vortex wake appears to be fully rolled up within one span of the trailing edge of the tip chord of the Mach 2.5 HSCT planform tested. The results of this section are suggestive in that the use of a modified span $b'=bA/C_L$ as a characteristic length makes the normalized roll-up distance x_r/b' a constant for all geometrically similar wings, a fact which may be exploited in subsequent analyses.

2.4 The far field: vortex instability

Well behind a cruising aircraft the flow field is dominated by two parallel trailing vortices. These far field vortices are subject to the sinusoidal instability, first described by Crow (1970), that leads to alteration of the organized pair into a number of elongated rings. The time scale for the onset of this instability corresponds to a downstream distance

$$x_c = 7.4\, bA/C_L \qquad (2)$$

or, in terms of the modified span introduced in the previous section, $x_c/b' = 7.4$. This illustrates that the distance to onset of the Crow instability is the same number of spans for any practical transport aircraft designed for efficient cruise. It must be kept in mind that the elapsed time to the Crow

instability is $t_c = x_c/U$, where U is the constant cruise velocity. Therefore, for two different large transport aircraft flying in the stratosphere where the sonic speed is approximately constant, the ratio of the onset times for the Crow instability to appear is $t_{c1}/t_{c2} = (b_1/b_2)(M_2/M_1)$, where M is the cruise Mach number. If aircraft 1 is a typical HSCT and aircraft 2 is a typical subsonic airliner the ratio of onset times is on the order of 10^{-1}.

2.5 The intermediate field: vortex decay

The intermediate region behind a cruising aircraft is also dominated by the two parallel trailing vortices that should decay through the effects of viscous dissipation, according to Jacob, Savas, and Liepmann (1997). They report that no accurate method for predicting this decay outside the laboratory exists although varying degrees of success have been achieved with empirical relations. Iverson (1976) presents a compilation of subsonic laboratory and flight test data for moderate to high aspect ratio wings along with a correlation for the decay of the observed maximum tangential speed. His correlation equation, given by

$$V_m\,[x/U\Gamma]^{0.5} = 5.8 \qquad (3)$$

is applicable provided that the vortex Reynolds number, $\Gamma/\nu > 10^6$, where V_m is the maximum tangential speed, Γ is the total circulation of the vortex, and ν is the kinematic viscosity. For elliptically loaded wings $\Gamma = 2C_L Ub/\pi A$ so that at distances sufficiently far downstream

$$V_m/U = 4.63(C_L/A)(x/b')^{-0.5} \qquad (4)$$

Prior to this decay region, at smaller values of x/b', a plateau level of essentially constant maximum tangential velocity has generally been observed. If dissipative effects are considered negligible, then the maximum tangential velocity may be approximated by $V_m = \Gamma/2\pi r_c U$, where r_c is the core radius, i.e. the radius at which the tangential velocity is a maximum. This can be written as $V_m/U = (b/\pi^2 r_c)/(A/C_L)$. The results of the low speed experiments of Devenport, *et al* (1996) and McAlister and Takahashi (1991) are well-represented by the correlation

$$V_m/U = 4.9/(A/C_L) \qquad (5)$$

at these lower values of x/b'. This result would imply that $r_c/b = 0.02$, which is smaller than typically reported.

It must be noted that most laboratory experiments are conducted under higher loading conditions than are typically found in cruise, i.e., at lower values of A/C_L and that Eq. 4 has not been validated for the supersonic range. Wang and Sforza (1997), indicate that the experimental database for vortices generated in supersonic flow is sparse, but they also point out that the few measurements available show the vortex swirl behavior to be much like that found at low speeds. However, the swirl angles are smaller than their incompressible counterparts. Indeed, the limited data available suggests a correlation given by

$$V_m/U = 0.75/(A/C_L)^{0.5} \qquad (6)$$

This result, which doesn't match the form of Eq.5, yields normalized swirls about 50% to 75% of that estimate, which is based on available low speed data.

The relations in Eqs.4, 5, and 6 are plotted in Figure 13 for practical flight values of A/C_L of 15 to 20, along with the location of the roll-up and Crow instability boundaries described previously. This diagram portrays the parameter space for practical subsonic and supersonic transport aircraft designs.

It is clear that more experimental studies of the details of the flow behind supersonic lifting wings are necessary. In the near field, the application of modern diagnostic techniques in wind tunnel simulations can be quite fruitful. This is evident in several recent low speed studies, e.g. Ramaprian and Zheng (1997), Chow, Zilliac, and Bradshaw (1997), and Rule and Bliss (1998). However, in the intermediate field, wall interference effects can make wind tunnel studies impractical. In particular, wave reflections crossing jet plumes and vortices can affect their downstream behavior. And, because of the fixed length of tunnel test sections, investigations in the far field are unattainable.

In low speed simulations of aircraft vortex wakes the problem of studying the far field has been circumvented by the use of towed models in long water tanks, historically a domain of naval architecture, as demonstrated most recently by Jacob, Savas, and Liepmann (1997). For supersonic speeds it is suggested that ballistic range techniques, coupled with optical diagnostics, would

provide much useful data since observations of wake temporal development could be made at a fixed laboratory location. Work of this nature has been carried out on both ballistic and powered projectiles, as described, for example, by Kuo and Fleming (1991). A low speed version of this approach, using a large (1/22 scale), catapult-launched transport aircraft model has been presented by Coton (1996). The difficulties with the ballistic range approach for supersonic speeds center on the need to launch a small, non-axisymmetric trimmed lifting model at high speed.

It is worth pointing out that no detailed laboratory experiments on trailing vortex flows have been carried out with powered models, i.e. on flows with zero net momentum. Wang, Sforza, and Pascali (1995) presented some exploratory flow visualization results at M=2.5 for an HSCT model with scaled jets designed to produce a thrust level equal to the drag. These preliminary experiments were carried out in the very near field and showed no obvious evidence of vortex-plume interaction. The test program was terminated prior to obtaining quantitative measurements in the wake.

3. THE JET PLUME FLOW FIELD

3.1 The supersonic jet in a supersonic stream

Wilder and Hindersinn (1953) presented one of the earliest investigations on supersonic jets (Mj) in co-flowing supersonic streams (M), where M_j>M, as part of a project aimed at improving methods for the design of propulsion wind tunnels. Their tests, carried out with two-dimensional nozzles, led them to conclude, among other things, that the spread of the jet in such cases is slight, as opposed to that for subsonic jets. A simple correlation for the jet angle (in degrees) was given as $\theta=0.2M_j/M$, where M_j and M are the jet exit Mach number. In addition, they found that jet temperature did not appear to have a substantial effect on the jet mixing process.

A comprehensive study of the structure of sonic and supersonic axisymmetric jets exhausting into stationary and moving environments was first presented by Love, Grigsby, Lee, and Woodling (1959). One of the motivations for this research was to evaluate the interference flow field caused by propulsive jets on flight vehicles. Like the contemporaneous work on inviscid supersonic vortex wakes described previously in section 2.1, concern was focused on near field interference effects on trailing control surfaces caused by the exhaust plumes from wing-mounted jets. The theoretical effort involved method of characteristics solutions for such flows and emphasized the prediction of flow boundaries and shock waves, while the experiments concentrated on schlieren photographs illustrating these same features.

Though the turbulent mixing characteristics of low speed jets were then, and still are, the subject of multitudinous investigations, the corresponding features of supersonic jets were not intensely studied until the mid-60s when interest in fuel injectors for scramjets started to grow. Schetz and Swanson (1973) noted that even with this incentive, experiments were still limited to rather low Mach numbers, so they carried out studies at around M=3.5. Since scramjet-related experiments, which are now popular again, have M_j<M and the jet is typically inclined at a substantial angle to the free stream, it is difficult to apply any results to the problem at hand. Dash and Kenzakowski (1996) present a modern review of jet flow field modeling which illustrates the dearth of data available in the open literature on supersonic-supersonic jet mixing and a corresponding lack of validated analyses. There are studies, like that presented by Reijasse, Corbel, B., and Delery, J. (1997) which address the this problem but emphasize the effects of the (usually substantial) wake of the vehicle afterbody structure on the downstream turbulent mixing process. Rodriguez, Desse, and Pruvost (1997) present interferometric results for a supersonic jet (M_j=1.8) in a supersonic stream (M=1.5). They show that the flow out of the jet stabilizes very rapidly and remains essentially constant over the region visualized, a distance of more than 10 jet diameters.

It is reasonable to assume that experiments, commissioned in support of missile plume technology, have provided data pertinent to this problem area, but that such results are presently restricted in circulation. Obviously, there exists a need for fundamental studies of supersonic jet mixing. Wind tunnel test rigs suitable for such a task are relatively easy and inexpensive to design, install, and operate. The challenges for such sorely needed investigations are found in the diagnostic techniques to be applied and the ability to perform measurements at large distances from the jet exit. It should be possible to design a test section for sufficient wave cancellation at the tunnel walls to permit probing the jet flow at greater distances

downstream Once again it seems appropriate to point out the possibilities inherent in ballistic range techniques for addressing these obstacles.

3.2 The supersonic jet in a weak downwash field

The basic premise of the present paper is that the jet plume, with velocity Uj oriented parallel to the line of flight, is exposed to the velocity field of the wing wake. This field is assumed to be composed of three velocity components: the aircraft speed along the line of flight U, the downwash w, and the sidewash v, the last of which is ignored here. Thus, in the slender body inviscid approximation, the jet plumes feel a small cross-flow velocity $w<<U$ normal to the jet velocity U_j. In other words, the jet is inclined at a small angle to the free stream. Margason's (1993) review, as well as the other papers collected in an AGARD conference devoted to jets in cross-flow, make no mention of small inclination cases.

Wilder and Hindersinn (1953) carried out schlieren studies for two-dimensional supersonic jets at initial inclination angles of 10° and 15° to a supersonic stream. They found that the jets smoothly turned back into the direction of the main flow, reducing the angular deviation to less than half its original value within 8 nozzle widths without suffering any noticeable change in spread rate. Ehlers and Strand (1958) presented a small perturbation analysis for determining the deflection of the jet centerline for such flows. A decade later Goldburg, Murman, Shreeve, and Wygnanski (1968) extended that method to attempt to account for the bending of the jet. Unpublished experiments performed in support of that research showed that the cross-section of the slightly inclined jets deformed into a kidney shape in the same manner observed for jets at large inclinations in both incompressible and compressible cross-flows.

All the experimental evidence for supersonic jets in supersonic streams shows that the jet changes very little in the downstream direction. As a simple analogy, consider the plume to be replaced by a slender cylinder at angle of attack $\alpha = -\arctan(w/U) \simeq -w/U$. According to Nielsen (1960) such a situation generates a pair of lee-side vortices of circulation $\Gamma \simeq \pi d U \alpha$, or $\Gamma \simeq \pi w d$, where d is the diameter of the cylinder. This corresponds to a pair of vortices below the cylinder rotating as to produce a local upwash between them.

The jet plume is actually inclined at a small angle to a free stream so it may be considered as a jet in a weak normal cross-flow. It is generally accepted that such a jet bends in the downstream direction, simultaneously deforming into a kidney-shaped cross-section, and ultimately developing into a pair of counter-rotating vortices. The trailing vortex pair produces an upwash along the trajectory of the transformed bending jet. This basic flow problem has stirred much controversy regarding the nature of the mechanism responsible for the observed behavior even though *ad hoc* approaches have often provided quite useful correlations, according to Coelho and Hunt (1989). In addition, the various analytic and semi-empirical approaches mentioned previously do not always give consistent results for the circulation to be expected in the vortices.

Assuming the jet deforms into a pair of counter-rotating vortices separated by a distance equal to the jet diameter d_j, thereby producing an upwash equal to w normal to the line joining the vortex centers, the jet vortex circulation becomes $\Gamma_j = \pi w d_j$. This is the same value observed for slender bodies at incidence, as described previously. Since the vortex system of the wing has been shown to roll up rapidly we can represent the centerline downwash velocity as $w=(4/\pi)^2(C_L/\pi A)U$ for a simple wing vortex wake system with only two trailing vortices. This downwash is fairly constant over most of the spanwise distance $|y|<b/2$, as shown by Spreiter and Sacks (1951). Using this simple approximation for w in the equation for Γ_j leads to a ratio of jet to tip vortex circulation

$$\Gamma_j/\Gamma = 8d_j/\pi b \qquad (7)$$

The downwash for more complex trailing vortex systems and more accurate values for the jet circulation may be accommodated readily in this model.

Fearn and Weston's (1974) low-speed experiments on a jet issuing normal to a free stream showed that the strength of the vortices produced was directly proportional to the ratio of jet velocity to free stream velocity and decreased slowly with distance downstream. This conclusion has been supported and generalized by subsequent investigators to show that the circulation is proportional to the square root of the jet to free stream momentum flux ratio. Here that quantity is $\phi = (\rho_j/\rho)^{1/2}u_j/w$ since the downwash w is the free stream velocity component impinging on the jet. Broadwell and Breidenthal

(1984) form a characteristic jet length, denoted by x_j, which, in the present notation, is given by

$$x_j/b' = 1.72(\rho_j/\rho)^{1/2}\,(d_j/b)(u_j/U)$$

where $(\rho_j/\rho)^{1/2}d_j$ is the scaled value of jet exit diameter typically appearing in studies of hot jets. They carry out a similarity analysis for the case of normal injection at low speed showing that the distance separating the jet vortices increases at the same rate as the vortex strength decays such that the product of the two remains constant. Applying their approach to the present case leads to a ratio of jet vortex strength to wing vortex strength given by

$$\Gamma_j/\Gamma \sim (A/C_L)(x_j/b')^{2/3}(x/b')^{-1/3} \qquad (8)$$

The constant of proportionality must be determined from experimental comparisons. However, this result suggests that for small downstream distances, $x<b'$, the jet vortex strength is constant and the ratio $G_j/G \sim (d_j/b)^{2/3}$, which is close to the result of the simple *ad hoc* analysis presented previously. This dependence on d_j/b leads to the speculation that the strength of a vortex is proportional to the length of the vortex sheet that rolls up.

Jacquin and Garnier (1996) present a table of typical parameters for a conventional large jet transport and for the Concorde; using these yields $\Gamma_j/\Gamma = 0.026$ and 0.18 (from Eq. 7), $\phi = 36.3$ and 43, and $x_j/b' = 0.0214$ and 0.15, respectively. This suggests that while the circulation ratio developed in the Concorde is much greater than that of the conventional large jet transport, it is still a rather small quantity. Furthermore, the momentum function ϕ is quite large, but approximately the same for both aircraft, indicating that the jet vortex circulation in the simple model mainly depends on the jet diameter to span ratio, d_j/b. Finally, the normalized jet characteristic length is on the order of the normalized roll-up distance so that both the wing and jet vortices should be rolled up within the same distance for a given aircraft.

It should be clear now that the study of supersonic jets at small angles to a supersonic free stream is another area ripe for experimental and analytic study. The facilities used for co-flowing supersonic jets discussed in the preceding section are also appropriate for studies of this type. The author and his colleagues have initiated investigations of such flows. A low speed case presented by Proot, Wang, Sforza, and Charbonnier (1998) examines the interaction between a jet mounted below the centerline of a delta wing at angle of attack and the surrounding wake flow, including the leading edge vortices.

This completes the proposed inviscid model for jet plumes immersed in the vortex wake of an aircraft. The relatively slow variation of jet properties thus far observed in experiments suggests that a turbulent boundary layer analysis could be superimposed on this model to treat the turbulent diffusion process, but that is not addressed here.

4. THE COMBINED WAKE MODEL

4.1 A model for plume-vortex interaction fields

The two major components of a cruising aircraft's flow field are the trailing vortex wake and the jet exhaust plumes, representing the steady state lift and thrust of the aircraft, respectively. For practical lift to drag ratios on the order of 10, the trailing vortex wake represents a significant perturbation to the jet plumes. An idealized model of this flow field suggested by Sforza (1997) involves placing the propulsive jet plumes in the cross-flow of a number of nearby parallel vortices, everything being located symmetrically about the centerline. In this model the momentum deficit wake due to the profile drag of the aircraft is considered of secondary importance. This is based primarily upon the fact that wake momentum deficits are not spatially concentrated like vortices and momentum-excess plumes but instead are distributed over the entire cross-sectional area of the aircraft. As a result, profile drag momentum deficits tend to decay rapidly, diffusing over increasingly larger transverse areas.

This model further assumes that the jet plumes, being immersed in the downwash produced by the, perhaps complex, trailing vortex wake system, each deform into twin counter-rotating vortices typical of jets in a cross-flow. This model of the complete aircraft wake flow field is comprised solely of vortex filaments thereby providing a simple and consistent means for analyzing the developing interaction of complex arrays of vortices and jet plumes. It is expected that if such a model proves valuable at the inviscid level localized diffusion effects of boundary layer type may be superimposed.

Application of this approach to the interaction between a jet plume and a delta wing vortex wake at low speed and comparison to flow visualizations has been presented by Wang, Proot, Sforza, and Charbonnier (1998).

4.2 Wake Model Calculations

A typical HSCT planform rapidly produces a complicated vortex wake while its propulsive jet plumes, immersed in the downwash field, also generates a vortex wake. The basic structure is an inviscid airplane wake model as shown schematically in Fig. 14. It is comprised entirely of trailing vortices that may be considered to interact according to the laws of vortex filaments. The resulting flow field depends solely on the vortex strengths and initial positions of those vortices in the transverse plane at the initial station. Such an approach provides a simple and efficient means for rapidly and economically evaluating the likely wake configuration for different design configurations.

The flow field generated by this model may be illustrated by calculation of a simple generic configuration. Consider an elliptically loaded wing of span b=25.5m with 2 single jet exhausts of diameter d_j=1.75m. The jets are mounted tangent to and under the wing, centered at |y/b|= 0.216 and z/b=0.069 (where x points to the nose and z points down). After roll-up the tip vortices are assumed to be located at $|y/b|= b_v/b=(\pi/4)$ and z=0 while the jet plume vortices are assumed to be situated on either side of the horizontal diameter of the jet exit. Normalizing distance with b and circulation with the tip vortex circulation Γ leads to 6 vortex filaments and 2 normalized circulation strengths.

Assuming that the initial roll-up location several spans downstream of the wing is sufficient to permit a two-dimensional vortex filament analysis with time steps $\tau=\pi b/4U$, the development of the flow field under mutual interaction is readily computed. For circulation ratios Γ_j/Γ on the order of 0.1 or less the effect of jet circulation is minimal and the jet vortices move along under the influence of the tip vortices as if passive particles, as shown in Figure 15a, where the ratio is taken as 0.1. This behavior occurs because the self-induced field of the jet vortex pairs serves mainly to move them up, against the downwash of the wing. Their effect on other regions of the flow is small because the counter-rotation provides substantial cancellation. The trajectory shown represents a distance of 20 vortex spans, or 15.7 wingspans.

Connecting corresponding data points of the two jet vortices provides a measure of the distance between the vortices. Note that as distance downstream increases this separation increases dramatically, suggesting substantial additional transverse strain rate on the jet mixing field, an effect which will certainly affect diffusion. Jacob (1998) presented flow visualization studies of the merger of two co-rotating trailing vortices. He observed that as the vortices revolve about one another, one vortex is distorted due to the velocity gradient upon it and is pulled into its companion vortex. Thus one vortex is essentially destroyed in the process of forming a single larger vortex with strength equal to the sum of the two original vortices. The final, post-merger, vortex is found to be stable and completion of the merger occurs in less than one orbit.

Though the present model suggests a value for the jet-to-wing circulation ratio on the order of 0.1, as used in the calculation, larger values may possibly be encountered in practice. As Γ_j/Γ increases from 0.1 the jet vortices finally begin to influence the motion of the tip vortices, as can be seen in Figure 15b, which is the same problem carried out for a circulation ratio of 0.5. Here the tip vortex moves outboard and the jet vortices are drastically separated. Such behavior has not been observed yet for aircraft so the model estimate for circulation ratio is probably sound. On the other hand, if trajectories of this sort could be produced they might have application for scramjet injectors. Of course, the number and placement of the jet exhausts also have an effect on motion in the wake, and the present model is quite appropriate for such parametric studies.

5. CONCLUSIONS

A review of the interaction between the vortex wake of a lifting wing and the jet plumes propelling it has been presented. The background of the problem has been described and the relevant past studies reviewed.

Introduction of the modified wing span $b'=bA/C_L$ as a characteristic length unified the parameter space for the vortex wakes of subsonic and supersonic cruise aircraft. The boundaries of vortex roll-up through vortex decay to onset of Crow instability all are found to be scaled by b' and the similarities between the vortex wakes of subsonic and

supersonic cruise transports are described. Experiments show maximum swirl to free stream velocity to be proportional to $(A/C_L)^n$ where n = -1 and –0.5 for subsonic and supersonic experiments, respectively.

Jet plumes are characterized as slightly inclined supersonic jets in a supersonic stream and therefore are assumed to produce trailing twin counter-rotating vortices. The strength of the trailing vortex system of such jet plumes is shown to be a function of dj/b, the ratio of jet exit diameter to wing span.

The interaction between the wing vortex wake and the jet plumes is then modeled as one occurring between a number of trailing vortex filaments of different strength. Calculations for a simple generic aircraft configuration showed that with circulation strengths expected in aircraft applications, the jet plume vortices merely move with the flow induced by the tip vortices. However, jet plume vortex circulation on the order of that of the tip vortex substantially affects the motion of the tip vortices. The ability to produce such circulation levels in other applications, such as scramjet injectors, may have practical significance.

6. ACKNOWLEDGEMENTS

The author wishes to thank Dr. Frank Wang for his helpful discussions during the preparation of this paper.

7. REFERENCES

Batchelor, G.K. (1964). Axial flow in trailing line vortices, *J. of Fluid Mechanics,* **20**, part 4, pp.645-658.

Betz, A. (1932). Behavior of vortex systems, *ZAMM,* **XII**.3.

Bilanin, A.J. and Donaldson C.duP. (1975). Estimation of velocities and roll-up in aircraft vortex wakes, *Jl. Of Aircraft,* **12**,7, pp. 578-585.

Broadwell, J.E. and Breidenthal, R.E. (1984). Structure and mixing of a transverse jet in incompressible flow, *Jl. of Fluid Mechanics*, **148**, pp. 405-412.

Chow,J.S., Zilliac, G.C., and Bradshaw, P. (1997). Mean and turbulence measurements in the near field of a wingtip vortex, *AIAA Jl.,* **35**, 10, pp. 1561-1567.

Coelho, S.L.V. and Hunt, J.C.R. (1989). The dynamics of the near field of strong jets in crossflows, *Jl. of Fluid Mechanics*, **200**, pp. 95-120.

Coton, P. (1996). Caracterisation et modelisation du sillage d'un avion a partir d'essais en vol de maquettes en laboratoire, in *The Characterisation and Modification of Wakes from Lifting Vehicles in Fluid,* AGARD CP-584, pp. 29-1 to 29-12.

Crow, S.C. (1970). Stability theory for a pair of trailing vortices, *AIAA Jl.*, **8**, 12, pp. 2172-2179.

Dash, S.M. and Kenzakowski, D.C. (1995). Turbulent aspects of plume aerodynamic interactions, AIAA Paper 95-2373, AIAA/ASME/SAE/ASEE 31st Joint Propulsion Conference and Exhibit.

Dash, S.M. and Kenzakowski, D.C. (1996). Future directions in turbulence modeling for jet flow field simulation, AIAA Paper 96-1775, 2nd AIAA/CEAS Aeroacoustics Conference.

Devenport,, W.J., Rife, M.C., Liapis, S.I., and Follin, G.J. (1996). The structure and development of a wing-tip vortex, *J. Fluid Mech.,* **312**, pp. 67-106.

Ehlers,F.E. and Strand, T. (1958). The flow of a supersonic jet in a supersonic stream at an angle of attack, *J. Aerospace, Sci., 25,* 8, pp. 497-506.

Fahey, D.W. *et al*, (1995). Emission measurements of the Concorde supersonic aircraft in the lower stratosphere, *Science,* **270**, 6 Oct., pp. 70-73.

Farlow, N.H., Watson, V.R., Lowenstein, M., Chan, K.L., Hoshizaki, H., Conti, R.J., and Meyer, J.W. (1974). Measurements of supersonic jet aircraft wakes in the stratosphere, Proceedings of the 2nd International Conference on the Environmental Impact of Aerospace Operations in the High Atmosphere, American Meteorological Society, Boston, MA, pp.53-58.

Fearn, R. and Weston, R.P. (1974). Vorticity associated with a jet in a cross flow, *AIAA Jl.,* **12**, 12, pp. 1666-1671.

Garnier, F., Jacquin, L., and Laverdant, A. (1996). Engine entrainment in the near field of an aircraft, in Proceedings of the International Colloquium CAO on Impact of Aircraft Emissions upon the Atmosphere, Clamart, France.

Gessow, A. (1977). Wake vortex minimization, NASA SP-409.

Gerz, T. and Ehret, T. (1996). Wake dynamics and exhaust distribution behind cruising aircraft, in *The Characterisation and Modification of Wakes from Lifting Vehicles in Fluid,* AGARD CP-584, pp.35-1 to 37-12.

Gerz, T. and Ehret, T. (1997). Wingtip vortices and exhaust jets during the jet regime of aircraft wakes, *Aerospace Science and Technology,* no.7, pp. 463-474.

Goldburg, A., Murman, E.M., Shreeve, R.P., and Wygnanski,I.J. (1968). A predictive method for the bending and mixing of a supersonic turbulent jet at a small angle to a supersonic stream. Boeing Scientific Research Laboratories Report D1-82-0777.

Hallock, J.N. (1977). *Proceedings of the aircraft wake vortices conference,* Federal Aviation Administration Report No. FAA-RD-77-68.

Iverson, J.D. (1976). Correlation of turbulent trailing vortex decay data, *Jl. of Aircraft,* **13**, 5, pp.338-342.

Jacob, J.D. (1998). Experimental investigation of co-rotating trailing vortices, AIAA 98-0590, 36th Aerospace Sciences Meeting and Exhibit

Jacob, J., Savas, O., and Liepmann, D. (1997). Trailing vortex wake growth characteristics of a high aspect ratio rectangular airfoil, *AIAA Jl.*, **35**, 2, pp. 275-280.

Jacquin, L. and Garnier, F. (1996). On the dynamics of engine jets behind a transport aircraft, in *The Characterization and Modification of Wakes from Lifting Vehicles in Fluid,* AGARD CP-584, pp. 37-1 to 37-8.

Jones, D.N. (1970). Introduction to jet-engine exhaust and trailing vortex wakes, USAF Air Weather Service Technical Report 226.

Kaden, H. (1931). Aufwicklung einer un-stabilen unstetigkeitsflache, *Ingenieur-Archiv,* **II** pp.140-168.

Kandil, O.A., Adam, I., and Wong, T-C. (1996). Far-field turbulent vortex-wake/exhaust plume interaction for subsonic and HSCT airplanes, AIAA Paper 96-1962, 27th AIAA Fluid Dynamics Conference,

Kuo, K.K., and Fleming, J.N. (1991). *Base Bleed - First International Symposium on Special Topics in Chemical Propulsion*, Taylor and Francis, Bristol, PA.

Love, E.S., Grigsby, C.E., Lee, L.P., and Woodling, M.J. (1959). Experimental and theoretical studies of axisymmetric free jets, NASA Technical Report R-6.

Margason, R.J. (1993). Fifty years of jet in cross flow research, in AGARD Conference Proceedings 534.

McAlister, K.W. and Takahashi, R.K. (1991). NACA 0015 wing pressure and trailing vortex measuements, NASA TP-3151.

Miake-Lye, R., Martinez-Sanchez, M., Brown, R., and Kolb, C. (1991). Plume and wake dynamics, mixing and chemistry behind an HSCT aircraft, AIAA paper 91-3158, AIAA Aircraft Design Systems and Operations Meeting.

Miranda, J.A. and Devenport, W.J. (1998). Turbulence structure in the spiral wake shed by a lifting wing, *AIAA Jl.*,**36**, 4, pp.658-660

Nielsen, J.N. (1960). *Missile Aerodynamics*, McGraw-Hill, NY

Nielsen,J.N., Stahara, S.S., and Woolley, J.P. (1974). Ingestion and dispersion of engine exhaust products by trailing vortices for supersonic flight in the stratosphere, AIAA Paper 74-42, AIAA 12th Aerospace Sciences Meeting.

Overcamp, T.J. and Fay, J.A. (1973). Dispersion and subsidence of the exhaust of a supersonic transport in the stratosphere, *Jl. of Aircraft*, **10**, 12, pp. 720-728.

Proot,M.M.J., Wang, F.Y., Sforza, P.M., and Charbonnier, J-M. (1998). Near-field vortex-wake/plume interaction at low speed, ASME Paper FEDSM98-4991, Proc. Of the 1998 ASME Fluids Eng. Div. Summer Meeting,.

Proctor, F.H. (1998). The NASA-Langley wake vortex modeling effort in support of an operational aircraft spacing system, AIAA Paper 98-0589, AIAA 36th Aerospace Sciences Meeting and Exhibit.

Quackenbush, T.R., Teske, M.E., and Bilanin, A.J. (1993). Computation of wake exhaust mixing downstream of advanced transport aircraft, AIAA Paper 93-2944, AIAA 24th Fluid Dynamics Conference.

(1996). Dynamics of exhaust plume entrainment in aircraft vortex wakes, AIAA Paper 96-0747, AIAA 34th Aerospace Sciences Meeting.

Ramaprian, B.R. and Zheng, Y. (1997). Measurements in rollup region of the tip vortex from a rectangular wing, *AIAA Jl.,* **35**, 12, pp. 1837-1843.

Reijasse, P., Corbel, B., and Delery, J. (1997). Flow confluence past a jet-on axisymmetric afterbody, *Jl. of Spacecraft and Rockets, 34,* 5, pp. 593-601.

Rizetta, D.P. (1996). Numerical investigation of supersonic wing-tip vortices, *AIAA Jl.,* **34**, 6, pp.1023-1028.

Rodriguez,O., Desse, J.M., and Pruvost, J. (1997). Interaction between a supersonic hot jet and a coaxial supersonic flow, *Aero. Science and Technology, 6,*pp. 369-379.

Rossow, V. (1997). Extended Betz methods for roll-up of vortex sheets, *Jl. of Aircraft*, **34**, 5, pp. 592-599.

Rule, J.A. and Bliss, D.B. (1998). Prediction of viscous trailing vortex structure from basic loading parameters, *AIAA Jl., 36,*2, pp. 208-218.

Sforza, P.M. (1970). Aircraft vortices - benign or baleful ?, *Space/Aeronautics*, April , pp. 42-48.

Sforza, P.M. (1997). Interaction of wing vortices and plumes in supersonic flight, *Proc. of the IUTAM Symposium on Dynamics of Slender Vortices*, Kluwer Academic Publishers, Dordrecht, The Netherlands.

Sforza, P.M. (1998). Shock-vortex interaction research, *Fluid Dynamics Research on Supersonic Aircraft,* NATO Research & Technology Organization AVT/VKI Special Course.

Smart, M.K., Kalkhoran, I.M., and Bentson, J. (1995). Measurements of supersonic wing tip vortices, *AIAA Jl., 33*, 10, pp.1761-1768.

Spreiter, J.R. and Sacks, A.H. (1951). The rolling up of the trailing vortex sheet and its effect on the downwash behind wings, *Jl. Aero. Sciences*, **18**, 1, pp.21-32.

Teske, M.E., Quackenbush, T.R., and Bilanin, A.J. (1997). Long-time aircraft vortex wake predictions and plume evolution consequences, AIAA Paper 97-1843, AIAA 28th Fluid Dynamics Conference.

Wang, F.Y., Sforza, P.M., and Pascali, R. (1996). Vortex-wake characteristics of a supersonic transport wing planform at Mach 2.5, *AIAA Jl*, **34**, 8, pp.1750-52; also (1995). AIAA 95-2284, 26th AIAA Fluid Dynamics Conference.

Wang, F.Y. and Sforza, P.M. (1997). Near-field experiments on tip vortices at Mach 3.1, *AIAA Jl*, **35**, 4, pp.750-753.

Wang, F.Y., Proot, M., Charbonnier, J.-M. and Sforza, P.M. (1998). Interaction of a jet with leading edge vortices, 8th International Symposium on Flow Visualization.

Wilder, J.G. and Hindersinn, K. (1953). Spreading of supersonic jets, *Aero. Engineering Rev., 12*, 10, pp.54-68.

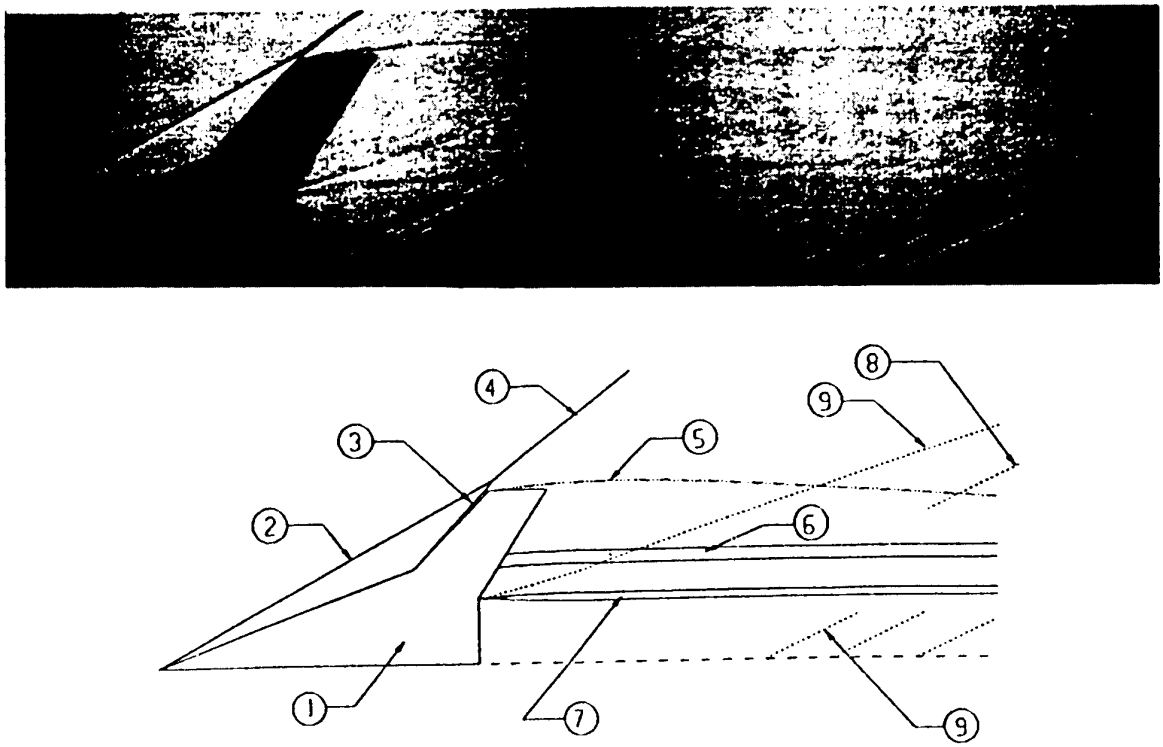


Figure 1. Shadowgraph of the vortex-wake flow.

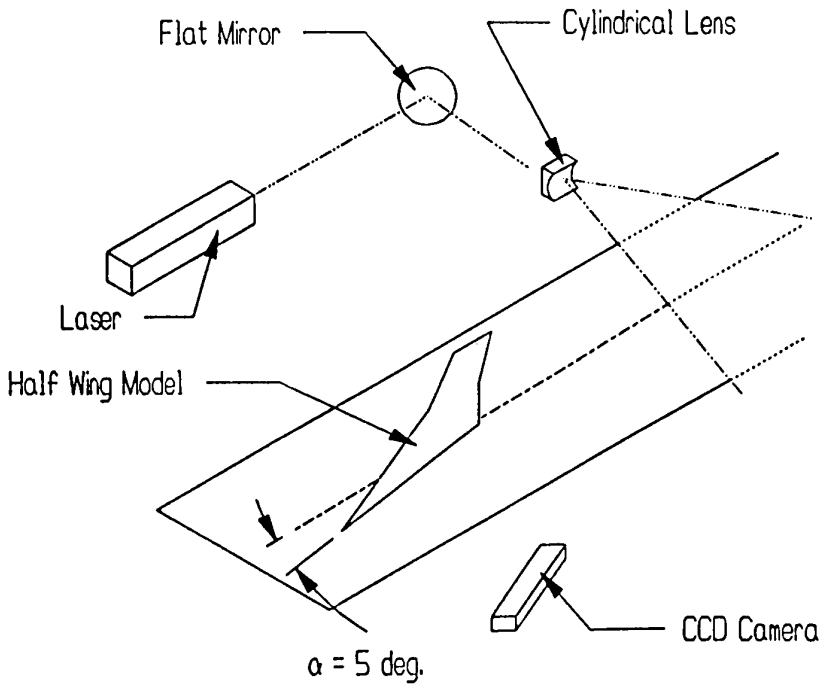


Figure 2. Schematic of the light sheet arrangement.

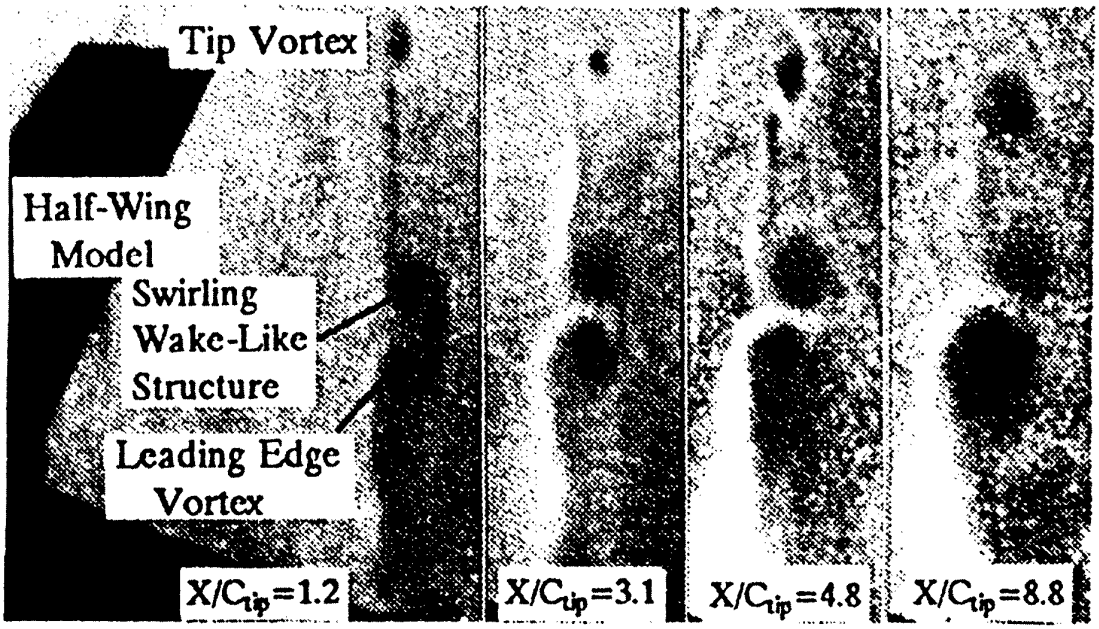


Figure 3. Vapor screen photographs.

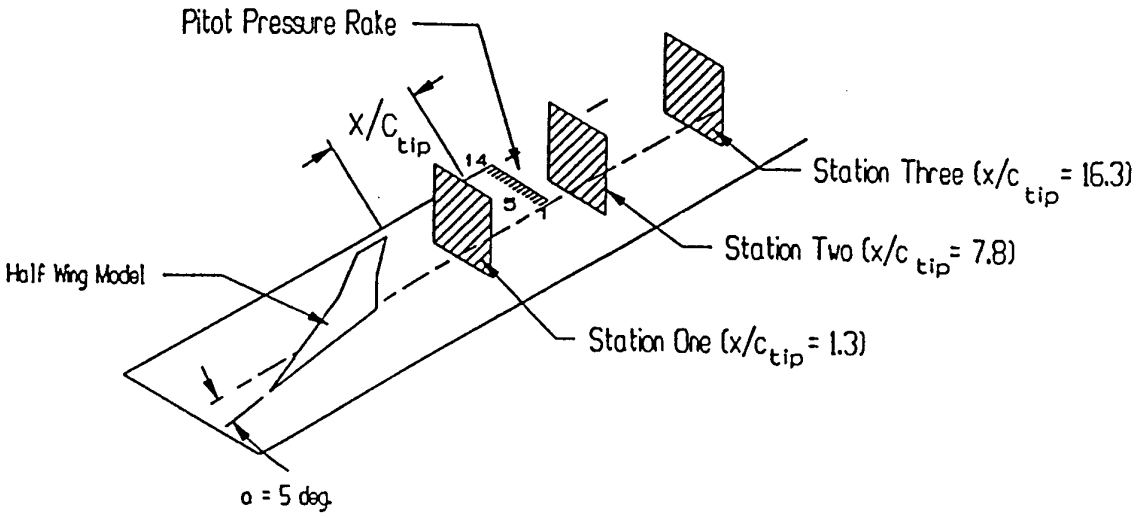


Figure 4. Schematic of pitot rake survey arrangement.

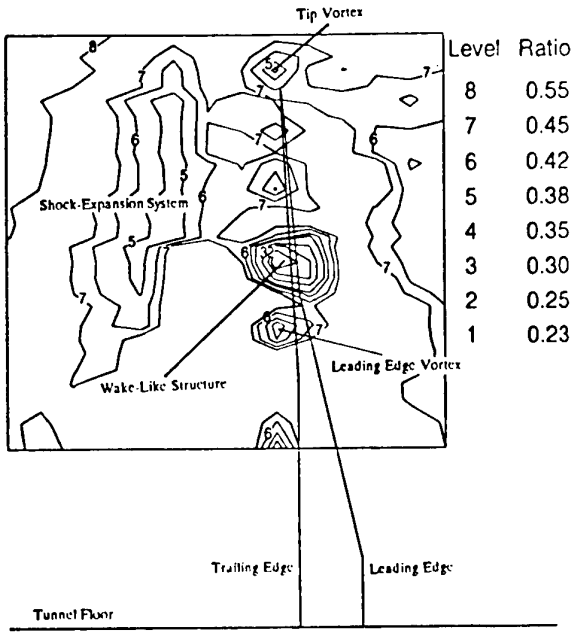


Figure 5a. $X/C_{tip} = 1.3$.

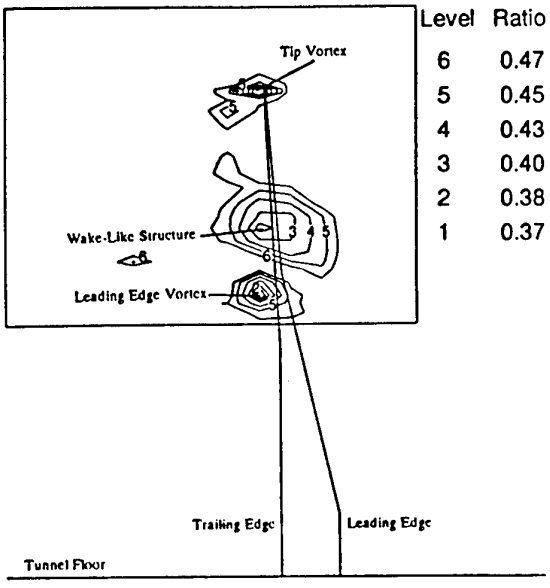


Figure 5b. $X/C_{tip} = 7.8$.

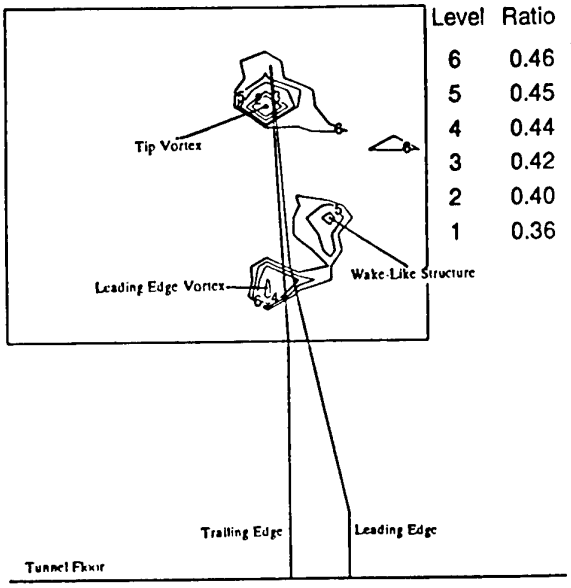


Figure 5c. $X/C_{tip} = 16.3$.

Figure 5. Pitot pressure contours shown to scale. Boxed region outlines survey limits and projection of half-wing on the measurement plane in superimposed for reference.

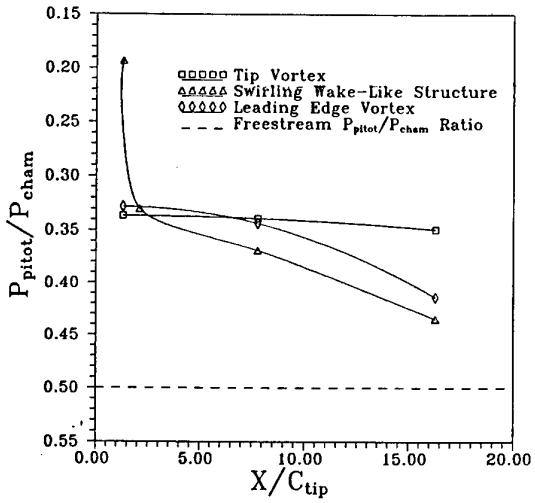


Figure 6. The pitot pressure recovery swirling characteristics structures. in the vortex-wake.

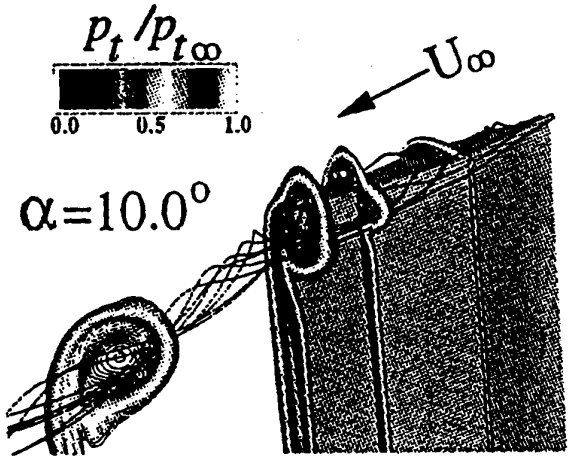


Figure 7. Particle paths and of the three crossplane total pressure contours at the wing tip and in the trailing-edge region from k-ε solution and α = 10.0. From Rizzeta (1996).

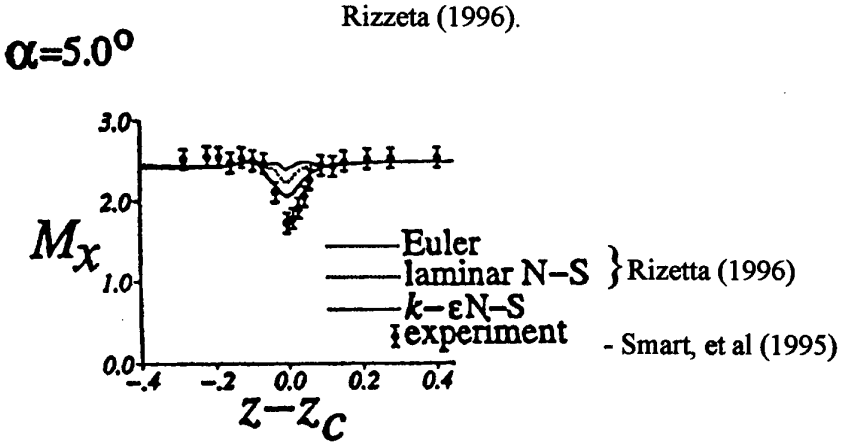


Figure 8a. Streamwise Mach number distributions through the vortex core for α = 5.0.

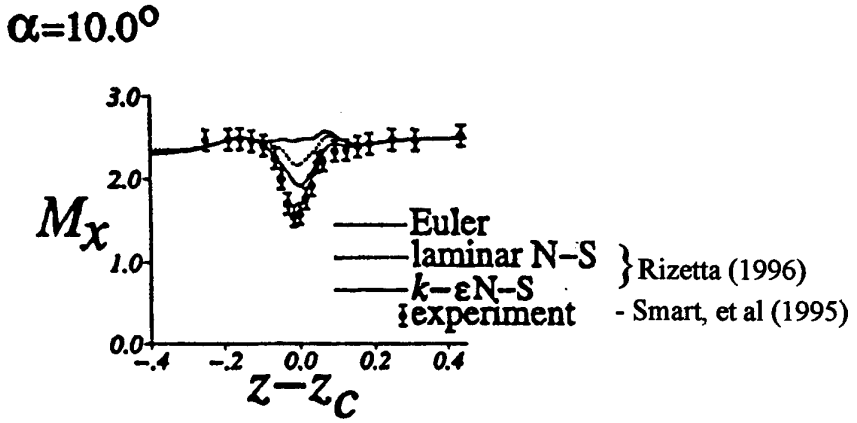
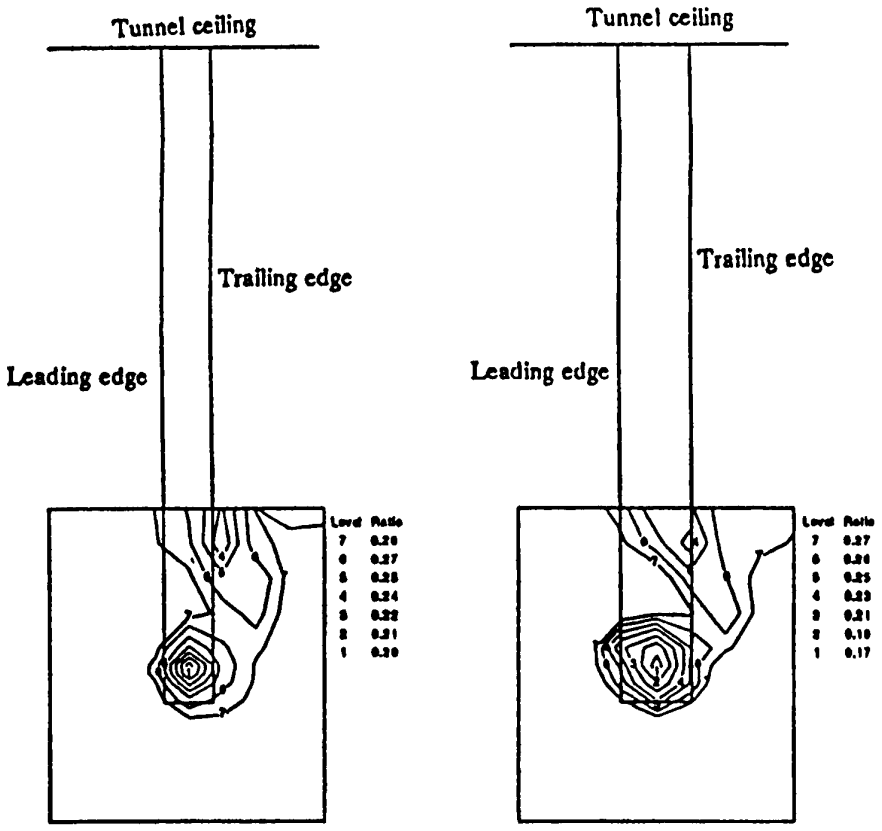
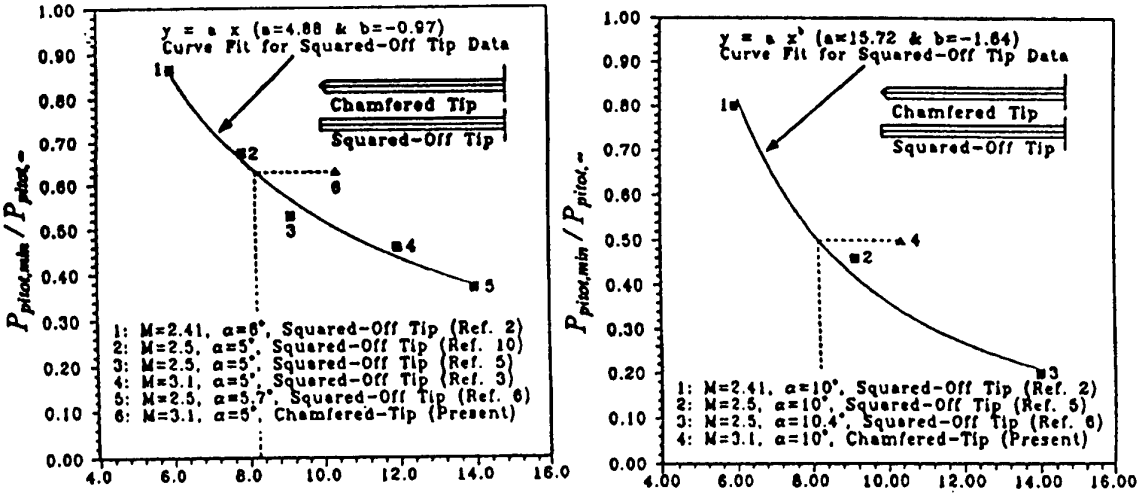


Figure 8b. Streamwise Mach number distributions through the vortex core for α = 10.0.



a) α = 5 deg b) α = 10 deg

Figure 9. Pitot pressure contours shown to scale; boxed region outlines survey limits and projection of wing on the measurement plane in superimposed for reference.



a) 5 deg $\leq \alpha \leq$ 6 deg b) 10 deg $\leq \alpha \leq$ 10.4 deg

Figure 10. Normalized minimum pitot pressure readings in the vortex cores correlated with thickness to chord ratios for squared-off and chambered wing tips.

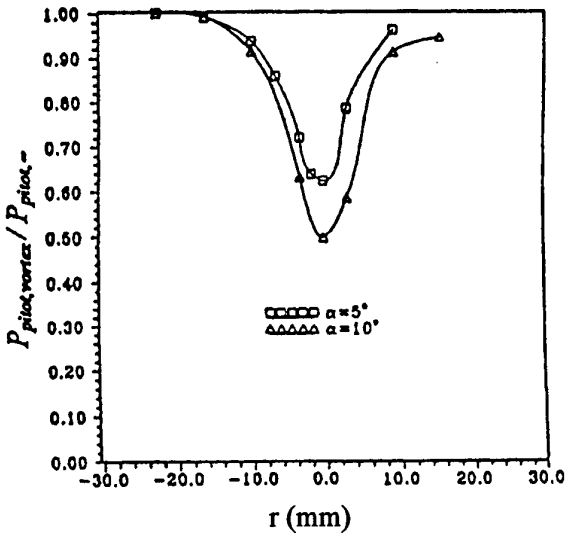


Figure 11. Normalized pitot pressure profiles.

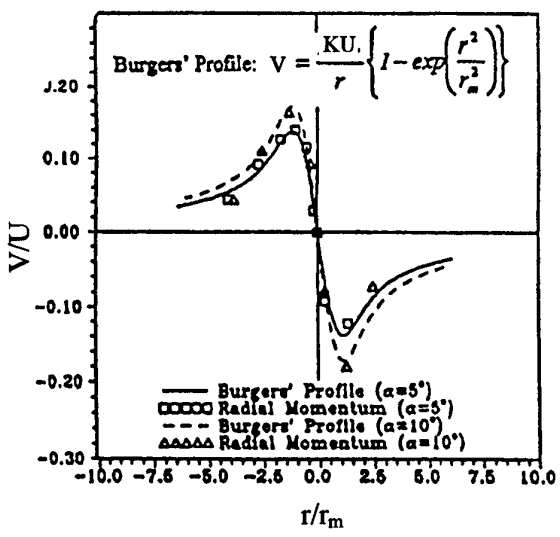


Figure 12. Vortex swirl profile; K and r_m are the characteristic strength and radius of the Burgers'vortex, respectively.

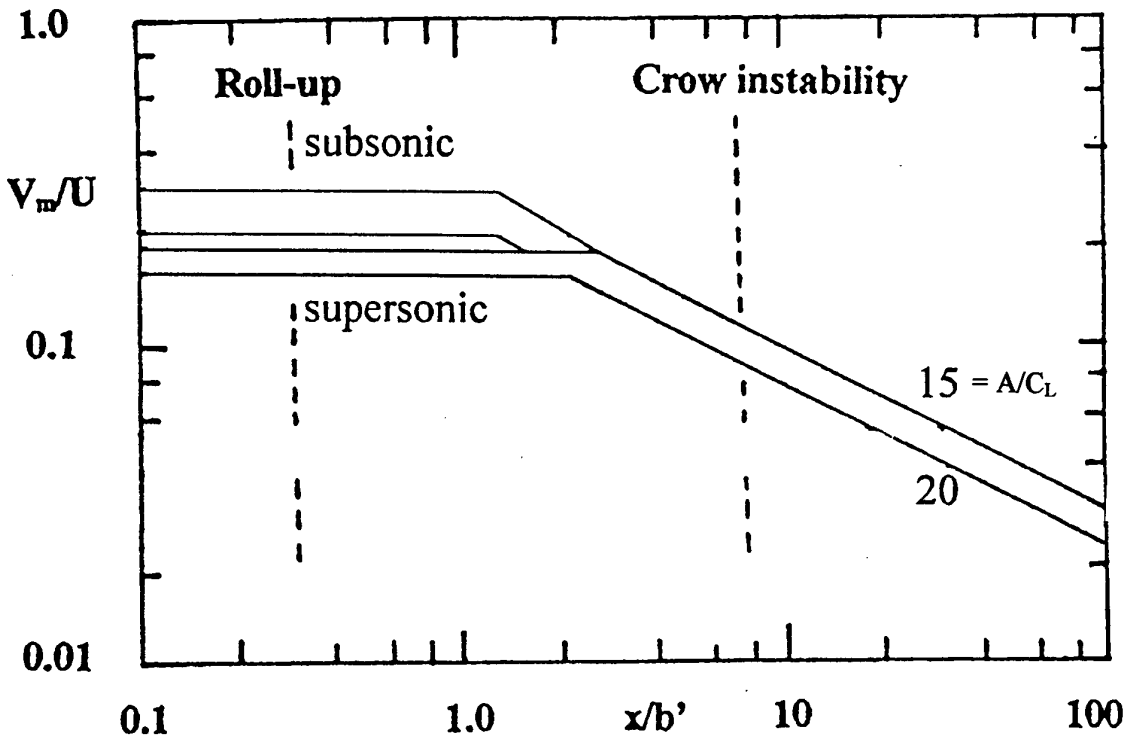


Figure 13. Normalized parameter space for maximum tangential speed of vortex.

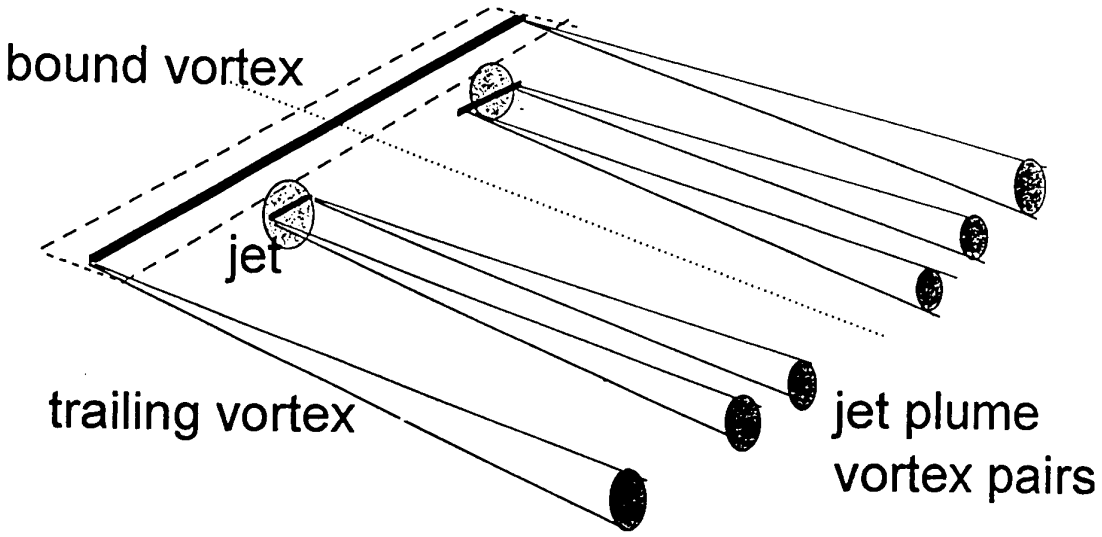


Figure 14. Schematic diagram of the combined vortex flow field model.

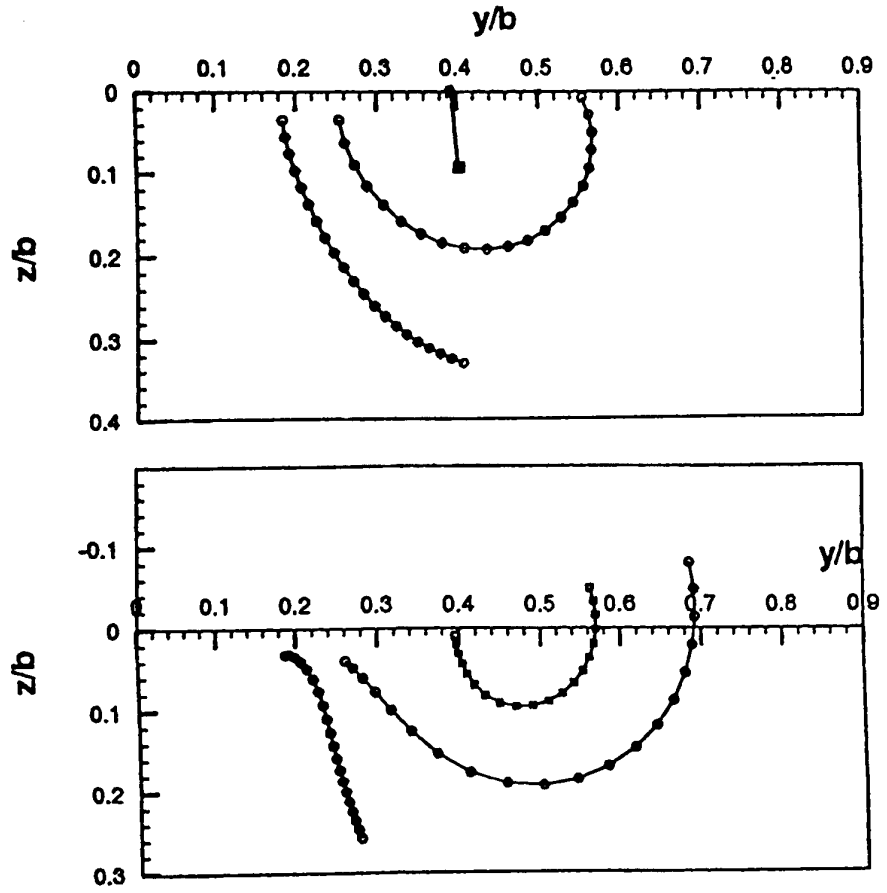


Figure 15. Vortex trajectories for: Γ_j/Γ = (a) 0.1 top; (b) 0.5, bottom.

STATUS OF NASA HIGH-SPEED RESEARCH PROGRAM

Allen H. Whitehead, Jr.
High-Speed Research Project Office
Environmental Impact Team
NASA Langley Research Center, MS/119
Hampton, Virginia 23665-5225, USA

SUMMARY

This paper provides an overview of the NASA High-Speed Research (HSR) Program dedicated to establishing the technology foundation to support the U.S. transport industry's decision for an environmentally acceptable, economically viable 300 passenger, 5000 n.mi., Mach 2.4 aircraft. The HSR program, begun in 1990, is supported by a team of U.S. aerospace companies. The international economic stakes are high. The projected market for more than 500 High-Speed Civil Transport (HSCT) airplanes introduced between the years 2000 and 2015 translates to more than $200 billion in aircraft sales, and the potential of 140,000 new jobs.

The paper addresses the history of supersonic commercial air transportation beginning with the Concorde and TU-144 developments in the early 1960 time period. The technology goals for the HSR program are derived from market study results, projections on environmental requirements, and technical goals for each discipline area referenced to the design and operational features of the Concorde.

Progress since the inception of the program is reviewed and a summary of some of the lessons learned will be highlighted. An outline is presented of the remaining technological challenges . Emphasis in this paper will be on the traditional aeronautical technologies that lead to higher performance to ensure economic viability. Specific discussion will center around aerodynamic performance, flight deck research, materials and structures development and propulsion systems. The environmental barriers to the HSCT and that part of the HSR program that addresses those technologies are reviewed and assessed in a companion paper (Ref. 1).

1.0 PROGRAM HISTORY AND ORGANIZATION

1.1 Vision Statement

The HSR vision statement in Fig. 1 contains the critical mission definition and properly characterizes the final objectives of the program. First and foremost, HSR is a technology program which supports the United States industry decision to produce the high-speed civil transport (HSCT). NASA does not design airplanes, nor does the agency play any role in the decision process to develop a new product like the HSCT. The vision statement dictates that the airplane must be both environmentally acceptable and economically viable and must meet the stated mission targets on payload, range and cruise speed. These requirements subsequently define a series of technology goals that provide the focus for each of the components of the program.

This paper will address the progress against performance goals supporting the economic viability, which is primarily driven by aeronautical technologies including aerodynamic performance, materials and structures, propulsion systems, flight controls, and flight deck developments. Another paper (Ref.1) addresss the specifics of those technologies underpinning the environmental acceptability, including a discussion of how these requirements have impacted the airplane design and the possible influence on the fleet operations of the HSCT.

1.2 History of Supersonic Transports

An understanding of the history of supersonic transport aircraft is useful in establishing the framework for our current undertaking. As depicted in Fig 2, in the early 1960's there were three potential supersonic transport entries into the marketplace.

The United Kingdom teamed with France and launched their SST program at about the same time as did the Soviet Union. The first to fly was the Soviet prototype TU-144 which took to the air on New Year's Eve, 1968, beating the Anglo-French Concorde prototype into the air by two months. There was no small measure of national pride involved in these developments to break the barrier to commercial supersonic airplane operations (Fig. 3). At the end of 1975, TU-144s began what the Soviet Ministry of Civil Aviation touted as the world's first commercial supersonic services, on a twice weekly basis. However, these flights did not carry passengers, but flew high-priority oil-field equipment, mail and agricultural foodstuffs. The first TU-144 passenger service began on November 1, 1977. This service was terminated less than a year later on June 6, 1978 after just 102 revenue flights due to severe operational difficulties with the aircraft and two accidents involving loss of life. The TU-144 suffered from poor air-conditioning, high interior noise levels, airframe vibration, and excessive fuel consumption (the TU-144 had to utilize its afterburners during the entire supersonic cruise phase). In all, 16 airworthy TU-144s were built. The English/French team faired better with their development of

Paper presented at the RTO AVT Course on "Fluid Dynamics Research on Supersonic Aircraft", held in Rhode-Saint-Genèse, Belgium, 25-29 May 1998, and published in RTO EN-4.

the Concorde which first began fare-paying passenger service on January 21, 1976. A total of 20 Concordes were constructed including two prototypes and two pre-production models. The Concorde was developed just prior to the establishment of FAR 36 noise rules in this country, and with its afterburner operation during takeoff, the aircraft required a noise rule waiver to allow its operation out of a few selected US. airports. The Concorde is still in operation, and is said to be profitable with current round-trip fares of around $8,500. Obviously, this extremely high fair premium is undesirable, and the Concorde, though a marvelous engineering feat, cannot be considered a commercial success because the taxpayers paid for the development and production costs.

In 1963 after precursor studies by NASA, President John F. Kennedy announced the commitment of the United States to develop a commercial supersonic transport (SST) under the direction of the Federal Aviation Administration (FAA) and with the support of the National Aeronautics and Space Administration (NASA). The design of the U.S. SST reached completion in 1968 and development began in earnest. The development proceeded to the full-scale mock-up stage when in 1972 the U.S. Congress terminated the program.

After the cancellation of the U.S. SST, NASA continued research in this area for about a decade with its Supersonic Cruise Research Program. This effort not only made great technical strides that established the foundation for the HSR program, but the program maintained the viability of the industry teams. There was some hope that the development program would be resuscitated, but this program was terminated in 1982 as shown in Fig 2. After a 3 to 4 year hiatus, the executive branch of the government issued a 'Call to Action' directive to NASA to initiate a set of system studies with U.S. industry to determine the technical and marketing feasibility for another attempt at developing a supersonic transport. The study results showed that the market would be responsive to the product if the airplane could meet aggressive technology targets. The industry studies recommended a two phase program with Phase I addressing the environmental issues that plagued the original U.S. SST. Phase II would address the more conventional aeronautical technologies to improve performance and economic potential. Phase I was successfully completed and the results from that environmentally-based program are reviewed in the companion paper (Ref. 1). The HSR Program is now in the fifth year of the Phase II program.

1.3 Market Perspective

The market evaluation that were a part of the Industry System Studies was completed independently by the Boeing Commercial Aircraft Group and the former McDonnell-Douglas Company. The study results clearly identified a viable market niche for the HSCT. The demands of a growing international economy, and the Asian market in particular, make a new supersonic airliner very attractive. The most obvious advantage of such a plane is sheer speed. A trip from Los Angeles to Tokyo, for example, would take just over 4 hours instead of over 10 hours on subsonic transports (Fig 4).

The importance of the increased cruise speed to an airline operator can be illustrated in Fig 5, where an airplane routing analysis prepared by Boeing compares supersonic and subsonic operations between Los Angeles (LAX) and Narita, Japan. As the figure illustrates, an HSCT can make two round trips between these two cities in about the same time as the subsonic transport can make a single trip. The Mach 2.4 cruise speed is important in this cycle because it allows the HSCT to avoid curfews or curfew penalties at either end and therefore maximizes the airline's utilization of the airplane. As for passenger comfort, note that the HSCT can depart LAX around 8 am in the morning and arrive in Japan between 6 and 7 am the same day after 4.5 hours of flight time. In this example, the subsonic jet leaves LAX around noon and arrives between 3 and 5 p.m. The passenger has been on the subsonic jet for 11.5 hours, suffering jet lag and needing a second day to recover from the experience!

These market studies also suggested that the average ticket premium that everyday passengers will pay for the increased convenience of a high-speed civil transport is between 20% and 30%. This small ticket premium, along with the aircraft cash operating cost and utilization rate, caps the ultimate price that airlines are willing to pay for the vehicle. This, in turn, will establish a production cost target for the manufacturers and enable an assessment of the HSCT as a sound investment opportunity.

The projected market for more than 500 High-Speed Civil Transport airplanes introduced between the years 2000 and 2015 translates to more than $200 billion in sales, and the potential of 140,000 new jobs.

1.4 Technology Requirements and Outlook

The possibility of an aircraft fleet of over 1,000 large supersonic transports early in the next century may seem remote today. However, we must remember that technological advances have continuously made the impossible happen. The human race has dreamed of sustained flight into the heavens for all of recorded time. As illustrated in Fig. 6 , technology made this dream a reality early in this century. Key technology leaps were required to transition from floating, falling, and gliding around the atmosphere to the air transportation system that we are familiar with today. The first economically viable aircraft were made possible by efficient internal combustion engines, cantilever wing design and metal construction techniques. Then, the fledgling air transportation system gained further momentum with the

advent of the jet engine and swept wing design. Further propulsion advances, composite construction technology and computer aerodynamic optimization will be the key to producing the first generation of economically viable high-speed civil transports. The next generation of supersonic transports, those beyond expected possibility early in the next century, may include supersonic laminar flow control and other boundary layer technologies for increased efficiency. Also, exotic "designer fluid mechanics" technologies such as plasma control or electro-gas-dynamics may be applied to later generation high-speed transport designs. Unique configuration solutions such as the "Oblique Flying Wing" or swept strut-braced arrow wings could also emerge as optimum solutions to the high-speed transportation market.

Many of these technical opportunities remain beyond the scope and time frame of the HSCT and HSR program. For the more near term requirements for the HSCT, Fig 7 displays the design and operational criteria driven by the environmental and economic goals in the vision statement. The chart compares the HSR program goals with the attributes of the Concorde. Basically, the challenge in this program is to produce an HSCT design which carries three time the number of passengers as the Concorde, has twice the range, and offers ticket prices only marginally higher than subsonic transports.

The two entries at the bottom of Fig 7 define the two of the most important environmental goals. The Concorde could not meet the noise standards at the time of its introduction into service so it operated under waivers. The HSCT will have to comply with the same certification requirement as any subsonic jet that is brought into service at the turn of the century. In the United States, that requirement is defined by the Federal Aviation Authority's Federal Aviation Regulation (FAR), Part 36. As will be discussed in the companion paper (Ref 1), the HSR noise goal is more restrictive than this mandated requirement. The second environmental issue is defined by the Emissions Index which measures the grams of NOx relative to the kilograms of fuel consumed. Early projections indicated that the value of this parameter must be between 3 and 8 in order to ensure that no significant ozone depletion can be attributed to HSCT operations. As is discussed in Ref. 1, this parameter drives the design of the HSCT combustor. The value of the Emissions Index for the Concorde is around 20, so this airplane again would be an environmental hazard to the ozone layer if there were a significant number of units in operation.

An excellent summary of the HSR program which covers both the environmental and performance issues can be found in Ref. 2. This report was prepared as a part of a National Research Council assessment of the program's planning and progress and covers some of the same areas with a somewhat different focus. Areas of particular interest in this review include the ability of technologies under development within HSR to meet program goals related to noise, emissions, service life, weight, range and payload.

1.5 Program Organization and Management

The current organizational structure of the HSR Phase II Program is shown in Fig 8. The HSR Program Director resides at the NASA Langley Research Center in Hampton, Virginia. The Airframe Technology office and most of its components shown in this chart are also in place at Langley. The Propulsion Technology office is run out of the NASA Lewis Research Center in Cleveland, Ohio. NASA's High-Speed Research Program has partnered with America's Aerospace industry to develop advanced technologies in the above identified in the Figure. The prime contractors are Boeing, Pratt and Whitney, General Electric Aircraft Engines and Honeywell; there are more than 70 subcontractors on the project. Unique in the history of the NASA/industry relationship is a series of management teams at every level of the program which make joint decisions on program priorities, budgets and planning. A consensus management process drives decision-making at each level.

This structure is useful for displaying the various technology components that will be briefly reviewed in this paper and in the companion paper by the same author (Ref. 1). The companion paper will address the four components listed under Environmental Impact and the Atmospheric Effects program element. We will not review the TU-144 program element which addresses a special set of experiments carried out in 1996 - 1997 on this airplane under a program with the Russian government.

HSR management at each level shown in Fig 8 tracks the progress on the program goals through a set of metrics that have been developed for each technology component and subcomponent. A metric is defined by a timeline chart which displays a series of projected milestone accomplishments related to an appropriate figure of merit for the technology. Typical figures of merit are lift-to-drag ratio, noise reduction, inlet pressure recovery, combustor efficiency, and component weight reduction. As progress is made on the metric, program risk is reduced and the particular technology is brought closer to the realization of its promised goal at the conclusion of the program. This process is also used to provide a status report on the overall progress of the HSR Program by integrating the results of the individual metrics to achieve a vehicle-level evaluation relative to the overall mission goals.

The technology projections embodied in the metrics can also be related to the maturity of the technology at any stage in the program. Technology maturity in the HSR Program is defined by a set of Technology Readiness Levels as shown in Fig 9. In general, most of the technology components project

final delivery of a readiness level of TRL = 6, in which a system or subsystem model or prototype has been demonstrated in a relevant environment. The TRL construction is tied to program risk, and can be a useful measure of the status of the vehicle development and the remaining technology investment that a potential manufacturer must consider prior to committing to the development of the HSCT.

2.0 CRITICAL TECHNOLOGY ELEMENTS

2.1 Technical Challenges

The solution to both the environmental and economic barriers can be viewed as the set of unresolved technical challenges (Fig 10 and Fig 11). Note that the economic and environmental barrier issues are inextricably related, given that the HSCT design must incorporate the best compromise between noise reduction, reduced emissions and performance in order to meet the stated mission requirements.

A propulsion system is needed that efficiently provides the required thrust for supersonic speeds while maintaining a comparable noise signature to that of subsonic aircraft. Light weight airframe materials and structural concepts are needed which provide greater strength at reduced weight, and are durable at extremely high temperatures. High aerodynamic efficiency is needed both during takeoff (to reduce noise) and during cruise phases of flight to reduce fuel consumption. Advanced flight controls and envelope protection technologies are also required for a well behaved and safe aircraft.

These issues define the critical technology elements that drive the HSR Program (Fig 12). These research areas receive top priority in the program decision-making, and the technology objectives are crucial for achieving the overall mission requirements. The notional drawing of the airplane depicts the basic characteristics of the HSCT. While the exact planform shape is technically-sensitive information, the basic design is comprised of a cranked delta wing, with the outboard panel configured to provide the required subsonic performance for take off, climb and approach. There are four individual engines slung beneath the wing. The fuselage will be partially waisted to reduce drag during transonic acceleration.

In December 1995, a single aircraft concept was chosen to focus the intensive technology development planned for the next three years of the program. This concept, the Technology Concept Aircraft (TCA) is not an actual design, but rather serves as a common reference point for the HSR technology development. The TCA is also used to evaluate technology options and to assess overall technical risk. The TCA evolved from separate Boeing and McDonnell Douglas HSCT designs. Computer modeling and wind tunnel tests were used to produce a single concept with optimized aerodynamic performance and operational characteristics. The selection allowed a significant narrowing of the focus for the areas of propulsion and airframe structural components.

2.2 Propulsion Technology Challenges and Status

There are primarily four unique challenges which set a Mach 2.4 HSCT propulsion system apart from current subsonic commercial transport and military tactical fighter engines: (1) high performance mixed compression inlets with high stability margins for safe operation , (2) the requirement for high specific thrust cycles for efficient super-sonic cruise which simultaneously achieve compliance with FAR 36 Stage 3 noise regulations , (3) the requirement for ultra-low nitric oxide emissions to prevent any significant impact to the Earth's protective ozone layer, and (4) a 30-fold increase in operating time at maximum temperature and stress. These criteria establish competing claims on the design of the airplane and even on the flight operating envelope.

2.2.1 Propulsion system trade studies

Engine trade studies outlined in Fig 13 constitute a set of component and system level propulsion assessments which must balance these competing requirements. The results of these trade studies contribute to component downselects, support the overall assessment of the engine performance (thrust and noise reduction), and provide input to the overall vehicle integration and evaluation. Installation issues such as boattail drag and spillage have been defined and assessed.

The current HSCT propulsion system definition and the individual propulsion components are presented in Fig 14 . Each of the inlet, engine and engine cycle and nozzle components have gone through a rigorous evaluation and a resulting downselect from multiple options. The major criteria contributing to the concept selection process are listed below each component in the figure.

2.2.2 Inlet concept downselect

The inlet is chosen as an example of the downselect process. The three designs shown on Fig 15 each were carried as individual research and development activities early in the program. Each concept had to meet the requirement of achieving the performance goals in a mixed compression mode while maintaining high stability margins. The database and analysis from this earlier work allowed a confident assessment of the advantages and risks associated with each competing design. Once the two-dimensional bifurcated inlet was chosen, future inlet work is focused on that design.

2.2.3 Nozzle size comparison

Progress in high-bypass turbofan engines for subsonic transports has generally allowed these airplanes to demonstrate noise levels well below the requirements established by national and international standards. For supersonic airplanes

there is a basic incompatibility between the supersonic cruise condition where power is most efficiently achieved by moving a low mass of air at high speed, and subsonic operations in the landing and takeoff modes where fuel efficiency and noise reduction demand that the engine move large volumes of air at low velocity. The HSCT designer is challenged to produce a "dual mode" propulsion system which can provide acceptable efficiency throughout the flight envelope and still meet the required noise constraints. The propulsion system for the HSCT requires a long inlet to sufficiently pressurize the air before entering the engine, and a large nozzle at the exit to provide required performance and noise reduction. The HSCT engine is nearly three times larger than current military supersonic engines as shown in Fig. 16. Noise reduction is the major driver on the size of the nozzle.

2.2.4 Propulsion materials

A major component of HSR is the development of advanced materials for the propulsion system (Fig 17). The major areas of concern are the combustor liner, exhaust nozzle materials, turbine airfoils, and compressor and turbine disks. There are two fundamentals factors associated with the development of the HSCT propulsion system materials. First, individual components will be much larger that comparable elements used in military or commercial aircraft. Second, HSCT propulsion system components will be required to operate at maximum temperature for an unusually long periods. Subsonic aircraft do not reach the operating temperatures projected for HSCT operations, and there are very few military aircraft that operate for extended time in a supersonic cruise mode where these high temperatures are reached and sustained. Thus there is very little data or experience with materials and propulsion components that have to operate in this hostile environment.

Liner material for the combustor is a challenge because active cooling with air changes the mixing and chemistry that is critical for low emission of nitric oxides, the prime culprit in ozone depletion. Ceramic matrix composites are the leading candidate material system for the 3500 degree F. and the 9000-hour life requirement for the liner. These composites have been demonstrated at design temperature and near mechanical load conditions using accelerated test techniques.

Other propulsion component material challenges are identified on Fig 17. HSCT turbine airfoils (vanes and blades) will likely consist of intricately cooled single-crystal castings of an advanced, oxidation resistant nickel-based superalloy. A thin ceramic coating will serve as a thermal barrier to reduce the average metal temperature in the airfoil. Special nickel alloys using powder metallurgy are being investigated for the compressor and turbine disks. High-temperature creep life and cyclic, fatigue durability issues drive the development.

The main components of the exhaust nozzle are the primary structure, convergent and divergent flaps, noise absorption liners, and thermal blanket. The current nozzle concept features a large nickel-based superalloy primary structure with a thin-walled casting to meet weight goals. Flap options include thin-walled castings of a nickel-base superalloy and a titanium aluminide intermetallic for the convergent and divergent flaps, respectively.

2.3 Airframe Technology Challenges and Status

2.3.1 Airframe materials and structures

The challenges in developing suitable airframe materials and structures for the HSCT are presented in Fig 18. Equilibrium skin temperatures that are maintained during the cruise portion of the flight envelope dictate the choice of material properties needed for the airplane.

The fraction of the operating empty weight for airframe structure is much smaller for a supersonic transport than for conventional subsonic commercial vehicles. This requires the use of innovative structural concepts and advanced materials to satisfy this stringent weight requirement. The operating environment is also more severe because of the high temperatures associated with the aerodynamic friction heating caused by supersonic cruise speeds. Major technology challenges include the effects of thermomechanical loading and manufacturing processes for reducing costs and risks.

Mach 2.4 drives the materials technology development requiring a 60,000 hour durability at 350°F skin temperature and a 30-percent reduction in structural weight relative to the Concorde. Conventional airplane materials such as aluminum and thermoset composites do not have the temperature capability, and titanium alloys are too heavy for the entire airframe.

To reduce structural weight, polyimide resin with carbon fibers has been developed. Polyimides have demonstrated mechanical properties greater than either epoxies or bismaleimides at 350°F. After three and a half years of isothermal testing, over half a lifetime has been demonstrated. Because it takes seven years to complete one lifetime, accelerated testing and analytical techniques are being developed for screening advanced resins.

A "building-block" approach outlined in Fig 19 is being used to develop the lightweight, damage tolerant structure for the HSCT and is consistent with the TRL approach described earlier. Small-scale elements are first designed, analyzed, fabricated and tested. When particular concepts yield favorable results, those concepts are selected for scale up to larger subcomponents and then analyzed and tested. Subcomponents

represent more complex structure and embody the characteristics of several elements combined. Finally, when concepts yield favorable results at the subcomponent level, one concept is selected for fabrication and test at the component level. The component represents a significant piece of structure, such as full-scale fuselage barrel or main wing box.

To reduce weight of the fuselage, outboard wing, strake and empennage, polyimide carbon fibers matrix composites (PMC) are being developed. A NASA patented polyimide resin called PETI-5 when combined with a vendor produced IM7 fiber has demonstrated mechanical properties greater than bismaleimides at 350°F. Currently only a "wet" prepreg is available for laboratory hand layup structures that require long cure times at high pressure in autoclaves to remove the volatiles. Dry prepreg is being developed that potentially has more affordable manufacturing processes such as resin film infusion and robotic layup. Durability isothermal tests after 35,000 hours of a model polyimide show no degradation, and PETI-5 has over 5,000 hours. Thermal mechanical fatigue tests that simulate the flight mechanical and thermal loads have been started. Because it takes seven years to complete one lifetime, accelerated testing and analytical techniques are being developed for screening enhanced PMC resins.

Structural design studies in support of material and structural concept downselects have incorporated current knowledge of these PMC materials. In Fig. 20 the approach followed to select fuselage and main wing box skin structure is depicted. The HSCT is represented by a finite element model with over 19,000 elements and a simultaneous strength and flutter opmization is performed. The four factors and the associated weighting factors are shown on the right side of the figure. The fuselage will have a PMC skin stringer construction, while the wing box will be composed of PMC honeycomb sandwich. At this time, titanium is only used in the main load-bearing members of the wing box such as the spar. Most of the airplane is composed of PMC materials.

2.3.2 High-lift systems

Advanced High-Lift Technology will be needed to produce an HSCT which will deliver the desired aerodynamic performance, while reducing take-off and landing noise levels (Fig 21). This presents a significant challenge, since the optimal wing planform for supersonic cruise is a highly-swept delta wing. In general, the lower the aspect ratio, the less lift per square foot of area is generated. The aspect ratio of the original HSCT wing planform was about 2.4, whereas the aspect ratio for Boeing's 777 subsonic aircraft is 8.4. High-lift efficiency is maximized by designing a system which has high levels of leading edge suction. This is a challenge for an aircraft which has a planform with a highly swept inboard part of the wing and significant amounts of cross flow on the low sweep outboard part of the wing. Additionally, a highly-swept planform exhibits a strong pitch-up characteristic as the angle of attack goes above design conditions. Hard noise constraints currently dictate more wing aspect ratio and less sweep for the outboard portion of this cranked delta. However, one HSCT high-lift benefit is that the relatively large mixer-ejector nozzles (mufflers) have been shown to provide a favorable "pumping effect" as they pull in the slower moving outside air from over the wing to mix with the fast moving hot jet primary flow.

2.3.3 Efficient supersonic flight

Supersonic performance (or cruise performance) is critically important to the viability of any future HSCT design (Fig 22). Supersonic performance has about 5-times greater impact on the economic viability (weight) than subsonic performance since 85% of the mission is planned to be supersonic. Newly developed state-of-the-art computational fluid dynamics (CFD) design, optimization, and flow-field analyses techniques provide a vital additional 10 percent of aerodynamic performance over optimized configurations developed with older methods. Validation of these CFD methodologies is accomplished with dedicated, highly-accurate wind tunnel test programs. In addition to the traditional wing and body design, CFD can also be utilized to optimally design the empennage and engine nacelle installations. CFD is also relied upon to provide answers for full-configuration and full-scale effects at actual flight conditions.

2.3.4 Flight envelope simulation

With an airplane that is over 300 feet long, the fuselage can be considered as a relatively flexible body supported by the wings. Subsonic transports tend to be "square," where as the HSCT length is about twice the width. One solution to controlling the undesireable flexing in the longitudinal axis is the use 3 surfaces: horizontal tail, wings, and canards. The horizontal tail and canards must be integrated with the flight control system to provide acceptable flying qualities. Many different dynamic modes must be investigated to insure a safe and certifiable airplane (Fig. 23). The pilot station must react to the pilot's control inputs in a way that gives proper feedback. Also, the propulsion system will be integrated with the flight control system to help prevent engine unstarts and handle other dynamic events. A totally integrated airframe and propulsion FCS requires new technology to accommodate multiple command and feedback signals. Full-envelope simulation studies are defined in Fig. 23 and are conducted in concert with the airplane technology development to provide an important tool to guide and validate the aerodynamic and flight control system technology development efforts. Every

phase of the flight profile will be investigated to identify and resolve any safety or control problems long before the HSCT ever takes to the air.

2.3.5 The external visibility system

Imagine flying a supersonic passenger jet at 1500 miles per hour with no front windows in the cockpit! In the HSR Program, engineers are working to develop the technology that would replace the forward cockpit windows in the HSCT with large sensor displays. These displays would use sensor images, enhanced by computer-generated graphics to take the place of the view out the front window.

Because of the nature of the design of a supersonic transport, the airplane must land and takeoff at angles that would preclude pilot visibility over the nose of the vehicle (Fig 24). The Concorde solves this problem by hinging the nose and drooping the front of the airplane to allow forward visibility during take off and landing. This approach adds weight and mechanical complexity to the airplane.

The HSR XVS (eXternal Visibility System) shown in Fig 25 has been developed to maintain a fixed nose and still provide the flight crew with the required view of the terrain. High-resolution displays will achieve operational capability which will be equivalent to today's subsonic aircraft. In addition this system will guide the pilot to the airport, warn of other airplanes near the flight path, and provide additional visual aids for operations in the vicinity of the airport.

During airport maneuvers, video cameras on the nose gear and on top of the vertical tail provide a panoramic view of the runway. Using differential global positioning satellite (GPS) data coupled with a digitized map database of the runways, the pilot can track the current airplane position. After takeoff, the computer overlays the sensor image with speed, altitude, and any other personalized selected data for the pilot. At cruise, the surveillance system uses the Traffic Collision Avoidance System (TCAS) and radar to warn the pilot of potential collisions. During weather conditions, radar is used to cut through the rain and fog. The radar data can be processed during airport operations to detect hazards on the runway that cannot be seen, and thus provide greater safety.

Eliminating the drooped nose allows the forward portion of the airplane to be configured for reduced drag, adding further benefit to the weight savings associated with elimination of the mechanical system associated with the drooped nose. The XVS will provide safety and performance capabilities that exceed those of unaided human vision.

3.0 SUMMARY—THE FUTURE OF HIGH-SPEED FLIGHT

The environmental and economic barriers to high-speed flight are very challenging. However, they are not insurmountable (Fig. 26). Technology will provide the key to unlock the door of a global supersonic transportation system. One can reasonably imagine that early in the next century, hundreds of large supersonic transports will continuously circle the globe. In that event, supersonic business-class jets will be developed which would utilize spin-off technologies and design innovations from the HSCT development. Everyone from the average tourist to the corporate executive will have affordable access to the convenience and efficiency of supersonic flight. The first production run of HSCTs will be followed by a series of derivatives with technology upgrades. Further into the next century, even more advanced technologies will be applied to the supersonic transportation system to improve efficiency, economics and utility.

ACKNOWLEDGMENT

This paper is constructed around a series of presentation charts developed by the technology area managers within the High-Speed Project Offices at NASA Langley Research Center in Hampton, Va. and at NASA Lewis Research Center in Cleveland, Ohio. Some of the charts were also developed from information generated on contract by Boeing. The author gratefully acknowledges the support from these sources. These charts and related background material represent the entire body of work accomplished within the HSR Phase I and Phase II programs from about 1990 to date.

REFERENCES

1. Whitehead, Allen H., Jr., "Impact of Environmental Issues on the Design of the HSCT", in RTO AVT/VKI Special Course on "Fluid Dynamics Research on Supersonic Aircraft", RTO Report R-833, June 1998.

2. Committee on High Speed Research, "U.S. Supersonic Commercial Aircraft - Assessing NASA's High Speed Research Program", National Academy Press, Washington, D.C., 1997.

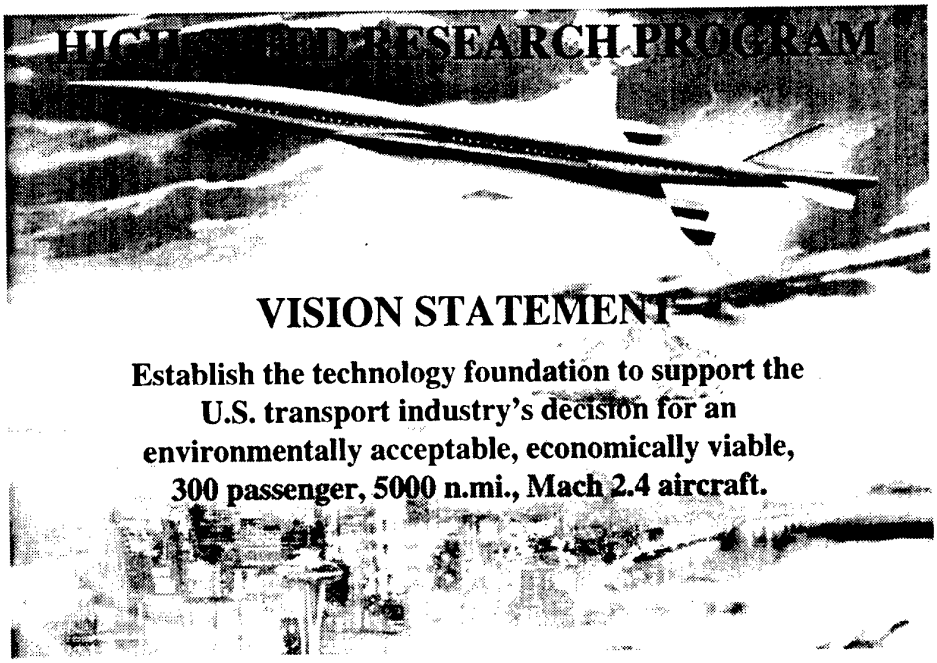


Figure 1. Vision statement.

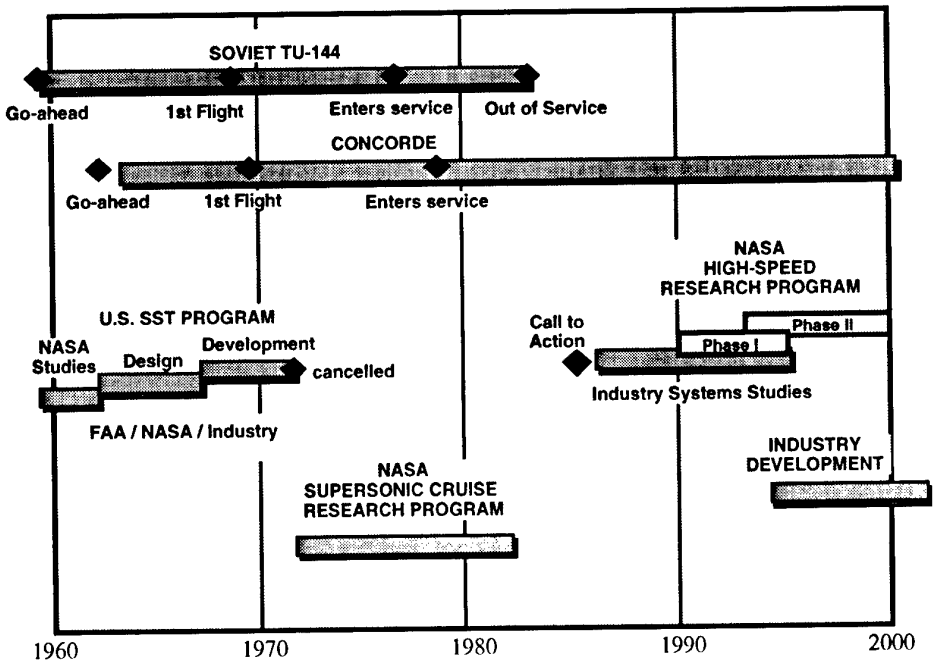
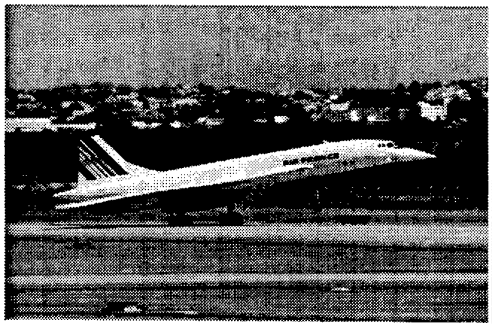


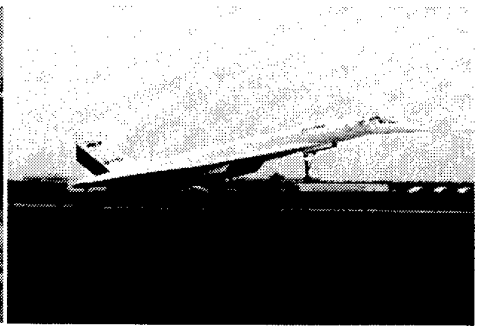
Figure 2. History of supersonic transport programs.

- Concorde



1976 entry into service
20 Built, 16 production models
$ 8,500 current round-trip ticket price

- Tu-144



1975 entry into service
16 "flying" models built
Only one flying today, as a testbed

Figure 3. The commercial barrier.

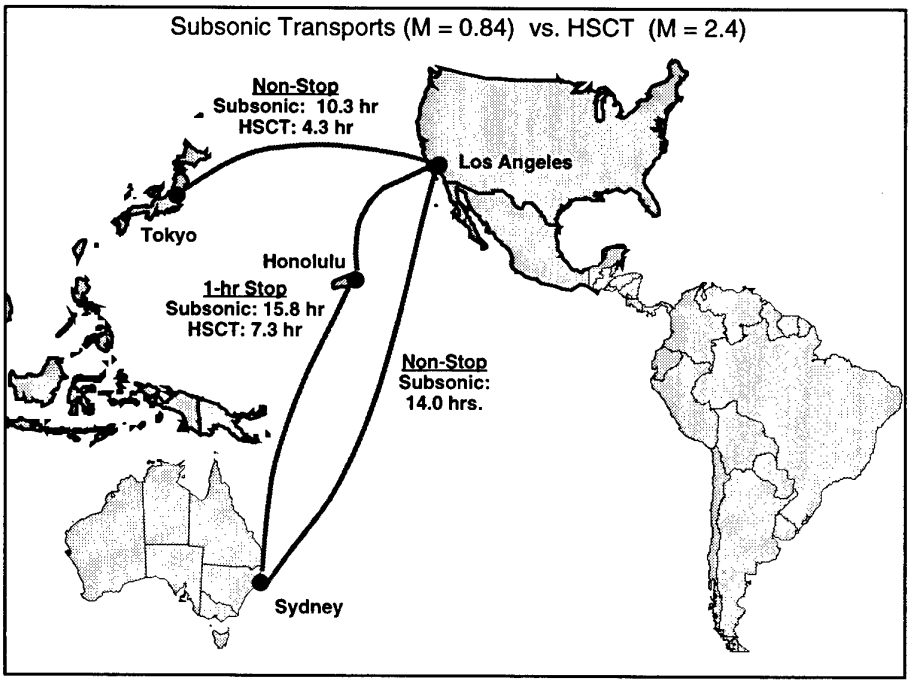


Figure 4. Trip time comparison.

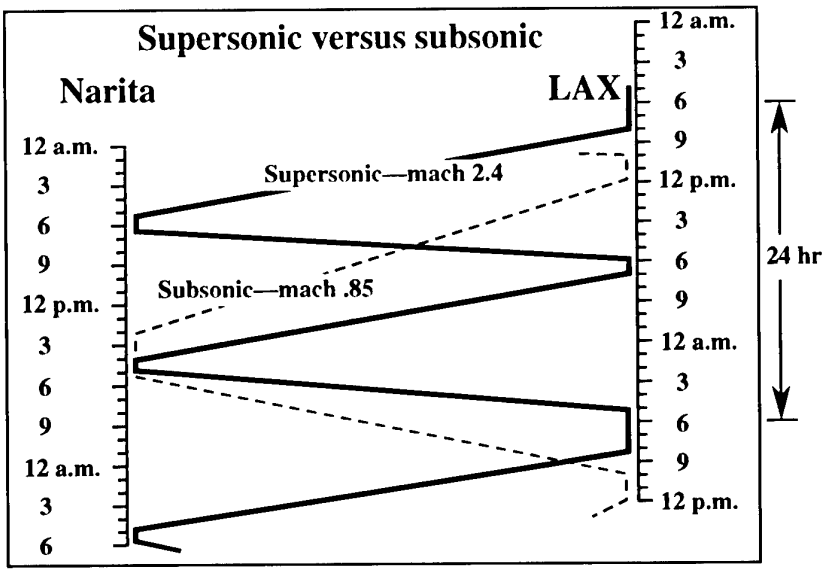


Figure 5. Los Angeles to Narita scheduling.

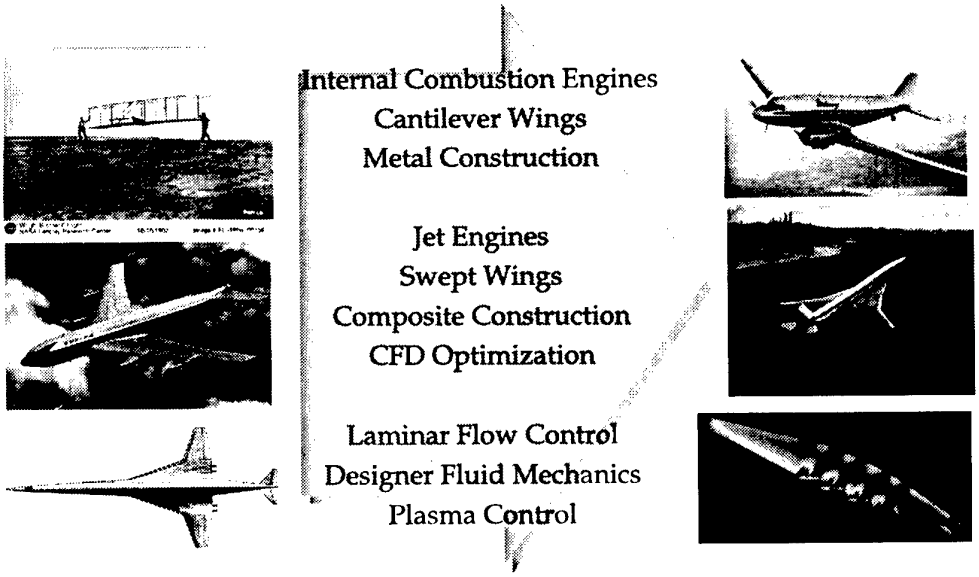
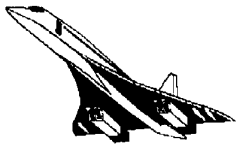
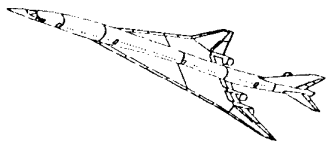


Figure 6. Technology leaps.





Concorde		HSCT Goals
North Atlantic	Market	**Atlantic & Pacific**
1976	Entry into Service year	**2006**
2.0	Speed (Mach No.)	**2.4**
3000	Range (nautical mi.)	**5000-6500**
100	Payload (passengers)	**250-305**
400,000	Takeoff Gross Weight (lb.)	**760,000**
87	Required Revenue (¢/RPM)	**10**
Premium	Fare Levels	**Standard**
Exempt	Community Noise Standard	**FAR 36 - Stage 3**
20	Emissions Index (gm/Kg fuel)	**3 - 8**

Figure 7. Initial program objectives.

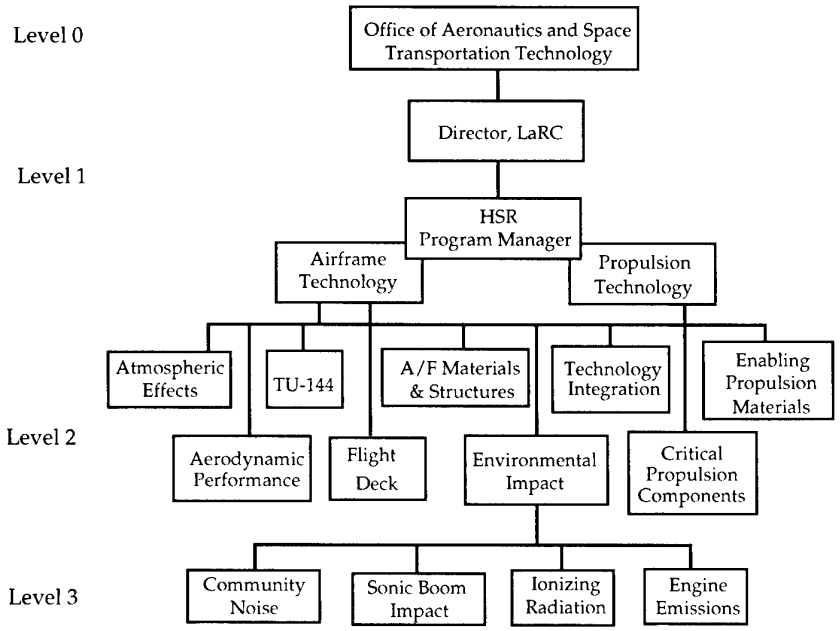


Figure 8. Organization of High-Speed Research Program.

9 - Actual system "flight proven" on operational flight

8 - Actual system completed and "flight qualified" through test and demonstration

7 - System prototype demonstrated in flight

6 - System/Subsystem model or prototype demonstrated in a relevant environment

5 - Component (or breadboard) validation in a relevant environment

4 - Component and/or breadboard validation in a laboratory environment

3 - Analytical & experimental critical function and/or characteristic proof-of-concept

2 - Technology concept and/or application formulated

1 - Basic principles observed and reported

Figure 9. Technology readiness levels.

- Ultra low NOx emissions levels to assure no adverse impact to the Earth's ozone layer
- Community noise levels (takeoff, cutback, approach) compatible with subsonic fleet
- High temperature engine/nozzle materials which have acceptable characteristics for durability, weight, performance, and safety
- Sufficient supersonic thrust while minimizing transonic and supersonic fuel burn

Figure 10. Environmental & economic barriers — propulsion system.

- Airframe Materials and Structures
  - Light weight and durable materials capable of temperatures to 350 degrees F
  - Light weight structural concepts
- Aerodynamic Performance and Flying Qualities
  - High takeoff aerodynamic efficiency for reduced noise
  - Optimized cruise aerodynamics for reduced fuel burn
  - Envelope protection for increased safety

Figure 11. Environmental & economic barriers — materials, structures and aerodynamic performance.

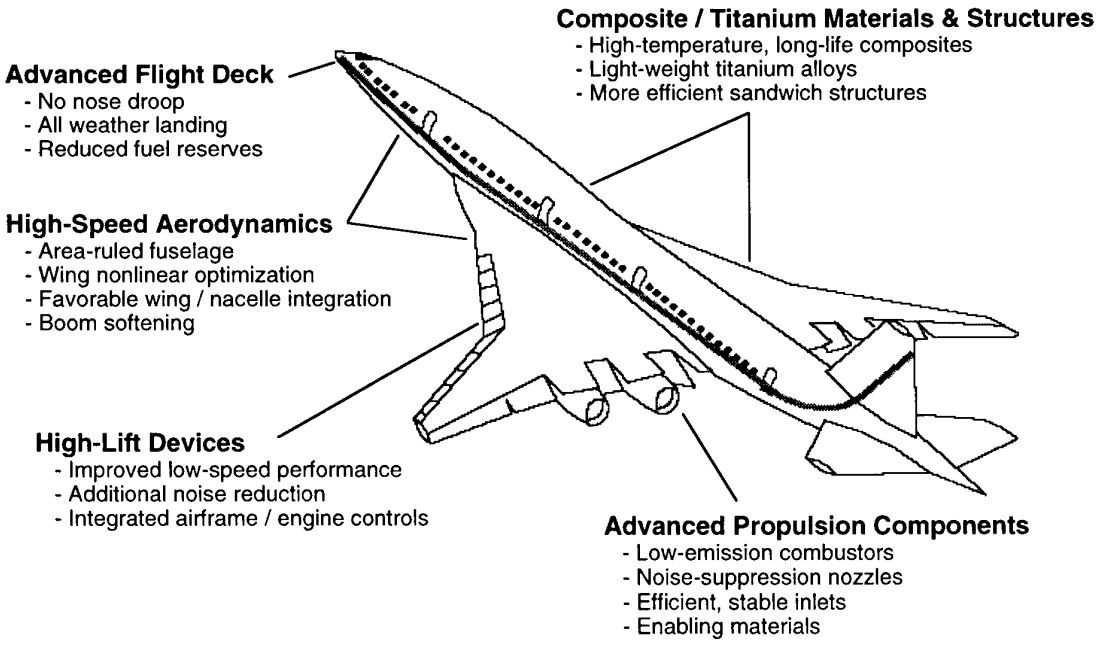


Figure 12. Technology applications.

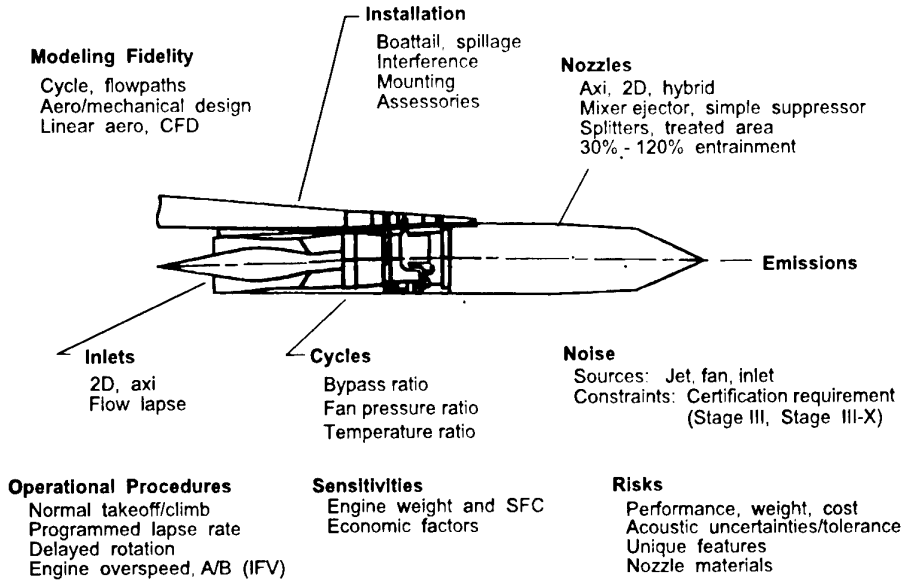
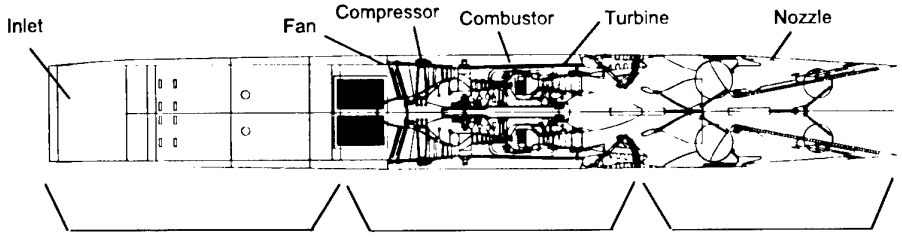


Figure 13. Propulsion system trades.

Propulsion Components Selected for Optimum Economics and Lowest Risk



2D Bifurcated Mixed-Compression Inlet

- Lowest overall risk
- Low mechanical complexity
- Lightest weight when required acoustic treatment area is included

Mixed-Flow Turbofan Engine

- Moderate-risk, conventional Turbomachinery
- Flexibility to match aircraft thrust requirements and noise suppression limitations

2-D Mixer-Ejector Exhaust Nozzle

- Moderate-risk noise suppression concept
- Avoids over-sizing of inlet and engine

Propulsion component selections meet environmental goals and achieve gross weight and good performance targets

Figure 14. Inlet/engine/nozzle system.

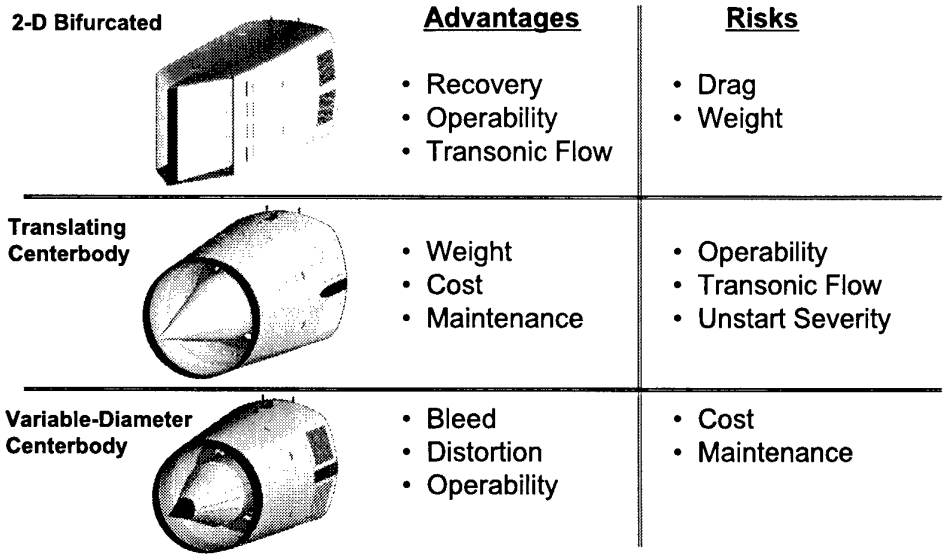
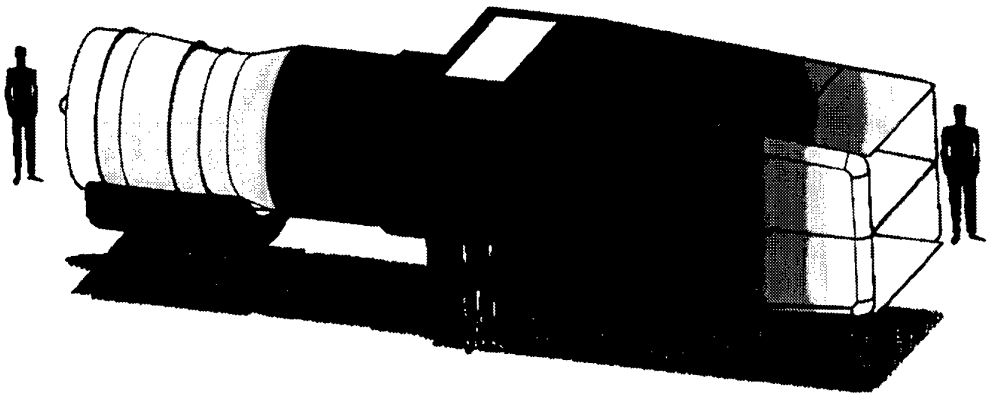


Figure 15. Inlet approaches.



The HSCT engine is nearly three times larger than current military supersonic engines.

Figure 16. HSCT engine configuration.

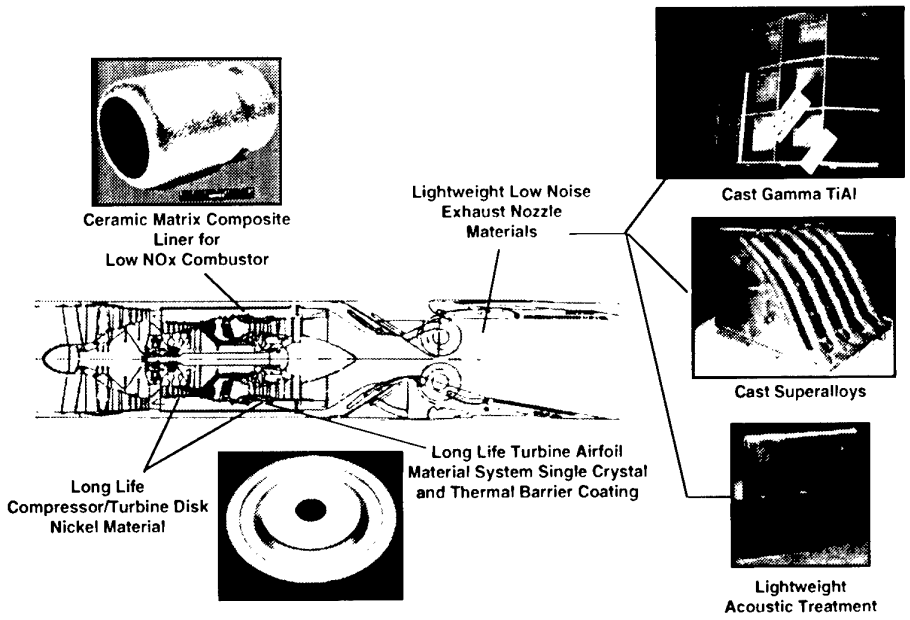
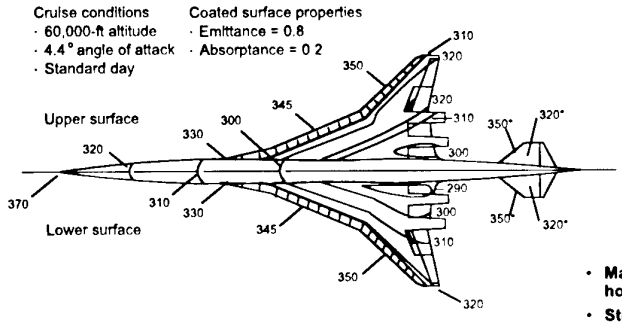


Figure 17. Enabling propulsion materials.

SKIN EQUILIBRIUM TEMPERATURES - MACH 2.4 CRUISE



CHALLENGES

- **Materials that are capable of 60,000 hours of durability up to 350 deg F**
- **Structures that are both lightweight and damage tolerant**
- **Airframes that have desirable dynamic, aeroelastic, and acoustic characteristics**
- **Materials, structural designs and manufacturing processes that are economically feasible**

Figure 18. Near term technical solutions — airframe materials & structures.

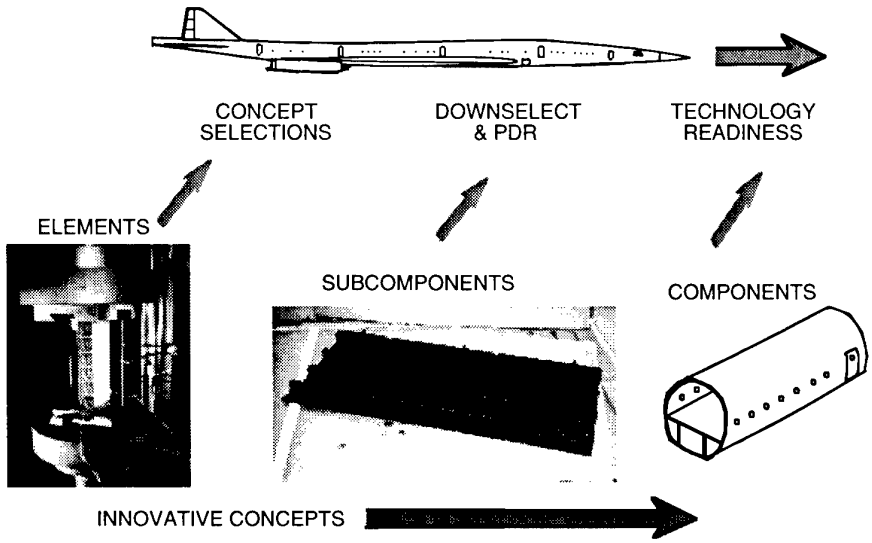


Figure 19. Materials and structuress technology — building block approach.

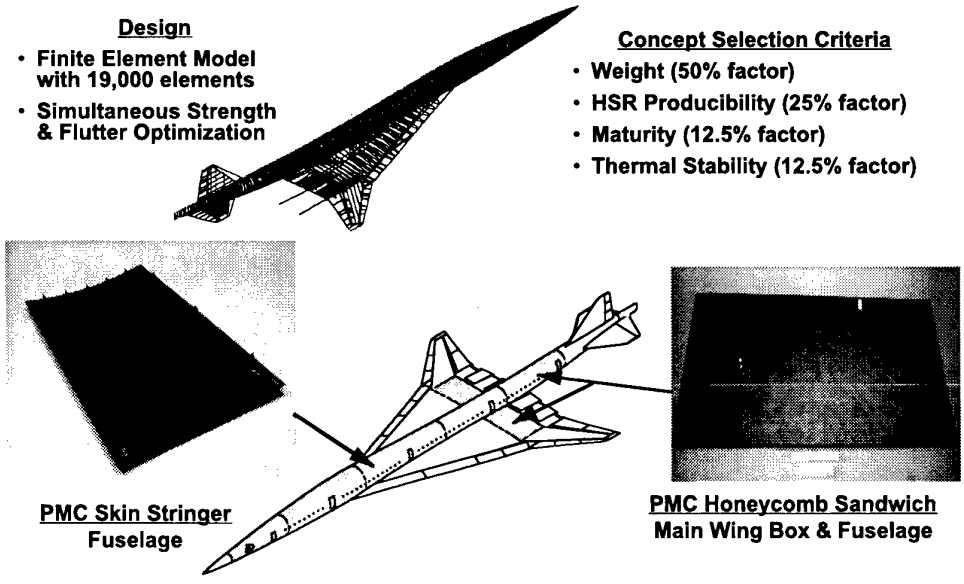
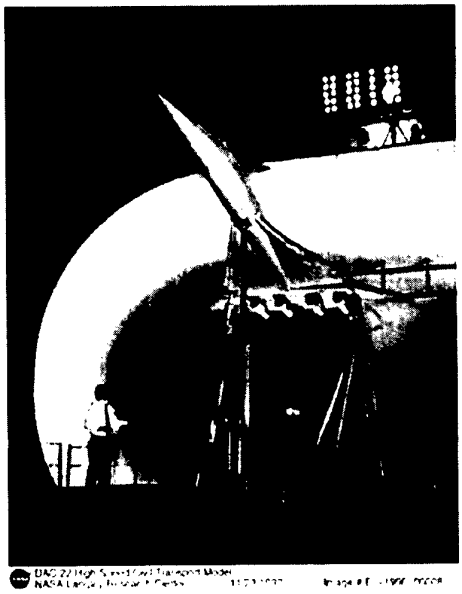


Figure 20. Structural design studies.



- High-Lift Technology advances are key to meeting Airport Community Noise Goals
- Planforms optimized for supersonic flight present a great challenge to low speed designers. Goal is to have a takeoff L/D > 10 versus 5 for the Concorde
- Large nozzles which pull in the colder air to mix with the hot jet will enhance the lift of the wings due to their pumping effects

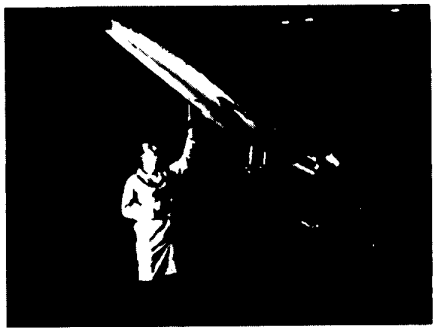
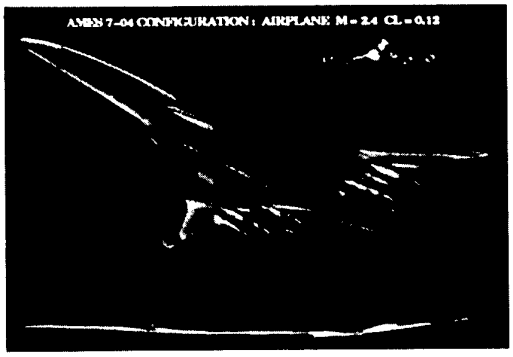
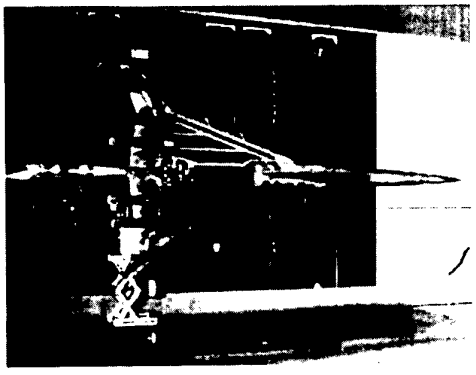


Figure 21. Efficient high-lift systems.



- Supersonic cruise efficiency is of primary importance - 85% of the nominal mission is flown at this condition
- Todays design advances are made possible by state-of-the-art computational fluid dynamics (CFD) codes and high-speed supercomputers



- Validation of the codes requires dedicated, highly accurate wind tunnel test programs
- Engine and empennage designs depend on CFD since these effects are difficult, if not impossible, to measure in a wind tunnel
- Full-Scale effects must also be predicted with CFD

Figure 22. Efficient supersonic flight.

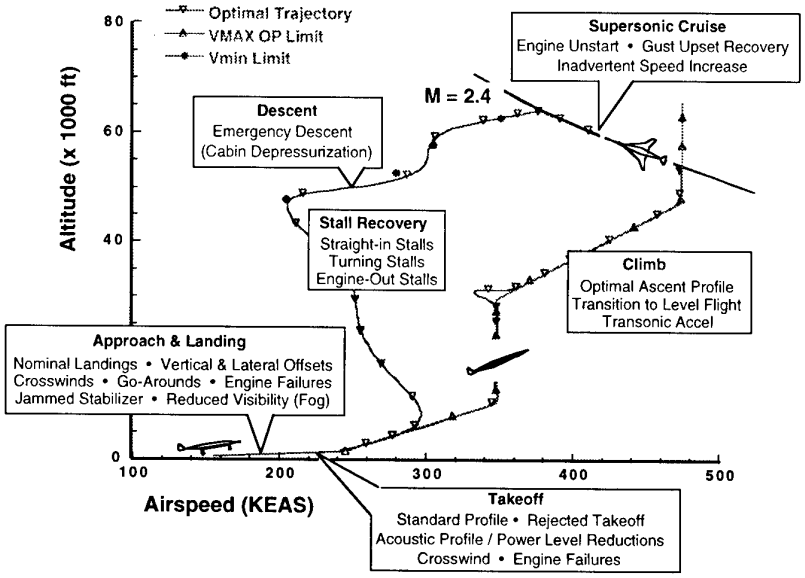


Figure 23. Full envelope simulation.

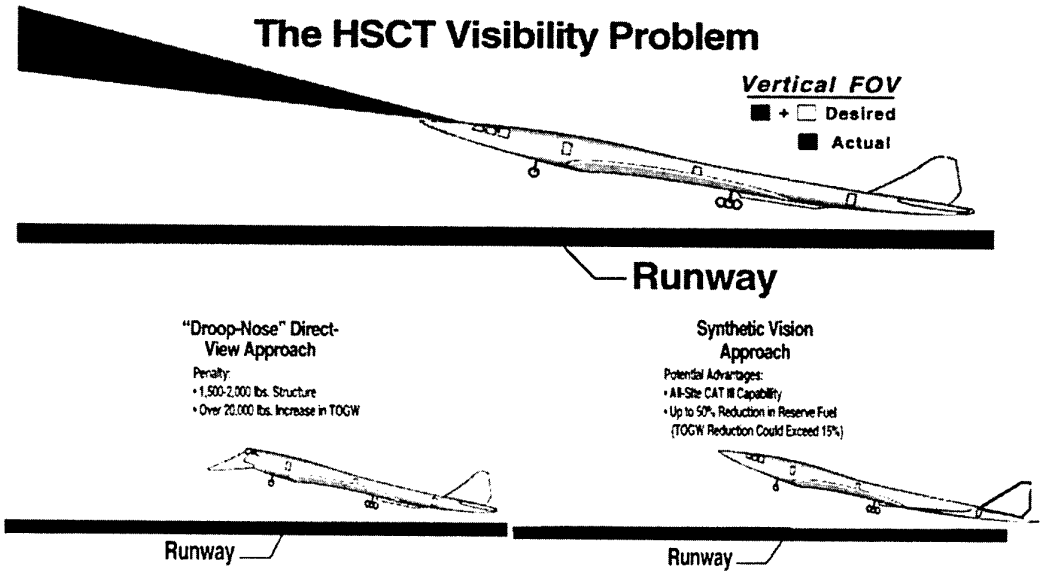


Figure 24. Two methods to achieve visibility.

- Operational Capability Equivalent to Today's Fleet (747, MD-11) Without Forward Facing Windows
- Increased Safety via Full-time Computer Monitored Surveillance utilizing multiple sensors (TCAS, Video, RADAR)



- No Increase in Pilot Workload
- Certifiable
- Pilot & Airline Acceptable
- No Special Handling (ground or flight)

Figure 25. EXternal vision system characteristics.

- Economic and Environmental Barriers to high-speed flight are real and represent a true challenge - however, they are not insurmountable
- Hundreds of HSCTs could fly early in the next century
- Supersonic business jets could also become available
- Future generations of HSCTs will employ even greater technologies

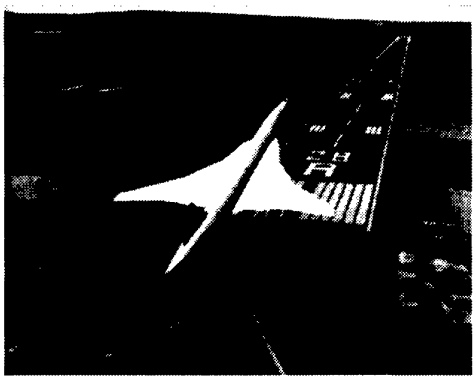


Figure 26. The future of high-speed flight.

GEOMETRY TOOLS FOR MULTIDISCIPLINARY OPTIMIZATION

Helmut Sobieczky
DLR German Aerospace Center
D-37073 Göttingen, Bunsenstr. 10
Germany

e-mail: Helmut.Sobieczky@dlr.de

Summary

Design tools for high speed design aerodynamics are developed using sets of mathematical functions to create curves and surfaces in 3D space, steady or moving for unsteady phenomena, adaptation and optimization. Coupled with fast grid generation, input for CFD verification of preliminary design variations may be created. Aerodynamic applications for conventional (HSCT) and novel (OFW) supersonic transport aircraft are illustrated, with future prospects to use geometry generation of internal structures, control surfaces and engines for multidisciplinary optimization. The geometry generator is a preprocessor to provide knowledge-based input for CAD and CFD methods.

1. INTRODUCTION

Renewed interest in Supersonic Civil Transport (SCT) or High Speed Civil Transport (HSCT) calls for extensive computational simulation of nearly every aspect of design and development of the whole system. CAD methods are available presently for many applications in the design phase. Nevertheless, work in early aerodynamic design lacks computational tools which enable the engineer to perform quick comparative calculations with gradually varying configurations or their components. To perform aerodynamic optimization, surface modelling is needed which allows parametric variations of wing sections, planforms, leading and trailing edges, camber, twist and control surfaces, to mention only the wing. The same is true for fuselage, empennage, engine and integration of these components. Considering the tight situation of available space for passenger, cargo and fuel volume, respective container geometry modelling and integration within the airframe should be added in a parametric study. This can be supported in principle by modern CAD methods, but CFD data preprocessing calls for more directly coupled software which should be handled interactively by the designer observing computational results quickly and thus enabling him to develop his own intuition for the relative importance of the several used and varied shape parameters.

The requirements of high speed air transport technologies are summarized in a new book on new concepts for supersonic transport aircraft, [1]:

Based on experience with the definition of test cases for transonic aerodynamics [2] and with design and optimization tools for supersonic and hypersonic configurations [3], some fast and efficient geometry tools for aerodynamic shape design are proposed [4]. This book chapter is actualized here with some new developments concerning the novel configuration of Oblique Flying Wing (OFW) .

2. GEOMETRY TOOLS

The geometry tools used here for high speed applications are adapted to contain some of the most important parameters of supersonic configuration design, to be varied in numerical early stage design and optimization studies and finally yield a suitably dense set of data needed as an input for industrial CAD/CAM systems.

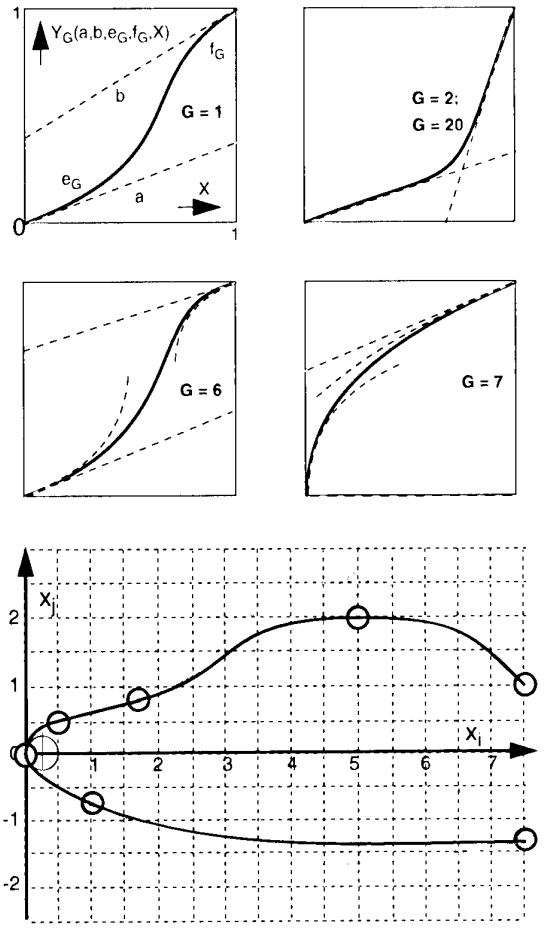
Focusing on surfaces of aerodynamically efficient aircraft components, we realize that the goal of surface generation requires much control over contour quality like slopes and curvature, while structural constraints require also corners, flat parts and other compromises against otherwise idealized shapes. When familiarity is gained with a set of simple analytic functions and the possibility is used to occasionally extend the existing collection of 1D functions, ground is laid to compose these functions suitably to yield complex 2D curves and surfaces in 3D space. This way we intend to develop tools to define data of aerospace vehicles with a nearly unlimited variety within conventional, new and exotic configurations. A brief illustration of the principle to start with 1D functions, define curves in 2D planes and vary them in 3D space to create surfaces is given.

---

* Sr. Research Scientist

Copyright (©) 1998 by author. Published by RTO AVT, with permission.

Paper presented at the RTO AVT Course on "Fluid Dynamics Research on Supersonic Aircraft", held in Rhode-Saint-Genèse, Belgium, 25-29 May 1998, and published in RTO EN-4.



key	u	F(u)	s_1	G	s_2	e_1	f_2
1	0.0	0.0	0.	7	0.25	4.	0.
1	0.5	0.5	0.	4			
1	1.7	0.8	0.25	6	0.	0.	-0.2
1	5.0	2.0	0.	6	-0.8	-0.2	-0.2
1	7.5	1.0					
2	0.0	0.0	0.	7	-0.5	4.	0.
2	1.0	-0.7	-0.5	20	0.	2.	
2	7.5	-1.3					

Fig. 1: Some basic functions Y_G in nondimensional unit interval (above). Construction of arbitrary, dimensional curves in plane (x_i, x_j) by peacewise use of scaled basic functions. Parameter input list (below), example with 2 parameters changed, resulting in dashed curves.

2.1 FUNCTION CATALOG

A set of functions Y(X) is suitably defined within the interval $0 < X < 1$, with end values at X,Y = (0, 0) and (1, 1), see Fig. 1, sketches above. We can imagine a multiplicity of algebraic and other explicit functions Y(X) fulfilling the boundary requirement and, depending on their mathematical structure, allowing for the control of certain properties especially at the interval ends. Four parameters or less were chosen to describe end slopes (a, b) and two additional properties (e_G, f_G) depending on a function identifier G. The squares shown depict some algebraic curves where the additional parameters describe exponents in the local expansion (G=1), zero curvature without (G=2) or with (G=20) straight ends added, polynomials of fifth order (G=6, quintics) and with square root terms (G=7) allowing curvatures being specified at interval ends. Other numbers for G yield splines, simple Bezier parabolas, trigonometric and exponential functions. For some of them e_G and/or f_G do not have to be specified because of simplicity, like G=4 which yields just a straight line. The more recently introduced functions like G=20 give smooth connections as well as the limiting cases of curves with steps and corners. Implementation of these mathematically explicit relations to the computer code allows for using functions plus their first, second and third derivatives. It is obvious that this library of functions is modular and may be extended for special applications, the new functions fit into the system as long as they begin and end at (0,0) and (1,1), a and b describe the slopes and two additional parameters are permitted.

2.2 CURVES

The next step is the composition of curves by a piecewise scaled use of these functions. Figure 1 illustrates this for an arbitrary set of support points, with slopes prescribed in the supports and curvature or other desired property of each interval determining the choice of function identifiers G. The difference to using spline fits for the given supports is obvious: for the price of having to prescribe the function identifier and up to four parameters for each interval we have a strong control over the curve. The idea is to use this control for a more dedicated prescription of special details of the geometry, hoping to minimize the number of optimization parameters as well as focusing on problem areas in analysis code development.

Characteristic curves ("keys") distinguish between a number of needed curves, the example shows two different curves and their support points. Below the graphs a table of input numbers is depicted, illustrating the amount of data required for these curves. Nondimensional function slopes a, b are calculated from input dimensional slopes s_1 and s_2, as well as the additional parameters e_G, f_G are found by suitable transformation of e_1 and f_2.

A variation of only single parameters allows dramatic

changes of portions of the curves, observing certain constraints and leaving the rest of the curve unchanged. This is the main objective of this approach, allowing strong control over specific shape variations during optimization and adaptation.

2.3 Surfaces

Aerospace applications call for suitable mathematical description of components like wings, fuselages, empennages, pylons and nacelles, to mention just the main parts which will have to be studied by parameter variation. Three-view geometries of wings and bodies are defined by planforms, crown lines and some other basic curves, while sections or cross sections require additional parameters to place surfaces fitting within these planforms and crown lines.

Figure 2 shows a surface element defined by suitable curves (generatrices) in planes of 3D space, it can be seen that the strong control which has been established for curve definition, is maintained here for surface slopes and curvature.

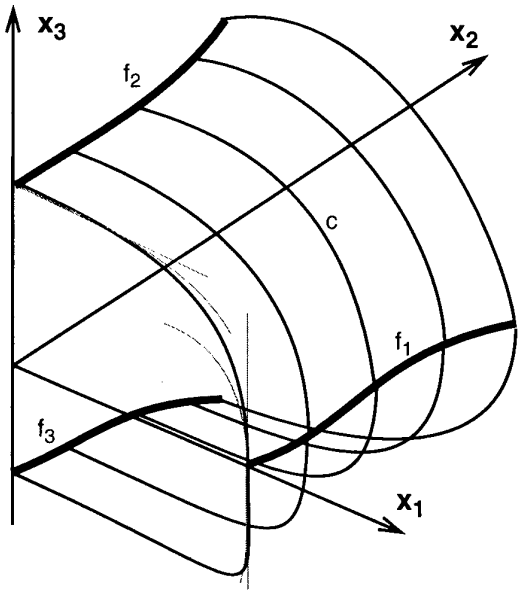


Fig. 2: Surface definition by cross sections c in plane (x_1, x_3) determined by generatrices f_i along x_2 and in planes (x_1, x_2), (x_2, x_3).

2.4 Airfoils

So far the geometry definition tool is quite general and may be used easily for solid modelling of nearly any device if a parametric variation of its shape is intended. In aerodynamic applications we want to make use of knowledge bases from hydrodynamics and gasdynamics, i. e. classical airfoil theory and basic supersonics should determine choice of functions and parameters. In the case of wing design we need to include airfoil shapes as wing sections, with data resulting from previous research. Such data will be useful if they are either describing the airfoil with many spline supports, or defining the shape by a low number of carefully selected supports, which can be used for spline interpolation in a suitably blown-up scale (Fig. 3a). For such few supports each point takes the role of a parameter, wavy spline interpolation may be avoided. An early version of this geometry tool was used to optimize wing shapes in transonic flow [5] by moving single wing section spline supports.

In a recent extension of this airfoil definition completely analytic sections with a set of minimum input parameters are given [6], Fig. 3b illustrates an airfoil family "PARSEC" with a minimum of 11 such parameters, additional ones for refinements are optional. Many known and optimized airfoils may be duplicated with good accuracy by this airfoil function.

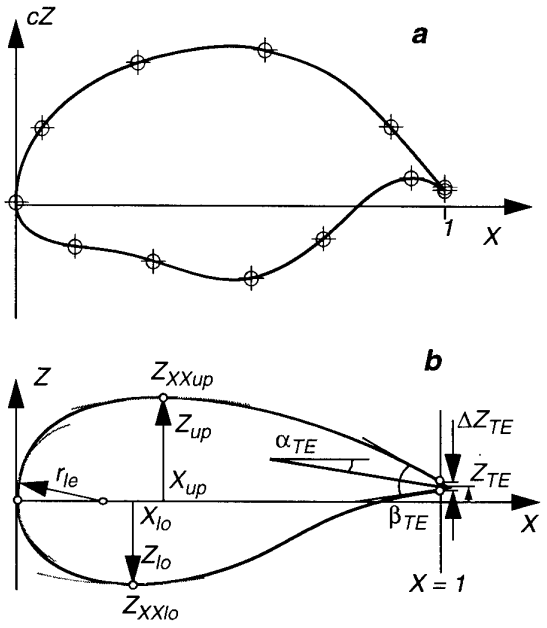


Fig. 3. Airfoil shape defined by a set of few spline supports in a blown-up scale, (a), and analytical definition of 'PARSEC' sections with 11 input parameters, (b).

2.5 Wings

Aerodynamic performance of aircraft mainly depends on the quality of its wing, design focuses therefore on optimizing this component. Using the present shape design method, the amount of needed "key curves" along wing span which is inevitably needed to describe and vary the wing shape, includes the following items:

key number	*purpose*
20	*spanwise section definition* $y_0(p)$
21	*leading edge* $x_{le}(y_0)$
22	*trailing edge* $x_{te}(y_0)$
23	*twist axis* $x_D(y_0)$
24	*dihedral: twist axis* $z_D(y_0)$
25	*twist axis* $y_D(y_0)$
26	*section twist in degrees* $\alpha_s(y_0)$
27	*section thickness factor* $\tau(y_0)$
28	*blending function* $r(y_0)$

The key numbers are just identification names: span of the wing y_0 in the wing coordinate system is a function of a first independent variable $0 < p < 1$, the curve $y_0(p)$ is key 20. All following parameters are functions of this wing span: planform and twist axis (keys 21-23), dihedral (24) and actual 3D space span coordinate (25), section twist (26) and a spanwise section thickness distribution function (27). Finally we select a suitably small number of support airfoils to form sections of this wing. Key 28 defines a blending function $0 < r < 1$ which is used to define a mix between the given airfoils, say, at the root, at some main section and at the tip. Practical designs may require a larger number of input airfoils and a careful tailoring of the section twist α_s to arrive at optimum lift distribution, for a given planform. For more details see [4].

Replacing the key 28 blending of several input airfoils by the 'PARSEC' analytical airfoils is a recent extension to the wing geometry tool, see [6]: The 11 input parameters are keys themselves, this way defined as functions along wing span.

Because of a completely analytic description of each wing surface point without any interpolation and iteration, other than sectional data arrays may be obtained with the same accuracy describing the exact surface.

2.6 Bodies and wing-body connections

Body axis is basically parallel to the x axis in the main flow direction, again some characteristic curves are a function of this independent variable. Here upper and lower crown line, side extent and suitable superelliptic parameters of the cross section are one possibility to shape a fuselage (keys 40 - 49). Other, more complicated bodies are defined by optional other shape definition subprograms. It is useful to define the body's horizontal coordinates because this allows an easy shaping of the wing root toward the body. The technique is called 'blended projection technique' and has been described in detail in some earlier presentations as reviewed in [4].

A new method to connect body and wing, or other components, by a fillet is explained in [7]:

Given surface data for two components, either with additional analytical gradient information or described by dense, accurate surface grids, is needed to shape a fillet as a connecting, additional component. Wing-fuselage junctions with their considerable potential to improve aerodynamic and structural efficiency, are shaped successfully with this technique. An application for high wing aircraft is outlined in Ref. [8].

Fig. 4 illustrates the approach:

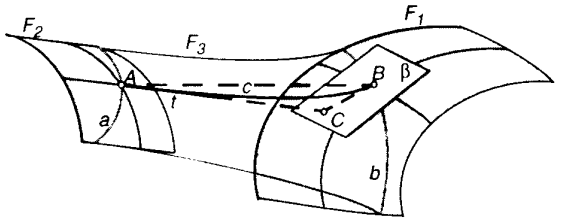


Fig. 4. Connecting two surface components by a fillet based on tangency conditions at predefined connection curves a, b.

3. Examples

Case studies for new generation supersonic transport aircraft have been carried out through the past years in research institutions and the aircraft industry. Our present tool to shape such configurations needs to be tested by trying to model the basic features of various investigated geometries. Knowing that the fine-tuning of aerodynamic performance must be done by careful selection of wing sections and twist distribution, our initial exercise is trying to geometrically model some of the published configurations, generate CFD grids around them and develop optimization strategies to find suitable section and twist distributions. This is still a difficult task but tackling its solution greatly contributes to building up a knowledge base for supersonic design. The initial phase of two case studies is illustrated next, the purpose of generating their geometry is the definition of test cases for CFD code development, parametric variations and finally identifying additional geometry parameters to arrive at a multidisciplinary optimization tool.

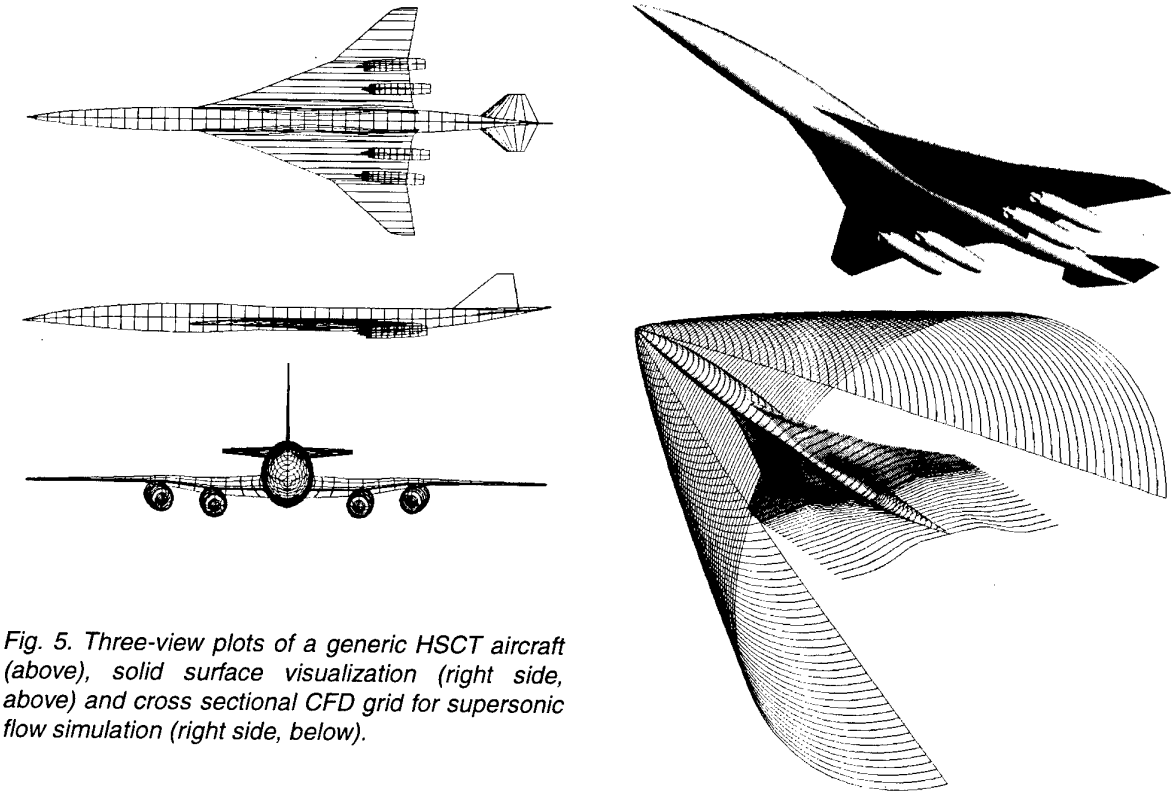


Fig. 5. Three-view plots of a generic HSCT aircraft (above), solid surface visualization (right side, above) and cross sectional CFD grid for supersonic flow simulation (right side, below).

3.1 Generic HSCT aircraft

The above graphics Fig. 5 illustrate geometry definition of a configuration generated from a Boeing HSCT design case for Mach 2.4 [9]. Fig. 8 shows a three-view and a shaded graphics visualization. The configuration consists of 6 components plus their symmetric images, engine pylons are not yet included. The wing has a subsonic leading edge in the inner portion and a supersonic leading edge on the outer portion. A minimum of support airfoils to get a reasonable pressure distribution is used: a rounded leading edge section in most of the inner wing and an almost wedge-sharp section in the outer wing portion define the basic shape of the wing. Wing root fillet blending, the smooth transition between rounded and sharp leading edge and the tip geometry are effectively shaped by the previously illustrated keys 27 and 28, while lift distribution along span is controlled by wing twist, key 26.

Fig. 5 shows an extension of the shape generation tool particularly useful for supersonic applications: A computational far field boundary is generated just like a fuselage in cross sections, a computational wake emanates from the wing trailing edge and the whole wing-body configuration is defined here by a cross section surface grid. Boundary conditions are given this way for CFD aerodynamic analysis, but also for sonic boom investigations and, with engine exhaust modelling included, for investigating jet contrails. The latter tasks are especially of interest for research on the environmental impact of HSCT aircraft.

3.2 Generic OFW aircraft

The already operational software and the tools under development stimulate us to study innovative aircraft concepts. The development of conventional HSCT configurations like the one modelled above, may still face crucial technology problems resulting in reduced chances to operate economically. An elegant concept avoiding some of these problems is the Oblique Flying Wing (OFW) for supersonic transport. Its high aerodynamic efficiency calls for ongoing in-depth investigation, continuing the work already done through the past years [10]. Geometry preprocessor tools seem ideally suited to aid such work by parametric shape variation and the implementation of inverse design methods based on gasdynamic modelling.

The new airfoil definition function for PARSEC wing sections was employed in our latest approach to create a parameterized OFW to study the influence and role of the various parameters 'manually' [11] before an automated optimization procedure can focus on the variation of all relevant parameters. The example for an OFW in the rela-

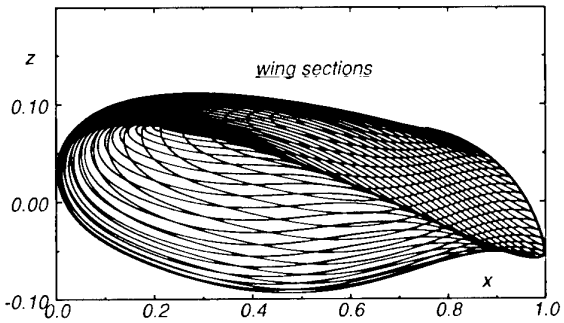
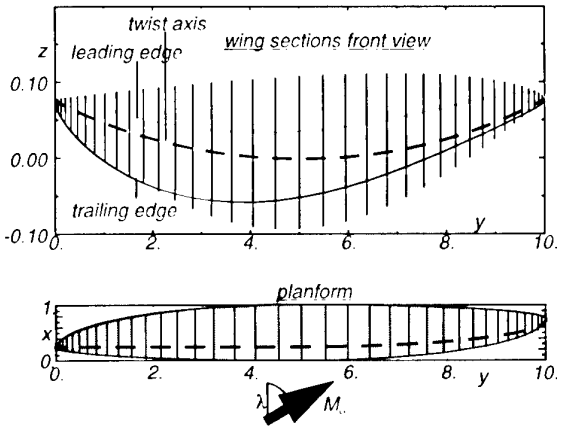


Fig. 6. Three-view of a generic OFW. Analytical wing section variation along span, paraboloic wing bending and asymmetric elliptic planform.



tively low supersonic Mach number of $M_\infty = 1.41$ at wing sweep of $\lambda = 60^o$ is illustrated in Fig. 6. Elements of the classical aerodynamic knowledge base for supersonic and transonic flows is applied here for selecting the suitable geometrical model functions:

Supersonic area rule, minimum drag body and elliptic load distribution along wing span is met by the shaping functions as well as the spanwise establishment of supercritical flow normal to the leading edge. Computational analysis with an Euler code at varying sweep angles and lift provides insight in the relation of optimum ratios of lift over drag to local flow quality like pressure distributions and the structure of the shock waves.

3.3 Components for multidisciplinary design optimization

The above example is an excellent test case for integrated predesign studies of aerodynamic, structural and economical performance: The known excellent aerodynamics of an OFW and the favorable structural conditions, - lift is produced where load is located, - invite to include models of internal structures like the wing box, room for passengers, cargo and fuel within the wing: constraints of minimum height defined by passenger size set wing chord and wing span as a function of passenger number. Thus the optimization of projected DOC may start using model geometries like those presented here, with extensions for the internal structure by 'box' models (Fig. 7).

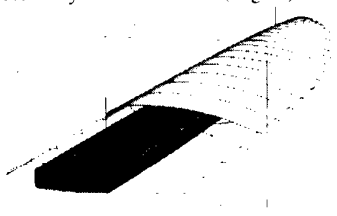


Fig. 7. Box model of internal structures

The same tool is useful for the definition of boundary conditions of the combined flux problem of turbine blade flow, heat transfer and coolant flow within the turbine blade (see ref. [12]) if a number of internal coolant passages is shaped using the box model.

The addition of geometry components for control surfaces and high lift devices for creating boundary conditions for low speed flight and flight stability simulation is an important addition to all aircraft shape models. The software outlined in this paper is being extended to include a multicomponent flap system and a slat, for high speed applications also simple sealed slat and flap surface models, as illustrated in Fig. 8. Some first studies with droop nose airfoils in unsteady flow have been carried out [13].

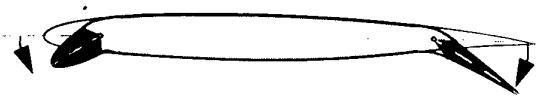


Fig. 8. Variable camber sealed slat and flap simulated by rotating a part of the wing geometry and connecting with elastic surface model

Aircraft fins are created using the wing tool, engines may be modelled by both the wing tool and as body definition. These parts almost complete the configurations as illustrated for the HSCT (Fig. 5) and the OFW (Fig. 9).

Conclusion

Software for supersonic generic configurations has been developed to support the design requirements in high speed aerodynamics and which should allow extensions for multidisciplinary design considerations. Based on simple, explicit algebra a set of flexible model functions is

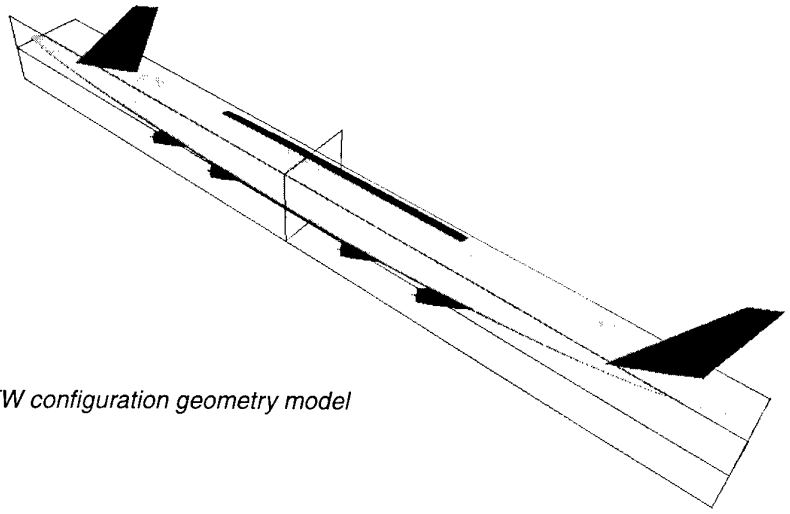


Fig. 9. Complete OFW configuration geometry model

used for curve and surface design which is tailored to create realistic airplanes or their components with various surface grid metrics. The explicit and non-iterative calculation of surface data sets make this tool extremely rapid and this way suitable for generating series of configurations in optimization cycles. The designer has control over parameter variations and builds up a knowledge base about the role of these parameters for flow quality and aerodynamic performance coefficients. Some basic gasdynamic relations describing supersonic flow phenomena in 2 or 3 dimensions have become guides to select key functions in the shape design; these and other model functions allow for the gradual development of our design experience if the generic configurations are used as boundary conditions for numerical analysis. With a number of efficient tools available now, the combination to an interactive design system for not only aerodynamic but also multidisciplinary optimization seems feasible.

References

[1] Sobieczky, H., (Ed.): New Design Concepts for High Speed Air Transport. CISM Courses and Lectures Vol. 366. ISBN 3-211-82815-X Springer Verlag Wien New York (1997)

[2] Sobieczky, H.: Gasdynamic Knowledge Base for High Speed Flow Modelling. Chapter 7 in Ref. 1, pp.105-120

[3] Sobieczky, H.: Configurations with Specified Shock Waves. Chapter 8 in Ref. 1, pp.121-136

[4] Sobieczky, H.: Geometry Generator for CFD and Applied Aerodynamics. Chapter 9 in Ref. 1, pp.137-158

[5] Cosentino, G. B., Holst, T. L.: Numerical Optimization Design of Advanced Transonic Wing Configurations. J. Aircraft, Vol. 23, pp 192-199, (1986)

[6] Sobieczky, H.: Parametric Airfoils and Wings. Notes on Num. Fluid Mechanics, Vol..., K. Fujii and G. S. Dulikravich (Eds.), Vieweg, to be published 1998

[7] Sobieczky, H.: Configuration Test Cases for Aircraft Wing Root Design and Optimization. Proc. 2. Int. Symp. Inverse Problems, M. Tanaka (Ed.) Elsevier Science, (1998)

[8] Sobieczky, H.: Geometry for Theoretical, Applied and Educational Fluid Dynamics. In: D. Caughey, M. Hafez, (Eds.), Frontiers of Computational Fluid Dynamics, John Wiley & Sons Ltd. (1997)

[9] Kulfan, R.: High Speed Civil Transport Opportunities, Challenges and Technology Needs. Taiwan IAA 34th National Conference, (1992)

[10] Van der Velden, A.: The Oblique Flying Wing Transport. Chapter 19 in Ref. 1, pp.105-120

[11] Li, P., Seebass, R., Sobieczky, H.: Manual Optimization of an Oblique Flying Wing. AIAA 98-0598, (1998).

[12] Dulikravich, G. S.: Thermal Inverse Design and Optimization. Chapter 13 in Ref. 1, pp.201-221

[13] Sobieczky, H., Geissler, W., Hannemann, M.: Numerical Tools for Unsteady Viscous Flow Control". Proc. 15th Int. Conf. on Num. Meth. in Fluid Dynamics. Lecture Notes in Physics, ed. K. W. Morton, Springer Verlag (1996)

IMPACT OF ENVIRONMENTAL ISSUES ON THE HIGH-SPEED CIVIL TRANSPORT

Allen H. Whitehead, Jr.
High-Speed Research Project Office
Environmental Impact Team
NASA Langley Research Center, MS/119
Hampton, Virginia 23665-5225, USA

SUMMARY

This paper provides an overview of the impact of environmental issues on the design and operation of the proposed High-Speed Civil Transport (HSCT). This proposal for a new generation commercial supersonic transport is being pursued by NASA and its U.S. industry partners in the NASA High-Speed Research (HSR) Program. A second related paper (Reference 1) describes the overall HSR Program, including a history of supersonic transport development that led to the present program, and a brief outline of the structure of the two-phase program and its management structure.

The specific objectives herein are to address the four major barrier environmental issues and show their impact on the design of the airplane and potentially, its mode of operation. A brief historical perspective shows how HSR Phase I addressed these environmental topics and, with the successful completion of that program, led to the successful advocacy for the Phase II effort that followed. The Phase II program elements were discussed in the earlier paper and addressed technology programs to enhance the economic viability of the HSCT.

Since many of the regulations that may effect the certification and operation of the HSCT are either not in place or well documented, a brief treatise is provided to address the status of the rules and the potential impact on the viability of the HSCT.

1.0 PROGRAM HISTORY AND BACKGROUND

1.1 Early Supersonic Transport Developments

The United States effort to produce a supersonic transport (SST) in the late 1960 time period was aborted in March 1971 when the U.S. Congress withdrew government funding for the project. As shown in Fig 1, the SST reached the full-scale mock up stage before cancellation. Both the Anglo-French and Soviet SST programs led to aircraft production and airline operations. While the TU-144 and Concorde prototypes were being flight tested, the U.S. SST Program was identifying formidable environmental and economic barriers to the successful introduction of the aircraft. The environmental issues included airport community noise, stratospheric ozone depletion, sonic boom impact, and crew/passenger radiation exposure. These environmental issues prompted extensive public discourse which ultimately led to diminished political support and the eventual cancellation of the US SST Program in March of 1971. In fact, the sonic boom issue resulted in the passage of a U.S. law prohibiting civil supersonic flights over the continental United States. Therefore, Concorde operations were relegated to those U.S. airports near the coastline to ensure that human and property exposure to sonic boom would be eliminated. Subsonic flight to reach inland cities would be allowed, but there is a huge economic disincentive for the Concorde to operate in that mode. Today, these environmental barriers must still be overcome for the successful development of a modern day supersonic commercial transport.

1.2 Environmental Technology Elements Within The HSR Program

Those four issues—noise, ozone depletion, sonic boom and atmospheric radiation—form the backdrop of the current HSR program organization. After the early market studies performed by Boeing and McDonnell Douglas, a clear message was delivered that there is a strong market potential for the HSCT. As seen in Fig 2, the elements of the HSR Phase I program addressed the environmental issues. A significant effort was also launched to address a technology with a lengthy maturation period, but with a huge potential payoff. The laminar flow control technology element will not be discussed in this paper other than to report that a very successful flight test program validated the potential benefits in aerodynamic performance. This technology could find its way onto a second generation HSCT if the specialized structural design and required subsystems are not series disincentives. Atmospheric radiation was not treated in Phase I, but was systematically addressed within Phase II.

By the end of the third year of the Phase I Program, substantial progress had been made in addressing the environmental barriers. These interim accomplishments are detailed in Fig. 3 and each will be discussed in detail in this paper. The first two accomplishments relate to the impact of engine emissions on the ozone layer. The atmospheric studies element supports the development of a set of independent models of the atmosphere which incorporate the basic chemistry and atmospheric transport of the exhaust products of the proposed HSCT. These models replicate the atmospheric processes that will predict the potential impact that the HSCT

Paper presented at the RTO AVT Course on "Fluid Dynamics Research on Supersonic Aircraft", held in Rhode-Saint-Genèse, Belgium, 25-29 May 1998, and published in RTO EN-4.

will have on the earth's ozone layer. The most pernicious exhaust ingredient in this regard is nitrogen oxide (NOx). In HSR Phase I, two competing engine combustor designs evolved which had the potential for delivering ultra-low levels of nitrogen oxide. The accomplishment was related to the successful demonstration of the NOx goal in a small-scale laboratory environment.

While significant progress was made in Phase I in reducing the propulsion noise, the airplane still needed additional noise reduction to achieve the challenging community noise goals. Additional reduction therefore has to be achieved through improved low-speed performance and advanced operational procedures. Within the sonic boom element, low-boom aerodynamic design methods were developed, tested and validated to show the degree of boom impact reduction that could be achieved. Since configuration shaping to reduce the boom comes at the expense of aerodynamic performance, these Phase I results set the stage for an early decision to eliminate supersonic overland flight. Market projections show that up to 15% of the projected route structure is overland which will dictate a requirement for reasonable performance at transonic speeds.

During the early stages of preparing for the second phase of the HSR Program dealing with economic viability, NASA had to convince the decision makers that sufficient progress had been made on the environmental barriers. The strategy to clearly focus on these barrier issues in a dedicated Phase I Program element was about to bring its reward. Not only was there demonstrable progress on the technology, but it was clear that the HSR team had properly addressed the politically sensitive issues that brought the original SST to a premature close. Phase II was officially approved at a budget line of around $1.6 billion (Fig 2).

In the discussion that follows, each of the four environmental areas will be addressed independently. Within each section, the HSR program goal will be defined and progress against that goal will be described. The outlook and status of regulations and proposed rule-making that impacts each environmental issue will be presented.

2.0 COMMUNITY NOISE

2.1 Noise Goals

The noise issues associated with the development of a supersonic transport bring a complex set of technical challenges to the design table. Before the designers can begin their work, however, noise goals must be established to guide both propulsion component design and airplane configuration evolution.

There is first a vexing question of "how much noise reduction is enough?" To begin the response to that question, one must both address the certification rules and potential community response. Noise certification rules are established in the United States through the Federal Aviation Regulations (FAR); the chapter applicable to noise levels of jet transports is Part 36 of the FAR. Any transport airplane introduced in the time frame for the HSCT introduction will have to meet noise criteria established by "FAR 36 Stage 3." The stage notation refers to successive levels of increased noise stringency that have been imposed on aviation. There is one school of thought that a "Stage 4" stringency could be imposed shortly after the turn of the century.

The certification procedure is a one-time event administered in this country by the Federal Aviation Administration (FAA). The current HSCT design concept has demonstrated levels of noise reduction that offer high confidence that FAR 36 Stage 3 certification can be achieved. However, this level of reduction will not satisfy the day to day community noise concerns. To ensure that the HSCT blends in at major international airports, noise levels must be low enough to be compatible with subsonic transport operations. In Fig 4, we see the trend of noise level reduction for subsonic jets from 1960. The Concorde, operating on noise waivers with its Olympus turbojet engines, exceeded sideline noise of its subsonic transport counterparts by about 20 dB! Subsequent supersonic propulsion technology developments made huge strides in noise reduction, but the parallel progress in noise reduction for subsonic transport turbofans established even more stringent goals for ensuring noise compatibility for the HSCT. As we see on Fig. 4, the HSCT goal is to achieve a noise level comparable to the noisiest large subsonic airliner in operation when the HSCT is introduced into service. The way to characterize this goal for the HSCT design community is with reference to the three certification stations. The goal is thus defined as 1 dB below the FAR 36, Stage 3 at the sideline and approach measuring stations, and 5 dB below the takeoff station (in the parlance of the HSR program, -1, -5, -1). The impact of this noise reduction challenge is best observed by noting that a 10 dB reduction is equivalent to reducing by one-half the noise perceived by the observer.

2.2 Airport Noise Compatibility

As with many environmental issues, we are dealing with the vagaries of "community tolerance" in defining margins of acceptability. The best strategy is to keep the HSCT noise 'footprint' within the same bounds as the subsonic transports operating from the same airports. In Fig. 5, the protocol followed for the one-time certification process is defined at the bottom of the chart, where noise data are recorded at the three monitoring stations located with reference to the runway. To

address the impact on the community, we must be concerned about the on-going operation of the airplane well beyond the environs of the airport.

The Federal Aviation Administration does have a guideline which addresses this community noise issue. This guideline addresses land use issues in the vicinity of airports, and is a useful technique to assess potential impact for the introduction of the HSCT into a selected airport. The FAA guide determines possible impact for new aircraft types or increased number of operations by employing a metric which generates noise contours from airport operations data (Ldn = Level day-night). The guideline asserts that if the proposed action would result in greater than a 17% increase in the 65 Ldn contour area, then further intense study of the proposal could be imposed. In Fig 6, the 65 Ldn boundary is depicted for the John F. Kennedy airport. Using the 17% growth area as a threshold limitation, a series of airport trade studies were initiated to determine a first-order relationship between various levels of assumed noise stringency for the HSCT and the number of projected operations from the airport. The outcome of the study is shown on the right of Fig 6 where relative cutback (i.e., takeoff) noise is plotted against fleet size for the JFK and Seattle/Tacoma airports. Since this metric integrates the number of operations from an airport, this guideline could ostensibly establish a potential limit on the HSCT fleet size.

2.3 System Integration Approach to Noise Reduction

HSCT noise reduction is a classical aircraft systems problem with highly coupled components; for example, the nozzle noise suppression effectiveness is dependent upon the flow conditions presented by the engine. Noise reduction strategies involve design innovation for most of the engine/nacelle components—fan, inlet, core and nozzle. Before the propulsion system can be optimized for noise reduction (and performance), the designer must understand and properly characterize the noise sources associated with the propulsion system components. A simplified illustration of these noise sources is presented in Fig 7 for the low bypass ratio engine applicable to supersonic transports and, in comparison, for the high bypass ratio engines typically employed on today's subsonic jets. The shape of the source noise envelope is representative of the magnitude and direction of the acoustic radiation pattern. With proper engine design and integration with the configuration and its flight envelope, jet shock noise will be minimized. The dominant noise source contribution for supersonic propulsion is the jet mixing noise which will be addressed below. Turbomachinery noise sources from the compressor, fan and turbine will play a contributing role in the approach condition. There are other noise sources such as airframe and combustor noise which play a lessor role and are not a major part of the HSR technology development.

In the early phase of HSR Phase II, a whole family of propulsion concepts and engine cycles were evaluated (Fig 8). Achieving the required noise reduction without undue loss in engine performance continues to be a major challenge in the propulsion program. The figure illustrates the strong influence that cycle selection has on exhaust velocity and, therefore, jet noise level. The HSR team evaluated two approaches to the problem. One was a variable-cycle engine, with valves that would divert the airflow around the compressor at subsonic speeds. That class of engine is representative of the low exhaust velocity concepts on Fig 8 such as the Inverted Flow Valve (IFV) engine. The noise reduction benefit comes at the expense of a more complex, higher risk design with highly loaded moving parts subjected to high temperatures. The second alternative was a compromise cycle called the mixed-flow turbofan which has been selected for the HSR technology development. Although this cycle does have a moderate bypass ratio to slow the jet flow, a mixer-ejector nozzle must also be included to provide most of the jet noise reduction. This nozzle entrains outside freestream air which is mixed with the hot-core jet exhaust to slow and cool the exhaust jet that reduces noise by about 16 dB. During supersonic cruise, external air entrainment is not required, so the ejector doors are closed to eliminate this source of drag. Small-scale nozzle wind-tunnel tests of the current HSCT nozzle design concept have demonstrated the projected level of noise attenuation while still meeting performance requirements. As discussed in Ref. 1, to keep nozzle weight at a minimum, advanced materials and manufacturing processes are being developed including thin wall castings of superalloys for the mixer, gamma titanium aluminides for the flap, ceramic matrix composite acoustic tiles for reducing mixing noise, and thermal blankets to protect the nozzle backside materials.

During approach and landing, the engines are throttled back and have reduced jet velocity and, in this phase of the flight envelope, turbomachinery noise is a key contributor to overall aircraft noise. To address this environmental compatibility challenge, NASA and industry are looking at both mixed compression inlet and low-noise fan concepts. Mach 2.4 operation requires a mixed compression inlet for efficient propulsion system operation where the shock structure is managed both externally and internally. Stability, high-recovery, and low distortion in the inlet must be balanced with low-noise, operability, and complexity. Two-dimensional bifurcated, axisymmetric translating centerbody and variable diameter centerbody inlets were considered and, as discussed in Ref. 1, the HSR team chose the bifurcated design.

As discussed in the previous section, the noise reduction challenge requires that the HSCT produce takeoff noise levels

that are 5 dB below certification requirements in order to provide compatibility with subsonic transports under the takeoff flight path. HSR study results have indicated that the final solution to the problem demands contributions to noise reduction beyond the propulsion system. Several of these sources are listed in Fig 9 and include the high-lift system and advanced operational procedures. Noise reduction can be achieved with high-lift leading and trailing edge wing systems which reduce thrust required for takeoff, climbout, and landing. These advanced high-lift concepts when combined with advanced landing and takeoff procedures such as automatic flap and throttle settings, more than double the low-speed lift-to-drag ratio relative to the Concorde

The December 1996 HSR Technology HSCT Baseline shown in Fig. 10 achieved an interim noise reduction of 3 dB below FAR 36, Stage 3 at a airplane weight penalty of about 4%; this was still 2 dB short of the HSR goal. One approach that was evaluated to achieve the remaining 2 dB reduction was to continue to oversize the engine. The airplane can reflect the benefit of the larger engine by reducing jet exit velocity and the associated jet noise at takeoff, or by increasing altitude during takeoff which increases the distance between the noise source and the ground observer. The latter application provides the largest benefit for the HSCT, but the weight penalty associated with this strategy will move the airplane into a region of unacceptable economics. The most effective strategy for achieving this additional noise reduction increment for this baseline configuration was to increase low-speed aerodynamic performance by a change in airplane wing aspect ratio. The yellow band in the chart shows the dramatic change in the weight trend for achieving the noise goal through planform change as compared to the engine oversize option.

2.4 Noise Prediction Methods

As with any advanced technology development program, a major component of the HSR program is the development and validation of the prediction tools. For noise prediction, each of the HSCT noise sources identified in Fig. 7 must be modeling and incorporated into an executive routine to calculate total configuration noise level. The individual source routines require a substantiating database for calibration and validation. For jet noise, for example, a major acoustic test program is underway to improve acoustic prediction confidence (Fig. 11). A series of mixer-ejector nozzle tests have been completed at one-seventh scale. The LSM, or large scale model, tests will step up the model scale and confidence for predicting product design acoustic levels.

Another noise test program contributed to the assessment of the climb-to-cruise acoustic prediction (Fig. 12). As shown in the insert on the top of the figure, there was a large disparity from two available codes in the noise prediction for the climb noise up to 70 miles from brake release. There simply was no data for these flight conditions and this class of engine, so the codes were well beyond their range of validity. To remedy this situation, a flight test was conducted at NASA's Dryden Flight Research Center using a modified F-15 aircraft. The data will also contribute to enhanced prediction techniques for ground attenuation. The test was completed last year, and the data is currently being analyzed prior to incorporation into the prediction codes.

2.5 Status of Noise Regulation Activity

Noise rule-making is a complex process involving a number of different types of organizations that cross international boundaries. Some of these entities are advocacy groups that lobby specific positions in the early stages of a regulatory activity. Other groups focus on the generation of data, trade studies and the preparation of position papers on focused issues. The international authorities charged with decisions on noise rules are identified at the top of Fig. 13. This chart presents a simplified diagram identifying many of the critical participants in the regulatory process and shows the interrelationships that promote the flow of data, information and opinions on regulatory issues. In particular, the chart includes a special SST Task Group under the ICAO Working Group 1, which provides a focus in the international arena for preliminary discussions on certification issues for the HSCT.

The three primary organizations are the FAA for the United States, the JAA (Joint Aviation Authorities) for Europe and ICAO (International Civil Aviation Organization). The United States, individual member states from the JAA, and other ICAO member states participate in ICAO's Committee on Aviation Environmental Protection (CAEP) working groups and subgroups to formulate recommended international noise standards which can be adopted as regulations by the United States, the JAA and many of the other ICAO member states. These CAEP groups and subgroups consist of representatives from 16 ICAO member states (Singapore joined in 1997) and industry lobby groups such as aircraft manufacturers, airline operators and airports.

The development of a supersonic aircraft noise standard has commenced in the ICAO-SST Task group. Two tasks have been initiated as follows:

> SST-1: (1) Identification of noise reduction technologies unique to future SSTs; and (2) estimated noise benefits at the certification conditions associated with future SST airplanes.
>
> SST-2: (1) A listing of the Annex 16 sections that are appropriate for future SST airplane designs; (2) a listing of the Annex 16 sections that should be considered for modification due to the unique technologies involved (e.g. automated flight

procedures) and (3) consideration of any new section for Annex 16 appropriate to unique technologies involved.

The SST-1 task was completed at the end January 1998 and current projections are that SST-2 task will be completed by the end of 1998.

The HSR Program will be afforded the opportunity to contribute to the supersonic transport noise rule-making discussions through a newly organized Environmental Impact Certification Issues Coordination Team (CICT). This group is chartered through an agreement between NASA and the FAA and includes industry participation. One of the group's prime functions is to

> "Identify, evaluate, catalogue, and prioritize airworthiness issues originating from new or unique HSR noise reduction technology that could warrant new certification procedures or otherwise influence standards which must be addressed for successful noise certification of the HSCT. Provide a forum for the review of technology information which contributes to this objective."

In all likelihood, there will be much more emphasis on subsonic aircraft within the regulatory community for developing cruise emissions rules and establishing increased noise stringency. Supersonic aircraft will be impacted by any decisions that evolve from these deliberations for subsonic transport aircraft.

3.0 ATMOSPHERIC IMPACT AND EMISSIONS REDUCTION

3.1 Background

The most publicized environmental concern about supersonic flight is the depletion of stratospheric ozone. Dr. Harold Johnston led a group of atmospheric scientists in the SST Congressional hearings in the early 1970's that raised the issue of the Earth's ozone shield to a global concern.

Ultraviolet rays break down stratospheric ozone into molecular and atomic oxygen. These molecules are later reunited in a reaction that forms new ozone that maintains a sufficient layer to protect the Earth from ultraviolet rays. The HSCT cruises at a nominal 60,000 feet which closely corresponds to the location of the maximum density of the earth's protective ozone layer. The nitrogen oxides emitted by the HSCT exhaust system break down through a photolysis process initiated by ultraviolet rays, and subsequently ozone is converted to molecular oxygen.

3.2 Atmospheric Modeling

The Atmospheric Effects of Stratospheric Aircraft (AESA) element was formed in Phase I of the High-Speed Research Program to address the ozone issue. An excellent summary of the most recent atmospheric assessment can be found in Ref. 2. Under this program element, an international team of scientists has applied global atmospheric models to predict the impact of nitrogen oxides, water vapor, and other exhaust emissions on ozone chemistry and climate change. The model results show that the amount of stratospheric ozone is determined by photochemical production and loss processes and by the transport of air throughout the atmosphere.

The AESA program task flow in Fig 14 displays how the inputs are created and fed into the transport models. The emission properties for the assumed HSCT engine are defined as a ratio of grams of each major exhaust constituent divided by kilograms of fuel consumed. Constituents of importance to the models include carbon monoxide and carbon dioxide, water, nitrogen oxide, and sulfur dioxide. The next step is to develop the operational scenarios that define how the HSCT flies within a simulated airline route structure. City pairs are identified and the number of flights between each city is calculated. Based on the characteristics of the particular HSCT design concept and the properties of its propulsion system, fuel burn and emissions are calculated for each city pair flight. These data are then summed to produce the emission inventory for the fleet. For the final data insertion into the models, the emission products are placed into cells defined by a 1° longitude by 1° latitude by 1 km altitude grid.

These 2- and 3-dimensional photochemical transport models are being calibrated through laboratory chemical kinetics tests and atmospheric observations (Fig 14). A converted U-2 spy plane called the ER-2 and balloons are providing global coverage to identify photochemical, radiative, and dynamic features of the stratosphere. The ER-2 has also been used to sniff the exhaust of the Concorde providing valuable data for near-field atmospheric interactions (Fig 15). Those data held a surprise for the research team in that the number of soot and sulfur particles was far higher than anticipated. These results emphasize the importance of proper characterization and understanding of the potential changes in aerosol chemistry due to these exhaust products.

3.3 Emissions Goal

During the early phase of the HSR program before any detailed propulsion components were designed or tested, the planning team assumed a range of tolerable emission levels. The goal was defined in terms of an NOx emission index (EI), defined as the ratio of the grams of NOx emitted by an HSCT at cruise altitude divided by the kilograms of fuel consumed.

The allowed range of values for this parameter at the initiation of the program was EI = 3 to 8. The stated program goal is that the airplane will have no significant impact on the ozone layer.

After the early results from the atmospheric studies were evaluated, the emissions goal was further narrowed. These emissions are developed during the fuel burn process, so the emissions index goal directly impacts the design of the one of the major propulsion components—the combustor. Fig. 16 presents a set of those early model results in which steady state ozone loss is plotted against annual production of NOx from projected HSCT operations. The bands represent the variations produced by the five independent atmospheric models that were a part of the AESA program. The chart shows two parametric variations of ozone depletion, one for an EI = 10 and another for EI = 5. Clearly, the higher value of the emissions index produces an unacceptable level of ozone loss for a reasonable fleet size. With these results in hand, the combustor emissions design goal was established at an EI = 5. The number of HSCT aircraft in the operational fleet is also a large factor; variations in projected levels of ozone loss are shown for fleet sizes of 500 and 1000 airplanes. This assessment thereby identifies a second environmental issue which could constrain fleet size.

3.4 Combustor Design Challenge and Current Status

To place this design challenge for the combustor in perspective, the Concorde generates a value of this NOx emissions index around 20. If the HSCT employed this type of conventional combustor design at the higher operating temperatures associated with Mach 2.4 cruise speeds, the value of EI would be driven to 35 or 40. The high level of NOx emissions from a current combustor design concept is attributed to fuel burn near stoichiometric air-to-fuel ratios; the key to reduced combustor emissions is to burn either fuel-rich or fuel-lean. Two alternative design options for achieving this objective are presented in Fig 17. One concept is a two-stage combustor design called rich burn, quick quench, lean burn design where fuel is initially burned rich, air is then added, and the products are burned lean. The challenge for this RQL design is an efficient mixing process to quickly quench the rich-burned products.

The second concept is the pre-mixed, pre-vaporized lean burn combustor (LPP) where flame stability and hardware complexity dominate the research. The small insert on this figure shows the results from the on-going combustor test program. Both concepts were tested at lab scale in the flame tube laboratory at NASA Lewis Research Center, and the results were well within desirable limits of NOx. Moving up to sector scale, the initial results showed a wide range of EI variation, but more recently as the hardware was tuned and test techniques improved, the sector scale results also produced levels in the range of EI = 5.

For both combustor concepts, liner material is also a challenge because active cooling with air changes the mixing and chemistry that are critical for low NOx. Thus, ceramic matrix composites are the leading candidate materials for the 3500°F environment and 9000-hour life requirements. These composites have been demonstrated at design temperature and near mechanical load conditions using accelerated test techniques. The combustor concept will be downselected this year, and a full-scale annular combustor with the selected liner material will be tested for final technology demonstration.

As with the approach to achieve the most efficient noise reduction, characterizing and manipulating engine exhaust characteristics is a highly-coupled process. Changes in trace species undergo significant change within the engine downstream of the combustor; therefore, turbine and exhaust nozzle processes are a critical part of the determination of atmospheric impact.

3.5 Emissions Rule-Making and Regulatory Status

The only emission standards that currently exist for supersonic aircraft apply to the landing-takeoff cycle (International Civil Aviation Organization (ICAO) Annex 16). No cruise emission standard for supersonic or any other aircraft currently exists. The path to such a rule is not yet well defined. In general, these two steps are likely:

- An international assessment of the ozone impact of an HSCT fleet conducted by the United Nations Environmental Program (UNEP) and the World Meteorological Organization (WMO), with support from NASA, NOAA, and other federal agencies around the world. The climate impact will be assessed by the Intergovernmental Panel on Climate Change (IPCC) in parallel with the UNEP/WMO assessment.

- The development of a supersonic cruise emission standard by the ICAO Committee on Aviation Environmental Protection (CAEP) with implementation in the United States by the Federal Aviation Administration and in Europe by the JAA (Joint Aviation Authority).

The preliminary discussion of a supersonic cruise emission standard was begun in early 1977 within the ICAO-CAEP Working Group 3 on emissions. The focus was on the development of rule criteria and not on rule options. In the United States both the FAA and the EPA will be involved in the emissions rulemaking process. The EPA is responsible for promulgating new aircraft emissions standards under the Clean Air Act, while the FAA is responsible for

implementing them through Federal Aviation Regulations (FAR).

4.0 SONIC BOOM

4.1 Low-Boom Configuration Studies

The initial program objective in 1990 was to develop design methods that would minimize the sonic boom impact to allow supersonic operations over both land and water. Efforts were initiated to define low-boom configurations, to develop validated sonic boom prediction techniques and to quantify the effects on marine life and human population. The design effort did result in significantly reduced sonic boom pressure levels on the earth's surface, but there was also a reduction in aerodynamic performance. The objective in the sonic boom configuration development was to avoid the coalescence of the shock system into a full "N-wave" shape at the earth surface. Fig. 18 presents an early analysis for a Mach 2 cruise condition. The low-boom design was able to develop and maintain a modified ramp signature which reduces the sharp pressure rise associated with the intense startle effect from the boom. The resulting pressure traces indicate a drop in the overpressure perceived on the ground from about 2.5 psf for the conventional aerodynamic design to below 1 psf for the boom-configured design. Atmospheric conditions as well as factors related to the airplane size and weight and the location and speed of the airplane all influence the sonic boom impact on the observer.

In the early phase of the program, sonic boom prediction techniques were developed, refined and validated through wind tunnel and flight tests. One flight test result and a comparison with a computational code is shown in Fig. 19. The data were acquired by an aircraft trailing the SR-71 flown out of NASA's Dryden Flight Research Center. Data and theory have shown excellent correlation in the near field of the sonic boom.

4.2 Sonic Boom Acceptability Studies

At about the same time that these results were documented, a series of studies of human response to sonic booms were completed. The three year effort to define acceptability criteria is depicted in Fig. 20. The studies began with laboratory experiments utilizing a 'boom box'—a cinder-block construction with massive speakers built into the door. The test subject is exposed to a series of computer-generated sonic booms and is asked to assess them in terms of level of annoyance. The boom signature variations included overpressure, shock rise time and basic signature shape. These results allowed sonic boom signature characteristics to be related to human response and thus quantify the benefits of boom shaping and provide guidance to the configuration design.

A similar system was then set up in a home environment to extend this understanding and continue the evaluation in a more realistic environment. The participants were exposed to various combinations of boom level and frequency of occurrence programmed to occur during various periods of family activity. From this work, an exposure metric was developed similar to the Ldn noise metric.

The final phase of these studies involved surveys of populations living in areas routinely exposed to sonic booms produced by high performance military aircraft. These HSR surveys were undertaken because existing guidelines were based on limited sonic boom data. The results from the HSR survey shown in Fig. 21 produced an unanticipated level of annoyance associated with the ever-present sonic booms. To gain a perspective on these results, calculations are shown that are representative of the boom levels for the current HSCT and for the low-boom configuration produced earlier in the program. Even the low-boom configuration would highly annoy over 25% of the population. Clearly, the HSCT will not operate supersonically overland! At this point in the program, the decision was made to limit the supersonic operation of the HSCT only to the overwater routes.

4.3 Overwater Supersonic Flight Impact

The emphasis of the work on sonic boom impact was then dedicated to research on overwater supersonic flight effects, including such topics as boom penetration into water and impact on marine mammals and ocean-going vessels.

The limitation imposed by the avoidance of sonic booms over land masses means that all aspects of sonic boom propagation, including atmospheric conditions and maneuver effects must be understood in order to intelligently plan flight tracks for sonic boom mitigation. The occurrence of secondary booms caused by refraction of the primary boom by the atmosphere must also be considered as well as focused booms created during transonic acceleration. Analytical methods have been developed that define a boom 'carpet' on the earth's surface as a function of all of the important atmospheric and vehicle operating characteristics. Based on this work, a boom buffer has been defined which constrain the flight tracks available to the HSCT when operating near coastlines.

The sonic boom characteristics during supersonic cruise have been documented with high confidence for the current HSCT configuration. The level of severity is determined by the magnitude of the front and rear shock amplitudes. The boom levels vary from 2.5 to about 3.8 psf depending on the weight of the airplane (decreases with fuel consumption). In contrast, the amplitude of a focused sonic boom occurring near the beginning of the climb phase can reach 8 to 12 psf on the

ground dispersed over a relatively small area. Human exposure to this level of boom impact is to be avoided at all costs. A simple algorithm has been developed to predict the impact point of the focused boom as a function of speed, altitude, winds and temperature (Fig. 22). The flight deck suite of instrumentation will likely incorporate a device based on this algorithm to provide pilot guidance for avoiding adverse impact.

4.4 Marine Mammal Response

Four main areas of research associated with defining the sonic boom impact on marine mammals have been identified by bio-acoustic and oceanographic experts:

(1) Sonic boom propagation into water

An analytical effort to determine propagation of booms across an air-water interface has been completed to allow the characterization of the boom below the water surface. At the Mach 2.4 cruise condition, most of the energy within an impinging sonic boom is reflected at the surface. That result is displayed on the right of Fig. 22 where sound pressure level associated with the boom is plotted against frequency. At 15 feet underwater, the boom spectra is well below the audible hearing curves of pinnipeds and whales. There is therefore a minimal underwater impact of the HSCT boom on marine mammals. Tasks (3) and (4) address the situation where the marine mammal is at the water surface or beached.

(2) Location of marine mammal species

The current HSCT route structure has been examined to identify locations of potential concern for marine mammal impact. In particular, special attention has been given to endangered species regarding feeding and breeding grounds and migratory routes. Locations of endangered species that are of potential concern have been identified.

(3) Impact of sonic boom on pinnipeds - response and habituation

The first phase of a study to examine the effects of booms on seals has been completed by the Department of Zoological Research (Smithsonian). During January 1997, extensive behavioral data and limited physiological data were acquired for gray seals exposed to three booms per day, averaging 0.84 psf and as high as 2 psf. Based on detailed analyses of the behavioral data, the booms were found to have no effect on any of the studied variables such as beach count, frequency of nursing, frequency of aggression, locomotion, activity, etc. The second phase of this task is scheduled for completion in 1998. Harbor seals, which have significantly different behavioral characteristics relative to gray seals, will be studied during their breeding season in May through June 1998.

(4) Impact of sonic boom on pinniped - potential hearing damage

Marine biologists are determining the effects of simulated sonic booms on the hearing of a range of marine mammal species. Both behavioral and physiological methods are being used to measure hearing thresholds before and after exposure to a range of boom signatures. Encouraging results have been obtained for both methods of hearing damage assessment.

4.5 Status Of Sonic Boom Rule-Making Process

The U.S. Endangered Species Act (ESA) applies to both domestic and foreign activities that may affect marine mammals. It prohibits the "taking" of marine threatened or endangered species within U.S. territorial waters or on the high seas. In common parlance, the term "take" refers to killing, capturing, or seriously injuring an animal. In legal terms, however, "take" includes harassment as well. The Endangered Species Act defines harass as "an intentional or negligent act or omission which creates the likelihood of injury to wildlife by annoying it to such an extent as to significantly disrupt normal behavioral patterns which include, but are not limited to, breeding, feeding, or sheltering". The Marine Mammal Protection Act (MMPA) defines "take" to include restraint or detention, negligent or intentional operation of an aircraft or vessel in the vicinity of an animal and any negligent or intentional act that results in disturbing or molesting a marine mammal.

The ESA provisions apply to any endangered or threatened animal, whether terrestrial or marine. The Marine Mammal Protection Act (MMPA) applies only to marine mammals; its governance is overseen by a commission appointed by the executive branch of the U.S. Government, the Marine Mammal Commission. Any activity in U.S. waters or international waters that takes marine mammals is in violation of the MMPA.

For the HSCT, proponents must show that sonic booms will not kill, injure, or harass marine mammals nor threaten endangered wildlife. Marine mammal research sponsored by NASA would be permitted as scientific research on marine mammals, but HSCT flights might require a small take exemption. Because the HSCT will almost certainly take large numbers of animals over large areas, an ongoing effort to clarify the law would be beneficial. Scientific research permits have been issued to harass large numbers of marine mammals in cases where the harassment is unlikely to have significant effects, but such permits are a rarity and have been the subject of controversy in the past.

The National Marine Fisheries Service (NMFS) is responsible for the enforcement of the Endangered Species Act and the Marine Mammal Protection Act, both of which are of

potential importance to HSCT operations. To date an HSR team has made regular visits to the NMFS facility in Silver Spring, Maryland to brief the status of the HSR program and to describe the research effort underway to collect data on sonic boom effects on marine life. The main area of concern seems to be the harassment of marine mammals, an issue that may have to be addressed in an Environmental Impact Assessment prior to launching an HSCT program. NMFS staff emphasized the need for a timely environmental assessment, well in advance of program launch.

5.0 ATMOSPHERIC IONIZING RADIATION

5.1 Radiation Sources and Potential Impact

Atmospheric ionizing radiation incident on the earth's atmosphere is attributable to three sources: (1) ever present galactic cosmic rays with origin outside the solar system; (2) steady state solar-generated cosmic rays that are modulated in intensity by the 11-year solar cycle; and (3) transient solar particle events that are at times very intense events associated with solar activity lasting several hours to a few days. These high-energy subatomic particles collide with atoms of oxygen, nitrogen and other atmospheric constituents, which spawns additional subatomic particles. Although the galactic and solar radiation penetrating through the atmosphere to the ground is low in intensity, the intensity is more than two orders of magnitude greater at commercial aircraft altitudes (Fig 23). The atmosphere acts as a radiation shield, so the higher cruise altitude of the HSCT results in higher incident radiation on the aircraft hull than for the lower-flying subsonic transports.

Ionizing radiation produces chemically active radicals in biological tissues that can alter cell function or result in cell death. An assessment of the biological effects of ionizing radiation on passengers and crew of an HSCT is beyond the scope of the HSR program. There is a rich archival database on this subject. A recommended report which deals directly with radiation safety related to supersonic transports (Ref. 3) includes a discussion of these radiobiological issues.

5.2 Historical Background

In the mid-1970 time period, the Langley Research Center (LaRC) performed atmospheric radiation studies under the SST development program in which important ionizing radiation components were measured and extended by calculations to develop an atmospheric ionizing radiation (AIR) model. In that program the measured neutron spectrum was limited to less than 10 MeV by the available 1960-1970 instrumentation. Extension of the neutron spectrum to high energies was made using theoretical models. Theoretical models of solar particle events showed that potentially high exposures may occur on important high latitude routes but acceptable levels of exposure could be obtained if timely descent to subsonic altitudes could be made.

As a result of this background atmospheric radiation data and the knowledge of the higher expected exposures in high altitude flight, an assessment study was initiated by the government-chartered National Council on Radiation Protection (NCRP) in conjunction with the HSR Program. Those results were published in July 1995 and recommended the need for additional studies as follows:

1. Additional measurements of atmospheric ionizing radiation components with special emphasis on high energy neutrons
2. A survey of proton and neutron biological data on stochastic effects and developmental injury for evaluation of appropriate risk factors
3. Develop methods of avoidance of solar energetic particles, especially for flight above 60,000 ft
4. Develop an appropriate radiation protection philosophy and radiation protection guidelines for commercial flight transportation, especially at high altitudes of 50,000 to 80,000 ft

Clearly, these issues must be addressed before the HSCT goes into commercial service to ensure the safety of the crew and passengers. The HSR Program endorsed these NCRP findings and developed a radiation research program element addressing several of the major issues.

5.3 HSR Atmospheric Ionizing Radiation Program Element

The focused goal of this program element is to develop an improved AIR model to reduce uncertainties in the atmospheric radiation components by twenty percent or less to allow improved estimation of the associated health risks to passengers and crew. Special emphasis was given to the high-energy neutrons in the altitude range of 50,000 to 70,000 ft. The results will be expressed in terms of an environmental AIR model able to represent the ambient radiation components including important spectral and angular distributions which will allow evaluation of aircraft shielding properties and the geometry of the human body. The model must be capable of representing the atmospheric radiation levels globally as a function of solar cycle modulation. The model must furthermore be capable of evaluating radiation levels during solar particle event increases in near real time using data from available satellite systems to allow risk mitigation and flight planning in the case of a large solar event.

To provide a sound scientific basis for determining atmospheric radiation exposure at HSCT cruise altitude, the

HSR Program supported a dedicated flight test with a high-altitude aircraft. In situ measurements have been acquired to quantify the ionizing particle field components in the atmosphere as a function of latitude and longitude and at altitudes up to 70,000 feet. The flight test results will provide a database for refining and validating environmental radiation models. Following the development of the AIR model, studies of impact of radiation exposure limitations on crew utilization and impact on passengers (especially frequent flyers) can be made to assess the need of developing a specific philosophy to control exposures in HSCT operations.

5.4 ER-2 Flight Test

The centerpiece of this HSR program element was a flight test program for acquiring the database needed to resolve current uncertainties in the AIR model. Flight tests were conducted with the ER-2 aircraft based at NASA Ames' Moffett Field; the flight test program was completed in June 1997. The ER-2 is a derivative of the Lockheed U-2, a high-altitude reconnaissance airplane utilized for intelligence missions. A sketch of the airplane is presented in Fig. 24 along with a listing and location of the instrumentation payloads. The flight project was an international collaboration devised by the science team at NASA Langley and the Environmental Measurements Laboratory of the Department of Energy, and included 12 domestic and foreign laboratories. A total of 15 instruments were placed on board the aircraft including Bonner spheres, bubble detectors, ion chambers, and scintillation counters.

Six missions were flown along the flight tracks parallel and perpendicular to line of constant geomagnetic strength as described in Fig. 25. The data are currently being analyzed and evaluated. An experimental calibration of the detectors in a neutron beam facility at the Los Alamos Laboratory is planned prior to final release of the data.

5.5 Potential Impact on HSCT Crew and Passengers

The radiation environment and exposure associated with the HSCT is not only dependent on altitude, but is also significantly impacted by the longitude of the flight path. Annual fuel burn profiles for projected HSCT routes in Fig. 26 were developed to build the scenarios for the atmospheric model studies, and the result shows the heavy concentration of operations at the higher latitudes. The earth's magnetic field deflects a significant part of the incident radiation from the mid-region of the earth's surface. For those northern latitudes associated with the Atlantic and Pacific corridors, the HSCT will experience near-maximum levels of radiation—in fact, the right hand insert in Fig. 27 shows that dosage rates can be five time the level at the equator. This figure also provides a visual reference for a comparison in exposure for the subsonic jet cruising at 40,000 feet.

Radiation exposure estimates have been made by Wilson, et. al. for the HSCT for several international routes (Ref. 3). The three HSCT routes chosen for analysis in Fig. 28 pass through the north magnetic polar cap and are among the most exposed routes. The supersonic flight crew exposures in mSv (millisieverts) are compared in this figure to subsonic transports flying the same routes. The uncertainty bars are based on a set of assumptions outlined in Ref. 3; these uncertainties will be reduced once the data from the ER-2 flight tests are incorporated into the NASA Langley AIR code. For reference, a worse case single event from a solar flare is displayed. The solar event is not a discriminator between subsonic and supersonic transports because an evasive action to reduce altitude must be assumed for the HSCT to avoid potentially hazardous exposure. The results of this crew exposure estimate are displayed for three annual block hour assumptions (900 hours is a nominal assumption under current subsonic transport airline operations).

5.6 Status Of Regulatory Process For HSCT Radiation

Over the last few years European and Japanese aircrew representatives have expressed concern over health risks associated with the radiation level in commercial jet aircraft. These discussions attracted public interest for three reasons when the International Committee on Radiological Protection (ICRP) published their new recommendations:

- The quality factors of neutrons were increased with the consequence of higher dose estimates than before for commercial jet transports.
- Simultaneously, the dose limits were lowered and now approach the annual doses received by some aircrew members.
- For these reasons, aircrews were recommended to be considered as "occupationally exposed."

The recommended limits by the ICRP are shown on Fig. 28 where it is seen that even for the lowest block-hour assumption for HSCT operations at this latitude, crew radiation monitoring would be required. The 20 mSv per year limit would be exceeded for the highest block hour assumption.

The crews of commercial air transports are now classified as radiation workers by the EPA, the FAA, and the International Commission on Radiological Protection (ICRP). The significance of the radiation-worker classification is clouded somewhat because of the nature of the radiation sources and composition. Ground-based radiation workers are exposed to man-made nuclear radiation from x-rays or gamma rays; whereas, airborne radiation workers are exposed to the naturally occurring radiation from neutron and protons

encountered at high altitude from cosmic rays. Guideline exposure limits for radiation workers are higher than for the public. Ground-based radiation workers are protected by a battery of regulations requiring precise monitoring of exposures, maintenance of cumulative-exposure logs, counseling and reporting requirements to the regulatory authorities in the event of an accident. At this time there are no known mandatory regulations for airborne radiation workers; however, there are pending European regulations for subsonic aircraft that may take effect as early as 2000.

In summary, aviation crew members are reported to receive more radiation than any other occupationally exposed radiation workers who are protected by a myriad of governing regulations. There are no protective laws in effect for aircrews at this time. This situation will most likely change for the subsonic fleet when the European regulations are imposed. Supersonic aircraft will have to respond to any such future regulatory provisions and, in addition, must deal with the additional issue of intense radiation pulses from solar flare events.

6.0 SUMMARY

This paper has addressed the impact of four environmental issues on the design, economics and program risk for the High-Speed Civil Transport. The following general comments are drawn from the work accomplished to date:

- Noise and Emissions
  - DO impact airplane and propulsion component design.
  - MAY impact flight profiles and flight corridors.
  - COULD dictate limits on fleet size.
- Sonic Boom and Ionizing Radiation
  - DO NOT impact HSCT design.
  - DO NOT appear to impose a significant environmental risk.
  - MAY require operational strategies and crew management to ensure community acceptance or regulatory compliance.
- Program risk will be impacted by:
  - Level of success in accomplishing HSR technology goals.
  - Reduction in prediction uncertainties through code validation.
  - Adoption of new regulations or increased stringency in existing noise or emission rules.

ACKNOWLEDGMENT

This paper is constructed around a series of presentation materials developed by the author and members of the HSR Environmental Impact team within NASA and at the Boeing Company. Additional sources included charts provided by personnel from the HSR Propulsion Program Office at NASA Lewis Research Center in Cleveland, Ohio. The author gratefully acknowledges the support from these sources. These charts and related background material overview the body of work accomplished within the HSR Phase I and Phase II programs from about 1990 to date.

REFERENCES

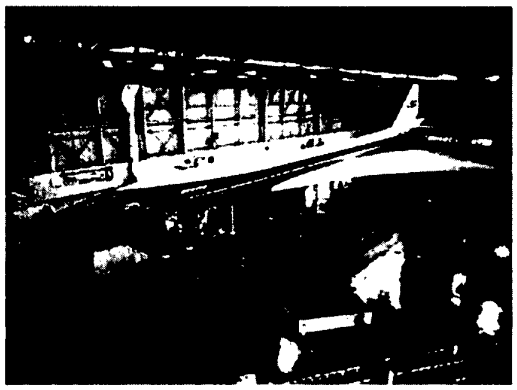
1. Whitehead, Allen H. Jr., "Status of NASA High-Speed Research Program", in RTO AVT/VKI Special Course on "Fluid Dynamics Research on Supersonic Aircraft", RTO Report R-833, June 1998.

2. Stolarski, Richard S., et. al., "1995 Scientific Assessment of the Atmospheric Effects of Stratospheric Aircraft", NASA Reference Publication 1381, November 1995.

3. Wilson, John W., et. al., "Radiation Safety Aspects of Commercial High-Speed Flight Transportation", NASA Technical Paper 3524, May 1995.

4. National Council on Radiation Protection and Measurements, "Radiation Exposure and High-Altitude Flight", NCRP Commentary No. 12, July 1995.

Boeing SST Full Scale Mock-Up



B-2707 Program Cancelled in March 1971

- **Community Noise**
  - Feasibility of economical compliance with certification and airport requirements
- **Stratospheric Ozone Depletion**
  - Predict HSCT ozone effects
  - Define feasible NOx reduction levels
  - Technical basis for accepability criteria
- **Sonic Boom Impact**
  - HSCT sonic boom predictions
  - Define feasible sonic boom reduction levels
  - Technical basis for acceptability criteria
- **Atmospheric Ionizing Radiation**
  - Assess high-altitude effects of radiation on passengers, crew and aircraft systems

Figure 1. Environmental impact on HSCT.

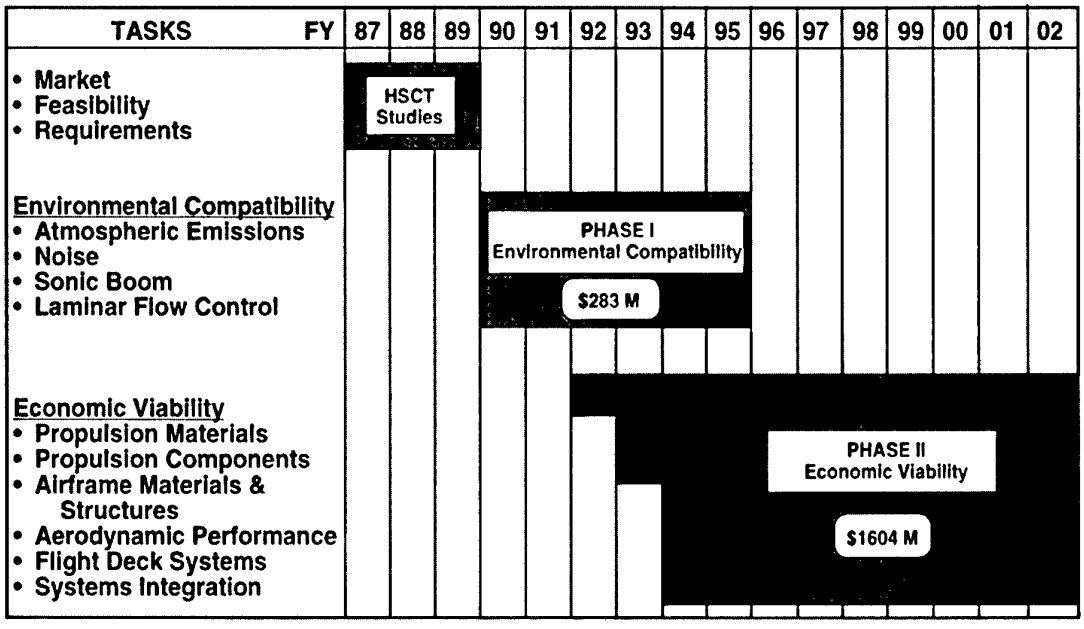


Figure 2. NASA/Industry High-Speed Research Program.

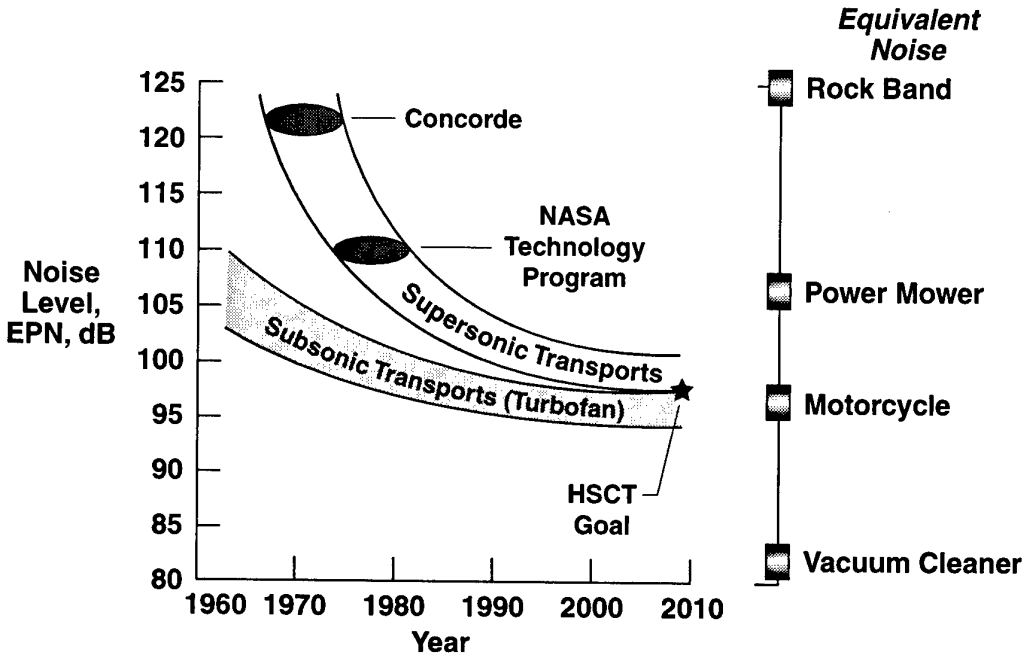


Figure 3. HSR Phase I progress.

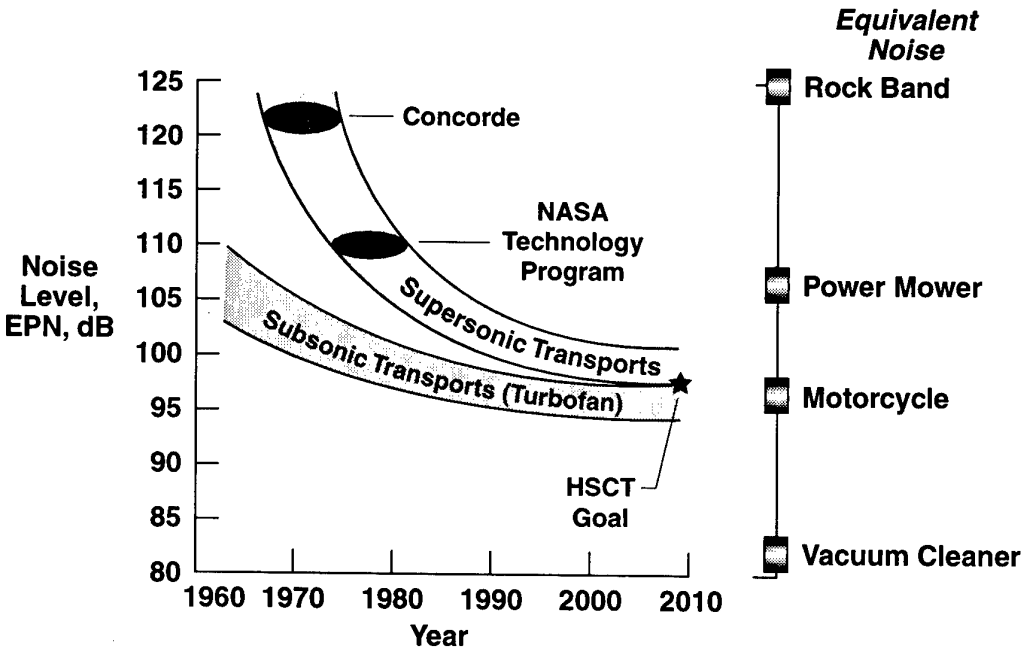


Figure 4. HSCT noise reduction challenge.

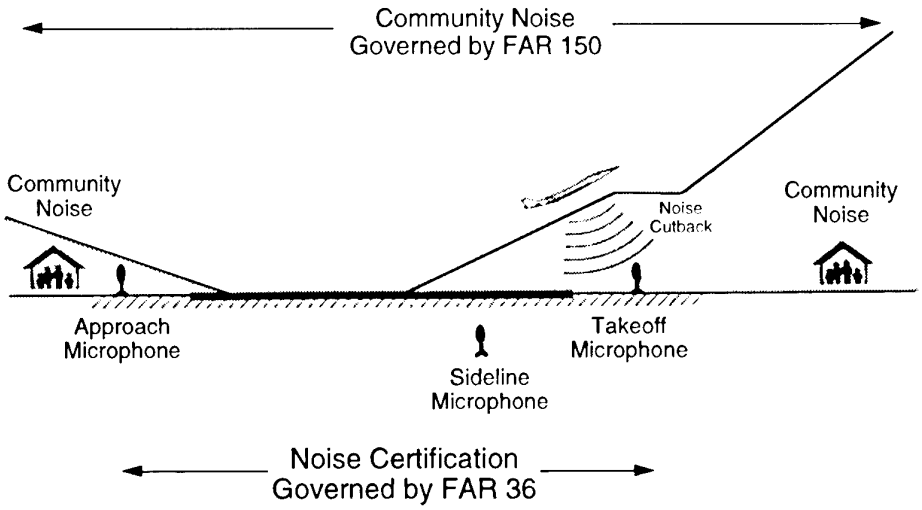
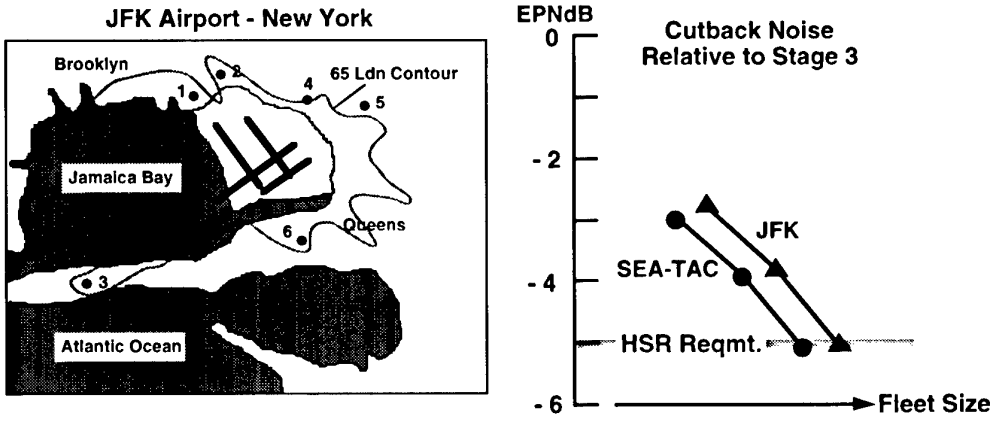


Figure 5. Noise regulations & guidelines.



Noise-Sensitive Area Analysis (FAA Guideline - FAR 150)
Recommends that if a change in aircraft operations produces more than a 17% growth in the 65 Ldn contour area, an impact statement may be required. Community points cannot exceed a 1.5 Ldn growth.

HSR airport noise studies have projected the growth of 65 Ldn contour area with assumed HSCT operations. The FAA guideline could establish potential limit on number of HSCT operations allowed at a given airport.

Figure 6. Airport noise compatibility.

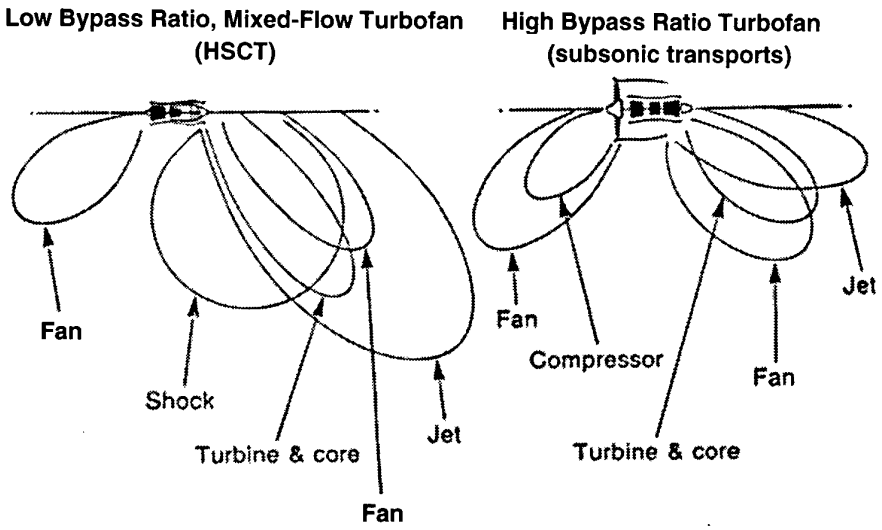


Figure 7. Engine noise sources.

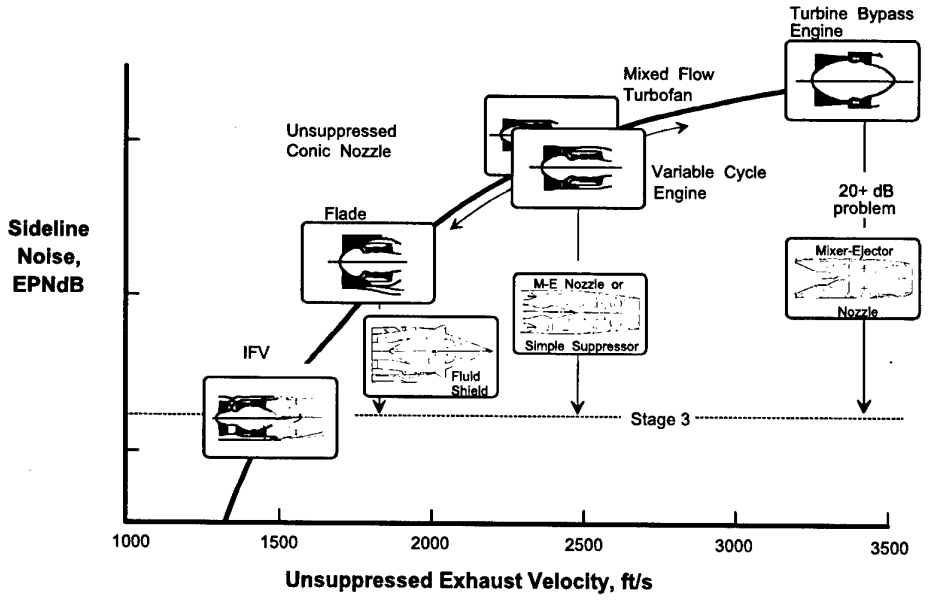


Figure 8. HSR propulsion system trades.

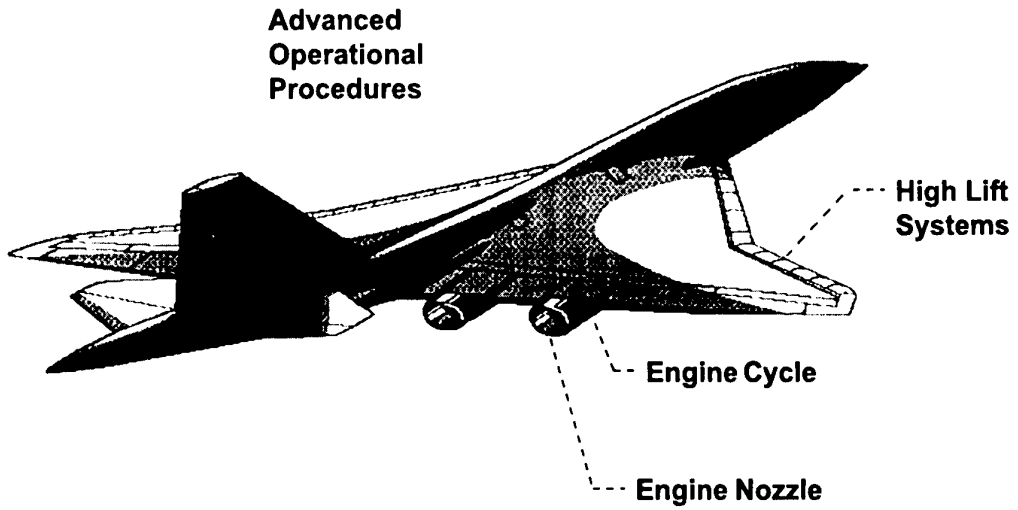


Figure 9. HSCT noise challenge.

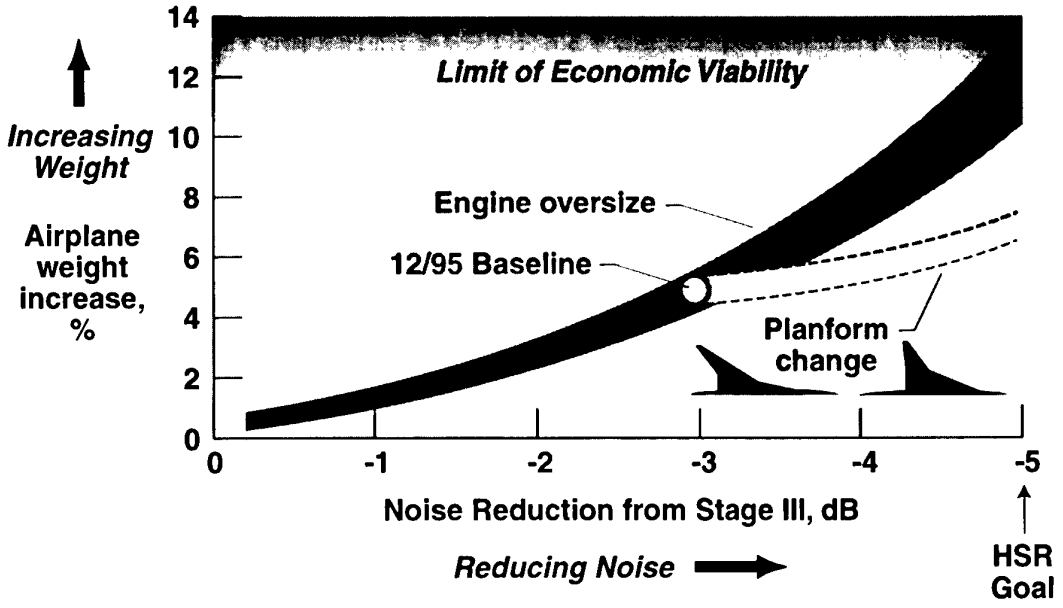


Figure 10. Community noise impact.

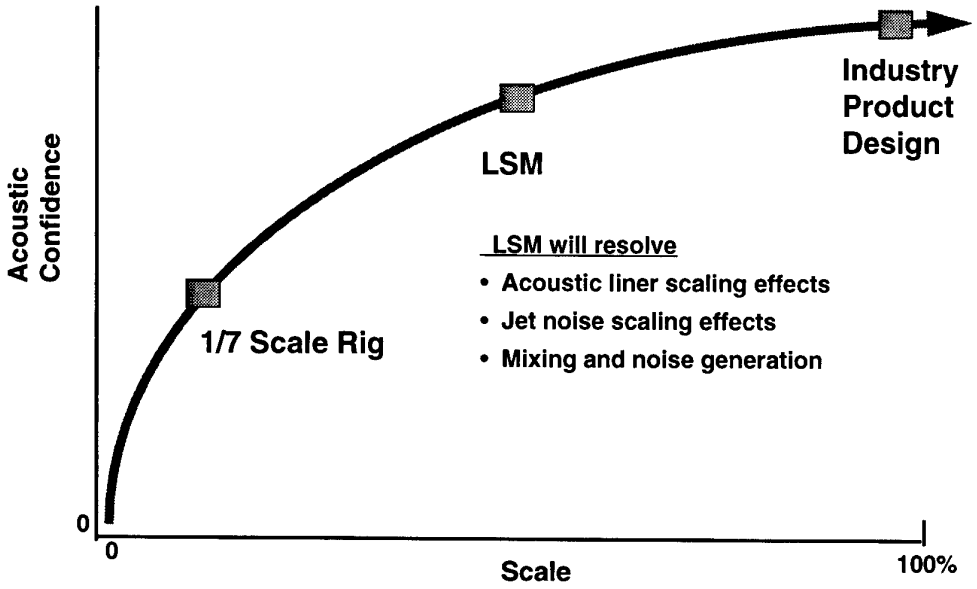
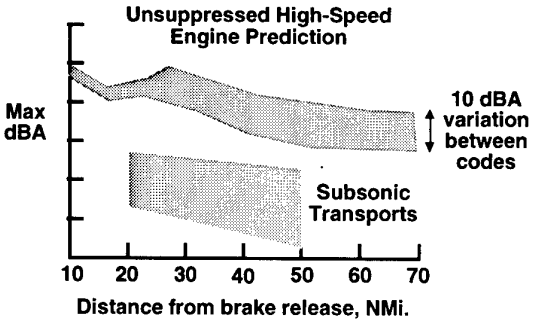


Figure 11. Large scale testing.





Test Objectives

- **Enhance and validate climb-to-cruise noise prediction codes**
- **Acquire a database for jet mixing and shock noise over a range of subsonic speeds**
- **Validate ground reflection codes**

Status

- **Successful completion of flight test program at Dryden Flight Research Center in 8/97.**
- **Data reduction and analysis underway; codes to be updated by end of FY.**

Figure 12. Improved noise prediction methods.

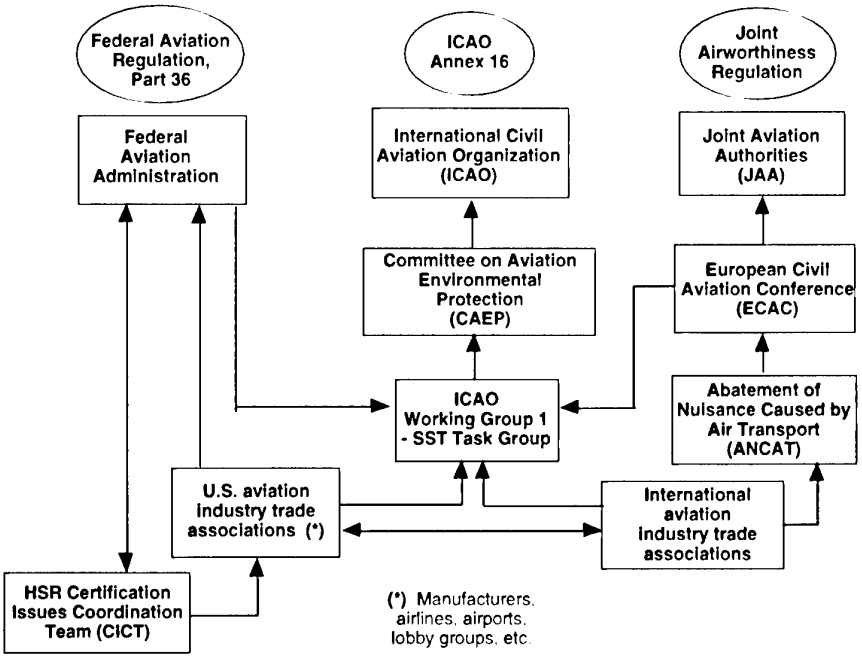


Figure 13. SST noise rule-making process.

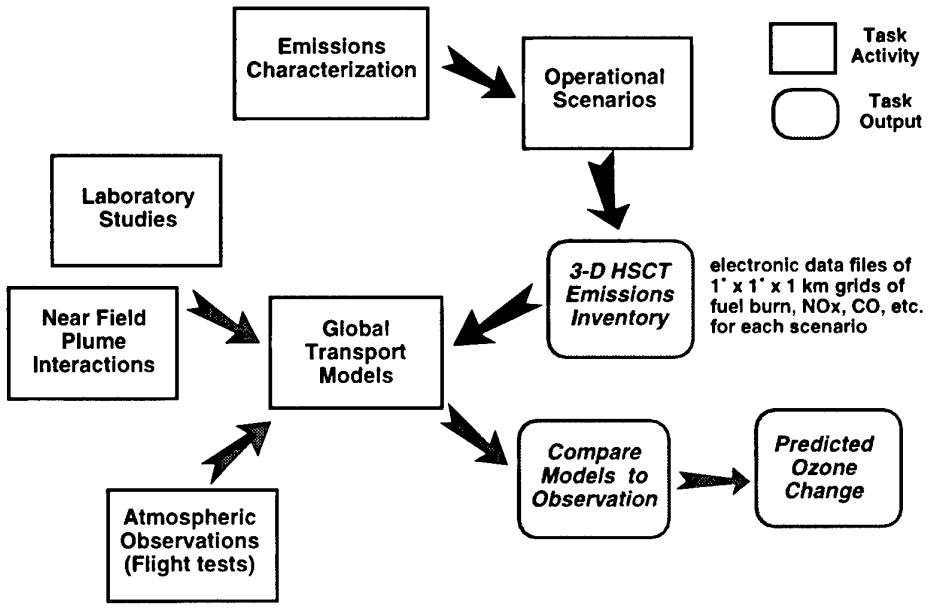


Figure 14. Atmospheric effects of stratospheric aircraft - task flow.

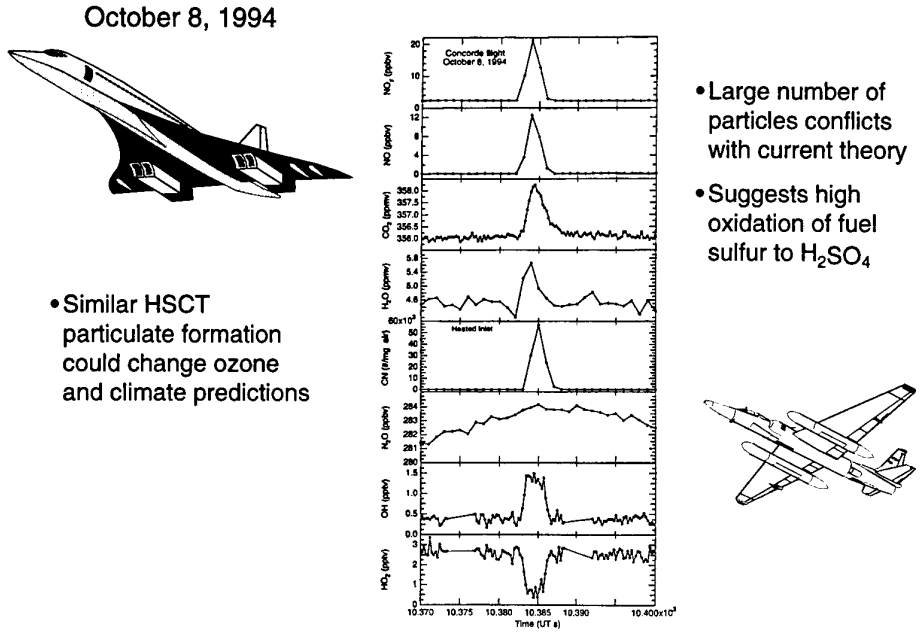


Figure 15. Concorde exhaust measurements.

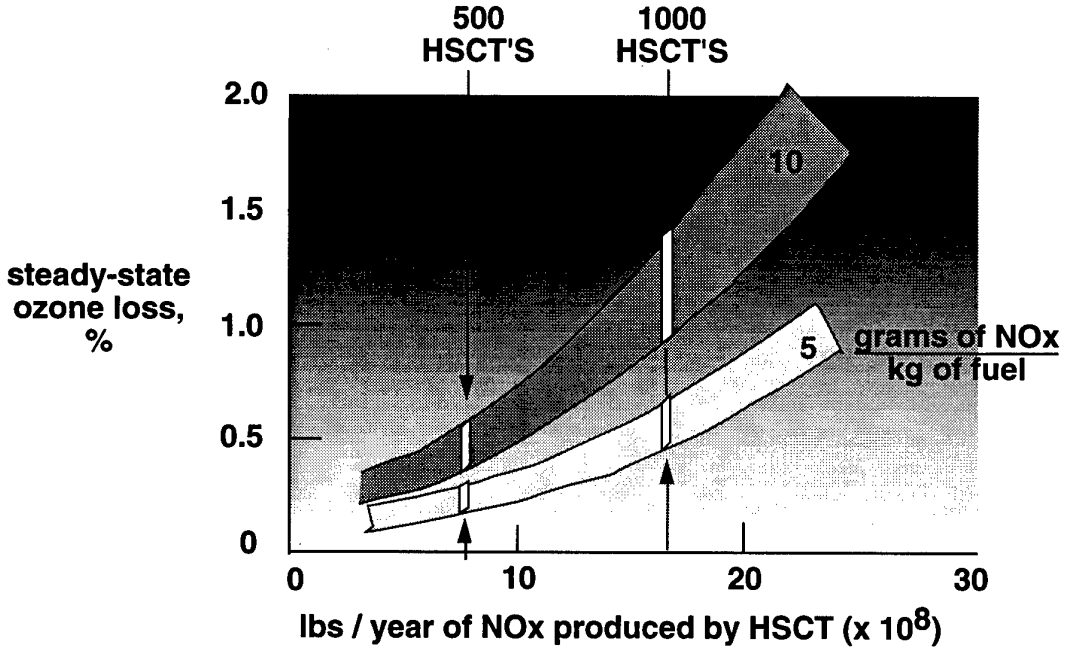


Figure 16. Potential HSCT impact on ozone.

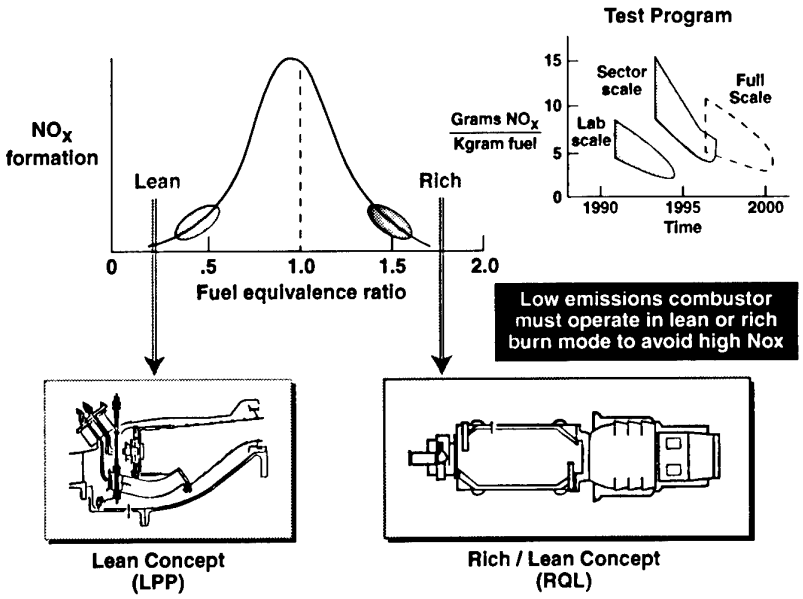


Figure 17. Low NOx combustor concepts.

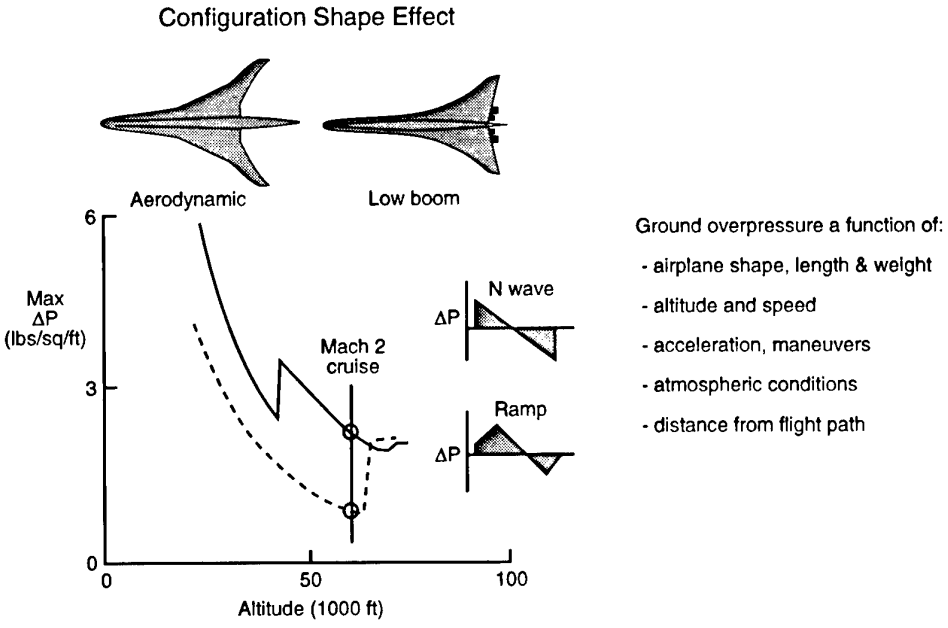


Figure 18. Sonic boom characteristics.

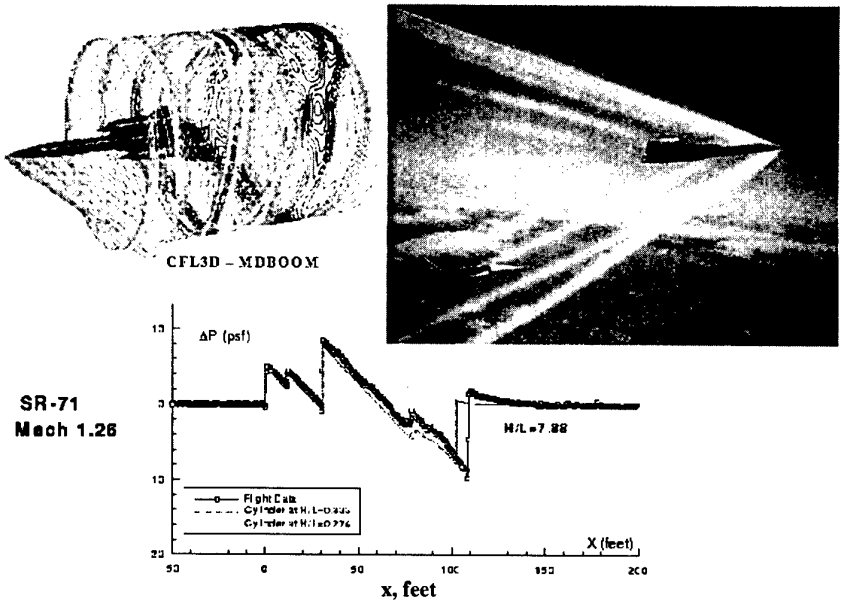


Figure 19. Sonic boom - flight test and CFD results.

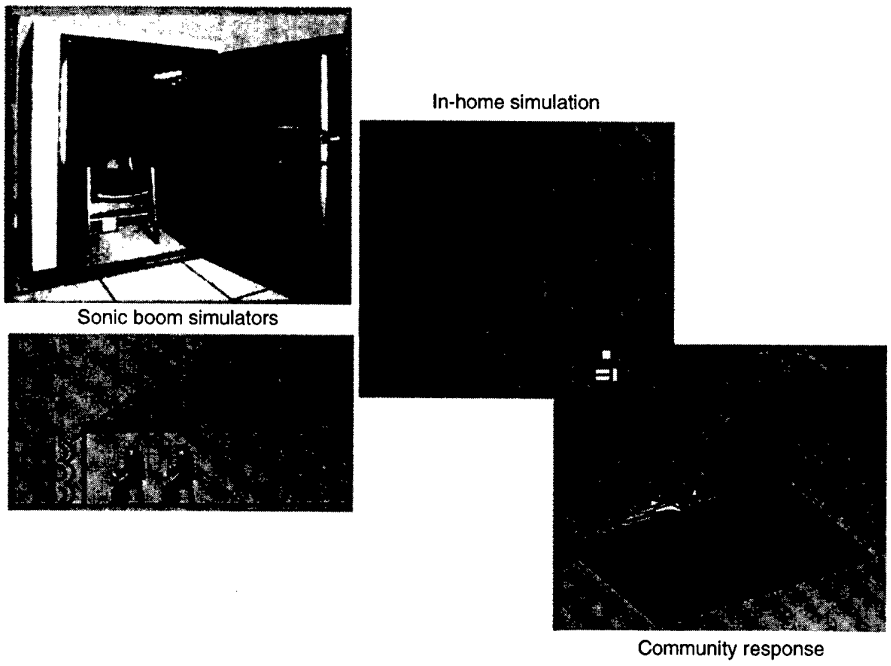


Figure 20. Sonic boom acceptability criteria.

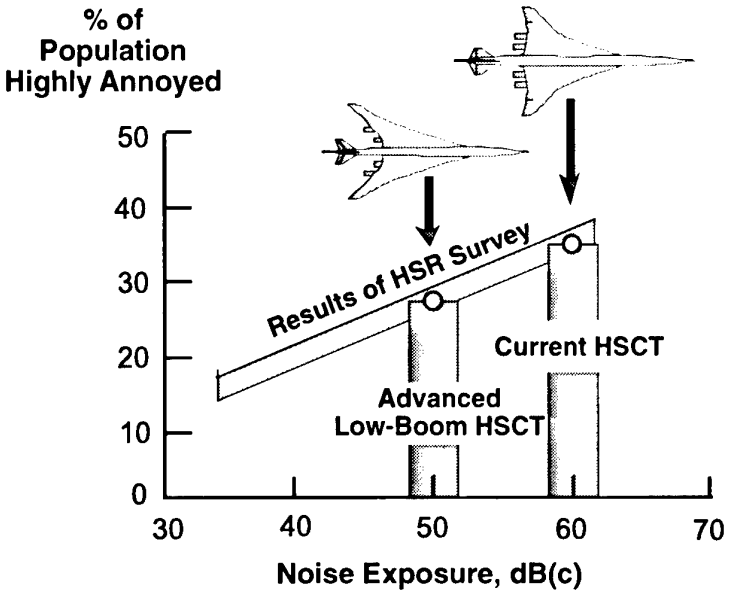


Figure 21. Human response to sonic booms.

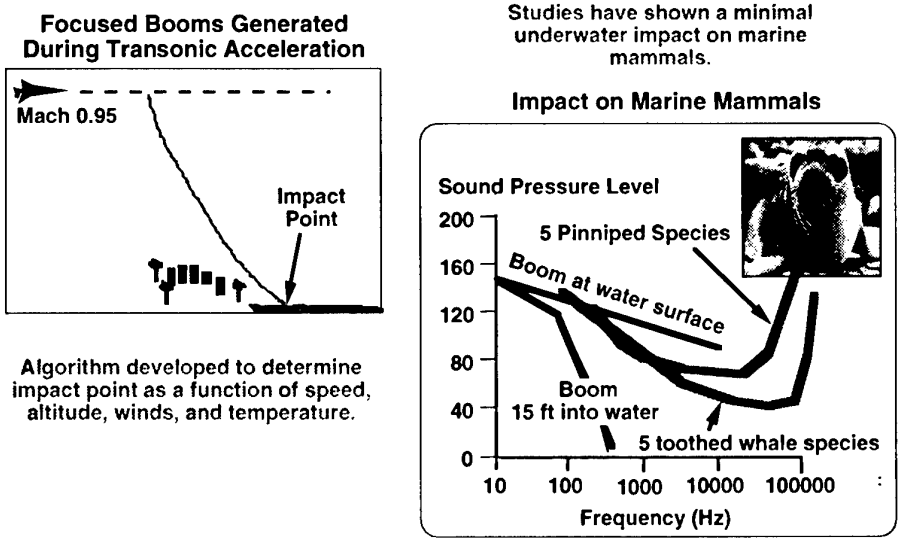


Figure 22. Sonic boom impact - marine mammals & focused boom.

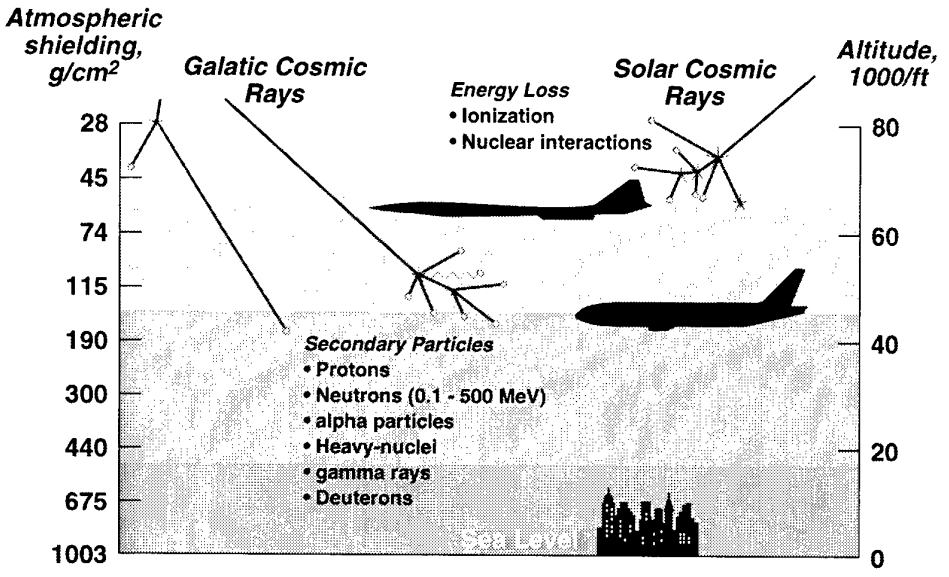


Figure 23. Atmospheric radiation exposure.

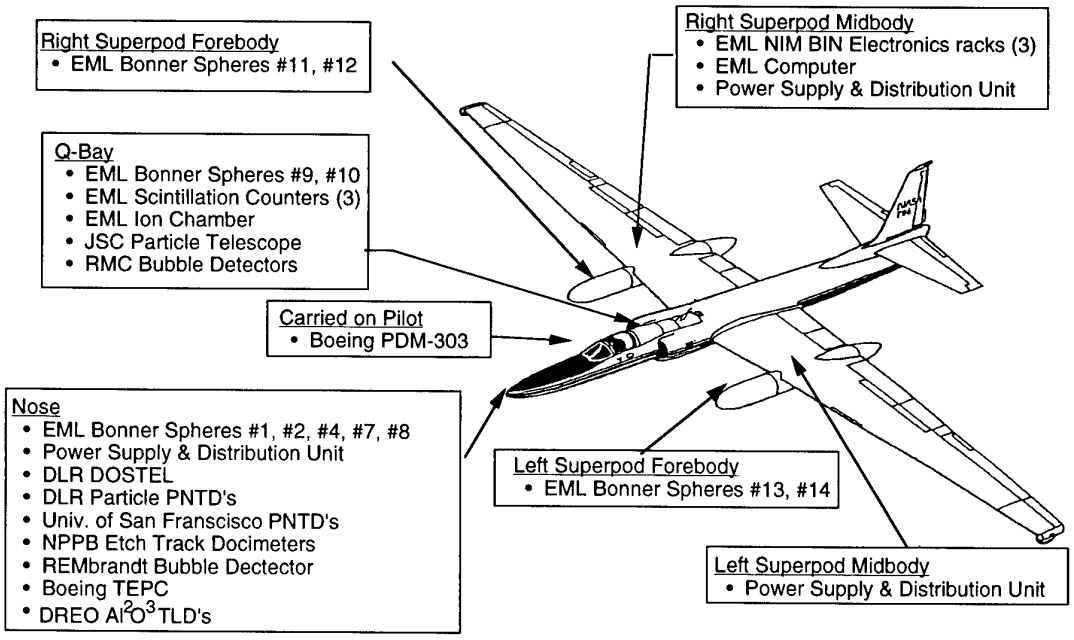


Figure 24. Atmospheric ionizing radiation measurements.

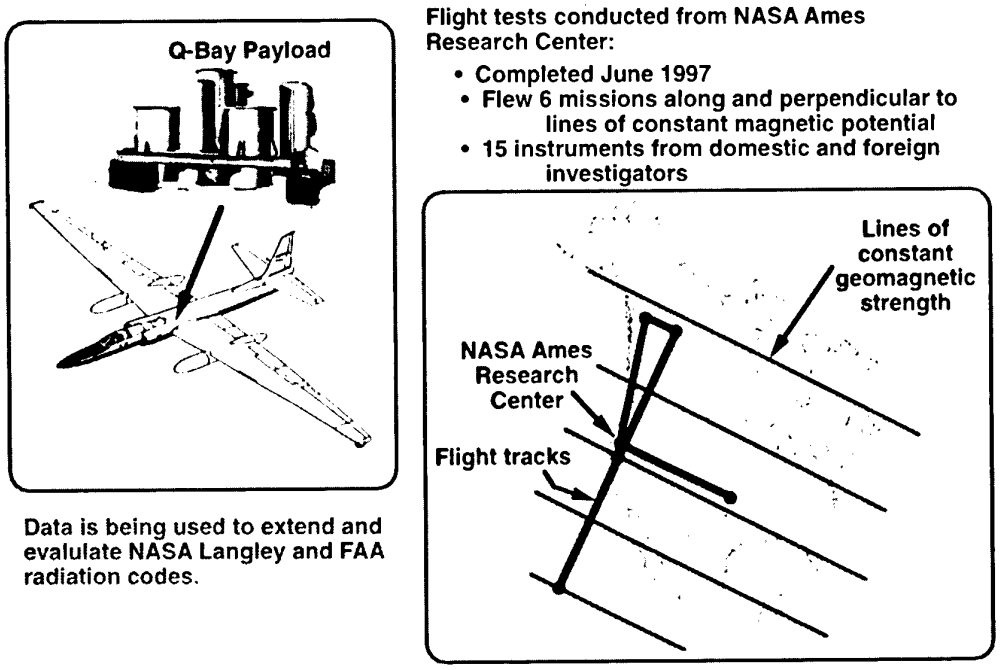


Figure 25. Atmospheric ionizing radiation - defining risk.

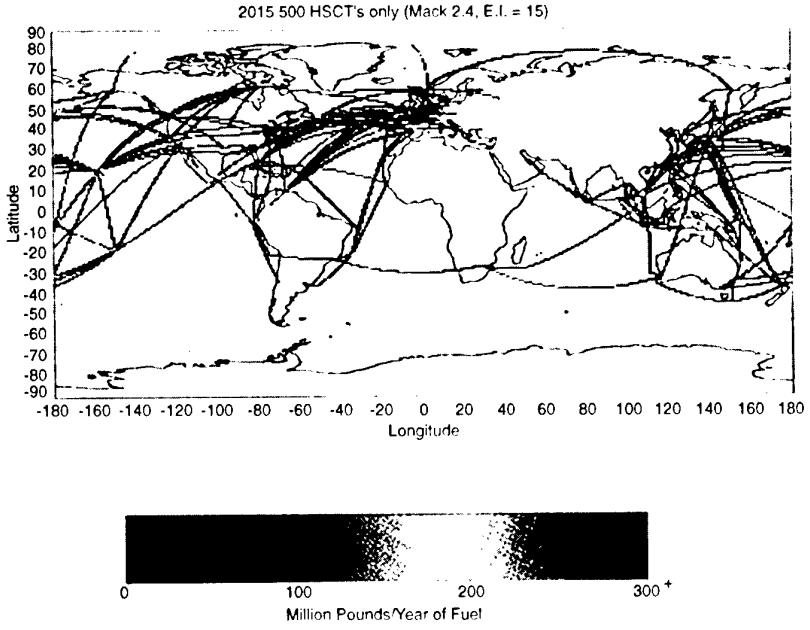


Figure 26. Projected air routes.

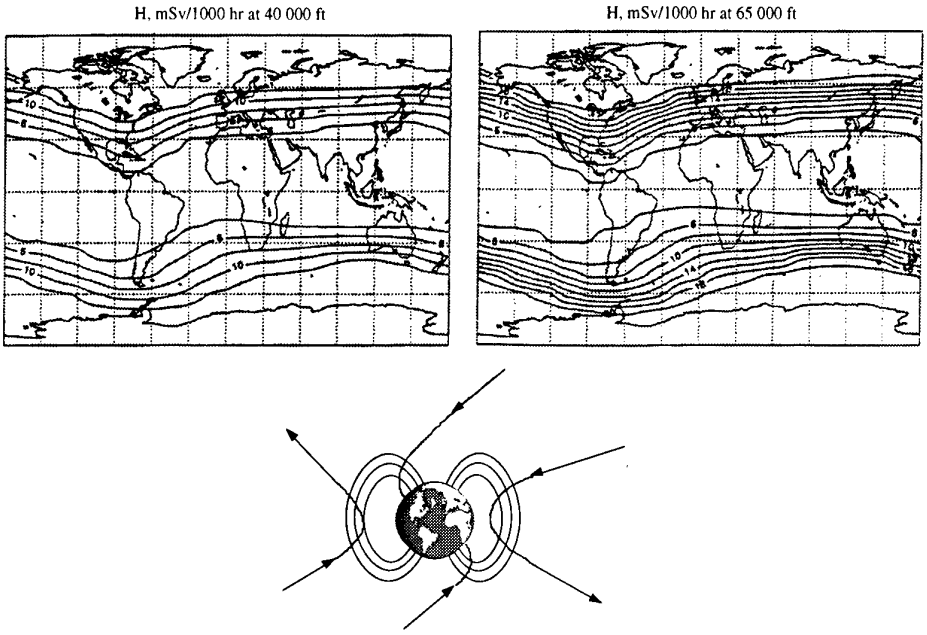


Figure 27. Galactic radiation exposure at solar minimum.

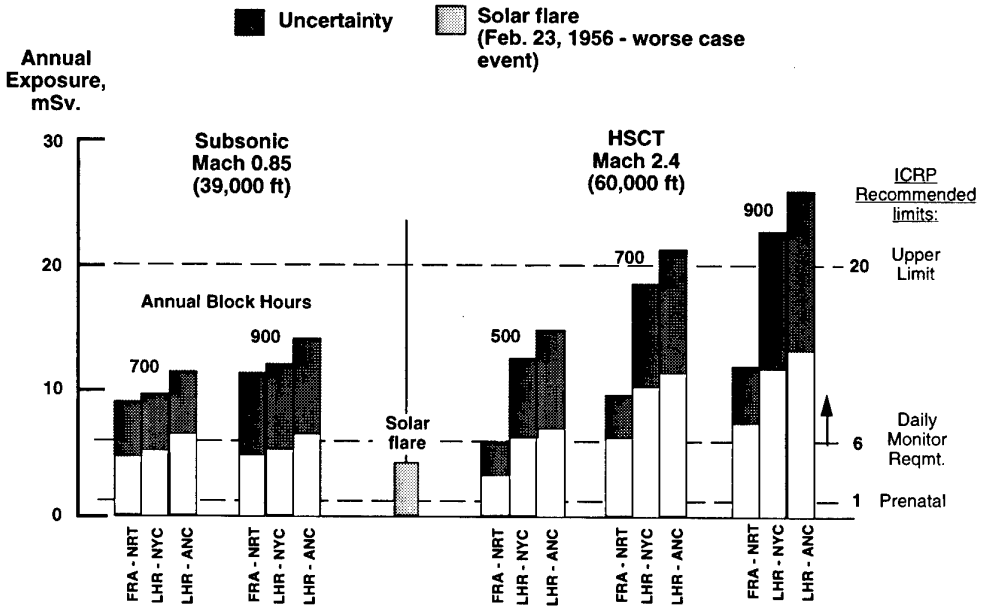


Figure 28. Annual crew exposures.

PROPULSION SYSTEM DESIGN FOR THE EUROPEAN SUPERSONIC CIVIL TRANSPORT AIRCRAFT

D. Prat

Aerodynamics Department

AEROSPATIALE Aéronautique

316, route de Bayonne F-31060 Toulouse Cedex 03

Project presentation

The three major European aircraft manufacturers have agreed on a common configuration for the future supersonic transport aircraft: the ESCT (European Supersonic Civil Transport aircraft). Daimler-Benz Aerospace, British Aerospace and Aerospatiale are working in close cooperation to make this project a reality. The technical feasibility of the future supersonic aircraft (SCT) depends on critical items such as high temperature materials, noise reduction during take-off, low NOx emissions, wave drag reduction, weight reduction, artificial vision...etc... In order to cope with these items, the European Supersonic Research Program (ESRP) has been established between the three above-mentioned aircraft manufacturers and their related national research establishments (NRE): DLR for Germany, DERA for Great Britain and ONERA for France. Within the ESRP project, aircraft manufacturers not only could work with their related NREs but also with the NREs from the other countries to give a better flexibility to the project.
The aim of ESRP is to provide and verify essential technologies for the development of an economically and environmentally viable SCT. Main fields covered within the ESRP are:

- Aerodynamics
- Propulsion integration
- Structure/materials
- Systems
- Technology integration

For each of these fields the major issues are addressed to ensure a full coverage of critical items while avoiding unintended duplication amongst the various partners. Aerodynamics represent 29% of the ESRP activity and if part of the 13.7% contribution from propulsion integration is also included in aerodynamics, it is more than one third of the overall effort that is spent on aerodynamic research for SCT. On the other hand, structure and materials represent 34%, and 16.2% is devoted to the systems.

In the aerodynamics field, compared to Concorde, a 30% improvement has to be achieved for the ESCT in supersonic cruise. Moreover, considering that it is a long range aircraft, long overland portions of flight have to be considered. The overland cruise is transonic at Mach=0.95. To cope with this particularity, the ESCT design is optimised both for supersonic and transonic speed. Typical target values for lift-to-drag ratio for these two regimes are:

- L/D ~ 9 at supersonic cruise (M=2.0)
- L/D ~ 15 at transonic speeds (M=0.95)

To achieve these ambitious objectives, every piece of the aircraft design has to be looked into in detail.

Aerospatiale involvement in Supersonic Civil Transport

Aerospatiale involvement in SCT design is important and is related to Concorde experience. Within the European framework, Aerospatiale is contributing to ESRP and European Community founded projects such as EUROSUP (Reduction of Wave and Lift -Dependant Drag for Supersonic Transport Aircraft) in the aerodynamics field. In France, there are some cooperations between SNECMA, ONERA and Aerospatiale mainly focused on propulsion integration (ONERA for the fundamental research, SNECMA for engine and exhaust definition and Aerospatiale for inlet design, nacelle design and overall integration). ONERA is also providing Aerospatiale with support for airframe technology development. Part of these research activities at ONERA are presented in a separate paper.
Aerospatiale activity in propulsion integration through both air intake design and nacelle design is an important activity, started in the early days of the supersonic story. An example of this activity is presented through an attached paper. This paper briefly explains the ESCT air intake and nozzle design and then focuses on propulsion system integration. It also includes an experimental validation for both air intake and propulsion system integration design. More detailed information about air intakes can be found in references [7,8].

Paper presented at the RTO AVT Course on "Fluid Dynamics Research on Supersonic Aircraft", held in Rhode-Saint-Genèse, Belgium, 25-29 May 1998, and published in RTO EN-4.

APPLICATION OF CFD METHODS TO PROPULSION SYSTEM INTEGRATION IN THE FUTURE SUPERSONIC TRANSPORT AIRCRAFT

D. Prat, T. Surply, D. Gisquet

Aerodynamic Department

AEROSPATIALE Aéronautique

316, route de Bayonne F-31060 Toulouse Cedex 03

Abstract

The economic viability of a future supersonic transport aircraft requires ambitious aerodynamic performance. Owing to its large impact on aircraft performance, the aerodynamic design of the future supersonic transport aircraft propulsion system is of utmost importance to Aerospatiale. However, it represents a particularly long and difficult task. The use of new CFD methods proved to be very helpful and powerful in designing the whole propulsion system. Through this process, Aerospatiale has developed know-how on both the internal and the external parts of the propulsion system.

Although the internal components of the propulsion system, i.e. the air intake, engine and nozzle have to be studied as a whole, the internal performance of a supersonic air intake is highly dependent on overall aircraft configuration. It therefore requires special care from the aircraft designer in the trade-off between internal performance (pressure recovery and operating characteristics) and external drag.
CFD methods, by simulating operating characteristics, provide a tool for better understanding the phenomena involved in flow physics. These tools, associated with overall expertise on intake design, were used to define and test a supersonic air intake.
The high level of information provided by modern CFD methods is a key point for both internal and external flow analysis. The code used by Aerospatiale was developed in cooperation with ONERA. It includes Euler and Navier-Stokes solvers with space marching and Parabolized Navier-Stokes capabilities for fully supersonic flows.
These last two capabilities allow complex industrial geometries to be studied while drastically reducing computing time. Considering the ability of the code to represent accurate physical phenomena, its Euler, as well as PNS and full Navier-Stokes capabilities, were used in the whole propulsion system integration process.
The external design of nacelles results from a careful analysis of the flow pattern on the wing's lower surface. A proposed geometry is obtained by minimizing the total drag while considering local flow conditions and the strong aerodynamic interactions of the nacelles.

The various levels of modelling of the CFD code provide an appropriate cost-effective answer to each type of physical phenomenon found in the flow pattern around the nacelles. This capability is essential for defining the best trade-off in the aerodynamic design of the propulsion integration. Experimental data are presented confirming the overall design process.

1. Introduction

The economic viability of a future supersonic transport aircraft requires ambitious aerodynamic performance. Owing to its large impact on aircraft performance, the aerodynamic design of the future supersonic transport aircraft propulsion system is of utmost importance to Aerospatiale. However, it represents a particularly long and difficult task. The use of new CFD methods proved to be very helpful and powerful in designing the whole propulsion system.
This paper presents various aspects of propulsion system design and integration for the second generation supersonic aircraft. Firstly, aircraft configuration and the CFD codes used for these studies are mentioned. Then, some internal elements of the propulsion system are presented through air intake and nozzle design. Propulsion system integration is detailed with the specific constraints it presents. A final design is proposed with the associated experimental wind tunnel data.

2. Configuration

The European Supersonic Civil Transport aircraft (ESCT) is a configuration defined by the three European partners, Aerospatiale, British Aerospace and Daimler-Benz

Copyright © 1997 by the authors. Published with permission.

Paper presented at the RTO AVT Course on "Fluid Dynamics Research on Supersonic Aircraft", held in Rhode-Saint-Genèse, Belgium, 25-29 May 1998, and published in RTO EN-4.

Aerospace. The general characteristics of this configuration are compared to Concorde characteristics in Figure 1.

Characteristics	Concorde	ESCT
Range (km)	6300	>10 000
Cruise Mach number	2,05	2,05
MTOW (t)	185	340
Passengers	100	250
Take-off thrust (kN)	170	230
Sideline Noise (EPNdB)	112,2	104,6
Flyover Noise (EPNdB)	119,5	105,2
Landing Noise (EPNdB)	116,7	105,2
Consumption kg/(seat.km)	0,1	0,05

Figure 1 : ESCT .vs. Concorde characteristics

Owing to increasing world-wide commercial exchanges, the design mission range has grown. As a consequence, part of the design mission is performed at 0.95 transonic Mach number for overland flight, the resulting aircraft takes dual supersonic as well as transonic flight design points into account. Major noises reductions from Concorde to the ESCT have to be achieved to comply with FAR 36 chap. 3 noise regulations. Low noise levels could be obtained through low nozzle exit velocity. For this reason, the ESCT configuration considers the relatively high by-pass ratio Mid Tandem Fan engines. The geometric description of the configuration (Fig. 2) presents a higher aspect ratio than for Concorde owing to transonic and subsonic cruise performance. Self stability for the wing is required as no tail is present.

Four nacelles are present under the wing fitted with the four MTF engines. Separate nacelles comply with safety considerations for engine burst and could minimize the propulsion system aerodynamic penalty.

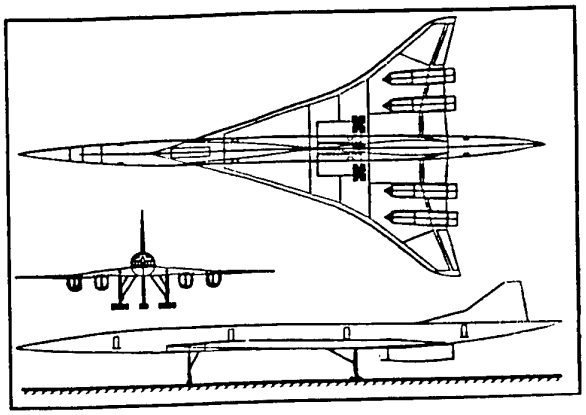


Figure 2 : ESCT configuration three view

Each nacelle contains two vertical two-dimensional mixed compression air intakes. The vertical layout of the two halves compared to the Concorde horizontal layout gives some possibilities to shorten the nacelles, again reducing propulsion system aerodynamic penalty.

Thus, this different propulsion system layout could give rise to higher aerodynamic performance through an appropriate design process.

3. Fluid Dynamics Code

The complexity of the geometries studied and the physical phenomena encountered, the accuracy required and the short calculation times were criteria which strongly influenced the choice of the solver and the numerical scheme.

The code selected at Aerospatiale,FLU3M was developed at ONERA and Aerospatiale to cover their need in compressible flow calculations governed by the Euler as well as Navier-Stokes equations[1,2].

The associated volume discretization is a structured multi-block approach. For complex industrial geometry, this approach is very suitable, providing calculation time and memory space saving through the implicit connectivity of such structured meshes. This approach also allows the scheme best suited to local flow characteristicsto to be used on each block.

However, the meshing of complex industrial geometries represents a difficult task. A specific application, ICEM CFD, allows Euler meshes to be generated with possible automatic remeshing using a COMAK module for some geometrical deformations through the design process. Navier-Stokes meshes are generated via ICEM and specific tools developed at Aerospatiale.

In addition to the choice of modelling, the CFD code offers the choice between different numerical schemes to discretize the convective flows[3]. These convective flows are all based on a upwind flux formulation, the second order in space being obtained by the Van Leer MUSCL approach associated with slope limiters to ensure the total variation diminishing (TVD) property. The good discontinuity capturing properties of such schemes allow complex supersonic flow to be correctly represented.

The finite volume space discretization of the schemes is related to the conservative formulation of the governing equations for better discontinuity capture and simple processing of degenerated cells. The implicit processing of the time discretization improves the convergence of these schemes whilst permitting a reduction in computation time.

For all supersonic flows, the governing system of equations could be written in a parabolized form[4] to express the non-dependence of flow to down-stream disturbances. As a consequence of this property, the flow could be solved with a space marching technique i.e. solved from up-stream to down-stream. For viscous flow, Parabolized Naviers-Stokes equations proved to be suitable for solving the flow around complex configurations[5,6]. Space marching calculations are only possible on a specific mesh topology as presented through the propulsion system integration example.

4. Propulsion System

The CFD codes described above are used to design and analyse both the propulsion system (i.e. internal flow) and its integration into the aircraft (i.e. external flow). Figure 3 shows a schematic view of the propulsion system, with its two air intakes dividing the flow through the engine and the nozzle.

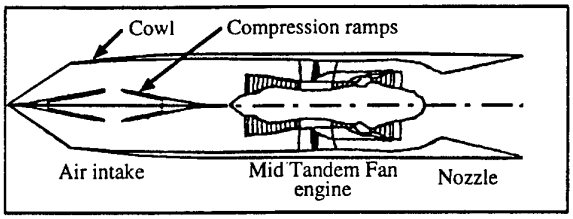


Figure 3 : Schematic layout of the propulsion system

Although these components may be analysed separately, one has to bear in mind that, to ensure a satisfactory operating characteristic of the air intake, it is necessary to bleed part of the flow (called secondary flow) off the air intake throat, while the main flow becomes subsonic. This secondary flow then circulates beside the engine, where it can ensure ventilation of its related components. It is then ejected through the nozzle, to achieve maximum efficiency of the whole propulsion system.

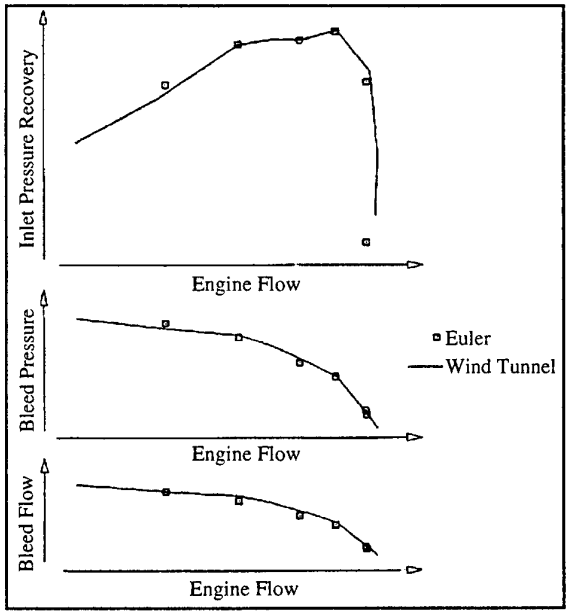


Figure 4 : Axisymmetric air intake operating characteristics : Euler prediction .vs. wind-tunnel test data.

The CFD code used at Aerospatiale successfully demonstrated its ability to simulate the flow in a supersonic air intake[7,8]. Figure 4 shows the main curves describing the operating characteristic of an axisymmetric intake in supersonic cruise conditions :

- Pressure recovery (average total pressure in front of the engine) ;
- Bleed pressure (total pressure in the bleed cavity) ;
- Bleed mass flow.

These curves are shown as a function of engine mass flow (simulated by a sonic throat aft of the air intake diffusor). Though Euler modeling of the flow provides a good simulation of the overall operating characteristics of the air intake, it is worth using Navier-Stokes modeling for detailed analysis of the flow where viscous phenomena are of importance (Fig. 5) :

- Boundary layer development in the intake diffusor ;
- Shape of the supersonic/subsonic shock line over the bleed area.

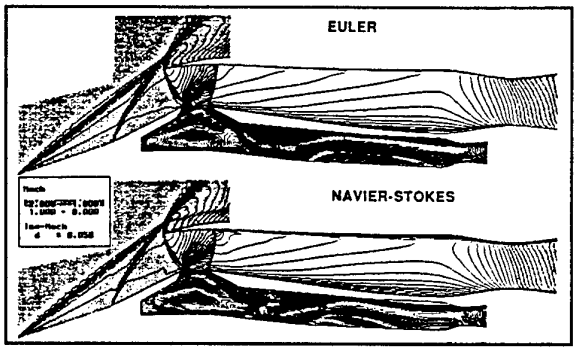


Figure 5 : Effect of flow modeling for an axisymmetric air intake.

The propulsion system of the new supersonic transport aircraft now under study (Fig. 2) has four separate engines, located under the wing. For each engine, the flow is fed through two opposite facing Concorde-like air intakes. In order to reduce external cowl drag, Aerospatiale has designed a new air intake with increased internal compression. Figure 6 shows the threedimensional Euler simulation of the flow in this air intake.

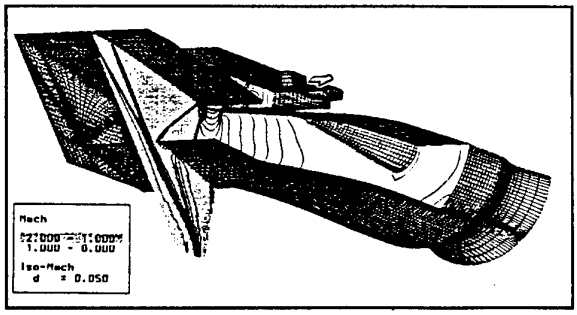


Figure 6 : Small cowl angle air intake for ESCT configuration.

One can notice the main geometrical features of this configuration : side exit of the bleed flow and rectangular to half circular diffusor. Visualisation of the flow through the inlet shows that owing to increased internal compression, the flow is fully supersonic up to the throat of the inlet.

A wind-tunnel model has been designed and manufactured. Several ramps and cowl angles have been tested in the ONERA S3 wind-tunnel in Modane (Fig. 7) to measure the effect of their shape and position on the performance and operating characteristics of the air intake, including start/unstart phenomena.
Owing to the pressurization of the wind-tunnel and the size of the model, a full-scale Reynolds number could be achieved. Results of the test, done in a Mach number range of 1.85 to 2.00 corresponding to the supersonic cruise of the aircraft showed good agreement with CFD predictions.

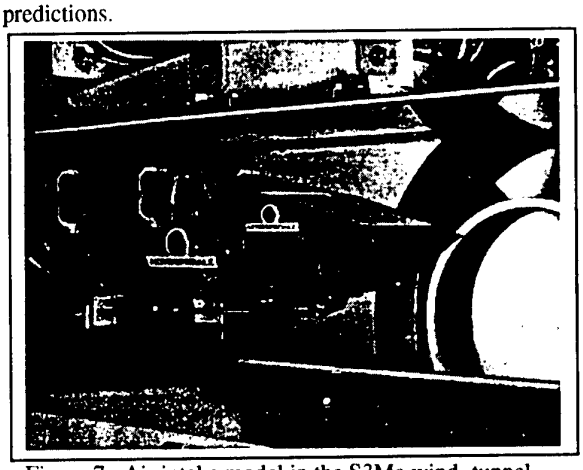


Figure 7 : Air intake model in the S3Ma wind-tunnel.

High pressure recovery was achieved with satisfactory inlet operating characteristics, in spite of the increase in internal compression with respect to Concorde.

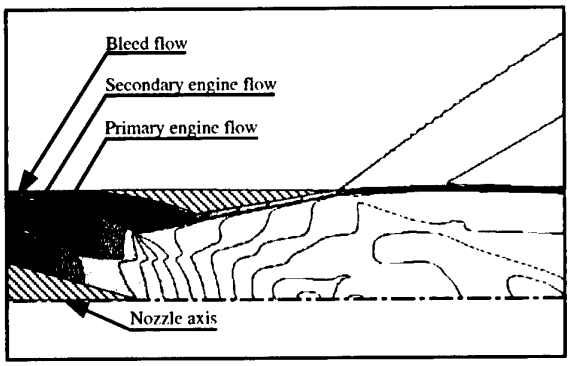


Figure 8 : Flow through the nozzle in supersonic configuration.

The secondary flow bled off from the air intake has to be ejected through the nozzle in order to improve the overall propulsion system efficiency. Figure 8 is an example of simulation of such a flow by CFD means.
Variation of the relative total pressure between the engine and the bleed flow allows the operating characteristics of the nozzles to be simulated. This operating characteristic is used for propulsion system optimization.

5. Propulsion System Integration

The propulsion system integration is based on the aircraft configuration and the propulsion system presented above. The definition and analysis of the propulsion system integration is achieved through two main steps :

- Aircraft design without propulsion system ;
- Nacelle design and positioning optimization.

Aircraft without nacelles

The aircraft design takes into account realistic constraints : - Structural constraints such as spar position and
minimum thickness of the wing.

- Configuration constraints for the landing gear, the fuel volume in the wing and all the moving surfaces (moving leading edge and elevons).
- Aerodynamic constraints for stability and sufficient leading edge radius for subsonic and transonic flight.

Propulsion system integration under the wing has to be considered at the very beginning of wing design to provide as homogeneous flow conditions as possible for the air intake. Wing design is obtained through both induced drag and wave drag minimization.

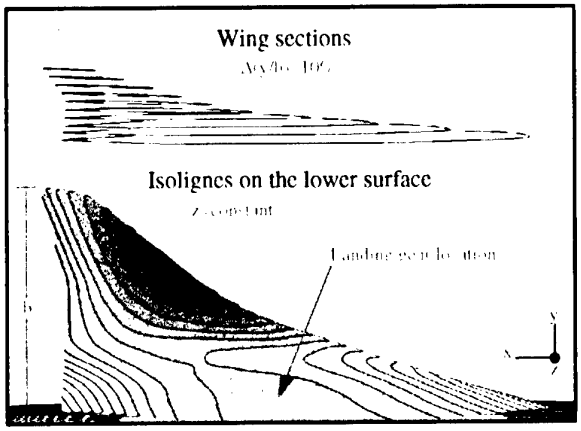


Figure 9 : Proposed ESCT wing

The lower surface of the proposed wing is presented on figure 9 . This design results from an optimisation process to provide the propulsion system good inflow conditions in a suitable angle-of-attack range around the cruise condition.

Nacelles

The initial nacelle shape (Fig. 10) is obtained through cross–section area evolution minimization.
Moreover, the nacelle shape should present sufficient volume for internal elements (air intake, diffuser, engine and nozzle), the many items of equipments associated with the engine, the bleed flow from the air intake and the structure. Main flow properties were taken into account for initial nacelle design but a refined analysis of the wing's lower surface flow is necessary to go further in nacelle design.
Propulsion system integration under the wing is based on the comprehension of the specificity of the flow under the wing. The present study will show that CFD methods are suitable for this task. Experiments will then be used only for validation purposes in the final design, drastically reducing the number of experiments for such a study and also reducing its cost.

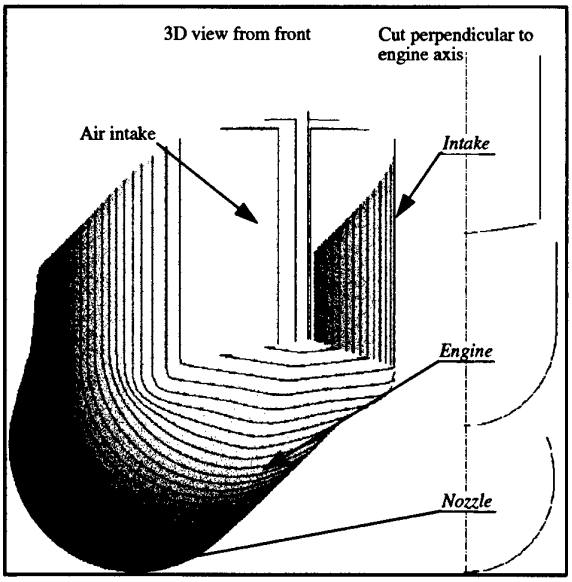


Figure 10 : Initial nacelle

Gridding

The first step of CFD analysis is the structured multi–block gridding of the volume around the complete configuration. Taking advantage of the space marching technique for all supersonic flows is possible by defining a specific mesh. An example of a 1.5 million node mesh spread out into a 70 block Euler mesh (Fig. 11) shows how the mesh is structured in slices perpendicular to the main stream direction for space marching purposes.
The propulsion system under the wing definitely complicates the mesh for taking the flow over the front part of the air intake into account. A good representation of the physical phenomena arising from air intakes is essential for achieving an accurate representation of the interactions between nacelles as well as those between the nacelles and the lower wing surface. It is thus necessary to take special care for gridding in this region. For the same geometry, meshing for a Parabolized Navier–Stokes application leads to a 2.6 million node, 128 block mesh .

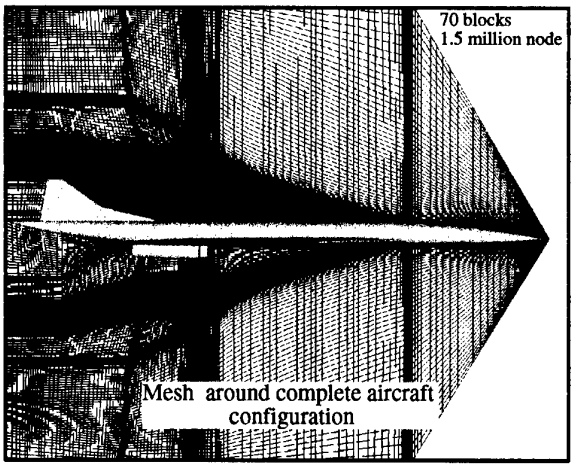


Figure 11 : Multi–block mesh

Incoming flow analysis

Considering that the flow is supersonic everywhere, no disturbances from the propulsion system will affect the flow upstream of the nacelles. The incoming flow characteristics are thus independent of the propulsion system. For propulsion system integration purposes, supersonic cruise conditions are considered. The positive angle–of–attack, combined with wing twist and camber creates compression under the wing and an outboard deflection of the flow.

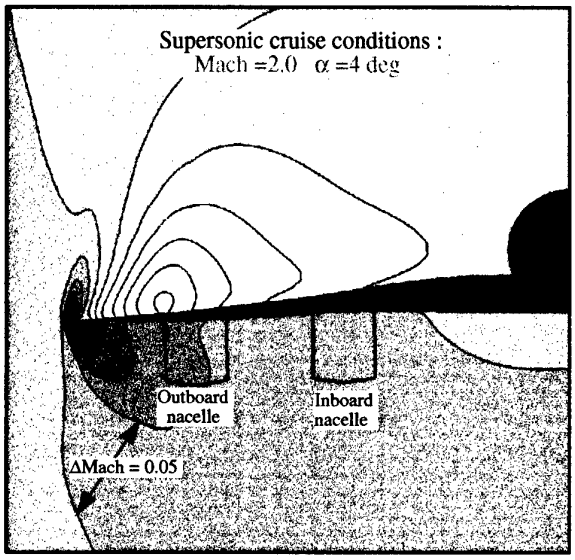


Figure 12 : Mach number in the air intake entry plane

These two characteristics vary along the span. Mach number distribution in the air intake entry plane (Fig. 12) leads to varying incoming flow conditions for each of the four air intakes. However, careful design of the lower wing surface may help to reduce these distortions.

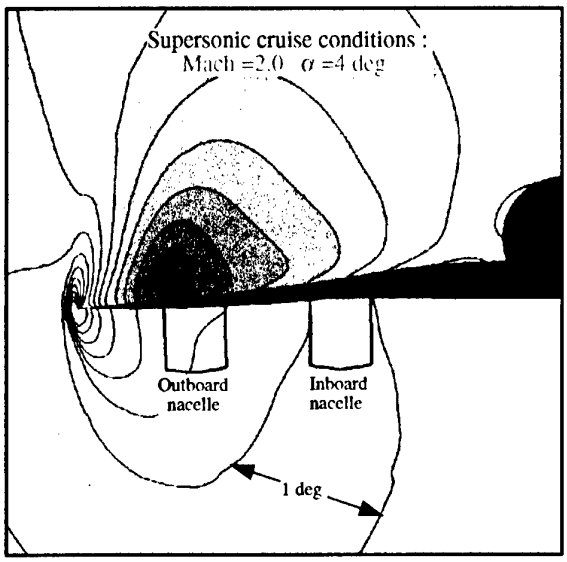


Figure 13 : Lateral deflection in the air intake entry plane

The analysis of the lateral deflection under the wing in cruise conditions (Fig. 13) again shows deflection gradients along the span. Near the wing leading edge, gradients become larger as tridimensionnal effects are increasing. In this figure, it appears that the outboard nacelle is at the beginning of this high gradient region. Lateral flow deflection analysis (Fig. 13) gives information for positioning air intakes. Actually, symmetrical intake inflow conditions are desirable for both efficiency and operating characteristics. Varying the angle between the air intake and the aircraft plane of symmetry also distributes the compression on the external cowl on the two sides of the nacelle, it therefore lowers the total drag generated by these compressions. The Euler solution gives sufficient information for incoming flow analysis for positioning purposes because compressible inviscid physical phenomena are predominant in this region.

Propulsion system adaptation

Through the analysis of the flow under the wing, it appears that initial nacelles have to be modified to ensure both good inflow conditions for the air intake and minimize installation drag.

Compression on the air intake and the external cowl results in high pressure on the external cowl and thus generates some drag. The compression wave from the air intake also puts high pressure on the wing downstream of this wave. This contribution generates lift combined with a small amount of drag. Cambering the front part of the nacelles will affect the relative compressions on each side of them and the associated contributions to aerodynamic coefficients.

If we first consider the initial uncambered configuration (Fig. 14), owing to the local flow outboard lateral deflection, the shock on the internal air intake of the external nacelle is much greater than the one on the opposite side.

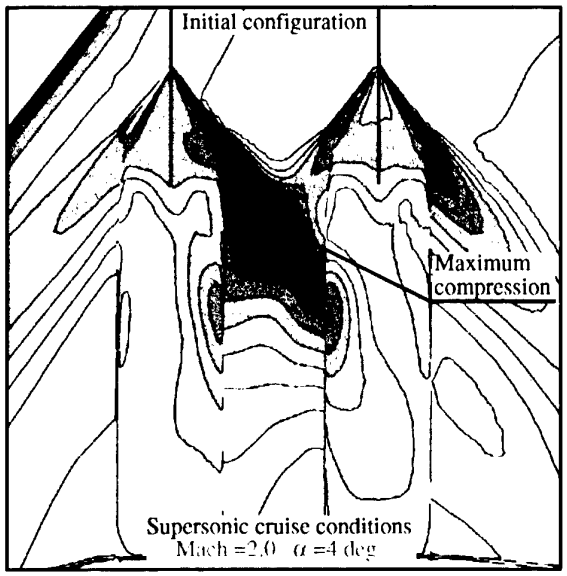


Figure 14 : Mach number on the uncambered propulsion system

For the inboard nacelle, the difference between the two sides of the nacelles is of less importance. The intersection between the compression waves coming from the two nacelles gives rise to a low Mach number region because of the high intensity of the incoming shock from the external nacelle. This strong compression creates negative pressure gradients in a region where the boundary layer is thick because of the great distance between this point and the leading edge. For this uncambered case, the minimum Mach number after compression is under the critical flow separation threshold found from various wind-tunnel result criteria. Thus, flow separation may occure in this area. Then, the uncambered configuration does not meet the criteria for good air intake inflow conditions and external low drag flow.

Considering the acceptable asymmetry of the incoming flow for the inboard nacelle, it is interesting to keep this nacelle unmodified to minimize the compression on its external side. This will contribute to lowering the compression in the region between the two nacelles.

The curved configuration (Fig. 15) lowers the compression between the two nacelles. For this configuration, the same analysis as for the uncambered case has shown no separation on the wing. The total installation drag is lowered and the lift due to the propulsion system has

increased. Incoming flow conditions are acceptables for both air intakes.

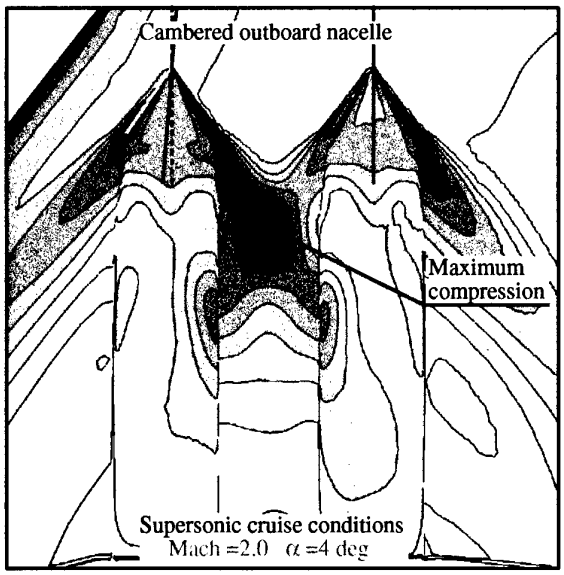


Figure 15 : Mach number on the cambered propulsion system

The final design has been reached through the cambering process with both good incoming flow properties for the air intake and reduced external drag with no separation. For this last configuration both boundary layer and PNS calculations have been carried out to capture boundary layer evolution accurately through the propulsion system influence on the wing lower surface.

Rear nacelle design

A specific study is needed for the definition of the external shape of the rear part of the nacelle. In this region, considering that the propulsion system nozzle is axisymmetric, a typical 3D surface will draw both upper surface and lower surface flow around the nozzle. Specific conditions for this region are :

- Different Mach number between upper and lower surface ;
- A rapid stream–wise evolution of the surface from the rear spar of the wing to the nozzle (the variable section nozzle puts additional geometrical constraints on this region) ;
- A thick boundary layer on the upper wing surface.

Large deviations combined with different Mach numbers between upper and lower surfaces produce shock waves at the flow mixing so that boundary layer separation might occur in this region. Studying this region requires solving the flow around the complete aircraft. Moreover, each new design results in a new mesh. As each nacelle has specific flow and geometric constraints, a big meshing effort is needed for the study. For this reason, the Euler approach with an automated meshing procedure ICEM CFD/COMAK has been used to reduce the design loop to one day for mesh generation, flow calculation and analysis. The resulting design (Fig. 16) is a trade–off between upper and lower flow deflections to minimize recompression at the intersection of these two flows on the surface.

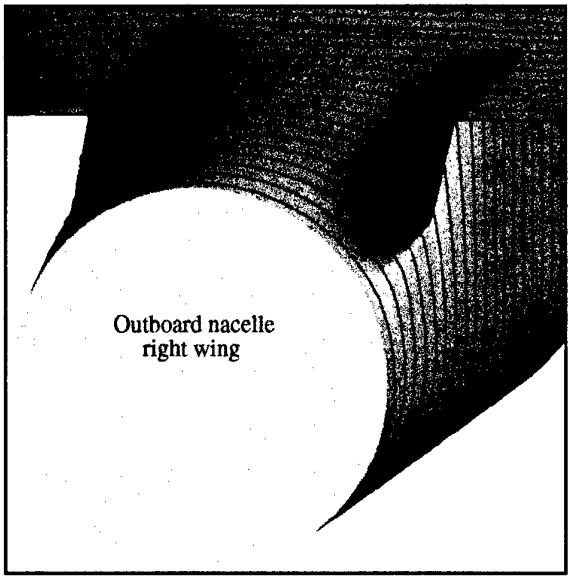


Figure 16 : Rear part of the outboard nacelle

Acceleration on the upper surface generates lift so that the overall drag penalty of this part of the nacelle at constant lift remains small compared to that of the propulsion system as a whole. Boundary layer calculations validated this design, showing no separation on the geometry.

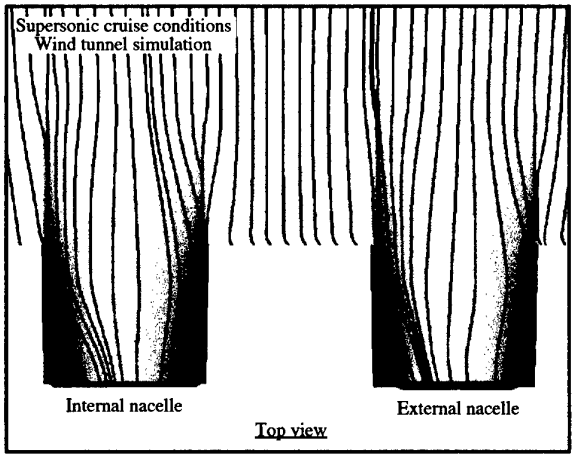


Figure 17 : Friction lines on the upper side of the propulsion system

Friction lines from boundary layer calculations at wind–tunnel Reynolds number (Fig. 17) are disturbed by the pressure gradients at the junction of the upper and lower

surface flow but deflections remain small enough to avoid separation.

Wind-tunnel model and test

The above-mentioned geometry is realistic with interesting calculated performance. Flow analysis showed good properties for flight conditions as well as for lower Reynolds number cases, thus justifying wind-tunnel testing. Experimental validation was carried out to consolidate the study.
Model sizing was governed by the ONERA S2Ma 1.75x1.94 m^2 supersonic test section dimensions chosen for the test. On one hand, a good representation of air intake geometry is only possible for a large model but on the other, wall shock reflection should not interfere with the model. A large 1:40 scale wind-tunnel model (Fig. 18) was built. It is approximately 2m long with a 1m wingspan.

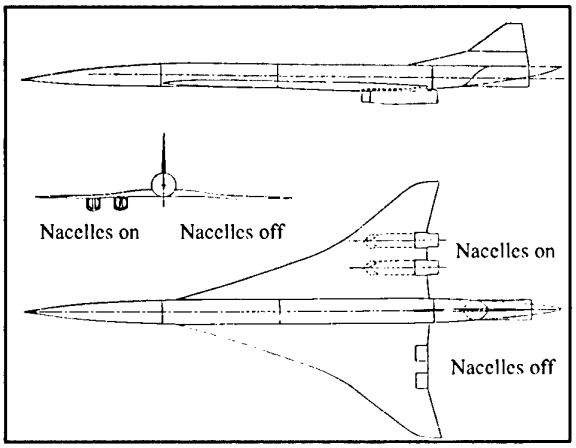


Figure 18 : Three-view of the wind-tunnel test model

The model is mounted on an internal, six component, strain-gage balance, it is equipped with static pressure ports on the wing surface to capture real flow features in particular around the propulsion system. Through-flow nacelles are equipped for internal pressure measurement and can be removed for the determination of the propulsion system installation aerodynamic coefficient.

After calibration of the nacelles, the internal drag of the nacelles can be determined from internal measurements during the test.
Installation aerodynamic coefficients are determined by the difference between the two configurations, i.e. with and without nacelles, after internal and base drag corrections. A picture of the model mounted in the ONERA S2Ma wind-tunnel is shown in Figure 19.

Thanks to the large size of the model and a pressurized wind tunnel, the test Reynolds number is as high as 1/10 of the supersonic cruise condition, this point allows accurate measurement for propulsion system integration studies.
The measurement sequence was set up using the considerable experimental experience acquired on Concorde to minimize measurement uncertainties. Oil flow visualizations were carried out in addition to force and pressure measurements.

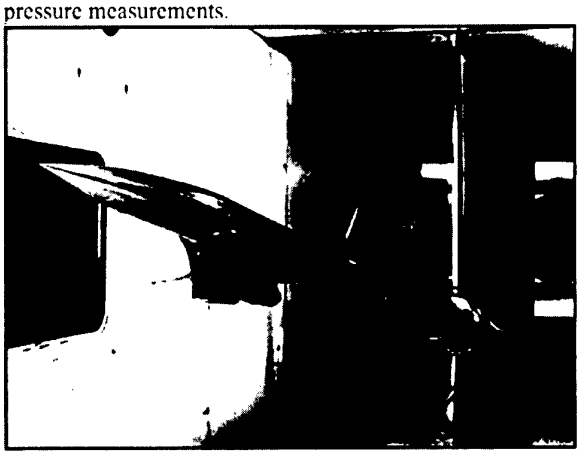


Figure 19 : Photograph of the wind-tunnel test model in the ONERA S2Ma wind-tunnel

Comparison of predictions to test data

Pressure measurements

The comparison of test data to the Euler prediction on the wing lower surface (Fig. 20) is presented for both configurations, with and without nacelles. In this figure, we have drawn the Mach number parameter as it is commonly used to study the propulsion system integration.
From this figure, it appears that the Euler solution agree well with test data for the nacelles-off configuration. Considering that Euler is an inviscid approximation, this point means that the flow structure is not modified by viscous effects i.e. no separations or important shock-boundary layer interactions are present.
Propulsion system influence is also well predicted for the level of recompression and the shock arrangement though experimental shock position is a bit upstream of that of the Euler solution.

Force measurements

Aerodynamic coefficients in the wind-tunnel conditions were estimated for the Euler solution adding friction drag from boundary layer calculations. A comparison with experiments is presented (Fig. 21) for the two configurations. The CFD estimation is in close agreement to experimental results for the configuration without nacelles.
From these results, it appears that Euler plus boundary layer calculations are accurate for capturing the governing physical phenomena around this configuration. Boundary layer calculation is a parabolic space marching process

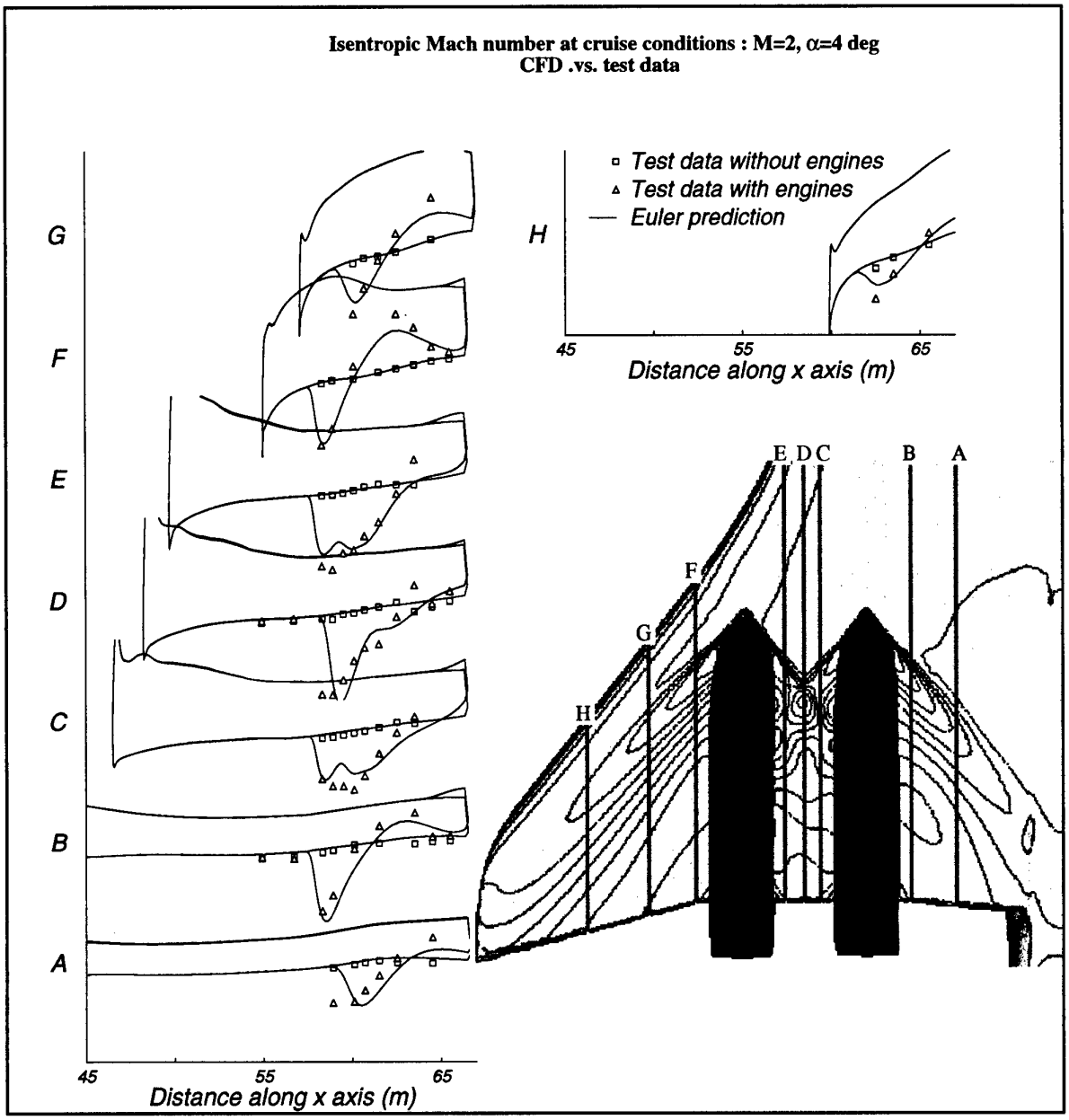


Figure 20 : Comparison of CFD predictions to test data on the lower wing surface with/without nacelles

which fails at boundary layer separation or flow structure modification (shock–boundary layer interaction). As for the nacelles–off configuration, neither separation nor shock–boundary layer interactions are present Euler plus boundary layer is well suited for this case.

For the configuration with nacelles, flow structure is much more complicated. However, predictions are also in close agreement with test results which means that :

- Internal and base drag are properly measured. The internal drag measurement method has been set up for Concorde and adapted to suit modern tools.
- The friction drag on the nacelles–on configuration is estimated by boundary layer calculations.
- Flow structure on the wing lower surface was accurately predicted with the Euler method. As no separations were observed on the surface, no viscous effects have modified the flow structure. Euler methods are then adapted to predicting flow development on the surface. Viscous effects are of importance for understanding physical phenomenon but showed little effect on integral coefficients.

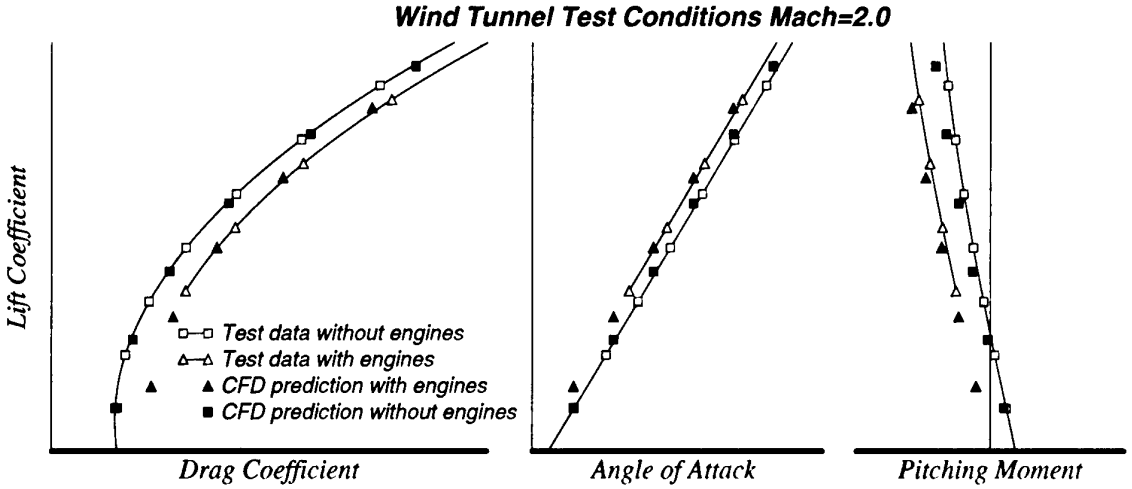


Figure 21 : Comparison of predicted aerodynamic coefficients to wind tunnel data

From the difference between the nacelles on and nacelles off configuration, the drag at constant lift due to the propulsion system integration can be determined. From the present study, it appears that a decrease of the propulsion system integration drag of 2 to 3% of the total aircraft drag can be achieved compared to Concorde.

6. Conclusion

Aerospatiale's aerodynamic study of the ESCT (European Supersonic Civil Transport) propulsion system has been presented through internal and external flow studies. The ability of current CFD methods to represent physical phenomena around complex geometry is a key point to the design and analysis of different parts of the supersonic propulsion system.

A low cowl angle air intake with good efficiency and operating characteristics has been developed to reduce propulsion system drag. Experiments on this design showed the good agreement between numerical and experimental results, comforting CFD approach accuracy for the prediction of the complex physical phenomena involved in air intake operation. Specific nozzle design was investigated including appropriate inputs from engine and secondary air intake bleed mass flow.

Propulsion system integration on a realist ESCT geometry was presented, including low cowl angle air intake and specifically designed wing. Through a refined analysis of the flow on the lower surface of the wing and around the nacelles, a propulsion system integration was designed. Wind-tunnel testing on a large model for propulsion integration purposes confirmed the promising calculated performances.

Aerodynamic design and evaluation of the propulsion system by CFD means proved to be efficient and accurate, drastically reducing wind-tunnel testing needs and associated costs. The level of performance achieved is encouraging for second generation future supersonic aircraft feasibility. Aerospatiale is continuing its research effort on supersonic aircraft to increase all the know-how acquired from Concorde's experience even further.

7. References

1. Dormieux, M. and Guillen,P.,"Design of a 3D Multidomain Euler Code", International Seminar on Supercomputing, Boston (USA), Oct.1989.
2. Borrel,M. and Guillen,P.,"Hypersonic Delta Wing Flow Calculations Using a Multidomains MUSCL Euler Solver", Workshop Hypersonic INRIA Sophia Antipolis, Antibes (France), Jan. 1990.
3. Hirsh,C., "Numerical Computation of Internal and External Flows", Vol.2, John Wiley, Chichester, 1990.
4. Korte, JJ.,"An Axplicit Upwind Algorithm for Solving the Parabilized Navier-Stokes Equations", NASA TP-003050, Feb. 1991.
5. Rai, MM., Chaussee, DS. and Rizit, YM. "Calculation of Viscous Supersonic Flows over Finned Bodies". AIAA 83-1667, 16th Fluid and Plasma Dynamics Conference, Danver.
6. Hollenback, D.M. and Blom, G.A., "Application of a Parabolized Navier-Stokes Code to an HSCT Configuration and Comparison to Wind Tunnel Test Data". AIAA 93-3537-CP.
7. X.Bousquet, T.Surply, D. Gisquet, "Numerical Simulation of the Airflow in Supersonic Air intakes : Application to the Future Supersonic Transport Aircraft". ICAS September 1992, Pekin.
8. X.Bousquet, "Simulation Numerique du Fonctionnement d'une Entree d'Air pour un Avion de Transport Supersonique". Colloque de mecanique des fluides de Toulouse, 7-8 Octobre 1993.

Overview of NAL's Program Including the Aerodynamic Design of the Scaled Supersonic Experimental Airplane

Kenji YOSHIDA
Advanced Technology Aircraft Project Center
National Aerospace Laboratory
6-13-1, Osawa, Mitaka, Tokyo 181-0015, Japan

ABSTRACT
NAL is promoting on un-manned scaled supersonic experimental airplane program consisting of an un-powered and a jet-powered airplanes. The main objective of the program is to establish an integrated design system with a CFD-based optimum method aiming at higher lift-to-drag ratio characteristics through flight tests of both experimental airplanes. Presently NAL has just designed an aerodynamic configuration of the first experimental airplane. This airplane plays a role of confirming supersonic drag reduction concepts incorporated in the design. Some of them are well known as an arrow planform, a warped wing and an area-ruled body, and they are used to reduce pressure drag. Furthermore as an original and challenging concept, natural laminar flow (NLF) wing design was tried to reduce friction drag. A target pressure distribution similar to a step function was derived from physical consideration with a current practical transition prediction code. The design process consisted of two stages. At the first stage, supersonic lifting surface theory and slender body theory were used. At the second stage, CFD (Navier-Stokes) code originally developed by NAL was effectively applied. Especially for the NLF wing design, a new inverse design method with CFD analysis was developed. Based on those concepts and tools, an optimum aerodynamic configuration was designed and the designed pressure distribution was validated by wind tunnel tests. Finally flight test plan for the airplane and further studies for an optimum design of jet-powered airplane are summarized.

1. INTRODUCTION

Several advanced technologies have been investigated and developed in the U.S.A. and Europe after Concorde was designed. At present time, those technologies makes it possible to develop a second generation SST. However, international collaboration is expected because huge development cost is anticipated.

Japan has little experience in designing an SST. To join such collaboration, a number of studies are necessary along the following two approaches. One is a design approach to catch up with current knowledge and technologies. Another is a fundamental research approach to provide new data on some advanced technologies.

National Aerospace Laboratory (NAL) has just started a flight test program with two kinds of un-manned scaled supersonic experimental airplanes. This program is promoted along both approaches. In this note, an overview of the program and details of the aerodynamic design of airplanes are described. On the other hand, several fundamental researches have already been conducted in Japan. An overview of the aerodynamic activities and details of special topics are summarized in another note on this course by the author.

Dr. Sakata, a leader of the NAL's program, presented the overview at the International CFD Workshop for Super-Sonic Transport Design on 16-17 March in Japan. Therefore referring to his paper[1], the overview of NAL's program is summarized in Chapter 2.

NAL has just designed the aerodynamic configuration of the un-powered experimental airplane. The design concepts, process, results are described in Chapter 3 and 4 . Then some results of wind tunnel tests are shown in Chapter 5. Finally the outline of flight test plan and further works for the design of jet-powered airplane are summarized in Chapter 6 and 7.

2. OVERVIEW OF NAL'S PROGRAM

To realize the second generation SST in early 21st century, high aerodynamic performance, high propulsion efficiency, light weight, and environmental compatibility are required. NAL has promoted some component researches and the development of two types of unmanned scaled supersonic experimental airplane in order to provide a technological base. This program consists of an un-powered and a jet-engine-propelled vehicles. The main subjects of the program include CFD-based aerodynamic design technology for high lift-to-drag ratio (L/D), composite structure technology for light weight, propulsion technology for high performance system, and associated control technology. The technological achievement of each component research will be applied to the experimental airplanes to be verified in the flight tests.

2.1. Outline of Program

The program was initiated in 1997 and will last until 2004 as shown in Fig. 1. The total cost of the program was estimated as much as 20 billion yen in eight years. NAL forms the SST project team consisting of the general affairs group, the experimental aircraft development group and component research group. To advance the program, collaboration and cooperation with some universities, industries and research institutes, including the foreign organizations are strongly encouraged.

The major research subjects being dealt in the program are categorized in four fields shown

Paper presented at the RTO AVT Course on "Fluid Dynamics Research on Supersonic Aircraft", held in Rhode-Saint-Genèse, Belgium, 25-29 May 1998, and published in RTO EN-4.

in Fig. 2. Aerodynamic design technology, CFD, composite materials and some of the propulsion theme are highly important. The program also includes the furnishing of the facilities, such as the small scale high-altitude supersonic engine test facility and the CFD research center.

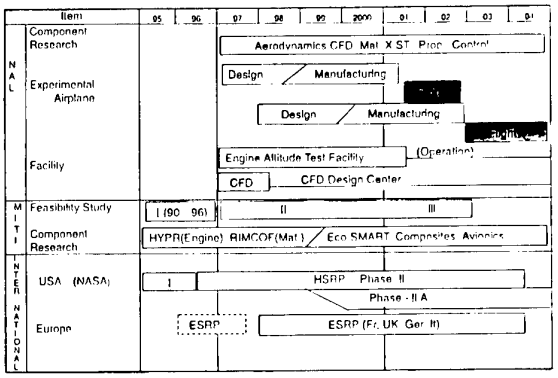


Fig. 1 NAL's Program Schedule[1]

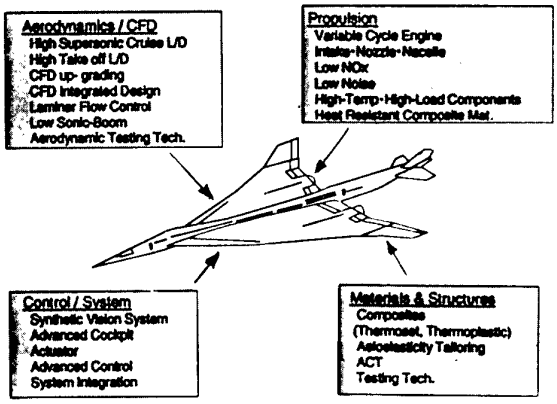


Fig. 2 Important Research Subjects[1]

2.2 Objective

One of the main goal of this program is to establish an aerodynamic design technology based on the CFD which will be validated by flight tests of the designed vehicles. In the aerodynamic design of the advanced SST, there are several standpoints in general. Such as reducing supersonic drag, reducing sonic boom, improving subsonic aerodynamic characteristics, compromising aerodynamics and structures, and suppressing aerodynamic noise. However in our program, improving lift-to-drag ratio (L/D) at supersonic and subsonic speed is most important.

Our first target is to develop an optimum CFD-based design system applying current drag reduction concepts and advanced technologies. Especially, fiction drag reduction is very effective and innovative, in spite of its difficult transition problem. Therefore, one of the final outputs is to propose the CFD-based aerodynamic design code with an optimum design method and a practical transition model.

The first type of scaled supersonic experimental airplane is a clean configuration without any propulsion system. Its goal is to establish a CFD-based inverse design system. Then the second type is a configuration with two jet engines, namely jet-powered vehicle. Its goal is to establish an optimized design technique for complete aircraft configurations, including airframe/nacelle integration.

2.3 CFD Technology

NAL has been promoting the CFD work using a large scale supercomputer, which had grown up to the Numerical Wind Tunnel (NWT). Fig. 3 shows comparison between conventional and inverse aerodynamic design methods by CFD. The inverse method creates a new design capability including the optimization of configurations aiming at high L/D and other features. Recently, NAL has tried to develop this technology, combining a CFD-based inverse method and an optimized pressure distribution for reducing drag.

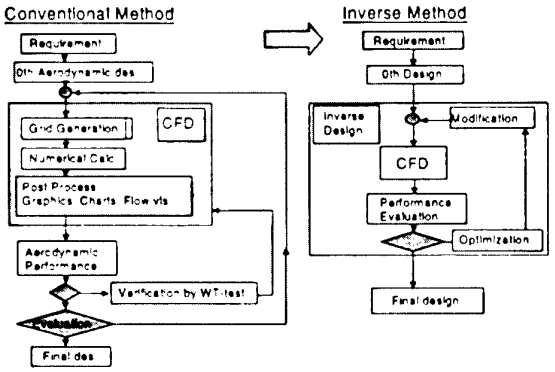


Fig. 3 CFD-based Design Technology[1]

Fig. 4 shows an outline of verification of the aerodynamic design technology through comparison of flight test and wind tunnel test data. The drag polar curves and pressure distributions will be compared with the design target and evaluated for establishing the design technology.

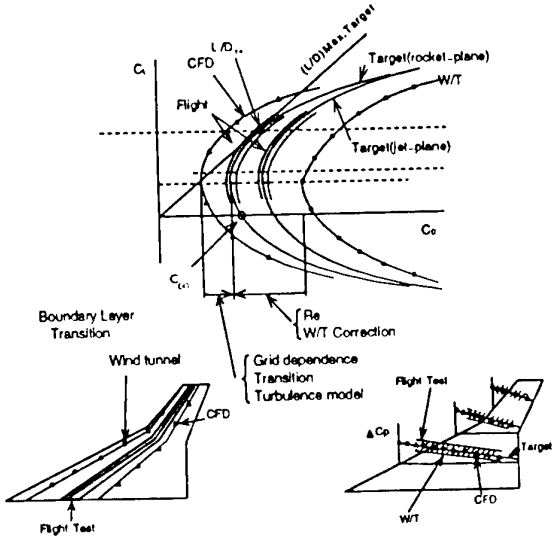


Fig. 4 Concept of Data Verification[1]

2.4 Development and Flight Test of Experimental Airplanes

1) Un-powered airplane
The un-powered airplane will be launched by a solid rocket booster. The design work of this vehicle was initiated in the middle of 1997 in cooperation with the industries' design team called SSET (Supers-Sonic experimental aircraft Engineering Team). Mitsubishi Heavy Industries, Ltd. (MHI), Kawasaki Heavy Industries, Ltd. (KHI), Fuji Heavy Industries, Ltd. (FHI), and Nissan Motors Co. are participating in the SSET.

NAL designed the aerodynamic configuration of the un-powered airplane with high L/D at M=2, using the CFD technology including the newly developed inverse method. The design concept and the configuration are shown in Fig. 8. The details are described in the following chapters.

After the design, many wind tunnel tests, and CFD calculations at off-design conditions were carried out. And the detailed design under several constraints will be started in 1998. The flight tests are planned to be performed in 2001. Fig. 5 shows the basic flight plan for accumulating the aerodynamic data. α-sweep and Reynolds-sweep at M=2 are the main flight pattern. The instrumentation for measuring the aerodynamic data including the boundary layer information, especially natural transition characteristics is extremely important. The design team makes effort for installation and integration of the object-fitted measurement system.

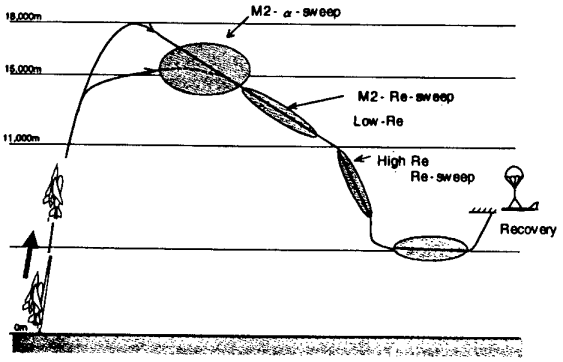


Fig.5 Concept of Flight Experiment (Un-powered Airplane)[1]

2) Jet-powered airplane
In order to develop a CFD-based aerodynamic design system for complete configurations and several advanced technologies, a jet-powered experimental airplane, which will fly in 2003, will be designed and manufactured. The basic concept is shown in Fig. 6. Modified warped wing with arrow planform, area-ruled body and laminar flow wing will be designed.

Two 8 kN turbojet engine integrated with air-intakes and nozzles will be installed under the wing. The outline of the propulsion system is shown in Fig. 7. A stable two-dimensional air-intake and simple nozzle are equipped. Location and diverter of the engine nacelle are the major design variables to obtain low aerodynamic drag. The CFD-based inverse method and optimization process will be developed and applied. Utilizing the data accumulated through wind tunnel tests of the airplane and air-intakes, the aerodynamic design will be completed in 2000.



Fig.6 Concept of the Jet-engine Powered Airplane[1]

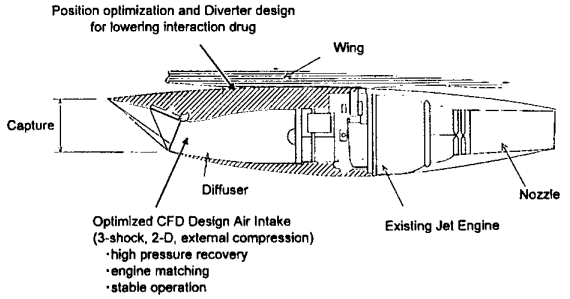


Fig. 7 Concept of the Propulsion System[1]

Table 1 Component research in NAL

Aerodynamics with CFD
-Boundary layer control for high lift/drag ratio
-Optimization and inverse method with CFD
-High-speed testing technology
Materials and structures
-Heat resistant thermoplastic and 3D thermoset
-Aeroelastic tailoring
Propulsion
-Air-intake and nozzle
-Variable cycle engine and component
Control and avionics
-Cockpit, FBL, GPS

2.5 Component Research

The component technology research in Table 1 conducted in NAL is expected to provide the database and technical base for the future. International and domestic cooperation is the key of the research.

3. DESIGN CONCEPTS

In the aerodynamic design of the first unpowered experimental airplane, we paid attention to reducing supersonic drag only, because this configuration is clean, namely an aerodynamically pure shape. The design point was set to M=2 and CL=0.1, which was a typical cruise condition for the expected second generation SST. Some design requirements such as fuselage length and volume, tail shape and position, were referred to the study of JADC(Japan Aircraft Development Corporation) and other foreign papers.

Our final design and supersonic drag reduction concepts incorporated in the design are summarized in Fig. 8. They are ①Arrow Planform, ②Warped Wing, ③Area-Ruled Body and ④Natural Laminar Flow (NLF) Wing. In the following sections, we described how we understood them, how we performed the aerodynamic design, and what we improved and devised.

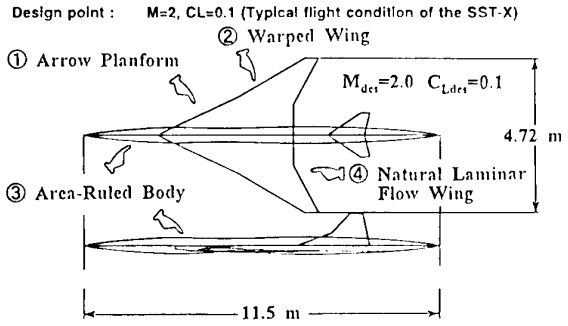


Fig.8 Design Concepts Incorporated in the Design[2]

Concepts ①, ②, ③ are well known to be very effective. The design procedure based on them has been well established. In our design procedure, first of all, a few candidate planform were selected according to a certain rule under some design constraints. At the second step, an optimum planform with a typical warped surface was selected through a warped wing design and estimation of the drag characteristics.

To design a complete warped wing, chordwise and spanwise thickness distributions are necessary. The spanwise thickness distribution is usually prescribed by considering structural constraint or referring to other data such as Concorde. The chordwise thickness distribution is important to realize natural laminar flow on the upper surface. One way to determine chordwise thickness distribution is to apply an inverse method. Another way is to use a prescribed distribution, for example, thickness distribution of NACA 6-series airfoil. And finally an area-ruled body was designed considering supersonic area distributions of wing and tails.

In our design, we tried to accumulate the effects of these concepts. Therefore, our designed configuration had a highly swept leading edge for the subsonic leading edge condition, a highly twisted and cambered wing designed using a numerical optimization, and a highly varied cross-sectional area distribution of fuselage following the exact solution by supersonic area-rule method. Furthermore, applying the NLF wing to a practical design was most challenging and original. In this sense, the designed configuration was a pure aerodynamic one.

However, our experimental airplane with this configuration must conduct flight tests even it is a scaled one. Therefore, aerodynamic configuration must be designed under several constraints such as ones from structure, flight performance, etc. Cooperative industries checked and improved this configuration from a standpoint of developing a real aircraft. One remarkable difference from the original SST configuration was tail length. It came from a parachute volume requirement. However there was little change in other constraints.

3.1 Arrow Planform

Selection of a suitable planform is effective in reducing lift-dependent supersonic drag. Jones[3] proposed an elliptic wing as an optimum planform using supersonic linear theory about a half-century ago. Furthermore he found an oblique elliptic wing was more effective in reducing wave drag. No other optimum planform with some constraints has been found.

According to a famous textbook[4] by Kuchemann, the following relation is useful to select a suitable planform.

$$C_D = C_{Df} + \frac{512}{\pi}\left(\tau p \frac{s}{l}\right)^2 K_0 + \frac{C_L^2}{2\pi}\frac{p}{s/l}\left[2\beta^2\left(\frac{s}{l}\right)^2 K_W + K_V\right]$$

$\frac{s}{l}$: *semispan – to – length ratio*

$p \equiv \frac{Wing\ Area}{2sl}$: *planform parameter*

$\tau \equiv \frac{Volume}{(Wing\ Area)^{3/2}}$: *Volume parameter*

$\beta \equiv \sqrt{M^2-1}$, K_0, K_W, K_V : *empirical coefficients*

The third term of the equation is a lift-dependent drag component. The formulation of this component is characterized by s/l and p under the first approximation of constant empirical coefficients. Because the effect of s/l in the first term of the third component is reverse to the second term, there is an optimum s/l. Therefore, the first principle for reducing supersonic drag is to select a planform with the optimum s/l. However, we can not exactly apply this principle, because planforms with this optimum value usually has a highly swept leading edge. Therefore in a

practical design, we have adopted a relaxed guideline of selecting subsonic leading edge. This was essentially valid, because it was found that sensitivity of drag near the optimum value on the s/l was very low through the numerical investigation of above equation.

Another way is to find an optimum planform among several candidates with lower drag using a supersonic lifting surface method. These candidates should be designed under the prescribed constraints, such as aspect ratio, taper ratio, leading edge sweep angle, trailing edge sweep angle, etc.

As described in the next chapter, planform with higher aspect ratio is aerodynamically desirable. To realize this situation under the structural constraints, arrow planform is very effective as reported in many technical papers.

3.2 Warped Wing

To reduce lift-dependent drag, one of the best ways is to adopt a combination of camber and twist distribution determined by an optimum load distribution. Such a cambered and twisted surface is usually called "warp". About a half century ago, a number of analytical investigations were performed[5,6]. Some optimum load distributions on typical planforms, such as delta, ogee and gothic type, were obtained under several aerodynamic constraints such as lowest drag, fixing aerodynamic center, fixing trailing edge position. However, these analytical solutions are not convenient for arbitrary arrow planform.

Carlson et al[7,8] developed a new numerical method for estimating drag and designing a warped surface in 1964, and they improved it in1974. This method is very effective to analyze various planform and warp effects. This method was also used in our design.

The key point of warp design for reducing drag is suppressing theoretical infinite load at leading edge. This usually leads to a certain leading edge droop, because leading edge separation vortex induced by local high angle of attack is generally due to highly swept leading edge. Therefore, to achieve an attached flow at leading edge, certain droop is necessary. This is the second principle for reducing supersonic drag.

Supersonic lifting surface theory indicates the minimum pressure condition achieved by the well-known Jones criterion, as stated above. However, Carlson et al. did not explicitly refer to Jones condition. To understand the warp concept which reduce lift-dependent drag, the author analytically investigated the relation.

In general, supersonic lifting surface theory formulates induced angle of attack α_i, lift coefficient C_L and lift-dependent drag coefficient C_{Di} as follows[3,8,9].

$$\alpha_i(S) = \iint_{A_F} dS_1 K(S - S_1) l(S_1)$$

where $S \equiv (x, y)$, $dS \equiv dydx$

$l \equiv \Delta C_p(x, y)$: *load distributi on*

x : *streamwise coordinate*

y : *spanwise coordinate*

$$K(S - S_1) \equiv -\frac{1}{4\pi} \frac{x - x_1}{(y - y_1)^2 \sqrt{(x - x_1)^2 - \beta^2 (y - y_1)^2}}$$

$A_F(S_1)$: *forward Mach cone region* , $x_1 < x - \beta |y - y_1|$

$$C_L = \frac{1}{S} \iint_{\sigma} dS\, l(S)$$

$$C_{Di} = \frac{1}{S} \iint_{\sigma} dS\, l(S)\, \alpha_i(S) = \frac{1}{S} \iint_{\sigma} dS\, l(S)\, \alpha_{iR}(S)$$

$$= \frac{1}{2S} \iint_{\sigma} dS\, l(S) \{\alpha_i(S) + \alpha_{iR}(S)\}$$

where $\alpha_{iR}(S) \equiv \iint_{A_R} dS_1\, K(S_1 - S)\, l(S_1)$

$K(S_1 - S) = -K(S - S_1)$

$A_R(S_1)$: *rearward Mach cone region* , $x_1 > x + \beta |y_1 - y|$

σ : *wing area region*

Here the formulation of C_{Di} above includes well-known "reverse flow theorem[3,10]". α_{iR} indicates the local incidence induced by reverse flow.

From this formulation, the following Jones criterion is derived[9] using a variational method with Lagrange multiplier, k.

$$l(S) = \bar{l}(S) + \delta l(S) \;\Rightarrow\; \alpha_i(S) = \overline{\alpha_i}(S) + \delta\alpha_i(S)$$

$$\Gamma\{l(S)\} \equiv C_{Di} - kC_L = \frac{1}{S} \iint_{\sigma} dS \left[\alpha_i(S) - k\right] l(S) = \bar{\Gamma} + \delta\Gamma$$

where $\delta\Gamma \equiv \frac{1}{S} \iint_{\sigma} dS \left[\overline{\alpha_i}(S) + \overline{\alpha_{iR}}(S) - k\right] \delta l(S)$

If $\bar{\Gamma}$ = *minimum*, $\delta\Gamma = 0$ *for any* $\delta l(S)$ *at given* C_L

$\therefore\ \overline{\alpha_i}(S) + \overline{\alpha_{iR}}(S) = k = const.$ *for* $S \Leftarrow$ *Jones criterion*

On the other hand, Carlson's method is summarized as follows.

$$l(S) = \sum_{n=1}^{N} c_n l_n(S) \quad , \quad l_n(S) : n - th\ given\ load$$

$$\Rightarrow\ \alpha_i(S) = \sum_{n=1}^{N} c_n \alpha_{i,n}(S)$$

$$\Rightarrow\ C_L = \sum_{n=1}^{N} c_n C_{L,n} \quad , \quad C_{Di} = \sum_{n=1}^{N} \sum_{m=1}^{N} c_n c_m C_{Di,nm}$$

where $C_{Di,nm} \equiv \frac{1}{S} \iint_{\sigma} dS\, l_n(S) \alpha_{i,m}(S) = \frac{1}{S} \iint_{\sigma} dS\, l_m(S) \alpha_{iR,n}(S)$

$$c_n = \overline{c_n} + \delta c_n \quad \Rightarrow \quad \Gamma(c_n) \equiv C_{Di} - k C_L = \overline{\Gamma} + \delta\Gamma$$

$$where \quad \delta\Gamma \equiv \sum_{n=1}^{N}\left[\sum_{m=1}^{N}\overline{c_m} A_{nm} - k C_{L,n}\right]\delta c_n$$

$$A_{nm} \equiv C_{Di,nm} + C_{Di,mn}$$

If $\overline{\Gamma}$ = *minimum*, $\delta\Gamma = 0$ *for any* δc_n *at given* C_L

$$\therefore \quad \sum_{m=1}^{N}\overline{c_m} A_{nm} - k C_{L,n} = 0 \quad for \ n = 1,\ldots,N$$

$$\Rightarrow \quad \overline{c_n} = k\sum_{m=1}^{N} A_{nm}^{-1} C_{L,m}$$

The relation between the formulation above and Jones criterion is as follows.

$$\sum_{m=1}^{N}\overline{c_m} A_{nm} = \frac{1}{S}\iint_{\sigma} dS \sum_{m=1}^{N}\overline{c_m}\{\alpha_{i,m}(S) + \alpha_{iR,m}(S)\} l_n(S)$$

$$= \frac{k}{S}\iint_{\sigma} dS\, l_n(S)$$

$$\therefore \quad \frac{1}{S}\iint_{\sigma} dS\left[\alpha_i(S) + \alpha_{iR}(S) - k\right] l_n(S) = 0, \quad n = 1,\ldots.N$$

This means Carlson's condition on optimum combination of coefficients is included within Jones criterion. However, the variety of elementary loads, for example, N=8 in their method in 1974, is less than Jones' theoretical consideration, namely N=∞. Therefore, drag of a warped surface designed with Carlson's method is generally larger than theoretical minimum by Jones. In a preliminary numerical study by the author, it was found drag reduction effect was about 85% of theoretical maximum reduction which is the difference between drag of flat plate and Jones optimum value.

Next as the second step, the author considered lift and drag characteristics of a warped wing using supersonic lifting surface theory. In linear theory, influence of angle of attack α_f is reflected through the combination of the following two loads.

$$l(S) = l_w(S) + l_f(S)$$

$l_w(S)$: *prescribed load at a warp design condition*

$l_f(S) = l_{u,f}(S)\alpha_f$: *load at a flat plate condition*

This means the dependency of α_f on load is the same as a flat plate, naturally supposed in linear theory. Under this assumption, lift and lift-dependent drag coefficients are formulated as follows.

$$C_L = C_{Ldes} + C_{Lf}$$

$$where \quad C_{Ldes} = \frac{1}{S}\iint_{\sigma} dS\, l_w(S)$$

$$C_{Lf} = C_{L\alpha_f}\alpha_f \quad , \quad C_{L\alpha_f} = \frac{1}{S}\iint_{\sigma} dS\, l_{wf}(S)$$

$$C_{Di} = K(C_L - C_{L0})^2 + \Delta C_{Di}$$

$$K \equiv \frac{1}{C_{L\alpha_f}}, \quad C_{L0} \equiv \frac{C_{Ldes} - \lambda}{2}, \quad \Delta C_{Di} \equiv C_{Di,des} - K\left(\frac{C_{Ldes} + \lambda}{2}\right)^2$$

$$\lambda \equiv \frac{1}{S}\iint_{\sigma} dS\, l_{wf}(S)\alpha_{i,des}(S), \quad C_{Di,des} \equiv \frac{1}{S}\iint_{\sigma} dS\, l_w(S)\alpha_{i,des}(S)$$

$$\alpha_{i,des}(S) = \iint_{A_F} dS_1 K(S - S_1) l_w(S_1)$$

In these formulations, remarkable features are obtained.

(1) Lift slope $C_{L\alpha}$ equals to the lift slope of a flat plate.
(2) K which characterize a polar curve is an inverse of a lift slope, and this is the same as flat plate condition.
(3) Drag reduction effect at design C_L increases as C_{L0} increases, unless ΔC_{Di} excessively increases.
(4) A theoretically optimum C_{L0} is obtained by the following relation.

$$\frac{C_{L0}}{\Delta C_{Di}} = \left[\frac{C_{Di,des}}{C_{L0}} - K C_{L0}\left(1 - \frac{C_{L,des}}{C_{L0}}\right)^2\right]^{-1} \rightarrow \max$$

$$\therefore \quad C_{L0} = \sqrt{\frac{\delta C_{Di,eff}}{K}} \quad where \quad \delta C_{Di,eff} \equiv K C_{Ldes}^2 - C_{Di,des}$$

$\delta C_{Di,eff}$: *drag reduction by warp effect*

3.3 Area-Ruled Body

First of all, to reduce wave drag due to volume, a wing and fuselage must be thin and slender. This means that aerodynamic configurations satisfying certain conditions in linear theory have lower drag. Then there is a further improvement in reducing such wave drag. This is the third principle for reducing supersonic drag, and it is a so-called "area-rule" technique for a fuselage design. This reduces drag due to volume based on interference drag between wing, tails and fuselage.

According to the supersonic slender body theory, wave drag due to volume is generally formulated in the following equation[10].

$$D_W = -\frac{q}{4\pi^2}\int_0^{2\pi} d\theta \int_0^{l}\int S''(x_1,\theta) S''(x_2,\theta) \ln|x_1 - x_2| dx_1 dx_2$$

$$where \quad S'' \equiv \frac{d^2 S}{dx^2} \ , \ q : dynamic\ pressure$$

Here θ is one of the coordinates indicate Mach cone. (Other coordinates are apex angle related to Mach angle and distance from the apex.) And S means the projection of oblique cross sectional area cut by each Mach plane on vertical plane to streamwise direction. (For convenience, we often call it "supersonic area".) This formulation was derived by von Karman and Hayes under assuming a pointed tail.

In general, a fuselage is approximately axisymmetric, and a wing and tails are non-axisymmetric. Then the following relations are assumed.

$$S(x,\theta) = S_f(x) + S_W(x,\theta)$$

where S_f : *supersonic area of fuselage*

S_W : *supersonic area of wing, H − tail, V − tail*

$$\text{Fourier expansion} : S'_W(x,\theta) = \sum_{n=0}^{\infty} A_{2n}(x)\cos(2n\theta)$$

$$A_{2n}(x) = \frac{1}{2\pi}\int_0^{2\pi} S'_W(x,\theta)\cos(2n\theta)\,d\theta$$

Under these assumptions, the formulation of wave drag is summarized as follows.

$$D_W = D_{Wing-Body} + (D_{Wing})_n$$

$$\text{where } D_{Wing-Body} \equiv -\frac{q}{2\pi}\int_0^l\int_0^l \left\{S''_f(x_1) + A'_0(x_1)\right\}\left\{S''_f(x_2) + A'_0(x_2)\right\} \cdot ln|x_1 - x_2|\,dx_1 dx_2$$

$$(D_{Wing})_n \equiv -\frac{q}{4\pi}\sum_{n=1}^{\infty}\int_0^l\int_0^l A'_{2n}(x_1)A'_{2n}(x_2)\,ln|x_1 - x_2|\,dx_1 dx_2$$

If a wing and tails are specified, it is difficult to reduce the second term $(D_{wing})_n$ due to its nonaxisymmetric feature. On the other hand, the first term $D_{wing\text{-}Body}$ corresponds to an axisymmetric part. For this part, a body with an optimum area distribution is well known "Sears-Haack body". Therefore, if the first term is the drag of Sears-Haack body, wave drag due to volume of complete configuration is reduced. To realize this situation, it is necessary to improve fuselage geometry in the way described below.

$$S''_f(x) + A'_0(x) = S''_{SH}(x)$$

$$\therefore \left\{S_f(x)\right\}_{Area-Ruled} = S_{SH}(x) - S_0(x)$$

where

$$S_0(x) \equiv \int_0^x A_0(x')dx' = \frac{1}{2\pi}\int_0^{2\pi} S_W(x,\theta)\,d\theta$$

$$S_{SH}(x) \equiv \frac{128\,V_{tot}}{3\pi l}\left\{\frac{x}{l}\left(1-\frac{x}{l}\right)\right\}^{\frac{3}{2}} : \textit{Sears} - \textit{Haack body}$$

Here V_{tot} is total volume of a complete configuration. This improved fuselage is generally called area-ruled body. This rule is the third principle of reducing supersonic drag.

3.4 Natural Laminar Flow (NLF) Wing

A cross-sectional shape of three dimensional wing, namely airfoil section is very important in designing an aerodynamic configuration at subsonic speed. However, it is supposed the effect of airfoil section is small at supersonic speed because of thin thickness and three-dimensionality due to low aspect ratio. The three concepts above are related to pressure drag reduction mainly and they have a large effect. On the other hand, reducing friction drag leads to another principle to improve L/D. One of the best ways is a laminar flow control, but there are a great number of problems to be solved through fundamental research. Another way is the NLF wing design.

Usually laminar airfoil concept is based on suppressing Tollmien-Schlichting (T-S) wave instability. For a low aspect ratio wing with highly swept leading edge, transition due to cross-flow (C-F) instability is dominant at forward part of wing. To design the NLF wing, first of all, an optimum pressure distribution suppressing C-F instability must be found.

As C-F instability is originated in cross-flow, the reduction of it is the first target of finding the optimum pressure distribution. It is generally impossible to eliminate cross-flow. The key point is to reduce the region generating cross-flow. Cross-flow is produced by any chordwise pressure gradient. At the front part of wing, there is always severe acceleration. Therefore, it is very effective to narrow this acceleration region. This leads to a pressure distribution with steep gradient at front.

After a mid-chord, T-S instability becomes dominant. To suppress this instability, well-known concept, namely gradual acceleration is effective. Fortunately, usual SST planform has supersonic trailing edge and no recover region of pressure distribution is necessary. As a result, an optimum pressure distribution should have steep acceleration at front and gradual acceleration from the front to trailing edge.

According to this consideration, Ogoshi[11] of KHI, a co-researcher in the joint study with the author, found an optimum pressure distribution for the NLF, using a current practical transition prediction code (SALLY code[12]). Fig. 9 and 10 show the NLF pressure distribution and estimated transition characteristics.

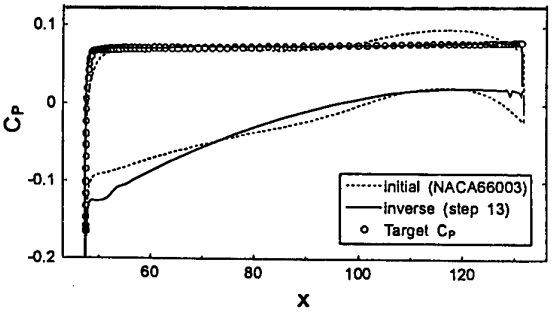


Fig.9 Target Pressure Distribution for NLF[11]

The SALLY code predicts so-called N-factor for both T-S instability and C-F instability. N-curve means an envelope on each integration of amplification rate of small disturbances with a wide variety of frequencies. As transition is physically caused by such amplified disturbances, it is generally expected there is a certain correspondence between transition point (exactly onset of transition) and N value. This N value is not predicted by any theory but empirically estimated through flight tests or quiet wind tunnel tests. At two-dimensional subsonic speed regime, an amount of information of this N value has

been obtained, however, we have only a few data on three-dimensional flow at supersonic speed. Therefore at present time, transition position on this optimum pressure distribution is not able to be predicted by the N characteristics of Fig. 10. However, lower N value in this figure shows the optimum pressure distribution has better transition characteristics.

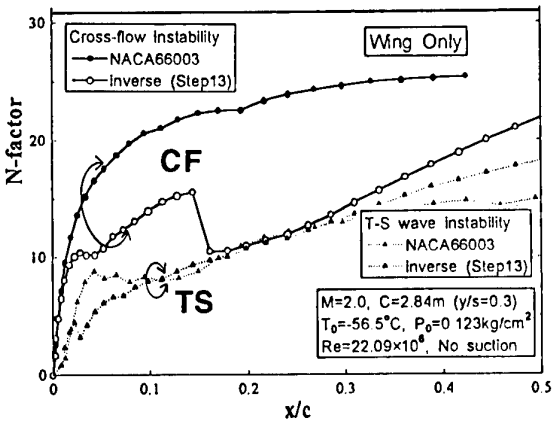


Fig.10 Evaluation of Amplification Factor[11]

The SALLY code has some assumptions, and the optimum NLF design pressure distribution above is just an approximated one. However, we decided this was a first step to challenge the advanced aerodynamic design.

Thus to design the NLF wing, we must solve a so-called inverse problem to achieve this pressure distribution. Jeong[13] and Matsushima[14] developed a new method using CFD analysis. Applying an optimum pressure distribution for a NLF wing and a CFD inverse method is the forth principle for reducing supersonic drag. The details of the NLF wing design is described in next chapter.

4. DESIGN PROCESS AND RESULTS

Our aerodynamic design process using design concepts or principles above consisted of two stages. At the first stage, a baseline configuration was designed using a supersonic linear theory, namely lifting surface and slender body theory. In this stage, NLF wing design concept was not included. At the second stage, some refinements of the baseline were conducted by CFD (Navier-Stokes) code, to break the limitation based on linear theory. Then to improve a lift-to-drag ratio(L/D), an optimum configuration was designed using the CFD code and applying the NLF wing concept. This code was developed by Takaki[15] of NAL and well validated through comparison with wind tunnel test results in other SST configurations without nacelles.

Improving L/D at supersonic cruise conditions is the main goal of the first type experimental airplane. The design point of M=2 and CL=0.1 was chosen, because it is a typical cruise condition for SST. The outline of a final designed configuration and incorporated design concepts are already shown in Fig. 8. Results at each process are described in the following sections.

4.1 First Design Stage based on Linear Theory[16]

1) Planform design

In general, parameters characterizing arrow planform are wing area (S), aspect ratio (AR), semispan-to-length ratio (s/l), taper ratio (λ), leading edge sweep angle (Λ_{LE}), trailing edge sweep angle (Λ_{TE}), and spanwise kink position (ε). In our planform study, some of those parameters were determined referring to a typical arrow planform proposed by Douglas. Major parameters were AR, s/l, $\Lambda_{LE,i}$(for inner wing), $\Lambda_{TE,o}$(for outer wing) and ε_T(for trailing edge). Here S was fixed at a typical value. The range of s/l was selected near its optimum value which was about 0.3 in this case as mentioned in previous chapter. On the other hand, AR was taken from 1.8 to 2.2, considering moderate balance between aerodynamics and structure.

First of all, according to these assumptions, ninety-nine candidate planforms were designed. Then the lift-dependent drag factor K defined in previous chapter of each planform was estimated as a flat plate wing using a lifting surface theory. One of the criteria selecting an optimum planform is to pick up planforms with lower K than Douglas one. As another criterion, planforms with lower derivative of K to Mach number at the design point were chosen. Finally eight planforms shown in Fig. 11 were selected for the next step.

2) Warp design

For each eight planform, optimum warped surface of its own was designed and lift-dependent drag at design point was estimated, using the Carlson's method. As shown in Fig. 11, the planform (hatched in the figure) with AR=2.2 and Λ_{LE}=66/61.2 degrees inner/outer was finally selected.

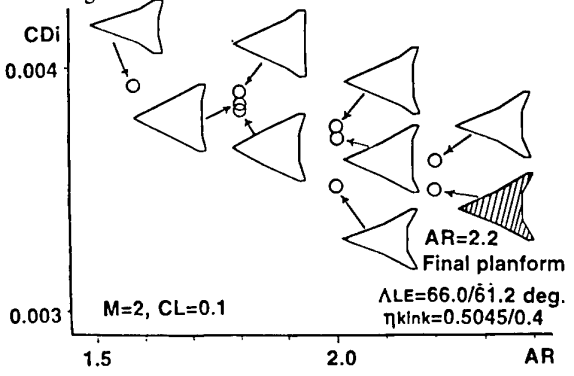


Fig. 11 Estimated Lift-dependent Drag for Warped Planforms[2]

As stated before, certain chordwise and spanwise thickness distributions are necessary to design a warped wing. The spanwise thickness distribution referred to a typical thickness distribution of foreign SST configurations, that is, a thickness ratio of 3.7% at a wing

root and 3% at a wing tip. In this stage, the chordwise thickness distribution was assumed to use a thickness distribution of NACA 4-digit series NACA0003 airfoil for simplicity. Fig. 12 shows the designed warp wing geometry.

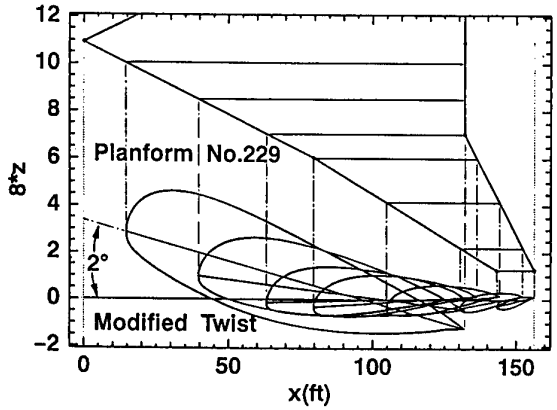


Fig. 12 Warped Wing Geometry[16]

3) Area-ruled body design

Before applying area-rule design, the tails and a wing location was determined. Since this is the first step, it was determined by referring to foreign similar SST configurations. Then according to the design procedure mentioned in Chapter 3, a supersonic area distribution of the area-ruled body was calculated as shown in Fig. 13. It was performed under the condition of M=2 and the requirement of volume capacity behind an empennage for parachute system used in a recovery phase of the flight test. This wing-body-tails configuration was called "1st Configuration".

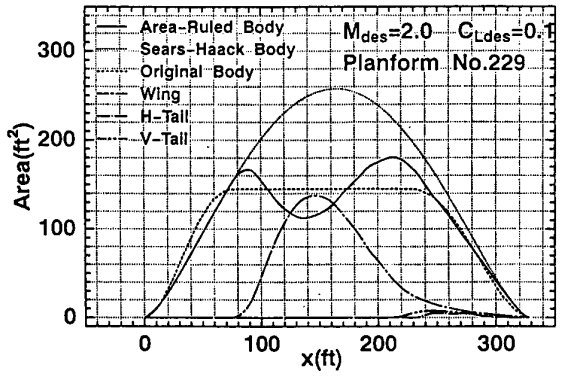


Fig. 13 Area Distributions of the 1st Configuration[16]

The aerodynamic characteristics shown in Fig.14 were predicted by linear theory about lift-dependent ($C_{DI}=C_{Dv}+C_{Dwl}$) and wave drag (C_{Dwv}), and by boundary layer theory with some empirical relations about friction drag (C_{Df}). This configuration was used as a start point at the next stage.

4.2 Second Design Stage based on CFD including Inverse Design Method[2]

1) CFD analysis of 1st configuration

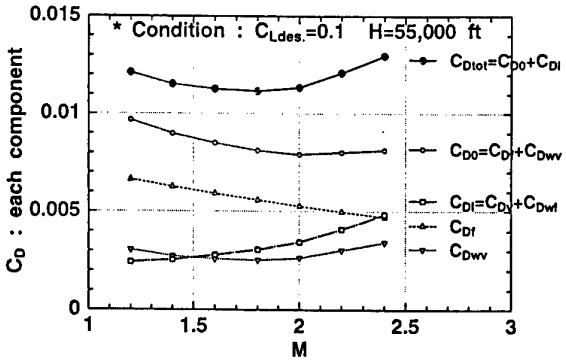
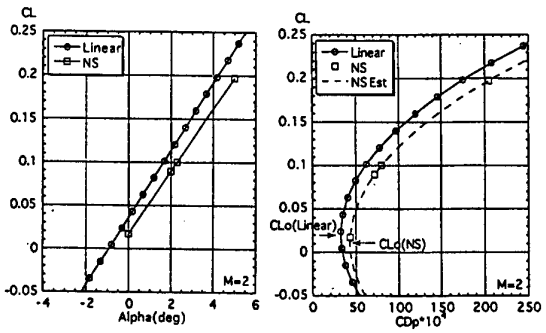


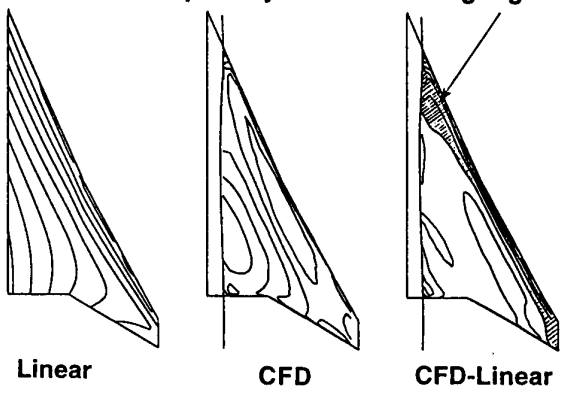
Fig. 14 Estimated Drag Breakdown

The 1st Configuration was analyzed at M=2 using NAL's CFD (Navier-Stokes) code under the full turbulent condition. Fig. 15(a) and (b) show the lift and drag characteristics computed by CFD, respectively. Comparing with the results by linear theory, good agreement of lift slope and K were obtained. However, there were the following major differences: (i) loss of lift at the same angle of attack, (ii) increment of minimum drag and (iii) loss of C_{L0}. In general, good agreement of minimum drag is not expected because of a turbulence model in CFD and an empirical relation in boundary layer theory.



(a) Lift vs. α (b) Drag Polar

• Load deficit near the leading edge, especially at an inner wing region



(c) Load Distribution

Fig. 15 Comparison of the Linear Theory and the CFD[2]

To consider the first and third difference, Shimbo[2,17] of NAL summarized an iso-load contour in Fig. 15(c). The left and center

correspond to the results of linear design and CFD analysis at M=2 and CL=0.1, respectively. And the right shows the difference between them. The hatching means a region where the load calculated by the CFD is smaller than the linear theory. A load deficit near leading edge at inner wing was found in the figure. This deficit originated in the influence of wing thickness and body, especially strong interference of an area-ruled body with static pressure on upper surface. They could not be treated by linear theory.

Decrease of C_{L_0} means the reduction of warp effect expected by the linear theory. As a first approach to improve the design, we considered to realize the drag reduction effect predicted by linear theory. Therefore some refinements including the influence of thickness and body were necessary.

2) Refinement by quasi-inverse design

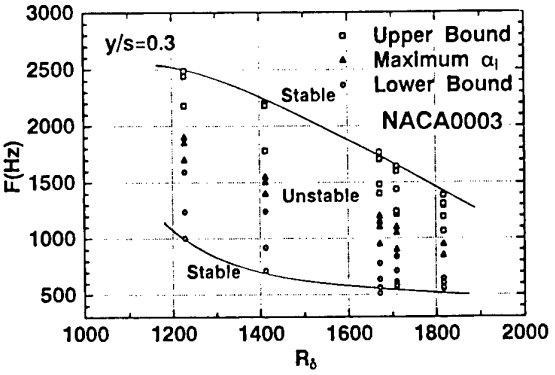
To recover the warp effect, removing the load deficit is necessary. Shimbo[2] designed a refined configuration through improving the camber near leading edge. He developed a simple quasi-inverse method for this purpose. This inverse method was formulated by two dimensional supersonic linear theory and applied to wing section every 5% semispan location.

To apply any inverse method, a target for load or pressure distribution is necessary. In his design, an optimum load distribution calculated by Kaiden of MHI using Middleton and Lundry's method[18] was used as a target, because their method, an extension of usual Carlson's method, could treat the effect of body on warped surface.

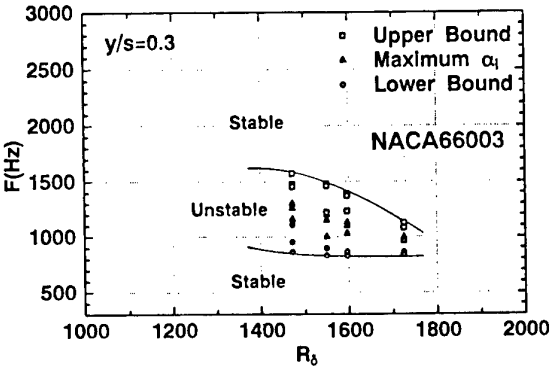
Shimbo's design procedure is as follows. The difference between the target load distribution and the CFD result made the increment of camber slope at each chordwise and spanwise location by the quasi-inverse method. Then a new camber was calculated by integrating the new camber slope modified with the increment. After a new wing was defined by adding the original thickness distribution to the new camber, CFD analysis was conducted.

Before designing, the chordwise thickness distribution was replaced with one of NACA 66-series airfoil, because better transition characteristics of NACA 66-series airfoil was reported by Ogoshi[11] using the SALLY code. Although the SALLY code was formulated on incompressible stability theory, the validity of his estimation at compressible condition was confirmed by the author using an originally developed compressible stability analysis code[19]. Fig. 16(a) and (b) show comparison of estimated unstable region at 30% semispan station with NACA0003 and 66003 thickness distributions.

Fig. 17(a) shows a drag reduction effect at each iterative step for one case with an original wing height relative to the body and the other case with a higher wing location. At the original height, the drag was rapidly decreased. This configuration at final step (indicated by "B" in the figure) was called "2nd Configuration". Fig. 17(b) indicates the deviation from the target load distribution by hatching. As shown in these figures, the quasi-inverse method was effective.

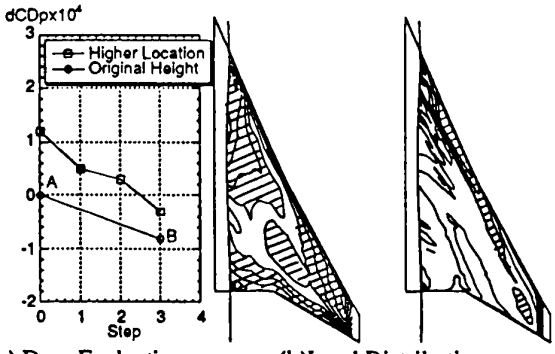


(a)NACA 0003 Thickness Distribution



(b) NACA 66003 Thickness Distribution

Fig. 16 Neutral Stability Characteristics



(a) Drag Evaluation (b)Load Distribution

Fig. 17 Results of the Quasi-Inverse Design[2]

3) Further improvement based on natural laminar flow wing concept

After improving pressure drag reduction, reducing friction drag is necessary to improve the L/D further. As mentioned in Chapter 2, one of such approaches is to reduce friction drag using natural laminar flow (NLF) wing concept.

The Reynolds number of the scaled experimental airplane is smaller than the full scale SST, because its body length is only 11.5 m.

In this situation, the turbulent friction drag occupies about a half of the total drag. Accordingly, the effect of the NLF wing concept was rather emphasized. And some flight test data on transition location and confirmation of the concept cover our handicap of having no large quiet supersonic wind tunnel. Therefore, it is a valuable challenge for us.

In this design stage, three-dimensional inverse method was used to predict the increment of wing geometry to achieve the target pressure distribution. This inverse method was newly developed in the cooperative research program between NAL and Tohoku University. The formulation of the method is based on supersonic lifting surface theory, and a panel method was used to solve the governing equation. The detail of formulation and method of solution was summarized in Ref. 13 and 14.

Fig. 18 shows a flowchart of the inverse design procedure. The target pressure distribution on the upper surface was the desirable one for the NLF wing described in Chapter 3. And the target on the lower surface was calculated by subtracting the optimum load distribution mentioned above from the upper surface pressure distribution. Then the 2nd Configuration was used as an initial geometry.

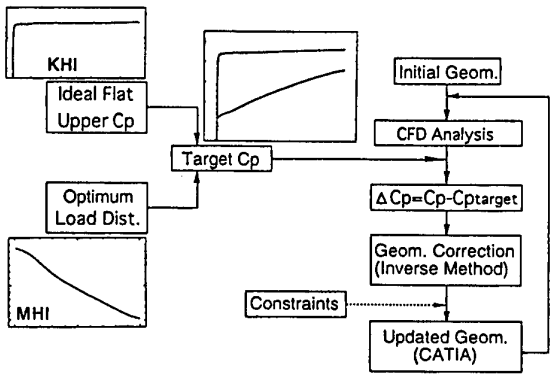


Fig. 18 Flowchart of the Inverse Design[2]

At each iterative process, wing geometry was modified by adding the increment computed by the inverse method to the original configuration at 14 spanwise stations with a certain relaxation and a weak constraint for a maximum wing thickness ratio. Then, a new wing geometry with fuselage for CFD analysis was re-defined through smoothing the modified geometry with the three-dimensional geometry generation software CATIA. Most time of one iteration was spent in this smoothing process. Therefore, within the time limit of the design, the modified wing configuration after ten iterations was chosen as the 3rd Configuration even though no complete convergence was obtained. Fig. 19 shows the designed wing geometry.

4) Evaluation of the 3rd configuration

Shimbo[2] evaluated the 3rd Configuration from the following viewpoints.

(1) Pressure distribution

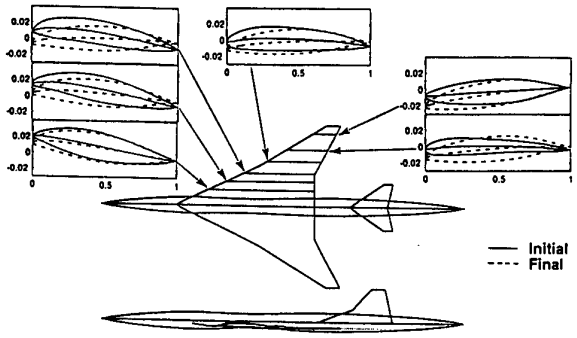
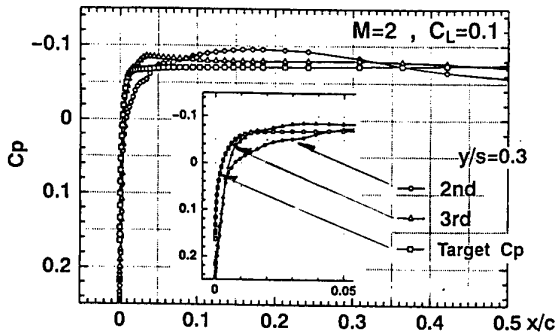
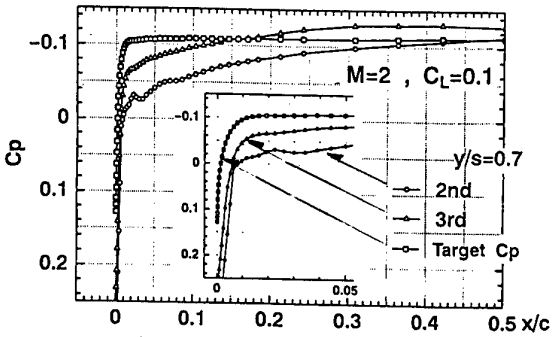


Fig. 19 Geometries of the 3rd Configuration[2]

Fig. 20(a) and (b) show the pressure distributions on 30% and 70% semispan locations at the design point, compared with the one of initial geometry and the target. These locations were chosen as a representative spanwise station at inner and outer wing portion. Both pressure distributions show better agreement with the target than the initial geometry as a whole. There are, however, slight and remarkable differences near leading edges at both 30% and 70% semispan locations.



(a) at 30 % Semispan Station



(b) at 70 % Semispan Station

Fig. 20 Comparison of Pressure Distributions[2]

(2) Load distribution and pressure drag

Fig. 21 shows the deviation from the optimum load distribution. In this figure, certain improvement of the load deficit near leading edge is obvious at 3rd Configuration. This means the inverse method is effective to improve the warp effect, too. However, the lift-dependent drag factor K increased. In total, pressure drag was not reduced much from the 2nd Configuration.

(3) Friction drag

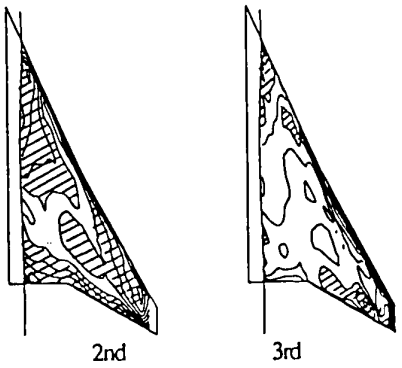
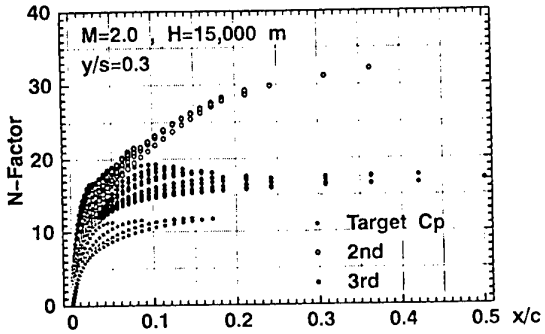
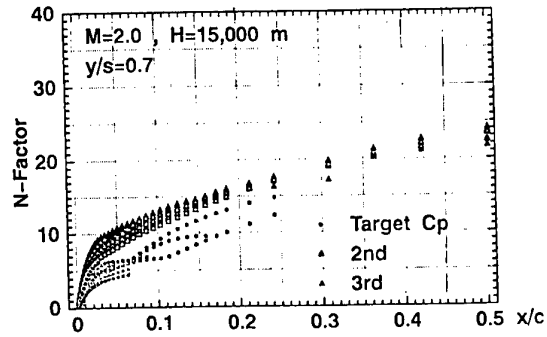


Fig. 21 CFD Results of the 3rd Configuration[2]

Fig. 22(a) and (b) show the N characteristics on C-F instability at 30% and 70% semispan location estimated by the SALLY code. They are compared with the 2nd Configuration and the target ones[16]. Certain improvement, namely the reduction of N values of 3rd Configuration from 2nd Configuration was obtained at both stations. However there was large difference compared with the target. This originated in slight difference of pressure gradient shown in Fig. 20 (close-up). The physical reason is understandable as stated above.



(a) at 30 % Semispan Station



(b) at 70 % Semispan Station

Fig. 22 Evaluation of the Transition Characteristics[2,16]

To evaluate friction drag, it is necessary to estimate transition position. Since the formulation of this code was based on an incompressible linear stability, each N value does not quantitatively reflect physical transition mechanism. Therefore, any reliable transition position could not be estimated. However, the difference of N characteristics is supposed to be valid. We can judge whether it has better transition characteristics or not.

In addition to the scaled supersonic experimental program, several fundamental researches have been conducted at NAL. One of them is to develop a practical transition prediction method. The author has investigated it using the e^N method based on three-dimensional compressible linear stability theory and some experimental data. The outline is described in another lecture note on this course by the author.

At this time, the friction drag was approximately evaluated under the following assumptions. The N value corresponding to natural transition due to C-F instability in flight test condition (at an altitude of 10 to 18 km) is expected to be 20~25. The transition at 30% semispan station was estimated at x/c=0.11 for the 2nd Configuration. For the 3rd Configuration, N was less than the critical value. In this configuration, transition due to T-S instability was expected to be dominant, and it was assumed at around x/c=0.5. On the other hand, the pressure distribution at 70% semispan station was not close to the target. A little improvement was obtained, and transition of both 3rd and 2nd Configuration was expected at x/c=0.31.

Then the friction drag was calculated with these estimated transition positions and empirical relations of friction coefficient in laminar and turbulent flat plate boundary layer. Here, a full turbulent flow was assumed on the lower surface. As a result, the friction drag of the 3rd Configuration was reduced about 0.0004 from the 2nd Configuration.

(4) Overall characteristics

The total drag of the 3rd Configuration was calculated using the estimated values above. It was improved by about 0.0005 from the 2nd Configuration. And it improved the L/D from 7 to 7.2 at the design condition of the experimental airplane.

5. WIND TUNNEL TESTS[2]

NAL conducted wind tunnel tests to validate our design. Two types of wind tunnel models with 8.5% scale to a real experimental aircraft as shown in Fig. 23, were used at 1m×1m supersonic wind tunnel at NAL. The first one was for a force measurement and mounted by a straight sting. The second one was for a pressure measurement and had 90 pressure taps. Since the main objective of the tests was not to confirm the NLF concept but to validate pressure distribution estimated by CFD, transition position was fixed at x/c=0.03 for both models to avoid unexpected laminar separation due to lower Reynolds number.

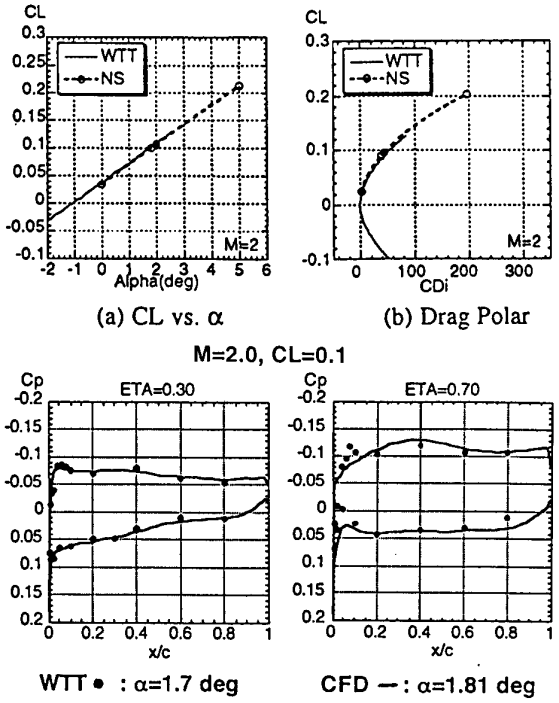
Fig. 24(a) and (b) show the lift and drag characteristics measured at M=2, compared with CFD (Navier-Stokes) analysis. Very good agreement in the lift was obtained. The drag polar curve was shifted to an origin of the plot, because friction drag was obviously different between these two. Lift-dependent drag factor K estimated by measured data was

confirmed to be nearly the same as CFD result.



Fig. 23 Wind Tunnel Test Model

Fig. 24(c) shows measured pressure distributions at 30% and 70% semispan stations at the design point of M=2 and CL=0.1, compared with CFD results. There is also very good agreement between the tests and CFD results.



(a) CL vs. α (b) Drag Polar

(c) Pressure Distribution

Fig. 24 Comparison with the Tunnel Test[2]

Through the wind tunnel tests, the CFD code in our design procedure was confirmed to be a reliable tool. And the design concepts on pressure drag reduction were approximately confirmed in the wind tunnel tests. However confirming the NLF wing design concept has not been conducted in any wind tunnel tests yet. This is very important work in our program. A further wind tunnel test will be planed this year.

6. FLIGHT TEST PLAN

NAL's scaled supersonic experimental airplane program is still in the very early stage of the whole program. That is, the fundamental aerodynamic design of the un-powered airplane has been just finished by NAL in collaboration with MHI and KHI. Then a real aerodynamic design under the several constraints (structure, equipment, flight dynamics, etc.) is started mainly by industries.

As mentioned in Chapter 2, the main objective of fight tests of the un-powered experimental airplane is to confirm the aerodynamic characteristics such as lift, drag, pressure distributions, surface and transition characteristics. In this sense, requests for the flight test are as follows:

(1) Flight Mach number should be kept between 1.95 and 2.05 to pay attention to M=2 condition.
(2) Lift coefficient should vary from -0.05 to 0.25 to obtain the drag polar curve.
(3) The design condition, M=2 and C_L=0.1, must be realized to measure transition at some high and low Reynolds number conditions.

In general it is not easy to satisfy these requests with the un-powered airplane. The possibility of such a flight has been investigated with a new control algorithm.

The outline of present flight test plan is summarized in Fig. 5. As stated before, the un-powered experimental airplane will be launched by using a solid rocket booster. The un-powered airplane will be ready to start a measurement at the specified flight test conditions after separating from the rocket at an altitude of about 18 km.

First, the α sweep test is conducted to obtain the drag polar curve. After the measurements, the design condition is maintained by varying its altitude. Then the first trial to measure the transition characteristics at lower Reynolds number is conducted for a few seconds, because it is difficult to keep this condition by un-powered vehicle. After the first trial, the flight condition is again adjusted to the design point at a lower altitude. Then the second transition measurement is conducted at higher Reynolds number. Finally the un-powered airplane is recovered with a parachute system. Such flight tests will be planed four times.

Since this experimental airplane is un-powered, there is little vibration. This situation is very effective in transition measurement. It is not generally easy to measure transition in flight test as well as wind tunnel test. Five transition measurement techniques, hot-film, thermocouple, unsteady pressure sensor, IR camera and Preston tube are under consideration. And several preliminary wind tunnel tests with simple models, for example, a sharp cone and a nose cone of the experimental airplane is planned to establish these techniques.

7. FURTHER STUDIES

At present, we are on the next stage for designing the second type of scaled supersonic experimental airplane. This airplane is a jet-powered one. In the aerodynamic design, an

optimum airframe/nacelle integration and an optimum intake design are very important.

NAL has already studied the intake design both experimentally and numerically. And the airframe/nacelle integration design has been just started using the CFD analysis. The outline of them are summarized in the following as further studies of the NAL program.

In addition, to design an optimum aerodynamic configuration, some investigations of new and innovative further design concepts are necessary. One example is to design an optimum warped wing satisfying Jones minimum drag criterion. Another is to apply nonlinear lift effect due to nacelle integration. Furthermore, some optimum design method using CFD which is different from inverse method, must be studied. NAL has also tried them.

7.1 Airframe/Nacelle Interference

In our program, a development of any engine system for the experimental airplane is not included because of limited program cost. As a candidate engine, a well-known YJ-69 was selected. The diameter of this engine, however, is fairly lager. Therefore large interference between airframe and nacelle is expected.

As a first step to design a baseline configuration of the jet-powered airplane, CFD analysis for interference between the airframe and such a large nacelle was conducted by FHI. Higaki[20] calculated L/D characteristics of the typical SST configuration with two large nacelles located at some locations. This configuration shown in Fig. 25 was designed at FHI's in-house study. Fig. 26 shows the calculated L/D compared with test results by FHI. Since such a configuration generates complex flow filed, qualitative agreement was enough effective to consider the flow phenomenon as a first step.

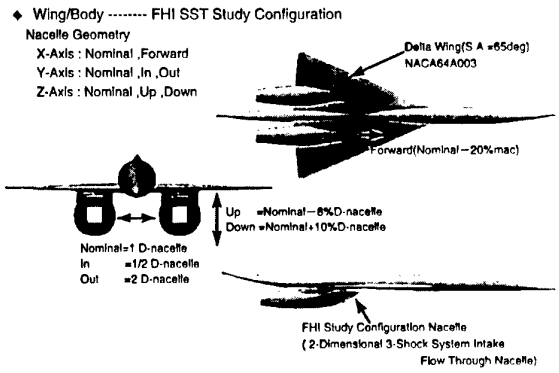


Fig.25 Model Configuration with Nacelle[20]

This study also analyzed breakdown of the drag as shown in Fig. 27. As a result, it was found that such nacelle and diverter produced very large drag. This study indicated a great amount of efforts were necessary to design the jet-powered experimental airplane.

7.2 Intake Design

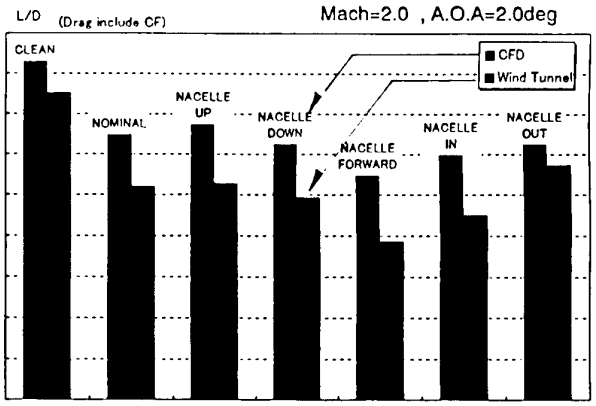


Fig.26 Comparison of the Test and the CFD[20]

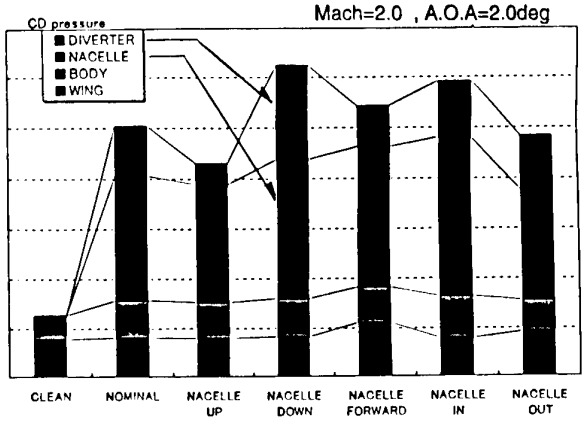
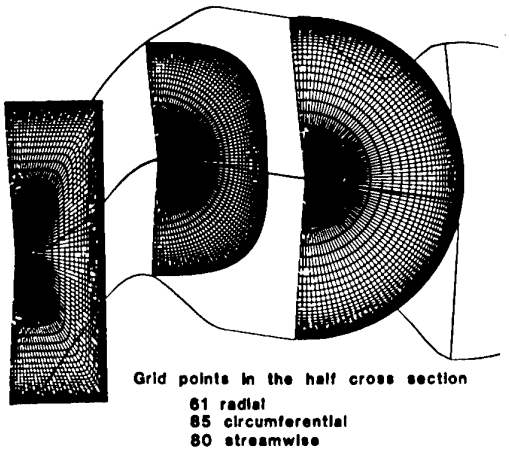


Fig.27 Drag Components by the CFD[20]



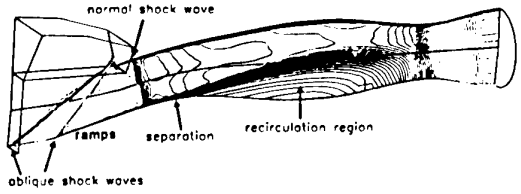


Fig. 28 CFD Results of the Designed Intake[21]

NAL has joined the MITI's HYPR program. And some experimental and numerical investigations for intake design of high speed aircraft has been conducted. Based on them, Fujiwara et al.[21] designed the intake for the jet-powered experimental airplane. At first, the intake of external compression type was designed using classical shock relation. Then he analyzed its flow feature and the effect of suction at throat using three-dimensional CFD(Navier-Stokes) code. Fig. 28 shows one of his results. Through his CFD analysis, some modifications of the intake were proposed. Then wind tunnel test is conducted this spring to confirm his design and to obtain some data on optimum suction condition.

8. CONCLUDING REMARKS

Overview of NAL's R&D program of unmanned and scaled supersonic experimental airplane was introduced. In the experimental airplane program, two types of airplane are planed. One is an un-powered and the other is a jet-powered airplane. The main goal is to develop an CFD-based optimized aerodynamic design system to be ready for contributing to development of a second generation SST. In detail, aerodynamic design system and its application to the un-powered airplane was described. Four design concepts for reducing supersonic drag, there are arrow shaped planform, warped wing, are-ruled body, and natural laminar flow (NLF) wing design were incorporated. As a design tool, CFD (Navier-Stokes) code, originally developed by NAL, was mainly used. Especially, a newly developed inverse design method with CFD analysis was very effective on the NLF wing design. The wind tunnel tests were conducted to validate the CFD analysis. The flight test plan of the un-powered airplane and some further studies for an aerodynamic design of the jet-powered airplane were summarized.

ACKNOWLEDGMENT

The author would like to express special thanks to the Kawasaki Heavy Industries, Ltd., the Mitsubishi Heavy Industries, Ltd., the Fuji Heavy Industries, Ltd. and Tohoku University for their cooperative efforts to the design program development and its application.

REFERENCES

1. Sakata, K., "SST Research Project at NAL", 1st International CFD Workshop on Supersonic Transport Design, Tokyo, March, 1998.
2. Shimbo, Y., Yoshida, K., Iwamiya, T., Takaki, R. and Matsushima, K., "Aerodynamic Design of the Scaled Supersonic Experimental Airplane", 1st International CFD Workshop on Supersonic Transport Design, Tokyo, March, 1998.
3. Jones, R. T., "Theoretical Determination of the Minimum Drag of Airfoils at Supersonic Speeds", J. Aeronaut. Sci., 19 (1952), pp. 813-822.
4. Kuchemann, F. R. S., "The Aerodynamic Design of Aircraft", Pergamon Press, 1978.
5. Smith, J. H. B. and Beasley, J. A., "The Calculation of the Warp to Produce a Given Load and the Pressure due to a Given Thickness on Thin Slender Wings in Supersonic Flow", A. R. C., R & M, No. 3471, 1967.
6. Tucker, W. A., "A Method for the Design of Sweptback Wings Warped to Produce Specified Flight Characteristics at Supersonic Speeds", NACA Rep. No. 1226, 1955.
7. Carlson, H. W. and Middleton, W. D., "A Numerical Method for the Design of Camber Surface of Supersonic Wings with Arbitrary Planform", NASA TN D-2341, 1964.
8. Carlson, H. W. and Miller, D. S., "Numerical Method for the Design and Analysis of Wings at Supersonic Speeds", NASA TN D-7713, 1974.
9. Ginzel, I. and Multhopp, H., "Wings with minimum drag due to lift in supersonic flow", J. Aeronaut. Sci. Vol.27, No.13, pp.13-20, 1960.
10. Ashley, H. and Landahl, M., "Aerodynamics of Wings and Bodies", Dover Publications Inc., 1965.
11. Ogoshi, H., "Aerodynamic Design of an Supersonic Airplane Wing - Application of the Natural Laminar Flow Concept to Airfoil", Proc. of the 47th Nat. Cong. of Theoretical & Applied Mechanics, Jan., 1998 (in Japanese).
12. Srokowski, "Mass Flow Requirements for LFC Wing Design", AIAA 77-1222, 1977.
13. Jeong, S., Matsushima, K., Iwamiya, T., Obayashi, S. and Nakahashi, K., "Inverse Design Method for Wings of Supersonic Transport", AIAA 98-0602, 1998.
14. Matsushima, K., Iwamiya, T., Jeong, S. and Obayashi, S., "Aerodynamic Wing Design for NAL's SST Using Iterative Inverse Approach", 1st International CFD Workshop on Supersonic Transport Design, Tokyo, Japan, March 16-17,1998.
15. Takaki, R., Iwamiya, T. and Aoki, A., "CFD Analysis Applied to the Supersonic Research Airplane", 1st International CFD Workshop on Supersonic Transport Design, Tokyo, Mar., 1998.
16. Yoshida, K., "Aerodynamic Design of NAL's High-speed Small Experimental Airplane", The 47th Nat. Cong. of Theoretical & Applied Mechanics 1998, pp. 333-334 (in Japanese).
17. Shimbo, Y., Yoshida, K., Iwamiya, T. and Takaki, R., "Linear and Non-Linear Aerodynamics/Design of a SST Configuration", Proc. of the 29th Fluid Dynamics Conference, pp. 369-372, 1997 (in Japanese).
18. Middleton, W. D. and Lundry, J. L., "A System for Aerodynamic Design and Analysis of Supersonic Aircraft", NASA Contractor Report 3351, 1980.
19. Yoshida, K., Ogoshi, H., Ishida, Y. and Noguchi, M. "Numerical Study on Transition Prediction Method and Experimental Study on Effect of Supersonic Laminar Flow Control", Special Publication of National Aerospace Laboratory SP-31, pp. 59-79, May 1996.
20. Higaki, K., "Numerical and Wind Tunnel

Test Study on the Nacelle Integration for NAL's Experimental Airplane", 1st International CFD Workshop on Supersonic Transport Design, Tokyo, Japan, March 16-17,1998.

21. Fujiwara, H. & Sakata, K., "Numerical Simulation of the Internal Flow through the Mach 2 Air-intake Designed for NAL's Experimental Airplane", 1st International CFD Workshop on Supersonic Transport Design, Tokyo, Japan, March 1998.

SHOCK-VORTEX INTERACTION RESEARCH

Pasquale M. Sforza
Graduate Engineering and Research Center
University of Florida, Shalimar, FL, 32579

SUMMARY

Supersonic cruise aircraft generate shock waves and vortices as a consequence of the flight speed and the forces generated, respectively. Interactions between these two produce flow disturbances which affect aircraft performance, stability and control. Research in the field is reviewed to provide an understanding of the state of the art. The important parameters in the interaction are the Mach number and the swirl to axial velocity ratio of the vortex. The phenomenon of vortex breakdown is described and a criterion for determining if a shock-vortex interaction is strong enough to provoke it is given. Models developed thus far for evaluating such interactions are presented. Experimental investigations of shock-vortex interactions are also discussed.

1. INTRODUCTION

Although the field of aerodynamics has included the concept of vortices as a fundamental analytical building block since its earliest days, there has been considerably less attention paid to the interaction of vortices with the various components of practical flight vehicles. Early studies on vortex generation in supersonic flight were carried out by NACA in the late 1940s and collected in a seminal paper by Spreiter and Sacks (1951). In this early period of research attention was focused on vortices as a means of determining the downwash field caused by lifting surfaces and its effect on downstream control surfaces of aircraft and missiles. In the case of missiles, the generation of vortices by the slender fuselages at angle of attack was of interest because of their effect on the forces and moments produced on the fuselage as well as on the aft control surfaces. Nielsen (1960) describes the work in this area carried out during the 1950s. In the 1960s, vortex-producing surfaces, such as canards and strakes, received much more attention as design features specifically intended to enhance the performance and control of aircraft and enjoyed wider application. At the same time it was recognized that vortices could have direct negative influences on flight vehicles, as described by Sforza (1970). Vortices streaming back from wing-fuselage junctions aggravated the deep stall control problem of T-tailed aircraft by virtue of the alteration of the angle and dynamic pressure of the flow encountering the high-mounted vertical tail. Furthermore, there are flow conditions in which the highly organized swirling structure of a vortex locally deteriorates to the point where the flow no longer retains the characteristics usually associated with a vortex. At that point the vortex is said to have experienced breakdown, and the definition of this state has been a subject of controversy in fluid mechanics for many years. Delta wing aircraft, which depend on the nonlinear lift increment afforded by the leading edge vortex formed above them, were found to develop stability problems caused by those same vortices. At high angles of attack one or both of the leading edge vortices may experience breakdown near the trailing edge causing the suction on nearby wing surfaces to deteriorate rapidly. If the breakdown occurs symmetrically over both wings an abrupt pitch-up is produced while the result of just one vortex breaking down is a rolling pitch-up.

Through the 1970s interest in vortices centered on those trailing from wings of heavy aircraft in terminal operations and in high altitude cruise. The former case concerned safety of following aircraft (Hallock, 1977) while the latter concerned questions of stratospheric pollution (Overcamp and Fay, 1973) and was particularly focused on the possible effects of a large fleet of SSTs on upper air quality. The abrupt collapse of efforts aimed at producing a large fleet of high-speed commercial aircraft dampened research on vortices produced in supersonic flight. Now, 20 years later, renewed interest in supersonic cruise vehicles, both commercial and military, has awakened corresponding attention to fundamental insights regarding their vortex wakes. Three basic problems illuminate the practical need for such information:

(a) *interaction* of vortices with shock waves and flow fields over downstream surfaces and through engine inlets. They can influence lift, drag, engine performance, and stability and control characteristics.

(b) *entrainment* of engine plumes into wing tip vortices (or fuel jets into scramjet

Paper presented at the RTO AVT Course on "Fluid Dynamics Research on Supersonic Aircraft", held in Rhode-Saint-Genèse, Belgium, 25-29 May 1998, and published in RTO EN-4.

injector vortices). Engine emissions (or fuel species) trapped in the vortex wake are subjected to conditions different than those in the free stream thereby altering the subsequent chemistry. This also has implications for the characteristics of wake signatures.

(c) *Confinement* of entrained material for long times after aircraft passage. This can increase residence times of possible pollutants.

The present paper is concerned with the interpretation and applications of the results of the few past and recent experiments to the first problem area, interaction of vortices with shock waves, while the latter two areas are discussed in a companion paper, Sforza (1998).

Shock waves and vortices are present virtually everywhere on vehicles traveling at supersonic speeds. Examples of situations where interactions between the two have substantial practical importance are shown in Fig. 1. Shock waves over lifting or control surfaces span large areas and are easy targets for streaming vortices from upwind surfaces. The interaction between the two will be shown to produce substantial pressure disturbances on the shock-generating surface. This may significantly alter the aerodynamic force field on that surface directly or by influencing the state of the boundary layer. A similar situation prevails when the vortex interacts with the shock compression system of an engine inlet. Localized regions of reduced stagnation pressure entering an inlet may produce a degree of flow distortion that will seriously degrade engine performance. It will be shown that vortices in supersonic flows are often characterized by stagnation pressure deficits in their cores.

2. NORMAL SHOCK INTERACTIONS

General characteristics of normal shock-vortex interactions

Experimental and numerical studies relevant to the shock-vortex interaction problem have focused on understanding the physics involved, particularly with respect to the phenomenon of vortex breakdown in supersonic flows. Most such studies have dwelt on the specific case of interaction of streamwise vortices with normal shock waves. Perhaps the first investigation of the problem was the experiments of Zatoloka, Ivanyushkin, and Nikolayev (1978) on a trailing vortex intercepting a normal shock wave in an engine inlet. They reported development of a stagnation zone as well as a distorted shock pattern as a result of such encounters.

The first substantive treatment of the normal shock-vortex interaction was presented by Delery, *et al* (1984). Experiments using laser Doppler anemometry and multi-hole conical probe measurements before and after the shock were accompanied by Euler calculations of the flow. In their experimental set-up a vortex formed by a swept wing at angle of attack within the subsonic portion of a wind tunnel was accelerated to supersonic speed through a nozzle, ultimately approaching a normal shock standing at the lip of a pitot type inlet. Preliminary experiments established the general behavior of the flow prior to intercepting the shock wave. The swirl, or tangential, component of the velocity had a high degree of rotational symmetry and the axial component of velocity was reasonably constant. The ratio of maximum swirl velocity to axial velocity external to the vortex, $\tau = V_{t,m}/V_{x,e}$, increased linearly with angle of attack of the vortex generator wing up to the point where vortex breakdown over the wing itself occurred.

At moderate values of swirl and lower Mach numbers, the passage of the vortex through the normal shock doesn't alter the basic nature of the flow. This is shown in Fig. 2 where the ratio of the maximum swirl downstream of the shock to the upstream axial velocity component is plotted against the upstream value of τ. If there were no change at all in maximum swirl component the data points would lie on the 45° line shown. Such behavior is found to occur up to a particular upstream value of τ for each test Mach number, while beyond that the swirl drops abruptly, signifying the onset of breakdown. More pronounced differences due to passage through the shock are observed in the axial component of velocity, as shown in Fig. 3. The axial component of velocity evaluated at the edge and at the axis of the vortex both before and after the shock is shown in Fig. 3 as a function of τ; all velocity components are normalized with respect to the free stream velocity. It is clear that increasing swirl at a given Mach number yields increasing evidence of vortex breakdown, as does increasing Mach number at fixed τ. Since the axial component of velocity drops through the shock, the local swirl ratio τ increases through the shock until breakdown occurs.

Their results also indicate that interactions involving vortex breakdown are characterized by

negative axial velocity on the vortex axis, a considerable reduction in maximum tangential velocity, and an increase in viscous vortex core radius, all of which are also symptomatic of vortex breakdown in incompressible flow. Some of these effects, as obtained at a Mach number of 2.28 by means of laser Doppler anemometry, appear in Figs. 4 and 5. The former shows the axial and tangential velocity profiles before and after passing through a normal shock for an unburst vortex while the latter depicts the same thing for a burst vortex. For the case where the vortex does not burst the only noticeable change in the flow field is the deceleration in the vicinity of the centerline of the vortex. However, in the case of the burst vortex the swirl decreases, the vortex dilates, and the axial component of velocity shows evidence of flow reversal. In either case, the effect of passage of a vortex through the shock field of an engine inlet can lead to distortion and unstart problems of variable magnitude. Construction of mean flow streamlines from the measured data for these two cases by conserving mass flow leads to the results shown in Figs. 6 and 7. It is evident from Fig. 6 that the unburst vortex case shows little effects from passage through the normal shock while Fig. 7 clearly suggests formation of a recirculation bubble. Unfortunately, no flow visualization experiments were performed in this investigation so that the structure of the flow had to be deduced solely from the available measurements.

Metawally, Settles, and Horstman (1989) and Cattafesta and Settles (1992) also studied interactions of vortices with normal shock waves. However, the vortices in these studies were formed by swirl vanes downstream of a nozzle and therefore have somewhat different characteristics from those formed by a lifting surface. Both papers report strong influence of vortex swirl rate and Mach number on the interaction, a vortex breakdown, and an oscillating bulged-forward shock. Their results suggested a hypothetical supersonic vortex breakdown model consisting of a region of reversed flow as well as a stagnation point downstream of a bulged-forward shock wave.

Kalkhoran's (1993) experiments showed that a head-on encounter between a trailing vortex and a sharp wedge at Mach 3 resulted in formation of a locally detached shock front far upstream of the wedge leading edge. In addition, the distorted vortex structure formed as a result of the interaction was found to include a slip surface separating a subsonic and a supersonic zone. All these studies involve vortices encountering normal shock waves that have subsonic flow downstream of the interception site. As a result, deceleration of the vortex axial velocity is accomplished in a manner similar to that in subsonic vortex breakdown. On the other hand, since supersonic flow is maintained downstream of an oblique shock wave, a vortex breakdown resembling the subsonic case will only be possible if a normal shock develops as a result of the encounter.

2.1 Vortex breakdown in normal shock-vortex interactions

Delery, *et* al (1984) presented a vortex breakdown criterion, established on the basis of their experiments, as shown in Fig. 8. The relatively simple correlation found depends solely on vortex swirl and shock strength and is applicable to cases where the upstream axial component of velocity in the vortex is approximately uniform throughout. Numerical calculations based on the Euler equations and axisymmetric flow pointed to a similar breakdown limit, as also shown on Fig.8. The agreement between the computations and the experimentally derived correlation indicates that, for the cases they studied, inviscid effects dominate the onset of vortex breakdown. However, the computed solutions did not have the same degree of success in predicting the observed post-breakdown flow structure, illustrating the need for more refined analyses.

Later, Delery (1994) presented a review of various aspects of incompressible and compressible vortex breakdown in which he describes the different schools of thought on this rather controversial subject. He concludes that it is well-established that vortex breakdown occurs under the action of an adverse pressure gradient which can induce a rapid deceleration in the axial motion until a stagnation point forms on the centerline of the vortex structure. He notes that the process depends on the swirl magnitude but is relatively insensitive to the Reynolds number and the local turbulent properties. Sarpkaya (1995) argues that these last two properties are important to vortex breakdown and shows a conical type of breakdown he obtained during experiments on vortices at high Reynolds number in a slightly expanding tube. He suggests that this type of breakdown configuration should be added to the other basic types, namely axisymmetric bubble, spiral, and double helix.

Mahesh (1996) developed an expression for the onset of breakdown in a normal shock-vortex interaction based on an *ad hoc* criterion that would signal incipient flow reversal on the vortex axis. Quantitatively, he speculates that breakdown occurs if the pressure rise across the shock exceeds the streamwise momentum flux ahead of the shock, when both terms are evaluated on the axis of the vortex. Closed form solutions are obtained for the cases in which either the stagnation temperature or the entropy is uniform in the flow. For the former case, the critical value of maximum swirl velocity may be approximated by $V_{t,m}/U = 0.48/M$ for $M>2$ and $\gamma = 1.4$.

Comparisons with the experimental results of Delery,*et al* (1984) and Metawally, Settles and Horstman (1989) show good agreement in the range $1.6<M<3.5$.The breakdown curve is shown on Fig. 8 along with the experimental and theoretical results of Delery, *et al* (1984). Mahesh's analysis is based on the assumptions that the flow is axisymmetric and that the axial velocity component is constant. Mahesh then extends his analysis to consider the effects of variations in the distribution of the axial velocity component on the prediction of the onset of breakdown. He shows that jet-like profiles of axial flow in the vortex delay breakdown to higher Mach numbers and that the reverse is true for wake-like profiles. This result is in keeping with general notions regarding such effects but there are no comparisons to any experiments. Smart and Kalkhoran (1997) argue that the appropriate metric for vortices with non-uniform axial velocity distributions is the maximum value of the ratio of V_t to V_x in the profile, i.e. $(V_t/V_x)_m=\tau_m$, rather than τ, which arose in previous studies where the axial velocity was essentially constant.

Kalkhoran and Smart (1997) presented another approach for evaluating the onset of breakdown in a vortex encountering a normal shock wave. They consider an inviscid axisymmetric flow with the vortex modeled as a slender whirling layer to which a number of simplifying approximations familiar in boundary layer integral methods are applied. Vortex breakdown is assumed to occur when the shock-vortex interaction leads to stagnation on the vortex axis after passing through the shock. The analysis shows that the maximum swirl at breakdown varies inversely with Mach number and comparisons with the experiments of Delery, *et al* (1984), Cattafesta, and Settles (1992), and Kalkhoran, Smart, and Betti (1996) show good agreement over a broad Mach number range. The breakdown curve proposed is also included on Fig. 8 with the other predictions discussed previously. It is clear that all the predictions lie fairly close to one another with the deviation between them increasing with Mach number.

Numerical studies based on the Navier-Stokes equations have also been carried out by Metawally, Settles, and Horstman (1989), Kandil and Kandil (1991), Kandil, Kandil, and Liu (1991), and Erlebacher, Hussaini, and Shu (1996). The analyses are based on the assumption of unsteady, axisymmetric, compressible flow and captured many of the observed characteristics of normal shock-vortex interactions. Several breakdown modes and post-interaction flow structure details were also uncovered in these studies. Metawally, Settles, and Horstman (1989) provided a description of the flow pattern observed in the breakdown interaction, reproduced here as Fig. 9. Formation of a recirculation bubble is accompanied by a "bubble" shock that bulges outward in the upstream direction. Either of two regimes of breakdown occurred in their investigations: a weak or a strong interaction characterized by a bubble shock with characteristic dimensions on the order of or much larger than the upstream vortex core diameter, respectively.

Kalkhoran, Smart, and Betti (1996) performed experiments on the interaction of wing tip vortices with the normal shock standing outside a pitot inlet at $M=2.49$ using multiple spark shadowgraphs to visualize the flow. This approach clearly showed an unsteady component to the shock-vortex interaction problem, as may be seen in Fig. 10. The two photographs show variations in the distorted shock structure for a vortex of moderate strength, $\tau_m=0.18$, at different times during the same test. The flow field appears to be divided into two roughly conical regions, a central portion showing evidence of turbulent flow and an outer portion, seemingly less disturbed, lying behind a conical shock. Since no quantitative data were available for the downstream regions the resulting flow structure was classified conservatively as a vortex distortion rather than a vortex breakdown. The strongly curved shock wave in the vicinity of the vortex axis indicates the presence of a high entropy layer in that region. They report that careful examination of the many flow photographs taken leads to the conclusion that it is the viscous

core of the vortex that dramatically expands radially to form the observed conical turbulent region. Experiments carried out using strong vortices, τ_m=0.32, lead to similar behavior, but at larger scales.

3. OBLIQUE SHOCK INTERACTIONS

3.1 General characteristics of oblique shock-vortex interactions

The normal shock-vortex interaction problems discussed previously all involve subsonic flow downstream of the interaction site. As such, the downstream boundary conditions can influence upstream portions of the flow and therefore the overall character of the interaction process. This ability to transmit information upstream is critical to many previous theories of vortex breakdown in incompressible flows, e.g. Benjamin (1962). In supersonic flows through oblique shock waves the Mach number behind the shock is supersonic so that upstream information transmission is not possible. It seems reasonable to expect that if a breakdown like that seen for incompressible flows is found in this case there must be present a strong oblique or a normal shock in evidence, at least locally.

Studies of oblique-shock vortex interactions are quite rare, despite the fact that such interactions are more likely to be encountered in practical flight vehicles than those involving normal shocks. Two reasons for the rather more common study of normal shock-vortex interactions are as follows: the larger pressure jumps available at a given Mach number make vortex breakdown easier to achieve and the flow before and after the shock may reasonably be considered axisymmetric.

Kalkhoran, Sforza, and Wang (1991) reported experiments on the interaction between wing tip vortices and oblique shocks generated at a downstream location. Though the shock waves were observed to deform as part of the interaction process, no vortex breakdown was apparent. The vortices were instead deflected by the oblique shocks in the same manner as the streamlines of the main flow. A somewhat similar experiment by Weger and Chokani (1991), also carried out at Mach 3, showed similar results. The lack of dramatic effects on the vortices in these experiments may be explained by the exploratory nature of the investigations that confined them to the generation of relatively weak shock waves.

Cattafesta and Settles (1992) studied impingement of their vane-generated vortices with oblique shock waves and did observe shock wave bulging but no apparent vortex breakdown.

Kalkhoran and Sforza (1994) studied the interaction resulting from the impingement of a wing tip vortex on an oblique shock wave produced by a sharp wedge airfoil at a free stream Mach number of 3. A schematic diagram of the experimental set-up is shown in Fig. 11. Changing the angle of attack of the vortex-generating wing provided a means to vary vortex strength. The location of the impingement point above the airfoil leading edge could be altered and cases where the vortex intercepted the shock at the airfoil leading edge or points above it were investigated. For heights sufficiently far above the leading edge the interaction served only to locally deform the shock with no evidence of breakdown of the vortex. As the leading edge was approached the nature of the interaction changed resulting in the formation of a localized conical shock structure whose apex was located substantially upstream of the undisturbed airfoil shock, as shown in Fig. 12.

Smart and Kalkhoran (1995) presented a comprehensive investigation of the effect of shock and vortex strengths on oblique shock-vortex interactions using an experimental set-up like that previously shown in Fig. 11. They varied vortex strength (τ_m=0.18 and 0.32, i.e., moderate and strong) by changing the angle of attack of the vortex generating wing and shock strength by adjusting the wedge angle ($20^\circ<\theta<30^\circ$) of the shock generating airfoil. The interaction of a moderate strength vortex with the wedge shock is quite steady and the main result is a slightly bowed out shock wave in the vicinity of the impingement point, which is a substantial distance above the wedge leading edge, as shown in Fig. 13. The vortex did not appear to be altered by the interaction but merely turned along with the rest of the flow behind the shock. This same behavior was noticed even as the wedge angle was changed through the desired range.

On the other hand, interaction of the strong vortex with the wedge shock was more dramatic, as shown in Figs. 14a-14c, and may be described with the aid of the schematic diagram of the interaction shown in Fig. 15. At the lowest value of shock strength (Fig. 14a), the shock wave is seen to bow out much in the same manner as the moderate strength vortex case of Fig. 13. As the

shock strength increases, the deformation of the shock is exaggerated to the point that it appears as a blunted conical shock protruding from the rest of the planar shock generated by the wedge. The shock wave produced by the interaction looks very much like that produced by a spherically capped cone in an inviscid supersonic flow. The lower portion of the conical shock in Fig. 14b is seen to extend down to the surface of the wedge at about the 30%chord location. This effect was verified by measurements of the pressure distribution along the wedge surface.

3.2 Breakdown in oblique shock-vortex interaction

Research emphasis has been placed almost entirely on breakdown in normal shock-vortex interactions because, in addition to being easier to produce experimentally and to analyze theoretically, it bears a strong resemblance to that encountered in incompressible flow. Mahesh (1996) extended his breakdown criterion for normal shock-vortex interaction to the case of oblique shock-vortex interaction simply by considering the Mach number normal to the shock rather than the Mach number itself as the pertinent parameter. The effects of three-dimensionality in such an approach is given little mention and, since there are no experimental results, no specific conclusions are drawn.

There have been no studies of vortex impingement on a series of oblique shocks, as might be found in the compression ramp of a high-speed engine inlet. The sequence of small pressure rises that characterizes such inlets may not induce a strong interaction. On the other hand, shock-vortex interactions at hypersonic speeds, which also have received no attention, offer the combination of strong shocks but small shock angles. It seems such cases would be marked by more complicated three-dimensional effects. The interest in hypersonic vehicles provides an incentive to extend the studies described here to that flight regime.

At present there is no accepted definition for what constitutes breakdown in these interactions. This, and the fact that the topic of vortex breakdown is so controversial, often leads to a reluctance to claim that a breakdown has occurred. The three-dimensionality of the problem also makes it extremely difficult to measure flow properties behind the shock and on the surface below the distorted vortex flow. This is a situation in which computational fluid dynamics can make an important contribution to the design of an experiment. By delineating the likely level and distribution of flow properties in a given experiment it is easier to plan an efficient mix of diagnostics to capture the essential features of a shock-vortex interaction. It is also possible to pick the combination of experimental conditions best suited to the facility and instrumentation available. Computational approaches that have demonstrated this level of credibility for the shock-vortex interaction problem are outline in the next section.

3.3 Oblique shock-vortex interaction effects on aerodynamic surfaces

Although some shock-vortex interactions produce only local shock wave deformation and no vortex breakdown, effects on the flow field over the shock-generating surfaces may be appreciable. Kalkhoran and Sforza (1994) performed a series of experiments aimed at discovering the extent of such effects. They studied the interaction between wing tip vortices of various strengths impinging on the oblique shock wave produced by a sharp wedge airfoil at a free stream Mach number of 3.

A schematic diagram of the flow field was previously depicted in Fig. 11. The 27° wedge-angle airfoil spanned the tunnel test section and could be traversed in the vertical direction to permit vortex impingement on the shock to occur at different heights above the leading edge. This airfoil was instrumented with 18 surface pressure taps in an array of 3 taps spanwise (Y-direction) and 6 taps chordwise (X-direction) spaced 5.08mm apart in either direction, as shown in Fig. 16. The baseline distribution of pressure coefficient $C_p=(p - p_{oo})/q_{oo}$ is depicted in Fig. 17 and shows good uniformity and close agreement with the theoretical value for supersonic two-dimensional wedge flow, i.e., $C_p=0.69$. The vortex generator was an unswept wing with a double wedge airfoil section mounted about 2 chords upstream of the leading edge of the test airfoil. Experiments were carried out at 3 angles of attack, namely, 5°, 7.5°, and 10°, corresponding to weak, moderate and strong vortices.

The downstream wedge airfoil was tested at 5 vertical (Z-direction) stations relative to the tip of the upstream vortex generator wing tip: h/c=0.4, 0.23, 0.067, -0.1, and –0.267. Here $h = Z_{tip} - Z_c$ is the vertical distance between the wing tip of the vortex generator and the chord-line of the airfoil and c is the chord of the airfoil. The distance h is merely a defined reference distance and does not

directly indicate the height of the vortex above the airfoil chord. Shadowgraph studies do show that positive values of h/c correspond to impingement above the chord-line whereas negative values correspond to impingement at or near the airfoil's sharp leading edge. Close encounters of the latter type are characterized by a high degree of unsteadiness. In general, the effect of the shock-vortex interaction is to reduce the pressure levels on the airfoil surface.

Pressure coefficient data based on time-averaged pressure measurements for all cases are shown in Figs. 18,19, and 20. In general, the effect of the shock-vortex interaction is to reduce the pressure on the airfoil surface near the leading edge with a recovery in pressure appearing as distance along the airfoil increases. The flow field is clearly highly three-dimensional. Recalling that the pressure taps are only 5.08mm apart, the spanwise pressure gradients appear to be quite large. Substantially more taps would be needed to completely define the pressure footprint arising as a result of the shock-vortex interaction.

Rizzetta (1995) carried out an extensive numerical simulation of this experiment for both the Euler equations and the mass-averaged Navier-Stokes equations. In the latter, turbulence is accounted for by means of the two-layer algebraic model of Baldwin and Lomax (1978). He noted that comparisons between the two flow models showed that most of the features of the flow were captured by the Euler equation formulation. This suggests that much of the behavior observed in such flows is fundamentally inviscid in character. Reasonably good agreement with the experimental data was achieved, particularly for the case of weak interaction. As the vortex strength increased the agreement suffered, and the calculations were unable to reproduce the large-scale and unsteady breakdown-type phenomena evidenced by the multiple-spark shadowgraphs used by Kalkhoran and Sforza (1994).

One of the limitations of the analysis was the lack of validation between the computed and actual vortex characteristics, especially for stronger interactions. To deal with this issue, Rizzetta (1997) attempted to simulate a later set of experiments on oblique shock-vortex interaction carried out by Smart and Kalkhoran (1995) which provided information on the vortex characteristics as well as the shock response. The importance of appropriate turbulence modeling in producing a good simulation of the flow in the vortex is demonstrated by the results shown in Fig. 21. Here a k-ε model like that of Jones and Launder (1973) coupled with a compressibility correction like that of Sarkar, *et al*, (1991) was used in the Navier-Stokes equations and the effect, particularly on Mach number profiles, is dramatic. As the effect of dissipation is increased, the axial Mach number develops a larger deficit in the vortex core. The same is true of stagnation pressure, but to a lesser extent.

Comparisons of computer-generated and shadowgraph flow field visualizations are presented in Figs. 22a-c. The agreement is quite good, except for the strongest interaction, Fig. 22c, where the computation under-predicts the extent of the shock wave distortion. The computer-generated result in Fig. 23 shows the surface of zero velocity parallel to the wedge surface, which encloses the space wherein the velocity is reversed. The presence of such a domain off the surface is taken by Rizzetta to denote vortex breakdown. This surface appears directly behind the normal portion of the distorted shock and completely within the subsonic region. It is important to note that in Rizzetta's calculation the vortex remains coherent after the breakdown event and the tangential velocity component is only minimally affected. The calculations for this case also provide the pressure signature on the wedge surface as shown in Fig. 24. These depict solutions of the Euler equations using different input vortex characteristics. One set uses the vortex characteristics obtained from solutions to the Euler equations for flow around the vortex generator while the other uses those obtained from the Navier-Stokes equations with the k-ε turbulence model. Both inviscid solutions displayed vortex breakdown, as narrowly defined earlier for these calculations, but those using the inviscid vortex input were steady while those for the turbulent vortex input oscillated with a fairly definite period. Thus the shaded portions of the curves in Fig. 24 represent the excursions in the unsteady solutions. The agreement in this sensitive three-dimensional problem is seen to be quite good, which bodes well for further applications of computational modeling to this problem

Quantitative measurements of the structure of the vortex behind the shock are not available at this time and represent an important research area. However, Kalkhoran and Smart (1996) have carried out laser light-sheet flow visualizations of the flow in this region under the strong interaction

conditions discussed previously. The photographs shown in Figs. 25a and b correspond to locations measured from the leading edge of the 75mm long wedge surface. The vortex structure does appear to be retained although at the farthest downstream station there appears to be evidence of enhanced mixing, perhaps caused by the turbulent conical region seen in the shadowgraphs.

4. CONCLUSIONS

A review of the characteristics of the interactions of vortices with shock waves has been presented. Vortices may pass through shock waves with little noticeable effect on their characteristics or they may break down, dramatically altering the original shock structure. The most important parameters of the process are the strengths of the vortex and the shock. The former is classically considered to be Γ/UL or V_t/U, but experiments in shock-vortex interactions suggest that $(V_t/V_x)_{max}$ is more appropriate. Shock strength appears to be adequately described by the normal component of the free stream Mach number. It is the combination of a strong shock and a strong vortex that leads to breakdown. Criteria for breakdown incorporating these parameters have been presented along with experimental support. The effects of oblique shock-vortex interactions on the surface generating the shock have been described. Computational approaches for the determination of the structure of a shock-vortex interaction have been discussed. They show that while the Euler equations can capture the essential features of the interaction, the Navier-Stokes equations with a sophisticated turbulence model is necessary to generate appropriate details of the impinging vortex.

5. ACKNOWLEDGEMENTS

The cooperation of Professor I.M. Kalkhoran in providing some of the work carried out by him and his students is gratefully acknowledged.

REFERENCES

Baldwin, B.S. and Lomax, H. (1978). Thin layer approximation and algebraic model for separated turbulent flows, AIAA 78-257, AIAA Aerospace Sciences Meeting and Exhibit.

Benjamin, T.B. (1962). Theory of the vortex breakdown phenomenon, *Journal of Fluid Mech.*, **14**, pp. 593-629.

Cattafesta, L.N. and Settles, G. (1992). Experiments on shock/vortex interaction, AIAA 92-0315, AIAA Aerospace Sciences Meeting and Exhibit.

Delery, J. (1994). Aspects of vortex breakdown, *Progress in the Aerospace Sciences,* **30**, pp. 1-59.

Delery, J., Horowitz, E., Leuchter, O., and Solignac, J.L. (1984). Fundamental studies on vortex flows, *La Recherche Aerospatiale*, English edition, No. 2, pp.81-104.

Erlebacher, G., Hussaini,M.Y., and Shu, C.-W. (1997). Interaction of a shock with a longitudinal vortex, *Journal of Fluid Mech.*, **337**, pp.129-153.

Jones, W.P. and Launder, B.E. (1972). The prediction of laminarization with a two-equation model of turbulence, *International Journal of Heat & Mass Transfer*, **15**, 2, pp. 301-314.

Kalkhoran, I.M. (1993). Vortex distortion during vortex-surface interaction in a Mach 3 stream, *AIAA Journal*, **32**, 1, pp.123-129.

Kalkhoran, I.M., Sforza, P.M., and Wang, F.Y. (1991). Experimental study of shock-vortex interaction in a Mach 3 stream, AIAA 91-3270-CP, AIAA 10th Applied Aerodynamics Conference.

Kalkhoran, I.M. and Sforza, P.M. (1994). Airfoil pressure measurements during oblique shock- vortex interaction in a Mach 3 stream, *AIAA Journal*, **32**, 4, pp. 783-788.

Kalkhoran, I.M. and Smart, M.K. (1996). Planar laser-sheet visualization of oblique shock wave-vortex interaction, AIAA 96-0046, AIAA Aerospace Sciences Meeting and Exhibit.

Kalkhoran, I.M. and Smart, M.K. (1997). Flow model for predicting normal shock wave induced vortex breakdown, *AIAA Journal*, **35**, 10, pp. 1589-1596.

Kalkhoran, I.M., Smart, M.K., and Betti, A. (1996). Interaction of a supersonic wing tip with a normal shock, *AIAA Journal*, **34**, 9, pp.1855-1861.

Kandil, O.A., Kandil, H.A., and Liu, C.H. (1991). Computation of steady and unsteady compressible quasi-axisymmetric vortex flow and breakdown, AIAA 91-0752.

Kandil, O.A. and Kandil, H.A. (1991). Supersonic quasi-axisymmetric vortex breakdown, AIAA 91-3311.

Mahesh, K. (1996). A model for the onset of breakdown in an axisymmetric

compressible vortex, *Physics of Fluids*, **8**, 12, pp.3338-3345.

Metawally, O., Settles, G., and Horstman, C. (1989). An experimental study of shock wave/vortex interaction, AIAA 89-0082, AIAA Aerospace Sciences Meeting and Exhibit.

Nielsen, J.N. (1960). *Missile Aerodynamics*, McGraw-Hill, NY.

Rizzetta, D.P. (1995). Numerical simulation of oblique shock-wave/vortex interaction, *AIAA Journal*, **33**, 8, pp. 1441-1446.

Rizzetta, D.P. (1997). Numerical simulation of vortex-induced shock-wave distortion, *AIAA Journal*, **35**, 2, pp. 209-211.

Sarkar, S., Erlebacher,G., Hussaini, M.Y., and Kreiss, H.O. (1991).The analysis and modeling of dilatational terms in compressible turbulence, *Journal of Fluid Mechanics*, **227**, pp.473-493.

Sarpkaya, T. (1995). Turbulent vortex breakdown, *Physics of Fluids*, **7**, 10, pp. 2301

Sforza, P.M. (1970). Aircraft vortices- benign or baleful?, *Space/Aeronautics*, April, pp.42-48.

Sforza, P.M. (1998). Vortex-plume interaction research, NATO Research & Technology Organization AVT/VKI Special Course, *Fluid Dynamics Research on Supersonic Aircraft*, von Karman Institute for Fluid Dynamics.

Smart, M.K. and Kalkhoran, I.M. (1995). The effect of shock strength on oblique shock wave-vortex interaction, *AIAA Journal.*, **33**, 11, pp. 2137-2143.

Spreiter, J.R. and Sacks, A.H. (1951). The rolling up of the trailing vortex sheet and its effect on the downwash behind wings, *Journal of the Aeronautical Sciences*, 18, 1, pp. 21-32.

Weger, J. and Chokani, N. (1991). Experimental design of a supersonic shock wave-vortex interaction at Mach 3, ASME Fluids Engineering Division, Vol 112.

Zatoloka, V., Ivanyushkin, A.K., and Nikolayev, A.V. (1978). Interference of vortexes with shocks in airscoops and dissipation of vortexes, *Fluid Mechanics, Soviet Research*, **7**, 4, pp. 153-158.

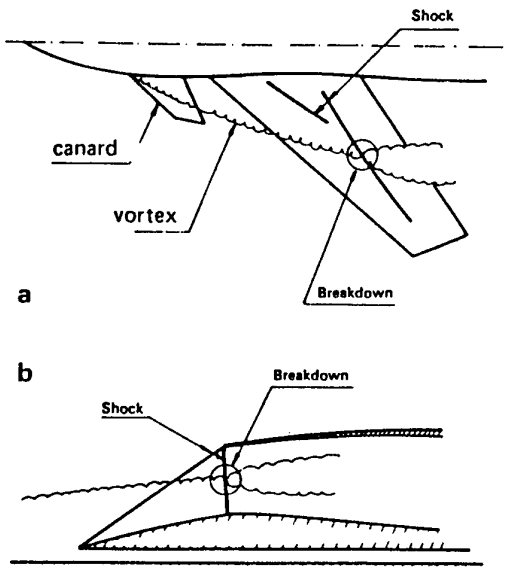


Figure 1. Examples of shock-vortex interaction. (a) Fighter plane flying at high angle of attack at transonic speed. (b) Supersonic air intake. (Delery, et al, 1984)

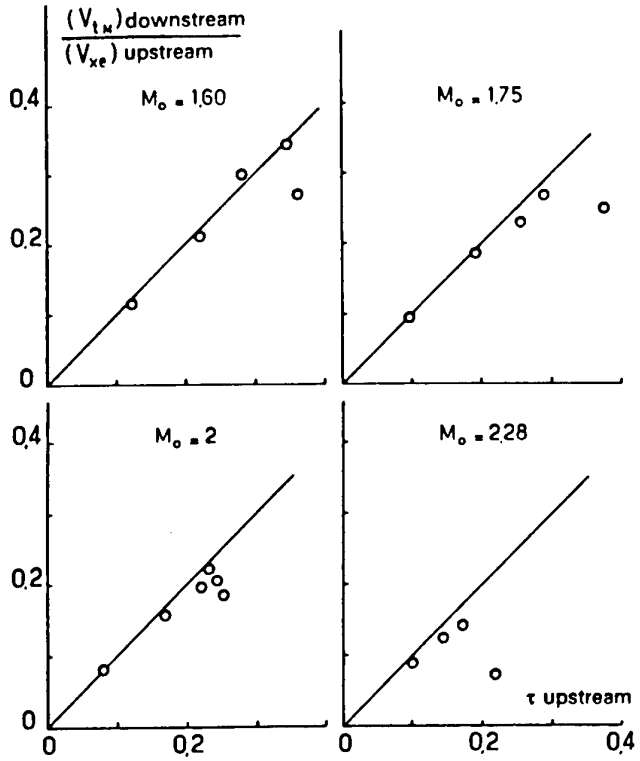


Figure 2. Effect of the shock on the maximum tangential component. (Delery, et al, 1984)

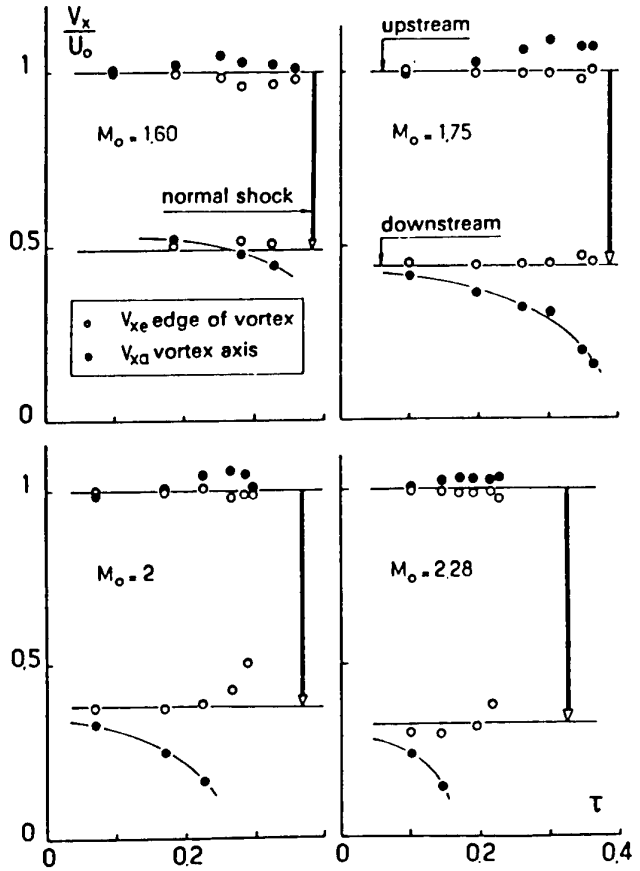


Figure 3. Effect of the shock on the axial component. (Delery, et al, 1984)

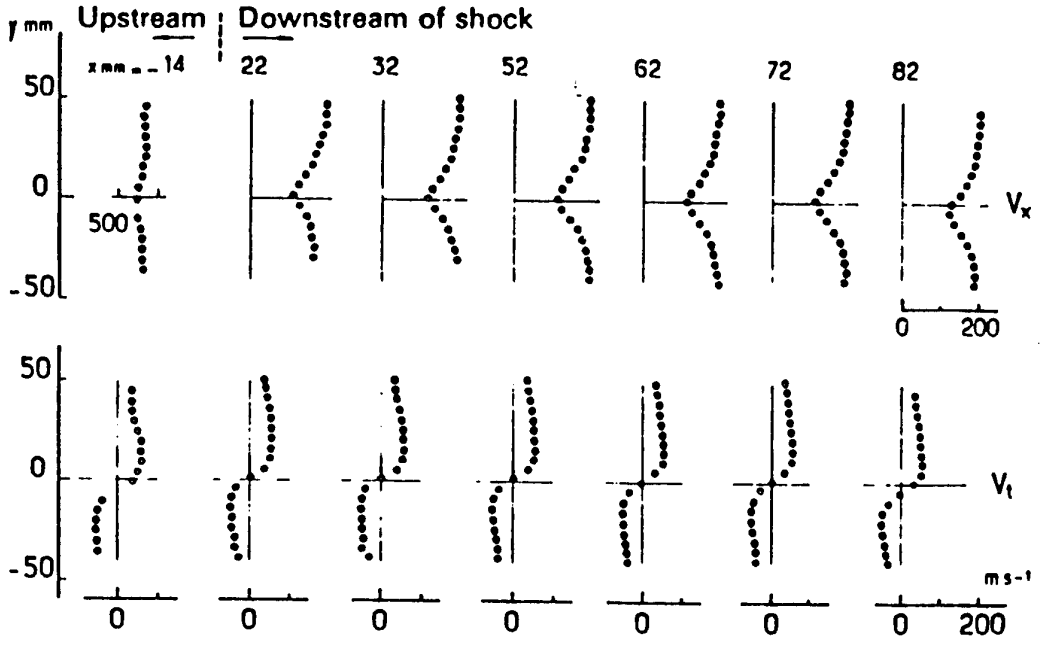


Figure 4. Axial and tangential velocity profiles.
Unbursted vortex ($\alpha = 10°$). (Delery, et al, 1984)

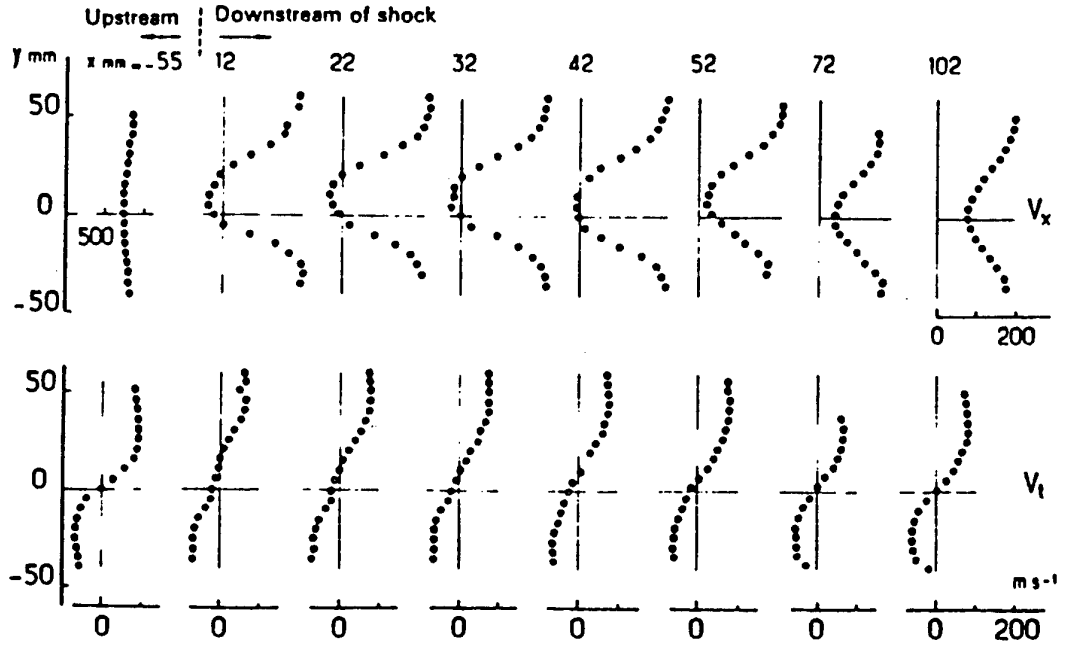


Figure 5. Axial and tangential velocity profiles.
Bursted vortex ($\alpha = 22.5°$). (Delery, et al, 1984)

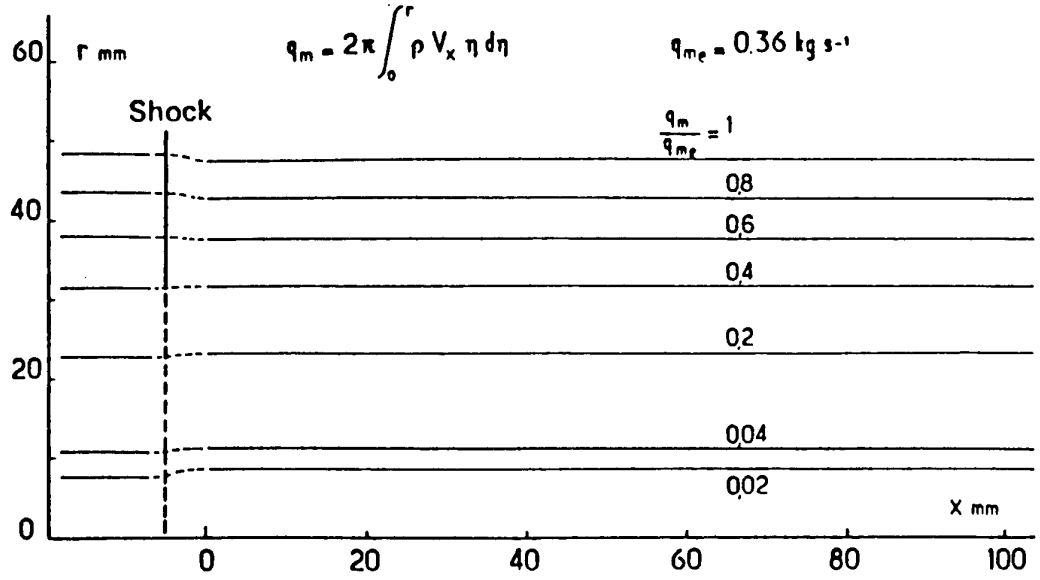


Figure 6. Mean meridian flow streamlines.
Unbursted vortex ($\alpha = 10^{\circ}$). (Delery, et al, 1984)

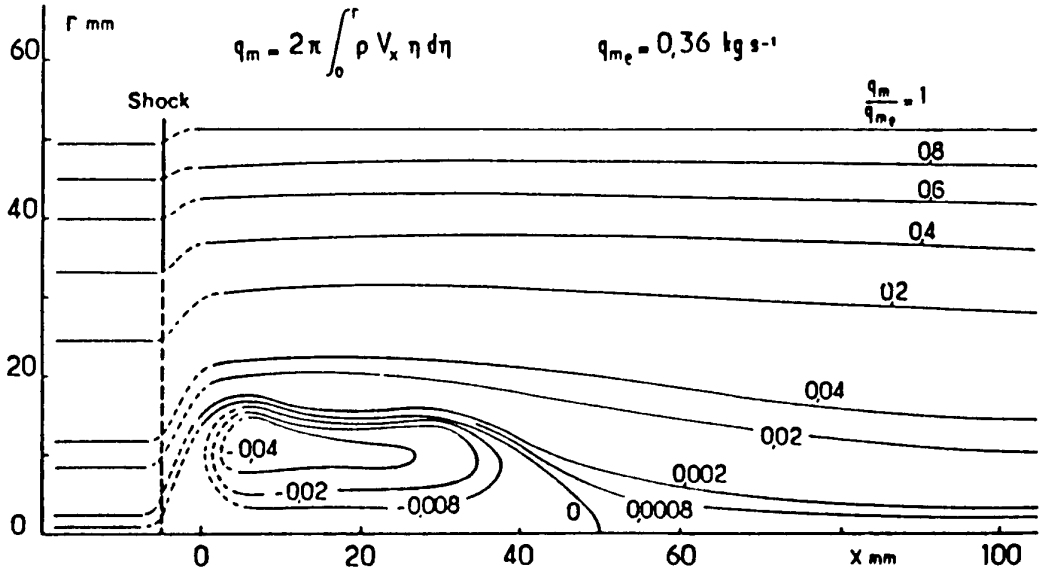


Figure 7. Mean meridian flow streamlines.
Bursted vortex ($\alpha = 22.^{\circ}$). (Delery, et al, 1984)

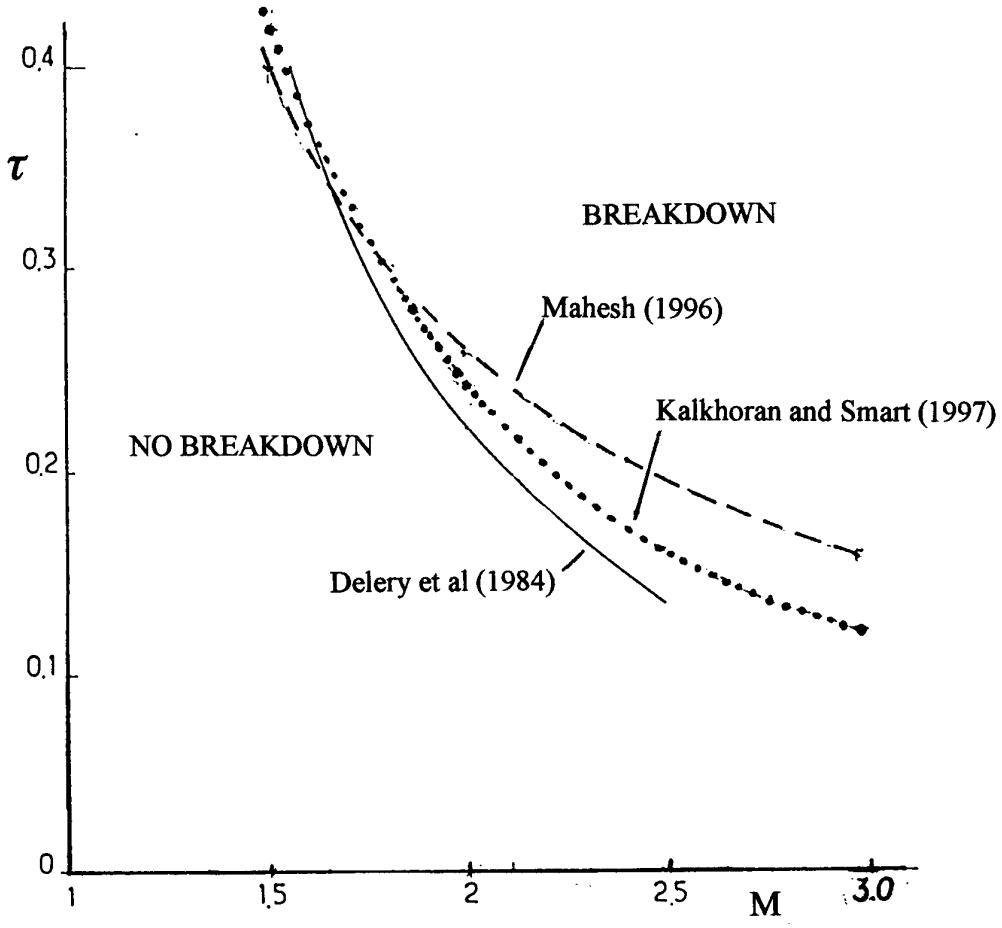


Figure 8. Breakdown limits for normal shock-vortex interaction according to various researchers. Uniform axial velocity component in vortex.

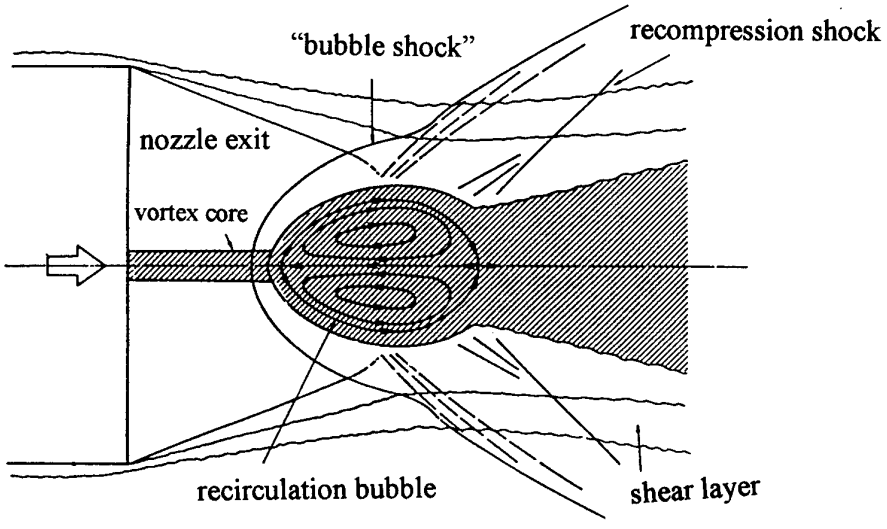


Figure 9. Shock vortex interaction for 'strong interaction'. (Metwally, Settles, and Horstman (1989)

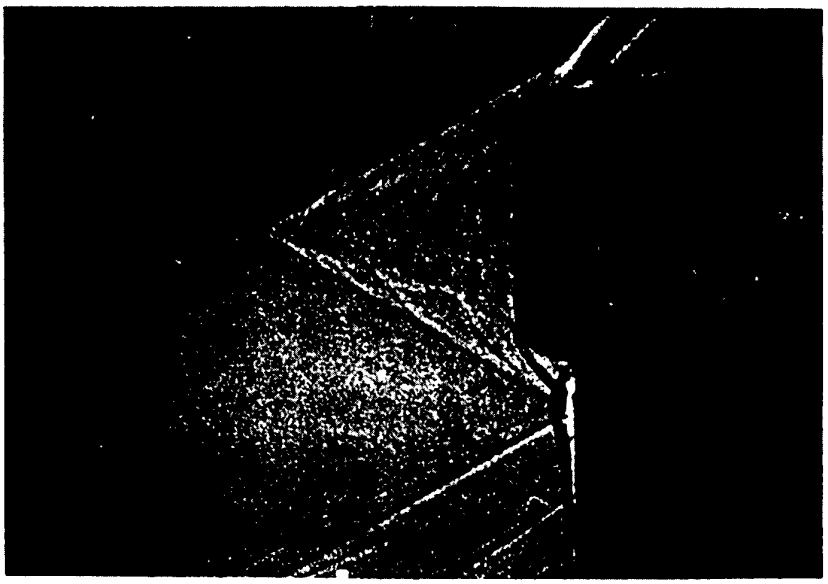


Figure 10a. $t = t_1$

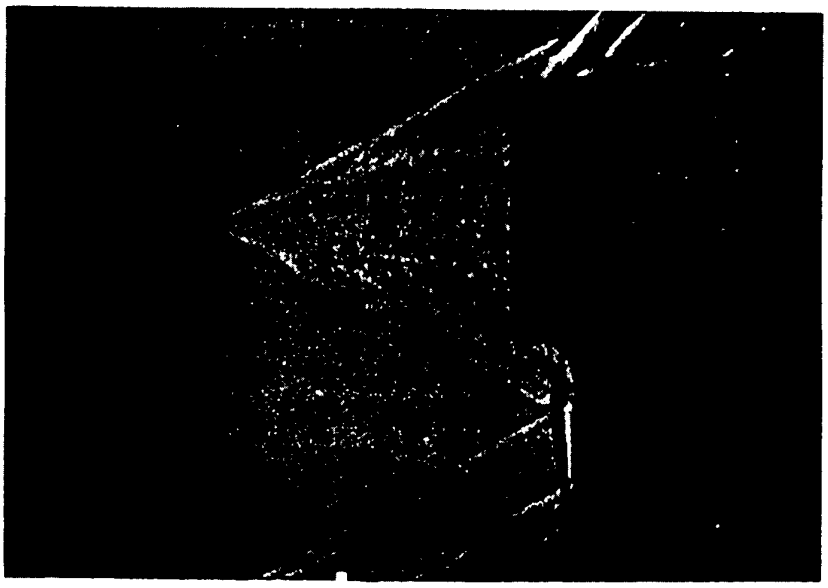


Figure 10b. $t = t_2$

Figure 10. Shadowgraphs of the flow at two different times during the interaction of a moderate vortex ($\tau_{max} = 0.17$) with a normal shock at Mach 2.49. (Kalkhoran, Smart and Betti, 1996)

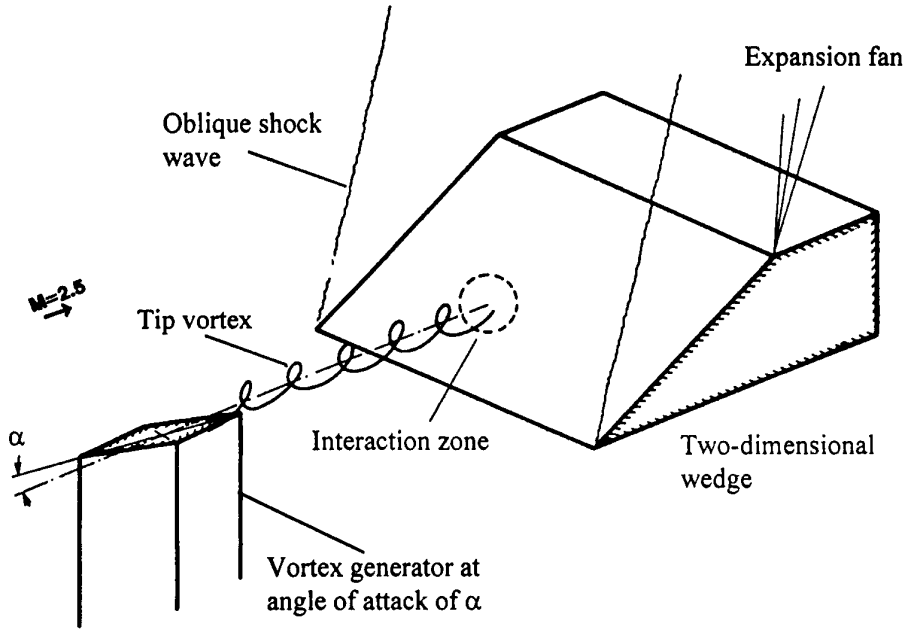


Figure 11. Schematic representation of the experimental arrangement for the oblique shock wave/vortex interaction experiments.

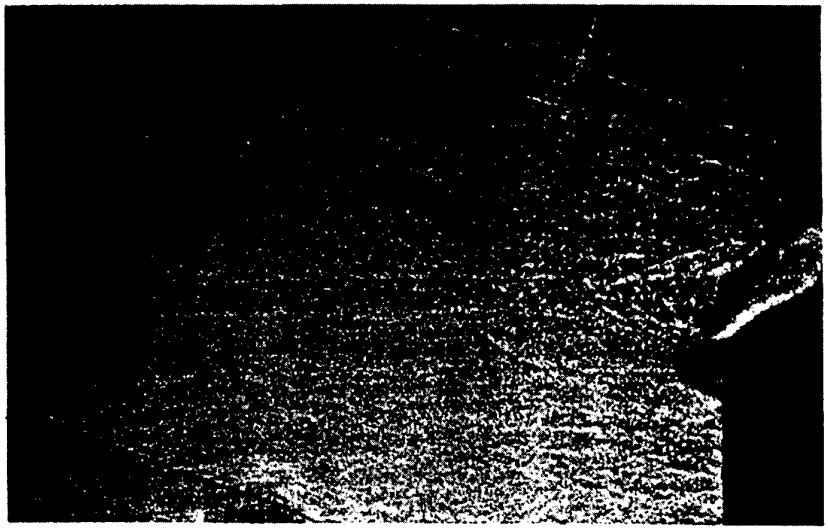


Figure 12. Shadowgraph of the flow during an oblique shock wave/vortex interaction at Mach 3. Flow is left to right. Note conical shock ahead of wedge shock. (Kalkhoran and Sforza, 1994)

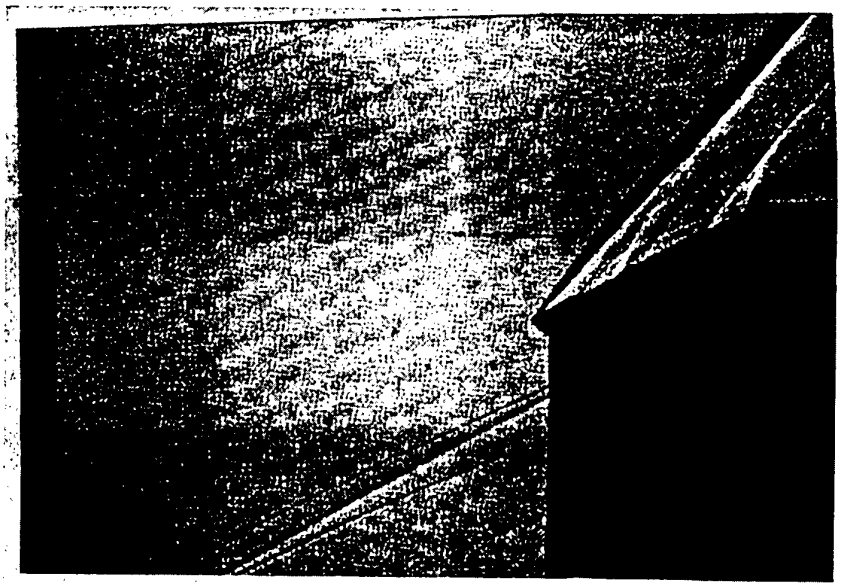


Figure 13. Shadowgraphs of the flow during the interaction of a moderate vortex(τ_{max} = 0.17) with a weak oblique shock with a flow detection of $\theta = 22^{\circ}$ at Mach 2.49. (Kalkhoran and Smart, 1995)

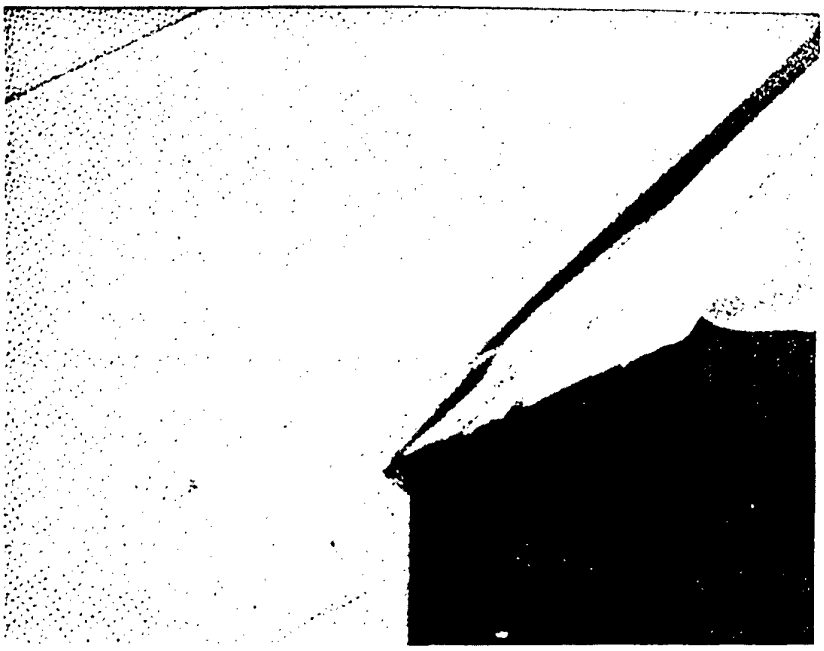


Figure 14a. $\theta = 22^{\circ}$.

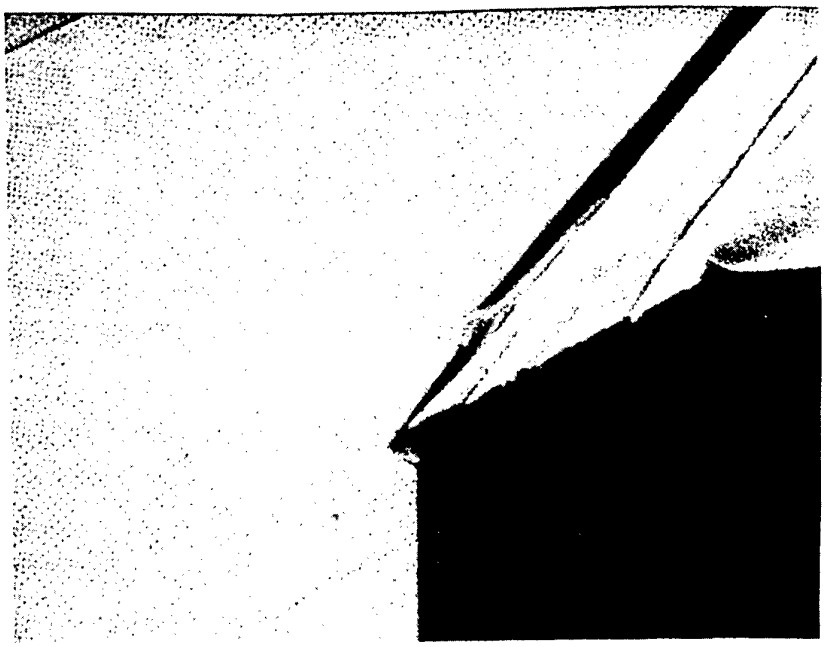


Figure 14b. $\theta = 25^{\circ}$.



Figure 14c. $\theta = 29^{\circ}$.

Figure 14. Shadowgraphs of the flow during the interaction of a strong vortex ($\tau_{max} = 0.32$) with oblique shocks of various strengths at Mach 2.49. (Kalkhoran and Smart, 1995)

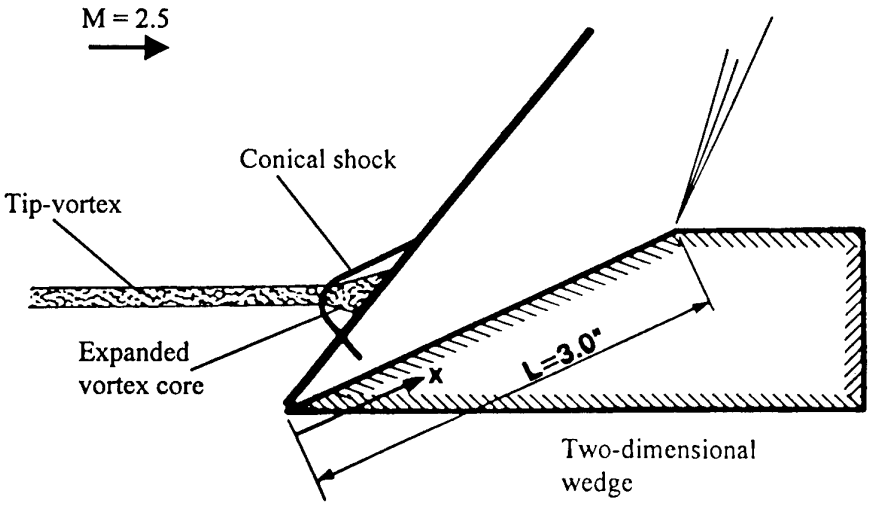


Figure 15. Interpretation of the observed flowfield during the interaction of a strong vortex and an oblique shock.

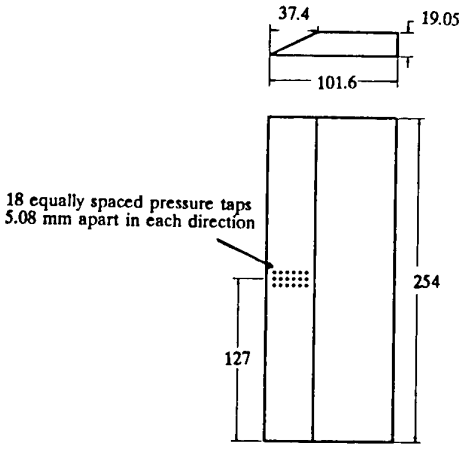


Figure 16. Geometry of the 27-deg shock-generator section.

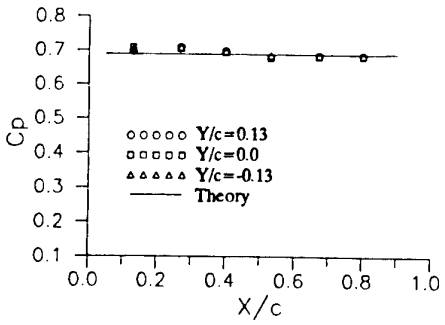


Figure 17. Baseline wedge pressure distribution. (Kalkhoran and Sforza, 1994)

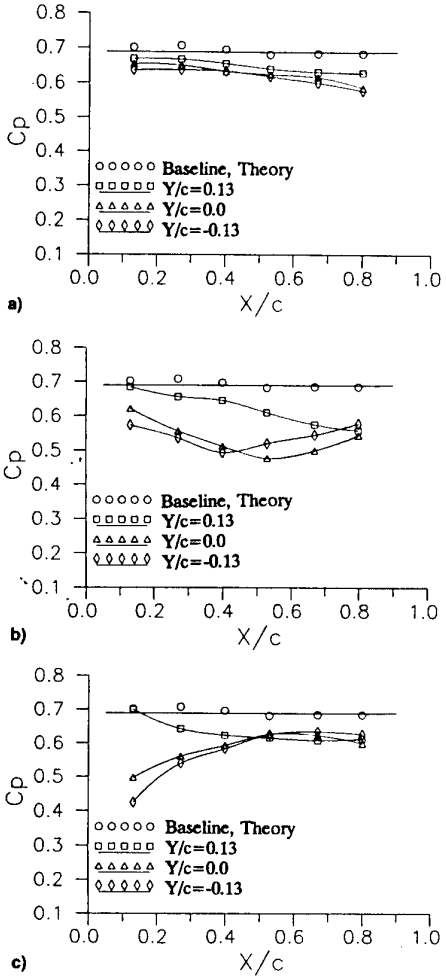


Figure 18. Wedge pressure coefficient distribution during the interaction for α_{VG} = 5 deg: a) *h*/*c* = 0.40,b) *h*/c -0.067, and c) *h*/c = -0.267. (Kalkhoran and Sforza, 1994)

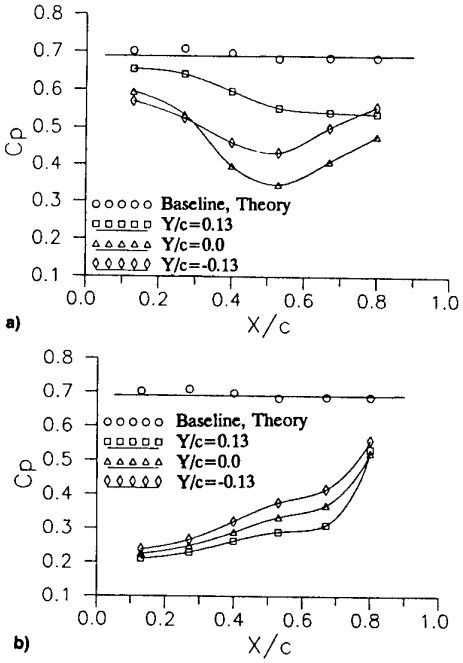


Figure 19. Wedge pressure coefficient distribution during the interaction for α_{VG} = 7.5 deg: a) *h*/c = 0.067, and b) *h*/c = -0.267. (Kalkhoran and Sforza, 1994)

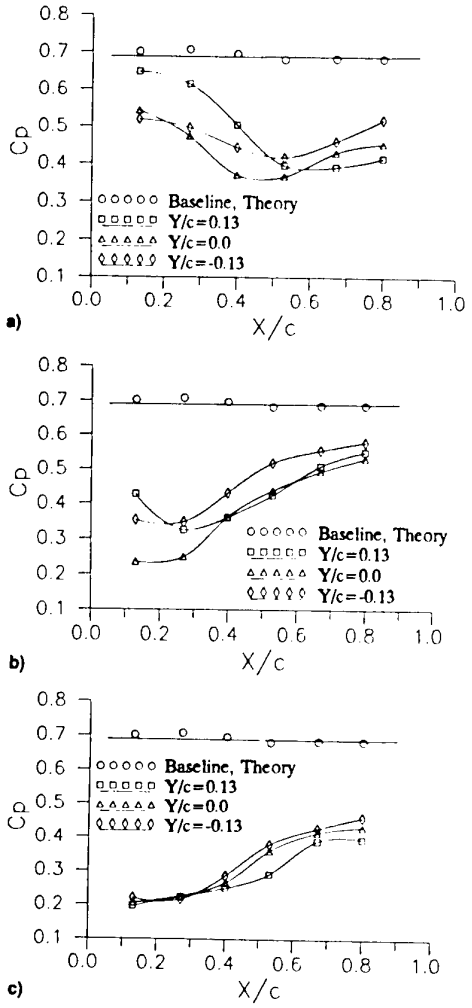


Figure 20. Wedge pressure coefficient distribution during the interaction for α_{VG} = 10 deg: a) *h/c* = 0.067, b) *h/c* -0.10, and c) *h/c* = -0.267. (Kalkhoran and Sforza, 1994)

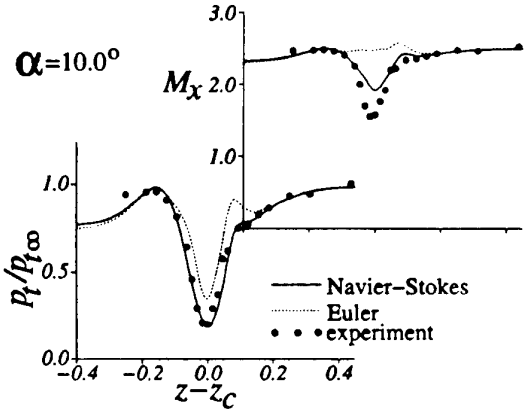


Figure 21. Total pressure and streamwise Mach number distributions through the vortex core at the upstream boundary for α = 10.0 deg. (Rizzetta, 1997)

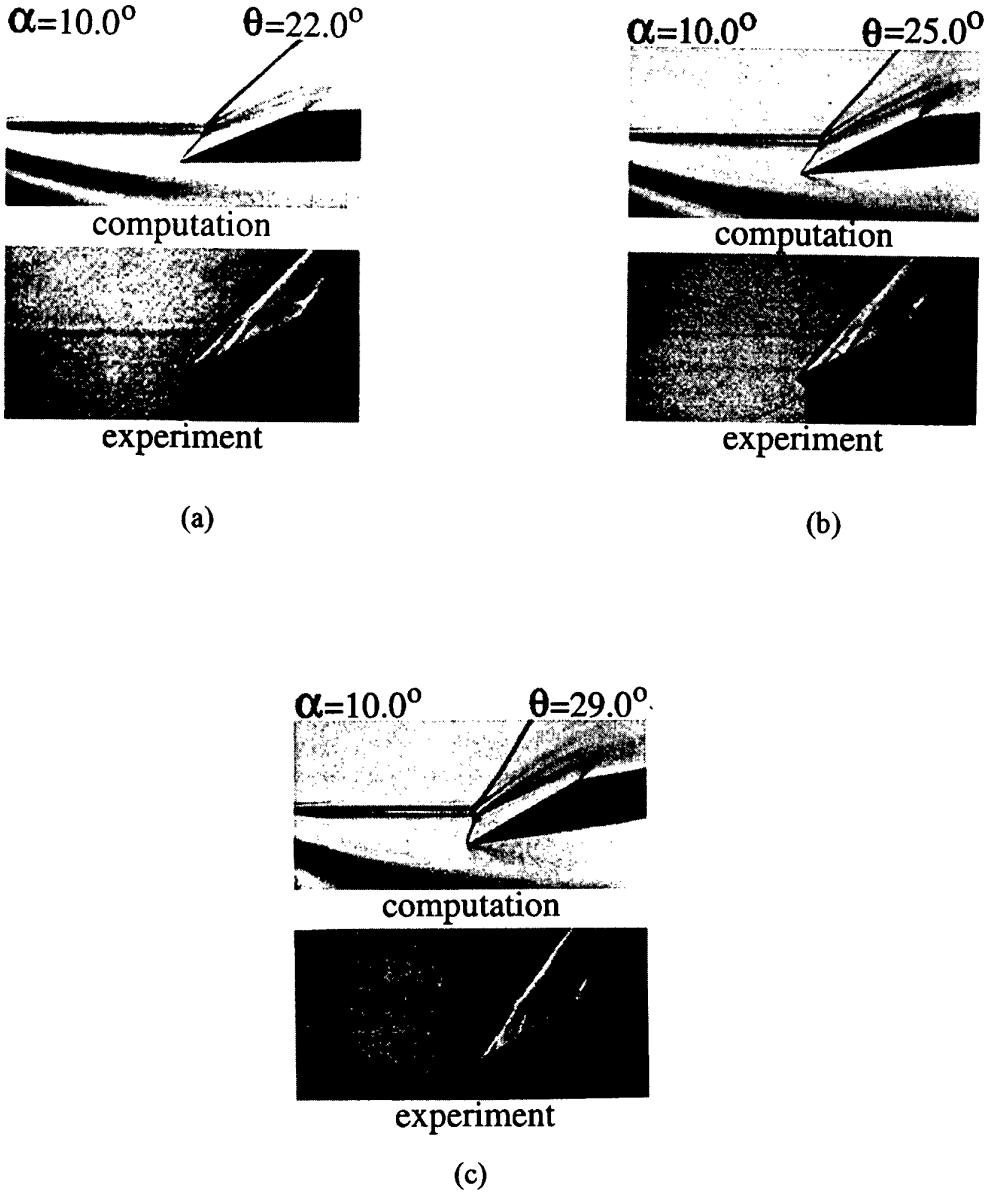


Figure 22. Comparison of computed and experimental oblique shock-vortex interactions at M = 2.49. Vortex generator angle of attack α and wedge angle θ shown on each set of results. (Rizzetta, 1997)

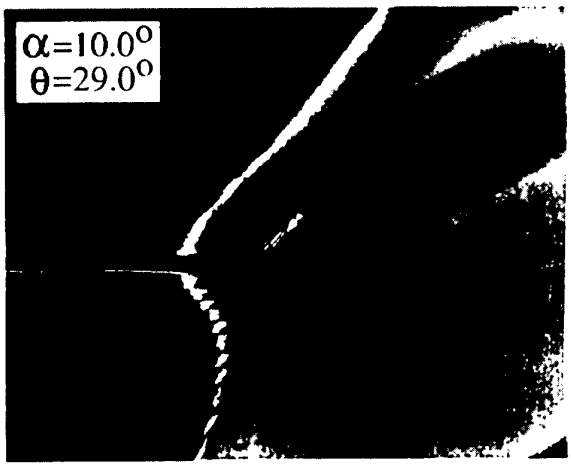


Figure 23. Computed Mach number contours, particle paths, and iso-surface of u = 0 and α = 10.0 deg and θ = 29.0 deg. (Rizzetta, 1997)

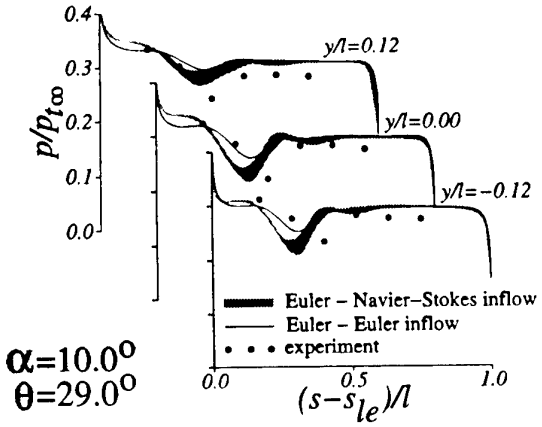
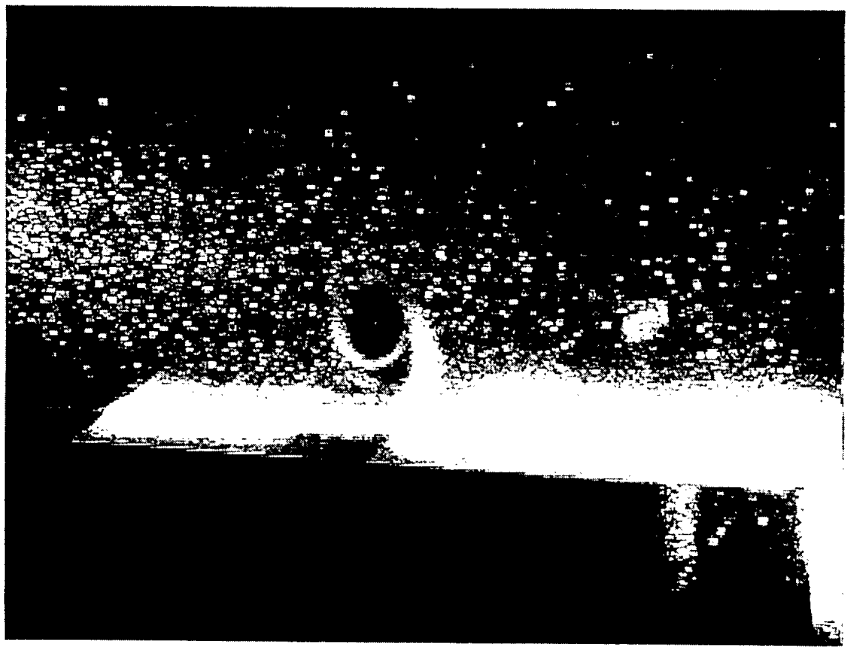
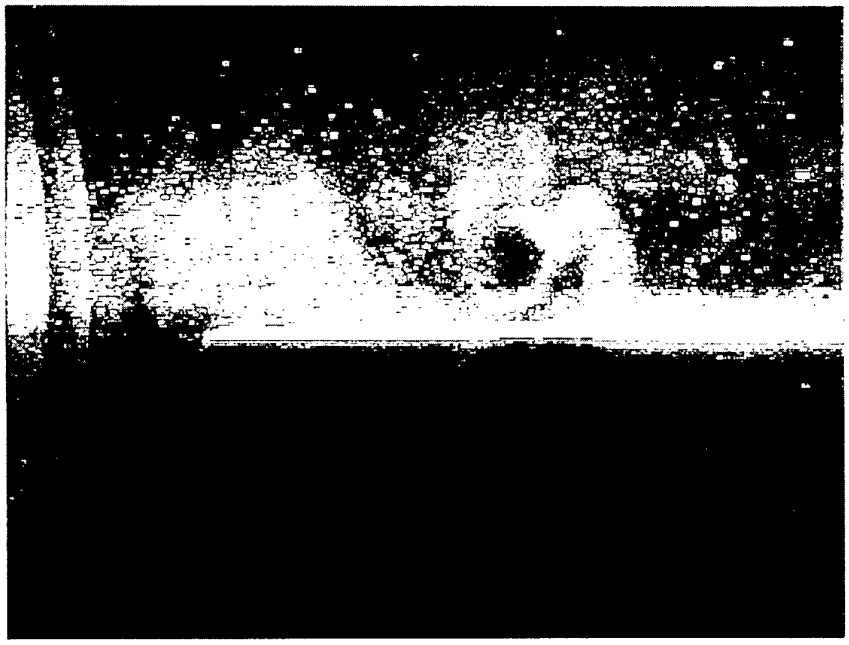


Figure 24. Computed wing surface static pressure distributions for α = 10.0 deg and θ = 29.0 deg. Experiments are those of Smart and Kalkhoran (1995). (Rizzetta, 1997)



(a). x = 12.7 mm.



(b). x = 66.6 mm.

Figure 25. Planar laser-sheet visualization of the flow during the interaction of a strong vortex ($\tau_{max} = 0.32$) with an oblique shock ($\theta = 29^{o}$) at Mach 2.49 and two locations downstream of the wedge leading edge. (Kalkhoran and Smart, 1996)

Aerodynamic Research for a Second Generation SST in Japan Including Laminar Flow Control & Low Sonic Boom Design

Kenji YOSHIDA
Advanced Technology Aircraft Project Center
National Aerospace Laboratory
6-13-1, Osawa, Mitaka, Tokyo, 181-0015, Japan

ABSTRACT
The outline of aerodynamic researches on a second generation SST in Japan and results of the individual research on the supersonic laminar flow control (LFC) and the low sonic boom design are described. LFC effect was examined by the wind tunnel tests of the warped delta wing model with a LFC device, and by the numerical analysis with originally developed e^N method together with a new assumption. As for the low boom technology, Darden's theory was applied for designing the aerodynamic configuration and its characteristics was investigated numerically in order to clarify the effects of nose shape and Mach number. Wind tunnel tests and Euler CFD analysis were performed for the evaluation. Further trial for improvements of lift-to-drag ratio and trim constraint is proposed with regard to real airplane design.

1. INTRODUCTION

Japan has little experience in designing and developing an SST. To take part in an international collaboration for a second generation SST in the near future, a number of studies are necessary along the following two approaches. One is a design approach to catch up present knowledge and technologies. Another is a fundamental research approach to provide new data on some advanced technologies.

National Aerospace Laboratory (NAL) has just started a flight test program with two kinds of un-manned scaled supersonic experimental airplanes. This program is promoted along both approaches. The detail of aerodynamic design of our airplane is summarized in another lecture note on this course by the author. It mainly corresponds to the study along a design approach.

On the other hand, several fundamental studies along a research approacn have already been conducted in Japan. In this note, an overview of those activities are summarized in Chapter 2, then details of two special topics, supersonic laminar flow control and low sonic boom design are described in Chapter 3 and 4, respectively.

2. OVERVIEW OF JAPANESE ACTIVITIES

2.1 Historical Review

Japan Aircraft Development Corporation (JADC) has promoted a feasibility study on conceptual design, targets for technology development, market and environmental issues since 1989. These studies are mainly conducted by three airframe companies--Mitsubishi Heavy Industries (MHI), Kawasaki Heavy Industries (KHI), Fuji Heavy Industries (FHI) and one engine company--Ishikawajima-Harima Heavy Industries (IHI).

A preliminary computer aided design (CAD) program and market analysis program were developed in the JADC study. The CAD program was based on some statistical and empirical database conducted aerodynamics, material and structural features, and engine performance proposed by the four companies above. The market analysis program was based on a number of database for market study conducted by JADC. Then several configurations were designed and demand from market were investigated. And some targets of technology which should be developed before the start of international collaboration program on a second generation SST, were made clear. And some of the targets have been investigated by MHI, KHI, FHI under a funding from the Society of Japanese Aerospace Companies (SJAC) from 1990 to 1995.

On the other hand, some fundamental researches have also been performed in National Aerospace Laboratory (NAL) in collaboration with MHI, KHI and FHI from 1992 to 1994. Recently NAL started a scaled supersonic experimental airplane program. Furthermore, to support it, NAL started cooperative research programs with universities. Some fundamental studies have been independently conducted at Tohoku University, University of Tokyo and Nagoya University.

2.2 Configuration Study

Yoshida and Hayama[1] experimentally investigated some basic aerodynamic concepts for supersonic drag reduction, namely, arrow planform, combination of camber and twist (warp), and area-ruled body. We examined an effect of each concept using simple test models without any nacelles and developed a fundamental aerodynamic design procedure based on supersonic lifting surface theory, slender body theory and boundary layer theory. Next Yoshida and Ogoshi[2] improved the design procedure and designed an optimum configuration shown in Fig. 1. The improvements of the procedure was confirmed by wind tunnel tests.

On the other hand, Yamazaki and Uchida[3] numerically investigated the first baseline configuration (Fig. 2), which was designed in the JADC study. Their CFD (Euler) analysis was the first in Japan concerning a configuration with nacelle. They showed clear difference in the drag between the configuration with and without nacelles as shown in Fig. 2.

Recently a new baseline configuration, shown

Paper presented at the RTO AVT Course on "Fluid Dynamics Research on Supersonic Aircraft", held in Rhode-Saint-Genèse, Belgium, 25-29 May 1998, and published in RTO EN-4.

in Fig. 3, has been designed in the JADC study. Suzuki et al.[4] analyzed aerodynamic characteristics using their CFD (Euler) code and pointed out the limitation of using linear theory as shown in Fig. 3.

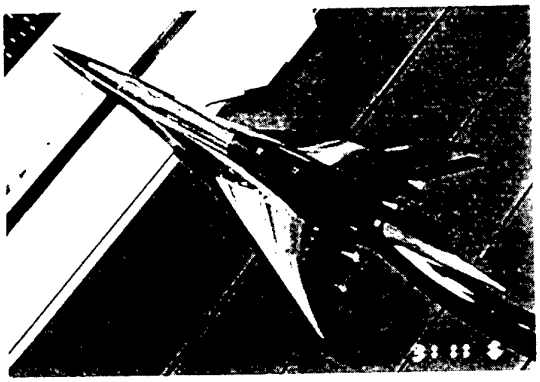


Fig. 1 Wind Tunnel Test Model[2]

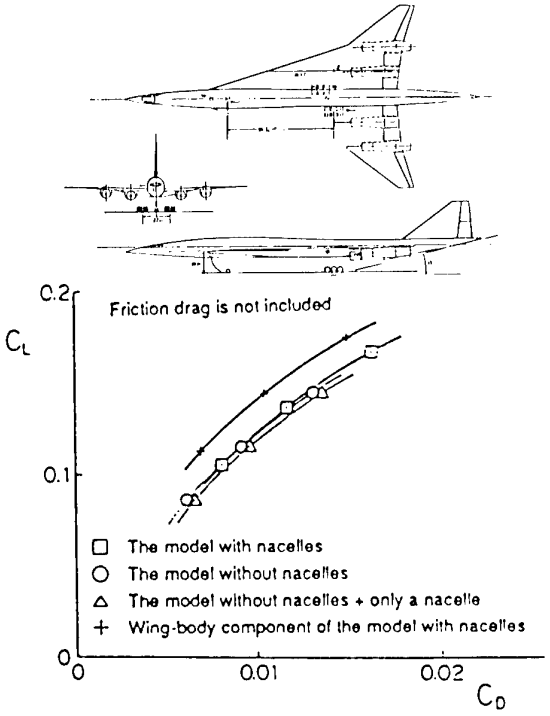


Fig. 2 Estimated Drag Polar by CFD[3]

2.3 Airframe/Nacelle Integration Study

The aerodynamic integration of an airframe/nacelle configuration is a difficult work in designing a real aircraft. Takami and Kawashima[5] conducted wind tunnel tests on a complete configuration with nacelles which were designed under a required mass flow condition estimated in the JADC study. They investigated an influence of spillage. Fig. 4 shows an oil flow pattern at no airflow condition for two nacelles mounted on the right wing.

Recently Kaiden et al.[6] analyzed a bleed and bypass effect of a typical second generation SST configuration with four nacelles, using a CFD (Navier-Stokes) solver and overset grid system indicated in Fig. 5. Fig. 6 shows surface streamlines from the nacelle at bypass off and 40% bypass condition. And they found the increments of lift and drag were about 1.0% and 0.5% per 10% bypass air, respectively.

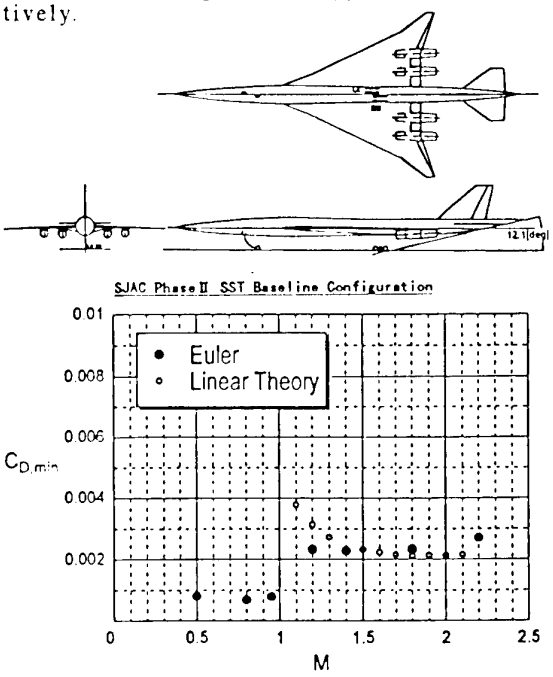


Fig. 3 Estimated Minimum Drag by CFD[4]

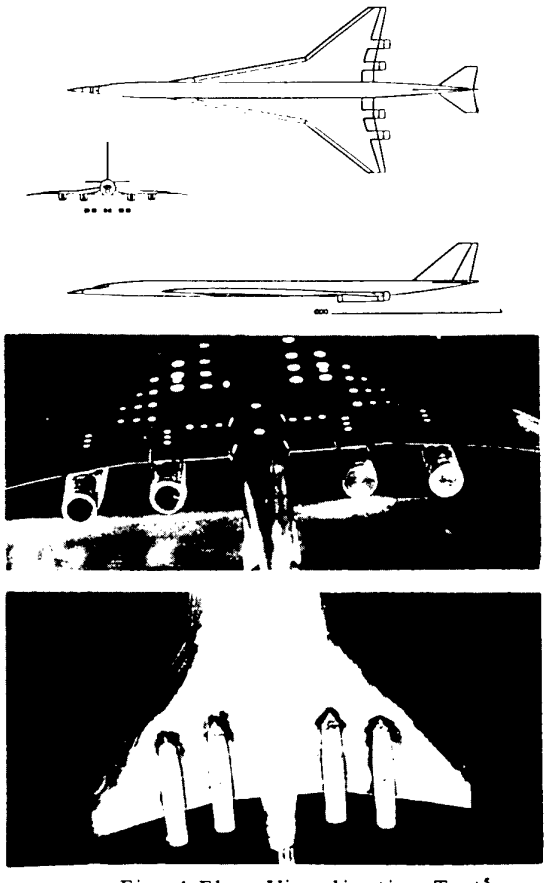


Fig. 4 Flow Visualization Test[5]

Higaki[7] also applied CFD (Euler) analysis to design a NAL's experimental airplane with jet propulsion system. Outline of her study is

summarized in another lecture note by the author.

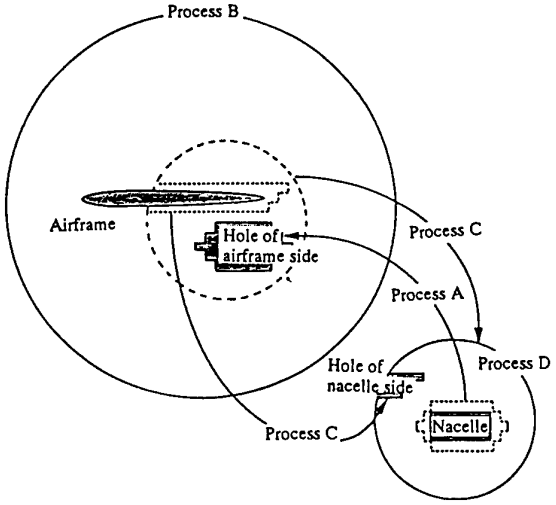


Fig. 5 Outline of Overset Grid System[6]

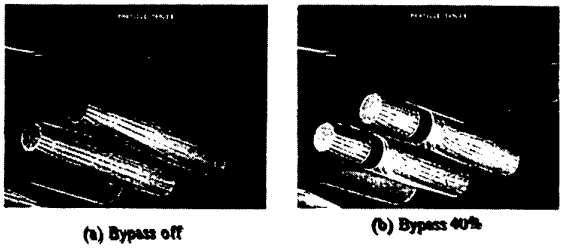


Fig. 6 Surface Streamlines on Nacelles by CFD[6]

2.4 Intake Design Study

Optimum intake design is another important work in the aerodynamic design of SST. Usually basic intake duct shape, namely, cross sectional area distribution is designed by shock relation and supersonic characteristics method, but there are some problems such as a bleed system, corner flow and unstart in the real design. CFD (Navier-Stokes) analysis is expected to solve them.

Fujimoto et al.[8], Fujimoto and Niwa[9] investigated an intake design using CFD (Navier-Stokes) analysis and compared it with a wind tunnel test. Fig. 7 shows the CFD results of a bleed effect on capturing a normal shock at throat. Then they also validated three dimensional analysis by comparing with their tests.

Recently Fujiwara and Sakata[10] also applied CFD (Navier-Stokes) to design an intake shape of the experimental airplane with jet propulsion. Their activity is summarized in another lecture note by the author. They plan a wind tunnel test of their designed intake in this spring.

2.5 Laminar Flow Control (LFC) Study

Through several researches on drag reduction technologies after the development of Concorde, pressure drag reduction technologies have fairly been optimized in their effects and procedures. However, the reduction of friction drag has not been solved yet. The most effective aerodynamic way is a well known laminar flow control (LFC), in spite of several problems which should be overcome in a real design.

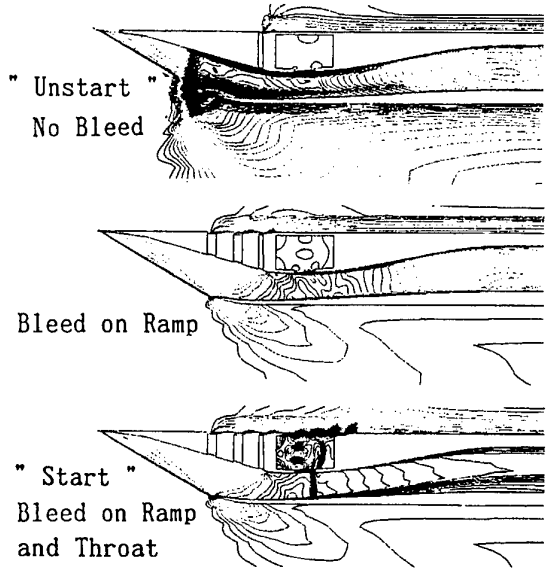
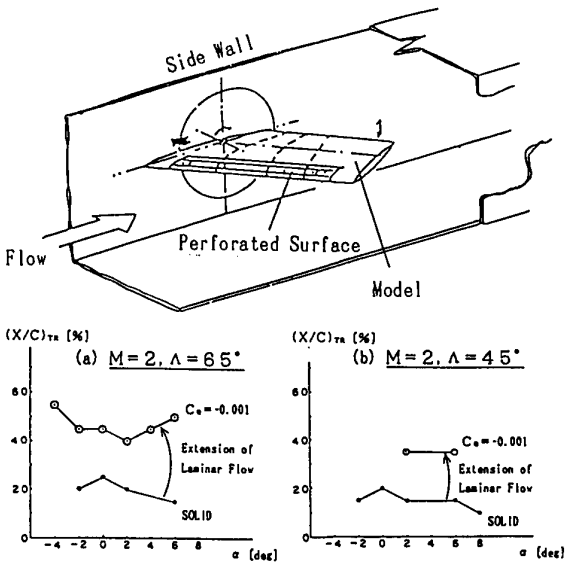


Fig.7 Mach Number Contours of Supersonic Intake at M=2.5[8]

Yoshida and Tani[11] investigated an effect of supersonic LFC experimentally and numerically. They used a simple swept wing model with NACA64A008 airfoil section and constant chord, and mounted it on the wall of FHI supersonic tunnel. The rearward movement of transition due to suction was confirmed by flow visualization as shown in Fig. 8.



Fog. 8 Supersonic LFC Effect on Transition Location[11]

At NAL, Ishida and Noguchi[12] have studied subsonic LFC applied to several airfoils and wings since 1984. In 1992 the author and

Ogoshi of KHI started a cooperative research on supersonic LFC with Ishida et al.. The detail of this study is described in the next chapter.

2.6 Sonic Boom Study

Sonic boom is one of the most important environmental issues. Since conventional supersonic aircraft usually has a sharp nose to reduce wave drag, its bow shock is weak. However, it has strong and multiple secondary shocks. Sonic boom is generated by the coalescence of these shock waves, in the propagation process. This pressure perturbation generally formed a so-called N-waveform.

Main parameters characterizing the N waveform are a peak pressure, a duration and a rise time. The peak pressure is usually used to indicate the acceptable level of the sonic boom. However, in the standpoint of human response, it is insufficient for evaluating sonic boom, and the rise time is more important. In general, we feel boom noise softer if the rise time is longer. It seems difficult to decrease the peak pressure, because it is determined by the aircraft size, absolute value of volume, and weight (lift). Therefore, shaping pressure waveform is very effective in reducing the sonic boom.

Two activities on the sonic boom issue have been performed in Japan. One is an acoustic study, namely, loudness study. Another is an aerodynamic study, namely, low sonic boom configuration design study.

Yamamoto et al.[13,14] has performed the loudness study. She investigated a human response and suitable metrics, such as an A-weighted sound exposure level (ASEL) and a PL proposed by Stevens, using frequency analysis and an originally developed sonic boom simulator shown in Fig. 9. Fig. 10 shows a typical test result on acceptability. The ordinate shows unacceptability (%) and the abscissa indicates loudness for several boom waveforms represented by each metric. She concluded the PL was the best in measuring a boom noise level, because the result by PL had a good correlation between unacceptability and loudness as shown in Fig. 10.



Fig. 9 Sonic Boom Simulatore[14]

On the other hand, the author conducted a low boom configuration study numerically and experimentally. The detail of this study is described in Chapter 4.

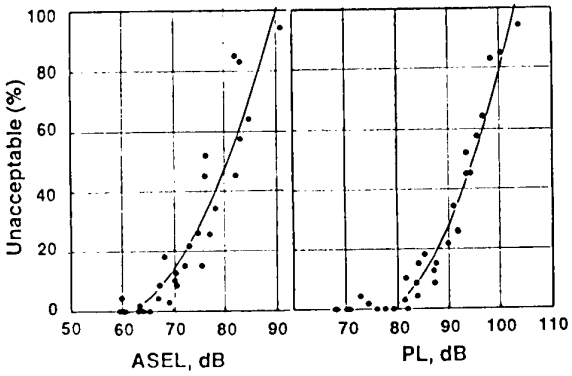


Fig. 10 Results of Simulator Test[14]

Makino et al.[15,16] also studied a low boom configuration and design procedure experimentally and numerically. Recently he pointed out the limitation of the author's design procedure based on supersonic linear theory and developed a new optimum design procedure using CFD (Euler) analysis. Fig. 11 shows a difference in geometry and equivalent area distributions, before and after applying his optimization technique. Their ground pressure signatures were also estimated and the improvement was confirmed as shown in Fig. 12.

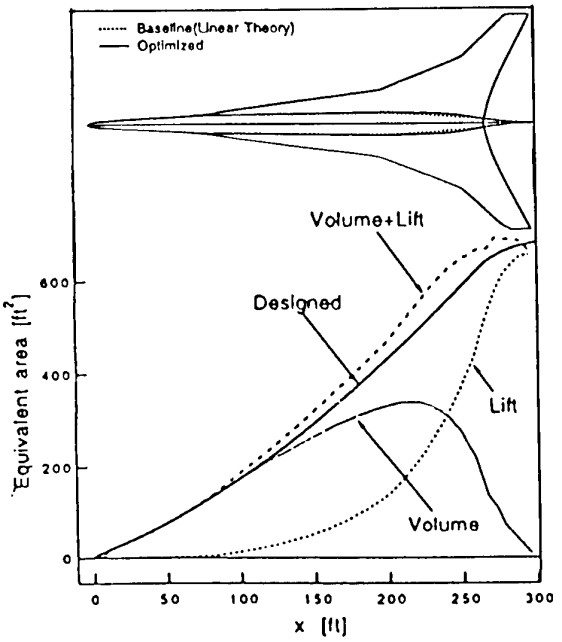


Fig. 11 Optimized Equivalent Area Distributions[16]

2.7 High Lift Device Study

High lift device (HLD) is also important because a second generation SST is required to have high performance in take-off and landing. Therefore vortex flap is expected to be an effective HLD for a low aspect wing like SST.

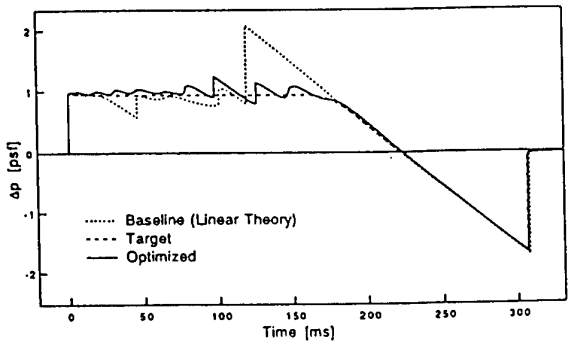


Fig.12 Estimated Ground Pressure Signatuers[16]

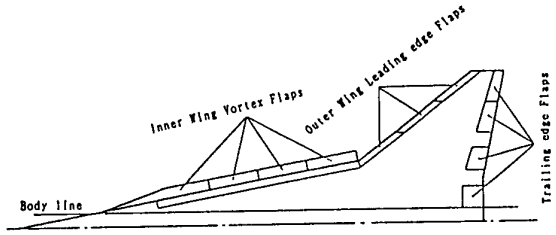


Fig. 13 Model Configuration of Vortex Flap Test[17]

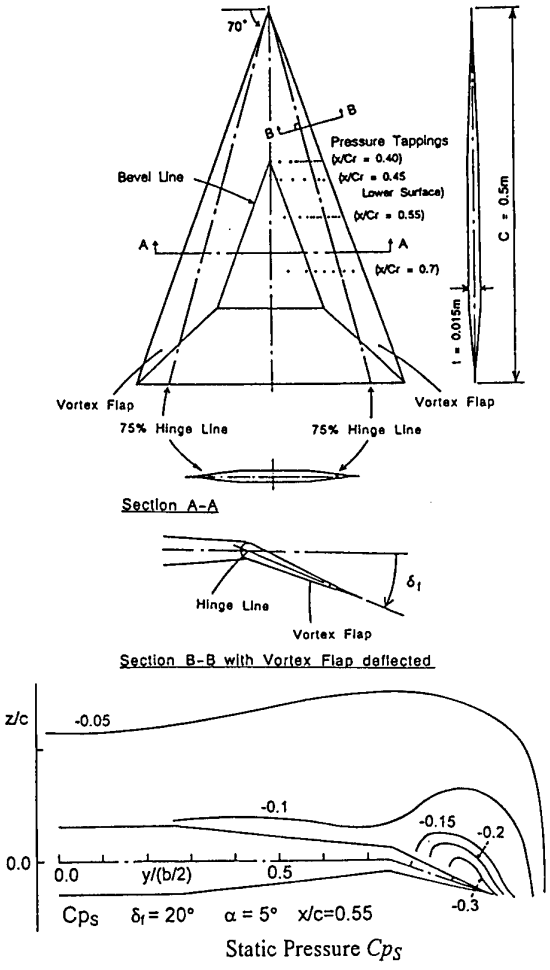


Fig. 14 Results of Vortex Flap Test[18]

Sato et al.[17] experimentally investigated an effect of HLD including the vortex flap shown in Fig. 13. They found the effect of the trailing edge flap to a L/D at CL=0.5 was larger than the one of leading edge flap.

Rinoie et al.[18] has investigated flow phenomena of leading edge vortex and optimum combination of the vortex flap parameters. Fig. 14 shows contours of measured static pressure near the flap of the test model shown in the figure. He confirmed the vortex flap could capture the leading edge vortex.

2.8 Optimum CFD Design Study

CFD analysis is well-known to be very effective and necessary in designing an optimum SST configuration. Recently Jeong, Matsushima and Iwamiya[19,20] developed an inverse design method by CFD, and it was applied to design an aerodynamic configuration of NAL's scaled supersonic experimental airplane. The outline and some results are described in another lecture note by the author.

Usually inverse method leads to local optimum solution. However, most designers will expect CFD has possibility to find a global optimum solution. Obayashi et al.[21] has tried it using a GA algorithm.

3.RESEARCH ON LAMINAR FLOW CONTROL

3.1 Background, Objective and Approach

1) Background

Laminar flow control (LFC) is well known to be the most attractive and effective technology in improving the lift-to-drag ratio (L/D). Its validity in subsonic speed has been confirmed by several wind tunnel tests and flight tests. However, supersonic LFC has not been established yet because of the following problems.

(i) Physical transition mechanism in three dimensional compressible flow is more complex than in low speed, due to the existence of Mach's second mode, for example.

(ii) Since supersonic wind tunnel of blow-down type is not usually quiet, any high quality test on transition is difficult.

(iii) Although e^N method is effective as practical transition prediction method, we do not have enough experimental data on supersonic flow to obtain an empirical relation between a typical N value and transition.

(iv) Most supersonic LFC tests which had been already conducted were limited to simple configurations, for example, a simple swept wing with constant chord length and no twist distribution[11], and a flat delta planform, etc.

As stated above, the author and Ogoshi started a research on supersonic LFC with Ishida and Noguchi in 1992. Our study was one of trials to solve those problems.

2) Objectives

Our objectives were as follows:
(A) To obtain fundamental and useful experimental data on transition phenomena, including to confirm a correct effect of supersonic LFC and to find an optimum suction distribution.
(B) To develop a practical transition prediction method based on an e^N method, including an investigation of stability characteristics and to find out empirical relations between the N value and transition.
(C) To establish a friction drag reduction technology with supersonic LFC, to find a desired pressure distribution for natural laminar flow (NLF) and to design a new original NLF wing.

3) Approach
Our study consisted of two approaches: one was a numerical approach and another was an experimental approach.

In the experimental approach, we first designed an original warped wing model which had a simple planform with a practical warped surface. Then we conducted wind tunnel tests to obtain useful data of natural transition characteristics and to investigate a sectional drag reduction effect by boundary layer suction.

In the numerical approach, we first developed two original programs analyzing stability characteristics and integrating an amplification rate of small disturbance, based on linear stability theory. Then we analyzed transition characteristics of our test model. Furthermore we tired to extend the present method to more general transition prediction system with linear stability theory and laminar profiles computed by CFD (Navier-Stokes) analysis.

3.2 Wind Tunnel Tests on LFC

1) Test facility
A quiet tunnel is necessary for a research on LFC. However, NAL's supersonic tunnel is not quiet because it is a blow-down type. On the other hand, NAL's transonic tunnel with 2m × 2m test section is quieter than the supersonic one, because it is a continuous flow type. For example, a low free-stream turbulence level was confirmed by a transition test on AEDC 10 degrees cone. Since our study was fundamental, we considered we could investigate main features using the transonic tunnel at M=1.4.

2) Test model
There are several LFC wind tunnel tests about relatively simple wings and configurations in the world, because LFC study is more fundamental than other design study. However there is few tests using a model with warped wing which is always applied in real SST design. Therefore, we designed a typical warped wing with simple delta planform, using Carlson's method[22].

The photograph of our originally designed test model is shown in Fig. 15. Our model was a half model and consisted of main wing and four cassettes which were located at a forward part of the wing (the region between 3 and 30% chord length and between 20 and 60% semispan location). They were a solid cassette for a pressure measurement test, an adiabatic cassette for a visualization test, a perforated cassette for the LFC test, and a hot-film cassette for a transition measurement test. The perforated cassette had about 60,000 tiny holes (0.1 mm in diameter) for suction of air. The semispan was 0.5 m, and root chord length was about 1 m. (The swept back angle of the leading edge was 65 degrees.)

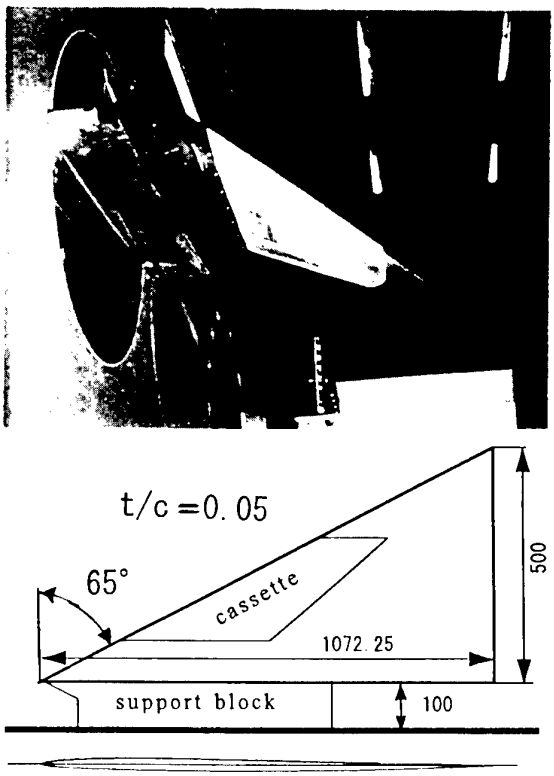


Fig. 15 LFC Test Model[24]

The transition phenomenon is very sensitive to turbulence in boundary layer on the tunnel wall. So we tried to set the half-wing model 0.1 m apart from the wall using a support block shown in Fig. 15. An influence of it was considered through our numerical study.

3) Test results for NLF characteristics[23]
Before conducting the LFC test, we carried out a flow visualization test with a liquid crystal to obtain the NLF characteristics of our model.

Comparing the color pattern on the surface with a reference pattern generated by a few tiny isolated roughness put near the leading edge, we approximately obtained NLF characteristics at several combinations of angle of attack and unit Reynolds number. The results are summarized in Fig. 16 and 17. Fig. 16 shows chordwise transition location in variation with unit Reynolds number, and Fig. 17 shows ones at various Reynolds number based on local chord length. It is found in Fig. 17 that the NLF characteristics are almost repre-

sented by one curve. This means the NLF characteristics had two dimensionality, and it was originated in warp.

4) Test results for LFC effect[24]

According to the obtained NLF characteristics, we chose 52% semispan as the best position for a wake measurement by a Pitot rake. Sectional drag was calculated by integrating measured total pressure loss shown in Fig. 18. However, our calculated sectional drag was not quantitatively exact, because Pitot rake was set near trailing edge under the limitation of tunnel facility. So we concentrated on the difference in drag at various aerodynamic conditions.

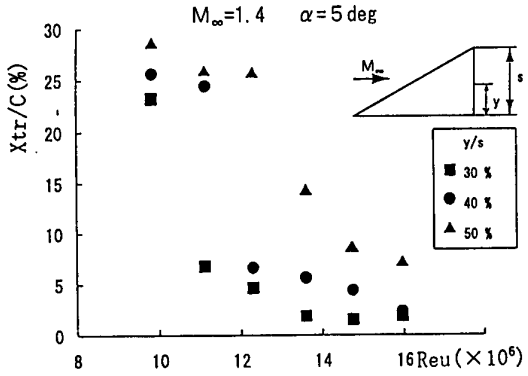


Fig. 16 Transition Location vs. Unit Reynolds Number[23]

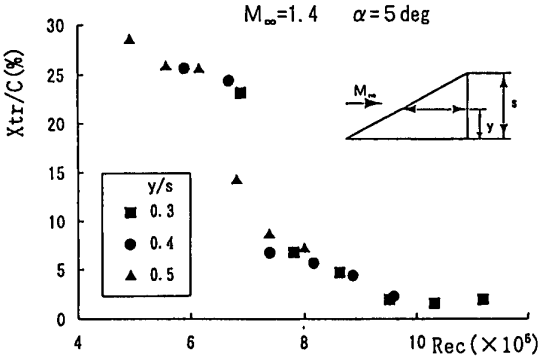


Fig. 17 Transition Location vs. Local Reynolds Number[23]

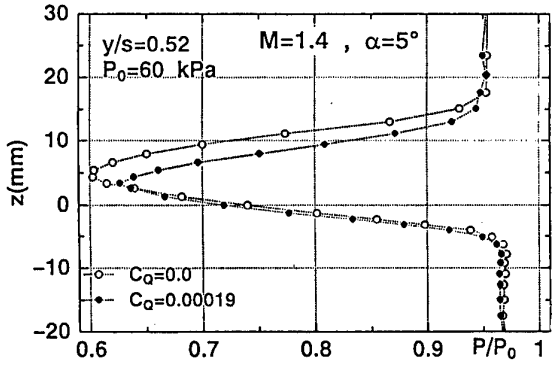


Fig. 18 Total Pressure Distribution in Wake

Fig. 19 shows the effect of LFC. C_Q means nondimensional mass flow by the suction. At Po=60 kPa, namely, relatively low Reynolds number, large drag reduction was depicted. It originated in existing wide laminar region at that condition.

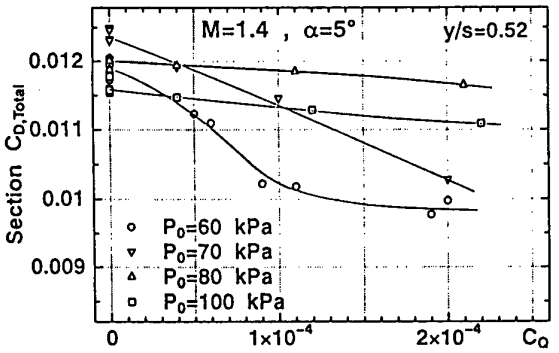


Fig. 19 Drag Reduction Effect vs. C_Q[24]

We could not directly measure the movement of transition position due to the suction. Therefore, there was a simple question whether this result was due to true transition movement or not. We considered it was true according to the following reasons. First, the main features of the boundary layer was not affected by even the maximum suction because C_Q was very small, that is, less than the value usually used in the LFC test.

Second, the behavior of LFC effect with a variation of the unit Reynolds number is summarized in Fig. 20. In this figure, two curves of sectional drag for no suction and maximum suction (C_Q=0.0002) are plotted. In this figure, the drag for no suction increases at relatively low Reynolds number as Reynolds number increases. On the other hand, it decreases at relatively high Reynolds number.

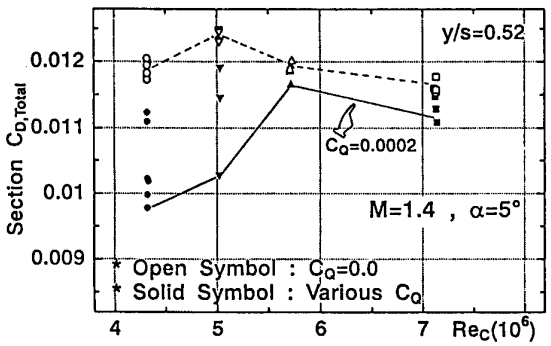


Fig. 20 Drag Reduction Effect vs. Local Reynolds Number[24]

This behavior is roughly explained as follows. In general, there are two factors related to the growth of boundary layer with the variation of Reynolds number. One is a transition movement, another is a growth rate. Transition moves forward as Reynolds number increases, but growth rate becomes small. The forward movement of transition increases the thickness of the wake, but the small growth rate reduces it. So we can understand from Fig. 20 that the factor on transition movement is dominant at relatively low Reynolds number

and the factor on growth rate is dominant at relatively high Reynolds number. Therefore, the drag reduction effect at relatively low Reynolds number reflects the control of transition movement.

3.3 Numerical Study on Transition Prediction Method[25]

Transition prediction is the most difficult problem due to its complex physical mechanism. However, transition prediction methods are strongly desired in the aerodynamic design. Since complete understanding has not been obtained yet, a prediction method based on boundary layer stability theory and some empirical relations is practical. One of such a practical prediction method is a so-called e^N method. This method is validated to be effective and very useful in two dimensional flow condition at low speed.

However, in a three-dimensional compressible flow condition, we feel practical e^N method has not been established yet, because there are some open questions: for example, how to select integral path of amplification rate, how to specify the relation among artificially introduced parameters (complex wave number in spatial theory), and how to understand the influence of higher mode of instability (Mack mode) on transition process. These are important themes of aerodynamic research at present.

On the other hand, in the aerodynamic design of the second generation SST, a transition prediction method, which can roughly and qualitatively estimate transition position, is very practical and useful. As a candidate method, an extension of current e^N method to three dimensional compressible flow is usually considered. Thus we originally tried to develop a transition prediction method based on three-dimensional compressible linear stability theory and the e^N method.

Transition Prediction method consists of two programs: a stability analysis program and a N-value calculation program. The former estimates eigenvalues of instability mode, and the latter calculates the integration of amplification of those eigenvalues.

1) Stability analysis method

We developed a system for calculating the eigenvalues and integrating the amplification rate of small disturbance, based on a three dimensional compressible boundary layer theory.

(1) Formulation

Present formulation is based on the following assumptions:

① simple plane wave disturbances

$$\{u',v',w',p',T',\rho',\mu'\} \equiv q'(x,y,z,t) = \tilde{q}(y)e^{i(\alpha x+\beta z-\omega t)}$$

Here, (x,y,z) are the coordinates in streamwise direction, thickness direction of boundary layer, and spanwise direction. (u,v,w) are the (x,y,z) components of velocity. (p,T,ρ,μ) are a pressure, temperature, density, and viscosity, respectively. And ω is a circular frequency (real) and α, β the components of wave number vector (complex).

② parallel mean flow

$$\{U,V,W,P,T,\rho,\mu\} = \{U(y),0,W(y),1,T(y),\rho(y),\mu(y)\}$$

Then the basic equation can generally be summarized in the following form [26,27].

$$\frac{d\varphi_i}{dy} = \sum_{j=1}^{8} a_{ij}\varphi_j \quad , \quad i = 1,.....8$$

where $\varphi_1 = \alpha\tilde{u} + \beta\tilde{w}$, $\varphi_2 = \frac{d\varphi_1}{dy}$, $\varphi_3 = \tilde{v}$, $\varphi_4 = \tilde{p}$,

$$\varphi_5 = \tilde{T}, \varphi_6 = \frac{d\varphi_5}{dy}, \varphi_7 = \alpha\tilde{w} - \beta\tilde{u}, \varphi_8 = \frac{d\varphi_7}{dy}$$

These quantities are non-dimensionalized by the boundary layer thickness and reference quantities at the edge of boundary layer, and the $a_{i,j}$ is related to the boundary layer profiles of velocity, temperature, etc.. Those details are described in Appendix I of Ref.25.

In general, the boundary condition in linear stability analysis is that all disturbances vanish at the wall and the edge of the boundary layer as follows:

$$\varphi_1 = \varphi_3 = \varphi_5 = \varphi_7 = 0, \ at\ y = 0$$

$$\varphi_1,\ \varphi_3,\ \varphi_5,\ \varphi_7 \rightarrow 0, \ as\ y \rightarrow \infty$$

Here the combination of the homogeneous basic equation above and such boundary condition lead to trivial solutions, except only one case where the matrix composed of the $a_{i,j}$ has an eigenvalue. Therefore, we must solve the so-called eigenvalue problem.

(2) Method of solution

To solve this eigenvalue problem, we adopted a method described in Ref. 27. The details are summarized in Appendix III of Ref. 25 and the main features are as follows:

① Integration from edge to wall by the 4th order Runge-Kutta-Gill method
② Application of analytical solution on the initial values at the edge (see Appendix II of Ref.25)
③ Use of the orthonormalization technique by Gram-Schmidt[28] to remove errors due to numerical integration (see Appendix IV of Ref.25)
④ Iteration by the Newton method with a "pseudo" boundary condition

(3) Validation of present formulation

As a first step, we tried to validate present formulation in two typical cases. One is a case of two-dimensional incompressible viscous flow, another is a case of two dimensional compressible inviscid flow.

The matrix composed of the $a_{i,j}$ is simplified under assumptions of two-dimensionality and incompressibility in the former case and inviscid condition in the latter case. Then it was confirmed that the governing equation completely led to a well-known Orr-Sommerfeld

equation and Mack equation, respectively.

(4) Numerical validation

As a next step, we numerically investigated eigenvalue characteristics in the following typical cases: (i) two-dimensional disturbance on incompressible flat plate boundary layer (Blasius flow[29]), (ii) two-dimensional disturbance on compressible boundary layer[30], (iii) three-dimensional disturbance on compressible flat plate boundary layer[31], and (iv) two-dimensional disturbance on incompressible infinite swept wedge boundary layer (Falkner-Skan-Cooke flow[32]). The detail of these validation studies was described in Ref. 25 and good agreements for all cases were obtained.

Fig. 21 and 22 show typical results for (ii) and (iii) among them. In Fig. 21, the estimated neutral stability curve on flat plate boundary layer at M=3 is indicated on the plane of nondimensional wavenumber ($\alpha_r \delta^*$) and Reynolds number based on displacement thickness (R_{δ^*}). In Fig. 22, the variation of maximum amplification rate $(-\alpha_i)_{max}$ is shown with a variation of mean flow Mach number. And ψ is the angle between the directions of mean flow and propagation of disturbance. As seen in these figures, we obtained good agreement with the results by Arnal[30] and Mack[31].

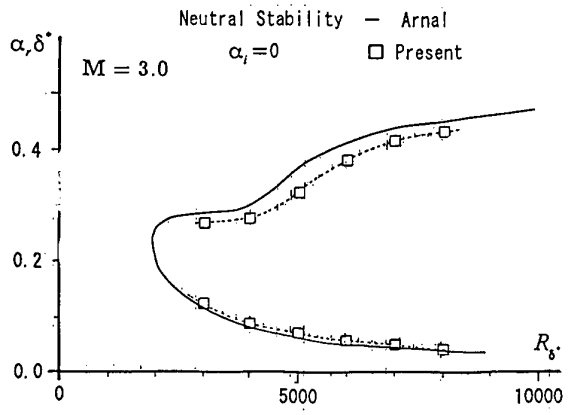


Fig. 21 Comparison of Neutral Curves at Flat Plate Flow[25]

2) Transition prediction method

As mentioned before, there are some problems, such as integral path and auxiliary relation in deriving the formulation of e^N method. We tried to investigate them as follows.

(1) Formulation

(i) Definition of amplitude of disturbance

According to the assumption of small plane wave disturbance, an amplitude A on three dimensional disturbance is defined as follows:

$$\ln\left(\frac{A}{A_0}\right) = \int_C \left(-\alpha_i dx_s - \beta_i dy_s\right) = \int_C d\sigma$$

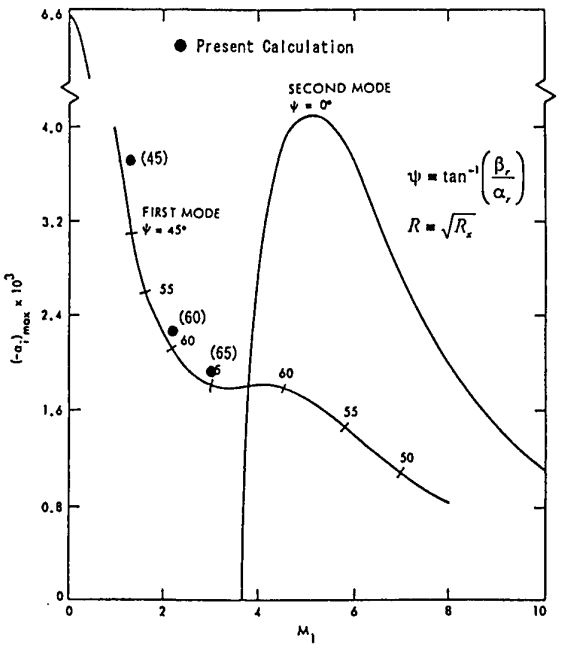


Fig. 22 Comparison of Maximum Amplification Rate at Flat Plate Flow[25]

where A_0 is the amplitude at a neutral point.

In this formulation, for convenience we adopted a so-called streamline coordinate, which was different from one in previous stability formulations. That is, the direction of the streamline at the edge of the boundary layer was indicated by x_s, the direction of crossflow by y_s.

(ii) Assumption for amplification of disturbance

To conduct the integration, it is necessary to specify the integral path. Thus some auxiliary relations between wave number (α_r,β_r) and amplification rate (α_i,β_i) are also necessary. Presently some models are suggested to solve this problem. Through detailed investigation of these models, we decided to adopt the following approach.

According to the assumption of specifying an amplification direction (θ) suggested by Mack, first of all, we can simplify the formulation as follows:

$$\frac{dy_s}{dx_s} = \tan\theta, \quad \beta_i = \alpha_i \tan\bar{\psi}$$

$$\Rightarrow \quad d\sigma = -\alpha_i (1 + \tan\bar{\psi}\tan\theta)\, dx_s$$

Here $\bar{\psi}$ is treated as a parameter.

Then we assume $\theta = 0$, because this assumption simplifies the present method. It is physically reasonable to consider that the most dominant direction is one of the streamline. Thus, we finally obtain the following relation.

$$d\sigma = -\alpha_i dx_s = -\frac{\alpha_i}{\cos\phi_e} dx_c$$

where x_c stands for a coordinate in the chord-

wise direction normal to the leading edge and ϕ_e is a local sweep angle at the edge. Although $\bar{\psi}$ is not explicitly included in this expression, influence of $\bar{\psi}$, namely β_i, is implicitly reflected by $\alpha_i(\psi,\bar{\psi},f,R)$.

Here $\psi \equiv tan^{-1}\left(\frac{\beta_r}{\alpha_r}\right)$, $f=\frac{\omega}{2\pi}$

(iii) Method of estimating N-factor

At present, it is known that there are several methods to estimate the N-factor based on the definition of the amplitude of disturbance above. In our approach, however, the first step is to understand mathematical features of present stability equation, and second step is to find out the best way of estimating N factor.

Therefore we calculated many eigenvalues for $\psi,\bar{\psi},f,R(x_c)$ in the specified parameter space, then estimated the N-factor based on the following Envelop Method[33]

$$N = \max_{\psi}\ \max_{\bar{\psi}}\ \max_{f}\left[\ln\left(\frac{A}{A_0}\right)_{\psi,\bar{\psi},f}\right]$$

$$\ln\left(\frac{A}{A_0}\right)_{\psi,\bar{\psi},f} = \int_C d\sigma = \int_{x_{c0}}^{x_c}\frac{-\alpha_i(x_c;\psi,\bar{\psi},f)}{\cos\phi_e(x_c)}dx_c = \int_{\xi_{c0}}^{\xi_c}\frac{f(x_c;\psi,\bar{\psi},f)}{\cos\phi_e}d\xi$$

$$f(x_c;\psi,\bar{\psi},f)\equiv -\alpha_i(x_c;\psi,\bar{\psi},f)\cdot\delta(x_c)\ ,\ \xi_c\equiv\frac{x_c}{\delta}$$

Here $\max_{\psi}\max_{\bar{\psi}}\max_{f}$ stands for choosing local maximum values for $\psi,\bar{\psi},f$ at every x_c respectively. Therefore N corresponds to an envelop for every curve.

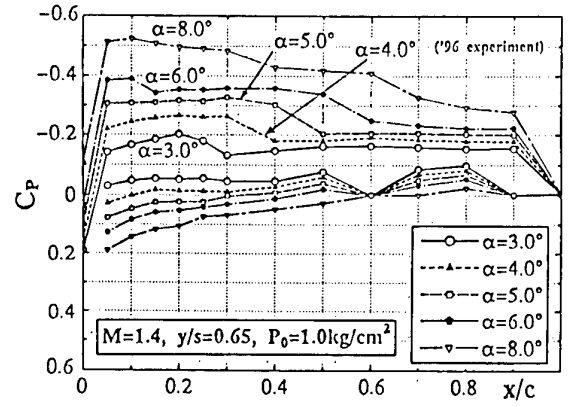
(2) Validation of present e^N method

To validate our e^N method, we investigated transition characteristics in the following two cases: (i) two-dimensional incompressible flat plate flow[33] (Blasius flow) and (ii) three-dimensional incompressible infinite swept flat plate flow with artificially introduced pressure gradient[34] (Falkner-Skan-Cooke flow). The details are described in Ref.25. In both cases, good agreement for the estimated N characteristics was obtained, compared with the results in Ref. 33 and Ref. 34.

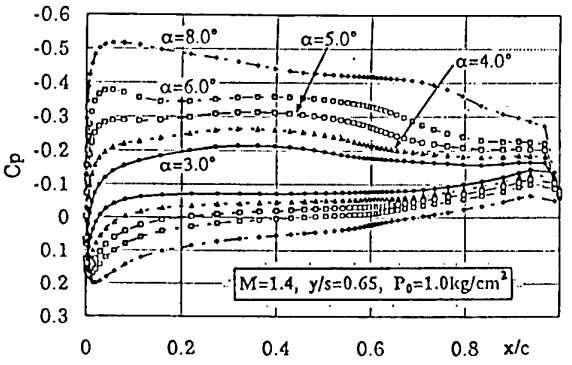
3.4 Numerical Study on Transition Characteristics Based on Test Results

1) Estimation of pressure distribution on test condition

Ogoshi et al[24,35], a co-researcher of the author, performed calculation of pressure distribution using CFD (Euler) solver with unstructured grid system, "UG3 code" which was originally developed by KHI. Fig.23(a) and (b) show measured and calculated pressure distributions respectively. Good agreement was obtained both qualitatively and quantitatively.



(a) Measurements



(b) Calculations by CFD

Fig. 23 Pressure Distributions on the LFC Test Model

Then he investigated an influence of the support block and the warp effect on pressure distribution. Fig. 24 shows the comparison of three pressure distributions of present tunnel model("96 model"), same wing model without the support block("93 model") and same planform without any warp and the block("Flat model"). It was summarized at same total C_L condition, but local C_l was different at each spanwise station.

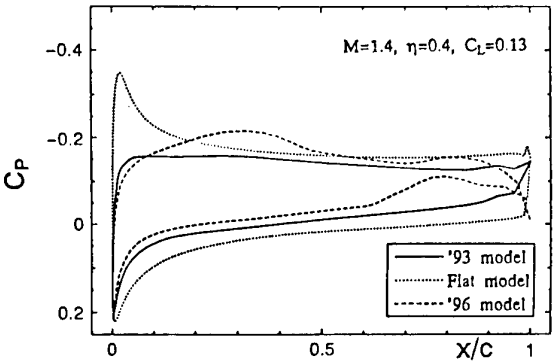


Fig. 24 Comparison of Calculated Pressure Distributions[24]

It was found that the pressure gradient of the "96 model" near the leading edge was relaxed compared with the "93 model" due to an influence of the strong bow shock by the support block, and the pressure distribution of the "93 model" after 10% chord was almost constant. And there was another remarkable influence of the support block at the aft part of the "96 model". It was reduced pressure region due to a strong expansion wave from the end of the support block. However there was little influence at the forward part of mid-span region.

On the other hand , it was confirmed that pressure distribution of the "Flat model" had a strong acceleration and deceleration near the leading edge, like the pressure distribution of a flat plate with a certain incidence in two-dimensional subsonic flow. Therefore, we obtained the result that the warp mainly worked on the suppression of strong acceleration near leading edge.

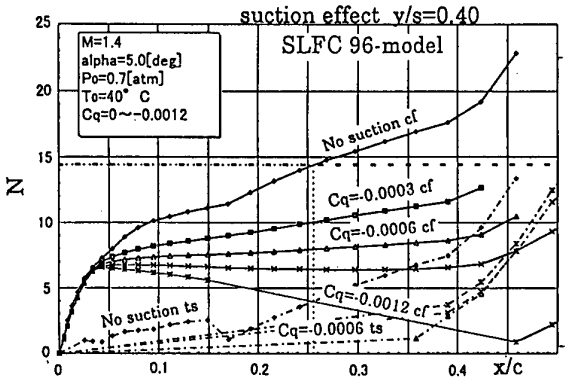
2) Analysis of N characteristics of natural transition

Our transition prediction method is not perfect, because the problem of the best strategy on integration path has not been solved yet. We do not have enough data to estimate the reliable N value corresponding to natural transition (Ntr). In general, it would be difficult to expect an unique and global N value on transition for general three dimensional compressible flow. The best way at present stage is probably to find out the relation of each Ntr value measured at several wind tunnel tests and flight tests.

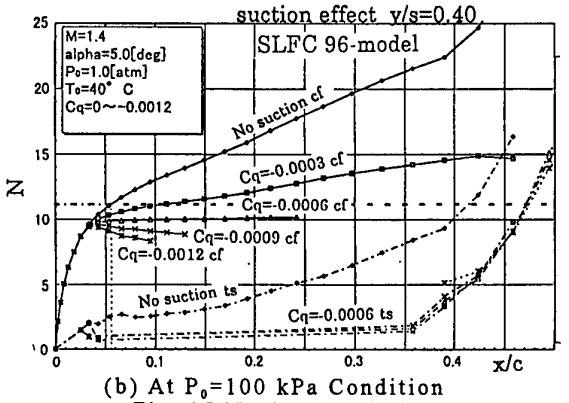
As a first step, Ogoshi and Inagaki[24,35] tried to analyze the N characteristics using so-called SALLY code[36], which is one of the practical transition prediction codes. Its stability analysis is based on incompressible stability theory, although the laminar boundary layer analysis is derived on compressible formulation by Kaups and Cebeci[37]. As our tests were conducted at M=1.4, this approach is generally effective, because remarkable compressibility effect, such as Mack mode appears at a little higher Mach number, for example above M=2.0 in a flat plate flow.

SALLY code estimates two kinds of N curve. One is due to T-S wave instability and another is due to crossflow (C-F) instability. Fig. 25(a) and (b) show both N curves of typical test cases including suction effect. "No suction cf" means N curve corresponding to natural transition due to C-F instability. Since natural transition location in Fig. 25(a) was almost observed near the position of about 25% chord in our visualization test mentioned before, Ntr could be estimated about 14.2.

According to this rule, we summarized Ntr on several test conditions in Fig.26. In this figure, we cannot find out a unique and global Ntr. One of the reasons is an increase of freestream turbulence with the increase of the unit Reynolds number. At y/s=0.5, however, the variation of Ntr is within about 2.5. Here this station was found to have a wider laminar region than other inboard stations in our test. Unless freestream turbulence varies, we would expect this indicates the existence of a unique and global Ntr.



(a) At P_0=70 kPa Condition



(b) At P_0=100 kPa Condition

Fig. 25 N Characteristics

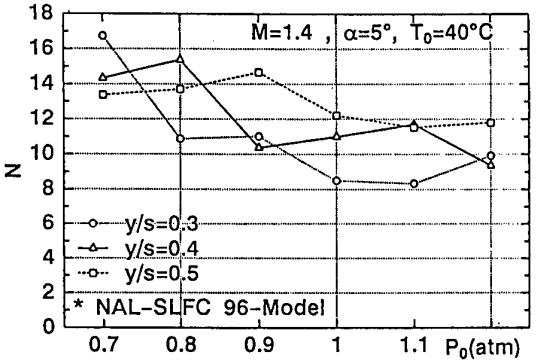


Fig. 26 Estimated Ntr

3) Consideration of supersonic LFC effect[24,35]

Then according to the Ntr summarized in Fig. 26, we analyzed the effect of supersonic LFC on transition location. Fig.25(a) also shows N characteristics at several suction condition. C_q=-0.0003 corresponds to about 150 % of the maximum suction in our test. These calculations do not exactly correspond to test conditions, because uniform suction is assumed in these calculations. The objective of this analysis is to find out whether the drag reduction by LFC in our test was due to the true rearward movement of the transition.

As shown in Fig. 25(a), remarkable rearward movement of transition location is expected, if the same Ntr is applied. Fig. 25(b) shows the results of higher unit Reynolds number than one in Fig. 25(a). In this case, Cq=-0.0003 suction has little effect on transition movement. And this behavior qualitatively corresponds to the test results shown in Fig. 20. Therefore we can understand the sectional drag reduction due to suction is originated in transition movement.

4) Consideration of warp effect and optimum pressure distribution for NLF[24,35]

Fig. 27 shows the N characteristics corresponding to pressure distributions indicated in Fig. 24. It was found that the N due to C-F instability of "Flat model " was the least against our expectation. The main reason is as follows. In general, cross flow is generated in the region with pressure gradient. Since strong pressure gradient exists near leading edge, cross flow is always induced and grows. In spite of strong pressure gradient of "Flat model", the chordwise region where cross flow grows is the narrowest. As a result, the N curve due to C-F instability could not become large.

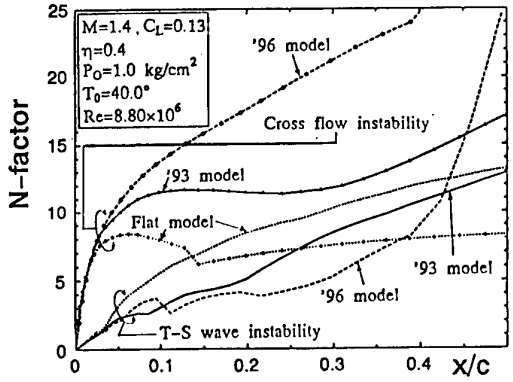


Fig. 27 Comparison of N Characteristics[24]

On the other hand, the N curve due to T-S instability of "Flat model" becomes larger than the other models because of strong adverse pressure gradient after the strong acceleration. If these N curves are compared at higher C_L condition, the N due to C-F instability of "Flat model" should have the largest value because of its strong suction peak. Therefore, the present analysis does not mean "Flat mode" has the best NLF feature and present warp has remarkable benefit in transition characteristics.

Through this analysis, however, the following information was obtained. To suppress the transition based on the C-F instability near the leading edge, pressure distribution with strong acceleration in the very narrow region, such as "Flat model" is favorable. Then, pressure distribution without any adverse gradient, namely, constant one like "93 model" with warp is effective in order to suppress the transition due to the T-S instability from mid-chord to rear region. Combining these characteristics, it is expected that the pressure distribution with a shape of so-called "step function" is very effective in achieving NLF.

Ogoshi[38] proposed a concrete pressure distribution based on this consideration. Then we applied it to the aerodynamic design of NAL's scaled supersonic experimental airplane, as a target pressure distribution on the upper surface. These details are written in another lecture note by the author.

3.5 Further Works

There are numerous studies to complete our transition prediction method and to develop an optimum aerodynamic design procedure including effective supersonic LFC. Thus, we are studying some of them as follows.

1) Relation of freestream turbulence and Ntr in our tunnel

It is important to obtain relation between freestream turbulence and Ntr in NAL's transonic tunnel. Using our prediction method, we analyzed N characteristics of a simple sharp cone with apex angle of 10 degrees ("AEDC 10 degrees cone"), because there is a large amount of transition data obtained in several wind tunnel tests and flight tests.

Fig. 28 shows calculated N characteristics at condition of M=1.2 and Re,unit=9 million, using similar solution of axisymmetrical compressible laminar boundary layer. By comparing it with our tunnel tests, it was found the N values on transition onset at M=1.2 was nearly 10.

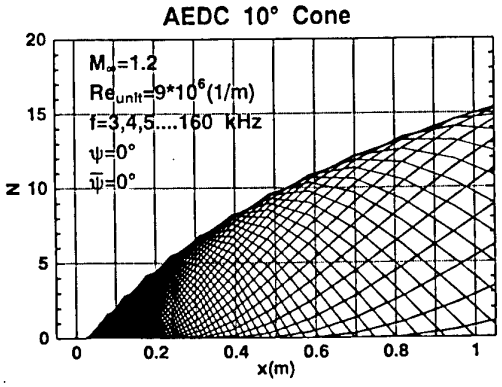


Fig. 28 N Characteristics of AEDC 10 degrees Cone at M=1.2

To obtain the relation between freestream turbulence and Ntr in our tunnel, such consideration must be conducted, for example, for the cases of several Mach numbers and Reynolds numbers on the AEDC 10 degrees cone, and for the cases of other simple configurations.

2) Consideration on natural transition of present tests using our prediction method

We tried to investigate N characteristics of the present test model in order to understand the relation among integral path, an auxiliary condition of parameters artificially introduced, and amplification rates of disturbance.

In this calculation, we used the same profile data of laminar boundary layer in the previous study by SALLY code.

The results are as follows. Since there are some parameters such as f, ψ and $\bar{\psi}$ in our method, the influence of these parameters on the amplification rate of disturbance should be investigated in detail.

(1) Influence of $\bar{\psi}$
First we investigated the influence of $\bar{\psi}$. In general, we supposed that the transition phenomenon of our model was mainly dominated by cross flow instability because of its highly swept leading edge. We paid attention to the condition of $\psi = 70^\circ$ as a representative case. Fig. 29 shows a calculated non-dimensional amplification rate $-\alpha_i \delta^*$ in variation of $\bar{\psi}$. Even though the difference in variation of $\bar{\psi}$ was very small, we found that the amplification rate had the maximum value at the condition of $\bar{\psi} = 0^\circ$

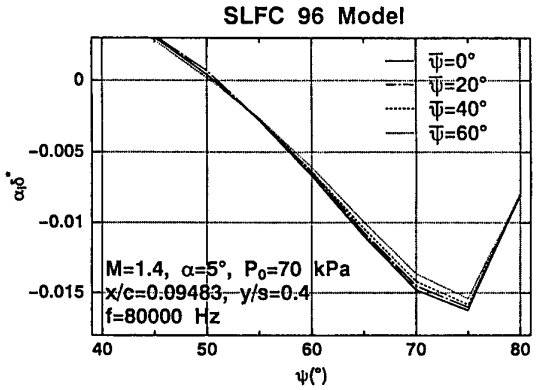


Fig. 29 Effect of $\bar{\psi}$ on Amplification Rate

(2) Influence of ψ
Next we investigated the influence of ψ at the condition of $\bar{\psi} = 0^\circ$. And we ascertained that the amplification rate at $\psi > 0^\circ$ was larger than that at $\psi < 0^\circ$. This is easy to understand considering the relation between the sweep angle and the direction of cross flow. Therefore the condition of $0^\circ < \psi < 90^\circ$ is enough for the present analysis.

Fig. 30 shows calculated eigenvalues with several ψ angles and frequencies. It was found that maximum amplification rate was obtained at $\psi = 70^\circ$. This is qualitatively understandable, because this calculation corresponds to disturbance near leading edge.

(3) Calculation of neutral curve
Fig. 31 shows neutral curves at several ψ angles in variation with Reynolds number based on the displacement thickness. Here the ordinate indicates a nondimensional streamwise component of wavenumber vector. This shape is apparently different from the neutral curve in Blasius flow, namely, wider unstable region at higher Reynolds number.

(4) Estimation of N-factor
Based on the calculated amplification rate, we estimated the N characteristics shown in Fig. 32. Comparing it with the test result, we can find the Ntr is nearly equal to 3.5. This value is about a quarter of previous Ntr value, 14 computed by SALLY code. The fact that Ntr based on compressible formulation is smaller than incompressible one is qualitatively valid, but this quantitative difference is larger than our expectation. Since this means there are some problems in our prediction method, more detailed study is necessary.

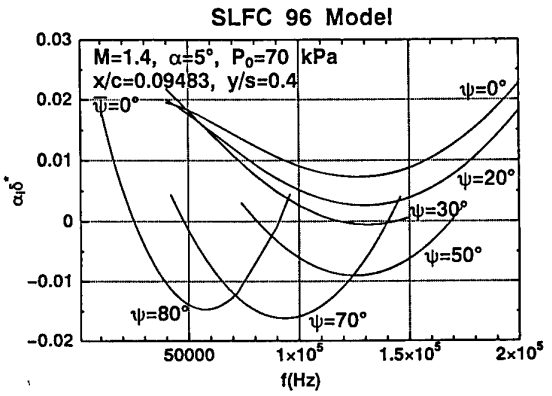


Fig. 30 Effect of ψ on Amplification Rate

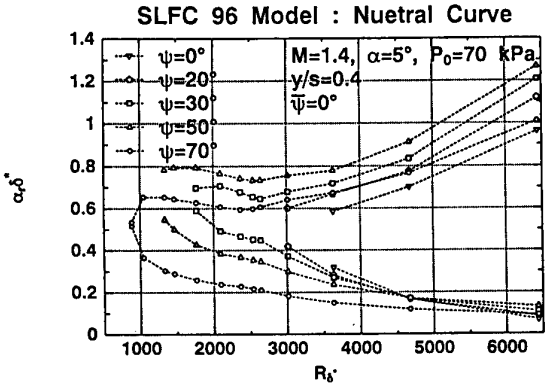


Fig. 31 Compressible Neutral Stability Curve of our LFC Test Model

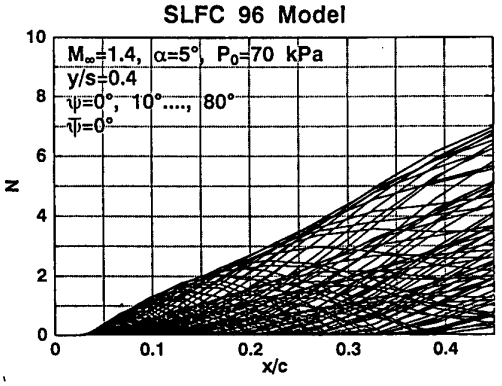
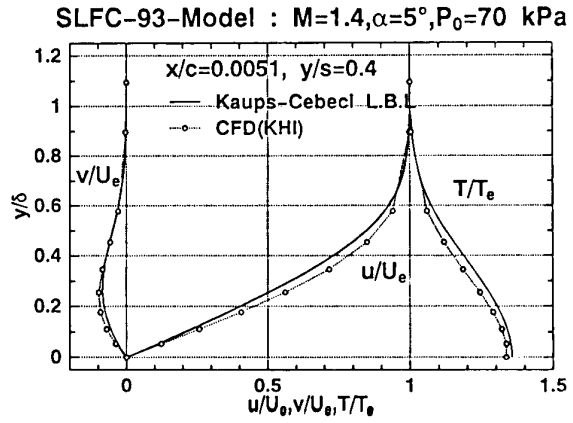


Fig. 32 Compressible N Characteristics

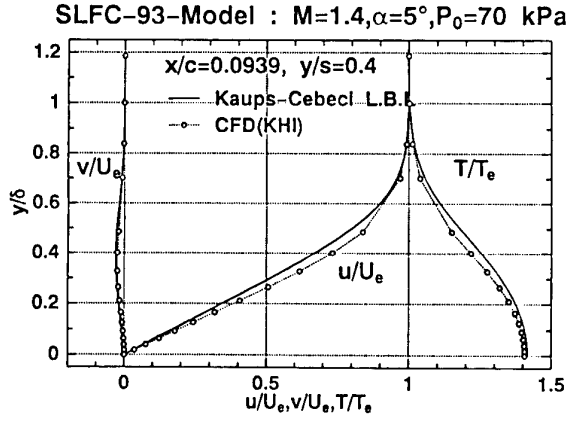
3) New transition prediction system
In our transition prediction system, laminar boundary layer was mainly calculated by the Kaups-Cebeci method. Although their method is very effective for high aspect ratio wings,

it has some errors in a flow field with strong three-dimensionality. In order to develop more precise prediction system, it is effective to use laminar boundary layer profiles computed by a Navier-Stokes code.

As a first trial, Ogoshi calculated them using KHI's CFD(Navier-Stokes) code. Fig.33(a) and (b) show streamwise velocity (u), cross-flow velocity (v) and temperature (T) profiles compared with ones by Kaups-Cebeci method. The differences in u, T profiles mainly originated in the selection of the height of boundary layer edge. On the other hand, the difference in v profile is expected to be based on physical property such as streamline curvature. As shown in Fig. 33 (a), there was a slight but important difference near the leading edge. However there was little difference at about 10% chord station shown in Fig. 33(b). So we expect high precision of stability solution near the leading edge. As a next step, we are planning to analyze the stability characteristics using those profiles and our method.



(a) Near Leading Edge



(b) At x/c=0.0939

Fig. 33 Laminar Boundary Layer Profiles

4) Wind tunnel test plan

Present consideration is not complete, because our tunnel test has some factors influencing transition, such as freestream turbulence, wall slot, wall boundary layer, and so on. Therefore numerous wind tunnel tests should be carried out using several models of which the transition position is well known.

As a first step, we have a plan of an improved test with the LFC test model using a reflector plate at root section to exclude the influence of the support block.

4. RESEARCH ON LOW SONIC BOOM DESIGN

4.1 Background, Objective and Approach

1) Background

(1) Low boom concept

The concept of boom minimization is based on suppressing coalescence of several shock waves generated by aircraft in supersonic flight. Such suppression generally requires strong bow shock at the nose, because it leads to less and weaker secondary shocks which reduce nonlinearity. To realize this situation, the cross-sectional area distribution of the aircraft must be carefully determined. This is provided by boom minimization method based on the works by Seebass-George[39] and Darden[40].

In sonic boom theory, so-called Whitham "F-function" plays a major role[41]. It is related to an "equivalent" cross-sectional area distribution which consists of area due to volume and lift. And pressure perturbations are proportional to the F-function. In 1969, Seebass and George found that minimum boom was produced by the F-function with the Dirac's delta function at nose. It means an equivalent area distribution should be infinite gradient at nose. Therefore, main feature of low boom configuration is characterized by the blunt nose. And it has strong bow shock and higher drag than a conventional supersonic aircraft. It is called "low-boom high-drag paradox[42]".

In 1977, Darden modified the Seebass & George method which was developed for an isothermal atmosphere. She considered the effect of the real atmosphere and improved the drag penalty due to the relaxation of nose bluntness[40]. She assumed the F-function with triangle roof shape in place of Dirac's delta function at nose. The width of the triangle roof shape, y_f controls the nose bluntness. In her tradeoff studies between drag and boom levels, it was found that there was an optimum value of y_f.

(2) Present problems[43]

However, there are some problems which should be solved to apply their low boom theory to SST design. They are summarized as follows:

(i) How we should solve the "low-boom high-drag paradox".

(ii) Since low boom theory only determines an equivalent area distribution, a fuselage geometry are not specified uniquely. It is not easy to design a fuselage geometry with a specified volume.

(iii) Their low boom theory is limited to the typical low boom waveform, namely, "flat-top" type and "peaky" or "ramp"

type. It can not treat arbitrary low boom waveform, such as "hybrid" type proposed recently.

(iv) In general, lift distribution, namely load distribution on wing surface has large contribution on sonic boom strength, because lift effect is integrated from the apex to the end of lifting surface. That is, it becomes maximum value at the end of lifting surface, and this maximum value is kept to the end of fuselage. Their low boom theory gives an equivalent area distribution with monotonous increase in order to reduce shock strength at aft-position. Therefore, slender wing with broader lengthwise lift distribution is very effective for low boom configuration. However, such a wing has large drag penalty in trim.

(v) At present, there is no criteria on acceptability of sonic boom from the stand point of human response. In the first stage of sonic boom study by NASA, about a half of boom strength by Concorde, that is 1.0 lb/ft^2(psf), was chosen as a target level for designing a low boom configuration. Recently the level has been reduced, furthermore. Since the effectiveness of low boom design concept is based on the target, the criterion is very important. A number of researches on human response such as using a boom simulator mentioned in Chapter 2 , are necessary.

(vi) If the target level for low boom is extremely severe, the possibility of supersonic overland cruise even by the low boom configuration is completely discarded. In such a situation, an unique solution is operational limitation. It requires precise estimation of so-called "boom corridor" by propagation analysis program. Presently its precision is not fairly high. Furthermore it can not accurately predict the rise time which is another important parameter on human response as stated in Chapter 2.

2) Objectives

Our study is one of trials to solve these problems from (i) to (iv), because (v) and (vi) are not pure aerodynamic design theme. Our objectives are as follows:

(A) To understand low boom design concept, and including to confirm the effect of it numerically and experimentally.

(B) Second, to develop an original design procedure for a low boom configuration, including to improve previous low boom theory and to find a solution to problems above.

3) Approach

Our approach consists of two steps:

In the first step, we conducted fundamental investigation of present low boom configuration numerically and experimentally. We developed a design procedure and program based on the combination of Darden's theory and our aerodynamic design concept. Then we investigated several characteristics of low boom configuration numerically, using supersonic linear theory and CFD(Euler) analysis. And finally we conducted wind tunnel tests to confirm the effect of low boom concept and validity of our design procedure.

In the second step, we tried to improve present low boom design procedure through some numerical and experimental investigations of the problems above.

As for the target level of boom strength, from the viewpoint of our objectives, the previous criterion by NASA, namely 1.0 psf was assumed as the first approximation. And after the advance of our study, more severe criterion will be considered.

This study by the author was conducted at Gifu Technical Institute of KHI in collaboration with Ogoshi and Yamakage et al. under the support by SJAC.

4.2 Fundamental Study on Low Boom Design[44,45,46,47]

1) Numerical study on design procedure and low boom characteristics

(1) Design procedure

In our study, first of all, we developed a low boom configuration design procedure and tools based on Darden's method, except estimating the effect of real atmosphere. This effect was treated according to the work done by Kawamura-Makino[48], because they derived a convenient analytical formulation.

Our design procedure demonstrated in Fig. 34 is based on the fact that boom minimization theory only produces an equivalent area distribution (Ae). Here Ae consists of area due to volume (Aw: wing, A_B: fuselage and Av: vertical tail) and lift (B). This fact means there is arbitrariness in designing wing, fuselage and tails, namely, infinite combinations among them are possible. We expect a possibility of designing an optimum configuration under this nonuniqueness.

Outline of our design process is as follows: First, from the standpoint of reducing drag, wing geometry is determined using usual supersonic lift-dependent drag reduction concepts[49,50], namely, application of suitable planform and warped wing. Then, from the viewpoint of reducing sonic boom, fuselage geometry is determined by boom minimization method under the assumption of axisymmetricity of fuselage.

The main feature of our design procedure is to replace the application of the area-rule concept with the low boom constraint, in designing an cross-sectional area distribution of the fuselage. Therefore, if an optimum wing geometry is designed with reduced lift-dependent drag under the low boom constraint, namely, broader lengthwise lift distribution, drag penalty is expected to be one due to the volume wave drag only. This means minimum drag penalty. However, it is generally difficult to design such an optimum wing, because planform suitable for low drag condition is

different from one for low boom condition. Therefore, a trade-off study between low boom and low drag is necessary.

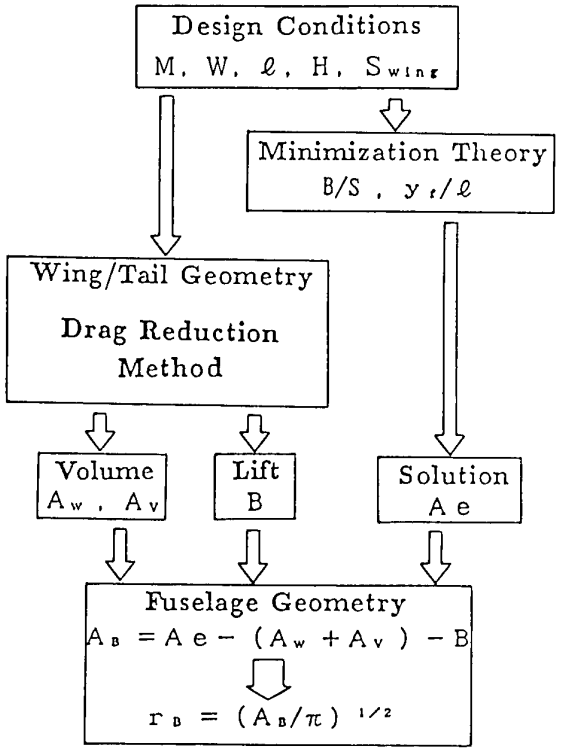


Fig. 34 Design Procedure of Low Boom Configuration Design[45]

(2) Nose bluntness parameter

One of such trade-off studies is to investigate an optimum nose bluntness parameter introduced by Darden. Although she had studied it, we originally analyzed it using our design procedure as a first step. In the study, we assumed "flat-top" type (demonstrated in Fig.37 later) for simplicity, as a typical low boom waveform. This waveform has a constant peak pressure, namely overpressure during the forward part.

Fig. 35 shows the numerical result[45]. The ordinate indicates the ratio of L/D and overpressure to the configuration with a blunt nose, the abscissa shows the nose bluntness parameter, y_f/l. For example, y_f/l = 0.0 means the blunt nose and the bluntness is relaxed as y_f/l increases. It is found that when y_f/l increases, the strength of overpressure increases linearly, but L/D varies nonlinearly. That is, L/D increases rapidly until y_f/l increases from 0.0 to about 0.07 and gradually above 0.07. Therefore, there is an optimum value of y_f/l between low boom and low drag approach, as indicated by Darden. Finally, y_f/l = 0.05 was chosen as a conclusion of the tradeoff study.

(3) Design Mach number

In the previous study by Boeing, M=1.7 was selected as the design Mach number of low boom configuration, in spite of M=2.4 for their conventional baseline configuration[51]. In order to understand this situation, we investigated the effect of design Mach number.

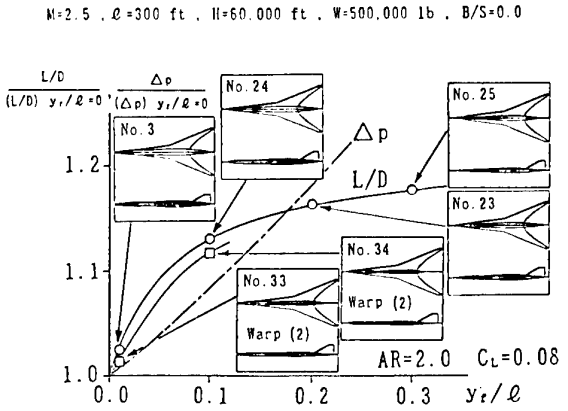


Fig. 35 Effect of Relaxed Nose Bluntness[45]

Fig. 36 shows the obtained result[46]. The ordinate indicates overpressure including the assumed target level indicated by dashed line, and the abscissa shows weight. According to the figure, it is supposed that the reason for the Boeing's choice is based on the following fact. The critical weight which satisfies the condition of overpressure below the target level, 1.0 *lb/ft²* (psf) is heavier at lower Mach number. This fact leads to some advantages for designing a real SST. Therefore, in designing an optimum configuration, it is also necessary to consider the variation of design Mach number.

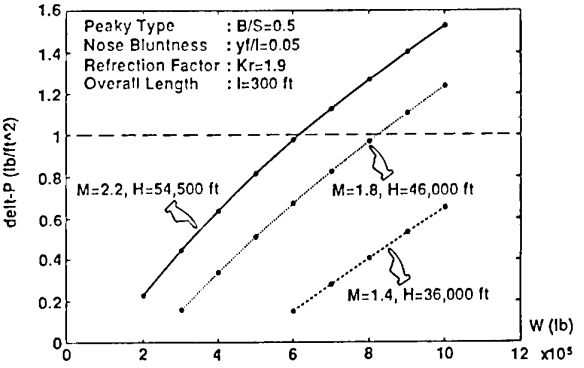


Fig. 36 Effect of Design Mach Number[46]

2) Wind Tunnel Tests on Validation of our numerical Study[46]

To confirm our numerical study, we conducted wind tunnel tests using originally designed low boom and low drag models shown in Fig. 37. The test Mach number was 1.4. This selection was due to the limitation of KHI's transonic tunnel facility we could use during this study. However if our design procedure would be validated at this Mach number, we could expect to use it at other Mach number, because sonic boom theory is fundamentally based on linear theory.

We designed six kinds of tunnel models shown in Fig. 38. The three models are wing-body type, namely, "low boom" configuration with blunt nose (No. 2), "low boom and low drag" configuration with relaxed blunt nose deter-

mined by the optimum bluntness parameter (No. 3) and "low drag" configuration (No. 1) designed as a comparison. And other models are axisymmetrical configurations which have exact equivalent area distributions by low boom theory, namely, No. 5 and No. 6 correspond to No. 2 and No.3 respectively. And as a comparison, No. 4 is a cone cylinder with a half apex angle of 10 degrees and same cross-sectional area as a sting support. Fig. 39 schematically shows radius distribution of them.

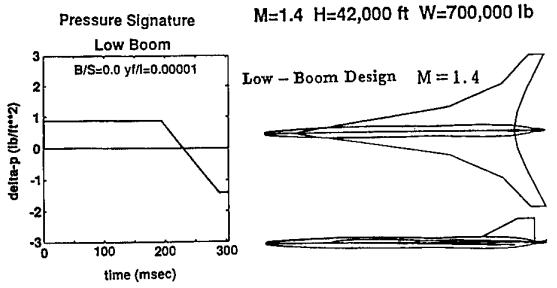


Fig. 37 Designed Low Boom Configuration[46]

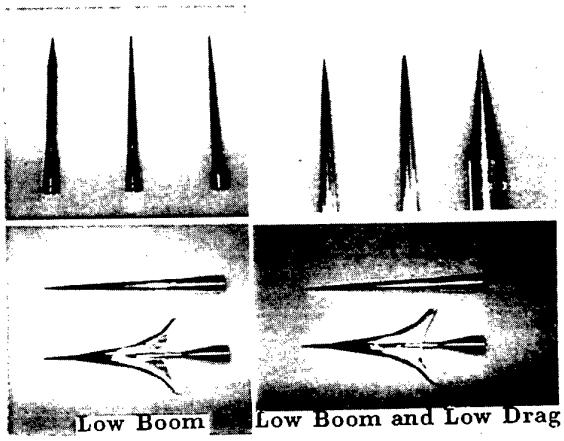


Fig. 38 Wind Tunnel Test Models[46]

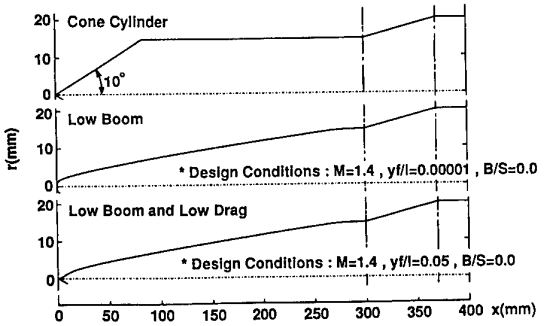


Fig. 39 Axisymmetrical Models with Exact Low Boom Solution[46]

In the wind tunnel tests, we measured a pressure distribution under those models by traversing a probe with one tiny hole on the surface from 167 % length upstream to downstream. Fig. 40 shows the test equipment.

○ **Test Equipment**

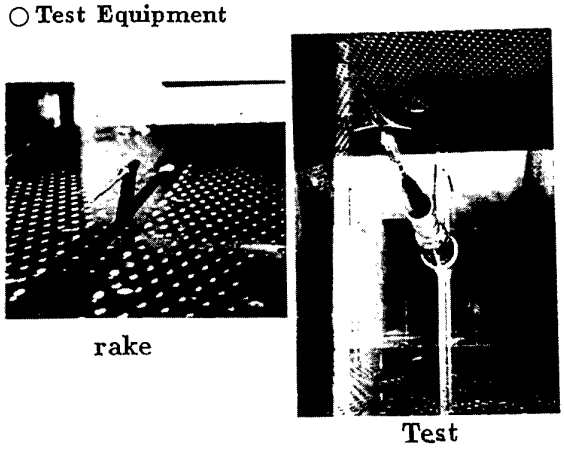
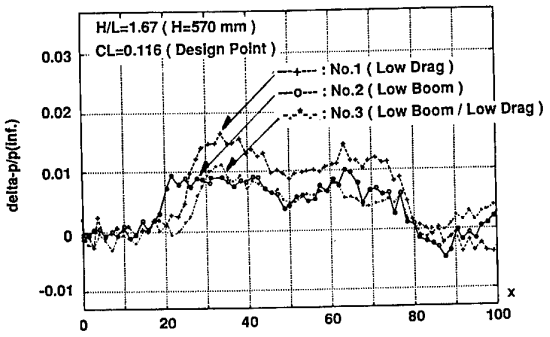
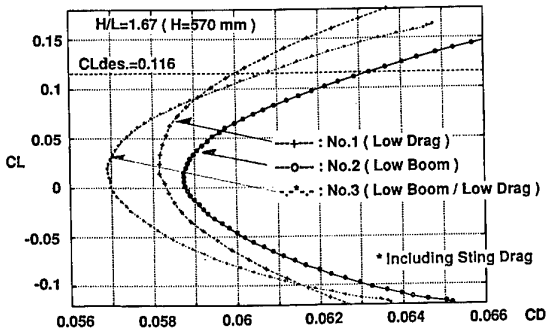


Fig. 40 Test Equipment[46]

The results of wing-body type are summarized in Fig. 41. Fig. 41(a) shows pressure signatures of forward part. The models were located on the height of 167 % body length above the probe. It was found that pressure rises of No. 2 and No. 3 were lower than that of No. 1, and it was confirmed that the signatures were roughly "flat-top" shape. However, some large fluctuation of pressure were also observed. They probably came from the nonaxisymmetric feature due to a short propagation distance.



(a) Measured Pressure Signatures



(b) Measured Drag Polar Curve

Fig. 41 Wind Tunnel Test Results[46]

Fig. 41(b) shows the polar curves. It was found that the drag of No. 1 was the smallest and the drag of No. 2 was the largest at design C_L=0.116. And the drag of No. 3 was reduced compared with No. 2, but it was lager than No. 1. Therefore it was confirmed that our "low boom and low drag" configuration (No. 3)

could reduce the drag of "low boom" configuration (No. 2) without large increase in overpressure.

As stated above, measured pressure signatures correspond to the signatures in near field. And for wing-body type, we could not realize axisymmetrical state which was the basis of low boom theory. Therefore, in order to validate Darden's theory, we conducted another test for axisymmetrical models.

Fig. 42 shows measured pressure signatures of forward part of No. 5 and No. 6, compared with the solution of low boom theory (indicated as "Design") and CFD (Euler) results mentioned later. It was observed that pressure signatures of both low boom configurations were qualitatively the "flat-top" shape except at nose , and the averaged values of the overpressure agreed with low boom theory and CFD results. The difference at nose was due to the short propagation distance in test condition. Therefore, we thought Darden's theory was validated in the test.

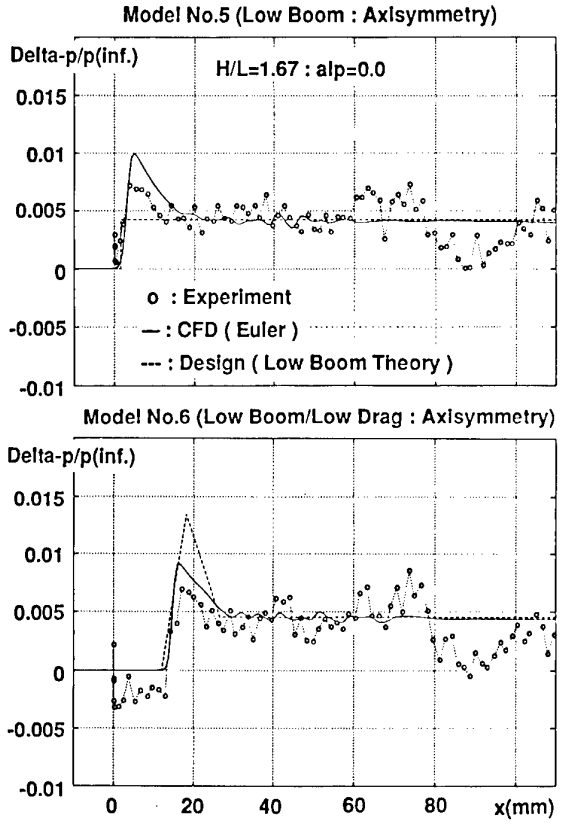


Fig.42 Comparison of Tests and CFD Results for Axisymmetrical Models[46]

However, a great number of small pressure fluctuations were also observed. Presently we have considered that the main reason was the influence of weak shock generated at a great number of holes on the tunnel wall surface due to transonic tunnel. In order to conduct more precise measurement, this situation must be improved, for example, using NAL's supersonic tunnel.

3) CFD Analysis of low boom configuration[46]

Since sonic boom theory is usually based on modified supersonic linear theory, it is impossible to estimate the characteristics of boom signature precisely in the flow field with strong nonlinearity, for example, the flow near the body or at high Mach number. On the other hand, CFD analysis is very useful to investigate such flow field.

We tried to apply KHI's CFD (Euler) code to our low boom configuration study. First we validated our Euler code from the viewpoint of sonic boom research, using simple configurations. They were axisymmetrical bodies with analytical solutions such as a parabolic body and Sears-Haack body. And we found good agreements[46,47].

Next we calculated pressure signatures of the same axisymmetrical tunnel models. In the calculations, we used special solution adaptive grids with the height of 20 times as long as the fuselage length (300 mm in Fig. 39).

Fig. 42 shows the calculated pressure signatures compared with the theoretical solution and test results. There was almost good agreement among CFD, theory and test at the averaged value. And near the nose, CFD results showed better agreement with test results, rather than theory. This is understandable considering its nonlinearity.

4.3 Research Activities on Several Problems of Low Boom Design[43,44,52]

In our fundamental study, the design procedure for low boom configurations with low drag characteristics was validated by wind tunnel tests and CFD analysis. However it is difficult to design an optimized low boom configuration, because our design procedure is so preliminary that it can not include several constraints, for example, fuselage volume, trim, structure and airframe/engine interference. Moreover it is necessary to optimize the low boom effect and to improve the L/D characteristics of low boom configurations. As stated in "Background" , there are some problems which we should solve.

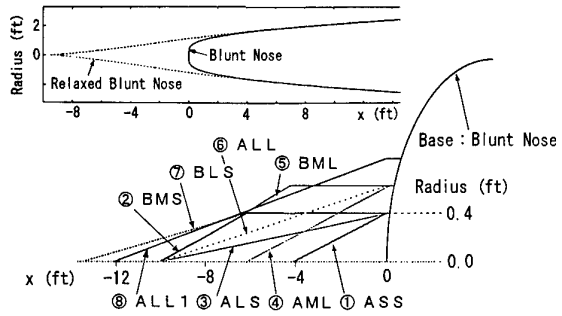
As the next step of our study, we tried to investigate them numerically and experimentally. And the following results were obtained.

1) L/D improvement devices[44]

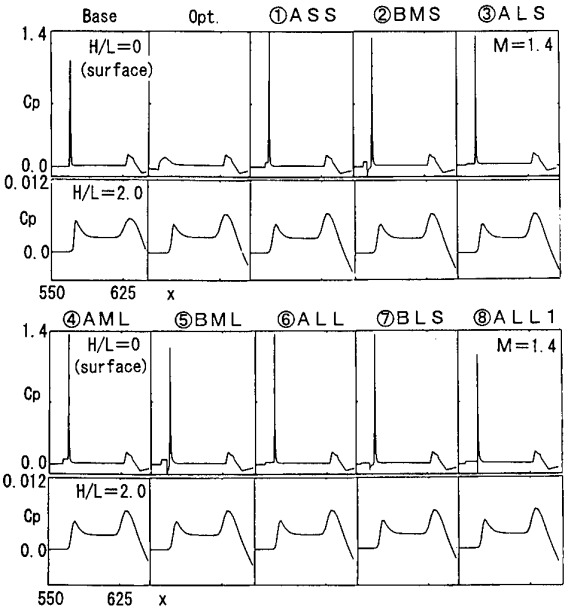
The key point of reducing wave drag of low boom configuration is to reduce strong bow shock at nose, keeping the effect of low boom characteristics at far filed. Darden's relaxed blunt nose is one of the excellent solutions. As another way, we considered the effect of spike such as a needle added on the blunt nose.

In general, a tiny and pointed spike generates weak oblique shock at nose and reduces strong bow shock at the rest part of the blunt nose. Therefore, drag due to bow shock is expected

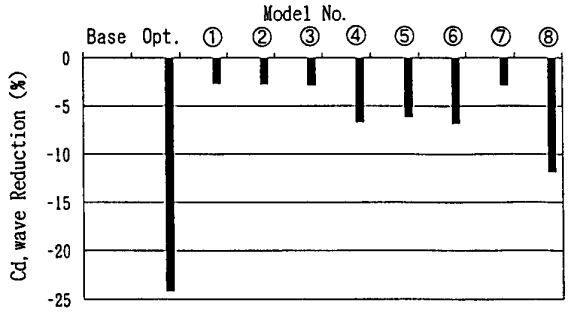
to be reduced. And it is supposed that the oblique shock is so weak that pressure signatures at far field are hardly changed. In application to real SST, movable spike is considered to be very effective.



(a) Spike Geometries



(b) Predicted Pressure Signatures



(c) Drag Reduction Effect

Fig. 43 Numerical Study on Spike Effect[44]

To verify this idea, we investigated the effect of several spikes shown in Fig. 43(a) using KHI's CFD (Euler) code. Fig. 43(b) shows the pressure distributions on the surface and at a certain propagation distance, r/L=2 in these cases (L: the reference length). In the figure, "Base" and "Opt" mean the blunt nose of low boom configuration (corresponding to No. 5 in our test model) and the relaxed blunt nose by Darden's theory (No.6), respectively. Although there was remarkable difference on the surface pressure distributions among them, there was little difference in propagated pressure distributions.

The drag reduction effect is summarized in Fig.43(c). As shown in this figure, we could confirm the drag reduction for all spikes. Therefore, such a tiny spike is surely effective in reducing wave drag due to front bow shock, and keeping low boom characteristics at far field.

However, we found that the Darden's relaxed blunt nose had the highest effectiveness in reducing drag. Therefore, our idea must be improved furthermore.

2) Consideration of Fuselage Volume[44]

In our design procedure, fuselage geometry is determined at final step. Therefore its volume does not generally satisfy a requirement for fuselage volume. To improve this situation, we must change wing geometry.

As a preliminary study to improve our design procedure, we investigated the relation between some parameters of wing geometry and fuselage volume of low boom configurations. Fig. 44 shows the relation among wing area (S_{ref}), maximum chordwise length of wing (l_w), semispan (s) and fuselage volume. From this figure, smaller l_w leads to larger fuselage volume and smaller S_{ref} at the condition of constant s, for example 81.24. Therefore, if the fuselage volume of a designed low boom configuration is smaller than the required value, re-design of the wing with smaller l_w is expected to be one of the most effective improvements. Naturally any iterative process is necessary through the trade-off analysis between low boom and low drag.

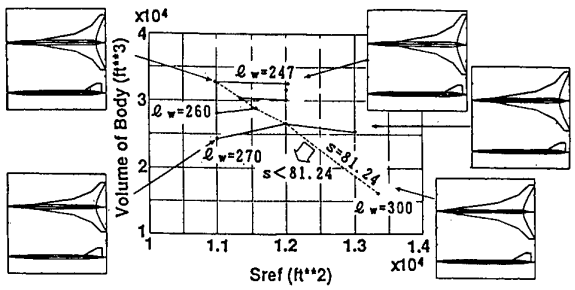


Fig. 44 Relation between Wing Geometry and Fuselage Volume[44]

3) New formulation based on arbitrary low boom waveform[44,52]

In treating an arbitrary low boom waveform, Darden's analytical formulation is not effective. Therefore we developed a following new formulation.

First of all, the outline of F-function shape corresponding to an arbitrary low boom waveform is assumed. However, in order to find the shape at front part, Darden's formulation is used. That is, the discrete value of F-function is specified except from x=0 (nose) to $x=y_f$ (introduced by Darden). In the rearward re-

gion from x=l (fuselage length), the F-function shape is automatically determined by the following mathematically compatible condition.

$$F(y) = -\frac{1}{\pi\sqrt{y-l}}\int_0^l \frac{\sqrt{l-x}}{y-x} F(x)dx \ , \ l \le y$$

Next, a corrected F-function is calculated, using the following relation which reflects nonlinearity of shock wave.

$$y_t = y - k\sqrt{r}F(y) \ , \ k \equiv \frac{(\gamma+1)M_\infty{}^4}{\sqrt{2\beta^3}}$$

Here this relation was derived at isothermal atmospheric condition. General expression for real atmospheric condition was summarized in Ref.53. Then a low boom waveform is estimated, using so-called "equivalent area condition[54]".

If peak pressure or overpressure of this estimated waveform is different from the target low boom waveform, the value of F-function is changed by multiplying a certain constant. This constant is predicted by the difference between the estimated waveform and the target. And if there is the difference between the estimated waveform and the target, such calculations must be continued until convergence.

Finally after convergence, the equivalent area distribution of desired low boom configuration is calculated by the following relation which is derived from the definition of F-function.

$$Ae(x) = 4\int_0^x F(y)\sqrt{x-y}\,dy$$

Fig. 45 shows one of examples. This target low boom waveform is a so-called "hybrid" type which was proposed by Boeing[55]. The estimated F-function was confirmed to have good agreement with Boeing's F-function. Therefore the low boom configuration with arbitrary target low boom waveform is designed through the calculated equivalent area distribution.

4) Consideration of trim problem[44,52]

As stated above, the "trim" problem is based on the fact that very slender and special planform is required for the low boom design. This means lift distribution must exist until the end of fuselage in order to satisfy the low boom condition completely. One solution is to move the wing forward. That is, it relaxes the reduction of overpressure at rearward position. This enables to apply a conventional planform which does not usually satisfy the lift condition at the end of fuselage.

To realize this situation, we improved present design procedure as follows: First, we design a warped wing with a conventional planform, from the viewpoint of reducing lift-dependent drag. Then we determine the streamwise position of wing, considering the trim condition.

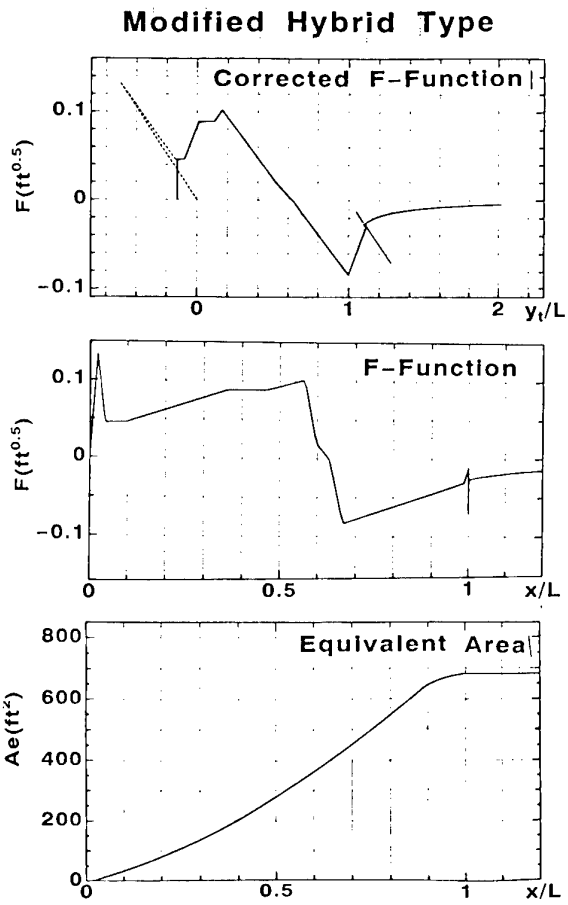


Fig. 45 Estimated Equivalent Area Distribution for Modified Hybrid Waveform[44,52]

Second, we assume that the length from nose to the rearward position of wing is a virtual length of low boom configuration. Then at the rearward position of the wing, we also assume that a virtual equivalent area increment corresponds to the increase of total weight. This area increment gives no negative volume in the region from the end of wing to the end of fuselage. According to the present design procedure with these assumptions, we can design a low boom configuration which has at least reduced overpressure at front part.

In this procedure, the increment of equivalent area and the shape of fuselage after the end of wing are parameters. In general, they must be optimized under the constraints of reducing overpressure at rearward position, its drag and trim penalty.

Fig. 46 shows one of results. This wing was designed at M=2.2 using low drag concepts, and then low boom configuration was designed at M=1.4. "Ramp" type low boom waveform shown in Fig.47 was used and parabolic shape of fuselage after the end of the wing was assumed.

From the estimated drag characteristics, the decrease in L/D of this low boom configuration was suppressed to about 0.3, comparing with a low drag configuration with the same

wing geometry shown in Fig. 47. Thus the trim problem is fairly improved. However, estimated rearward overpressure at ground increased as shown in Fig. 47. This is mainly based on the rear fuselage shape. That is, present parabolic shape is not effective. Therefore it is necessary to find an optimum shape as a further work.

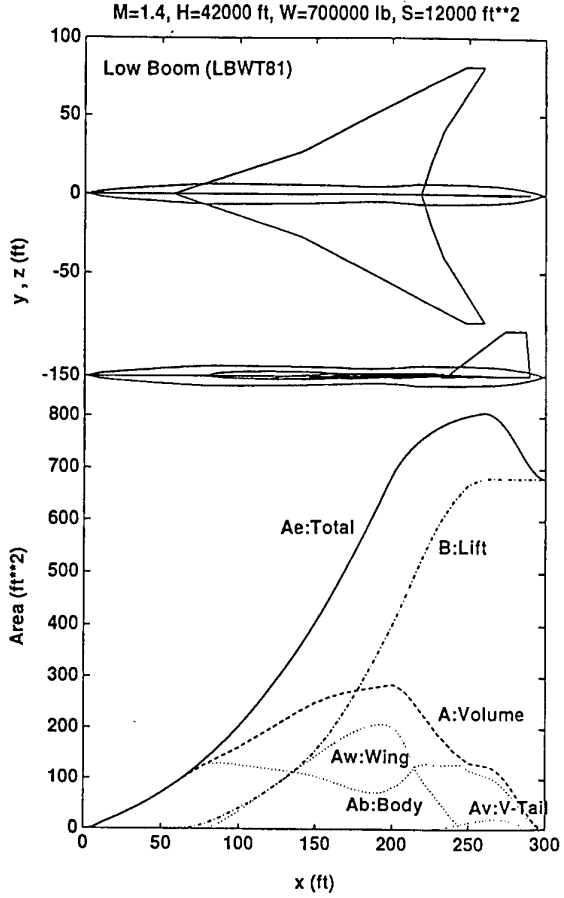


Fig. 46 A New Designed Low Boom Configuration[44,52]

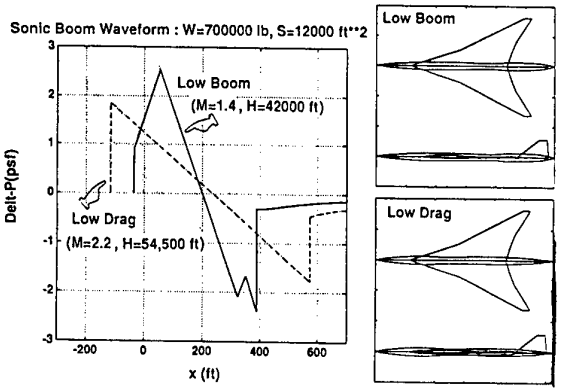


Fig. 47 Estimated Pressure Signatures at Ground[44]

4.4 Further Works

As mentioned above, our trial to present problems on low boom design study is incomplete. Therefore, first one of further works is to continue our present study. Then advanced study for the (v) and (vi) in "Present problems" is necessary. Furthermore, we think the following nonlinear CFD design study is more important.

In our low boom design study, CFD analysis is confirmed to be very effective. As mentioned above, our design procedure is based on a modified linear theory by Whitham and Darden. We think this theory is effective to understand fundamental features of low boom configuration qualitatively. To optimize a low boom configuration, however, we should apply CFD analysis to the design.

As introduced in Chapter 2, recently Makino has succeeded in optimizing the low boom configuration (shown in Fig.37) designed by our procedure. He showed the difference in equivalent area distribution of his configuration and the solution by Darden's theory. And he pointed out this was due to the nonaxisymmetric feature of the wing, nonlinearity of shocks at the kink of leading edge and trailing edge, and three-dimensionality of shock propagation. Thus he tried to improve the equivalent area distribution using an optimum design algorithm. Finally he designed an optimum configuration with an exact solution of equivalent area distribution. (See Fig. 11)

Furthermore he estimated the propagation of low boom waveform and confirmed the "flat-top" waveform was achieved at ground by the optimum low boom configuration. (See Fig. 12) As his design procedure is very effective, wind tunnel test for validation is expected.

5. CONCLUDING REMARKS

A number of aerodynamic research activities on a second generation SST is conducting in Japan. They covers supersonic drag reduction concepts, airframe/nacelle integration, intake design, supersonic LFC, low boom design, HLD, and optimum CFD design. Their state of arts were summarized. Selectively details on supersonic LFC and low boom configuration design, in which the author has mainly conducted, were described. First objective of those studies is to understand current technologies and to develop a certain design procedure and tools. Second is to confirm the characteristics and their effects through original CFD analysis and experimental tests. Then third is to research important problems which are presently unsolved, and to find some new ideas or concepts.

In the supersonic LFC study, a transition prediction system based on the current e^N method and original test data on natural transition was developed. The LFC effect was also confirmed through the wind tunnel test using the originally designed warped wing model.

In the low boom configuration design study, a design procedure based on Darden's boom minimization method and drag reduction technologies was developed, then validated by wind tunnel test and CFD analysis. CFD was also applied to solve the present problems on low boom configuration design and to obtain some improvements.

ACKNOWLEDGMENTS
Most of the author's studies were supported by the in-house research program of Kawasaki Heavy Industries, Ltd., and the joint research program with NAL and NAL's supersonic research program. Some of them were conducted under the SJAC. The author would like to thank MHI, KHI, FHI for information about their activities.

REFERENCES

1. Yoshida, K. and Hayama, K., "Experimental and Numerical Study of Aerodynamic Characteristics for Second Generation SST", SAE Tech. Paper Series 912056, pp. 695– 707, 1991.
2. Yoshida, K. and Ogoshi, H., "Study on Aerodynamic Configuration of an SST", Kawasaki Technical Report No. 126, 1995 (in Japanese)
3. Yamazaki, T. and Uchida, T., "CFD analysis of the aerodynamic characteristics of SST", 7th European Aerospace Conference, The Supersonic Transport of Second Generation, Toulouse, France, pp.125-130, October, 1994.
4. Suzuki, W., Fujimoto, A. and Takasu, T., "Aerodynamic Design of SJAC Phase-II SST Configuration", 1st International CFD Workshop on Supersonic Transport Design, Tokyo, Japan, March 16-17, 1998.
5. Takami, H. and Kawashima, E., "Aerodynamic Characteristics of a Next Generation High-Speed Civil Transport", AIAA 92-4229, AIAA Aircraft Design Systems Meeting, Hilton Head, SC, August 24-26, 1992.
6. Kaiden, T., Shibata, M. and Iwamiya T., "Numerical Simulation with Bleed and Bypass Effects of Nacelles on SST", 1st International CFD Workshop on Supersonic Transport Design, Tokyo, Japan, March 16-17,1998.
7. Higaki, K., "Numerical and Wind Tunnel Test Study on the Nacelle Integration for NAL's Experimental Airplane", 1st International CFD Workshop on Supersonic Transport Design, Tokyo, Japan, March 16-17,1998.
8. Fujimoto, A., Niwa, N. and Sawada, K., "Numerical Investigation of Supersonic Inlet with Realistic Bleed and Bypass Systems", Journal of Propulsion and Power, Vol. 8, No. 4, July – August, pp.857-861, 1992.
9. Fujimoto, A. and Niwa, N., "Experimental and Numerical Investigation of Mach 2.5 Supersonic Mixed Compression Inlet", AIAA 93-0289, 31st Aerospace Sciences Meeting & Exhibit, Reno, NV, January 11-14, 1993.
10. Fujiwara, H. & Sakata, K., "Numerical simulation of the internal flow through the Mach 2 air-intake designed for NAL's experimental airplane", 1st International CFD Workshop on Supersonic Transport Design, Tokyo, Japan, March 1998.
11. Yoshida, S. and Tani, Y., "An Experimental and Numerical Study on Supersonic Laminar Flow Control", AIAA 93-3960, AIAA Aircraft Design, Systems and Operations Meeting, Monterey, CA, August 11-13, 1993.
12. Ishida, Y., Noguchi, M., Sato, M. and Kanda, H., "Numerical and Experimental Study of Drag Characteristics of HLFC Airfoils in High Subsonic, High Reynolds Number Flows", SAE Tech. Paper Series 930034, pp.243-253, 1993
13. Tokuyama, A., Sakai, K. and Taya, H., "Experimental Study of Sonic Boom Acceptance", AIAA 93-3961, 1993.
14. Sakai, K., Yoshida, K., Yamamoto, A. and Ogoshi, H., "Research of Sonic Boom Evaluation Method and Boom Minimizing Technique for Next Generation Supersonic Transport", Kawasaki Technical Report, No. 134, pp.46-51, 1997 (in Japanese)
15. Makino, Y, Sugiura, T., Kaido, A., Watanuki, T., Kubota, H. and Aoyama, T., "The Effect of the Body Configuration on the Sonic-Boom Intensity", AIAA Paper 96-2466 CP, The 14th AIAA Applied Aerodynamics Conference, 1996.
16. Makino, Y., Watanuki, T., Kubota, H., Aoyama, T. and Iwamiya, T., "Low-Boom Design Method by Numerical Optimization", AIAA Paper 98-2246, 4th AIAA/CEAS Aeroacoust. Conference, Toulouse, France, June 1998.
17. Uchida, T., Sato, K., Kawashima, E. and Takami, H., "Longitudinal Aerodynamic Characteristics of a Supersonic Transport of Second Generation", 7th European Aerospace Conference, The Supersonic Transport of Second Generation, Toulouse, France, October, pp.169-177, 1994.
18. Rinoie, K., Fujita, T., Iwasaki, A. and Fujieda, H., "Behaviors of Leading-Edge Separation Vortex Formed on a Delta Wing Vortex Flaps", Proc. of the 20th Congress of the International Council of the Aeronautical Sciences (ICAS), pp.2252-2259, Sorrento, Napoli, Italy, 8-13 September, 1996.
19. Jeong, S., Matsushima, K., Iwamiya, T., Obayashi, S. and Nakahashi, K., "Inverse Design Method for Wings of Supersonic Transport", AIAA Paper 98-0602, 36th Aerospace Sciences Meeting & Exhibit, Reno, NV, January 12-15, 1998.
20. Matsushima, K., Iwamiya, T., Jeong, S. and Obayashi, S., "Aerodynamic Wing Design for NAL's SST Using Iterative Inverse Approach", 1st International CFD Workshop on Supersonic Transport Design, Tokyo, Japan, March 16-17, 1998.
21. Yoshino, N., Nakahashi, K. and Obayashi, S., "Aerodynamic Optimization of Supersonic Wings Using GA and Unstructured Grid" 11th Computational Fluid Dynamics Symposium, pp.431-432, 1997 (in Japanese).
22. Carlson, H. W. and Middleton, W. D., "A Numerical Method for the Design of Camber Surface of Supersonic Wings with Arbitrary Planform", NASA TN D-2341, 1964.
23. Noguchi, M., Yoshida, K., Ogoshi, H., Komatsu, Y. and Ishida, Y., "Transition Measurement using Liquid Crystal on a Three-dimensional SST wing Model at Supersonic Speed", J. of the Visualization

Society of Japan, Vol. 17, Suppl. No. 1 pp.225-228, 1997 (in Japanese).
24. Ishida, Y., Yoshida, K., Noguchi, M., Ogoshi, H. and Inagaki, K., "Supersonic Laminar Flow Control on a Warped Delta Wing", Proc. of the 29th Fluid Dynamics Conference, pp.73-76, 1997 (in Japanese).
25. Yoshida, K., Ogoshi, H., Ishida, Y. and Noguchi, M., "Numerical Study on Transition Prediction Method and Experimental Study on Effect of Supersonic Laminar Flow Control", Special Publication of National Aerospace Laboratory SP-31, pp. 59-79, May 1996.
26. Mack, L.M., "Boundary-Layer Linear Stability Theory", Special Course on Stability and Transition of Laminar Flow, AGARD Rep. No.709, 3-1～81, 1984.
27. El-Hady, N.M., "Nonparallel Stability of Three-Dimensional Compressible Boundary Layers, Part I - Stability Analysis", NASA CR-3245, 1980.
28. Tatsumi and Gotoh, "Stability Theory of Flow", Sangyou Tosyo, 1976.
29. Schlichting, H., "Boundary-Layer Theory", Seventh Edition, McGraw-Hill Inc.
30. Arnal, D., "Stability and Transition of Two-Dimensional Laminar Boundary Layers in Compressible Flow over An Adiabatic Wall", La Recherche Aerospatiale No.1988-4.
31. Mack, L.M., "Linear Stability Theory and the Problem of Supersonic Boundary-Layer Transition", AIAA J. Vol.13, No.3, pp.278-289, 1975.
32. Rosenhead, L., "Laminar Boundary Layer", Dover Publications Inc., 1961.
33. Arnal, D., "Boundary layer transition: prediction based on linear theory", AGARD FDP/VKI Special Course on Progress in Transition Modeling, AGARD Report 793, 1993.
34. Meyer, F. and Kleiser, L., "Numerical Investigation of Transition in 3D Boundary Layers", AGARD-CP-438, 16-1, 1989.
35. Ogoshi, H., Inagaki, K., Yoshida, K., Noguchi, M. and Ishida, Y., "Study for Supersonic Laminar Flow Control on a Warped Delta Wing", Proc. of the Aerospace Computational Simulation Technology Symposium '98, 1998 (in Japanese).
36. Srokowski, A.J., "Mass Flow Requirements for LFC Wing Design", AIAA Paper 77-1222, AIAA Aircraft Systems & Technology Meeting, Seattle, Washington, August 22-24, 1977.
37. Cebeci, T., Kaups, K. and Ramsey, J.A., NASA CR-2777.
38. Ogoshi, H., "Aerodynamic design of a Supersonic aircraft wing – Application of the Natural Laminar Flow concept to Airfoil", Proc. of the 47th Nat. Cong. of Theoretical & Applied Mechanics, pp. 341-2, 1998 (in Japanese).
39. Seebass, R. and George, A.R., "Sonic Boom Minimization", J. of Acoust. Soc. of Am., Vol. 51, pp. 686-694, 1972.
40. Darden, C. M., "Sonic Boom Theory—Its Status in Prediction and Minimization", J. Aircraft, Vol.14, pp. 569-576, 1977.
41. Carlson, H. W. and Maglieri, D. J., "Review of Sonic Boom Generation Theory and Prediction Methods", J. Acoust. Soc. Am., Vol.51, pp. 675-685, 1972.
42. Brown, J. G. and Haglund, G. T., "Sonic Boom Loudness Study and Airplane Configuration Development", AIAA 88-4467, 1988.
43. Yoshida, K. and Yamamoto, A., "Study for Low Sonic Boom Technology on an SST", Proc. of the 34th Aircraft Symposium, November 1995. (in Japanese)
44. Kawasaki Heavy Industries, Ltd., "Study on Low Boom Technology", the Soc. of Japanese Aerospace Companies (SJAC) Special Report No. 0702 (Kakushin-Koukuki Gizyutu-Kaihatsu Center), 1996 (in Japanese)
45. Yoshida, K. and Tokuyama, A., "Improving the Lift to Drag Characteristics of Low Boom Configuration", AIAA 92-4218, 1992.
46. Yoshida, K., "Experimental and Numerical Study for Aerodynamics of Low Boom Configuration", AIAA 94-0052, 1994.
47. Yoshida, K., Yamamoto, A., Futatsudera, N. and Hagiwara, S., "Study on Aerodynamic Characteristics of Low Boom SCT", 7th European Aerospace Conference, The Supersonic Transport of second Generation, Toulouse, France, pp. 227-245, October 1994.
48. Kawamura, R. and Makino, M., "The Effect of Atmospheric Nonuniformity on Sonic Boom Intensities", Univ. of Tokyo, ISAS Rept. No.416, 1967.
49. Yoshida, K., "Fundamental Study on Aerodynamic Configuration of Second Generation SST --- Two Examples Based on KHI Aerodynamic Research", J. of the Japan Soc. for Aeronaut. and Space Sci., Vol. 42, No. 486, pp. 403-415, July 1994 (in Japanese).
50. Yoshida, K. and Hayama, K., "Experimental and Numerical Study of Aerodynamic Characteristics for Second Generation SST", SAE-912056, 1991.
51. Boeing Commercial Airplanes, "High-Speed Civil Transport Study", NASA CR-4233, 1989.
52. Yoshida, K., "Low Sonic Boom Configuration of an SST", Journal of Japan Society of Fluid Mechanics, Vol.16, No.6, pp.484-489, 1997 (in Japanese).
53. Kawasaki Heavy Industries, Ltd., "Study on Low boom / Low Drag Configuration", the Soc. of Japanese Aerospace Companies (SJAC) Special Report No. 0203 (Kakushin-Koukuki Gizyutu-Kaihatsu Center), 1991 (in Japanese)
54. Middleton, W. D. and Carlson, H. W., "A Numerical Method for Calculating Near-Field Sonic Boom Pressure Signatures", NASA TN D-3082, 1965.
55. Haglund, G. T., "HSCT Designs for Reduced Sonic Boom", AIAA 91-3103, 1991.

THE AERODYNAMICS OF THE FUTURE SUPERSONIC TRANSPORT AIRCRAFT : RESEARCH ACTIVITIES AT ONERA

J.J. THIBERT

Office National d'Etudes et de Recherches Aérospatiales
29, Avenue Division Leclerc
BP 72 Châtillon Cedex, France

SUMMARY

The paper gives an overview of the ONERA activities concerning the aerodynamics of the future supersonic transport aircraft.

In a first part detailed comparisons between CFD and wind tunnel data are presented and discussed.

The second part adresses the problem of the drag prediction in cruise flight conditions from wind tunnel data. Skin friction coefficients values measured in flight are compared to the results of boundary layer computations.

The third part is devoted to wing designs with numerical optimisation techniques. Several examples are presented and discussed.

Results concerning riblets and laminar flow control are given in a fourth part which also presents experiments carried out for attachment line contamination investigation. A quiet supersonic tunnel for basic research on supersonic laminar flows is also presented.

The last part of the paper deals with activities on air intakes aerodynamics. After a brief recall of supersonic air intakes operational modes and a description of the Concorde air intake, comparisons between CFD and wind tunnel data on a generic 2D intake are presented. Basic experiments on intake internal flow are described and the problem of the internal shock control is addressed. Examples of the use of CFD for auxiliary air intakes design are given.

1. INTRODUCTION

ONERA has been involved for several years in close cooperation with Aerospatiale and SNECMA in research concerning the future supersonic transport aircraft (SCT). This research programme which is supported by the French governmental agencies (DGAC, SPAé) aims at the development of tools, methodologies, and technologies to be used for this new aircraft. ONERA activities concern propulsion, structures, material, environment, noise and aerodynamics.

ONERA is also participating in the EUROSUP project supported by the European Commission.

This paper give an overview of the ONERA activities in the aerodynamic field carried out in the framework of the national and of the European programmes.

These activities have been oriented towards CFD code assessment for performance prediction and in particular for the drag, the development of numerical optimisation tools for multipoint designs, drag reduction technology investigations and air intake aerodynamics.

Predesign studies carried out by the European manufacturers indicate that this new aircraft will probably have the main characteristics shown in **figure 1**. The weight breakdown for a typical range of 5 500 nm given in **figure 2** shows that the payload represents about 8 % of the gross weight while it is about 20 % for a subsonic long range aircraft.

* PASSENGERS : 250 * (3 classes)
* RANGE : • 5500 nm. (at entry into service)
  • 6500 nm. (later version at higher T.O. weight)
* CRUISE SPEED : • SUPERSONIC : MACH 2.05
  • SUBSONIC : M = 0.95
* CRUISE ALTITUDE : 50 000 < Z < 65 000 ft
* ENVIRONMENT : • POLLUTION : minimum NO_x injection near ozone layer to be defined
  • NOISE : FAR 36, stage 3 regulation around airports
  • SONIC BOOM : no supersonic flight over inhabited area

FIGURE 1 - Future SCT Aircraft - Main characteristics

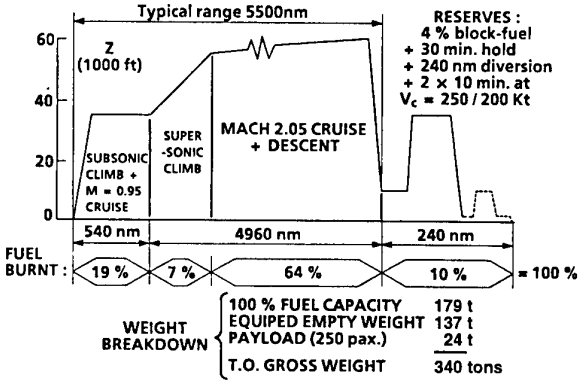


FIGURE 2 - Weight breakdown for a 5 500 nm trip

Paper presented at the RTO AVT Course on "Fluid Dynamics Research on Supersonic Aircraft", held in Rhode-Saint-Genèse, Belgium, 25-29 May 1998, and published in RTO EN-4.

The fuel part in the D.O.C. will probably be around 35 % while it is only 27 % for a subsonic aircraft. The relatively low payload and the high part of the fuel in the D.O.C. make this aircraft very sensitive to the aerodynamic performances. Compared to Concorde this aircraft will be bigger as shown in **figure 3** with about a double span and an aspect ratio around 2. The wing planform is chosen to provide high L/D at supersonic and transonic speeds and the expected gains compared to Concorde are about 40 %. Thus the drag is the key issue for this aircraft. This is why the aerodynamic research activities at ONERA have been oriented to this main topic.

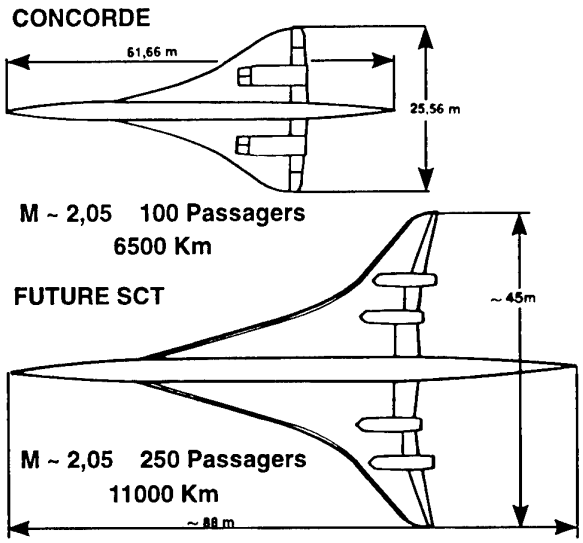


FIGURE 3 - Concorde and future SCT aircraft size comparison

2. PERFORMANCE PREDICTION

The aerodynamics of Concorde was based on approximate theoretical methods and intensive wind tunnel tests. CFD will play a much larger role for the next SCT aircraft since Navier Stokes, Euler codes and boundary layer codes are in principle able to predict the performances for all the flight conditions. However these tools have to be carefully assessed in order to determine their accuracy.

ONERA has developed these last years 2 main finite volume Euler/Navier Stokes codes, one for transonic and low supersonic speed flows (CANARI code) based on a centred scheme, the second one for supersonic and hypersonic flows (FLU3M code) based on an upwind scheme. The last one will be described later in the paper. The first solver [1] uses multidomaine structured grids with potential overlapping. Time integration is the explicit multistage Runge Kutta, accelerated by the Lerat-Sides implicit method [2].

Dissipative terms are the blended 2nd and 4th differences of Jameson and al [3]. Boundary conditions are based on the characteristic relations and various turbulence models are available.

This code has been used to compute the Aerospatiale ASTF configuration (wing + fuselage + fairings + fin) which was tested in the ONERA S2MA transonic + supersonic wind tunnel. (**figure 4**)

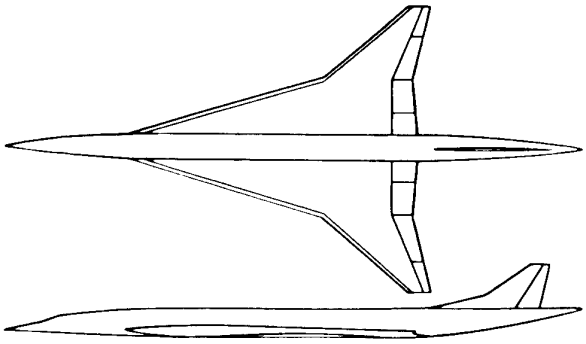


FIGURE 4 - ATSF Configuration
- General arrangement

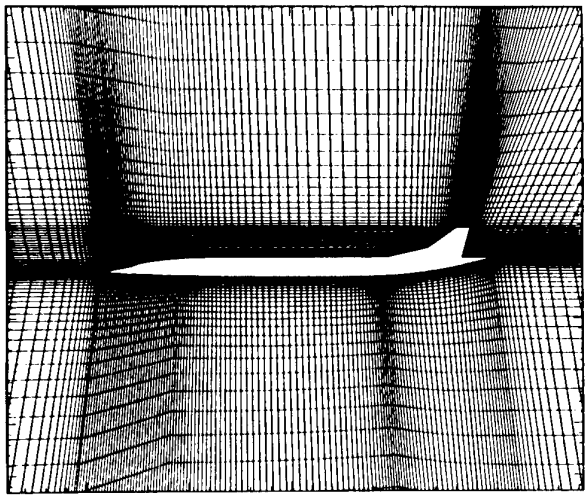


FIGURE 5 - ATSF Configuration
- Computational grid

Computations have been carried out on a grid of 1.2 million mesh points generated with the ICEM-CFD system (figure 5).

The topology is simple with 5 sub-blocks, of which 4 are H-H type, all extending from upstream to downstream infinity.

The Euler option (inviscid flow) was used and boundary layer computations were done without coupling with the 3C3D code [4] developed at ONERA-CERT. In this method Prandtl equations are integrated along the local streamlines, which are sub-characteristics lines. The discretization of the equations is done in the plane tangent to the surface of the aircraft, using a coordinate system which respects the metric properties of the fuselage to express the velocity derivatives. This is done by orthogonally projecting the body fitted coordinate system and the velocity field in the tangent plane at the considered points. Then, the integration of the boundary layer equations could be performed using their local cartesian form, even in areas where the mesh is not regular. Several turbulence models are implemented in the code. For the computations presented in this paper a mixing length formulation with the wall damping function of the Cebeci model has been used.

Euler computations were done for Mach =2.,0.95, 0.25 at two angles of attack per Mach number. Severe convergence criteria were set for the decrease of residuals (4 orders of magnitude) and lift coefficient oscillation (10^{-4}), resulting in computations of about 500 iterations in supersonic flow, 10 000 in transonic flow, and 1 300 in subsonic flow. Boundary layer computations were not done for the subsonic test-cases, as the flow separated on the upper surface of the wing. For the transonic computations transition was enforced at the location of the boundary layer trip used on the model. In supersonic flow, boundary layer computations were done with free transition like on the wind tunnel model.

2.1 Supersonic cruise Mach number

Figure 6 presents the comparisons at Mach 2. The lift is slightly over-predicted by the Euler computations (**figure 6a**) and the pictching moment is a little bit too much nose down (**figure 6c**) but the differences are small and consistent with what can be expected in inviscid flow. The computed pressure + friction drag is lower by about 5 counts than the experimental drag. This difference is about the same for the two lift levels which means that the drag increment due to the lift is correctly predicted (**figure 6b**).

Figure 6d presents the comparison of the pressure distributions for the two computed lift levels. The agreement is very good on the upper surface while on the lower surface of the inboard section small deviations appear near the trailing edge which can be due to small differences in the geometry between the model and the computation. The iso Cp contours plotted in **figure 6e** on the upper surface for the cruise lift level are also in very good agreement. The low pressure areas coming from the inboard leading edge and spreading over the outboard wing are less well defined for the experimental data due to an insufficient number of pressure measurement points.

FIGURE 6 - Performance prediction at Mach 2

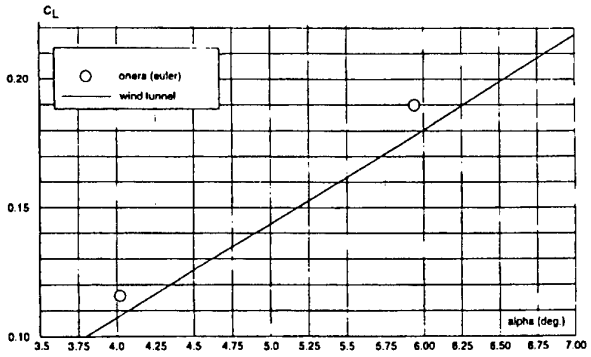


FIGURE 6a - Lift

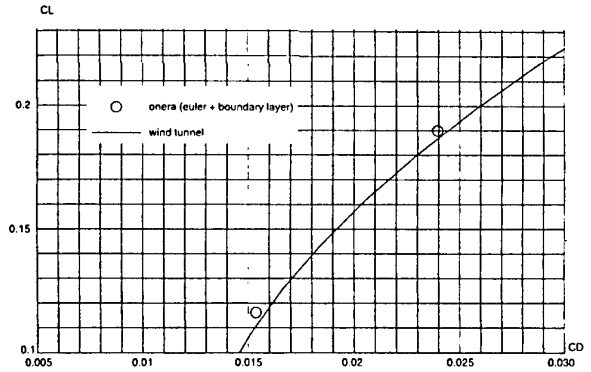


FIGURE 6b - Drag

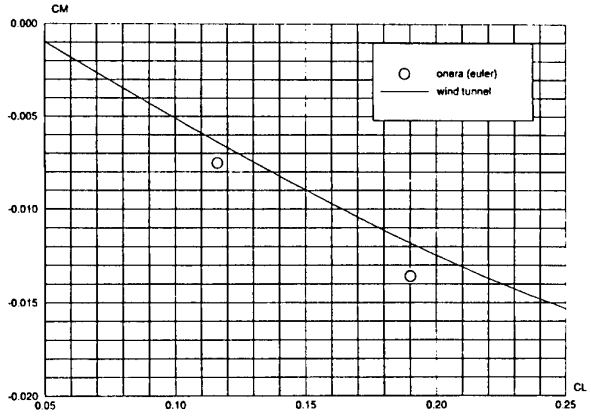


FIGURE 6c - Pitching moment

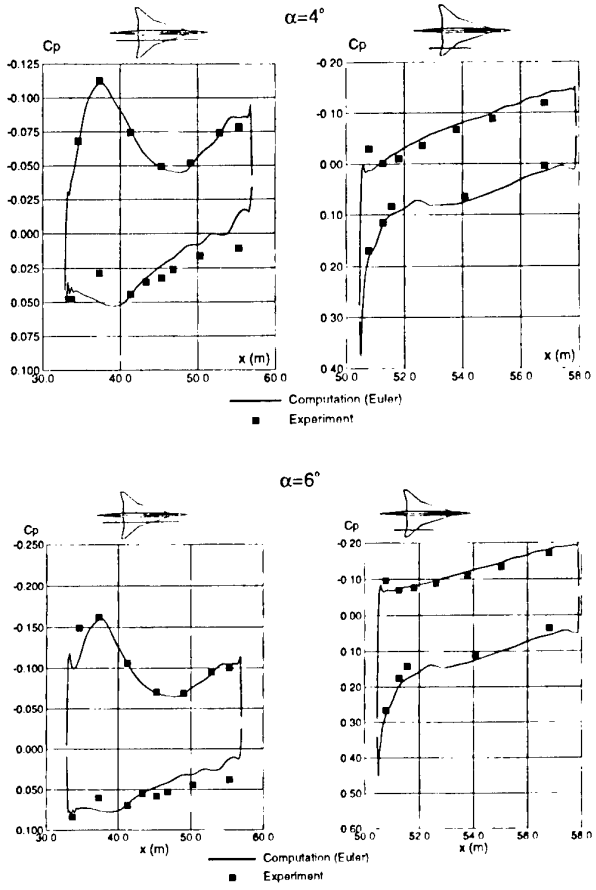


FIGURE 6d - Pressure distributions

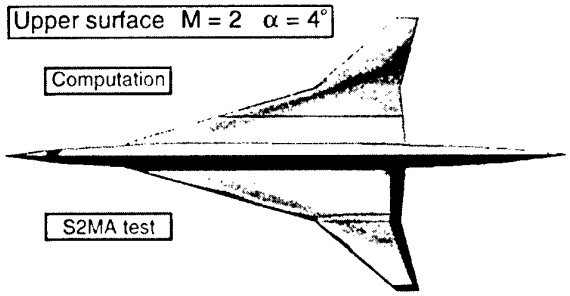


FIGURE 6e - Iso Cp contours

2.2 Transonic cruise Mach number

Values of lift coefficient are plotted against the angle of attack in **figure 7a**. A given C_L is obtained at an angle of attack which is between .5° and .7° lower in the computations than in the experiment. The slope computed is higher than the experimental one. These larger differences than in supersonic flow can be ascribed to stronger viscous effects. The computed pressure + friction drag under-predicts the drag by about 20 counts (**figure 7b**) but the increase of the drag with the lift is quite well predicted. The pitching moment plotted in **figure 7c** shows that the computed values are more negative than the measured one due to too large aft loading on the wing.

The pressure distributions are plotted in **figure 7d** for the two lift levels. For the inboard part of the wing the agreement is good even if the rear compression is sharper and closer to the trailing edge in the computations. The agreement is not so good on the outer part of the wing, the vortical flow developing along the wing leading-edge being not predicted in the computations. This vortical flow is clearly visible on the experimental pressure distributions which exhibit a rounded shape near the leading edge. The extent and the intensity of this vortical flow area increase with the lift as shown in **figure 7d**. In the computations the leading edge expansion is much more sharper and the load on the aft part of the wing is over-estimated.

FIGURE 7 - Performance prediction at Mach 0.95

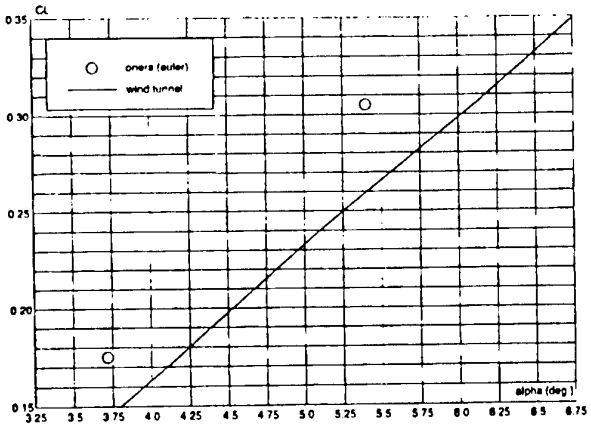


FIGURE 7a - Lift

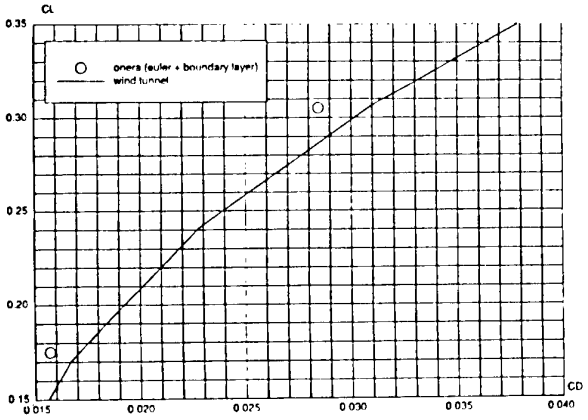


FIGURE 7b - Drag

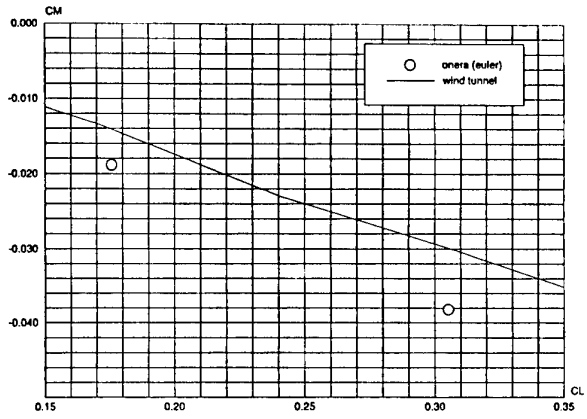


FIGURE 7c - Pitching moment

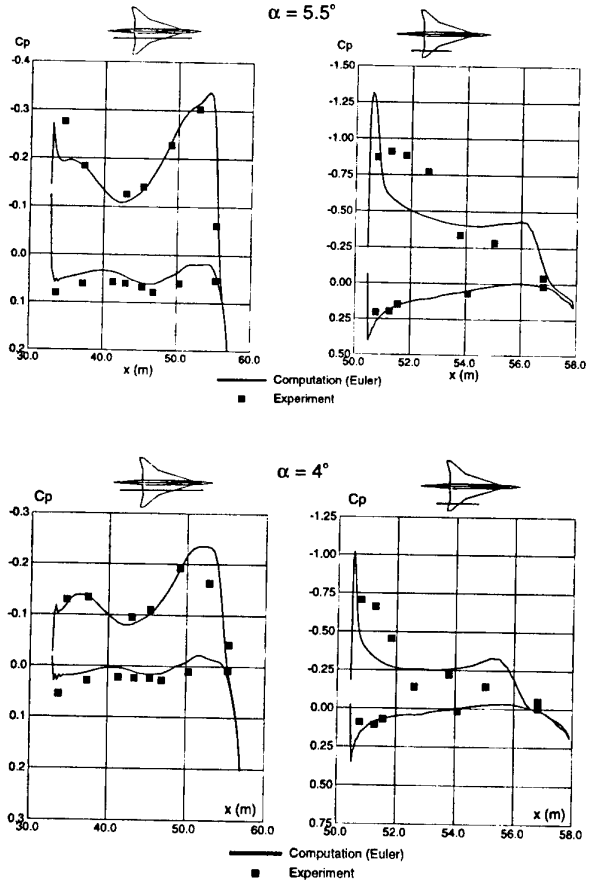


FIGURE 7d - Pressure distributions

For this Mach number coupled Euler codes or Navier Stokes codes are needed to improve the performamce prediction accuracy even if the main features of the flow are given by Euler codes (**figure 7e**).

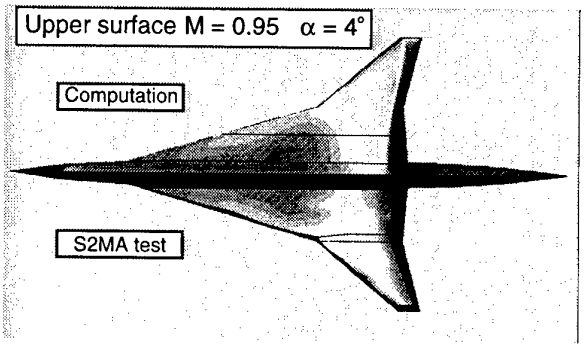
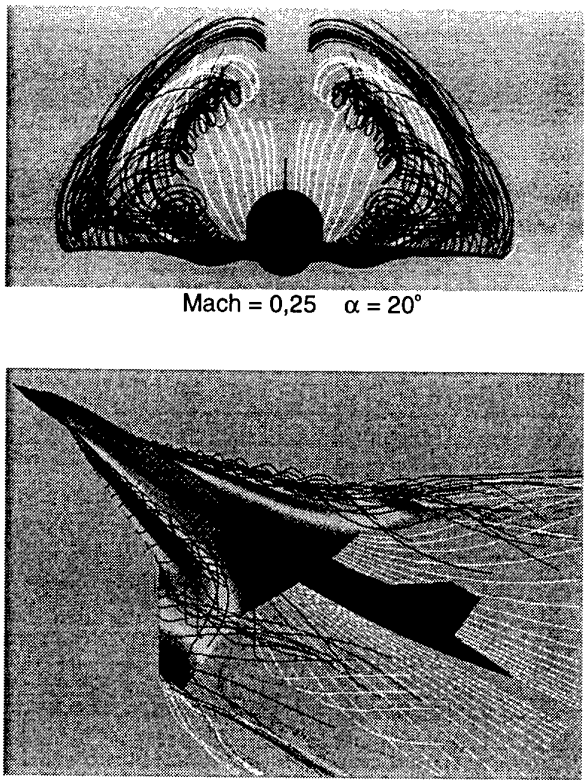


FIGURE 7e - Iso Cp contours

2.3 Low speed

At low speed (Mach 0.25) and high angle of attack **figure 8** shows the complexity of the flow with there vortices interacting on each other. One vortex originates from the wing apex ; the second one is coming from the kink in the planform and the third one is the tip vortex.

The flow being separated on the upper surface only inviscid Euler computations were done.



Mach = 0,25 α = 20°

FIGURE 8 - Flow pattern at Mach 0.25

The lift, drag and pitching moment curves are plotted respectively in **figure 9a, b, c**. Computations over-predict the lift at a given angle of attack but the slope $C_{L\alpha}$ is well predicted. The drag is under-predicted by about 13 % with these inviscid computations but the induced drag is fairly predicted. The pitching moment is more negative in the computations than in the experiment.

These comparisons show however than the Euler code give the main feature of the flow and this is confirmed by the pressure distributions plotted in **figure 9d**. On the inboard part of the wing, the vortex originating from the wing apex is captured but it is less strong than in the experiment and located too much inboard. On the outer part of the wing the vortex originating from the kink in the planform is also located too much inboard in the computation.

As shown on the comparisons of the pressure distributions, the effects of the two vortices which extend above the wing seem more diluted in the computations. This can be due to discreapencies in the trajectories or/and in the intensities of these vortices.

FIGURE 9 - Performance prediction at Mach 0.25

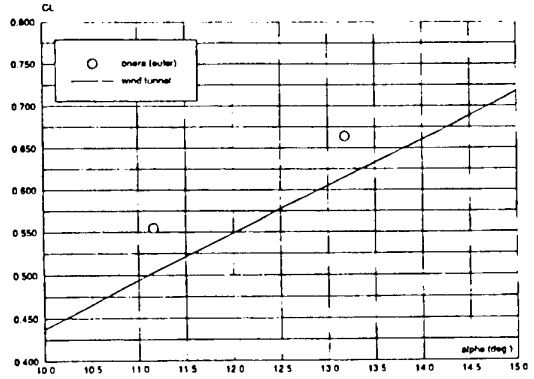


FIGURE 9a - Lift

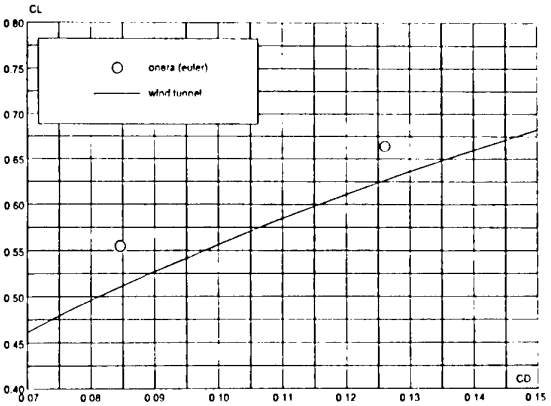


FIGURE 9b - Drag

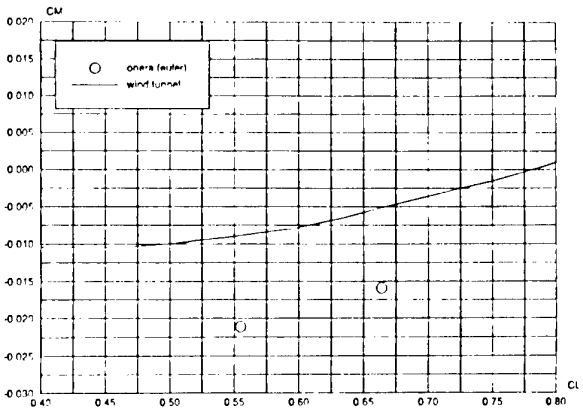


FIGURE 9c - Pitching moment

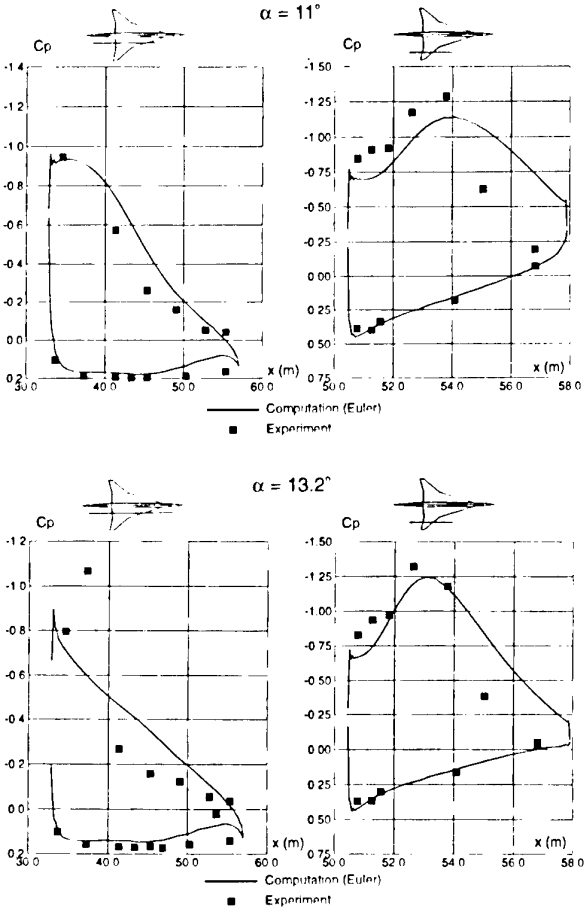


FIGURE 9d - Pressure distributions

Figure 9e shows that the apex vortice formation occurs downstream in the computation and that the trajectories of the vortices are not correctly predicted mainly for the one originating from the kink.

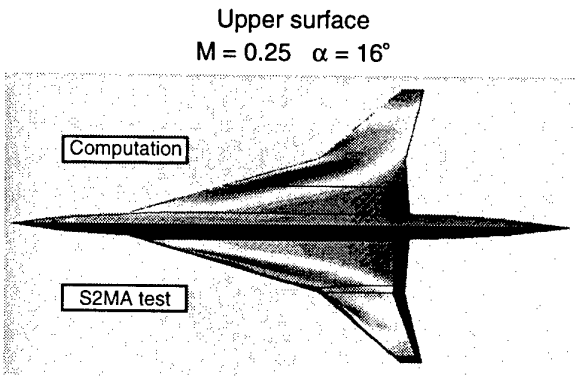


FIGURE 9e - Iso Cp contours

In order to complement the comparisons between Euler computations and experimental data at low speed and high angle of attack, other experiments have been performed on the same model in the S2 Chalais-Meudon low speed wind tunnel with LDV flow field measurements. The three components of the velocity have been measured in three planes above the wing (**figure 10a**).

The axial vorticity distributions computed and measured in these three planes are compared in **figure 10b** for an angle of attack of 20°. In the first plane, the two vortices coming from the apex and the leading edge crank are well predicted. Downstream, for station 2, the inner vortex is more diffuse in the computation than in the experiment. Behind the trailing edge, at station 3, the computed vortices are completely diffused while there are still visible in the experiment. For this station the tip vortex is hardly visible both for experiment and for computation.

FIGURE 10 - Vortex flow prediction at Mach 0.25

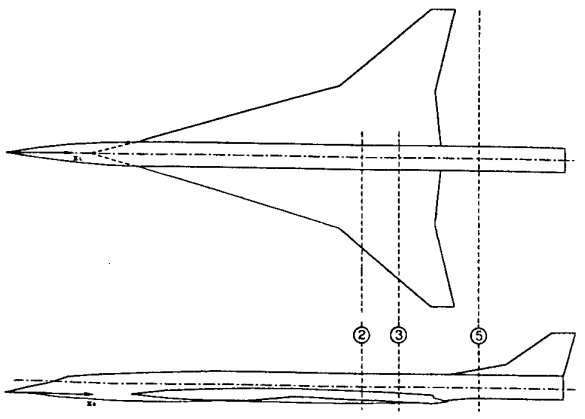
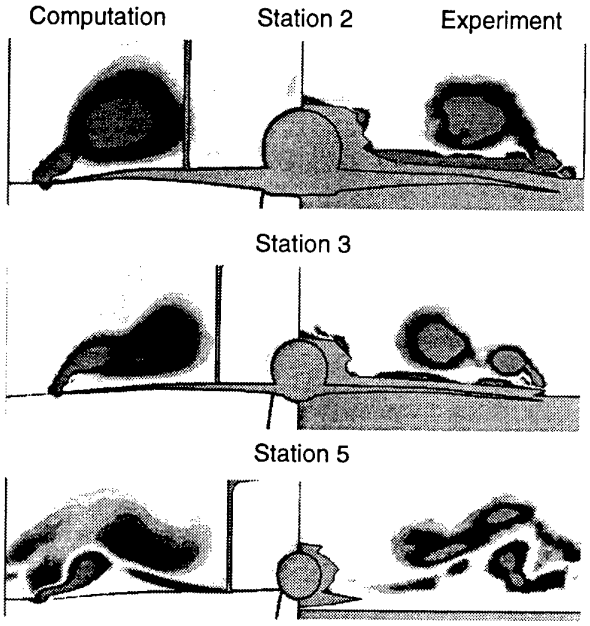


FIGURE 10a - Location of the measurement planes



Mach = 0,25 α = 20°

FIGURE 10b - Axial vorticity distribution

2.4 Conclusion

The comparisons between computational solutions and experimental data shows improved levels of agreement as go from subsonic to supersonic regime. This applies for pressure distributions as well as for values of overall forces and moment coefficients.

Euler solutions give the mean features of the flow for all the flight conditions but suffer from too much dissipation in particular for the vortex flow prediction development. Even if the accuracy in the prediction of the drag is no sufficient at transonic speed and at low speed the variation of the drag with the lift is correctly predicted which allow to use this type of method for design purpose. Euler + boundary layer solutions improve significantly the drag prediction but coupled methods will certainly be better at transonic speed.

Navier Stokes code seems to be of practical interest only at low speed and high angle of attack for predicting vortex flows if their numerical dissipation can be mastered and if an adequate turbulence model is used.

3. WIND TUNNEL/FLIGHT EXTRAPOLATION

Figure 11 presents the drag breakdown at Mach 2 for the cruise lift level. In wind tunnel conditions (Re ~ 13 10^6) the friction drag is about 43 % of the total drag. Reynolds number correction applied to the friction drag to extrapolate the drag to flight conditions (Re ~ 160 10^6) reduces drastically the drag.

On the figure the full payload as well as 1 ton of payload have been expressed in term of drag to point out that the drag correction from wind tunnel to flight is higher than the full payload. This illustrate the degree of accuracy needed for wind tunnel data and for Reynolds number corrections because errors mean questionable predicted payload/range.

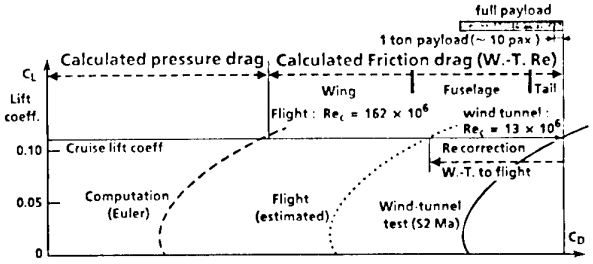


FIGURE 11 - Drag breakdown at Mach 2

Accurate Reynolds number correction implies reliable skin friction laws for high Reynolds numbers, this is why flight test measurements have been performed on a Concorde aircraft in order to measure the local skin friction. These measurements were carried out by Aerospatiale and ONERA/CERT [5]. Six measuring blocks were installed on the aircraft , each one constiting of two Preston tubes, one static probe and one thermocouple to measure the wall temperature as shown in **figure 12**.

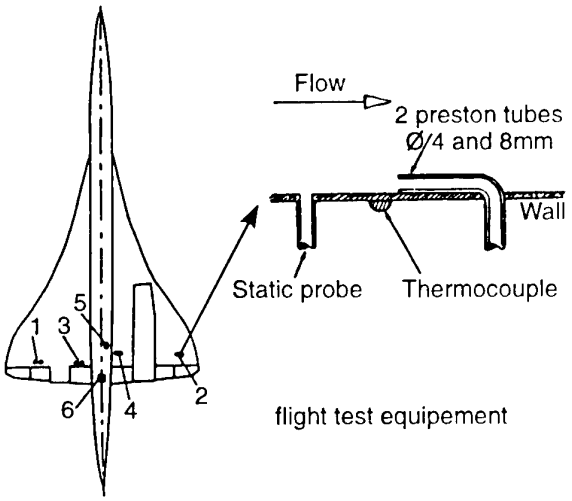


FIGURE 12 - Flight test equipement

The Preston tubes were calibrated using the Hopkins and Keener relation which require the knowledge of flow parameters at the outer edge of the boundary layer. These conditions were computed by assuming that the total stagnation pressure remained constant all over the aircraft. From the evaluation of the temperature outside the boundary layer it is possible to deduce the friction temperature Tf assuming a recovery factor of 0.89. This value is compared to the wall temperature Tp given by the thermocouples for all the measuring stations in **figure 13** and for all the flight conditions. It can be noticed than for a given flight conditions the 6 values are consistent. For the subsonic flights the difference between Tp and Tf are within The range ± 2 %. For the supersonic flights the difference is higher but remains under 5 %, the aircraft skin being colder than the adiabatic wall.

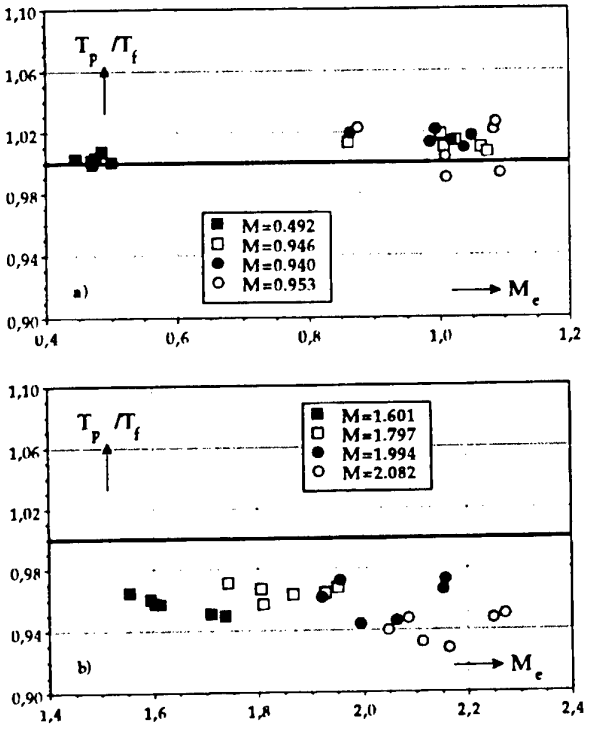


FIGURE 13 - Evolution of the Tp/Tf ratio

All the data provided by the smaller Preston tubes are plotted in **figure 14** in a (Cfi, Rel) diagram, Cfi being the incompressible skin friction coefficient and Rel the local Reynolds number which ranges from 47 10^6 up to 488 10^6. Whatever the Reynolds number is the maximum variation between the measured Cfi and the value given by the empirical law of Michel is close to 25 %.

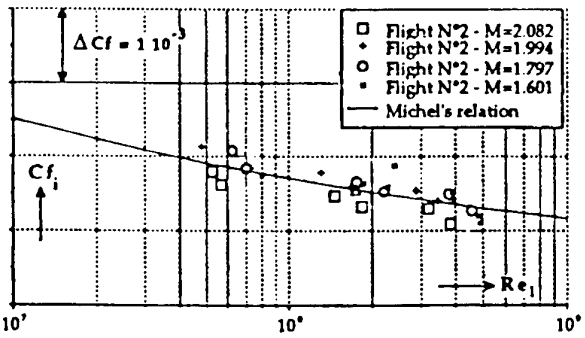


FIGURE 14 - Concorde Flight test - skin friction data

Comparisons have also been made with three dimensional boudary layer computations carried out with the 3C3D code using the pressure distributions computed by Aerospatiale with the FLU3M Euler code. An examples is given **in figure 15** for two Mach numbers : 0.5 and 2.

The results given by the Michel law are also plotted in the figure. The agreement is good particularly on the wing and the differences between the 3C3D computations and the measured values are much smaller than between the measurements and the values given by the Michel law.

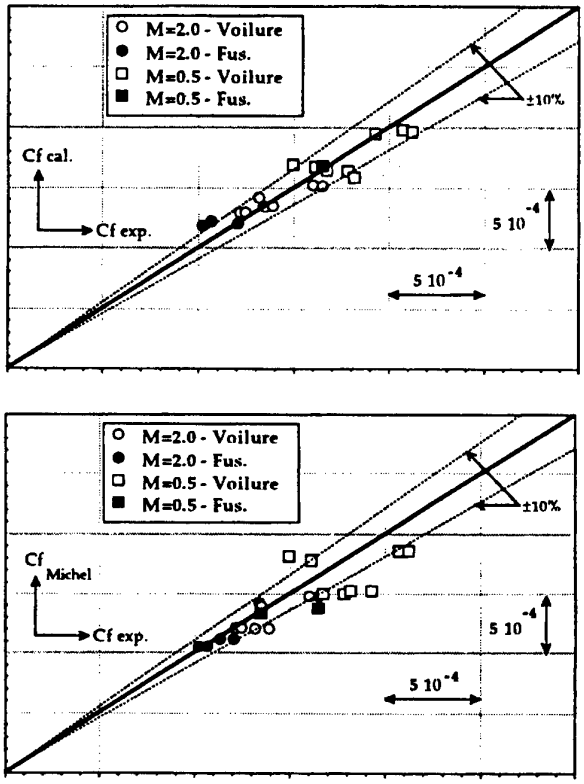


FIGURE 15 - Skin friction coefficient - Comparisons between computations and flight test data

4. WING DESIGN BY NUMERICAL OPTIMISATION

4.1 Description of the optimisation code

The future SCT aircraft will probably fly overland at transonic speed. Thus its design will be a compromise between supersonic and transonic performances. Numerical optimisation techniques are powerful tools for this kind of multipoint design.

They have been used at ONERA for several years to improve airfoil and wing designs at transonic speed [6] [7].

For these applications the number of design variables was rather low and the aerodynamic computations were performed with potential codes.

Three years ago the method was extended to allow wing-body configuration optimisation with Euler codes and to deal with a great number of design variables. The general organisation of the ONERA optimisation code is described in **figure 16**. The code is built around the CONMIN and COPES codes [8] [9] with :

- a geometry generator which modifies the wing -body geometry,
- a geometric constraints module,
- a grid generator,
- an Euler code.

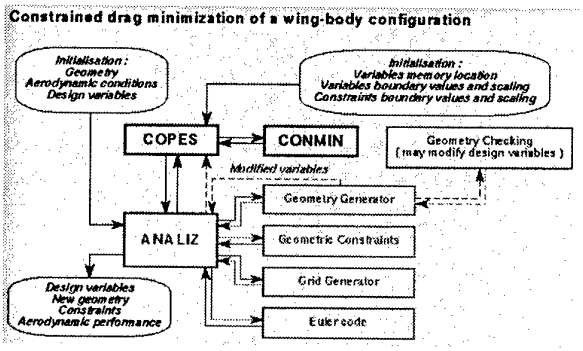


FIGURE 16 - Structure of the ONERA optimisation code

All these routines are controlled by the ANALYZ routine which ensure the interfaces. More details about this code can be found in [10]. Bezier curves are used for wing twist, camber and thickness modifications and specific modules have been built for wing planform and wing location controls. The twist and camber laws at each design section are actually controlled by 5 design variables according to the sketch show in **figure 17**. The section twist angle is the first design variable. The two others define the camber law of the section with one Bezier's curve of degree 3 having 4 control points. The thichness laws of the design sections are controlled by 4 or 10 design variables as shown in **figure 18**. The four main design variables are the maximum thickness and its location, the leading edge radius and the trailing edge slope of the thickness law. If a finer tuning is needed, 6 extra design variables can be added.

The twist and camber laws defined by the set of design variables are always considered in an incremental form as variations of the twist and camber laws of the initial wing. The thickness law is considered in an absolute form and each design section is rebuilt by adding the new thickness law to its initial mean camber line before adding twist and camber deformations. After the deformations have been computed at each point of the design sections, they are interpolated along the span and then added at each point of the initial wing.

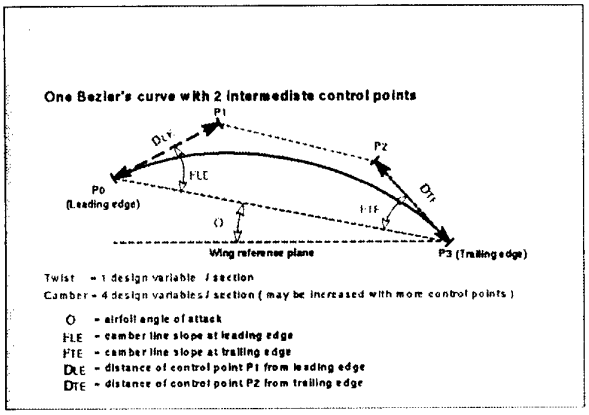


FIGURE 17 - Twist and camber control

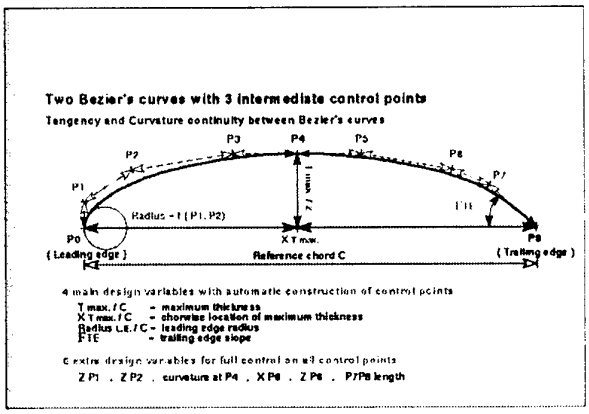


FIGURE 18 - Thickness control

The grid generator builds an 0 type grid around the wing or the wing-body configurations to be optimised. This topology has been retained because it reduces the number of cells while allowing a good level of refinement near the aircraft surface. The grid is built using simple fast algebraic methods, so it can be wholly rebuilt each time the geometry has been modified. The outer boundary of the grid is spherical and put at a distance form the surface which depends on the aerodynamic conditions. An examples of the mesh for a wing-body configuration is shown in **figure 19.** Typical mesh sizes are about 30 000 cells and the Euler code is the one described before.

The surface grid has been chosen to give to the body surface grid an H type topology relative to the wing body intersection. The grid is built in such a way that the aircraft skin is swelling up to the outer boundary with a number of layers between the aircraft and the outer boundary.

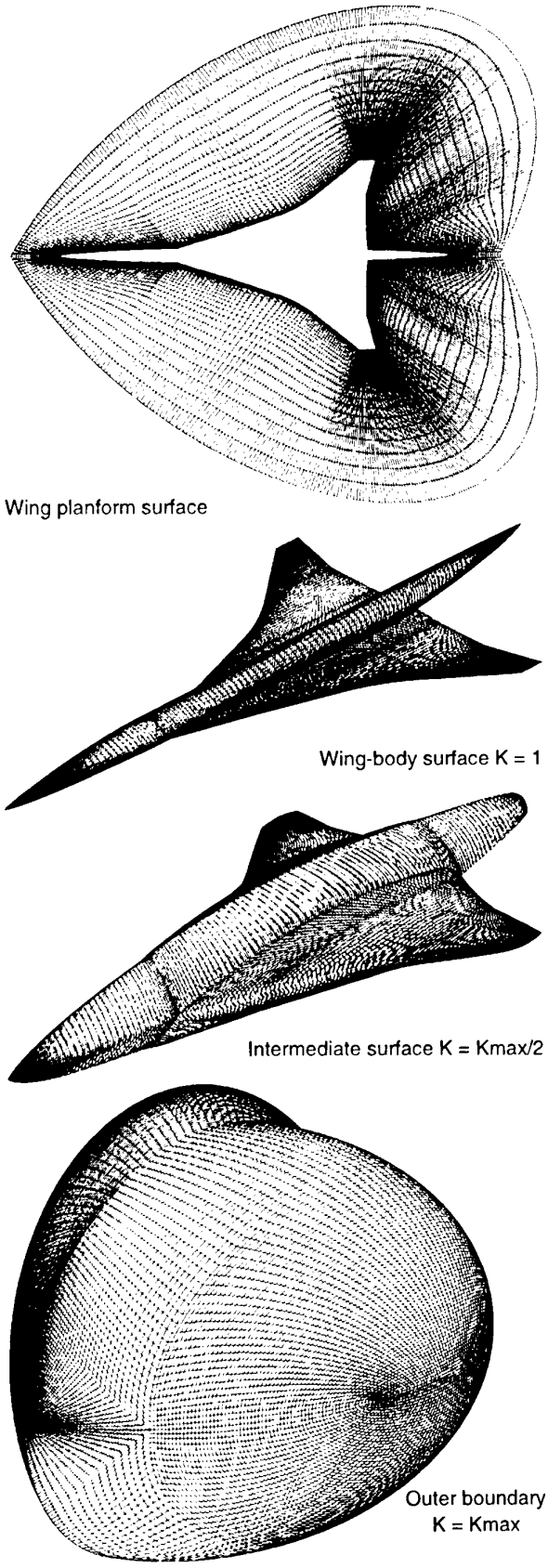


FIGURE 19 - Wing-body configuration at M=2,, α=4°

4.2 Wing optimisations

The code has been applied to the optimisation of the ATSF configuration. The objective was to reduce the inviscid drag by modifying the twist and the camber laws. Three optimisations were performed starting with the same initial shape :

- single point optimisation at Mach 2,
- single point optimisation at Mach 0.95,
- dual point optimisation.

For each case 25 design variables were used and about 20 cycles were needed for each optimisation. The three optimised wings have been computed in a fine grid in order to improve the drag prediction accuracy. In **figure 20a** the performances of the initial wing and of the optimised ones are compared at Mach 2 and for an angle of attack of 4° (supersonic cruise conditions). The supersonic single point optimisation reduces the drag of the ATSF wing by 4 per cent, the transonic optimisation by 3.2 per cent and the dual points optimisation by 2.5 per cent. The lift cannot be maintained during the transonic optimisation for the given angle of attack. The pressure distributions show that the supersonic optimisation decreases the maximum velocity on the upper surface mainly on the trailing part of the low pressure area which follows the highly swept leading edge (**figure 20b**). The transonic design reduces too much the load at the leading edge of the outer wing while the two points design seems to be in between the two single points designs. The performances for the transonic cruise point (Mach 0.95 α=4°) are presented in **figure 20c**. The drag reduction is 5.4 per cent for the supersonic design, 17.5 per cent for the transonic design and 9.8% for the two points design. The lift is kept approximately constant for this case. Pressure distributions drawn in **figure 20d** show that while the supersonic design has a small effect, the transonic design eliminates almost completely the velocity peak along the leading edge mainly on the outer part of the wing but increases slightly the Mach number before the shock. For the two points design pressure distributions are in between those given by the two single point optimisations.

FIGURE 20 - One point and two points optimisation of the ASTF wing

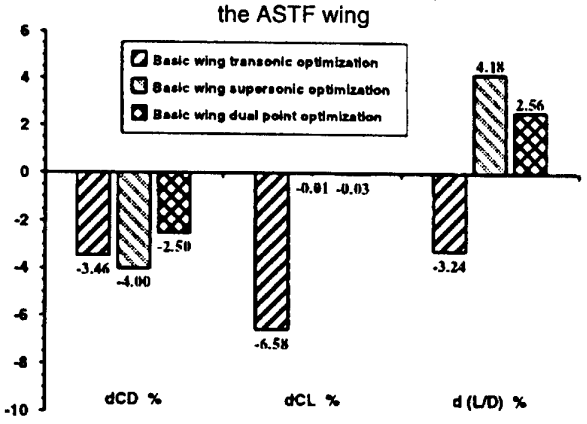


FIGURE 20a - Performance comparison at M=2., α=4°

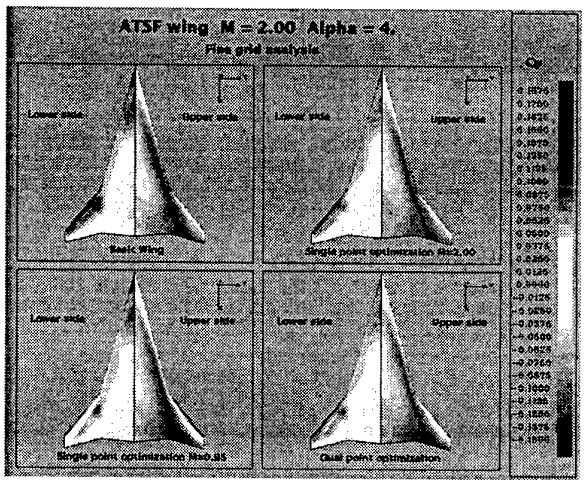


FIGURE 20b - Iso Cp contours at M=2.

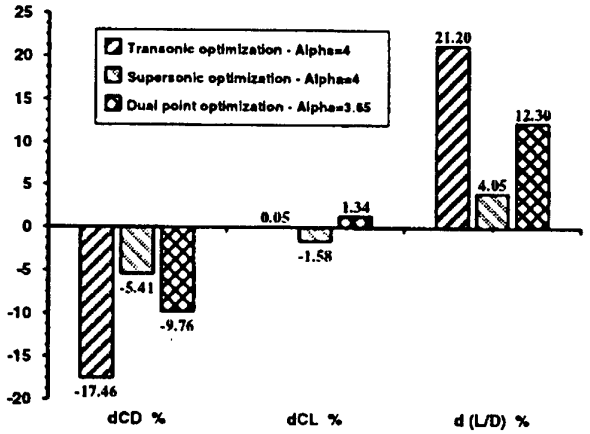


FIGURE 20c - Performance comparison at M=0.95, α=4°

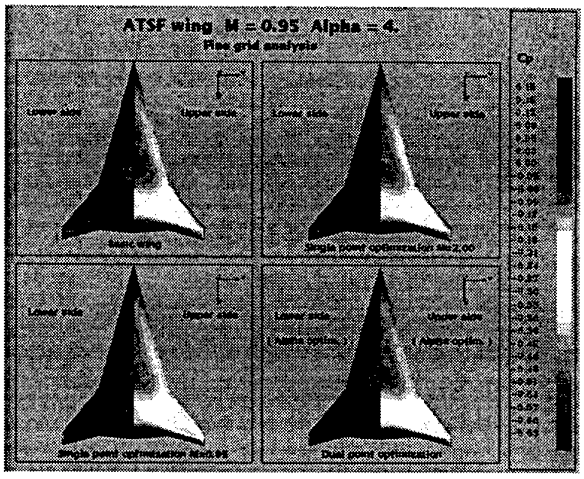


FIGURE 20d - Iso Cp contours at M=0.95.

4.3 Wing-body optimisations

The wing-body optimisation code has been checked on a simplified geometry of the European Supersonic Civil Transport (ESCT) configuration shown in **figure 21**. The first stage of the optimisation process was the optimisation of the thickness law at M=2 and zero angle of attack starting from the decambered wing. Five design sections with four design variables were used so the thickness law was entirely controlled by 20 design variables and each optimisation cycle requires 22 evaluations of the objective function. After 12 minimisation cycles the inviscid drag was decreased by about 14 %.

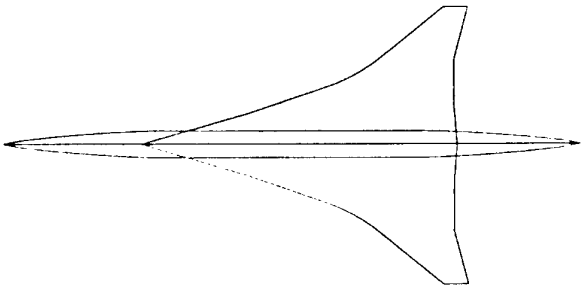


FIGURE 21 -ESCT configuration

The second step of the optimisation process was the optimisation of the twist and of the camber starting with the uncambered wing designed previously. The angle of attack was set at 4° and 25 design variables were used. The objective function was again the inviscid drag and constraints were put on the minimum value of the lift and on the maximum angle of the fuselage. The history of the optimisation is shown in **figure 22**. Some modifications on the constraints as well as several restarts of the optimisation were needed to reach a satisfactory solution after 100 cycles. The final geometry combines the improvements of the thickness law as well as of the twist and the camber laws.

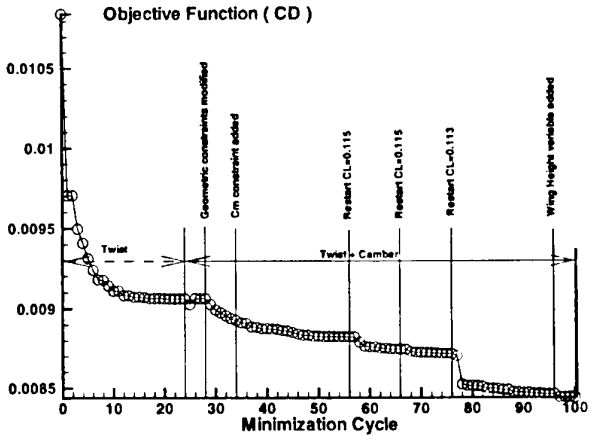


FIGURE 22 - History of the twist + camber optimisation

A fine grid analysis has been performed on the datum configuration and on the final supersonic design for the same lift coefficient close to the aimed value of 0.115 at M=2. The results are shown in **figure 23**. The lift to drag ratio is 14.2 for the optimised geometry while it is about 12 for the datum configuration. The comparison of the pressure distribution show that the optimisation has greatly reduced the low pressure area along the leading edge of the inboard part of the wing as well as its extension over the outer part of the wing. The flow velocity is also reduces along the leading edge of the outboard part of the wing.

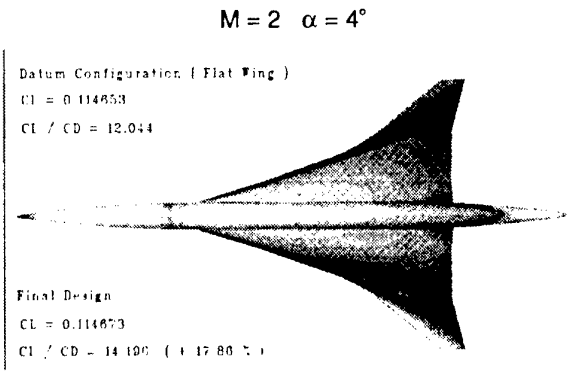


FIGURE 23 - ESCT supersonic design
- Iso Cp contours

An another optimisation exercice has also been performed on the ESCT configuration starting from the supersonic design discussed above. For that case the slat leading edge deflections were determined in order to optimise the L/D for the transonic cruise point. The control surfaces are shown in **figure 24**. The leading edge of the wing has been split in three parts on which different deflections can be applied. The optimisation computes the best combination of the slats together with the value of the angle of attack, the lift being constrained to a value of 0.2. Since the computations are made in inviscid flow, some constraints were also put on the pressure coefficient at the hinge to avoid too large an expansion. Sixty cycles were needed to obtain a good solution. The L/D is increased by 14.8 per cent with the slat deflections given in **figure 24**. The leading edge droop reduces the velocity in that region but increases the velocity slightly ahead of the rear shock. The final angle of attack is very close to the starting value and the slat deflection decreases from inboard to outboard. The maximum normal Mach number on the rear part could be reduced with a simultaneous optimisation of the upward deflection of the trailing edge flaps. Computations with a coupled Euler method would be needed to verify if the low pressure peaks along the hinge line are not too strong.

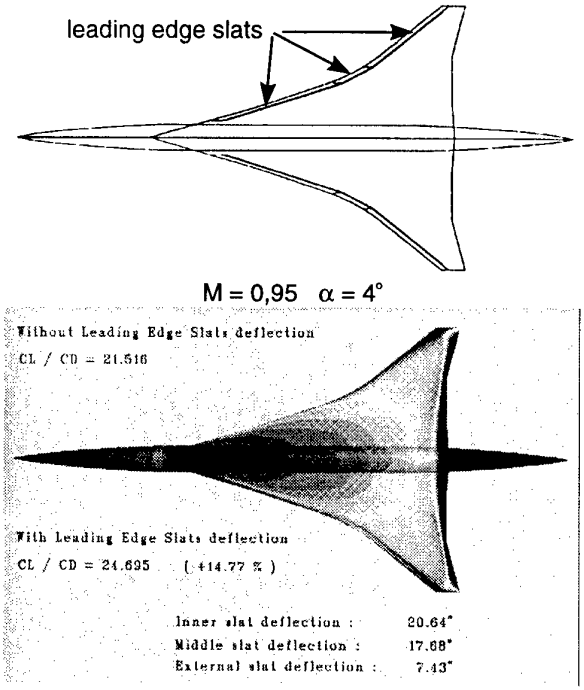


FIGURE 24 - Leading edge slat deflections optimisation. ESCT configuration

These examples show that significant improvements of the L/D can be obtained through the use of numerical optimisation. Multipoint capabilities as well as the possibility to deal with geometrical constraints make this type of method very attractive for such design even if the computing time is quite large.

5. DRAG REDUCTION TECHNOLOGIES

Since ONERA has been involved for some years in research aiming at the drag reduction of subsonic aircraft [11] [12] it seems worthwhile to investigate the potential drag benefit for supersonic transport aircraft by using these techniques.

5.1 Turbulent skin friction drag reduction

Riblets have proven to be efficient in the reduction of the turbulent skin friction drag in wind tunnel and in flight [13]. They have also been tested in supersonic flow on a simplified cone-cylinder model [14] for Mach numbers between 1.6 and 2.5 and Reynolds numbers ranging from 5.5 to 22.5 million per meter (**figure 25**). The pressure distributions along the model, for M=2 are plotted in figure 25 (x=o refers to the junction between the cone and the cylinder part of the model). The Cp values on the cone are in good agreement with the shock relations and the ones at the junction between the cone and the cylinder are also very close to those given by the two-dimensional Prandtl-Meyer formulation.

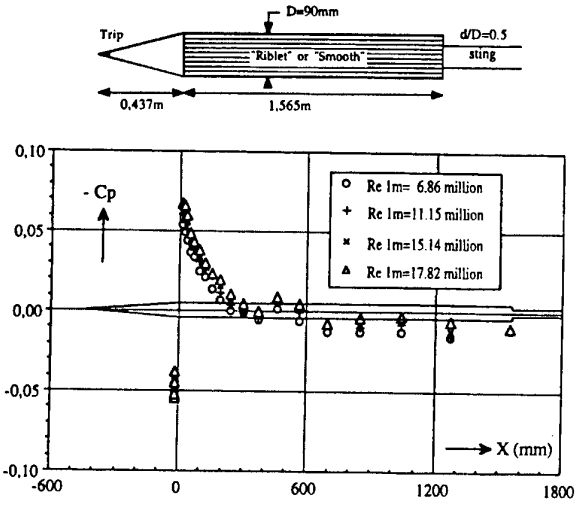


FIGURE 25 - Pressure distribution at M=2

The Reynolds number does not have too much effect on the pressure distribution. For different freestream conditions, the internal balance gives the total drag from which the external pressure drag, the base drag as well as the internal pressure drag have to be subtracted. These last two forces are obtained from pressure measurements at the base and inside the cavity of the model. The values of the viscous drag coefficient of the reference model (smooth surface) are plotted versus the unit Reynolds number for three values of the Mach number in **figure 26a**, the reference surface is the projected surface. In that diagram, the values of the computed drag coefficients, using an integral boundary layer method, are also given. The agreement between the computed and estimated values of Cd is rather good since the difference does not exceed 4 %. An example of the results with riblets is given in **figure 26b** for a height of 0.051 mm. The net overall drag decreases are obtained over the whole Reynolds number range.

FIGURE 26 - Viscous drag data

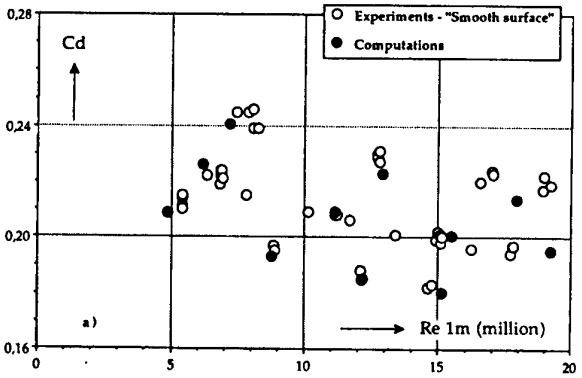


FIGURE 26a - Viscous drag comparisons

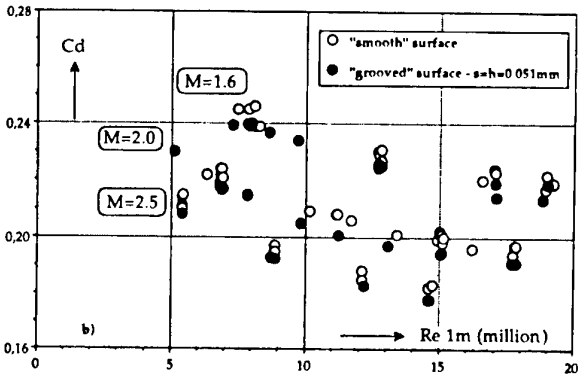


FIGURE 26b - Viscous drag with and without riblets

The dependence of the results to the Mach number or to the Reynolds number can be avoided by plotting the results using the non dimensionalized height hp^+. As shown in **figure 27** a maximum of 6 per cent of skin friction drag reduction has been measured for a height of the riblets expressed with the wall variables of about 10. This is slightly lower than in subsonic flow but it can provide for the complete aircraft a total drag reduction between 1 and 2 per cent depending on the surface area on which riblets are applied.

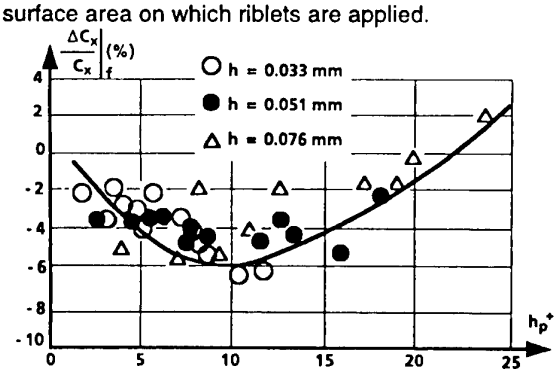


FIGURE 27 - Skin friction drag reduction with riblets in supersonic flow

5.2 Laminar flow control

The configuration chosen for the evaluation of drag reduction through laminar flow control is the ESCT presented in the previous section. The study was done for the supersonic cruise condition (Mach = 2).

Euler computations were first made on the wing body geometry (**figure 28a**). The mesh presented in **figure 28a** has about 2 millions grid points. Special attention has been paid for the mesh near the leading edge in order to compute accurately the pressure distribution as shown in **figure 28b** for a section located at 30 per cent of the span. Five hundred iterations were needed to decrease the residuals by 4 orders of magnitude resulting in 4 hours CPU on a CRAY YMP 8/8128 computer.

FIGURE 28 - ESCT configuration M=2, α=4°

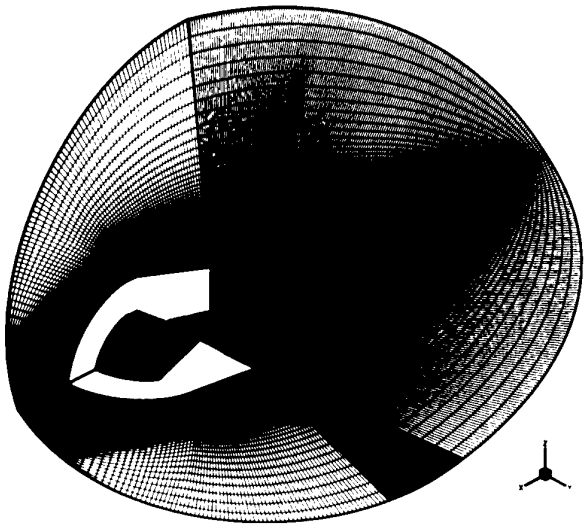


FIGURE 28a - ESCT configuration M=2, α=4°

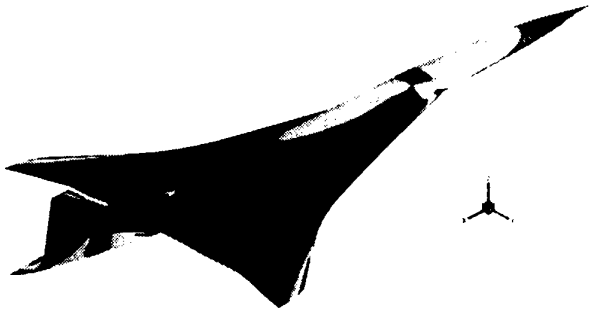


FIGURE 28b - Computed pressure distribution

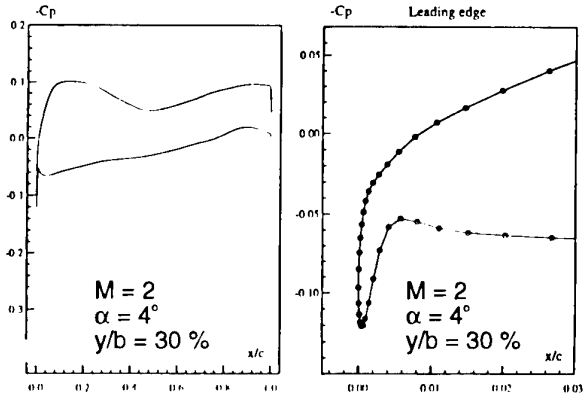


FIGURE 28c - Pressure distribution - 30 % span section

Boundary layer computations were then performed and the transition location was predicted with a data base method [15] for TS instabilities and with a semi empirical criteria [16] for the cross flow instabilities. These predictions were checked with linear stability computations [17] for some cases. **Figure 29a** shows that for a constant suction applied between 0 and 20 % of the chord it is possible to move the transition downstream up to 30 % of the chord in the inner part of the wing. This figure shows also that the simple criteria are in good agreement with the stability computations for predicting the transition location.

Figure 29b presents the results of stability computations without and with suction. Without suction, cross flow instabilities trigger the transition near the leading edge. Suction applied between 0 % and 20 % of the chord decreases significantly the total amplification factor.

The next step consisted in the optimisation of the suction distribution both in the streamwise and in the spanwise directions in order to minimise the sucked mass flow rate. With five independent suction chambers along the leading edge, through which different suction velocities can be applied, it is possible to achieve higher drag reduction than by keeping the same suction velocity all over the span. This arrangement allows the suction mass flow to be largely reduced as shown in **figure 29c**. The transition location on the upper surface ranges from 25 % of the chord near the wing root to 60 % of the chord at the tip. The total aircraft drag reduction has been estimated at about 4 % with a suction mass flow of 6 kg/s. Taking into account the power needed for the suction the fuel consumption reduction is about 3 %.

FIGURE 29 - ESCT configuration Wing Laminarisation

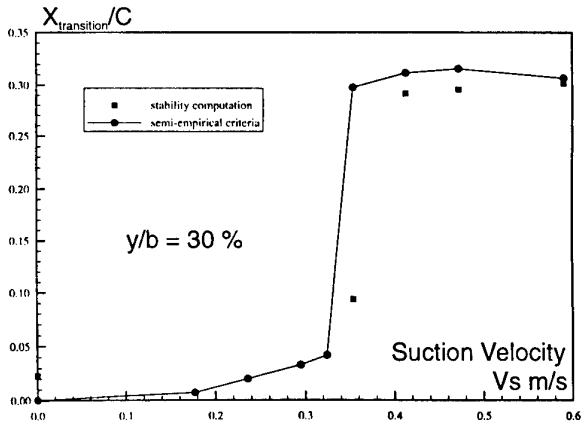
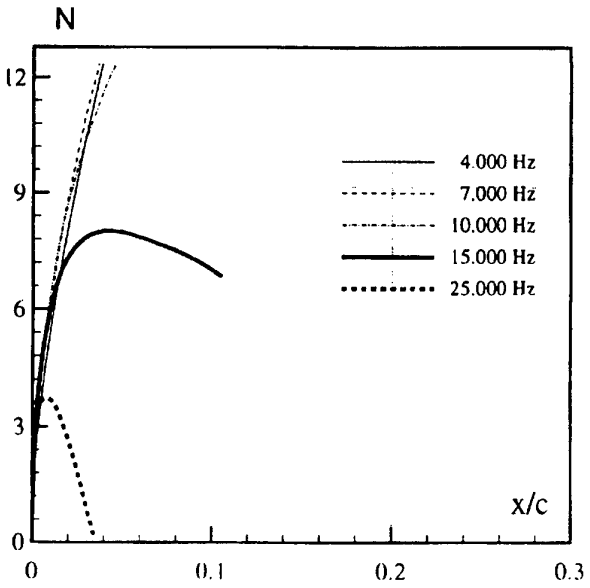


Figure 29a - Transition location versus suction velocity



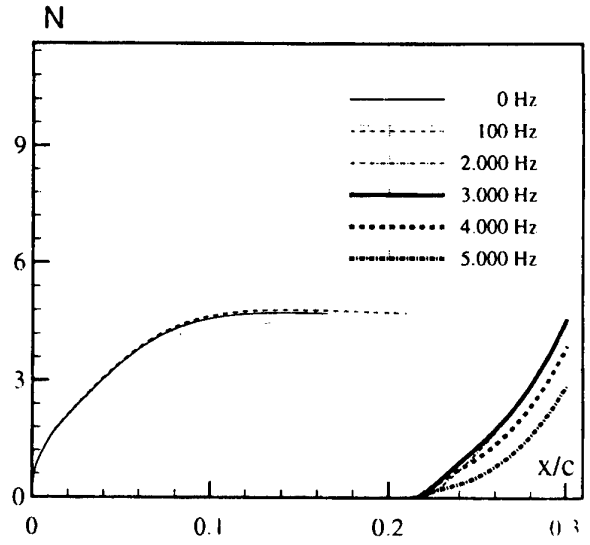


FIGURE 29b - Stability computations

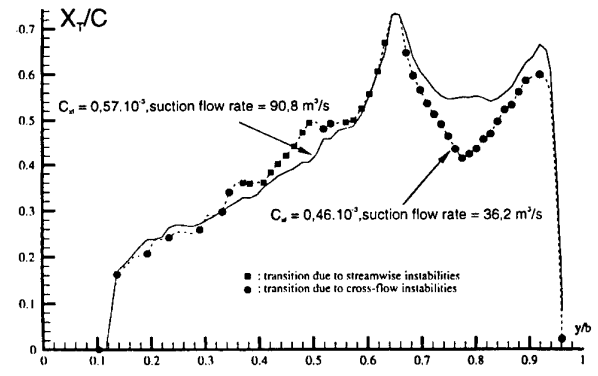


FIGURE 29c - Transition location on the wing upper surface

This study shows that with a turbulent wing design potential gains by applying laminar flow control are relatively low. They probably can be increased significantly through the optimisation of the pressure distribution and this is being investigated at the moment.

Anyhow the application of Laminar Flow Control on Supersonic aircraft will raise difficult technical problems due to the small thickness of the wing.

5.3 The ONERA "quiet tunnel"

Experimental laminar flow studies in supersonic flow cannot be performed in conventional wind tunnels since the transition Reynolds number in these wind tunnels are very low due to the noise and to the turbulence level. This is illustrated in **figure 30** where are plotted the values of the transition Reynolds number measured in flight on cones (symbols) and the ones measured in wind tunnels (full line). As shown in this figure only the NASA Langley quiet tunnel allows Reynolds numbers similar to the flight values to be reached.

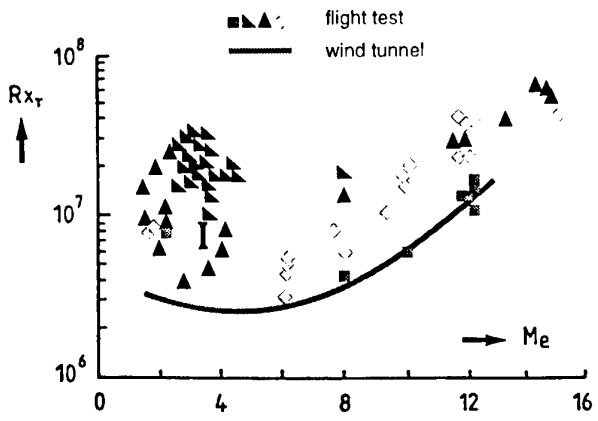


FIGURE 30 - Transition Reynolds numbers in supersonic flow

This is why ONERA decided some years ago to modify an existing wind tunnel in order to obtain a quiet tunnel. The R1Ch wind tunnel is a blow down wind tunnel with a Mach 3 nozzle. The exit diameter is .3 m and the stagnation pressure can vary between 0.5 bar and 10 bar.

A general view of the tunnel is presented in **figure 31**. Special cares were taken for the design of the tunnel to achieve the objective [20] :

- The noise coming from the upstream part of the circuit has been minimised ;
- The nozzle boundary layer is sucked just upstream of the throat (**figure 32**) ;
- The shape of the nozzle has been defined so that the transition occurs at a distance of about 1 m from the throat ;
- The roughness of the nozzle is very small (≤ 2 microns).

This should allow a "quiet flow" over a distance of about.45 m for a stagnation pressure of 10 bar to be obtained.

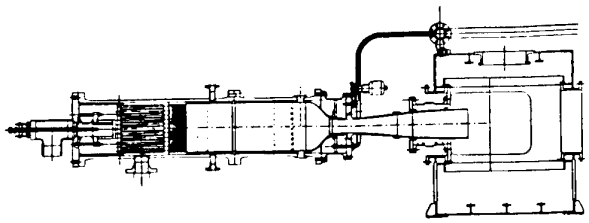


FIGURE 31 - General view of the ONERA quiet tunnel

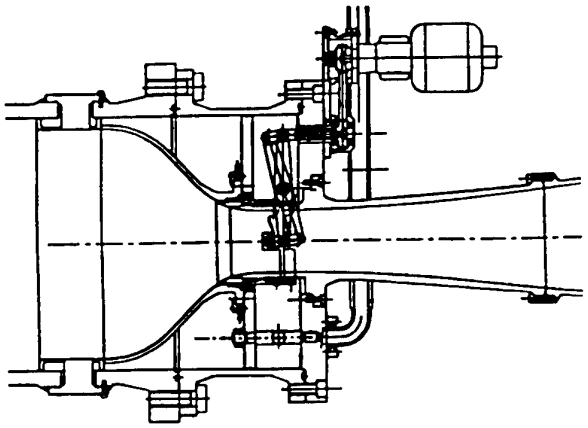


FIGURE 32 - Throat suction system

The flow quality in the test section is very good with local Mach number deviations less than 0.01 in the major part of the flow and up to .05 on the centerline where the Mach waves focus.

The unsteady measurements carried out on this new tunnel presented in **figure 33** shows that the level of the pressure fluctuations in the settling chamber is very low for a wide range of frequencies. However heat flux measurements on a flat plate have shown that the transition Reynolds number is less than expected. Boundary layer measurements at the exit nozzle show that the suction has almost no effect. These disappointed results have been ascribed to the suction slot geometry.

Test with other geometries of the suction slot lip will be carried out in the near future.

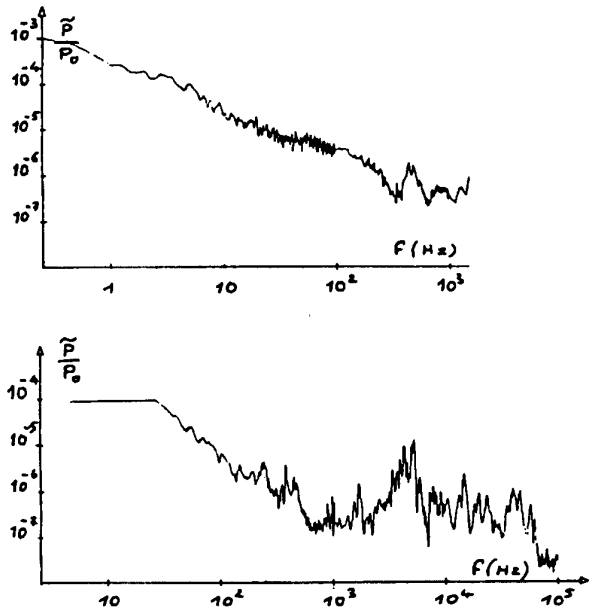


FIGURE 33 - Pressure fluctuations in the settling chamber

5.4 Leading edge contamination

In order to apply Laminar Flow Control the attachment line on the wing has to be laminar. Several solutions have been successfully tested for transonic swept wings at ONERA [18] but no experience exists for supersonic wings. This is why as a first step two experiments have been performed in order to investigate leading edge flows on swept wings in supersonic flow. The main objective was to assess the criteria proposed by Poll for leading edge contamination.

The first experiment [19] was carried out on a cylinder placed with a sweep angle in the jet exhaust of the supersonic R1 Chalais-Meudon wind tunnel. A flat plate generates a turbulent boundary layer at the attachment line of the cylinder (**figure 34a**). The flat plate is placed at zero angle of attack with respect to the incoming flow direction. The tests were carried out at Mach 3. for two sweep angles of the cylinder (20° and 30°). The cylinder is equipped with pressure taps and thermocouples from which the state of the boundary layer can be determined through the value of the Stanton number. **Figure 34b** shows a diagram with the evolution of the Stanton number versus $\overline{R}^*$. Laminar and turbulent theoretical boundaries are indicated on this diagram. The experimental data points plotted on this diagram show that leading edge contamination occurs for $\overline{R}^* \geq 250$.

FIGURE 34 - Attachment line contamination on a swept cylinder

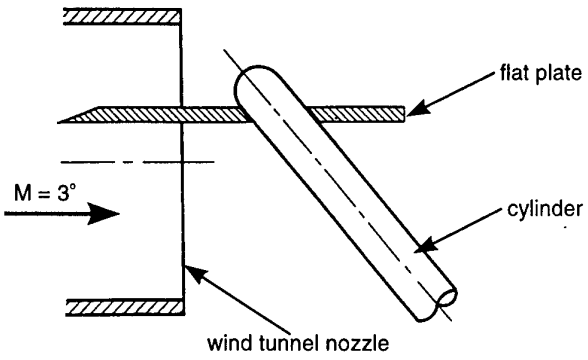


FIGURE 34a- Test set up

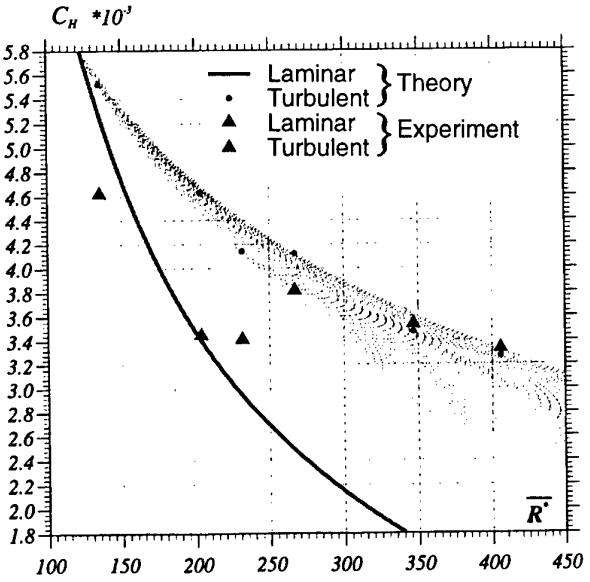


FIGURE 34b - Test data

This value has also been confirmed by an another experiment on a swept wing whose leading edge was designed to provide in the wind tunnel conditions $\overline{R}^*$ values close to the flight values. The wing was tested in the supersonic S5 Chalais-Meudon wind tunnel for Mach numbers 2 and 2.5 (**figure 35a**). Pressure distribution around the leading edge and wall temperature measurements allow to compute $\overline{R}^*$. The state of the boundary layer is determined through hot films signals as shown in **figure 35b.** For $\overline{R}^*$ values < 200 the signals indicate a laminar boundary layer. For $\overline{R}^* \sim 200$ turbulent spots appear and for $\overline{R}^* > 250$ the signals show that the boundary layer is turbulent.

FIGURE 35 - Leading edge contamination on a swept wing

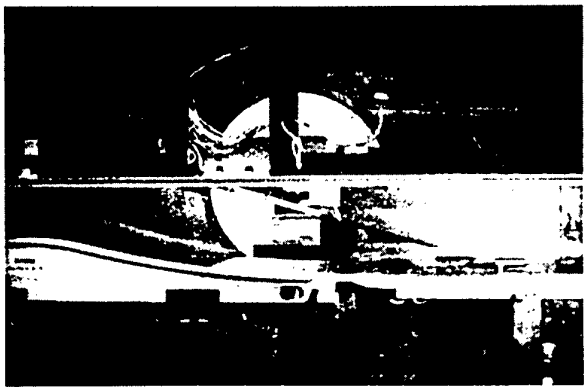


FIGURE 35a - Test set up

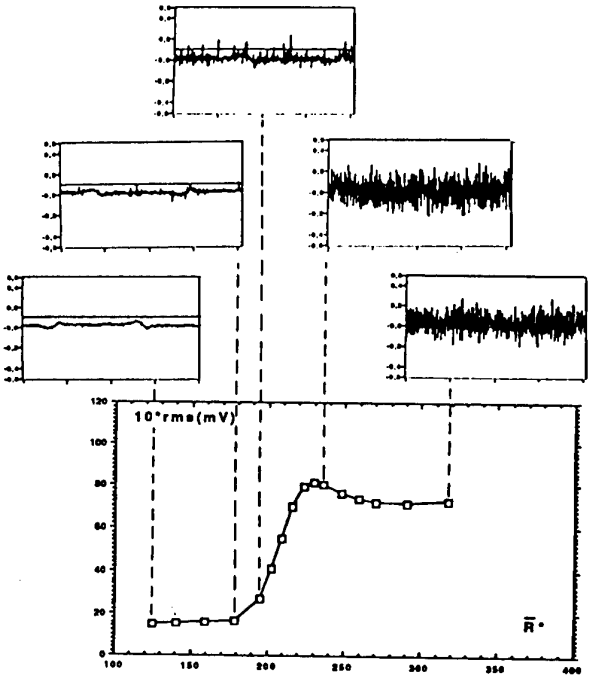


FIGURE 35b - Leading edge hot film signals

These studies are being pursued in order to investigate various passive devices which could avoid leading edge contamination.

Additional experiments were performed on the cylinder presented in **figure 34a** in order to investigate the effects of roughness elements placed on and off the attachment line. When the roughnesses are placed on the attachment line the transition occurs for $\overline{R}^* \geq 250$ when the ratio k/η is higher than 2, k being the height of the roughness and η* the characteristic length given by $\eta^* = (\nu_e^*/du_e/dx)$ on the attachment line.

For lower values of k/η* the transition occurs for higher values of $\overline{R}^*$ as shown in **figure 36**.

When the roughness elements are placed off the attachment line higher values of $\overline{R}^*$ are needed to trip the boundary layer. In other words, for a constant value of $\overline{R}^*$, the minimum roughness height which is necessary to trigger transition increases when its location moves downstream of the attachment line. Thus the attachment line is the location where a laminar boundary layer is the most sensitive to roughness elements. A complete analysis of these experiments can be found in Arnal et al [21]

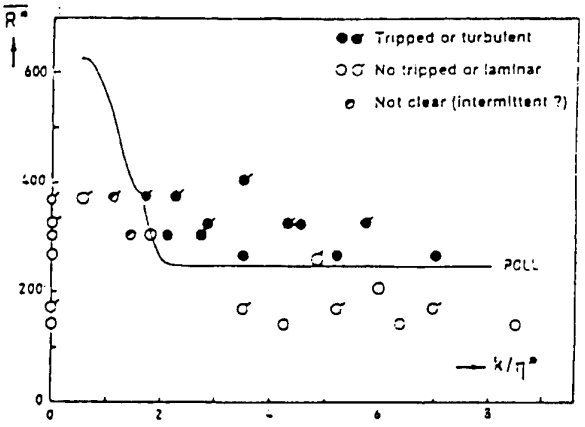


FIGURE 36 - Roughness effect on the attachment line boundary layer

6. AIR INTAKE AERODYNAMICS

An another major issue for the next supersonic transport aircraft is the air intake performance since a one per cent loss in the pressure recovery at Mach 2 would give a penalty of two per cent for the payload.

6.1 Main parameters

The role of the air intake is to reduce the flow velocity from Vo to a subsonic value V2 at the compressor face, with the minimum total pressure losses.

This velocity V2 (and the corresponding Mach number M2) can be expressed as functions of Mo and of the altitude Z if the rotational speed N is kept constant at its maximum continuous value Nmax and by choosing a maximum value for M2 for an extreme flight condition (M2 max=0.55 for Mo=0.5 and Z ≥11 kms).We then obtain the law M2=f (Mo) plotted in **figure 37**. Taking this law and a typical intake pressure recovery law is as the one plotted in **figure 38** allow the mass flow ratio m_R and the A_{CO}/A_E ratio to be computed as functions of Mo as shown in **figure 39**.

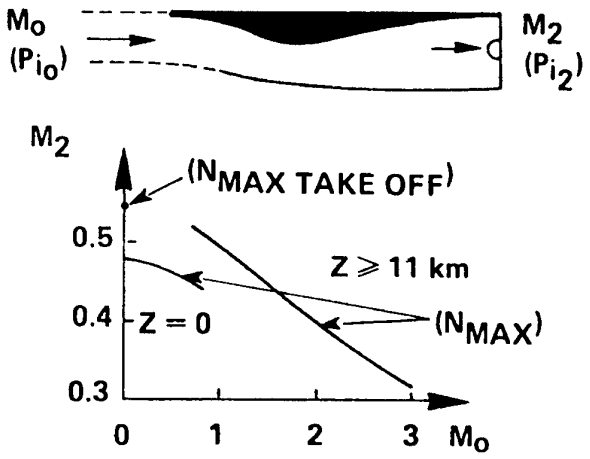


FIGURE 37 - Compressor face Mach number versus Mo and Z

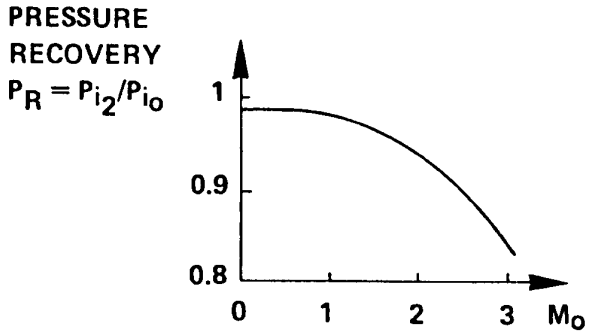


FIGURE 38 - Intake typical pressure recovery law

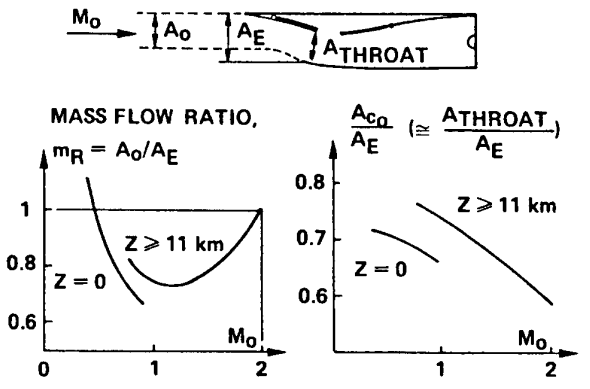


FIGURE 39 - Evolutions of the mass flow ratio and of the throat section with Mo (M=2. Design)

The variation of A_{co} (the critical section for the inflow which is close to the value of the internal throat section A_{coL}) with Mo shows the need for a variable throat section and the figure gives the magnitude of this variation. When the Mach number is lower than the cruise value (2 in the figure), the decrease of the ratio A_o/A_E indicates the amount of the flow which has to be deviated upstream of the air intake. This gives a drag penalty which can be reduced by using an internal by-pass. This is the solution adopted for the Mid Tandem Fan engine (MTF). The by-pass ratio must be kept at a small value in order to avoid a too large increase of the engine diameter which would increase the drag. Thus at subsonic speeds auxiliary air intakes are necessary to increase the mass flow needed by the engine (**figure 40**).

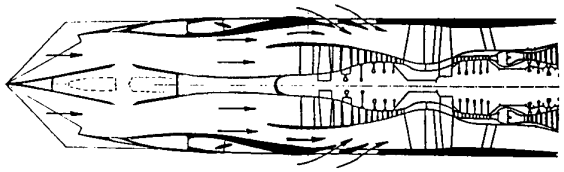


FIGURE 40 - Mid Tandem Fan engine

6.2 Concorde air intake

Figure 41 presents the scheme of the Concorde air intake with a description of the flow for the cruise conditions (M=2). The external compression of the flow is given by two ramps. The second ramp is movable in order to allow the throat section to vary. The Mach number at the entry plane is about 1.4. The cawl which has an angle of 12° at the lip generates a curved oblique shock wave which interacts with the free jet surface of the internal boundary layer bleed. This interaction gives an expansion zone which ends by a straight shock.

The boundary layer bleed collects a part of the wing boundary layer as well as the boundary layer which develops on the ramps, thus increasing the efficiency of the diffuser located downstream.

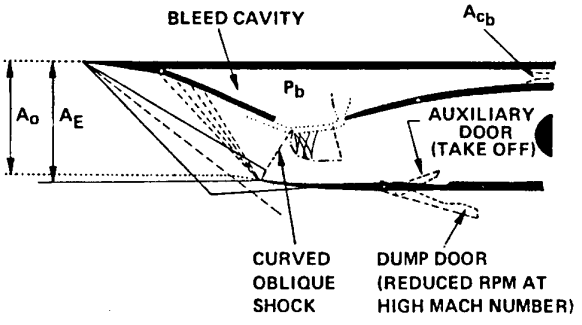


FIGURE 41 - Concorde air intake

The bleed is also very important for the air intake operating behaviour as shown in **figure 42**.

When the engine mass flow is reduced, the other parameters being kept constant, the flow which cannot enter the engine goes in the bleed and the pressure Pb increases.

The air intake operating condition starting for example from supercritical becomes critical.

The pressure recovery being about the same for these two conditions, it means that the nominal operating condition can be a little bit supercritical. The margin between this condition and the critical one is then used as a stability margin. If the engine mass flow is further decreased, the bleed pressure Pb will exceed a certain value and the oblique shock wave will be no more attached to the lip and the air intake will enter in the subcritical operating conditions.

The increase of the bleed flow exhaust throat area Acb, keeping the other parameters constant, leads first to a decrease of the value of Pb without any variation of the bleed mass flow. Thus the intake operating condition goes from critical to supercritical for the same engine mass flow. It is then possible to decrease the engine mass flow which will increase the bleed mass flow and the pressure Pb and to find again the critical operating condition.

A larger stability margin is thus obtained if the bleed flow exhaust throat area Acb is increased when the engine mass flow is reduced that is to say when the pressure Pb increases. This is automatically performed on the Concorde air intake. More details about the Concorde air intake can be found in [22] [23].

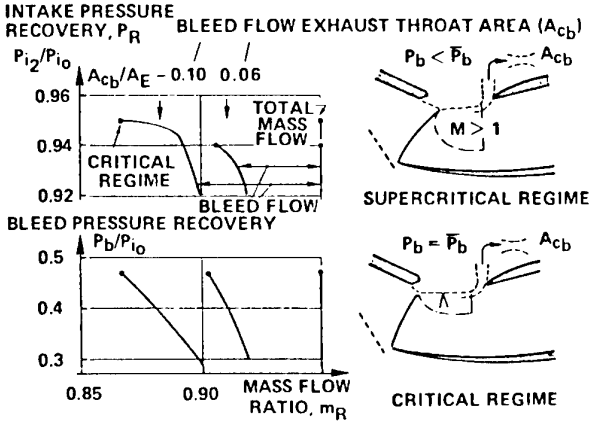


FIGURE 42 - Intake pressure recovery and bleed flow characteristics

This air intake was optimised through intensive wind tunnel testing. It exhibits very good performances in term of efficiency, stability and control. For the future SCT aircraft the objective is to have the same performances together with a reduction of the external drag. This can be achieved by increasing the internal compression and thus using mixed type compression air intake like those shown in **figure 43**. This type of air intake has low cawl drag but suffers from low margin between the adaptation and unstart phenomena. To increase this margin an advanced control system will be needed.

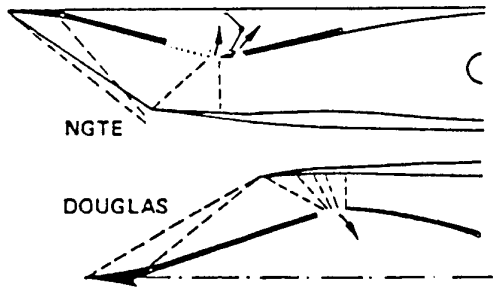


FIGURE 43 - Examples of mixed compression air intakes

6.3 Air intake performances prediction

The two ONERA Euler/Navier Stokes codes developed at ONERA are currently used for air intakes aerodynamic studies. The first one (CANARI code) which uses a centred scheme has already been described in a previous section of the paper. The second one (FLU3M code) is a finite volume, cell centred code which uses an upwind scheme with MUSCL extrapolation and has a second order accuracy in space on regular meshes [22]. Van Leer, minmod and other limiters are available in order to satisfy Total Variation Diminishing condition. For viscous calculations, Roe's scheme is used together with Harten correction and minmod limiter. An ADI factorisation technique is applied for implicit time stepping.

A generic 2D simple compression ramp air intake model shown in **figure 44a** has been used for parametric studies in the S3 Modane supersonic blow down wind tunnel. Experimental data include wall static pressure distribution, and detailed pitot probings at various locations.

These data have been used to assess the Euler/Navier Stokes codes. 3D inviscid FLU3M computations were performed at Mach 2 for different operating conditions. **Figure 44b** shows that the computational results exhibit flow features which are close to the ones given by the schlieren picture for the critical regime.

FIGURE 44 - Shematic 2D air intake - CFD codes assessment

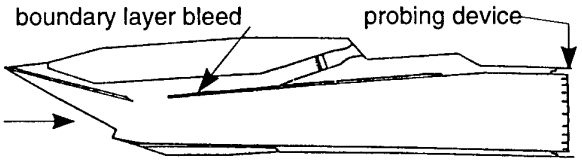
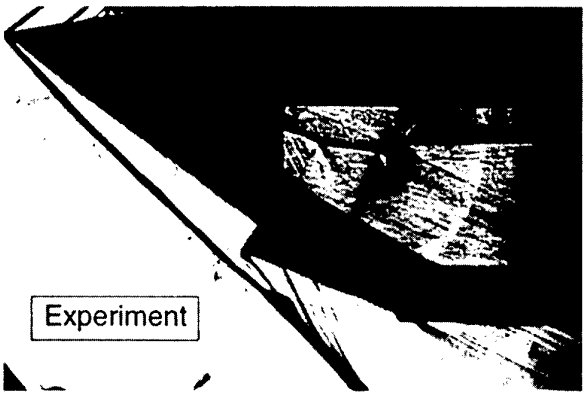


FIGURE 44a - Wind tunnel model



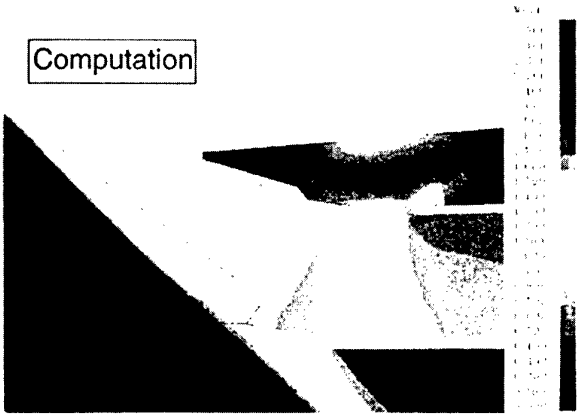


FIGURE 44b - Flow field comparison for the critical regime

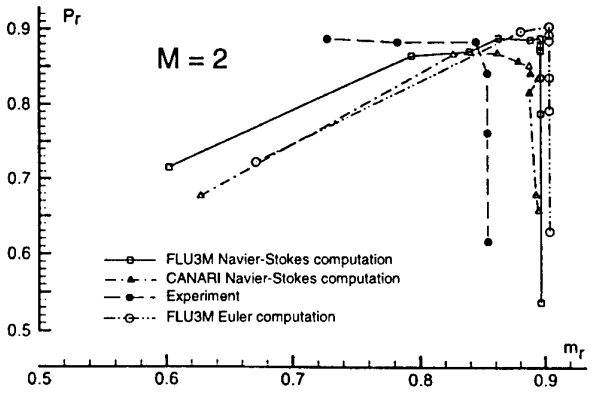


FIGURE 44c - Air intake performance

2D Navier Stokes computations with the Jones-Launder k-ε turbulence model are presented in **figure 44c**. The pressure recovery is quite well predicted with both codes but the mass flow is over predicted due to the lateral flow spillage which is not accounted for in these 2D computations. The total pressure profiles plotted in **figure 44d** show that the codes predict the pressure profile quite well at the end of the diffuser.

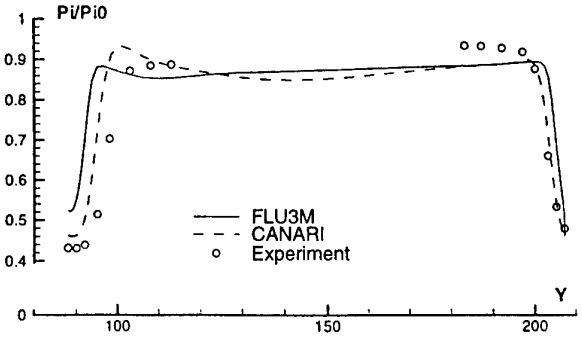


FIGURE 44d - Total pressure profiles at the end of the diffuser

For a cruise Mach number of 2.4 which is also being investigated by the manufacturers, axisymetric air intakes provide some advantages compared to 2D geometries. For this Mach number mixed compression air intakes are needed in order to avoid too large a cowl drag. Such an air intake, designed by Aerospatiale, has been computed with the FLU3M code and the results are presented in **figure 45**. The flow field for the critical regime shows that the supersonic compression is achieved both by the centerbody and the internal cowl, the subsonic compression taking place inside the diffuser downstream of the inlet throat.

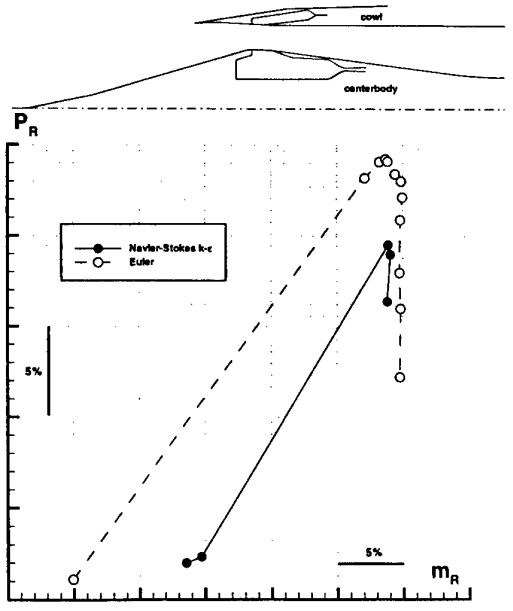


FIGURE 45 - Axisymetric mixed compression air intake Performance prediction at M=2.4

The operating characteristic curves obtained from Euler and Navier Stokes computations are plotted in **figure 45**. Both calculations indicate that there is no stability margin as expected for this type of air intake. The maximum pressure recovery predicted by Navier Stokes calculations is clearly lower than the inviscid value because the unstart of the inlet occurs earlier in viscous flow. An increase of the bleed flow would likely increase the efficiency computed in viscous flow.

6.4 Air intake shock control

Mixed compression air intakes need a control system to provide sufficient margins between the design operating conditions and the unstart of the inlet. This will probably be achieved with internal boundary layer bleed(s) located on the compression ramp side and with a passive or an active shock boundary layer control device located on the cowl side. To design such a control system CFD and experiments will be used. On the experimental side detailed measurements are needed to provide a better understanding of the flow which will help in its modelisation. This is presently being done on a special test rig shown in **figure 46a**.

A supersonic nozzle delivers an upstream flow at a Mach number of 1.3/1.4 which is representative of the Mach number ahead of the last compression shock in the real air intake. The location of this shock can be adjusted with the throat located downstream. The test rig allows various geometries of the main boundary layer bleed to be tested and different shock control systems can be mounted on the upper side of the channel. Detailed flow field measurements can be performed with five holes probes and LDV. **Figure 46 b** shows an example of the flow field obtained with 2 independent suction areas through porous plates mounted on the opposite side of the main boundary layer bleed.

FIGURE 46 - Test set up for basic studies of air intakes



FIGURE 46a - Test rig

When increasing the Number of independant suction chambers while keeping the same suction mass flow the efficiency is increased as shown in **figure 46c**.

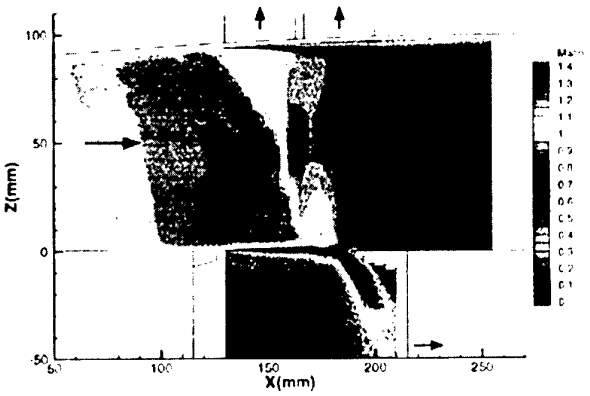


FIGURE 46b - Detailed flow measurement

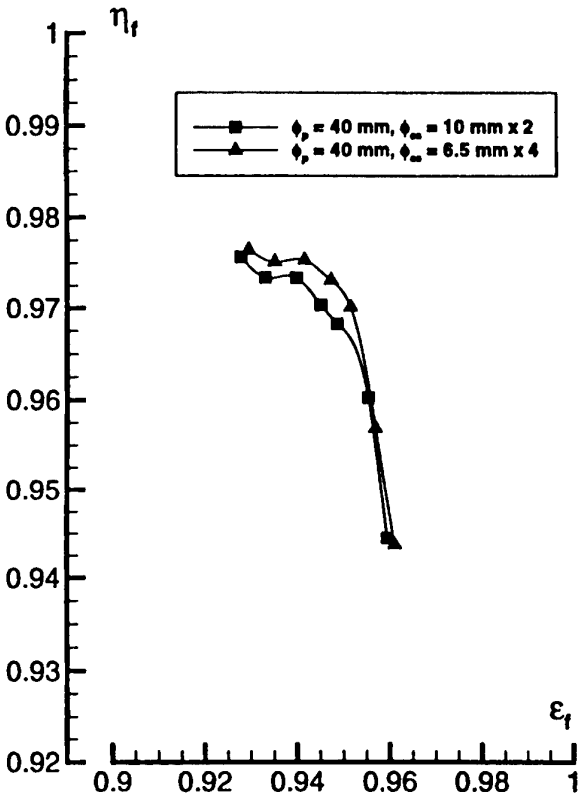


FIGURE 46c - Effect of the suction on the efficiency

Due to the great number of parameters to be investigated for the design of such a control system CFD will certainly be useful but unsteady, time accurate 3D Navier Stokes codes are needed. These codes are under development at ONERA and **figure 47** presents an example of unsteady 2D Euler computations using the ALE technique [23] for the simulation of a quick change of the mass flow rate of a 2D air intake.

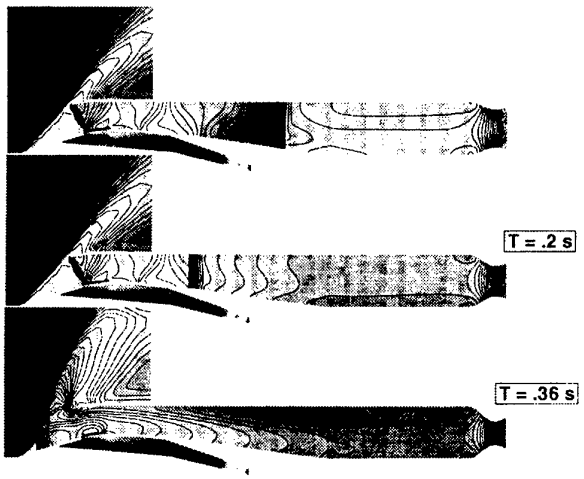


FIGURE 47 - Unsteady 2D Euler computations

6.5 Auxiliary air intakes

To improve the transonic cruise efficiency a bypass engine will probably be used for the future SCT aircraft but the bypass ratio will be small in order to reduce the engine diameter.

Thus, auxiliary air intakes will be used in order to increase the engine mass flow at subsonic speeds. The secondary flow passing through the fan will come both from the main air intake and from the auxiliary air intakes (**figure 40**).

In order to provide the fan with a flow having a high pressure recovery and low distortion, a careful design of the shape of these auxiliary air intakes is needed. This design has also to take into account geometrical constraints and has to be such that the nacelle drag is not increased too much. **Figure 48** illustrates how CFD can help in the design of these air intakes. The figure compares flow fields computed in 2D with the Navier Stokes CANARI code on three different axisymetric geometries (two flush inlets and a scoop inlet). The flush inlets have different curvature laws for the internal lip which generate more or less acceleration. The scoop inlet which exhibit a higher cross section allows to increase the fan mass flow compared to the flush inlets.

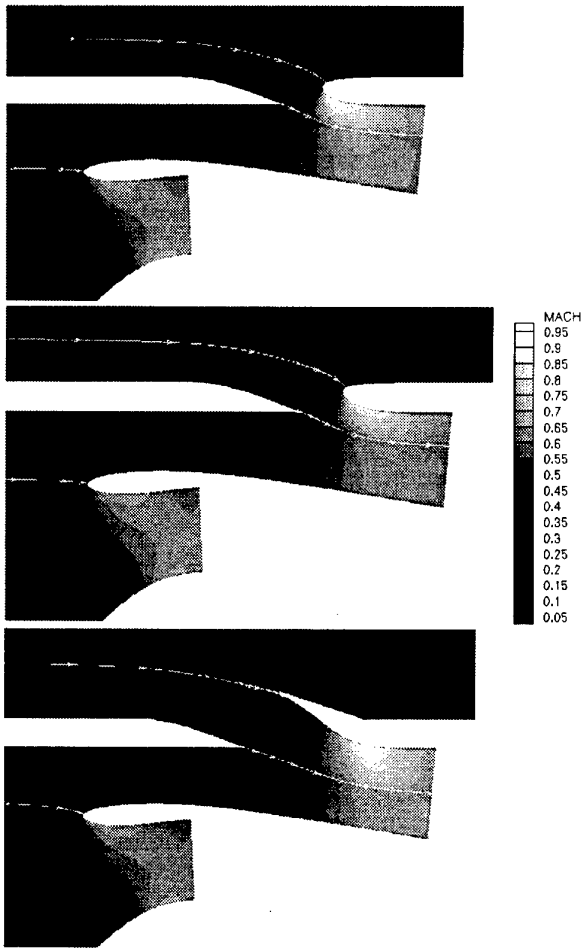


FIGURE 48 - Auxiliary air intakes - Computed flow field

7. CONCLUSION

During these last few years ONERA activities on supersonic transport aircraft aerodynamics have been oriented towards CFD code assessment for performance prediction and in particular for the drag, the development of numerical optimisation tools for multipoint designs, drag reduction technology investigation and air intake aerodynamics.

From these studies the following conclusions can be drawn :

- Euler and Boundary Layer codes are able to predict the general feature of the flow around supersonic transport aircraft configurations for all the flight conditions. The accuracy concerning the drag prediction is quite satisfactory for supersonic cruise but not so for transonic cruise. At low speed and high angle of attack Euler codes exhibit two much artificial dissipation.

- The degree of accuracy needed for the prediction of the drag of this new aircraft needs further improvement of the Euler codes and the assessment of other codes like coupled codes and Navier Stokes codes.

- Measurements of skin friction coefficient on a Concorde aircraft have been compared to an empirical skin friction law and to 3D boundary layer computations. The analysis has pointed out the better accuracy of the 3D boundary layer computations. However complementary work will be needed since one could question the validity of two-layer method or mixing length scheme at very high Reynolds number values.

- Numerical optimisation techniques have proven to be efficient for multipoints designs but they suffer from too large computing time and thus new algorithms have to be developed to reduce this computing time.

- Drag reduction technologies which have been extensively investigated for subsonic transport aircraft can also be used for supersonic aircraft. While riblets seems to be promising, laminar flow control provides small gains at least for the actual wing designs. Specific laminar designs are needed to evaluate the potential benefit but also to see if such designs are practical. Anyhow difficult technical problems will have to be solved for laminar flow control applications.

- The final adjustment of the research quiet tunnel which is being done will alow to perform basic research on Laminar Supersonic Flows.

- Experiments on a swept cylinder and on a swept wing have shown that the leading edge contamination occurs is supersonic Flow for $\overline{R}^*$ values greater than 250 and that roughness height which is necessary to trigger the transition increases rapidly when its location moves off the attachment line.

- CFD tools are able to predict correctly air intake performances near adaptation. They have still to prove their capacity for off design performance prediction as well as for shock control system designs which are needed for mixed compression air intakes.

- Basic experiments on internal air intake flow are being performed in order to improve the ouderstanding of the boundary layer bleed behaviour and in order to investigate shock control devices which can be used for mixed compression air intakes.

- Comprehensive wind tunnel test are needed both for external and internal aerodynamic studies in order to get more confidence in using the CFD tools and also to better understand complex flow mechanisms.

ACKNOWLEDGEMENTS

The author would like to thank D. ARNAL, D. BARBERIS, E. COUSTOL, D. DESTARAC, Ph. DUVEAU, R. GRENON, P. LEMEE and R. THEPOT for providing results presented in the paper and also E. COUTURE and B. GUERIN for the preparation of the manuscript.

The author would also like to thank Aerospatiale and SPAé (Service des Programmes Aéronautiques) for giving the authorization to publish some of the data presented in the paper.

REFERENCES

[1] - VUILLOT A.M., COUAILLER V., LIAMIS N.
"3D turbomachinery Euler and Navier Stokes Calculations with a multidomain cell-centred approach".
AIAA paper 93-2576, Monterey, 1993.

[2] - LERAT A., SIDES J., DARU V.
"An implicit finite volume method for solving the Euler equations. "
Lecture notes in Physics. Vol. 17, pp 343-349, 1982.

[3] - JAMESON A., SCHMIDT W., TURKEL E.
"Numerical solution of the Euler equations by finite volume methods ."
AIAA paper 81-1259, 1981

[4] - HOUDEVILLE R.
"Three-dimensional boundary layer calculation by a characteristic method using Runge-Kutta time stepping schemes."
5th Symposium on Numerical and Physical Aspects of Aerodynmic Flows, Long Beach, January 1992.

[5] - COUSTOLS E. and ARNAL D.
"Skin friction Prediction and reduction".
International CFD Workshop for Supersonic Transport Design, Tokyo, March 1998.

[6] - THIBERT J.J.
"One point and multi-point design optimisation for airplane and helicopter application."
AGARD FDP/VKI Special course on Inverse Methods for Airfoil Design for Aeronautical and Turbomachinery Applications. AGARD report n° 780 paper n° 10.

[7] - DESTARAC D., RENEAUX J.
"Applications de l'optimisation numérique à l'aérodynamique des avions de Transport."
La Recherche Aerospatiale, 1993 n° 2 p. 39-55

[8] - VANDERPLAATS Garret N.
"CONMIN- A fortran Program for Constrained Function Minimization".
NASATMX 62, 282 - August 1973.

[9] - VANDERPLAATS Garret N.
"COPES - A Fortran Control Program for Engineering Synthesis."

[10] - GRENON R.
"Numerical Optimization in Aerodynamic Design with application to a Supersonic Transport Aircraft".
NAL International Workshop on Supersonic Transport Design, Tokyo, March 1998

[11] - RENEAUX J., THIBERT J.J., SCHMITT V.
"ONERA activities on drag reduction"
ICAS paper 90-3.6.1

[12] - SCHMITT V., HINSINGER R.
" Advanced transport aircraft aerodynamics in cooperation with Airbus Industrie".
La Recherche Aerospatiale, 1996, n° 4, p. 265-277.

[13] - COUSTOLS E., SCHMITT V.
"Synthesis of experimental Riblet studies in transonic conditions in Turbulence Control by passive means"
COUSTOLS E. Ed, Klumer Academic Publisher, 1990

[14] - COUSTOLS E. and COUSTEIX J.
" Performances of riblets in the Supersonic regime"
AIAA JOURNAL, VOL 32, n° 2. Technical notes.

15] - ARNAL D.
"Transition prediction in transonic flow"
IUTAM Symposium Transsonicum III. DFVLR - AVA Göttingen 1988.

[16] - COUSTOLS E.
"Stabilité et transition en écoulement tridimensionnel : cas des ailes en flèche."
Thèse de Docteur-Ingénieur ENSAE (Juin 1983).

[17] - ARNAL D.
"Boundary layer Transition predictions based on Linear Theory."
AGARD FDP/VKI Special Course on Progress in Transition Modelling - AGARD Report n° 793.

[18] - RENEAUX J., PREIST J., JUILLEN J.C., ARNAL D.
"Control of attachment line contamination."
2nd European Forum on Laminar Flow Technology.
Bordeaux (France), June 10, 1996 - ONERA TP 1996-84.

[19] - ARNAL D.
"Etude des possibilités de réduction de Traînée par laminarisation."
7th European Aerospace Conference EAC 94 Toulouse,
October 1994.

[20] - PAPIRNIK O., RANCARANI G., DELERY J., ARNAL D.
"Conception et qualification de la soufflerie silencieuse R1Ch de l'ONERA".
AGARD Conference on Aerodynamics of wind tunnel circuits and their components. MOSCOU 30/9 - 3/10, 1996
ONERA TP 1996-175

[21] -ARNAL D., LABURTHE F.
"Recent supersonic transition studies with emphasis on the swept cylinder case".
Conference on Boundary layer Transition and Control. Cambridge, April 1991.

[22] - LEYNAERT J.
"Transport Aircraft intake design"
VKI - Lecture series 1988-04 Intake aerodynamics - ONERA TP 1988-18.

[23] - LEYNAERT J.
"Les prises d'air et arrière-corps de moteur des avions subsoniques et supersoniques. Eléments généraux."
25e colloque d'Aérodynamique Appliquée, Talence, October 1988 ONERA TP 1988-132.

[24] - CAMBIER L., DARACQ D., GAZAIX M., GUILLEN Ph., JOUET Ch., LE TOULLEC L.
"Améliorations récentes du code de calcul d'écoulement compressible FLU3M."
AGARD Séville, Espagne 2-5 Octobre 1995.

[25] - THIERRY G.
"Simulations d'écoulements de fluides parfaits autour de corps déformables. Applications à l'aéroélasticité des lanceurs."
Thèse de doctorat de l'Université de Paris Nord, 1998.

Aspects of Wing Design for Transonic and Supersonic Combat Aircraft

B. Probert, Aerodynamics Department (W310P)
British Aerospace, MA&A, Warton, Lancashire, PR4 1AX England

SUMMARY

This paper describes some aspects of high speed design, mainly wing design, for combat aircraft. This is done by first reviewing the fundamental features and problems posed by high speed transonic and supersonic flow and the means of alleviating them. The resulting empirical / simple rules and methods allow an initial baseline configuration to be developed which is further optimised using the most appropriate design processes - involving the use of a number of CFD codes, which are described. Each process is then illustrated by briefly considering the design of four types of high speed aircraft each optimised for a different, but overlapping, flight envelope The current need for processes to treat the design of novel configurations which have low observabilty is mentioned and finally current ways of working are reviewed and suggestions made for future developments in the areas of design processes, aerodynamic improvements/fixes and the potential of new physical phenomena.

INTRODUCTION

This paper considers certain aspects of wing design related aerodynamics for subsonic, transonic and supersonic flow. The authors experience lies in the field of military aircraft design and the contents will obviously reflect this fact but some of the broad descriptions and conclusions will also relate to commercial aircraft applications.

A major difference between military and civil aircraft design lies in the greater number of design requirements, viewed in the (M,C) plane, to be achieved by the military configuration. It is not possible to concentrate too much effort on a single design point e.g. altitude cruise, at the expense of other important considerations e.g. turn rates, low altitude high speed dash etc. The design thus becomes a search for the best compromise - or better, the best balanced configuration which comes closest to meeting the overall objectives. At the extremes of the configuration range we have the unswept wing which is usually limited to subsonic flight and much of its characteristics can be described by appealing to two dimensional aerofoil properties. Years of experience with this type of aircraft both in flight and experiment means that flow features are well understood. At the other end, for sweeps beyond 60°, the flow features though very different are still orderly with concentrated vortical flow being the dominant feature at low speed and swept shocks with vortex separation at high speed. At supersonic speeds available theories hold reasonably well for the attached flow condition. However this class of aircraft has poor airfield performance and high lift dependent drag. The above shortfalls i.e the subsonic performance of unswept wings and the poor manoeuvrability and field performance of highly swept wings means that the designer may need to look at the intermediate sweep region, 20° to 60°, with all the associated mixed flow complexities in order to obtain the balance which he is seeking.

It should also be mentioned that the term 'balance' relates to the mix of aerodynamic performance and the overall weapons system capability. The aim is to maximise aircraft agility, defined as efficiency of the weapon system as a whole (ref. 1). In this context aerodynamic efficiency plays only a part since 'agility' brings in many other disciplines. The search for aerodynamic efficiency and controllability will form the main subject of this paper.

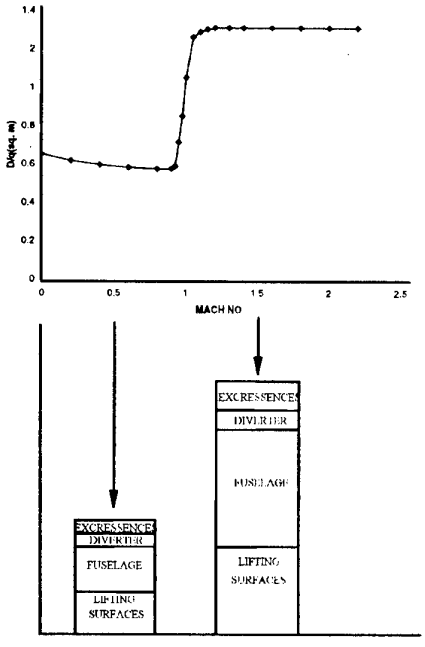
The theme will be to review the fundamental features of high speed flows, the problems posed and the means of overcoming them by configuration choice and detail design. Such design work depends heavily on available methods and procedures and a section is devoted to briefly cover examples of CFD capability. The general problems which emerge will feature to various degrees depending on the precise operating requirement of a particular aircraft. Here this is illustrated by breaking the problems down to four flight regimes and considering the detail wing design of an aircraft in each. Finally, current and future trends which may strongly influence aerodynamic progress are mentioned.

SOME FUNDAMENTAL FEATURES OF HIGH SPEED FLOW

From the aircraft performance viewpoint it is worth considering the gross effect of various wing geometric parameters on the flow development, but first we look at the broad effect of supersonic flow on the configuration drag.

A drag breakdown at zero lift for a typical combat aircraft at subsonic and supersonic speeds is shown in fig. 1.

Fig 1 - Typical Variation of Drag with Mach Number Combat Aircraft

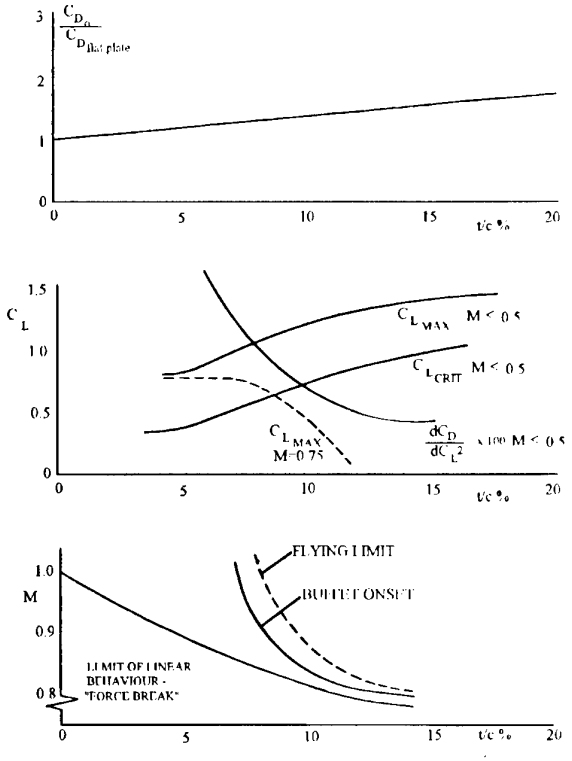


Paper presented at the RTO AVT Course on "Fluid Dynamics Research on Supersonic Aircraft", held in Rhode-Saint-Genèse, Belgium, 25-29 May 1998, and published in RTO EN-4.

The dominant increase at supersonic speeds is due to the wave drag component consisting of fuselage, lifting surface and interference drag, collectively known as drag due to volume. At lifting conditions the lift dependent wave drag produces a further contribution. At subsonic and transonic speeds the lift dependent drag varies inversely with the square of the wing span, thus maximising span is desirable for manoeuvre performance whilst at supersonic speeds the lift dependent drag is strongly influenced by the longitudinal area distribution. Typically the wing contribution to zero lift wave drag on a combat aircraft is in the region of 25% and this contribution is dominated, for a given sweep, by the wing thickness as supersonically the drag varies with the square of the thickness to chord ratio.

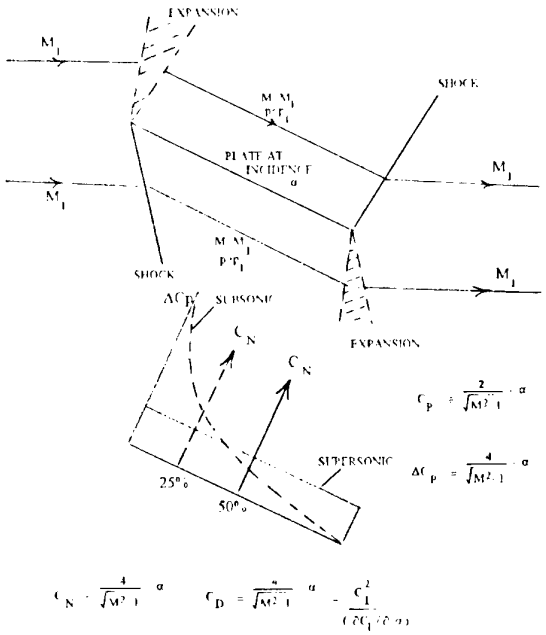
However an increase in thickness at low subsonic speeds is often beneficial, increasing maximum lift, but as speed increases eventually becomes detrimental as shock waves begin to form leading to drag rise, separation, buffet and eventually shock stall. Typical boundaries for the above are shown in fig. 2.

Fig 2 - Effect of Aerofoil Thickness on Various Characteristics



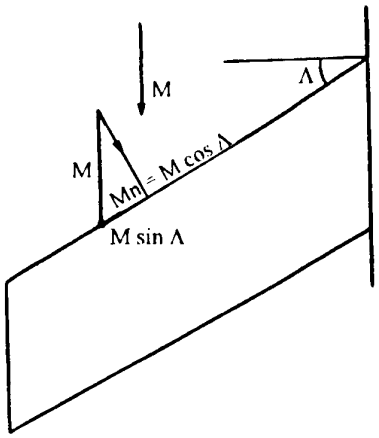
Another significant effect of increased speed is the change in pressure/ loading over the lifting surface leading to a rearward shift in the aerodynamic centre position. This is illustrated simply by looking at the 2D flat plate development in supersonic flow in fig. 3.

Fig 3 - Lift Development in Subsonic and Pure Supersonic Flows



For the subsonic case the distribution has the classic LE suction type of distribution which results in a centre of pressure at 25% chord. For the supersonic LE condition this is absent and for the 2D case leads to a centre of pressure position at 50% chord. For a practical 3D configuration the a.c. shift lies in between these extremes.

Fig 4 - Swept Wing Relationships

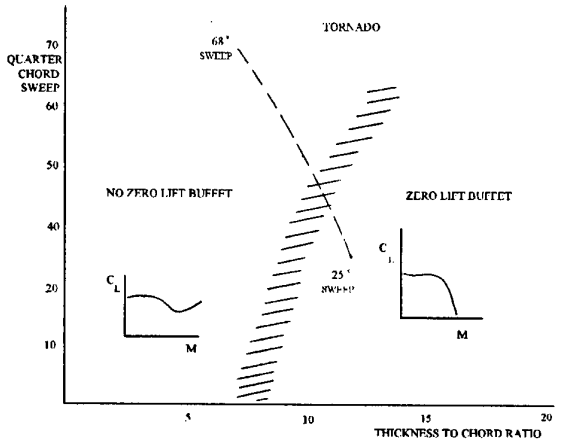


3D Quantity	Value for Equivalent 2D Aerofoil	2D Symbol
M	M cos Λ	M_n
C_L	$C_L \sec^2 \Lambda$	C_{Ln}
C_P	$C_P \sec^2 \Lambda$	$(C_P)_n$
α	$\tan^{-1}(\tan \alpha \sec \Lambda)$	
$C_{DPRESSURE}$ (t/c)	$C_{DPRESSURE} \sec^3 \Lambda$ (t/c) sec Λ	$(C_{DPRESSURE})_n$ $(t/c)_n$

The effect of thickness can be obviated by the incorporation of wing sweep which works by reducing the component of Mach number normal to the leading edge, since it is the normal component which leads to shock development and problem regions. From this 2D to 3D simple sweep relationships can be derived as shown in fig. 4. These are often useful in the early stages of design.

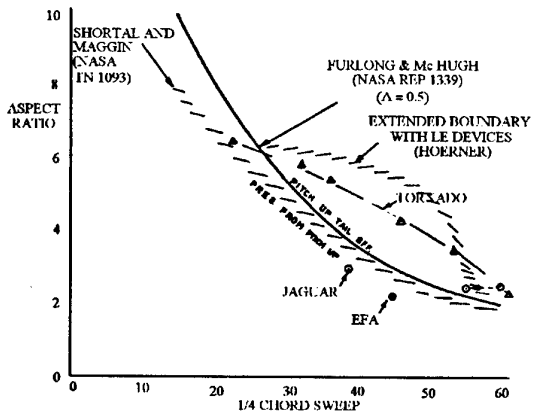
Combining thickness and sweep effects one can derive the boundaries shown in fig. 5 where it is interesting to note that to obtain a transonic 'corridor' whereby the aircraft can fly from subsonic to supersonic speeds the maximum wing thickness must be less than 7 %.

Fig 5 - Combination of Sweep and Thickness



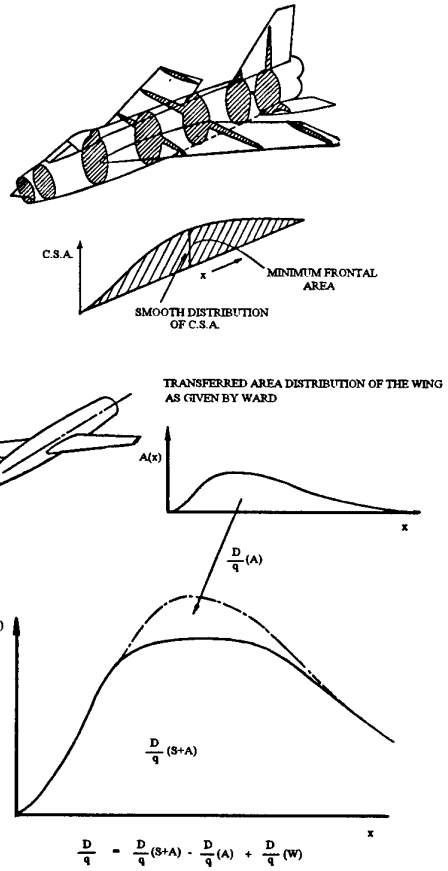
However sweep cannot be increased without eventual detrimental effect on other aerodynamic parameters, notably longitudinal stability. Increasing sweep increases the loading on the outer wing leading to flow separation, possible loss of lift in that region and eventually to pitch up. An useful guide to the limit on sweep as a function of wing aspect ratio is shown in fig 6. The designer transgresses this boundary at his peril in the early stages of design but, as the figure shows, a properly positioned tailplane and/or a powerful LE device may allow the nominal boundary to be exceeded. However both of these options will need detail development. Further the correlation was developed from a large data base of conventional wing planforms Its application to novel LO configurations is not yet established but should still serve as an initial guide.

Fig 6 - Pitch-up Boundaries



The above examples are extremely well known and do form the basis of initial project considerations for a conceptual design. Starting the detail design from a realistic base is obviously the sensible approach. The first approach to detail design lies with the improvement of the longitudinal volume distribution using supersonic area rule type methods. A number of variants are available, the approach adopted in Fig. 7 is based on a transfer of area rule and has been in use at MA&A for many years. The basic concept is to minimise the streamwise slopes of the cross sectional area distribution and the method is based on far field integration of the wave drag. This approach has been very successful over the years and still forms the corner stone of initial project design work.

Fig 7- Shaping for Supersonic Flight and The Supersonic Area Transfer Rule



The author apologises that the above is rather simplistic but does serve to illustrate that the basic features of high speed flow need to be considered at the outset of a project design layout. What follows is a description of the various procedures for refining the design. This calls for reliable design methods and before describing each procedure it is worth considering the computational methods available to the designer.

COMPUTATIONAL METHODS

The tremendous advances in CFD methods over the last 20 years have exerted a powerful influence on aircraft design capability. Instances of application are too numerous to mention so I will confine myself to specific illustrations to emphasise certain aspects of design. As already mentioned,

supersonic area rule methods, based on linearised theory have been available for over 40 years and still provide useful design guidelines. Linearised theory lifting surface methods have played, e.g. Refs. 2, 3, and still play, a large part in aircraft design with each firm having their own, possibly in house developed, favourite. Inverse versions of such methods, where the geometry is derived from a specified loading or pressure distribution, are easily derived. Such methods have been coupled with empirically derived limits on flow features e.g. limiting LE suction levels and limits on suction levels which could lead to shock formation and separation (Ref 4). Such methods do not consider thickness effects.

So called panel methods, where thickness effects are included, are usually based on the linear Prandtl-Glauert equation with a correction for compressibility when required. These methods have been used at BAe to improve on the far field methods' initial design to increase locally fuselage volume without increasing drag. The panel methods give useful information at low incidences through the Mach number range but all the above methods are not usually classed under the heading of CFD.

This seems to be reserved for methods which solve the non linear flow equations admitting discontinuities i.e. shock waves. The earliest methods considered the small perturbation form of the transonic flow equations. A two dimensional version was coupled with an integral boundary layer method in Ref. 5 and was used for many years as a successful aerofoil design code at BAe. Later, and with a fair amount of ingenuity on the part of the code developers, 3D versions were produced which could tackle complex geometry's, including stores (Ref 6). Such methods, used with care and including special LE treatment, provided good quality results for a number of years. An example is shown for the configuration in fig 8A, a 42° sweep wing-body combination, which is designed to a high standard of wing design. The comparison of the TSP method with experiment is shown in fig 8B and is impressive.

Fig 8A - Swept Wing Body - 42º Sweep, AR=3.3

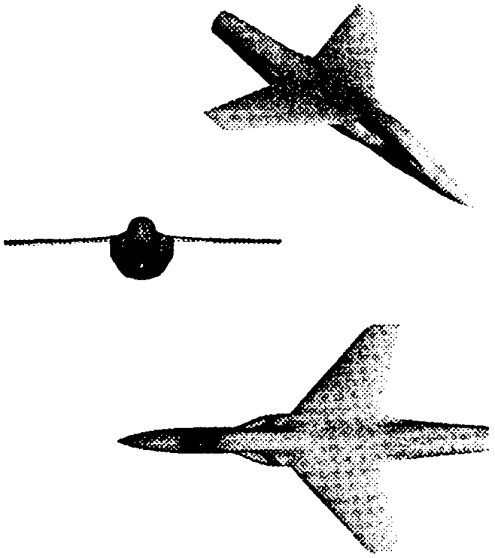
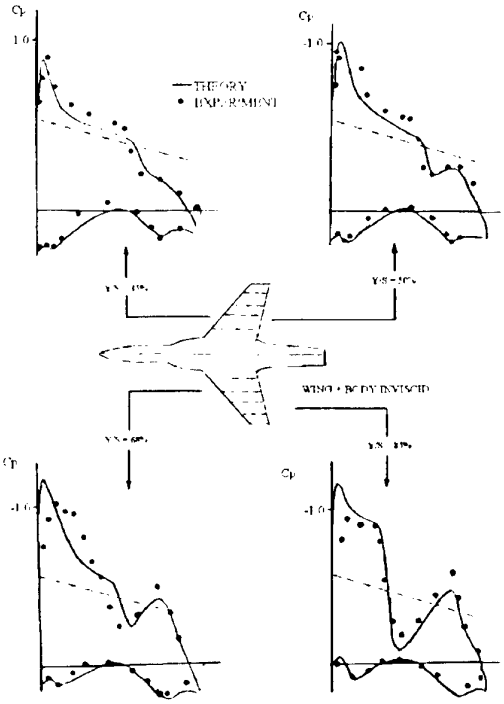


Fig 8B - Comparison of Theory and Experiment
Transonic Small Perturbation Theory
Wing + Body (Inviscid) - M=0.88, a=6.6°



However progress elsewhere, coupled with the need to cover more highly swept planforms, led to the switch to methods which solved the full potential equations. These methods, in highly developed forms, are actively used today particularly for civil aircraft design, where wing sweeps are low and shock waves are weak. Thus the isentropic assumptions are not limiting. Such methods have also provided good results on military configurations (ref 7). Fig 9A shows the configuration and a comparison of the FP result with experiment is shown in fig 9B. at an incidence close to the manoeuvre design point, where we have significant shock strength on the outer wing. Experimental pressure tap data was only available on the wing upper surface. Comparison is very good.

Fig 9A - GA of Model 2091/4

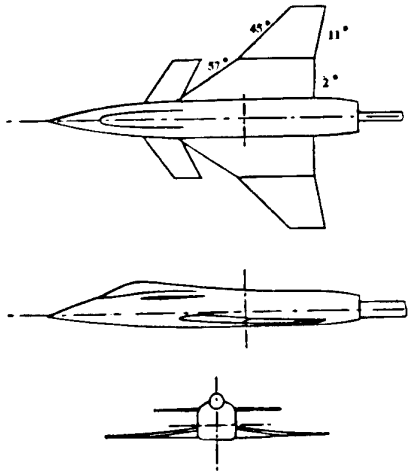
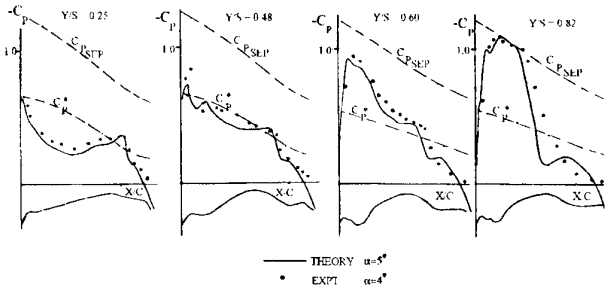
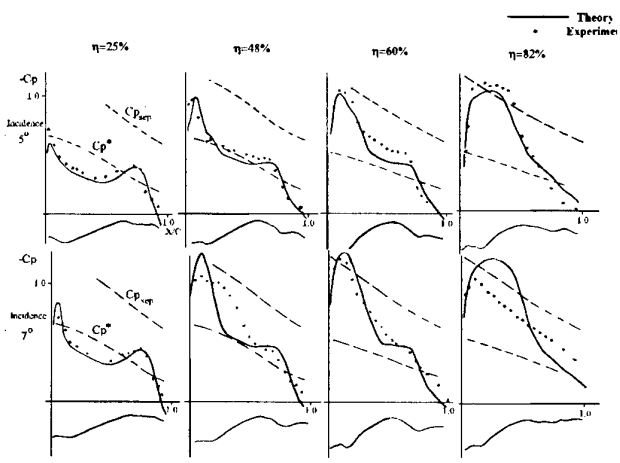


Fig 9B - Theory v Experiment - Full Potential Method Mach 0.9 - Wing + Simple Body



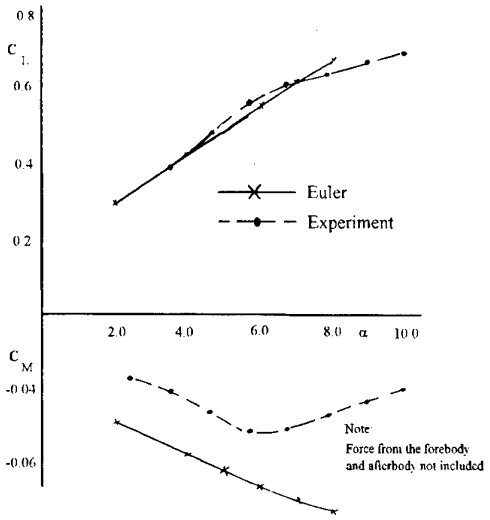
More recently, during the last 10 years and in line with the need for the treatment of stronger shock waves for military aircraft, the development and increasing application of methods based on solutions of the Euler equations have been prominent. These methods have proved to be robust in use and have achieved good comparison with experimental data. Examples for the same configuration as in fig 9A. are shown in fig 10A.

Fig 10A - Theory v Experiment - Euler Method Mach 0.9 - Wing + Body



Even at this higher incidence, with regions of flow separation, the Euler (Ref 8) code gives a reasonable comparison. The code used at the time could only cope with a simple representation of the body, and this led to a poor comparison of the pitching moment data, as seen by the comparison with experimental data in fig 10B. We will return to this point later.

Fig 10B - Comparisons Between Euler Theory and Experiment - M = 0.9 - M2091/4



Further comparisons of Euler at supersonic speeds also gave good results as shown for M=1.1 and 2.0 in figs 10C. and 10D.

Fig 10C - Euler Theory v Experiment Wing + Body - Mach 1.10 α=6

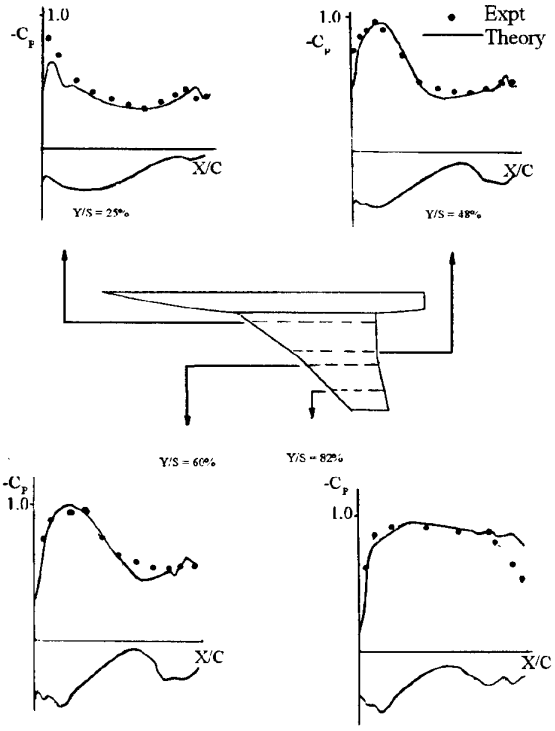
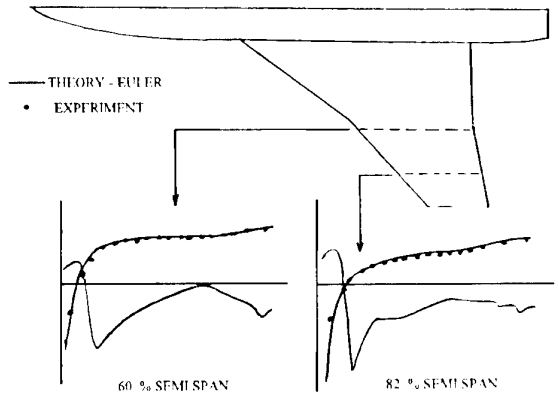


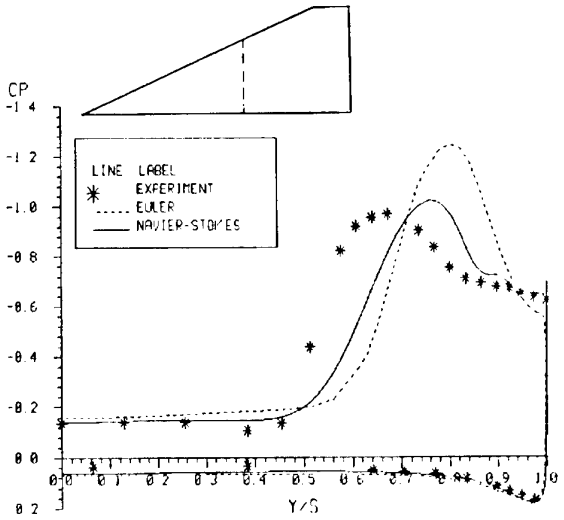
Fig 10D - Supersonic Comparison - Euler v Experiment M=2.0 / α=4°



The need for better treatment of complex geometries led to the development of Multiblock Euler codes for the prediction of vortical flows (Ref. 9). These provide a powerful diagnostic tool and have been used extensively on many aircraft projects. In addition to the complex geometry capability reasonable results have been obtained in the prediction of vortical flows on sharp edges. However care is needed when dealing with rounded leading edges due to grid dependency.

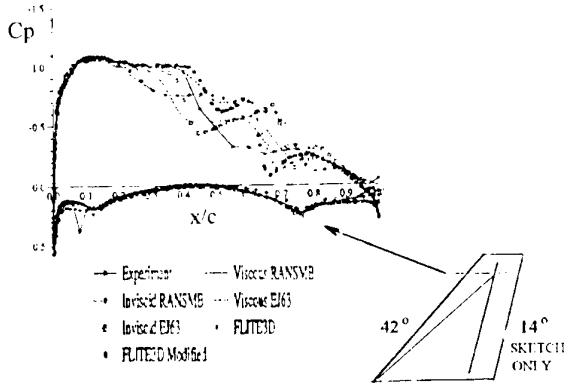
More recent developments have resulted in methods based on the Reynolds time averaged equations with a variety of turbulence models. These have improved the prediction of vortical flows and have also shown promise in the prediction of shock induced separation. A comparison of an Euler and Navier Stokes (Ref 10) solution for a highly swept 65° planform is shown in Fig. 11 The latter solution captures the secondary separation line and moves the attachment line closer to experiment.

Fig 11 - Comparison of Euler, Navier Stokes and Experiment - 65° Wing Sweep Mach 0.85 / α=10°



A fundamental necessity in obtaining good results with such methods is the provision of a suitable computing grid. Again, advances in surface conforming grids on complex configurations via the multi block approach have provided high quality, possibly benchmark, results in many instances. Set up times have been a problem but current developments on 'fast response' unstructured grid codes are now reaching the standard set by the structured codes - for inviscid flow. An example is given in fig. 12 for the wing-body combination shown in fig. 8A at one spanwise station. A number of methods are compared, including a structured grid Navier Stokes method (RANSMB, Ref 11) and an Euler method (with and without viscous coupling). If we add the incremental change in shock position, observed from the Euler results, to the unstructured Euler result (FLITE3D, Ref 12) it promises to give a good match with experiment. Pressure losses due numerical dissipation are also low from this program thus the method shows good potential for future applications.

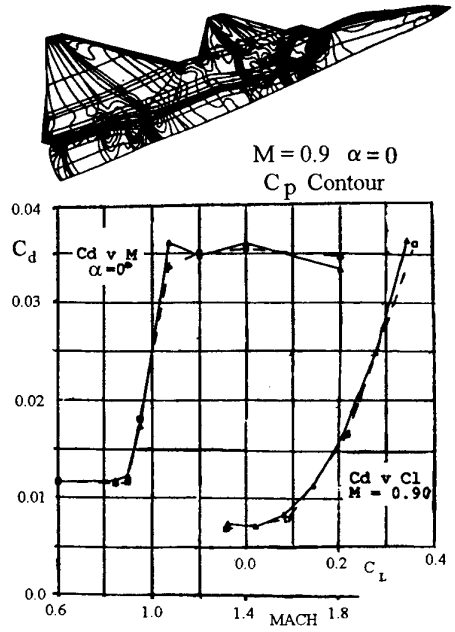
Fig 12 - SMARM Configuration - Mach 0.88 / a=6.6° 68% Station



All of the above types of CFD methods have been used at MA&A over the years with the bulk of detailed design completed using Euler codes with and without viscous coupling. Often the design emphasis is based on achieving a desirable form of upper surface pressure distribution which is likely to produce low drag or good stability characteristics- preferably both.

However, increasingly the prediction of drag from CFD is improving so that reliance on the predicted force data is playing an increasing role in decision making between configurations. In some instances, normally civil configurations, drag accuracy can be improved by considering the far field components of drag-viscous,wave and vortex and thus avoid the notoriously unreliable near field pressure drag integration, plus skin friction. For the more closely integrated military configuration where the body and wing are often blended it is difficult to successfully achieve such a process and resource is often made to direct surface pressure integration. In many instances excellent agreement with experiment has been obtained as shown in fig. 13 for a complex wing - body - foreplane configuration. However the recommended way of proceeding is still to think in terms of using CFD to calculate drag increments due to design changes and applying these to an experimental baseline.

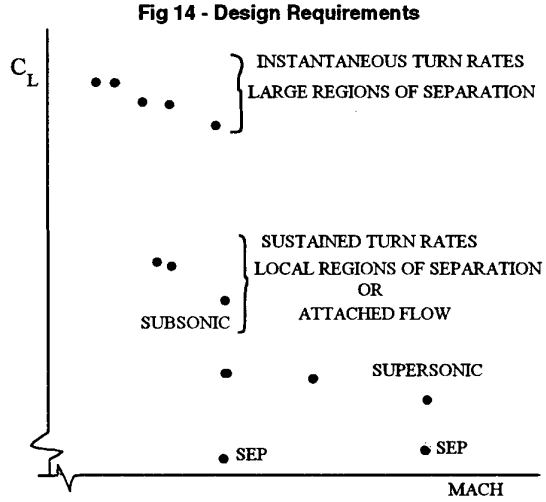
Fig 13 - Example of CFD in Design Euler Multiblock



DESIGN REQUIREMENTS

For a military aircraft these are numerous and a typical set are given in fig 14 which cover both a wide Mach number and lift coeff. range hence emphasising both subsonic and supersonic manoeuvre requirements. The same figure illustrates the type of flows expected and hence the challenge posed to any design method. It is evident that the major part of the flight envelope will have strongly separated flow regions hence calling for extensive low and high speed wind tunnel development in parallel with CFD design activity. Looking at this another way, only a small portion of the envelope is rigorously theoretically predictable.

Fig 14 - Design Requirements



Coupled with these requirements are the constraints set by the capabilities of the flight control system, the need to obtain a stiff low mass structure with adequate spar depth and consideration of installed store interference. These points will have different levels of importance depending on the flight regime covered by the aircraft. For present purposes it is intended to illustrate the different aspects of wing and configuration design by considering four aircraft types -

1	Wing Sweep < 35°	Subsonic aircraft
2	35° < Wing Sweep < 50°	Transonic biased aircraft with moderate supersonic capability
3	50° < Wing Sweep < 60°	Supersonic biased aircraft with very good transonic manoeuvre
4	Wing Sweep > 60°	Supersonic aircraft

The above are very broad classifications and no doubt there will be some exceptions. It is obvious that a variable sweep wing configuration e.g. TORNADO fulfils many of these roles, in the aerodynamic sense, as was intended. However, this was achieved at the expense of weight and cost. The effect of wing loading on STR performance means that it is not classed as an Air Superiority aircraft. The basic design of each of the above will have many common features but the detailed design will be very different. For example, the simple 2D to 3D sweep relations will only play a large role in the design of type 1. and to some extent in type 2. Even in type 2. the role of the 2D section may only be to provide an equivalent form of upper surface pressure distribution. We now consider each design in turn.

THE SUBSONIC WING - but with supercritical upper surface flow.

The example chosen is the minimum sweep of the TORNADO wing (25°) The multi role requirements demanded excellent field performance, good supersonic performance and 'reasonable' manoeuvre performance. The variable sweep wing helps considerably in this respect from the aerodynamic viewpoint. The bulk of the aero design concentrated on wing sweeps between 25° and 45° with fully swept high supersonic cases mainly serving as fallout from the transonic area. The variable sweep greatly alleviates the wing design problem, as the dominant thickness problem is 'taken out' by the sweep effect as shown in fig. 15. Of course the configuration layout reflects strongly the multi role capability of the aircraft. A principal factor is the outboard location of the wing pivot in order to minimise the aerodynamic centre shift as the wing sweeps - fig. 16. The resulting nib fairing acts like a strake improving high incidence performance at low main wing sweeps.

Fig 15 - Tornado - Variation of Thickness to Chord Ratio With Wing Sweep

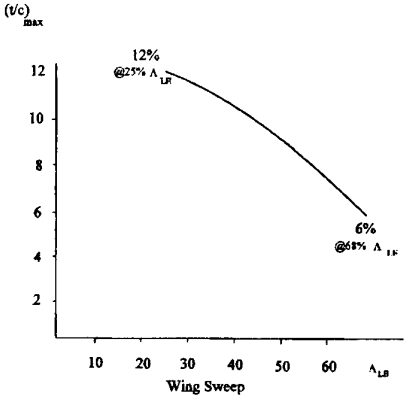
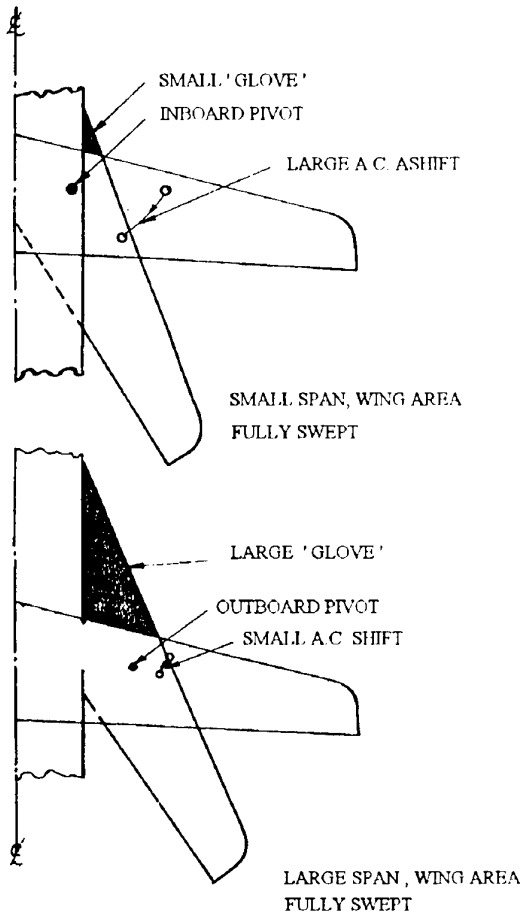


Fig 16 - Effect of Pivot Position on A.C. Shift With Sweep



The wing was sized for a manoeuvre design point and thus demanded powerful high lift flaps and slats for the demanding field performance. In addition high speed combat utilised the slat and some flap (Transonic slat design is still difficult currently even with the best CFD method available). A good standard of design was achieved by combining subcritical theory, empiricism and much wind tunnel data. This demanded a large slat extension at manoeuvre which resulted in a hockey stick track shape to cater for the landing case.

As mentioned the low sweep design cases were based on 2D aerofoil data involving much wind tunnel testing and converting to 3D using geometric sweep concepts. The level of agreement between actual 3D and 2D experimental pressures are shown in fig 17. Agreement is good validating the design approach. Currently such a design would be achieved without resource to 2D test data since CFD codes are adequate for the task. It is worth pointing out the aerodynamic, but not actual, benefit of the VG concept. Fig. 18 shows a comparison of L/D at a high subsonic Mach number compared with a fixed wing. The advantages of increased span are obvious.

Fig 17 - Example of 2D to 3D Pressures Tapered Wing - Mid Semi-span

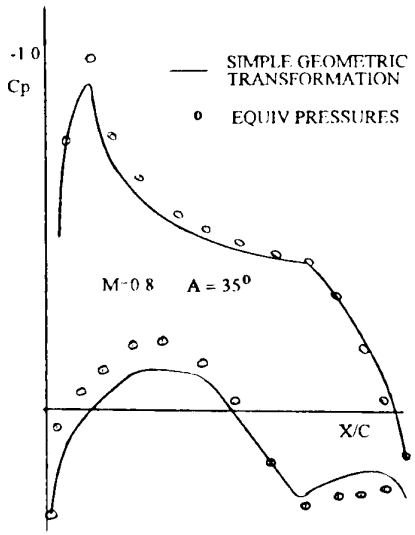
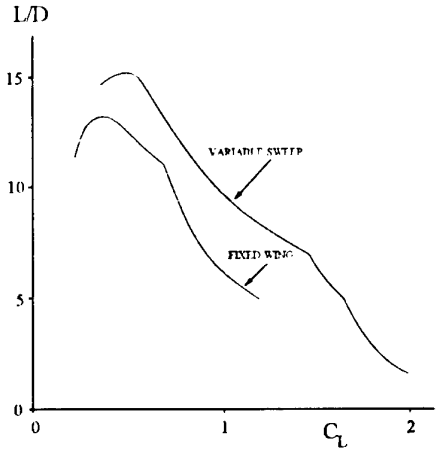


Fig 18 - Aerodynamic Benefit of Variable Sweep M=0.9

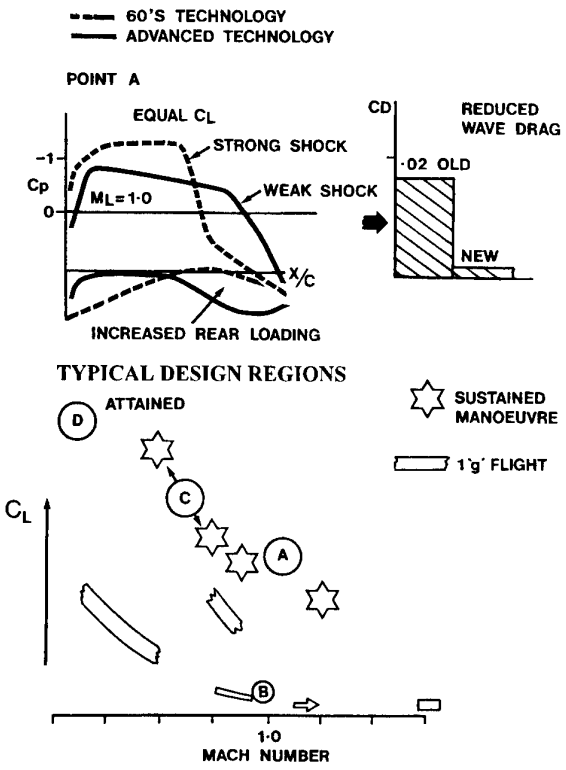


THE TRANSONIC BIAS WING

In this example (Ref 13), improvements to the basic wing are obtained through the use of supercritical aerofoil technology, variable camber and aeroelastic tailoring. The wing and configuration considered is the 42° sweep case already shown in fig 8A. The requirements assume a high turn rate at M = 0.9 and a good subsonic dash speed. The configuration is fitted with a tailplane.

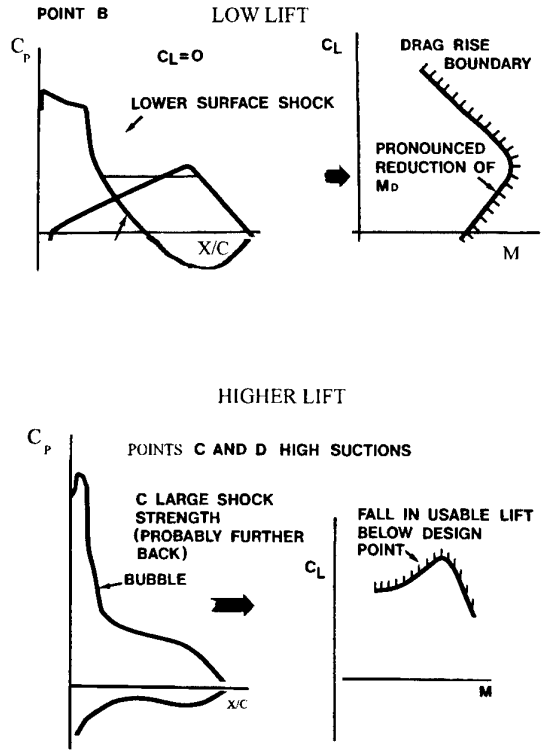
The supercritical concept is an extension of the constant near sonic roof top aerofoils e.g. ESDU data sheets, but with the near sonic level replaced by a supercritical controlled region. The terminal shock wave is weak and so for a given lift distribution the resulting wave drag is reduced. This calls for careful design of the upper surface curvature but the gains over older conventional aerofoils are significant as shown in fig 19A. A reminder of typical design requirements is shown in fig. 19B where the main design point for 'supercritical' development lies within the STR region A.

Fig 19A/B - Main Flow Features Supercritical Wing



Off design conditions at low lift (fig 20A) or lower Mach number,high lift (fig 20B) can pose problems for these aerofoils through lower surface shock formation for the first and LE shock bubble separations for the second. However incorporation of variable camber with lower surface design can reduce the first of these effects where small up deflections of LE and TE flap greatly extends the potential flight Mach number at low lift coefficients.

Fig 20 A/B - Off Design Considerations



This type of design can usually be achieved with the use of CFD codes alone since the aim is to achieve attached flow throughout. Fig 21A indicates a theoretical design exercise which designed the upper surface for a high 'g' manoeuvre point and the lower surface shape for a low speed high speed 'dash' requirement, with an intermediate design to serve as additional verification. The resulting experimental drag rise boundaries shown in fig. 21B vindicated the design approach. Additional LE down flap deflection will obviously improve the high lift performance at lower Mach numbers.

Fig 21A - Benefits of Variable Camber Theoretical Design - Equivalent 2D Aerofoil Section

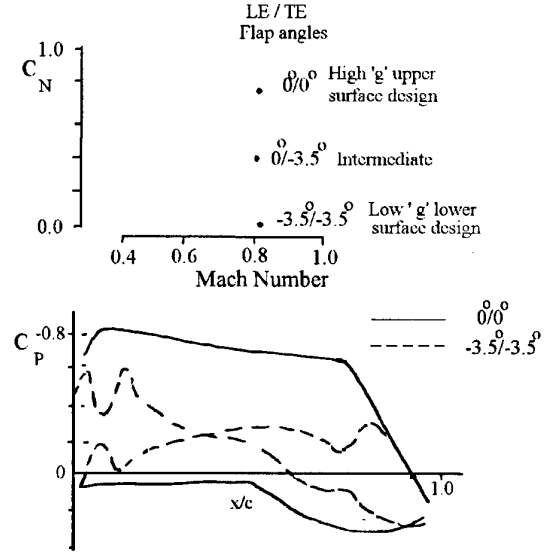
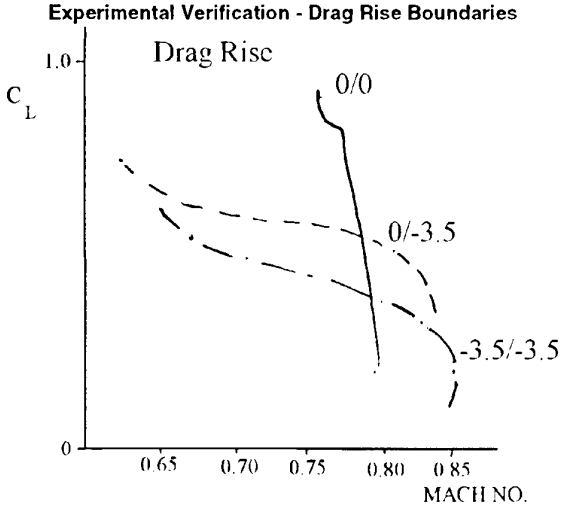
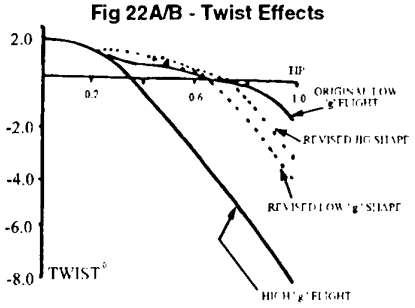


Fig 21B - Benefits of Variable Camber Experimental Verification - Drag Rise Boundaries

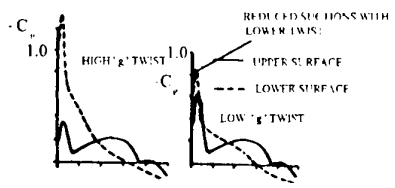


Good comparison between CFD and experiment for this case has already been shown in fig 8B. This type of design approach aims to achieve a smooth upper surface at the high 'g' design point and thus the idealised geometry contains the aeroelastic deformation of the wing. To achieve a jig shape for manufacture this deformation must be determined and subtracted from the ideal high 'g' shape. This is an iterative process between aerodynamics and structures. For the wing considered here the ideal twist requirement is close to 10°, whilst the initial twist assumed for a wing build '0g' shape was 3.5°, as seen in fig 22A. This implied that an aeroelastic increment of 6.5° was needed to achieve an optimum design. However detailed structural work using a conventional aluminium alloy skinned multi spar wing structure gave only approximately 4° of twist implying that extra twist would have to be built in to the wing '0g' shape. This was thought to be acceptable when combined with variable up flap deflection to alleviate potential lower surface problems near the wing tip. Fig 22B illustrates the benefit of reduced twist in the outer wing region.

Fig 22A/B - Twist Effects



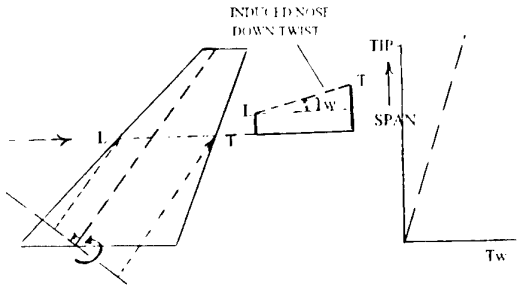
Pressures Near the Wing Tip (h=0.87)



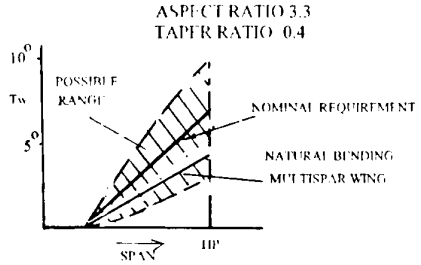
It is worth noting that the nose down twist induced streamwise on a swept back wing under positive 'g' is in the right direction from the aerodynamic viewpoint - fig 23A. If aeroelastic tailoring had been adopted using composites then a twist increment over and above that due to natural bending could have provided a further small advantage. The range of twist possibilities available with different composite ply orientations are shown in fig 23B . In this example almost 2/3 of the required twist is achieved from the natural wing bending of a conventional structure.

Fig 23A/B - Aeroelastic Considerations

Twist Due to Bending



Aeroelastic Tailoring



This wing was also considered for manufacture (Ref 14) where the geometry was simplified, from an initial 8 control station wing definition to a three control definition. This was an iterative process involving CFD and aeroelastic and loading calculations as indicated in fig. 24. This resulted in only minor changes to its performance, as indicated in fig. 25 where L/D distribution are shown at moderate and high subsonic Mach numbers. The final results with this type of approach and careful design are impressive and shown in fig. 26 compared with a 60's technology design. Gains in L/D of 50% are evident at high manoeuvre lift conditions.

Fig 24 - Productionisation

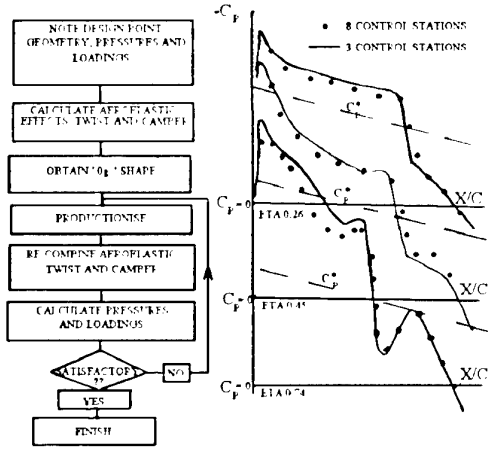


Fig 25 - Experimental Results

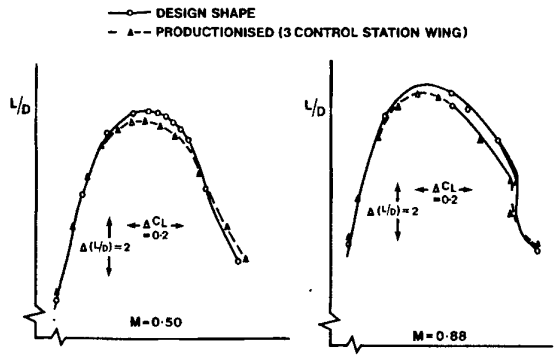
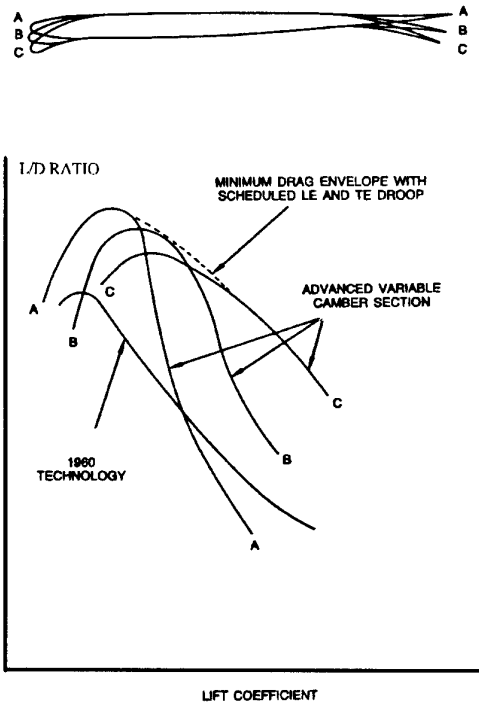


Fig 26 - Effect of Advanced Variable Camber Wing Design on Lift / Drag Ratio

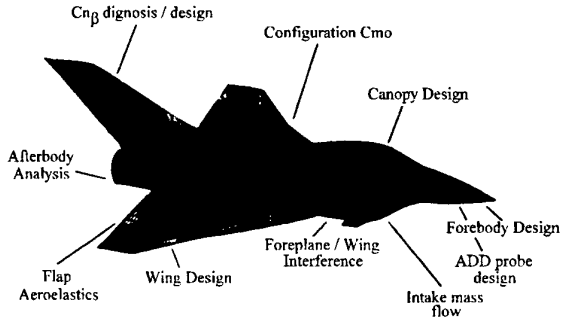


SUPERSONIC BIAS

Here illustrated by EAP (Experimental Aircraft Programme) design and later EFA (European Fighter Aircraft - now EF2000), CFD was used for many parts of the airframe as indicated in fig. 27 but here we only look at the wing design problem.

Obviously here a high LE sweep is called for, ideally swept sufficiently such that the LE is subsonic to achieve some leading edge suction at the main supersonic manoeuvre point. However there are many other important points to consider which affect and constrain the wing design.

Fig 27 - Areas of CFD Application Canard Delta - EAP



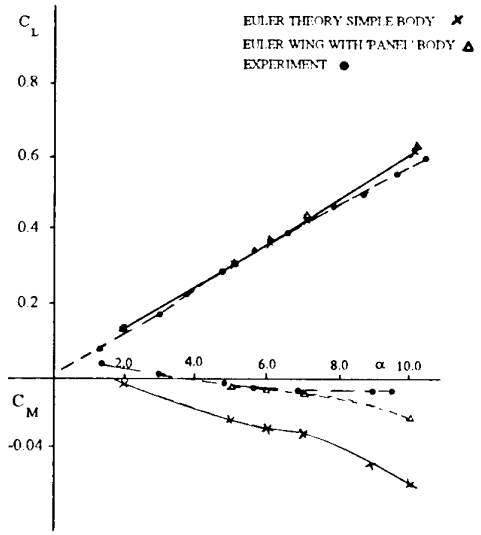
The foreplane-wing layout has many advantages in this flight regime since it suffers from a smaller aerodynamic centre shift with Mach number than a tailed configuration, and hence gives benefits in trim drag. It also gives cleaner afterbody lines with no adverse tailplane / afterbody pressure drag interference. Coupled with relaxed longitudinal stability and a powerful flight control system this type of configuration works well over a wide Mach number range. A constraint on the wing design lies in the area of aeroelasticity. For the tailed configuration considered earlier benefits were obtained through wing twist variation. This was since the tail could be used for roll control allowing a flexible wing. Differential foreplane is ineffective for roll thus the wing must be stiffer to provide adequate roll via ailerons or flaperons. In addition on a delta wing the effective flexural axis is relatively unswept and any wing bending produces very little streamwise twist. Thus any wing twist required for aerodynamic performance has to be 'built in' twist. An excessive amount will compromise the high speed dash case.

However the swept LE wing can produce problems away from the supersonic region, principally in the formation of LE vortices and possible shock / vortex interactions. Also the presence of a control surface ahead of the wing and a complex fuselage shape means that we must consider an integrated approach from the outset and cannot think in terms of a wing in isolation design. Due to the complex nature of the problem it has been found that EULER codes, at least, are required to provide accurate estimates as incidence develops. These have been successful when used with empirical design rules. Example results have already been seen in fig. 10A.

The main important parameters which the wing designer needs to consider or influence are mentioned below. It is surprising how basic configuration features which are not directly related to the wing can exert a strong influence on the design process.

The first of these is the complex fuselage shape and wing location which can lead to strong interference even at zero incidence. As we have seen in the Euler result shown in fig. 10B for a wing - body case the inadequate representation of the body has lead to a poor prediction of zero lift moment. To improve this capability a hybrid approach was adopted which combined the effect of the body, as calculated by a BAe panel method, and the Euler code for wing alone. This gave a much improved match with experiment for zero lift moment and stability as shown in fig. 28. this is an example where the designer makes use of, at the time, inadequate tools but improvises to obtain an effective design procedure.

Fig 28 - Comparison - Modified Euler v Experiment Mach 0.9



Application of this procedure to the EAP project showed the complexity of wing - body interference as shown in fig 29. It is apparent that the contribution from the wing alone is benign at zero lift and is dominated by interference effects. The procedure also compared well with experimental results as shown in fig. 30 and therefore was used to guide basic design work on the EFA in this low incidence region. A typical target zero lift pitching moment distribution through the Mach number range is shown in fig 31 where the transonic hump is limited by the loads on the foreplane. Such a basic requirement can thus limit the scope of the wing design as small variations in camber can produce large interference effects. The zero lift moment can also strongly influence drag at supersonic speeds through its effect on trim drag. This will be considered later.

Fig 29 - Pitching Moment at Zero Lift

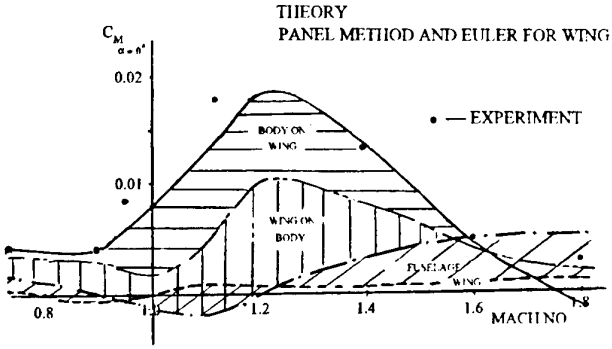


Fig 30 - Evaluation of Hybrid Method Against Experimental Data

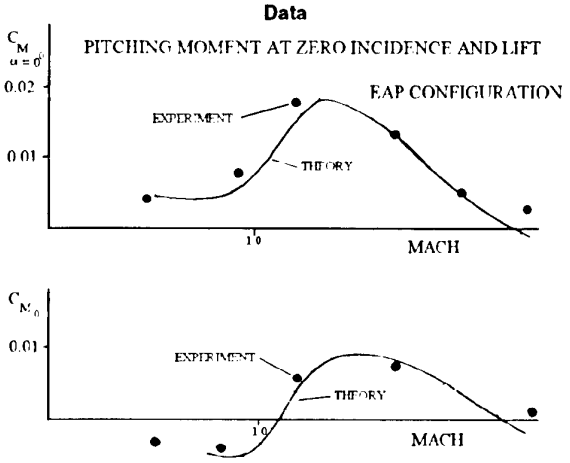
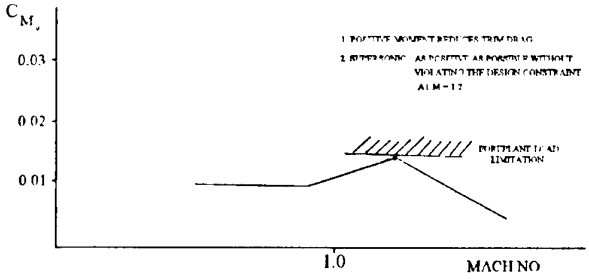
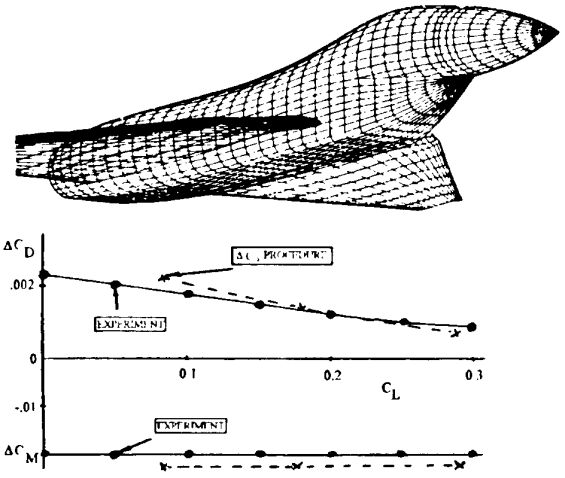


Fig 31 - Design Targets for Moment at Zero Lift



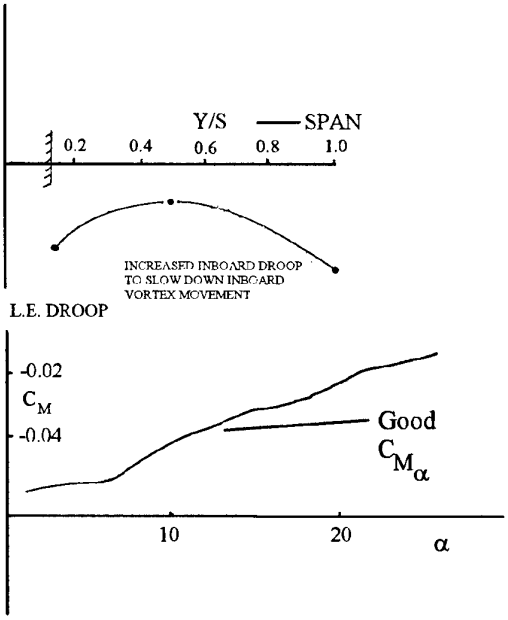
The same procedure was also used to assess and design out trim drag problems. A typical prediction of the TE flap contribution to drag and moment, a prerequisite in the estimation of trim drag, compares well with experiment - fig. 32. Here again incremental predicted force data was used and applied to a known experimental baseline configuration to obtain trimmed aircraft drag estimates. It was also calculated, and confirmed experimentally, that use of TE flap to trim was more efficient than the use of the foreplane.

Fig 32 - Evaluation of ΔC_D, ΔC_D Project Procedure
BAe High Speed Wing Development Model
ΔC_D, ΔC_M Due to 5° Trailing Edge Flap - M=1.4



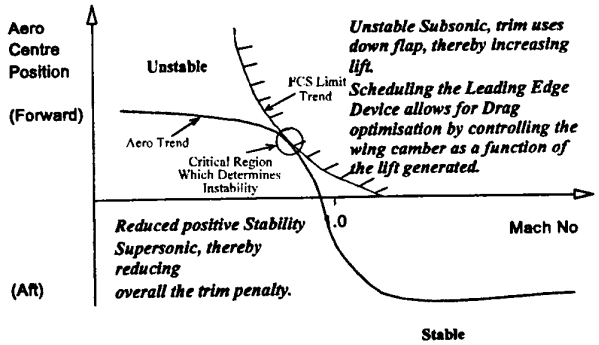
The leading edge separation was controlled using a combination of Euler CFD with an empirical LE separation criterion and wind tunnel data. Fig 33 shows that careful optimisation of the leading edge region, in particular near the wing apex can control the inboard vortex movement leading to regular force behaviour to high incidence. Additional control, particularly at high subsonic speeds is available with LE 'flap', where care is taken to maximise the upper surface radius in the region of the hinge. Effectively forming a slotless slat device. This device is scheduled with incidence and demands high actuation rates due to the high agility of the aircraft.

Fig 33 - Design of Leading Edge to Provide Vortex Control - Mach 0.90



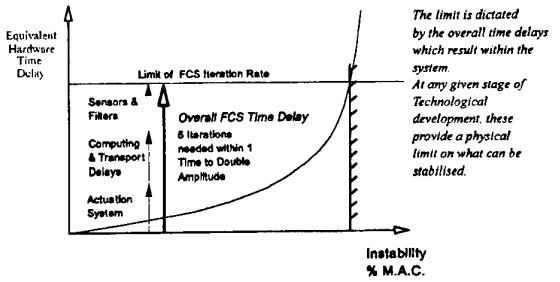
The overall aircraft stability level, resulting from the capability of the Flight Control system, strongly influences the lift dependent drag of the configuration. A typical aerodynamic stability trend with Mach number is shown in fig. 34 where the capabilities of the FCS system are superimposed.

Fig 34 - Longitudinal Stability - Variation with Mach Number



The two boundaries come together at a fairly high subsonic Mach number and at low altitude. Thus it is the low altitude subsonic Mach number region which sets the permissible stability level. From the performance viewpoint the aircraft should be as unstable as possible, allowing use of large flap angles to trim with consequent reductions in drag and supersonically, trim drag. However this must respect the need to recover the aircraft from high incidence and the FCS limits, set by a limit on the time to double amplitude fig. 35.

Fig 35 - Flight Control Systems Why is there a limit on Instability?



Examples of the effect of zero lift moment on trim drag are shown in fig. 36A. The effect is significant. Similarly the effect of basic instability level on lift dependent drag is significant - fig. 36B. Both examples are at the main BVR (Beyond Visual Range) manoeuvre Mach number of 1.6.

Fig 36A - Effect of Zero Lift Moment on Trim Drag

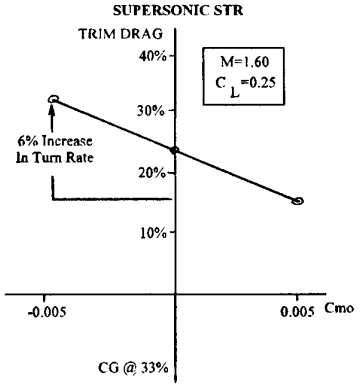
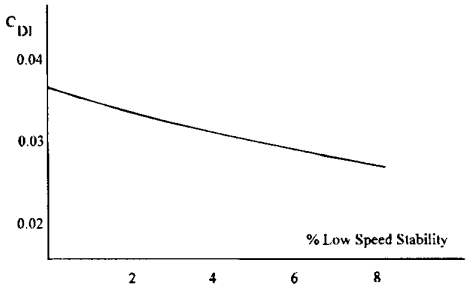


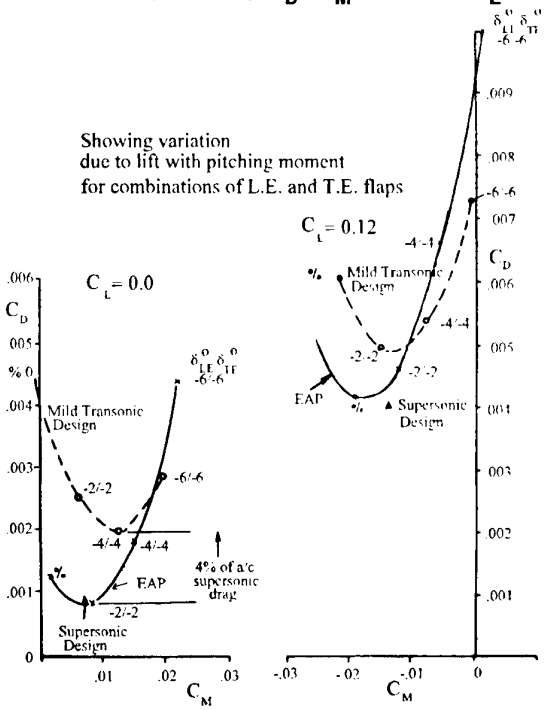
Fig 36B - Effect of Stability on Drag due to Lift M=1.6, C_L=0.25



The search for a configuration with excellent supersonic performance coupled with good transonic and subsonic performance is difficult. It was found that the best balance was achieved by designing for the supersonic manoeuvre point, using a combination of linear and EULER methods with wind tunnel data, and achieving the sub / transonic requirements with LE and TE flap. The alternative of designing for the transonic cases and decambering to achieve the supersonic cases was not as successful. This is illustrated in fig. 37 for early work done on the Experimental Aircraft Programme. The

predicted drag values for different types of wing design each with scheduled LE and TE flap are plotted against pitching moment at constant lift coefficient. This approximates to comparisons at trimmed conditions. 'Transonic', 'mild transonic' and 'supersonic' designs were investigated but even the mild 'transonic' option was found to give unacceptably large (4 %) zero lift drag penalties. The final design selected was based on a refinement of a supersonic inverse design calculation. This was also the conclusion reached in ref 15.

Fig 37 - Supersonic Drag - Lifting Surface Theory M=1.4, Wing and Body, C_D v C_M at Constant C_L



A typical exchange rate between mean wing camber levels, subsonic STR and supersonic 1g drag was established early in the design work. This serves as an useful guide to permissible camber levels - see fig. 38. The advantages of incorporating detail shaping, twist and camber are shown in fig. 39. The final design provided large gains in the high subsonic flight regime compared with a planar wing with
scheduled flaps, with only a small penalty in supersonic lift drag. For the supersonic STR point the design requirement was met.

Fig 38 - Exchange Rate

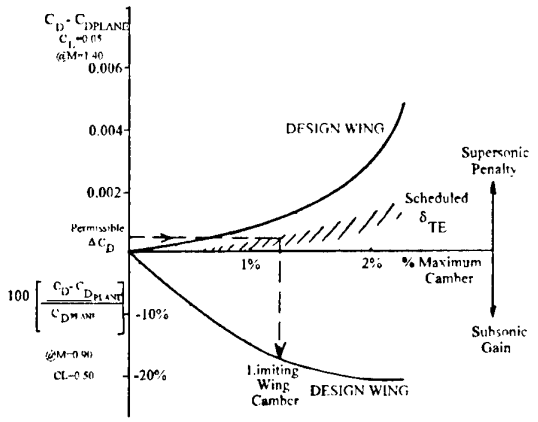
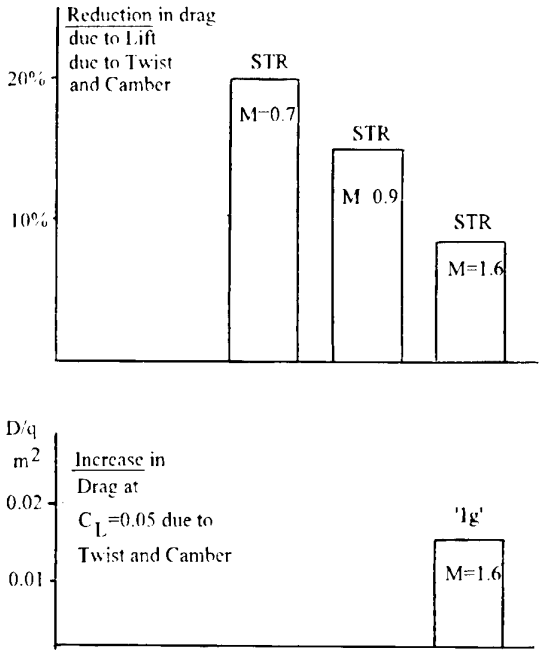


Fig 39 - Twist and Camber on 53° 'D' Wing



SUPERSONIC WING

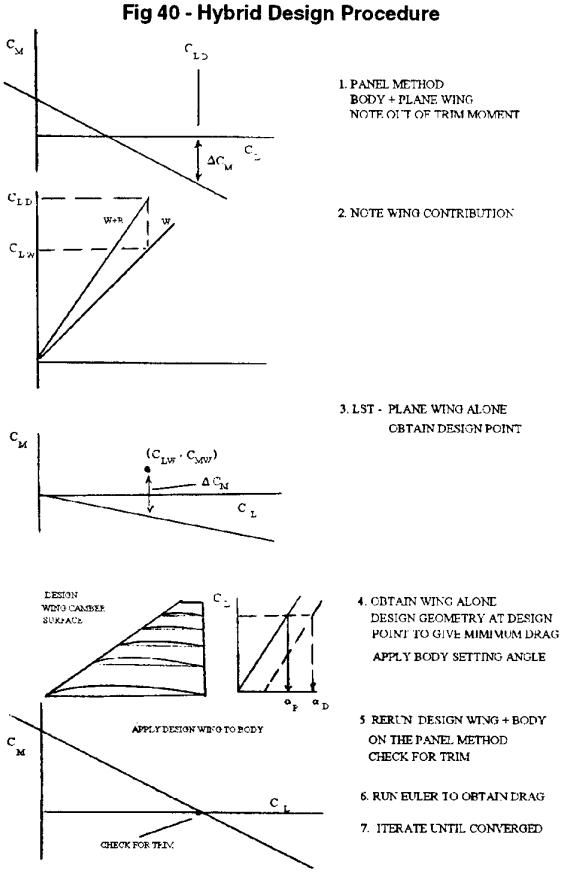
Here we have a more extreme form of the previous planform swept to 60° and beyond, possibly with a cranked subsonic leading edge planform. Extensive literature is available on the basic flow features (Ref. 16) and design methodology on such wings - the majority based on linearised theory with empirical improvements to account for finite levels of LE suction or limiting suction levels to avoid shock induced separations (Ref. 17). Excellent review papers have been written (Ref 18) on this subject. However the majority of designs based on linearised theory have concentrated on cruise conditions with the aim of achieving minimum drag and attached flow. Even for this case linearised theory on its own is not successful in achieving an optimum solution. Inherent singularities at the LE and the centre line results in over cambered regions. This results in the optimum performance being achieved at a much higher lift coefficient than desired (Ref. 19). The designer thus needs to factor his design lift coefficient in an empirical way.

For a combat aircraft, even without a supersonic cruise requirement there may well be a supersonic manoeuvre requirement, as seen in fig. 14. Linearised theory even used in conjunction with experimentally based empirical limits may be inadequate for this task - though such rules do serve to give the designer a physical 'feel' of what is possible to achieve. This is often not available from an inviscid CFD code. However, and in addition, a complex wing-body-control surface is unlikely to be adequately represented using a linearised approach.

An interim hybrid development has been successfully used at BAe (MA&A) to partly overcome these deficiences. The rather tortuous procedure is illustrated in fig. 40, where the main aim is to design an efficient wing taking into account the effects of the rest of the configuration. Trimmed conditions are assumed throughout and the process has been found to converge to adequate accuracy in three to four iterations.

However proper treatment of this area needs a fully non-linear code for the whole configuration but even these need empirical rules to limit the calculated pressures.

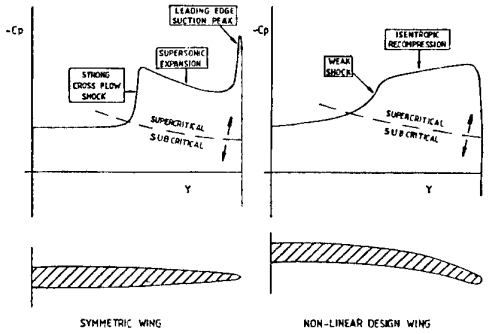
Fig 40 - Hybrid Design Procedure



The approach advocated in refs 20, 21 concentrates on reducing the strength of the cross flow shock. However to apply the method a non linear e.g. Euler or FP code is required to predict the shock in the first place. The geometry is then modified via a change (increase) in LE radius and spanwise camber to reduce the shock strength. Taken in isolation this method has produced large reductions in drag which was a benefit of using non-linear codes. However it is also important to consider the effect of such changes on the longitudinal stability variation with incidence and to check that the drag gains are not cancelled by trim drag changes.

Such an exercise (Ref. 22) was undertaken in an attempt to improve the drag of the swept delta wing of the previous section. The basic wing body configuration and the design concept are shown in fig. 41. The calculations were done using an Euler code and the wing upper surface isobars at the main design point are shown in fig. 42. The cross flow development at a range of incidences are shown in fig. 43 where it is noticed that at the main design point C = 0.28 the shock strength is possibly just strong enough to promote a separation on the outer wing. A large number of designs were tried, in an attempt to improve on the supersonic and transonic performance of the DATUM twisted and cambered wing, by applying analytic forms to streamwise and spanwise camber, LE blunting, twist and the LE and TE flaps. Only three of these results are considered here.

Fig 41 - Design Modifications to the Spanwise Pressure Distributions



General Arrangement of the Q85/3 Configuration

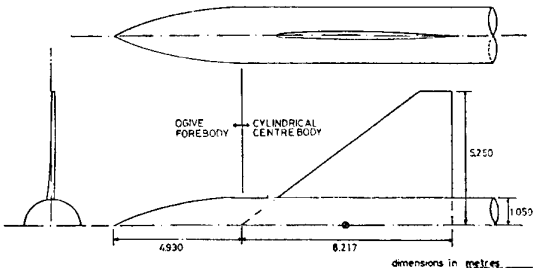
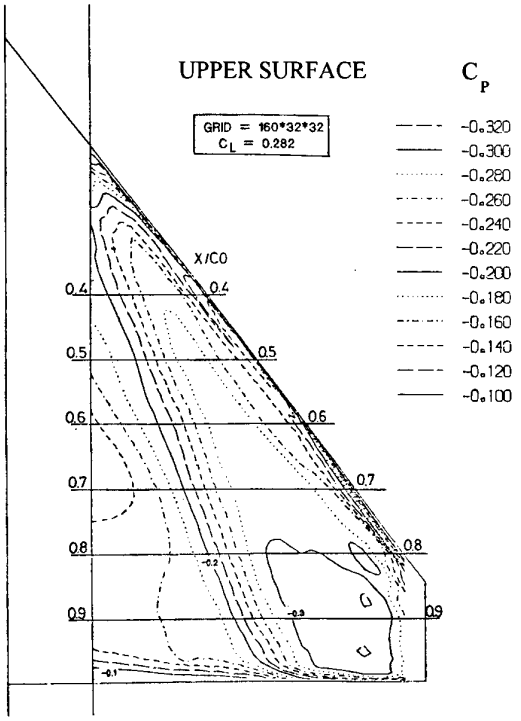


Fig 42 - Datum Wing M1.6 / a=7.3°



WING ISOBAR PATTERN AT THE SUPERSONIC MANOEUVRE DESIGN POINT: M=1.6, n=4'g' FINE GRID

Fig 43 - Wing Spanwise Pressure Distributions at M=1.6

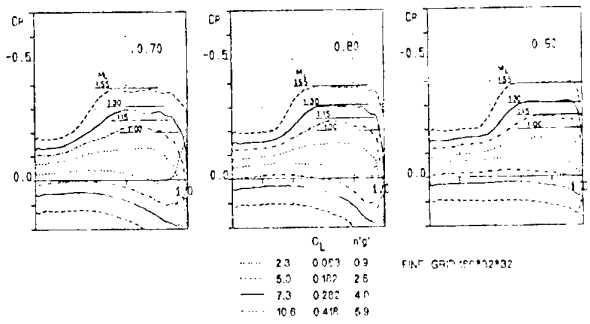


Fig 44 shows basic wing drag (minus ideal vortex drag), pitching moment, and trimmed drag as a function of lift coeff. The results shown are for the datum twisted and cambered wing (labelled DATUM), a wing with the twist and camber removed (labelled SYMMETRIC), and the final redesigned wing (labelled FINAL) which has 50% greater twist than the datum and less camber - especially over the inner wing. The upper fig. shows that the untrimmed drags of the datum and final wings are similar with the symmetric giving a drag increase. However the final wing has a more positive pitching moment which greatly reduces trim drag and gives a 0.004 (40 drag counts) reduction in total drag relative to the datum. Note that the symmetric wing moment is in a sense to increase trim drag. However the FINAL wing has much inferior performance at the transonic case M = 0.9 as shown in fig. 45.

Thus, though the supersonic manoeuvre condition could be improved through this design approach, the negative inboard camber and increased twist would violate the 'C_{M_0}' constraint imposed on this design. In addition, as seen in fig. 45, the subsonic / transonic performance is much inferior than the DATUM. gThe 'balance' required between sub / trans / supersonic must be considered at all times.

Fig 44 - Refinement of Wing to Optimise C_{Do} Trim

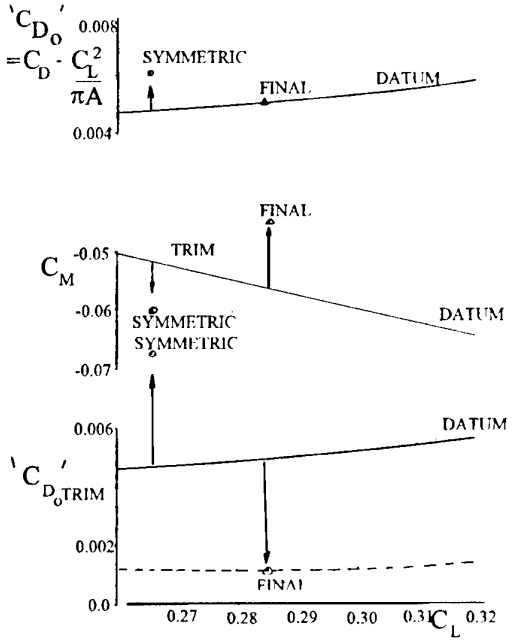
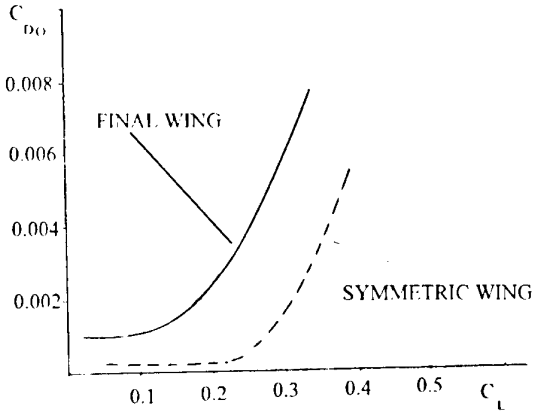
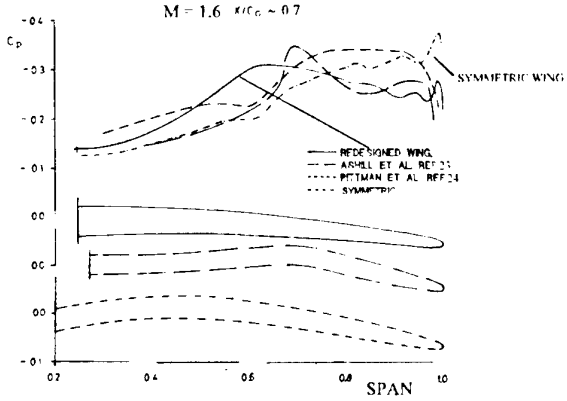


Fig 45 - Effect of Redesigned Wing on Drag at Mach 0.9



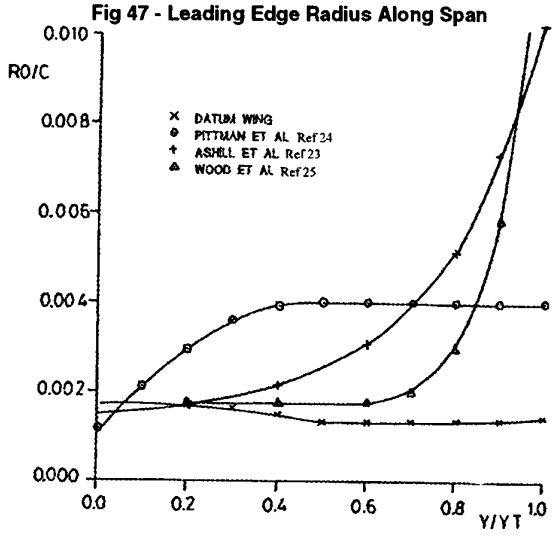
The cross flow profiles for these cases at a key longitudinal station are shown in fig. 46 where an apparently near ideal profile is obtained with the symmetric wing and a far from ideal one with the final wing. This is though the basic drag of the FINAL wing is less than that of the SYMMETRIC case, as seen in the top figure of fig. 44. It is thus conjectured that the use of wing pressures alone at supersonic speeds to judge the implied drag benefits of different designs is not enough. The local flow development is different to the classic 2D supercritical flows on which the cross flow concept is based. Thus the overall force data should also be used and, of-course, trimmed conditions compared.

Fig 46 - Comparison of Various Wings for Supersonic Manoeuvre



The above design problem also raises the vexed question of the use of blunt leading edges in supersonic flow. Various researchers have proposed different solutions, fig. 47, and much work has been done on aerofoils which show a benefit with blunting in supersonic flow. However it is difficult to maintain this benefit over a wide lift range. In practice detail design should investigate the possible options but it is worth noting even when the wing LE is subsonic the wing-root junction may unsweep the Mach lines and cause a local drag increase (Ref 26) which can cancel out any drag gains elsewhere along the span.

Fig 47 - Leading Edge Radius Along Span



RECENT AND FUTURE DEVELOPMENTS

These are divided into processes, aerodynamic developments and flow physics and will be covered very briefly.

PROCESSES

CFD.

A current design challenge for the military aircraft wing designer is to obtain satisfactory aerodynamic performance from novel configurations which achieve low observability. This also poses a challenge to the CFD codes, where existing evaluations against conventional experimental data bases may not be suitable. In addition body faceting, chines, sharp leading edges will provoke separated regions at low incidences thus calling for an improvement in separated flow predictions. To meet this challenge both Euler and Navier Stokes codes have been evaluated on a number of such configurations. An example for a 50° lambda wing is shown in fig. 48A, B, C. The first figure shows good agreement with the force data to a high incidence and the theoretical surface skin friction lines (fig 48B) are close to the experimental data. The experimental data lies in between the results from the two turbulence models. The wings in this example were of symmetric section and the fuselage was of simple circular cross section and did not strongly influence the wing flow. Predictions at high subsonic Mach number are shown in fig 48C, where potential problem regions are indicated over the rear of the outer wing. It remains to be seen whether the N - S code will be as successful on full configurations and this topic is the subject of ongoing investigation. However on the simple configuration presented here the use of Navier Stokes for design with separated flows is a possibility.

Fig 48a - Novel Wings - Comparison of Theory with Experiment - 50º Lambda Wing

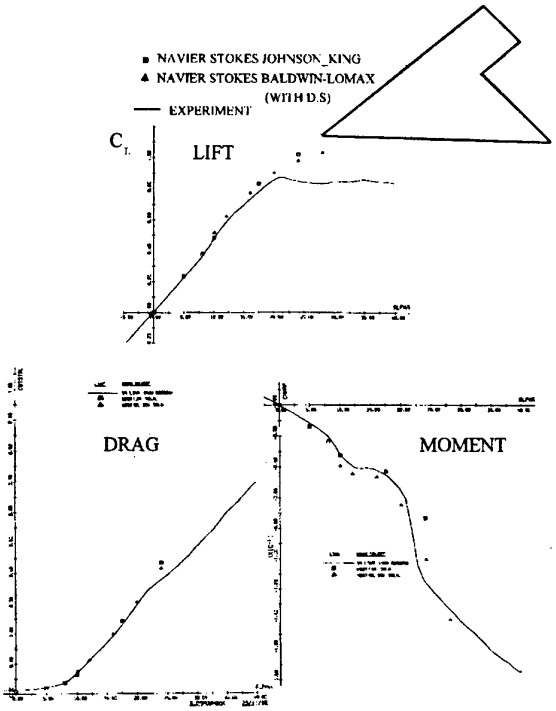


Fig 48b - Skin Friction Lines

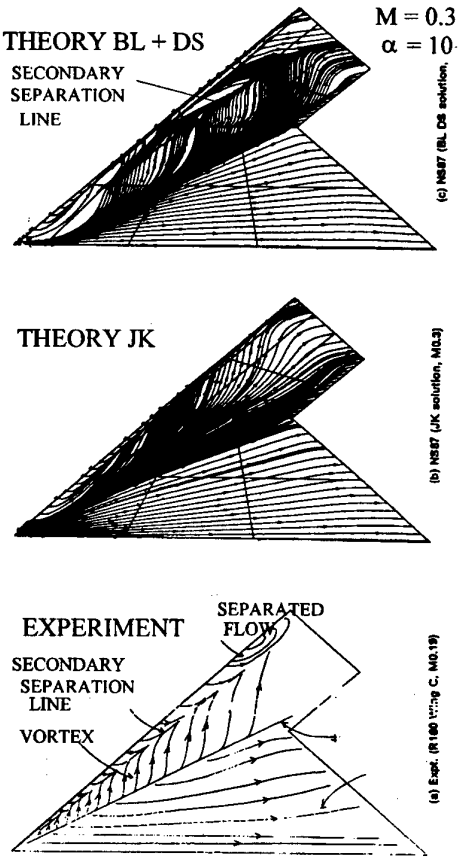
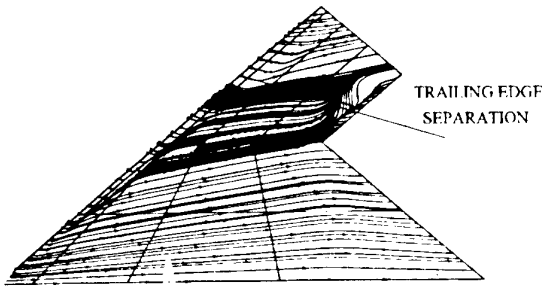
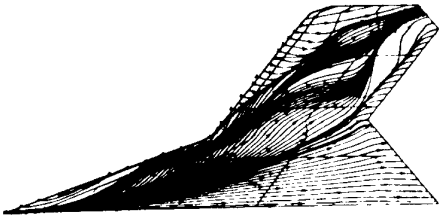


Fig 48c - Transonic Prediction Navier Stokes - M=0.95



INCIDENCE = 6.5°

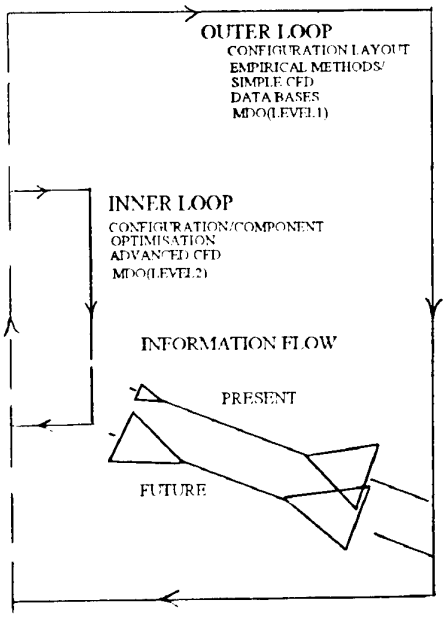


INCIDENCE = 8.5°

NUMERICAL OPTIMISATION AND MULTIDISCIPLINARY OPTIMISATION

As will have been noticed from this paper the process of aerodynamic design is significantly iterative and it is natural to expect that numerical optimisation could play a major role in future developments. It is only recently that such methods have been developed for routine(?) use for the non linear flow codes e.g. Euler. The system which is most familiar to the author is that of Ref. 27 and has produced, again with user defined empirical limits and user 'nursing', a good standard of design on a number of configurations. It is likely that such methods will be needed at an earlier stage in the design process, as long as proper evaluation of the underlying CFD has taken place, due to the less certain data base available on novel configurations. Eventually it might be expected that the outer (coarse) and inner (detailed) design loops shown in fig 49 will merge. In the same time frame it is expected that MDO (Multi Discipline Optimisation) procedures will be developed, these merging across the disciplines. Pilot schemes are already in place linking aerodynamics, structures and low observability.

Fig 49 - Current and Future Ways of Working



AERODYNAMIC DEVELOPMENTS

To alleviate the strength of shock waves and to possibly increase buffet penetration external ramps / bumps have been proposed (Ref 28). These are still under evaluation but little data is available on their effectiveness or otherwise on 3D configurations. Wing body blending holds promise of reduced supersonic drag but is configuration dependent and the subject of detail design. From the current military perspective the emphasis is on STOVL with supersonic capability. As such these are non ideal shapes for supersonic flight and it is a matter of doing the best one can at supersonic speeds from an inherited 'poor datum' shape.

FLOW PHYSICS

A significant development over the last 5 years has been the growth in collaborative, and technology exchange, activities between the FSU and western countries. BAe have identified a number of topics which may hold promise in aerodynamic, structural and chemical areas. One topic which could influence supersonic and hypersonic flight is the use of plasmas to reduce drag - wave drag and possibly skin friction drag. This has aroused interest in both the U.K. and the U.S.A. and is the subject of ongoing collaborative programs in both countries. A principal short term aim is to repeat and validate the FSU claims for supersonic drag reduction and to apply the effects to flight conditions of interest to BAe. A longer term aim is to develop an understanding of the observed phenomenon and to increase plasma efficiency.

CONCLUSIONS

Essentially for combat aircraft the numerous design requirements and constraints demand that a broad look is initially taken on wing design aspects before starting the detail design. It is often beneficial to undertake global calculations on a minimum / maximum range of wing parameters so that the initial wing base line definition can be tailored to suit the evolving configuration. When the configuration, especially

fuselage, intake, afterbody are firming up then detail design can begin. This takes a different form depending on the type of aircraft, and hence the type of wing flow, under consideration. In the future it is expected that increased use of Navier Stokes codes will figure in the control of separated flow, by design, while the role of numerical optimisation for detail design will spread into the early phases of configuration design.

REFERENCES

1. AGARD Flight Mechanics Panel WG-19 AR-314. Operational Agility
2. Carmichael, R.L. and Woodward. F.A., "An integrated approach to the analysis and design of wings and wing - body combinations in supersonic flow", NASA TN D - 3685, Oct 1966
3. Woodward, F. A., Tinoco, E. N. and Larsen, J. W., "Analysis and design of supersonic wing - body combinations including flow properties in the near field. part 1 - Theory and applications", NASA CR - 73106,1967
4. Middleton, W. D. and Lundry, J. L. " A computational system for aerodynamic design and analysis of supersonic aircraft", NASA CR - 2715, March 1976.
5. Hall. M.G. and Firmin. M.C.P." Recent developments in methods for calculating transonic flow over wings. ", I.C.A.S. Paper 74-18, 1974
6. Albone. C.M. "Numerical solutions for flow past wing body combinations. " IUTAN symposium Transsonicum II Ed. K. Oswatitsch
and D. Rues.Springer-Verlag, 1976.
7. Forsey. C.R. "The calculation of transonic flow over wing body combinations using the full potential equations" - ARA Report 59
8. EJ65 user guide - Euler Viscous coupled single block code
9. EJ83 user guide - Euler multi block code
10. Lucking. M. "The Warton contribution to the BAe M-B-Navier Stokes assessment exercise" BAe-WAe-RP-GEN-00828 March 1993.
11. Benton J.J. "3D multiblock N-S code "RANS-MB" Current status and possible future developments". ADE-ETR-R-RES-CM-3769 Jan 1993.
12.Booth. G.D. "Further assessment of the unstructured FLITE3D suite of codes using T40,W4,SMARM and generic missile test cases".
13. Holt, D. R. "Some particular configuration effects on a thin supercritical variable camber wing", AGARD CP - 285 Subsonic/transonic configuration aerodynamics(May 1980)
14. Probert, B. and Holt, D. R. "Advanced combat aircraft wing design", ICAS Congress(1980)
15. Bradley. R.G. "Practical aerodynamic problems - Military aircraft transonic perspective - NASA/Ames Research Centre-Moffet Field ,CA 94035(Feb 18-20,1981)
16. Rogers, E. W. E. and Hall, I. M., "An introduction to the flow about plane swept -back wings at transonic speeds", Journal of the Aeronautical Society, Vol. 64, Aug 1960,pp.449-464.
17. Kulfan, R. M. and Sigalla, A. "Real flow limitations in supersonic airplane design", AIAA Paper 78 - 147 Jan 1978
18. Kulfan, R. M. "Wing geometry effects on leading - edge vortices", AIAA - Aircraft Systems and Technology Meeting (Aug 20-22,1979,NY)
19. Carlson , Mann. "Survey and analysis of research on supersonic drag due to lift minimisation with recommendations for wing design", NASA TP 3202 1992
20. Mason, W. H. aand Daforno. G. "Opportunities for supersonic performance through non linear aerodynamics", AIAA paper 79-1527,July 1979
21. Mason W. H. "SC - A wing concept for supersonic manouvre", AIAA 83 - 1858 July 1983
22. Stanniland, D. R. "Supersonic manoeuvre design guidelines for a highly swept military aircraft wing", ARA Model Test Note Q85/3, June 1990.
23. Ashill, P. , Fulker. J. , Simmons. P, "A study of flows over highly swept wings designed for manoeuvre at supersonic speeds", RAeS Conference "Aerodynamic design for supersonic flight", April 1988.
24. Pittman, J.L.,Miller. D. S.,Mason. W. H. "Supersonic non linear attached flow wing design for high lift with experimental validation", NASA TP 2336
25. Wood. R. M.,Bauer. S.S.,"Evaluation of a three dimensional empirically derived wing at supersonic speeds". AIAA-88-0481 1988
26. Fulker. J.L. ,Ashill. P.R.,Shires. A. "A theoretical and experimental investigation of the flow over the 'supersonic' leading edge of
wing body configurations.
DRA/AP/TM9341/1.0(Aug 1993)
27. Lovell. D. A. and Doherty. J.J. "Aerodynamic design of aerofoils and wings using a constrained optimisation method", DERA,EAC 1994 paper 3.21,Oct 1994.
28. Ashill. P.R. ,Fulker. J. L.,Shires. "A novel technique for controlling shock strength of laminar flow aerofoils", DRA Tech Memo.

REPORT DOCUMENTATION PAGE

1. Recipient's Reference	2. Originator's References	3. Further Reference	4. Security Classification of Document
	RTO-EN-4 AC/323(AVT)TP/6	ISBN 92-837-1007-X	UNCLASSIFIED/ UNLIMITED

5. Originator Research and Technology Organization
North Atlantic Treaty Organization
BP 25, 7 rue Ancelle, F-92201 Neuilly-sur-Seine Cedex, France

6. Title

Fluid Dynamics Research on Supersonic Aircraft

7. Presented at/sponsored by

A Special Course on "Fluid Dynamics Research on Supersonic Aircraft" held at the von Kármán Institute for Fluid Dynamics (VKI) in Rhode-Saint-Genèse, Belgium, 25-29 May 1998.

8. Author(s)/Editor(s)	9. Date
Multiple	November 1998
10. Author's/Editor's Address	**11. Pages**
Multiple	332

12. Distribution Statement There are no restrictions on the distribution of this document. Information about the availability of this and other RTO unclassified publications is given on the back cover.

13. Keywords/Descriptors

Fluid dynamics
Supersonic aircraft
Research projects
Aerodynamics
Supersonic transports
Design
Lift
Drag
Laminar flow
Flow control
Vortices
Environmental impact
Sonic boom
Emission control
Turbulent boundary layer
Computational fluid dynamics
Integrated systems

14. Abstract

Contains the lecture notes prepared for a Special Course on 'Fluid Dynamics Research on Supersonic Aircraft' organised by the RTO Applied Vehicle Technology Panel (AVT). The Course was held at the von Kármán Institute for Fluid Dynamics (VKI) Institute, Rhode-Saint-Genèse, Belgium 25-29 May 1998.

The following topics were covered: History & Economics of Supersonic Transports, Supersonic Aerodynamics, Sonic Boom Theory and Minimization, Multi-Point Design Challenges, Vortex Plume Interactions, Propulsion System Design. Presentations on the major world wide supersonic transport programs were also included.

The material assembled in this publication was prepared under the combined sponsorship of the RTO Applied Vehicle Technology Panel, the Consultant and Exchange Program of RTO, and the von Kármán Institute (VKI) for Fluid Dynamics.

NORTH ATLANTIC TREATY ORGANIZATION

RESEARCH AND TECHNOLOGY ORGANIZATION
BP 25 • 7 RUE ANCELLE
F-92201 NEUILLY-SUR-SEINE CEDEX • FRANCE
Télécopie 0(1)55.61.22.99 • Télex 610 176

DIFFUSION DES PUBLICATIONS
RTO NON CLASSIFIEES

L'Organisation pour la recherche et la technologie de l'OTAN (RTO), détient un stock limité de certaines de ses publications récentes, ainsi que de celles de l'ancien AGARD (Groupe consultatif pour la recherche et les réalisations aérospatiales de l'OTAN). Celles-ci pourront éventuellement être obtenues sous forme de copie papier. Pour de plus amples renseignements concernant l'achat de ces ouvrages, adressez-vous par lettre ou par télécopie à l'adresse indiquée ci-dessus. Veuillez ne pas téléphoner.

Des exemplaires supplémentaires peuvent parfois être obtenus auprès des centres nationaux de distribution indiqués ci-dessous. Si vous souhaitez recevoir toutes les publications de la RTO, ou simplement celles qui concernent certains Panels, vous pouvez demander d'être inclus sur la liste d'envoi de l'un de ces centres.

Les publications de la RTO et de l'AGARD sont en vente auprès des agences de vente indiquées ci-dessous, sous forme de photocopie ou de microfiche. Certains originaux peuvent également être obtenus auprès de CASI.

CENTRES DE DIFFUSION NATIONAUX

ALLEMAGNE
Fachinformationszentrum Karlsruhe
D-76344 Eggenstein-Leopoldshafen 2

BELGIQUE
Coordinateur RTO - VSL/RTO
Etat-Major de la Force Aérienne
Quartier Reine Elisabeth
Rue d'Evere, B-1140 Bruxelles

CANADA
Directeur - Gestion de l'information
(Recherche et développement) - DRDGI 3
Ministère de la Défense nationale
Ottawa, Ontario K1A 0K2

DANEMARK
Danish Defence Research Establishment
Ryvangs Allé 1
P.O. Box 2715
DK-2100 Copenhagen Ø

ESPAGNE
INTA (RTO/AGARD Publications)
Carretera de Torrejón a Ajalvir, Pk.4
28850 Torrejón de Ardoz - Madrid

ETATS-UNIS
NASA Center for AeroSpace Information (CASI)
Parkway Center, 7121 Standard Drive
Hanover, MD 21076

FRANCE
O.N.E.R.A. (Direction)
29, Avenue de la Division Leclerc
92322 Châtillon Cedex

GRECE
Hellenic Air Force
Air War College
Scientific and Technical Library
Dekelia Air Force Base
Dekelia, Athens TGA 1010

ISLANDE
Director of Aviation
c/o Flugrad
Reykjavik

ITALIE
Aeronautica Militare
Ufficio Stralcio RTO/AGARD
Aeroporto Pratica di Mare
00040 Pomezia (Roma)

LUXEMBOURG
Voir Belgique

NORVEGE
Norwegian Defence Research Establishment
Attn: Biblioteket
P.O. Box 25
N-2007 Kjeller

PAYS-BAS
RTO Coordination Office
National Aerospace Laboratory NLR
P.O. Box 90502
1006 BM Amsterdam

PORTUGAL
Estado Maior da Força Aérea
SDFA - Centro de Documentação
Alfragide
P-2720 Amadora

ROYAUME-UNI
Defence Research Information Centre
Kentigern House
65 Brown Street
Glasgow G2 8EX

TURQUIE
Millî Savunma Başkanliği (MSB)
ARGE Dairesi Başkanliği (MSB)
06650 Bakanliklar - Ankara

AGENCES DE VENTE

NASA Center for AeroSpace Information (CASI)
Parkway Center
7121 Standard Drive
Hanover, MD 21076
Etats-Unis

The British Library Document Supply Centre
Boston Spa, Wetherby
West Yorkshire LS23 7BQ
Royaume-Uni

Canada Institute for Scientific and Technical Information (CISTI)
National Research Council
Document Delivery,
Montreal Road, Building M-55
Ottawa K1A 0S2
Canada

Les demandes de documents RTO ou AGARD doivent comporter la dénomination "RTO" ou "AGARD" selon le cas, suivie du numéro de série (par exemple AGARD-AG-315). Des informations analogues, telles que le titre et la date de publication sont souhaitables. Des références bibliographiques complètes ainsi que des résumés des publications RTO et AGARD figurent dans les journaux suivants:

Scientific and Technical Aerospace Reports (STAR)
STAR peut être consulté en ligne au localisateur de ressources uniformes (URL) suivant:
http://www.sti.nasa.gov/Pubs/star/Star.html
STAR est édité par CASI dans le cadre du programme NASA d'information scientifique et technique (STI)
STI Program Office, MS 157A
NASA Langley Research Center
Hampton, Virginia 23681-0001
Etats-Unis

Government Reports Announcements & Index (GRA&I)
publié par le National Technical Information Service
Springfield
Virginia 2216
Etats-Unis
(accessible également en mode interactif dans la base de données bibliographiques en ligne du NTIS, et sur CD-ROM)

Imprimé par le Groupe Communication Canada Inc.
(membre de la Corporation St-Joseph)
45, boul. Sacré-Cœur, Hull (Québec), Canada K1A 0S7

NORTH ATLANTIC TREATY ORGANIZATION

RESEARCH AND TECHNOLOGY ORGANIZATION
BP 25 • 7 RUE ANCELLE
F-92201 NEUILLY-SUR-SEINE CEDEX • FRANCE
Telefax 0(1)55.61.22.99 • Telex 610 176

DISTRIBUTION OF UNCLASSIFIED RTO PUBLICATIONS

NATO's Research and Technology Organization (RTO) holds limited quantities of some of its recent publications and those of the former AGARD (Advisory Group for Aerospace Research & Development of NATO), and these may be available for purchase in hard copy form. For more information, write or send a telefax to the address given above. **Please do not telephone**.

Further copies are sometimes available from the National Distribution Centres listed below. If you wish to receive all RTO publications, or just those relating to one or more specific RTO Panels, they may be willing to include you (or your organisation) in their distribution.

RTO and AGARD publications may be purchased from the Sales Agencies listed below, in photocopy or microfiche form. Original copies of some publications may be available from CASI.

NATIONAL DISTRIBUTION CENTRES

BELGIUM
Coordinateur RTO - VSL/RTO
Etat-Major de la Force Aérienne
Quartier Reine Elisabeth
Rue d'Evere, B-1140 Bruxelles

CANADA
Director Research & Development
Information Management - DRDIM 3
Dept of National Defence
Ottawa, Ontario K1A 0K2

DENMARK
Danish Defence Research Establishment
Ryvangs Allé 1
P.O. Box 2715
DK-2100 Copenhagen Ø

FRANCE
O.N.E.R.A. (Direction)
29 Avenue de la Division Leclerc
92322 Châtillon Cedex

GERMANY
Fachinformationszentrum Karlsruhe
D-76344 Eggenstein-Leopoldshafen 2

GREECE
Hellenic Air Force
Air War College
Scientific and Technical Library
Dekelia Air Force Base
Dekelia, Athens TGA 1010

ICELAND
Director of Aviation
c/o Flugrad
Reykjavik

ITALY
Aeronautica Militare
Ufficio Stralcio RTO/AGARD
Aeroporto Pratica di Mare
00040 Pomezia (Roma)

LUXEMBOURG
See Belgium

NETHERLANDS
RTO Coordination Office
National Aerospace Laboratory, NLR
P.O. Box 90502
1006 BM Amsterdam

NORWAY
Norwegian Defence Research Establishment
Attn: Biblioteket
P.O. Box 25
N-2007 Kjeller

PORTUGAL
Estado Maior da Força Aérea
SDFA - Centro de Documentação
Alfragide
P-2720 Amadora

SPAIN
INTA (RTO/AGARD Publications)
Carretera de Torrejón a Ajalvir, Pk.4
28850 Torrejón de Ardoz - Madrid

TURKEY
Milli Savunma Başkanliği (MSB)
ARGE Dairesi Başkanliği (MSB)
06650 Bakanliklar - Ankara

UNITED KINGDOM
Defence Research Information Centre
Kentigern House
65 Brown Street
Glasgow G2 8EX

UNITED STATES
NASA Center for AeroSpace Information (CASI)
Parkway Center, 7121 Standard Drive
Hanover, MD 21076

SALES AGENCIES

NASA Center for AeroSpace Information (CASI)
Parkway Center
7121 Standard Drive
Hanover, MD 21076
United States

The British Library Document Supply Centre
Boston Spa, Wetherby
West Yorkshire LS23 7BQ
United Kingdom

Canada Institute for Scientific and Technical Information (CISTI)
National Research Council
Document Delivery,
Montreal Road, Building M-55
Ottawa K1A 0S2
Canada

Requests for RTO or AGARD documents should include the word 'RTO' or 'AGARD', as appropriate, followed by the serial number (for example AGARD-AG-315). Collateral information such as title and publication date is desirable. Full bibliographical references and abstracts of RTO and AGARD publications are given in the following journals:

Scientific and Technical Aerospace Reports (STAR)
STAR is available on-line at the following uniform resource locator:
http://www.sti.nasa.gov/Pubs/star/Star.html
STAR is published by CASI for the NASA Scientific and Technical Information (STI) Program
STI Program Office, MS 157A
NASA Langley Research Center
Hampton, Virginia 23681-0001
United States

Government Reports Announcements & Index (GRA&I)
published by the National Technical Information Service
Springfield
Virginia 22161
United States
(also available online in the NTIS Bibliographic Database or on CD-ROM)

Printed by Canada Communication Group Inc.
(A St. Joseph Corporation Company)
45 Sacré-Cœur Blvd., Hull (Québec), Canada K1A 0S7

ISBN 92-837-1007-X